Water stable isotopic composition on the East Antarctic Plateau: measurements at low temperature of the vapour composition, use as an atmospheric tracer and implication for paleoclimate studies

Mathieu Casado

NNT : 2016SACLV058

THÈSE DE DOCTORAT

DE L'UNIVERSITÉ PARIS-SACLAY
PRÉPARÉE À L'UNIVERSITÉ VERSAILLES SAINT-QUENTIN EN YVELINES
ECOLE DOCTORALE N°129 : Sciences de l'Environnement d'Ile de France
***Spécialité** : Océan, Atmosphère, Climat et Observations Spatiales*

PRÉPARÉE AU
LABORATOIRE DES SCIENCES DU CLIMAT ET DE L'ENVIRONNEMENT
ET AU
LABORATOIRE INTERDISCIPLINAIRE DE PHYSIQUE

Par

Monsieur Mathieu CASADO

Water stable isotopic composition on the East Antarctic Plateau :

measurements at low temperature of the vapour composition, use as an atmospheric tracer and implication for paleoclimate studies

Thèse présentée et soutenue à Paris, le 6 Septembre 2016
Composition du jury :

Monsieur	Colin Christophe	Président
Monsieur	Krinner Gerhard	Rapporteur
Monsieur	Ricaud Philippe	Rapporteur
Madame	Merlivat Liliane	Examinatrice
Monsieur	Cacciani Patrice	Examinateur
Madame	Landais Amaelle	Directrice de thèse
Monsieur	Kassi Samir	Co-directeur de thèse
Monsieur	Kerstel Erik	Co-directeur de thèse

La composition des isotopes stables de l'eau sur le plateau Est Antarctique : *mesure à basse température de la composition de la vapeur, utilisation comme un traceur atmosphérique et implication pour les études paléoclimatiques*

Mots clés : Antarctique, isotopes, spectroscopie, climat, reconstruction

Les carottes de glace permettent de reconstruire le climat du passé, à partir entre autre de la composition isotopique de l'eau ($\delta^{18}O$, $\delta^{17}O$ et δD). Sur le plateau Est Antarctique, les températures très froides et les faibles accumulations permettent de remonter le plus loin dans le passé (jusqu'à 800 000 ans) mais compliquent l'interprétation du signal isotopique. Premièrement, les reconstructions des variations de température dans les carottes de glace à partir des isotopes de l'eau se basent sur des modèles pour décrire l'évolution de la composition isotopique de la vapeur et de la phase condensée le long du cycle de l'eau. Ces modèles, qui ont été développés au cours des dernières décennies, reposent sur la connaissance de coefficients du fractionnement isotopique associé à chaque transition de phase et sur des hypothèses pour représenter la micro-physique des nuages.

Lors de la formation de flocons de neige à basse température, 2 types de fractionnements isotopiques doivent être pris en compte : le fractionnement isotopique à l'équilibre, associé à la transition de phase vapeur-glace et le fractionnement isotopique cinétique lié aux différentes diffusivités des différents isotopes. A basse température, les déterminations des coefficients du fractionnement du fractionnement à l'équilibre présentent d'importantes différences et n'ont jamais pu être mesurées à des températures inférieures à -40 °C. Or la température moyenne annuelle à Dome C est de -54 °C atteignant jusqu'à -85 °C l'hiver. Les diffusivités des différents isotopes quant à elles n'ont jamais été mesurées à des températures inférieures à 10 °C. Toutes ces lacunes résultent dans des incertitudes importantes sur le lien entre la composition isotopique et la température dans des conditions comme celles du Plateau Est Antarctique.

De plus, dans ces conditions froides et arides, les processus physiques qui affectent la composition isotopique de la neige après la déposition des flocons deviennent importants compte tenu du faible apport annuel de précipitation. Pour estimer l'impact de ces processus de post-déposition sur la composition isotopique, il est nécessaire de bien caractériser le fractionnement isotopique à l'interface neige/atmosphère pour des températures allant jusqu'à -90°C.

Afin d'améliorer les reconstructions quantitatives de température l'étude des processus affectant la composition isotopique de la glace à très basse température est donc primordiale. Dans cette optique, ma thèse a été à l'interface entre les études de processus au laboratoire et en Antarctique et le développement instrumental afin de pouvoir réaliser des mesures isotopiques encore inédites, en particulier à très basse humidité. D'un côté, j'ai développé d'un nouveau spectromètre infrarouge aux performances bien au-delà des instruments commerciaux. En effet, la fréquence du laser est stabilisée par rétroaction optique par une cavité ultra-stable jusqu'à un niveau de stabilité de l'ordre du hertz. La lumière est ensuite injectée dans une cavité CRDS hautes performances avec une sensibilité de $10^{-13} cm^{-1}.Hz^{-1/2}$. Ceci permet de mesurer la composition isotopique avec une précision inférieure au ppm.

En parallèle, des expériences au laboratoire ont permis de renforcer les connaissances sur les processus affectant les isotopes de l'eau, en particulier le fractionnement lié à la transition de phase vapeur - glace et le fractionnement cinétique lié aux différentes diffusivités des différents isotopes en modélisant le fractionnement lié à la diffusion près d'un point froid. Enfin, durant une campagne en Antarctique, j'ai pu réaliser parmi les premières mesures de la composition isotopique de la vapeur et de la glace en Antarctique et appliquer les modèles physiques des processus à des données de terrain. Ces mesures montrent que le cycle de sublimation/condensation contribue de manière importante à la composition isotopique de la neige sur le plateau Est Antarctique.

.

Water stable isotopic composition on the East Antarctic Plateau :
measurements at low temperature of the vapour composition, utilisation as an atmospheric tracer and implication for paleoclimate studies

Key words : Antarctica, isotopes, spectroscopy, climate, reconstruction

Ice cores enable reconstruction of past climates, from among others water stable isotopic composition ($\delta^{18}O$, $\delta^{17}O$ et δD). On the East Antarctic Plateau, very cold temperature and low accumulation provide the longest ice core records (up to 800 000 years) but embrangle the interpretation of isotopic composition. First, reconstructions of temperature variations from ice core water isotopic composition are based on models used to describe the evolution of the isotopic composition of the vapour and of the condensed phase over the entire water cycle. These models have been developed during the last decades and depend upon precise determinations of isotopic fractionation coefficients associated to each phase transition and upon hypotheses to describe cloud microphysics.

During the formation of snowflakes at low temperature, two types of isotopic fractionations need to be taken into account : equilibrium fractionation, associated to the vapour to ice phase transition and kinetic fractionation associated to the difference of diffusivity of the different isotopes. At low temperature, determinations of equilibrium fractionation coefficients present important discrepancies and have never been realised for temperature below -40 °C. However, mean annual temperature at Dome C is around -54°C reaching -85°C in winter. For the diffusivities of the different isotopes, they have never been measured at temperature below 10°C. All these gaps result in important uncertainties on the link between isotopic composition and temperature, especially for cold and dry conditions such as encountered on the East Antarctic Plateau.

Furthermore, because of the very low amount of precipitation, physical processes affecting the isotopic composition of the snow after the deposition of snowflakes can results in an important contribution to the isotopic budget. In order to estimate the impact of the post-deposition processes on the water vapour isotopic composition, it is necessary to characterise the isotopic fractionation at the snow/atmosphere interface for temperature down to -90°C.

In order to improve isotopic paleothermometer performances, it is primordial to study processes affecting snow isotopic composition. Toward this goal, my Ph-D has been at the interface between monitoring of processes affecting isotopes, both in laboratory experiments and field studies, and instrumental development to push the limits of water vapour isotopic composition trace detection. On one hand, new developments in optical feedback frequency stabilisation applied for the first time to water isotopic composition monitoring provide performances beyond any commercial instrument and can be used for thorough processes studies. The laser frequency is stabilised by optical feedback from an ultra-stable cavity to the hertz level. Then, the light is injected in high performances cavity with a sensibility of $10^{-13} cm^{-1}.Hz^{-1/2}$. This enables measuring isotopic composition with a precision below the ppm level.

On the other hand, laboratory experiments have supported theories about isotopic fractionation associated to the vapour to ice phase transition and to kinetic fractionation linked to the difference of diffusivities of the different isotopes. Finally, these physical models have been collated to field measurements realised at Dome C in Antarctica, which are among the first water vapour and snow isotopic composition measurements realised inland Antarctica. These measurements show how important is the contribution of the sublimation condensation cycles to the snow isotopic composition budget on the East Antarctic Plateau.

.

Acknowledgments

First of all, I am grateful to my Ph-D advisor Amaelle Landais for bringing me along in this adventure. It does not feel like we spent 3 years working on this project and yet here we stand. Your support and trust have been incredibly important to me, even when I was coming to you with the craziest ideas, you always enthusiastically consider the discussion. I also wish to thank Samir Kassi, my co-supervisor, who never gives up and manages, step-by-step, to transform every desperate situation into a successful measurement. And, I also want to thank Erik Kerstel for his support and his valuable teachings during this whole project.

I want to acknowledge all the members of my jury for your evaluation of my work and to all make it to the defence, for coping with this dense and long manuscript and for supporting me through the obtention of a PhD, it means a lot to me, thanks a lot to Christophe Colin, Patrice Cacciani, Gerhard Krinner, Liliane Merlivat and Philippe Ricaud.

I'm truly indebted to M. le Référent for showing me the ancient ways of mass spectroscopy and coffee brewing. Discussions all around the world with Anaïs Orsi have been both useful and fun, I hope we will be able to do more of those adventures together. I also wish to thank the entire team GLACCIOS and in particular Valérie Masson-Delmotte for introducing me to the water isotope world and Dominique Genty for all those discussions about vintage photography. Thanks to Jean Jouzel, Hans-Christian Steen-Larsen, Francoise Vimeux, Olivier Cattani and Benedicte Minster for your help and advises. I'd also like to thank Anne-Marie L'ezine for introducing me the first to the LSCE, and Masa and Pascale for introducing me to climate sciences.

This PhD has been built on the collaboration between LSCE and the *Laboratoire Interdisciplinaire de Physique* and I was happy to be a part of the team. Thanks a lot to Guillaume Méjean, you scrap the hell out of a wall and still are able to have passionate discussion about anything. Special thanks to Johannes Burkart for sharing with me your passion for science. Thanks to Aurélien Gourrier to always find time for a nice discussion. Infinite thanks to Peter Cermak whom resolution can make miracles happen through the endless night of measurements. Thanks to all the LAME team, not so gammy after all, I will remember the numerous discussions at coffee break with Roberto Grilli, Jean-Luc Martin, Thibaut Desbois, Serge Beguier. Thank a lot to Alain Campargues for interesting discussions about spectroscopy.

These three years would not have been the same without all my fellows both in Paris and in Grenoble, I'm thinking in particular of Alexandre, Fred, Johannes, Tim,

Joseph, Camille, Marine, Alexandra, Alienor, Katharina, Rachel, Tommaso, Bernard, Janek, Mathias, Etienne, Christophe, Clément, Inga, and probably many others.

I have been lucky to go for a field campaign at Concordia and I wish to thank all my mates in this amazing adventure, in particular Philippe, Christophe, Etienne, Doris, Le P'tiot, Elsa, Olivier, and I'm thankful to my colleagues in LGGE that helped make this campaign become possible. I'm also thankful to all the people I've been lucky enough to work with abroad and in France during this PhD.

I'd like to thank my family and I hope I'll be able to share more of my scientific adventures with you in the future. I need to thank my flatmates for coping with me and feeding me during the redaction of my thesis.

Contents

Chapter 1

Introduction

> La météorologie ne pourra devenir une science véritablement exacte que le jour où les phénomènes qui s'y rattachent auront été étudiés sur tous les points du globe, et l'Antarctique, [...], reste toujours une vaste tache d'inconnu. *
>
> *Pourquoi faut-il aller dans l'Antarctique ?*
> JEAN-BAPTISTE CHARCOT

Past climate reconstructions

As the cold trap of the water cycle, Antarctica's ice has archived variations of climate in the past. Ice traps dusts, air bubbles and dissolved compounds which are preserved on long time scales (up to 800 000 years), locked and frozen in time. The composition in stable heavy water isotopes ($H_2{}^{18}O$, $H_2{}^{17}O$ and $HD{}^{16}O$) over the light, principal one ($H_2{}^{16}O$) is one of the tools used to realise past climate reconstructions [Dansgaard, 1964; Lorius et al., 1969] among greenhouse gases concentration trapped in air bubbles [Raynaud et al., 1993], inert gas isotopic composition trapped in air bubbles [Severinghaus et al., 1998; Landais et al., 2004], borehole thermometry [Cuffey and Clow, 1997]... Along the last decades, several deep ice cores have been drilled in Greenland [North Greenland Ice Core Project members, 2004; NEEM community members, 2013] and in Antarctica [Petit et al., 1999b; EPICA, 2004, 2006; WAIS Divide Project members, 2013] providing multiple reconstructions of the climate variations.

∗. Meteorology will only become an exact science when all the phenomena involved in it will have been studied all around the world, and Antarctica, [...] still remains a vast unknown area.

Past climates study reveals successive glacial and interglacial cycles characterised by a period of 100 000 years [Imbrie and Imbrie, 1980] as illustrated on Figure 1.1. These cycles are controlled by the variations of energy received from the solar radiation in the high latitudes of the Northern hemisphere Milankovitch [1941]. The decrease of solar radiation at the high latitudes of the Northern hemisphere increases the quantity of snow accumulated over the year. Because the surface covered in snow is larger, the global albedo increases. It creates a positive feedback loop because more solar radiations are then reflected which decreases even more the temperature and can increase the accumulation of snow and trigger a glacial period. The variation of the amount of energy received by the solar radiations is mainly controlled by the orbital parameters. First, there is the eccentricity which corresponds to the deformation of the Earth orbit from a perfect circle into an ellipsoid: the deformations are small (1.7 to 5.8 %) and change slowly with two typical frequencies at 100 000 years and 400 000 years. Second, the obliquity represents the tilt between the rotational axis of the Earth with the orbital axis: it imposes the latitudinal repartition of the solar radiation and directly controls the amplitude of the seasonal cycle, the obliquity varies between 22.1° and 24.5° with two pseudo-periodicity around 41 000 years. And third the precession controls the synchronisation of the season (determined by which hemisphere face toward the sun) with the position of the earth on the ellipsoid with a periodicity of 19 000 years and 23 000 years. The variations of the orbital parameters create small variations of solar irradiance, but as the climatic system is strongly non linear, these small variations are enough to trigger an hysteresis cycle, hence the glacial-interglacial cycles [Paillard, 1998].

The hydrological cycle is predominant in the Earth climate system and all three phases of water (vapour, liquid and ice) play an important role in the radiative balance and redistribution of heat. First, the oceanic masses cover 72% of the Earth surface and are actively regulating the climate through an important and complex thermohaline circulation. Second, water vapour, as the most important greenhouse gas (60% of the natural greenhouse effect [Kiehl and Trenberth, 1997]), warms the atmosphere by trapping infrared radiations but can also cool the atmosphere through the increase of albedo by the clouds. Third, as explained above, snow and ice albedo effects strongly impact the climate, but frozen water can also impact the climate through fresh water input in the thermohaline circulation creating large, rapid temperature fluctuations [Dansgaard et al., 1984; Bond et al., 1993]. Because stable water isotopes are involved at each step of the hydrological cycle [Dansgaard, 1954], they can be used as a faithful proxy of past atmospheric temperature [Dansgaard, 1964].

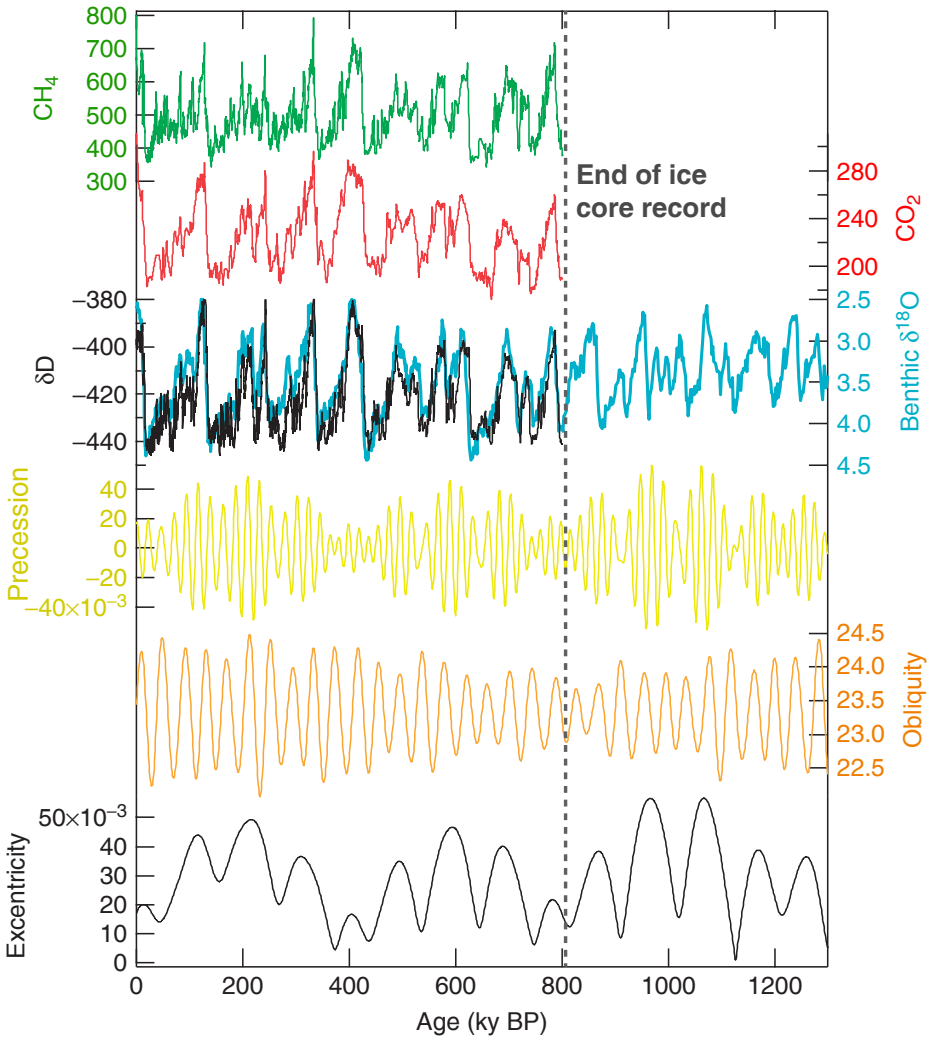

Figure 1.1: Methane (green, ppbv) and carbon dioxide (red, ppmv) concentrations from the air bubbles of the EPICA ice core and δD (black, permil) of the ice of the EPICA ice core, compared to benthic isotopic composition (blue, permil), precession, obliquity and eccentricity as predicted by the Milankovitch theory [Jouzel and Masson-Delmotte, 2010]

Studying Antarctica

Antarctica is a very important place for paleoclimate science. First, because of the extent of the ice sheet, both vertically and horizontally, it is an archive of the Earth global climate and presents as well local particularities due to the large range of climatic conditions encountered. Present ice cores span with unchallenged reconstruction power over the last 800 000 years and they are expected to be able to reach up to 1.5 million years [Fischer et al., 2013]. Second, Antarctica is isolated enough and mostly free of direct anthropogenic contamination, which leads to better preserved archives. Finally, the importance

of Antarctica's ice sheet in global climate makes it dire to understand the dynamics of local climate to temperature variations, especially in the context of climate change. Indeed, mass balance of Antarctica's ice sheet is very sensitive to climate variations with rapid ice-sheet collapse triggered by coastal melt highlighting the vulnerability of the Antarctic ice sheet in the context of climate change [DeConto and Pollard, 2016]. These ice sheet mass losses are associated with direct impact on the global climate, in particular large sea level rising [Dutton et al., 2015].

Several deep ice cores have been drilled providing either long spanning records of several hundred thousand years (Vostok, Dome C...) or high resolution records of the last 80 000 years of the West Antarctic ice sheet (WAIS Divide). New technological developments, in particular infrared spectroscopy, enable to access to high resolution and even continuous measurement of ice core isotopic composition profiles. Indeed, the ability of infrared spectrometers to continuous measure has been transferred to ice cores study through sampling in Continuous Flow Analysis (CFA) systems [Gkinis et al., 2011]. By extracting liquid water during the progressive melting of an ice core, it is possible with a peristaltic pump to continuously vaporise the water and analyse it. Even more impressive, a common effort of the Laboratoire de Glaciologie et de Geophysique de l'Environnement (LGGE) and of the LIPHY has developed an infrared spectrometer deployed inside the drill of the ice core, enabling measurements of the ice isotopic composition and methane content in situ when the ice is being drilled [Grilli et al., 2014].

Water stable isotope signal

Interpreting stable water isotopic composition signal is not as straightforward because of the multitude of processes leading to the formation of the snow in remote Polar Regions: evaporation at the oceanic surface, advection of air masses, snow flake/rain drop formation in mixed phase conditions in clouds, re-evaporation during precipitation events, mixing of different air masses and even post-deposition processes such as sublimation-condensation cycles at the diurnal scale. Indeed, each of these processes is associated with one or several fractionation of water isotopes.

In addition, the fractionation processes are not perfectly constrained at low temperatures such as encountered in remote Polar Region. At the phase transition between vapour and ice, the fractionation associated with the phase transition at thermodynamic equilibrium (equilibrium fractionation) has only been measured down to $-40°C$ [Merlivat and Nief, 1967; Majoube, 1971a; Ellehøj et al., 2013] and the different determinations already

differ significantly at $-20°C$. Kinetic fractionation during molecular diffusion is not constrained any better with only a few experimental determinations of the diffusivity ratios of the different isotopes [Merlivat, 1978a; Cappa et al., 2003; Luz et al., 2009], all of them realised at positive temperatures.

This creates important uncertainties on theoretical relationship between water stable isotopic composition and temperature as highlighted by Guillevic et al. [2013]. As a result, stable isotopic composition from ice core is generally calibrated against an independent estimation of temperature variations, for instance a borehole thermometry record [Cuffey and Clow, 1997] or from nitrogen and argon isotopic composition temperature record [Orsi et al., 2014]. Still, these methods only provide a discrete calibration for one period, one time scale and one location and cannot be generalised for the interpretation of the isotopic composition as a temperature proxy.

At the first order, all three stable isotopic compositions ($\delta^{18}O$, δD and $\delta^{17}O$) are still directly related to local average temperature. Additional information can be extracted from combination of the isotopic compositions in secondary parameter or excess. The deuterium excess $d-excess = \delta D - 8 \times \delta^{18}O$ as defined by Dansgaard [1964], provides additional information such as the relative humidity during evaporation at the source of the moisture [Gat, 1996; Uemura et al., 2008], during re-evaporation in convective zones [Risi et al., 2008], the temperature variations at the source of the moisture [Vimeux et al., 1999] or can be used to tune supersaturation using its spatial variations [Ciais and Jouzel, 1994; Werner et al., 2011]. The excess in ^{17}O, defined by $^{17}O - excess = ln\left(\delta^{17}O+1\right) - 0.528\, ln\left(\delta^{18}O+1\right)$ [Barkan and Luz, 2007; Landais et al., 2008] can be used as an indicator of relative humidity at the source of the moisture during evaporation [Uemura et al., 2010b] or temperature during condensation of the snow in very cold regions [Landais et al., 2012b; Winkler et al., 2012; Schoenemann et al., 2014]. The second order parameters are still relatively rarely used in Polar Regions as they are not so simple to interpret as they also combine several signals such as relative humidity and temperature at the source and the local temperature in Polar Regions [Jouzel et al., 2007] or even the precise trajectory of the air masses during the advection of moisture [Bonne et al., 2015].

Main scientific questions

The frame of my Ph-D is to improve the performances of paleoclimate reconstructions from ice core isotopic composition, by better quantifying the climatic information recorded by the ice isotopic composition, especially for remote Polar Regions. This motivates an

important effort to understand the processes involved in the fractionation of water stable isotopes both in the atmosphere and at the snow surface, in particular at low temperature and low humidity, using both laboratory experiments and field studies. This goal has been separated in several scientific questions, the first one is:

- **What is the primary contribution to snow isotopic composition on the East Antarctic Plateau ?**

The snow isotopic composition is not solely determined by the isotopic composition of the successive precipitation events and is affected by several post-deposition processes. First, wind transports flakes and erodes the snow surface in a fashion dependent on topography (from the local to the regional scale) which redistributes the snow [Sokratov and Golubev, 2009]. Modelling approaches highlight that only during strong wind events can occur permanent deposition of snow [Groot Zwaaftink et al., 2013]. It also creates gradual movement of the snow dunes associated with artificial variations of the isotopic composition in the ice structure [Ekaykin et al., 2002; Frezzotti et al., 2002; Ekaykin et al., 2004]. Second, surface snow measurements in Greenland indicates that the isotopic composition can be altered directly by the exchanges with the local vapour [Steen-Larsen et al., 2014a]. Already in Greenland, this modification can contribute for a significant amount of the signal despite important annual accumulation. On the East Antarctic Plateau, it is not clear whether this kind of post-deposition process should have more or less impact on the snow isotopic composition: the precipitation rate is much lower than in Greenland, and therefore we expect these exchanges to have a larger relative contribution in Antarctica but the temperature is lower and therefore the humidity level, which limits the contribution of these exchanges.

One of the limits to obtain a better constrain on the archival of climatic signal by snow isotopic composition is that, at this range of temperature, the associated fractionation processes are poorly constrained. This raise the second question of my Ph-D:

- **How to determine quantitatively isotopic fractionation during the formation of snow at low temperature ?**

This question includes mainly the impact of the fractionation during the vapour to ice phase transition and the fractionation associated with diffusion processes. An important amount of studies have been led in the 60's, 70's and 80's exploring the processes influencing isotopic composition under the direction of Dansgaard, Lorius, Merlivat and Jouzel. At this time, measuring isotopic composition of water was mainly realised by mass spectrometry and required a chemical transfer. To explore the influence of one

physical process affecting the isotopic composition, they had to realise complex and time consuming laboratory setups and they laid the foundations of the isotopic paleothermometry. Experiments on fractionation processes have been so far still mainly realised by mass spectrometry. Indeed, even though Ellehøj et al. [2013] tried to implement an infrared spectrometer to determine the isotopic composition of the vapour left over the equilibration chamber, below $-10°C$, the precision of the infrared spectrometer was direly reduced and led Ellehoj et al to mainly use the data obtained by mass spectrometry.

Still, as stated above, important discrepancies remain in the determination of both equilibrium fractionation and kinetic fractionation coefficients, in both cases, especially at low temperatures. In laboratory setups or in the field, processes affecting the vapour or the vapour to ice phase transition are the main troublemakers in cold conditions. Indeed, only traces of water vapour remain in the air at the temperature encountered on the East Antarctic Plateau leading to reduce precision of the measurement of the isotopic composition of the vapour in these conditions.

To overcome this measurement issue, analytical developments are crucial to push the detection limit and therefore realise processes studies. This leads to the next question of my Ph-D:

- **How to measure water vapour isotopic composition for climatic conditions as encountered on the East Antarctic Plateau ?**

Nowadays, commercial plug and play instruments based on infrared spectroscopy are available and can measure continuously isotopic composition with precision equivalent to mass spectrometry. Infrared spectrometry builds on several aspects of physics to provide high sampling rate, non destructive, water vapour isotopic composition measurements. With telecommunication developments, laser diodes in the near-infrared region have been widely studied. Indeed, optical fibre main material has a minimum of absorption in this region near $1400\,nm$. Through the development of telecommunication, efficient and affordable diode lasers, photodiodes, mirror and other optical, electro-optical and accousto-optical components have been conceived.

In the last decades, development of resonant cavities have opened new possibilities to reduce the size of the sample analysed and increase the power of measurement at the same time. Combined with the computer evolution, stand alone infrared spectrometers are now able to measure isotopic composition continuously in the field and in laboratories.

These new instruments are routinely deployed to measure water vapour isotopic composition in tropical and temperate regions [Tremoy et al., 2011; Steen-Larsen et al., 2014b]. In Polar Region, only a few measurements have been realised due to low humidity content increasing the need for calibration and special care to prevent condensation in the inlets [Steen-Larsen et al., 2013; Bonne et al., 2014]. Indeed, absolute humidity decrease exponentially with temperature, reaching easily the limits of the instruments below $-30°C$. In Antarctica, before the beginning of my Ph-D, only two campaigns measured water vapour isotopic composition inland Antarctica: Olivier Cattani at Dome C in 2006/07 by cryogenic trapping and whose results are presented in Section 6.2 and Janek Landsberg (Ph-D defended in 2014) at Troll Station in 2012 but the results were impaired by sampling problems and were never published [Landsberg, 2014]. Continuous measurement of water vapour by infrared spectroscopy stays very limited at low humidity and therefore leads to the last question of my Ph-D:

- **What are the limits of the isotopic composition measurements of water vapour by Infrared spectrometry ?**

New developments in infrared spectroscopy over the last years enabled one to measure down to very low humidity, such as encountered in central Antarctica. New commercial instruments, from Picarro for instance, are now able to measure below $1000\,ppmv$ and include $^{17}O-excess$ [Steig et al., 2014] with routine precision around $0.1‰$ for $\delta^{18}O$.

At the Laboratoire Interdisciplinaire de PHYsique (LIPHY), Daniele Romanini, Erik Kerstel and Janek Landsberg have developped an infrared spectrometer able to measure triple isotopic composition in trace of water vapour down to $10\,ppmv$. New developments in optical feedback frequency stabilisation realised by Johannes Burkart (Ph-D defended in 2015) enabled comb-assisted spectroscopy of CO_2 gas with unchallenged precision. My thesis builds on all these initiatives to expand the possibilities to measure water isotopes in the vapour at low humidities as encountered in Antarctica combining cryogenic trapping for mass spectrometry measurements, the use of several generations of commercial instruments from Picarro, the use of the instrument developed by Janek Landsberg and the development of a new range of infrared spectrometer for water vapour isotopic composition measurements based on optical feedback frequency stabilisation. At the Laboratoire des Sciences du Climat et de l'Environnement, using the expertise of Olivier Cattani and Hans-Christian Steen-Larsen (Ph-D defended in 2010), three campaigns were organised to monitor water vapour isotopic composition inland Antarctica: one at Kohnen station by François Ritter in 2013 and two at Dome C by myself in 2014 and Frederic Prié in 2015.

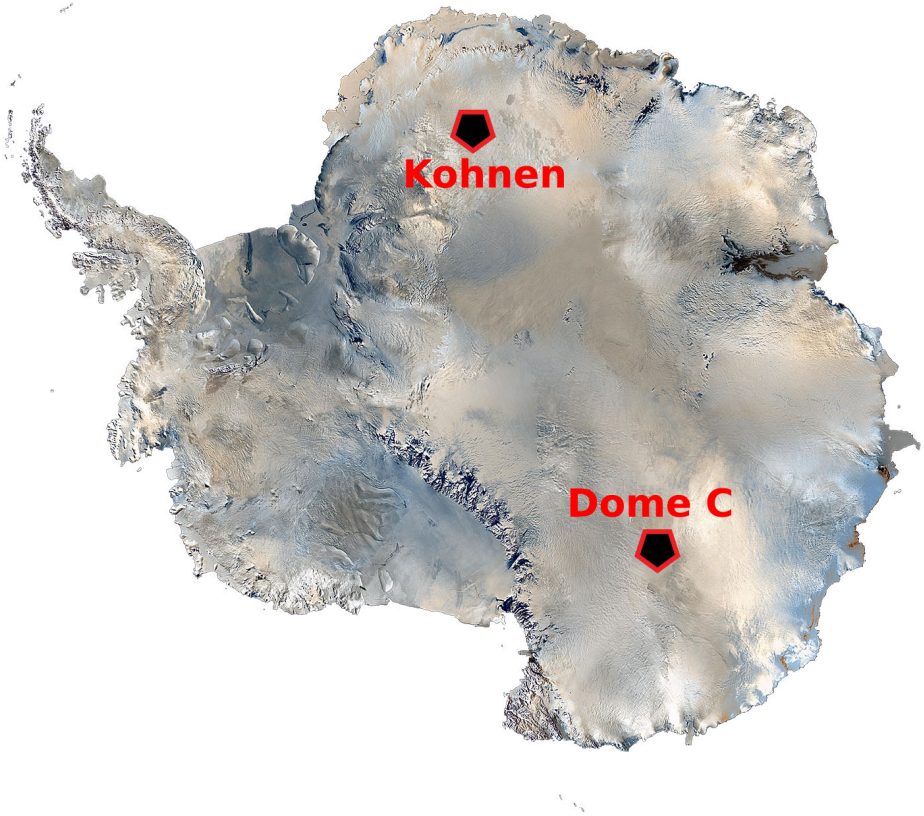

Figure 1.2: Satellite picture of Antarctica with the two inland stations where water vapour isotopic composition was monitored during my Ph-D

- **Applications to atmospheric dynamic and link with modelling**

Finally, water isotopes study is actually going beyond the sphere of paleoclimate science, even in Polar Regions. Continuous monitoring of water vapour isotopic composition has enabled one to use water stable isotopes as an atmospheric tracer. For instance, using several continuous monitorings in the North Atlantic region, Bonne et al. [2015] highlight the interest of using d-excess to monitor atmospheric rivers. These phenomena are particularly important because they account for a significant contribution to high latitudes moisture budget [Liu and Barnes, 2015]. Water isotopes have also been commonly used to tune supersaturation in remote Polar Regions where very few measurements exists [Ciais and Jouzel, 1994; Winkler et al., 2012].

Vapour isotopic composition is also necessary to improve the performances of climatic models: accurate description of isotopic composition as a tracer in climate models requires an important amount of data to set precise parametrisation. Water isotopes have been routinely implemented into Global Circulation Model (GCM) and provide dynamic representation of the isotopes in Polar regions useful for the interpretation of ice core data [Hoffmann et al., 1998; Schmidt et al., 2005; Risi et al., 2010; Werner et al., 2011]. In parallel of my Ph-D, the implementation of water isotopes in the regional model MAR [Gallée and Gorodetskaya, 2010], which include the complete physics of the water cycle in Polar Region, has been realised by Mathias Moys and should provide important insights of the local dynamic of water isotopes. Additionally, the implementation of water isotopes in the snow model CROCUS [Brun et al., 2011] has been realised by Alexandra Touzeau and should provide important insights of the post deposition processes in the snow firn.

Organisation of the manuscript

In this manuscript, we will address several aspects of water stable isotopes in low humidity and temperature conditions: how to measure water isotopes accurately at low humidities ? How equilibrium and kinetic fractionation are parametrised at low temperature ? How isotopic composition is affected by climatic parameters during snow formation and after deposition ? This PhD had an important experimental part through the development of a new infrared spectrometer, developments on existing infrared spectrometer: the HiFI realised by Janek Landsberg; and also the developments a new humidity generator to be able to calibrate infrared spectrometers at very low humidities. It includes the results from several laboratory experiments: spectroscopy of the water vapour at the LIPHY, cloud chamber experiments at the Laboratoire Interuniversitaire des Sciences Atmospheriques (LISA), equilibrium fractionation coefficients determination at the LSCE, and from two field campaigns at Concordia among which I took part in the first one. It also includes the analysis of snow samples gathered by several winterover crew at Concordia.

In the Chapter 2 are detailed the water isotopes physical properties. First, from a thermodynamic point of view, it focuses on how phase transition affects the isotopic composition and details two experiments that have studied the phase transition between vapour and ice. Then, the large panel of out of equilibrium processes affecting the isotopic composition is reviewed and applied to the formation of snow in Antarctica. Finally, all these information is placed in the context of an isotopic paleothermometer.

In the Chapter 3, we detail the measurement of isotopic composition and provide an idea of the limits of infrared spectroscopy before I started my Ph-D. First, a quick overview of mass spectrometry is realised in order to explain the pros and cons of the method, in particular the rather good precision versus the time consuming preparation of the samples and the necessity of regular calibration. Then, a detailed review of how to measure water vapour isotopic composition by infrared spectroscopy includes basic physics underlying the measurement techniques. The purpose is to clarify the possibilities with both methods in order to optimise behaviour with mass spectrometry and infrared spectroscopy and to clearly state the present limits.

In the Chapter 4, we present the new developments in infrared spectroscopy realised during my Ph-D in order to push the limits further. First, we realised new reference spectra of water vapour in order to improve the spectroscopy fit parameters on which are relying all infrared spectrometers to estimate the concentration. These results show that one of the principal limits is the frequency stabilisation of the laser. These results motivated the construction of a new ultra stable cavity as a frequency reference. This cavity has been characterised and placed in the context of previous prototypes and we describe the first results from this cavity to realise spectra of water vapour. The efforts on these two aspects of spectroscopy: are mandatory to realise instruments able to measure at lower humidity water stable isotopic composition, in the laboratory or on the field.

In the Chapter 5, we focus on experimental investigations on the fractionation processes with two main aspects: the isotopic fractionation associated with the vapour to ice phase transition and diffusion led kinetic fractionation. First, we go back on fractionation during the phase transition between vapour and ice and try discriminate over the two existing determinations [Merlivat and Nief, 1967; Ellehøj et al., 2013]. We present perspectives of a new experiment to be realised. Then, we revisit the experiment of Jouzel and Merlivat [1984] extending a similar impact of kinetic fractionation on $^{17}O-excess$ than on $d-excess$ and exploring with a new theoretical background the impact of the difference in diffusivities of the different isotopes.

In the Chapter 6, we focus on field study of stable isotopes on the East Antarctic Plateau. First, we describe the water vapour isotopic composition monitoring realised during my Ph-D at Dome C. Because this is the first campaign measuring on the East Antarctic Plateau with humidity levels down to 200 $ppmv$, it was important to validate the measurement techniques. This led to an important amount of validation of the data through Allan Variance calculation, regular calibrations, comparison with cryogenic trap-

ping realised in parallel, and the first results. These results are also compared with the similar results from Kohnen station where the climatic conditions are in between the one found at Dome C and at NEEM (Greenland). Then we study in parallel vapour and snow isotopic composition in order to understand how the isotopic composition archives temperature signal in a place where annual accumulation of snow contributes as much as sublimation/condensation cycles to the mass budget.

In the Chapter 7, a comprehensive discussion of the impact of these results is provided to conclude this manuscript. Finally, this manuscript is completed by a summary in French (Annexe A), a description of my Ph-D in a context larger that simply scientific point of view (Annexe B), some technical aspects (Annexe C) and an additional article about the acquisition of isotopic composition for surface snow in East Antarctica in which I was involved (Annexe D).

Chapter 2

Water isotopes physical properties

In this section, we will define all the notions we will be using later on. This section is based on the state of the art of water isotopic composition physical properties including thermodynamic, diffusion, turbulence and distillation processes. These properties are fundamental to understand the history that led a moist air toward being precipitated in remote Polar Regions and therefore essential to analyse the ice isotopic composition in paleoclimate studies. These properties are directly used by models incorporating isotopes, including global climate models. They mainly involve the thermodynamic properties of moisture along the water cycle. First, we will describe the thermodynamic properties involved at the phase transition at thermodynamic equilibrium, then move on to out of equilibrium processes also affecting the different isotopes and finally explain why this is important in the isotopic paleothermometer.

2.1 Thermodynamic properties

2.1.1 Saturated vapour pressure

When a gas is in contact with its condensed phase, particles can freely exchange between the two phases. At thermodynamic equilibrium, the net flux is equal to 0. If the thermodynamic conditions are enabling both phases to exist, the vapour reaches its saturated vapour pressure. Then, the number of particles leaving the surface is equal to the number of particles striking and "joining" this surface at this time, i.e. $P_{sat}(T)(1-R)/\sqrt{2\pi mT}$ where P_{sat} is the saturated vapour pressure, R a mean "reflection coefficient" for particles colliding at the surface [Landau and Lifshitz, 1958]. Using the Clausius-Clapeyron formula, one can calculate the saturated vapour pressure with:

$$\frac{dP_{sat}}{dT} = \frac{L_v(T)P_{sat}}{R_v T^2} \tag{2.1}$$

where L_v is the latent heat and R_v the gas constant. In the case of water for climatology studies, the variations of L_v against temperature, and therefore of P_{sat}, cannot be neglected. Approximations validated toward measurements are used as there is no analytical solution of such problems considering the degree of complexity involved. Unless stated otherwise, we will use within this manuscript the Goff and Gratch formula [Goff and Gratch, 1945] for vapour at equilibrium with liquid water :

$$\begin{aligned} log\ P_{sat} = &-7.90298\left(\frac{373.16}{T}-1\right)+5.02808\ log\left(\frac{373.16}{T}\right)... \\ &-1.3816\ 10^{-7}\left(10^{11.344\ (1-T/373.16)}-1\right)... \\ &+8.1328\ 10^{-3}\left(10^{-3.49149\ (373.16./T-1)}-1\right)+log\ (1013.25) \end{aligned} \tag{2.2}$$

Where T is expressed in K. For the case of vapour at equilibrium with ice :

$$\begin{aligned} log\ P_{sat} = &-9.09718\ \left(\frac{273.15}{T}-1\right)-3.56654\ log\ \left(\frac{273.15}{T}\right)... \\ &+0.876793\ \left(1-\frac{T}{273.15}\right)+log\ (6.1173) \end{aligned} \tag{2.3}$$

Even though this formula slightly underestimates the vapour pressure of ice, in the range of $-100°$C to $+100°$C, the error is only on the order of 0.1 % which is not relevant considering the precision obtained with humidity and temperature measurements.

As the number of particles striking the surface is mass-dependent, different isotopes have different saturated vapour pressures. Therefore, there is a fractionation at the interface between the phases. For instance, in the case of the isotopic exchange of H_2O and HDO between a liquid phase and a gaseous phase, we have, using the formulation from Criss [1999], chapter 2:

$$(H_2O)_l + (HDO)_g = (HDO)_l + (H_2O)_g \tag{2.4}$$

where the equilibrium constant $K = \dfrac{[(HDO)_l][(H_2O)_g]}{[(H_2O)_l][(HDO)_g]}$ is directly linked to other state thermodynamic variables. In the case of an equilibrium between a gas and a liquid phase with two different isotopes involved such as described above, the relationship between the Gibbs free energy and the equilibrium constant is given by :

$$\Delta G_f^0 = -RT\,lnK \tag{2.5}$$

where R is the gas constant, T the absolute temperature (Kelvins) and the standard Gibbs free energy of the particular reaction ΔG_f^0 is expressed in $kcal.mol^{-1}$. Tables usually provide values of the Gibbs free energy at standard conditions of pressure and diverse ranges of temperature. For instance, Lide [2004] provides the thermodynamic data associated with each element involved in the exchange equation (2.4) at 25°C. We obtain for the reaction (2.4) a value $\Delta G_f^0 = 45\, cal.mol^{-1}$ which gives a value of $K = 1.079$. This means that the ratio of number of HDO molecules by H_2O molecules in the condensed phase is 1.079 times higher than in the vapour and therefore, the heavy isotopes are more importantly found in the condensed phase than in the vapour. This property is classically called equilibrium fractionation and the value found here is in agreement with experiments. As the values for the Gibbs free energy ΔG^0 associated with isotopic exchanges are very small, thermodynamic data can not necessarily be known with enough precision to make useful predictions to estimate isotopic fractionation, especially as there is a very strong dependence on the Gibbs free energy associated with each element with temperature.

2.1.2 Equilibrium fractionation

As the flux of molecules sticking on the surface is greater for the heavy isotopes ($H_2{}^{18}O$, $H_2{}^{17}O$, or $HD{}^{16}O$) than for the light isotope ($H_2{}^{16}O$), they remain in larger quantity in the condensed phase than in the vapour. More generally, the molecules are preferably found in the phase in which they bound the strongest. In the case of water isotopes for the range of temperature observed on earth, the heavy isotopes are preferentially found in the condensed phases rather than in the vapour, but it is not necessarily the case. In order to express the quantity of the heavy isotope X compared to the light one, we use the isotopic ratio R^X:

$$R^X = \frac{abundance\ of\ heavy\ isotopes}{abundance\ of\ light\ isotopes}$$

The quantity of heavy isotopes is much lower than the light ones, thus we usually report isotopic composition compared to a reference value:

$$\delta X = \frac{R^X}{R^X_{ref}} - 1 \tag{2.6}$$

Because the values of δX are very small, it is expressed in ‰. In the case of water, R_X^{ref} is the standard value given by the International Atomic Energy Agency (IAEA) named V-SMOW after Vienna Standard Mean Ocean Water and SLAP after Standard Light Antarctic Precipitation. The values of the standards are given in Table 2.1. Determination of the absolute isotopic composition of a sample is rather complicated as we will see in section 6.2.

Table 2.1: Values of the standard V-SMOW and SLAP with a factor 10^{-6} [Baertschi, 1976; de Wit et al., 1980; Martin and Gröning, 2009] .

	$H_2{}^{18}O/H_2{}^{16}O$	$H_2{}^{17}O/H_2{}^{16}O$	$HD{}^{16}O/H_2{}^{16}O$
R^X_{V-SMOW}	2005.20 ± 0.45	379.9 ± 0.8	155.75 ± 0.08
R^X_{V-SLAP}	1893.91 ± 0.45	???	89.12 ± 0.07

The equilibrium fractionation has been defined as the ratio of saturated vapour pressure between each heavy isotope and the principal one ($H_2^{16}O$). If a water sample is introduced in a box, after a time long enough for thermodynamic equilibrium to settle, the vapour partial pressure reaches the saturated vapour pressure; the partial pressure of the heavy isotope is equal to its saturated vapour pressure as well and:

$$\alpha_{eq}^{HDO}(v \leftrightarrow l) = \frac{P_{sat}^{HDO}}{P_{sat}^{H_2^{16}O}} \tag{2.7}$$

This definition is not commonly used. Using Raoult's law which links the partial vapour pressure to the composition of the liquid (solid) phase it lies above and to the saturated vapour pressure of the compound i: $P_v^i = X_l^i P_{sat}^i$, we can simplify this expression. Again, in the case of HDO, we obtain:

$$\frac{P_{sat}^{HDO}}{P_{sat}^{H_2^{16}O}} = \frac{P_v^{HDO}}{P_v^{H_2^{16}O}} \frac{X_l^{H_2^{16}O}}{X_l^{HDO}} = \frac{R_v^{HDO}}{R_l^{HDO}} \tag{2.8}$$

This leads us to another definition of the equilibrium fractionation coefficient, much more convenient to use in climate science:

$$\alpha_{eq}^{HDO}(v \leftrightarrow l) = \frac{R_v^{HDO}}{R_l^{HDO}} \tag{2.9}$$

This notation is equivalent to the equilibrium constant of equation (2.4). The same notation can be applied for phase transition between solids, liquids or gases and generalised for $H_2^{17}O$ and $H_2^{18}O$. This notation is directly related to the equilibrium constant associated with the reaction of the transfer of molecules between the two phases. The saturated vapour pressure P_{sat} can be determined from equation 2.5: as we saw $\frac{P_{sat}^{HDO}}{P_{sat}^{H_2O}} = 1.079$ at 25°C which is the correct value for equilibrium fractionation between liquid water and vapour at this temperature. As saturated vapour pressure is sensitive to temperature through the Clausius Clapeyron (equation 2.1), so is the equilibrium fractionation coef-

ficient. As we will see in the next sections, the equilibrium fractionation coefficient is well known for the liquid/vapour phase transition of water, but for the ice/vapour phase transition, it is not very well constrained and under $-40°C$, the equilibrium fractionation coefficients of the different heavy isotopes are just extrapolated.

Another notation is sometimes used in order to directly compute the impact of equilibrium fractionation on the δ values using:

$$\varepsilon_{eq} = (\alpha_{eq} - 1) \tag{2.10}$$

In the case of small ε, it is then possible to write:

$$\varepsilon^i_{eq}(v \leftrightarrow l) \approx \delta^i_v - \delta^i_l \tag{2.11}$$

If this expression is more convenient to use directly with δ isotopic composition, it is not always valid, in particular at low temperature α^{HDO}_{eq} is not small enough for such an approximation.

2.1.3 Statistical thermodynamics

Classical statistical thermodynamic provides tools to roughly estimate the variation with temperature of the saturated vapour pressure of different isotopes and therefore of the equilibrium fractionation coefficients. These estimations are provided by experimental determinations of the thermodynamic state variables but the theoretical background fails to predict their variations. Indeed the differences in the chemical potentials of the pure isotopes only differ by a constant no matter which phase [Landau and Lifshitz, 1958], resulting in roughly equal saturated vapour pressure for all isotopes. To infer theoretical formulas for either Gibbs free energy or saturated vapour pressure, quantum statistical thermodynamic is necessary.

In the case of equilibrium fractionation of water between different phases, the stoichiometry of the exchange equation allows us to write $\alpha_{eq} = K$ (equation (2.4)). Also the net volumes are not changing and PV remains constant. The Helmholtz free energy associated with the isotopic exchange reaction is therefore equal to the Gibbs free energy change providing a direct link between K and Q, the partition function. The partition function can be expressed from the Boltzmann distribution law:

$$Q = \sum_j g_j e^{-\frac{\varepsilon_j}{kT}} \tag{2.12}$$

where g_j refers to the degeneracy of level j, ε_j is the j^{th} level of energy, k is the Boltzmann constant and T is the temperature. Calculating these quantum effects can only be done analytically for monoatomic elements by solving the Shrödinger equation with an adapted potential. For polyatomic molecules, more complicated theory are to be used. By applying a correction to the thermodynamic chemical potential of the liquid, acceptable expression of the saturated vapour pressure can be found. Water molecule physical properties make it really complex to model. Urey [1947] simplified the system by analysing separately the different atoms in the molecule and the three contributions (rotational, vibrational and the zero point energy (ZPE) associated with the energy of the lowest vibrational state) to each degree of liberty to the partition function with:

$$\frac{Q^i}{Q} = \prod_{k=1}^{3n-6} \underbrace{\frac{\sigma}{\sigma^i}\frac{U_k^i}{U_k}}_{Rotational} \underbrace{\frac{e^{-U_k^i/2}}{e^{-U_k/2}}}_{ZPE} \underbrace{\frac{1-e^{-U_k}}{1-e^{-U_k^i}}}_{Vibrational} \tag{2.13}$$

where σ is the symmetry number, U_k is the ratio of the energy of the transition k and of the thermal energy $U_k = \frac{h\nu_k}{kT}$, the subscript i refers to the heavy isotope i whereas no subscript refers to the main isotope ($H_2^{16}O$) and $3n-6$ is the number of vibrational modes, n being the number of atoms (for instance, in the case of water, $n=3$) [Criss, 1999]. At high temperature when U_k becomes small, this formula can be developed in power series with :

$$ln\left(\frac{Q^i}{Q}\right) = ln\left(\frac{\sigma}{\sigma^i}\right) + \sum_{k=1}^{3n-6}\left(\frac{{U_k}^2 - {U_k^i}^2}{24} - \frac{U_k^4 - U_k^{i4}}{2880} + \frac{U_k^6 - U_k^{i6}}{181440} + ...\right) \tag{2.14}$$

In that case, the ratio of partition function provides with an expression of the equilibrium fractionation coefficient dependency with temperature. This calculation is fundamental in the determination of water isotopes equilibrium fractionation [Van Hook, 1968]. As $U_k \propto \frac{1}{T}$, we find that the dependency of $ln\left(\frac{Q^i}{Q}\right) \propto \frac{1}{T^2}$ and therefore, the dependency of α_{eq} against the temperature. At low temperature, similar calculations predict a dependency of $1/T$. Combining those two approaches in a more general power serie development, Bigeleisen and Mayer [1947] predict the dependency of the isotopic fractionation coefficient with:

$$ln\,\alpha_{eq} = \frac{A}{T^2} + \frac{B}{T} + C \tag{2.15}$$

where the term $\frac{B}{T}$ is small against the others. The theoretical formula calculated with this principle and determination of the coefficients A, B and C by Van Hook [1968] will be compared to the experimental determinations in the next section.

2.1.4 Determination of equilibrium fractionation coefficient

Instead of measuring the thermodynamic Gibbs energy linked to the phase transitions, equilibrium fractionation coefficients have been directly determined. For liquid-vapour phase transitions, the different experimental determinations of the equilibrium fractionation for the different molecules have provided satisfactory agreement [Craig et al., 1963; Merlivat and Nief, 1967; Majoube, 1971b]. The theoretical determination from Van Hook [1968] which solves Eq. 2.14 to estimate the variations of α_{eq} is in agreement with these data and validates the theoretical background previously described. Determining experimentally equilibrium fractionation coefficient for ice and vapour is not as easy as it seems. Indeed, to measure only equilibrium fractionation at the solid/vapour phase transition, one needs to build very specific systems where only the influence of the fractionation due to the phase transition affects the measurements. We will describe here the two principal ones: a) Merlivat and Nief [1967] (and later on Majoube [1971a] for $\delta^{18}O$) and b) Ellehøj et al. [2013]. These two methods are radically different and provide two independent determinations of the α_{eq}.

Merlivat and Nief [1967] used a method developed by Boato et al. [1962] to measure isotopic fractionation in vapour flux of Argon. It relies on a closed volume connected at one end to a reservoir of water vapour of known isotopic composition (R_0^i) as presented in Fig. 2.1. The other end of the volume is cooled down below 0°C at a stable temperature by eutectic baths. At first, the volume is empty and a leak dN from the reservoir is opened. When the vapour pressure at the cool part of the volume reaches the saturated vapour pressure, the vapour condensates and ice is formed (some experiments lead to supercooled liquid water as well). After a while, a profile of humidity and isotopic composition is formed, lead by molecular diffusion from the leak from the reservoir to the condensing surfaces. This profile eventually reaches a permanent regime which is when the measurement takes place.

In a permanent regime, there is no more accumulation of neither moisture nor isotope in the volume, therefore the quantity of all isotopes of water going through the leak is equal to the one condensing. This results after a while on the isotopic composition of the ice being roughly the same as the isotopic composition of the reservoir $R_S^i = R_0^i$ for each isotope i. At the ice/vapour interface, equilibrium fractionation occurs, the link between the isotopic composition of the vapour near the interface and the ice is $\alpha_{eq}^i = R_S^i/R_v^i =$

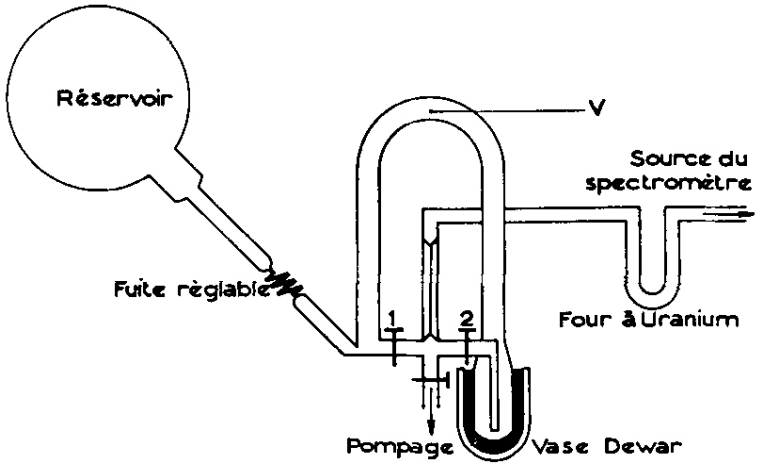

Figure 2.1: Merlivat and Nief experimental set up.

R^i_0/R^i_v. The isotopic composition in the vapour is therefore defined by:

$$R^i_v(x) - R^i_0 = R^i_0 \left(\frac{1}{\alpha^i_{eq}} - 1 \right) exp \left(\frac{-vz}{D^i} \right) \tag{2.16}$$

where v is the speed of the water fluxes in the linear volume, z the curvilinear length of the volume V and D^i is the diffusion coefficient of the isotope i. By measuring the isotopic composition of the vapour very close from the condensation surface, Merlivat and Nief obtain an estimate of the composition of the first vapour. By measuring the isotopic composition very close from the origin of the leak, they obtain an estimate of the isotopic composition of the original vapour, and therefore of the condensate. This results in a measurement of the equilibrium fractionation coefficients through:

$$\alpha^i_{eq}(T) = \frac{R^i_v(z=l)}{R^i_v(z=0)} = \frac{R^i_0}{R^i_v} \tag{2.17}$$

This method relies on two criteria for the fluxes:

- The flux to the spectrometer must be negligible compared to the flux of the leak: $d_{spectro} << dN$. In the case of Merlivat and Nief [1967], this flux was less than 1% than the flux entering the volume;
- The number of molecules condensing by unit of time, which is equal to the leak as we saw earlier, dN must be several orders of magnitude smaller than the number of collisions due to the thermal agitation $N_{col} = P\Delta tS/\sqrt{2\pi mk_BT}$.

By forcing the flux of water vapour and isotopes in a closed system, Merlivat and Nief

[1967] manage to create an experiment where the entire isotopic composition profile is determined by the boundary condition of isotopic composition in the vapour at the vapour/ice interface. This experiment was realised using different eutectic bath, therefore at different temperatures providing the dependency of the equilibrium isotopic fractionation coefficient with temperature for HDO. Majoube [1971a] realises a similar experiment and extends the determination to the case of $H_2^{18}O$ for a vapour to ice transition and to both $H_2^{18}O$ and HDO for a vapour to liquid transition [Majoube, 1971b].

Ellehøj et al. [2013] rely on a completely different setup taking advantages of the new developments in infrared spectrometry allowing reliable continuous monitoring of water vapour isotopic composition (see section 3.2.2.1). They created a constant flux of moisture with known isotopic composition which was going through an equilibration chamber where part of the vapour was condensing (see Fig. 2.2). In this case, the quantity of moisture condensing and remaining in the vapour after the equilibration chamber is determined by the saturated vapour pressure at the temperature of the chamber. Finally, the infrared spectrometer precision was not good enough to infer directly the isotopic composition of the residual vapour and they used a cryogenic trapping device to analyse by mass spectrometry the remaining vapour isotopic composition (see section 3.1.2).

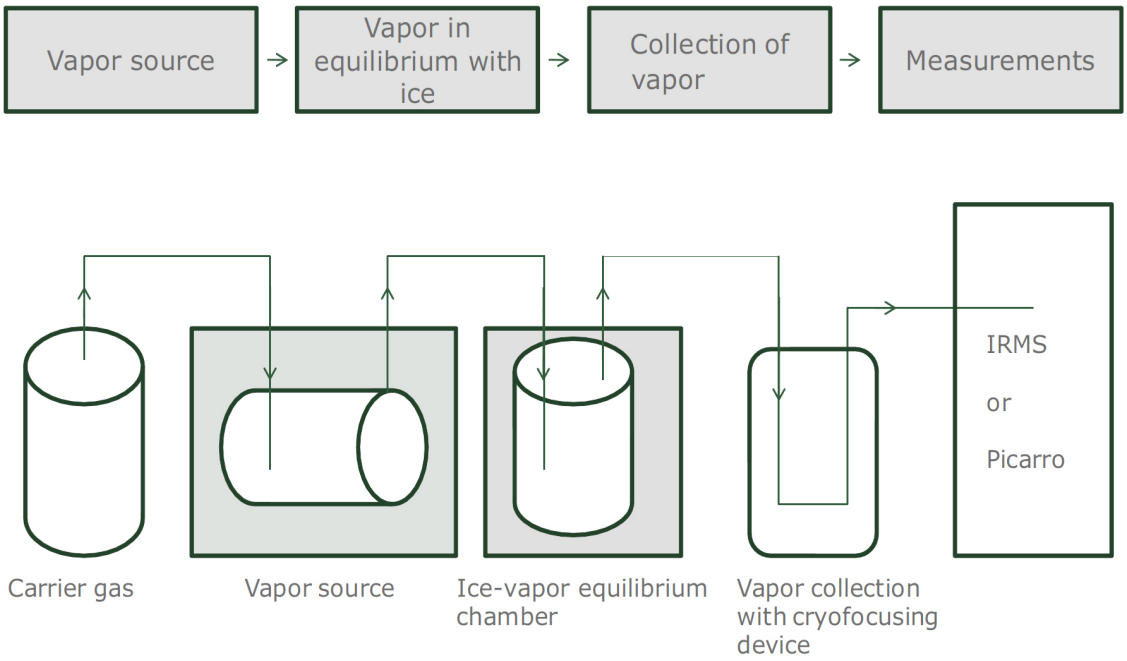

Figure 2.2: Ellehoj et al experimental set up.

The air carrier flux is conserved through the equilibrium chamber but the mass of water vapour changes: $m_{vap}(in) = m_{ice} + m_{vap}(out)$. For the isotopes, the mass conservation

is expressed by: $m_{vap}(in)\delta(in) = m_{ice}\delta_{ice} + m_{vap}(out)\delta(out)$. By combining these two relationships and the equilibrium fractionation definition $\alpha_{eq} = (\delta_{ice}+1)/(\delta_{vap}+1)$, Ellehøj et al. [2013] obtain a measurement of the equilibrium fractionation coefficient from the isotopic composition of the vapour injected to the chamber, out of the equilibration chamber and the thermodynamic conditions:

$$\alpha_{eq} = \frac{\delta_{vap}(in) - \delta_{vap}(out)}{(\delta_{vap}(out)+1)(1-g)} + 1 \tag{2.18}$$

where $g = m_{vap}(out)/m_{vap}(in)$ is directly linked to the temperature and the partial pressure of water of the gas. For this experiment, the set up is imitating a more realistic situation as the phase transition occurs at pressure conditions close to atmospheric ones. In addition, two different instruments were used to measure the isotopic composition of the vapour : an infrared spectrometer and a mass spectrometer. The infrared spectrometer was also used to monitor the permanent regime and therefore estimate how reliable are the experiments results. This experiment suffered some experimental issues, in particular the infrared spectrometer was one of the first generation of Picarro analyser was not able to infer precisely the isotopic composition at low humidity.

The results of these two experimental determinations are presented in Fig. 2.3. The datapoints have been fitted with the theoretical dependence with temperature. Indeed statistical thermodynamics predict a temperature dependency of the equilibrium fractionation in $1/T^2$ (see Eq. 2.15 in section 2.1.3) which is compatible with the experimental determination described above. There is a relatively good agreement between the different determinations in the case of a vapour/liquid transition (not shown) but in the case of a vapour/solid transition, important discrepancies appear, especially in the case of HDO.

Interestingly, theoretical determinations [Van Hook, 1968] were agreeing with Merlivat and Nief [1967] determination of α^D_{eq} but not with Majoube [1971a] determination of α^{18}_{eq}. For α^{18}_{eq}, the experimental determinations of Ellehøj et al. [2013] and Majoube [1971a] remain compatible but differ from theory. The extrapolations of the temperature dependency of the equilibrium fractionation from Ellehøj et al. [2013] and Majoube [1971a] still differ significantly below $-40°$C therefore it is not possible to discriminate one extrapolation over the other. Indeed, the discrepancies in the determination of the equilibrium fractionation coefficient are even more important at low temperatures where no datapoint was gathered and formula are only extrapolated (dashed lines on figure 2.3). All this creates an important uncertainty on the determination of the isotopic fractionation at phase transition at low temperature and is a motivation for the present work: ice

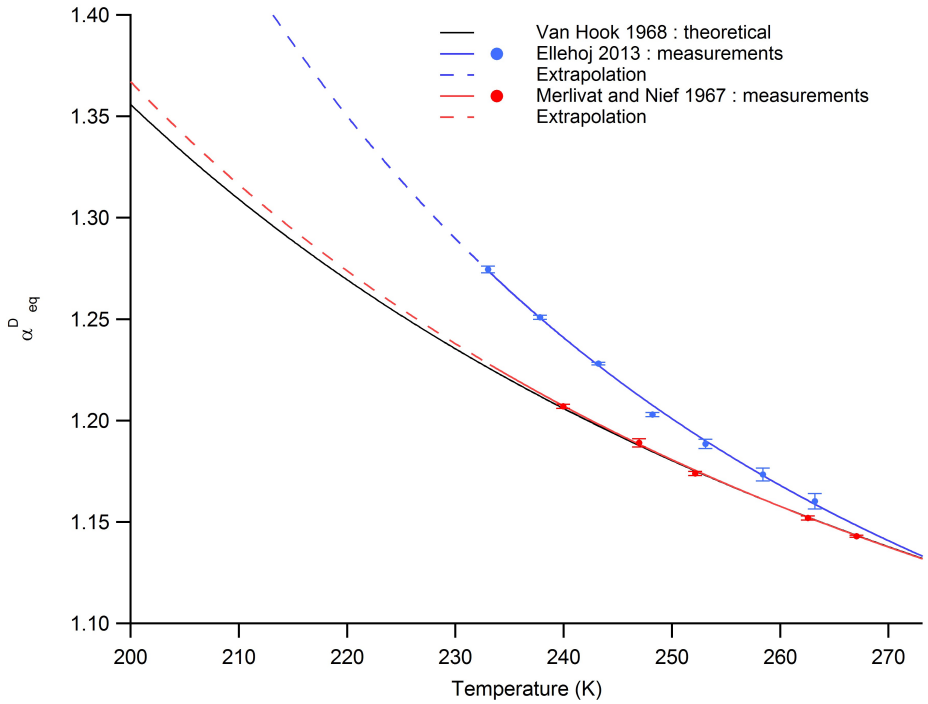

(a)

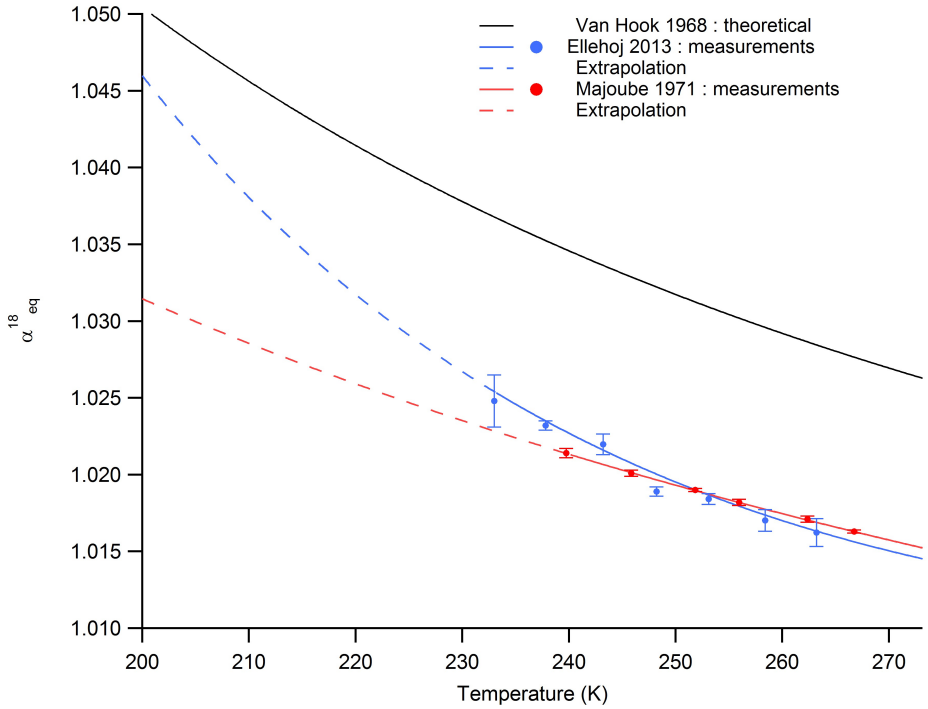

(b)

Figure 2.3: Equilibrium fractionation temperature dependency from theoretical [Van Hook, 1968] and experimental [Merlivat and Nief, 1967; Majoube, 1971a; Ellehøj et al., 2013] for (a) the case of HDO and (b) the case of $H_2^{18}O$

cores are gathered in place usually far below 0 °C and all these uncertainties hamper the interpretation of the isotopic composition reconstructions.

In the case of α_{eq}^{17}, only theoretical determination of the dependence of the equilibrium fractionation coefficient with temperature has been realised by Van Hook [1968] by comparing it to α_{eq}^{18} with a relation characterised by: $\frac{ln\left(\alpha_{eq\,s\,v}^{17}\right)}{ln\left(\alpha_{eq\,s\,v}^{18}\right)} = 0.528$. Barkan and Luz [2005] measured a few points (at 11.4 and 41.5 °C) and found which are in agreement with the calculation from Van Hook [1968]. Landais et al. [2012b] used field data from Greenland and also found a ratio of 0.528 for the ratio of the fractionation coefficients between vapour and ice.

2.2 Out of equilibrium processes

Kinetic fractionation is a term enveloping a wide range of fractionation processes which do not involve two phases at thermodynamic equilibrium. In the case of phase transition, under or over saturated transitions often happen at every step of the water cycle (evaporation in subtropical regions, in the clouds, in the mist, even over the inlandsis). Under or over saturated phase transitions can result from the wind, diffusion or the lack of condensation nucleus. Wind and diffusion also generate fractionation: transport of heavy isotopes is less efficient than the light isotope one.

2.2.1 Evaporation over an isolated water body

First evidences of out of equilibrium fractionation processes were highlighted by Craig et al. [1955, 1963] for wind driven rapid exchanges between a liquid reservoir and the atmospheric boundary layer. In this case, the boundary layer is isolating the ocean/atmosphere interface from the free atmosphere adding additional fractionation effect to the isotopic composition of the moisture escaping the boundary layer.

Craig and Gordon [1965] represent the isotopic fractionation processes during the evaporation and advection of moisture through different layers. First, the surface of the ocean is considered to have an isotopic composition slightly different from the rest of the reservoir. At the interface between the ocean and the atmosphere, equilibrium fractionation is implemented. Above, the atmosphere is separated in 3 layers: a) a laminar layer of height z_m characterised by moderate wind speed, b) a turbulent layer where the vertical gradient of wind speed is located and c) the free atmosphere (see Fig. 2.4). For each of these layers is attributed a difference in the isotope transfer rates and therefore a

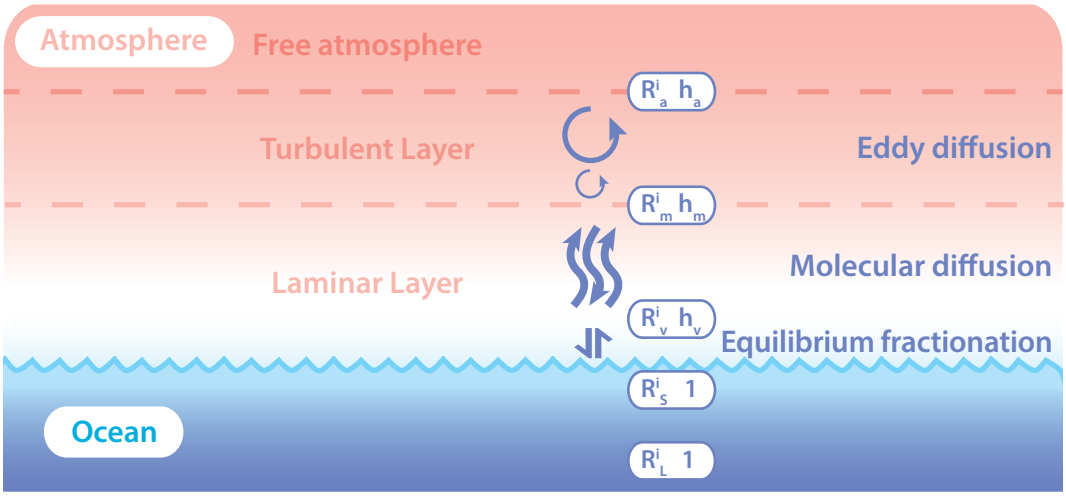

Figure 2.4: Craig and Gordon model illustration, h is the relative humidity of the different levels of the atmosphere and R^i the isotopic ratio

fractionation. In the end, the isotopic composition of the moisture escaping in the free atmosphere is determined by the combined transfer function of diffusion near the ocean surface, equilibrium fractionation at the interface, molecular diffusion in the laminar layer and eddy diffusion in the turbulent layer.

The approach of Craig and Gordon [1965] is to associate with each layer described above a flux for water and heavy isotopes and a resistance by analogy to Ohm's law. For each layer described in Fig. 2.4, we defined the isotopic composition of the layer X by R^i_X, the relative humidity h_X and the resistance ρ^i_X. As on the schematic, the subscript L corresponds to the deep water layer, S to the surface water layer, v to the surface vapour layer, m to the interface between the laminar and the turbulent layer and a to the free atmosphere. Starting from the bottom, in the ocean, the flux of water over the whole column is defined by the evaporation rate at the surface because of the continuity law, therefore :

$$E = -\frac{dN}{dt} = \phi(1-h_v) = \frac{P_{vsat}\chi}{\sqrt{2\pi MkT}}(1-h_v) \tag{2.19}$$

where ϕ is the vaporisation flux, M is the molecular mass, k is the Boltzmann constant, χ is the condensation coefficient. Note that in climate models, ϕ is often calculated differently. The isotope flux on the other hand is not fully determined by what is happening at the surface. Craig and Gordon suppose the existence of the laminar layer under the surface of the ocean where diffusion of heavy isotope in water is responsible of fractionation

with a heavy isotope flux defined by :

$$E_L^i = \frac{(1+E\rho_L^i)R_L - R_S}{\rho_L^i} \tag{2.20}$$

where $\rho_L^i = Z_L/D_L^i C_L$ is the resistance associated with each isotope through the ocean sub-surface layer and R_L and R_S are the isotopic composition of respectively the deep ocean and of the water at the surface. This resistance will mainly be necessary to estimate time constant to reach a stationary state and the gradient of isotopic composition in the water will vanish once the transient state ends.

At the interface, the evaporation rate of the heavy isotopes is driven by the equilibrium fractionation through this formula :

$$E^i = \phi^i(\alpha_{eq}^i R_S^i - h_v R_v^i) = -\frac{dN^i}{dt} \tag{2.21}$$

where $\phi^i = \phi/(\sqrt{M^i/M}\chi/\chi^i)$ is the ratio of the condensation rate of $H_2^{16}O$ to the rate for the pure isotopic species. This provides with interfacial resistances of $1/\phi$ for $H_2^{16}O$ and K/ϕ for heavy isotopes. Above, in the laminar layer, molecular diffusion is limited the fluxes toward the free atmosphere through :

$$E_m = \frac{h_v - h_m}{\rho_m} \tag{2.22}$$

$$E_m^i = \frac{h_v R_v^i - h_m R_m^i}{\rho_m^i} \tag{2.23}$$

where the resistances are defined by $\rho_m = z_m/DC$ and $\rho_m^i = z_m/D^i C$ with C the absolute water vapour concentration and D and D^i the diffusion coefficient of water and heavy isotope in the air respectively.

This model does not provide easy applications in this form as it requires enormous dataset. Indeed, to take advantage of this model, isotopic composition profiles from inside the ocean all the way up to the free atmosphere are necessary. Still, Cappa et al. [2003] study an interesting steady state application of this model. Considering that the ocean and the free atmosphere are two infinite reservoirs, in a permanent regime, there is not accumulation of neither water vapour nor heavy isotopes in the boundary layer. Therefore, the flux of water at the interface between the turbulent layer and the free atmosphere should be equal to the flux at the surface of the ocean:

$$K\frac{h_v - h_a}{z_a C} = \phi(1 - h_v) \tag{2.24}$$

where K is a diffusivity coefficient taking into account both molecular and eddy diffusion in one parametrisation. An analogue equation can be written for the heavy isotopes. In the case of equilibrium, the flux isotopic ratio $R_E = \frac{E^i}{E}$ (not to mix up with an isotopic composition) can be expressed as :

$$R_E = \frac{K^i}{K}\frac{R_{eq} - R_a h_a}{1 - h_a}\frac{1 + K/\phi z}{1 + K^i/\phi^i z} \tag{2.25}$$

with R_{eq} the isotopic composition of the vapour at equilibrium with the ocean. In this case, the effective fractionation is defined by $\alpha_{eff} = R_E/R_L$, leading to:

$$\alpha_{eff} = \frac{R_E}{R_L} = \underbrace{\frac{K^i}{K}\left(\frac{1 + K/\phi z}{1 + K^i/\phi^i z}\right)}_{Kinetic\ effect}\ \underbrace{\left(\frac{\alpha_{eq} - h_a R_a/R_L}{1 - h_a}\right)}_{Equilibrium+humidity\ effect} \tag{2.26}$$

This formulation still is simplified when used in models to describe kinetic effects during the evaporation of water vapour over the ocean. Indeed, in the kinetic effect factor, the terms $K/\phi z$ and $K^i/\phi^i z$ are very small and the fractionation linked to diffusion processes can be expressed as $\alpha^i_{diff} \approx \frac{K^i}{K}$. The diffusion lead fractionation processes will be described later on in section 2.2.4 for the simple molecular diffusion and in section 2.2.5 for the parametrisation of turbulent diffusion in models. In addition, Merlivat and Jouzel [1979] introduced the closure assumption stating that in steady state while the evaporation at the ocean being the lone source of moisture, then the isotopic composition at the top of the free atmosphere is determined by the flux isotopic ratio, thus $R_a = R_E$. Using these two assumptions, it is possible to obtain a simpler expression, closer to what is used in models:

$$\alpha_{eff} = \frac{\alpha_{diff}\left(\alpha_{eq} - h_a \alpha_{eff}\right)}{1 - h_a} \tag{2.27}$$

In order to describe accurately the water cycles involved in the formation of ice in Polar Regions, the transport toward continental Polar Regions is often computed using a Rayleigh distillation.

2.2.2 Rayleigh Distillation

In order to use the isotopic composition of the ice in remote region of Antarctica, we need to calculate the isotopic composition of the moisture transported toward there. After the evaporation at the ocean which can be described using a Craig and Gordon model, we consider the transport of air parcel under moist pseudo-adiabatic conditions: each time condensation occurs (toward both liquid or solid phase), the condensed phase is removed

from the air parcel. In this case, we obtain successive distillation of the water vapour present in the air masses, and in particular an evolution of its isotopic composition. By analogy with chemical binary systems, we can apply the Rayleigh distillation principle [Rayleigh, 1902]. Indeed, every time condensation occurs, the isotopic composition of the condensed phase R_c^i is determined by the temperature (through the equilibrium fractionation α_{eq}^i and the isotopic composition of the vapour R_v^i:

$$R_c^i = \alpha_{eq}^i R_v^i \tag{2.28}$$

As the newly formed condensate is immediately removed from the air parcel, to maintain the mass balance for each isotope, the number of molecules of the isotope i is determined by:

$$R_v^i(t+dt)N(t+dt) = \left(R_v^i(t) - dR_v^i\right)\left(N(t) - dN\right) + \alpha_{eq}^i dN \tag{2.29}$$

where dR_v^i is the variation of isotopic composition of the vapour and dN is the number of molecules of water removed from the system. We therefore obtain a direct expression of the fundamental Rayleigh differential equation:

$$\frac{dR_v^i}{R_v^i} = \left(\alpha_{eq} - 1\right)\frac{dN}{N} \tag{2.30}$$

This equation can be simplified by introducing the fraction of remaining water $f = \dfrac{N}{N_0}$, leading to:

$$d\,ln\,R_v^i = \left(\alpha_{eq}^i - 1\right) d\,ln\,f \tag{2.31}$$

This differential equation is very general and can be applied to a wide range of cases. First, let us consider the case when the fractionation coefficient is constant, originally treated by Rayleigh [1902]. Then, we obtain that the isotopic composition at each step of the distillation is determined directly by $\dfrac{R^i}{R_0^i} = f^{\alpha_{eq}^i - 1}$, where R_0^i is the initial condition when $f = 1$. With this simple equation, as α_{eq}^i is constant, R^i can refer equivalently to the isotopic composition of both the condensed phase or the vapour (as $R_v^i = \alpha_{eq}^i R_p^i$ and $R_{v0}^i = \alpha_{eq}^i R_{p0}^i$ with R_p^i the isotopic composition of the precipitation). Therefore we obtain for the precipitation:

$$\frac{1+\delta_p^i}{1+\delta_{p0}^i} = f^{\alpha_{eq}^i - 1} \tag{2.32}$$

If the fractionation coefficient is rarely constant along an air masses trajectory in particular in Polar Region where the temperature varies a lot, this equation can be used to estimate the local slope of the different isotopic composition (for instance δD as a function of $\delta^{18}O$). Indeed, the fraction of remaining water will be the same for the different isotopes

and the temperature variations can be neglected, the Rayleigh model gives for instance:

$$\frac{1+\delta D}{1+\delta D_0} = \left(\frac{1+\delta^{18}O}{1+\delta^{18}O_0}\right)^{(\alpha_{eq}^D-1)/(\alpha_{eq}^{18}-1)} \tag{2.33}$$

Therefore, the instantaneous slope between δD and $\delta^{18}O$:

$$\frac{d\delta D}{d\delta^{18}O} = \frac{\alpha_{eq}^D - 1}{\alpha_{eq}^{18} - 1}\left(\frac{1+\delta D}{1+\delta^{18}O}\right) \tag{2.34}$$

Fig. 2.5 presents the isotopic composition of precipitation from the GNIP network. Even if important variations in the isotopic fractionation coefficient are created by a wide range of temperature, the isotopic composition relationship between $\delta^{18}O$ and δD can be linear. For instance, Jouzel et al. [1987] found that the observed annual precipitation slope is very close to the one of the meteoric water line: $\delta D = 7.97\,\delta^{18}O + 8.6$ with a correlation coefficient $r = 1.00$. Even though the ratio $\frac{\alpha_{eq}^D - 1}{\alpha_{eq}^{18} - 1}$ keeps rising as the temperature drops, the decrease in $\left(\frac{1+\delta D}{1+\delta^{18}O}\right)$ counterparts this increase. This effect can even provide with slopes lower than 8, for instance in the case of the vapour isotopic composition in Greenland [Steen-Larsen et al., 2013] where the slope is around $6.5‰/‰$ and even way lower as we will see in the case of Antarctica (See chapter 6).

2.2.3 Second order (excess) parameters

This recurrent slope of 8 in precipitation from large part of the world and important correlation between the different isotopic composition motivated for the creation of a second order parameter. In the case of HDO, Dansgaard [1964] defined the d-excess against the composition of $H_2^{18}O$ by:

$$d - excess = \delta D - 8\,\delta^{18}O \tag{2.35}$$

The slope of 8 being predicted by equilibrium fractionation in a Rayleigh distillation, using the d-excess as a second order parameter enables one to see the influence of out of equilibrium processes.

In the case of $H_2^{17}O$, even though a natural linear relationship with $\delta^{18}O$ occurs, a more complex power relationship links more precisely the isotopic ratios [Craig, 1957; Mook and Grootes, 1973] as illustrated by Fig. 2.6:

$$\frac{R^{17}}{R_{SMOW}^{17}} = \left(\frac{R^{18}}{R_{SMOW}^{18}}\right)^{\lambda} \tag{2.36}$$

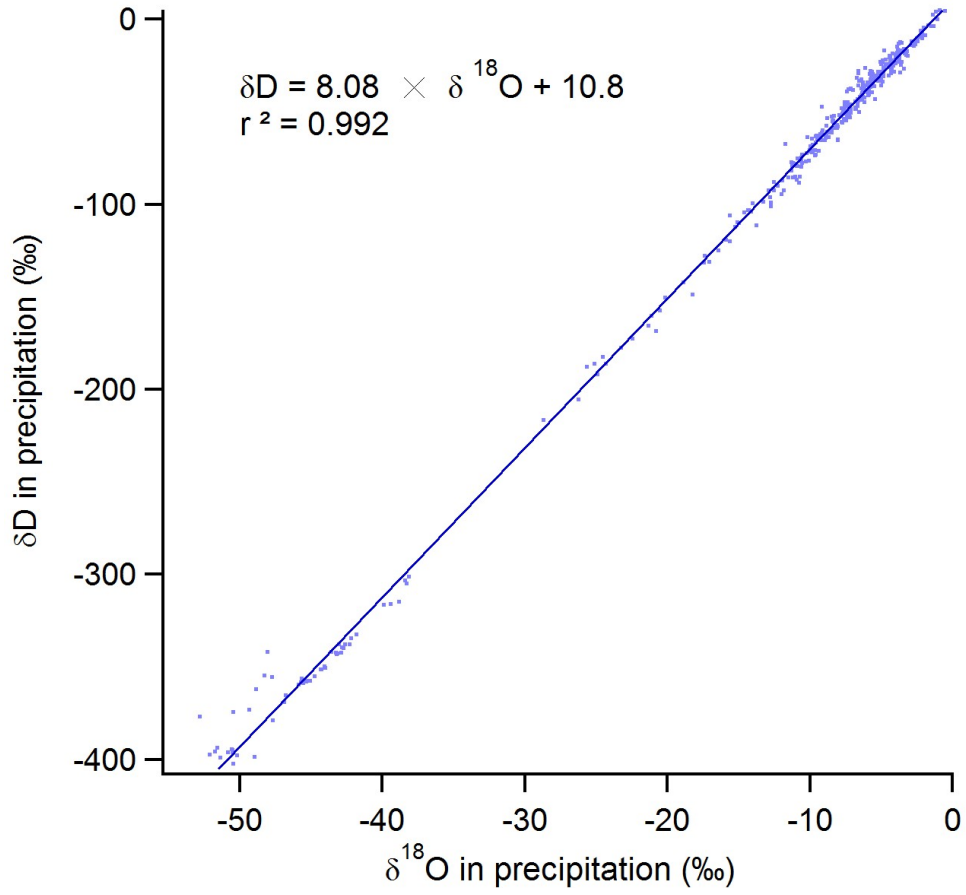

Figure 2.5: Annual δD vs $\delta^{18}O$ in precipitation from the GNIP network [Schotterer et al., 1996]

The observed coefficient in this case has been determined by Meijer and Li [1998] as 0.5281 ± 0.0015. Using this slope, Barkan and Luz [2007] defined $^{17}O-excess$ by analogy with $d-excess$ by:

$$^{17}O-excess = ln\left(\delta^{17}O+1\right) - 0.528\, ln\left(\delta^{18}O+1\right) \tag{2.37}$$

The ratio of logarithm of equilibrium fractionation of $H_2^{17}O$ and $H_2^{18}O$: $ln\,\alpha_{eq}^{17}/ln\,\alpha_{eq}^{18} = 0.529$ (which is independent of temperature) is slightly different from this slope because of the ratio of isotopic compositions in the Rayleigh distillation (as for the slope for the definition of $d-excess$, see Eq. (2.34)). This implies that equilibrium fractionation only slightly affects $^{17}O-excess$ as detailed more in section 5.2.2.

As the ratio of isotopic fractionation $\dfrac{\alpha_{eq}^{D}-1}{\alpha_{eq}^{18}-1}$ strongly depends on the temperature, its values changes and in particular, at low temperature, it can rise up to 10. Therefore, in the Rayleigh distillation, during the advection of air masses, $d-excess$ is affected by

equilibrium fractionation because of the gradient of temperature from the source of the moisture to the site of final precipitation. This makes $d-excess$ an interesting tracer of the processes that affected the moisture during its transport. $^{17}O-excess$ is mostly affected by kinetic effect, for instance during the evaporation, or later on in this manuscript due to molecular or turbulent diffusion. The kinetic fractionation impact on $d-excess$ and $^{17}O-excess$ will be detailed in section 5.2.2.

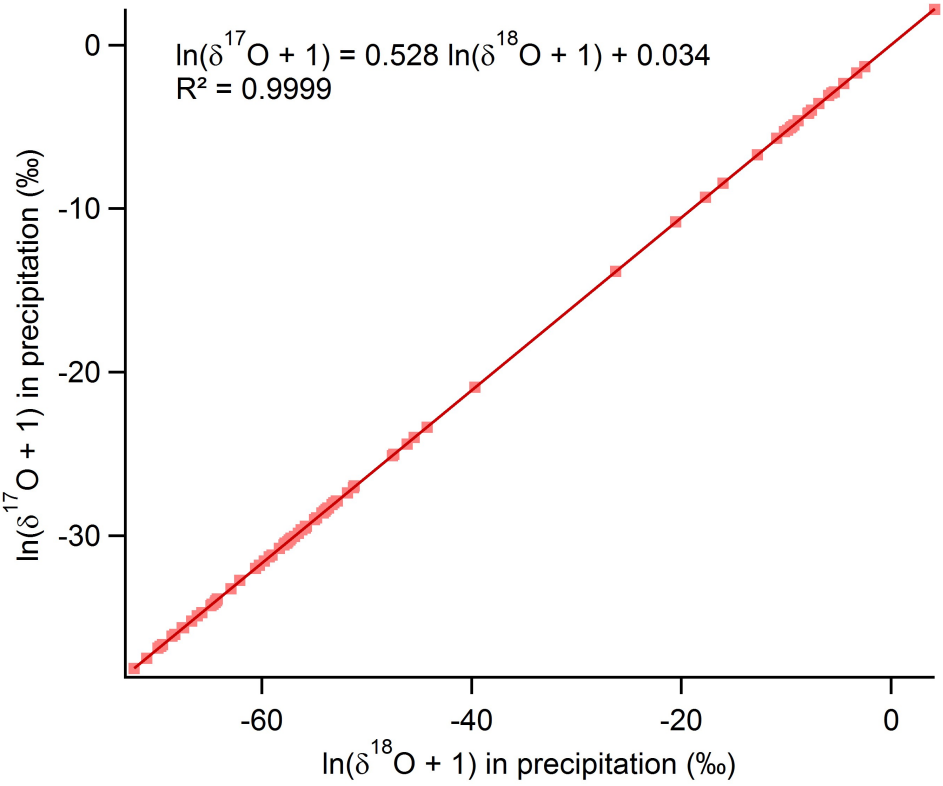

Figure 2.6: $\delta^{17}O$ vs $\delta^{18}O$ in precipitation from Luz and Barkan [2010] and Touzeau et al. [2016]

2.2.4 Molecular diffusion

In the Craig and Gordon approach, there is a diffusive layer characterised by a resistance. Merlivat [1978a] realised an experiment to analyse the difference in diffusion coefficients for the different water isotopes in an air matrix. The principle of the measurement described in the article is to follow the composition of two flasks connected by a pipe. Initially, one is filled with nitrogen and water vapour of known concentration and isotopic composition and the other is filled at the same pressure of nitrogen. The pipe is maintained opened and only molecular diffusion is displacing molecules from one flask to the other. Using a serie of experiments, she obtained values for the relative diffusion

coefficient of :

$$\frac{D_{HDO}}{D_{H_2O}} = 0.9755 \pm 0.0009 \tag{2.38}$$

$$\frac{D_{H_2^{18}O}}{D_{H_2O}} = 0.9723 \pm 0.0007 \tag{2.39}$$

The experiment were realised in nitrogen and not in dry air, therefore a model was used to estimate the values above. Kinetic theory of gases in a rigid elastic spherical molecules model [Rosenboum, 1941] predicts that:

$$\frac{D^i}{D} = \left(\frac{M}{M^i}\frac{M^i + M^{mat}}{M + M^{mat}}\right)^{1/2} \left(\frac{\Gamma + \Gamma^{mat}}{\Gamma^i + \Gamma^{mat}}\right)^2 \tag{2.40}$$

where M, M^i and M^{mat} are the molecular masses of the main isotope, the heavy isotope and the atmospheric matrix respectively and Γ, Γ^i and Γ^{mat} their respective diameters. To interpret quantitatively the data, Merlivat had to introduce differences in the molecular diameters of the different species calculated from the Virial coefficients. As no values for these diameters existed in the literature, only qualitative validations of these could be realised. This diameter modification has a stronger effect in the case of HDO than in the case of $H_2^{18}O$.

Another determination of diffusion coefficient was realised by Cappa et al. [2003] with an independent method in which a stream of air was circulating above a water surface. The results differ a lot as they found :

$$\frac{D_{HDO}}{D_{H_2O}} = 0.9839 \tag{2.41}$$

$$\frac{D_{H_2^{18}O}}{D_{H_2O}} = 0.9691 \tag{2.42}$$

If Cappa et al. [2003] claim that the evaporative cooling of the liquid surface is necessary to estimate the fractionation and argue against the "diameter effect" highlighted by Merlivat, the argument does not really work to compare to Merlivat's results as no evaporation took place. In addition, new measurements of Luz et al. [2009] validated the results of Merlivat [1978a] and additionally highlighted the impact of temperature over the ratio of diffusion coefficients.

As the "speed" associated with the diffusion of the different isotopes is different, fractionation occurs during the molecular diffusion processes and an example of the impact will be detailed in section 2.2.6.

2.2.5 Turbulent diffusion

In numerous situations, molecular diffusion is completely erased by turbulence. In this case, it is necessary to consider the impact of eddy diffusion, or turbulent diffusion. Merlivat and Jouzel [1979] parametrised the impact of the combination of molecular diffusion and turbulence on isotopic fractionation. Using wind tunnel experiments [Merlivat, 1978b] and a theoreotical evaporation model [Brutsaert, 1975], they highlighted the impact of windspeed on the relative contribution from molecular diffusion to kinetic fractionation. In particular, Merlivat and Jouzel [1979] framework takes into account a discontinuity in the fractionation coefficients between a smooth and a rough regime as illustrated on Fig. 2.7.

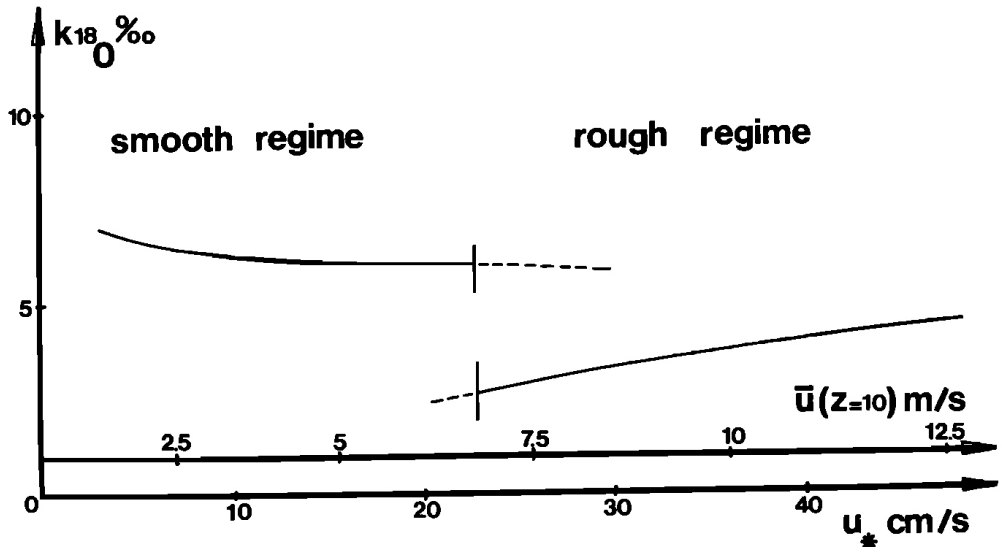

Figure 2.7: Variation of kinetic fractionation coefficient of $H_2^{18}O$ with wind speed, a discontinuity occurs around $7\,m\,s^{-1}$ [Merlivat and Jouzel, 1979]

This framework is obtained by distinguishing different cases for kinetic fractionation according to the wind speed:

- the static case, if wind speed tend to $0\,m\,s^{-1}$, only molecular diffusion impacts the kinetic fractionation factor and we obtain like in previous section $\alpha_{diff} = \frac{D^i}{D}$
- the laminar case, when wind speed is inferior to $5\,m\,s^{-1}$, part of the molecular diffusion impact is erased and $\alpha_{diff} = \left(\frac{D^i}{D}\right)^{2/3}$
- turbulent case, when wind speed is superior to $5\,m\,s^{-1}$, a larger part of the molecular diffusion impact is erased and $\alpha_{diff} = \left(\frac{D^i}{D}\right)^{1/3}$

A large number of studies have explored different parametrisations of $\alpha_{diff} = \left(\frac{D^i}{D}\right)^n$ with different values of n from pure turbulent diffusion ($n = 0$) to pure molecular diffusion ($n = 1$) [Cappa et al., 2003; Barkan and Luz, 2007; Uemura et al., 2010b].

We have seen the macroscopic impact of diffusion led fractionation in the Craig and Gordon model (section 2.2.1), it also impacts the cloud microphysics and in particular the snow formation which has a strong impact in paleoclimate studies from Polar ice cores.

2.2.6 Snow formation

In remote Polar Regions, the density of condensation nuclei is low enough to enable strong supersaturation to occur. In this case, once some ice crystals have been formed in the cloud, they behave as condensation nuclei and there is a transfer of molecules from the vapour to the ice. This transfer is limited by the diffusion toward the condensation nuclei and not by the moisture amount nor the available energy. As the diffusion "speed" of the heavy isotopes ($H_2^{18}O$, $H_2^{17}O$ and HDO) is limited compared to the main isotope $H_2^{16}O$, this results in a kinetic fractionation during the formation of the snow flakes in the clouds. Jouzel and Merlivat [1984] provide with a theoretical framework to estimate the fractionation associated with diffusion in this context. They consider a flux of water molecule toward the surface directly proportional to $D(p_v - p_{sat})$ where D is the diffusivity, p_v the partial pressure and p_{sat} the saturated vapour pressure over ice. For the heavy isotopes, a similar expression can be written with in addition a relationship between the heavy isotope partial pressure to the vapour partial pressure:

$$p_v^i = p_v R_{SMOW}^i \left(1 + \delta_v^i\right) \tag{2.43}$$

and between the heavy isotope saturated vapour pressure and the water saturated vapour pressure:

$$p_{sat}^i = p_{sat} R_{SMOW}^i \frac{1 + \delta_{ice}^i}{\alpha_{eq}^i} \tag{2.44}$$

As the diffusion of molecules in ice is extremely low, the composition of each ice layer is considered to be fixed by the ratio of fluxes of heavy and light isotopes toward the ice:

$$1 + \delta_{ice}^i = \frac{1}{R_{SMOW}^i} \frac{\Phi^i}{\Phi} \tag{2.45}$$

where Φ and Φ^i are the fluxes of molecules of water and of heavy isotope i respectively. This brings to:

$$1+\delta^i_{ice} = \frac{D^i\left(p_v(1+\delta^i_v) - p_{sat}(1+\delta^i_{ice})/\alpha^i_{eq}\right)}{D(p_v - p_{sat})} \tag{2.46}$$

From this equation, they obtain an effective fractionation coefficient taking into account the equilibrium fractionation at the phase transition and the kinetic effect due to diffusion toward the ice such as:

$$\alpha^i_{eff} = \frac{\alpha^i_{eq} S_i}{\alpha^i_{eq}\frac{D}{D^i}(S_i - 1) + 1} \tag{2.47}$$

where S_i is the supersaturation against ice. If this equation is widely used in models including water isotopes, it requires an estimation of the supersaturation which is a critical point. Jouzel and Merlivat [1984] use a parametrisation of the supersaturation against temperature such as $S_i = 0.99 - 0.006\,T$. This model has been tested in a cloud chamber experiment and will be described in section 5.2.2.

2.3 Toward an isotopic paleothermometer

All these processes will affect the isotopic composition of all the water cycle (Fig. 2.8). We already saw in section 2.2.1 one description of fractionation occuring during the evaporation at mid-latitudes. During the advection toward Polar Regions, isotopic composition of precipitation decrease poleward due to the successive distillations under colder and colder conditions. We will first describe how Rayleigh distillation (section 2.2.2) can be directly applied to meteoric water and then how all this different processes enable estimate of past temperature from ice isotopic composition.

2.3.1 Application of the Rayleigh distillation to meteoric waters

On the full scale of the water cycle, the formulas described in section 2.2.2 are not able to describe the distillation of the moisture. Indeed, the temperature gradient along the trajectory of the air masses from the evaporation site in the sub-tropics toward remote Polar Regions is such that the fractionation coefficient cannot be considered constant anymore. In the formation of meteoric water in more realistic case, it is necessary to consider a variable fractionation coefficient. Dansgaard [1964] proposes a discrete segmentation of the cooling process using the mean temperature of each stage of the cooling process to provide with an estimate of the mean fractionation faced by the moisture.

The major biases of this approach are first that it does not take into account the intermittency of the precipitation and second that only one source of moisture is taken into

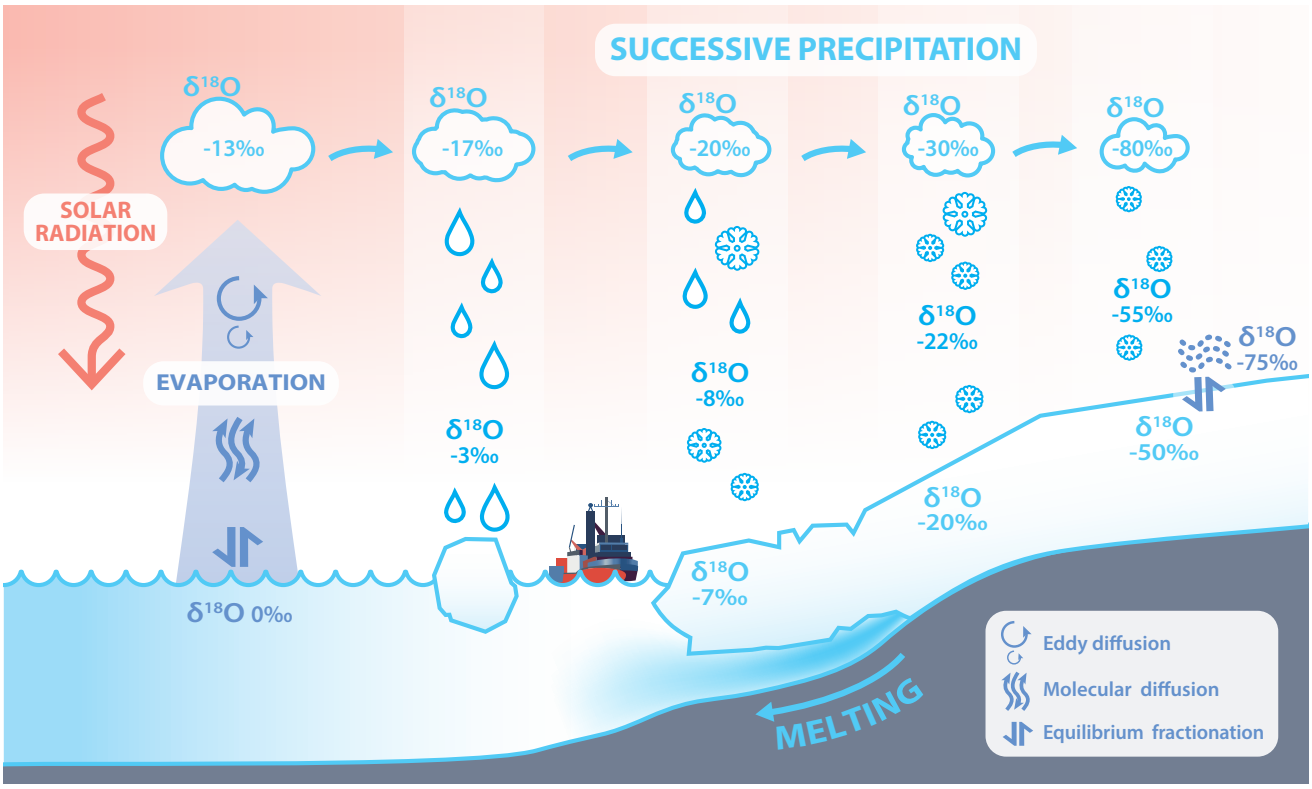

Figure 2.8: Scheme of the isotopic fractionation associated with each step of the water cycle toward Antarctica

account. In the case of a real air parcel, models can compute Rayleigh distillation calculations taking into account the real temperature for each condensation event. To compute the impact of different sources for the vapour, it is necessary to realise back-trajectory of the air masses to estimate the relative importance of the different inputs of moisture. At LSCE, Ciais and Jouzel [1994] developed the Mixed Cloud Isotopic Model (MCIM) which computes the successive distillation in the cloud at different temperatures along the air masses trajectories. It takes into account the micro-physical properties, in particular mixed phase conditions (possibility of water under vapour, liquid and ice phases in the air parcel) and kinetic fractionation. The mixed-phase is handled by distinguishing 3 different regimes. First, above a certain threshold of temperature ($T > T_S$), only liquid and vapour can exist in the air parcel. This results in saturated vapour pressure being calculated above liquid water and fractionation at the phase using the liquid-vapour equilibrium fractionation coefficient. Then, below T_S, ice can appear in the cloud but liquid droplets can still exist. This is called a Bergeron-Findeisen regime [Bergeron, 1935]. The vapour partial pressure is in between the saturated vapour pressure of the liquid droplets P^L_{sat} and of the ice crystals P^I_{sat}. There is a partial evaporation of the droplets into the vapour which condensates into ice crystals, both phase transition associated with fractionation. Finally,

below a second threshold T_W, the liquid phase completely disappears.

By computing the isotopic fractionation (equilibrium and kinetic) at each step of the water cycle, it is possible to compute the evolution of the vapour isotopic composition all along the hydrological cycle, and therefore to estimate the precipitation isotopic composition. It is possible to include realistic temperature variations, for instance obtained from back trajectory analysis. Nevertheless, the MCIM (and globally Rayleigh type models) does not take into account neither vertical mixing with (unsaturated) air masses along the water mass trajectory [Winkler, 2012] nor mixing of several air masses of different origins.

2.3.2 Isotopic thermometer

The foundation of isotopic thermometry is based on the work of Dansgaard [1964] and Lorius et al. [1969] who have been able to highlight the relationship between isotopic composition of snow and the local mean annual temperature in Polar Region. This method is part of a long list of methods using ice core to reconstruct past climates. Using the isotopic composition of samples obtained during transect in both Antarctica and Greenland, they obtained a linear relationship between the yearly average δ isotopic composition and the average local temperature. Different slopes are obtained according to the region (Fig. 2.9), indeed the air masses have different origins and histories which are reflected by the slope of the linear relationship. Jouzel et al. [1987] used the spatial slope to estimate the temporal variations of temperature from Vostok ice core isotopic composition.

The use of stable water isotopes to infer temperature at long time scale is still not so direct. Jouzel et al. [1997] show using simulations that the temporal slopes are significantly lower than the spatial slopes obtained at present day and does not remain constant over time. The variations in the slope of isotopic composition vs temperature have been linked to different processes. First, differences in the seasonality of precipitation between glacial and interglacial periods sensibly affects the relationship between temperature and isotopic composition in Greenland [Fawcett et al., 1997; Krinner et al., 1997]. If in interglacial periods, the precipitation occurs regularly through the whole year, during glacial period, they seem to only occur during summer due to a modification of the storm track trajectory. This results in recording a temperature signal biased toward summer conditions in glacial periods in Greenland and therefore underestimate the variations of temperature between interglacial and glacial period. Modifications in the large scale circulation can also imply the mixing of different moisture sources [Charles et al., 1994], a complete change of the moisture sources [Sime et al., 2013] or the conditions in which they are generated [Boyle,

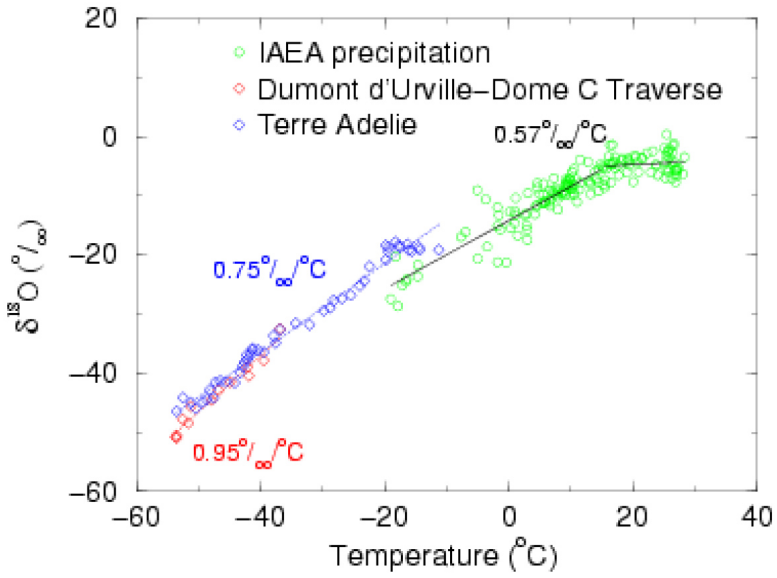

Figure 2.9: Isotopic composition of the precipitation compared to the yearly average of the temperature of the site.

1997].

The use of second order parameters like $d-excess$ or $^{17}O-excess$ can enable to estimate the modifications of the source climatic conditions as they preserve the information on the evaporation conditions [Landais et al., 2008; Jouzel et al., 2013]. For instance, using the impact of kinetic processes over $d-excess$, Gat [1996] has been able to estimate the relative humidity over the ocean during the evaporation and Risi et al. [2008] have been able to estimate the re-evaporation in the convective zone. $d-excess$ can also be used to track down the kinetic impact due to diffusion during the cloud formation and help tune supersaturation spatial evolution [Ciais and Jouzel, 1994; Werner et al., 2011] to implement in Eq. (2.47). Vimeux et al. [1999] also used $d-excess$ to estimate changes in the moisture sources temperature conditions in the Vostok ice core associated with obliquity's variations over the last 150 000 years. The interpretation of $d-excess$ signal still remains challenging as it is affected by several factors such as the relative humidity of the source, the local temperature in Polar Region [Jouzel et al., 2007] and the path followed by the water masses [Bonne et al., 2015].

$^{17}O-excess$ is also controlled by relative humidity during evaporation and re-evaporation processes and is not redundant compared to $d-excess$. Indeed, at higher latitudes, they show different variations because the relationship between $\delta^{17}O$ and $\delta^{18}O$ is not temper-

ature dependent whereas the one between δD and $\delta^{18}O$ is [Luz et al., 2009; Majoube, 1971b,a], $^{17}O-excess$ keeps the signature of relative humidity acquired at low latitudes as illustrated in Fig. 2.10 [Luz and Barkan, 2010]. In very isolated regions in East Antarctica, $^{17}O-excess$ also depends of the condensation temperature as the influence of kinetic fractionation increases when temperature decreases [Landais et al., 2012a; Winkler et al., 2012].

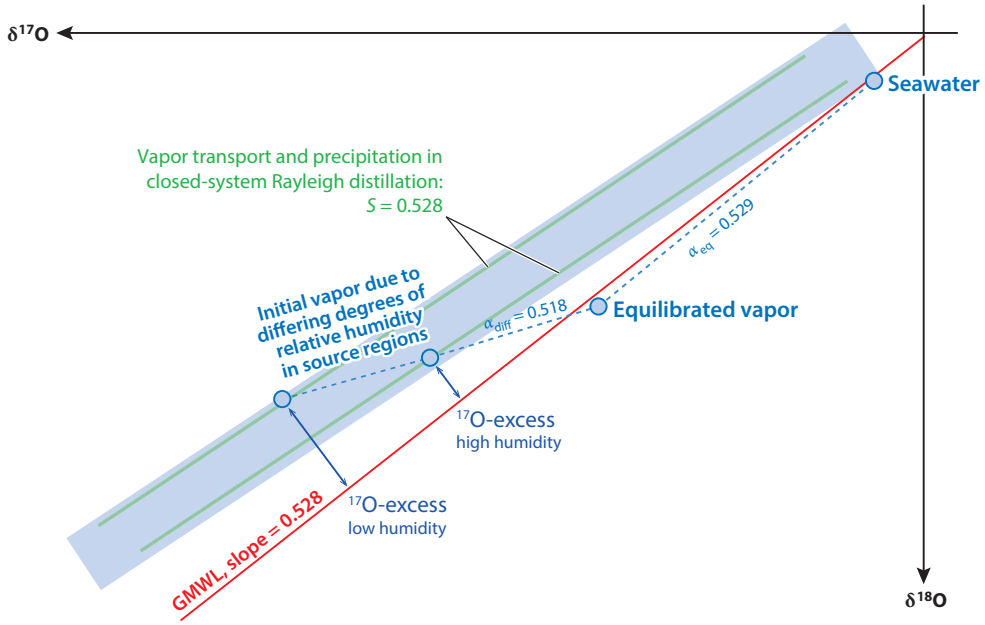

Figure 2.10: Schematic illustration of the impact of kinetic fractionation on $^{17}O-excess$ at evaporation: during evaporation, kinetic fractionation due to the difference of diffusivities acting with a slope of 0.518 creates a positive $^{17}O-excess$ signal; the amplitude of the kinetic fractionation at the evaporation is directly linked to the local humidity. Modified from Bao et al. [2016].

Efficient isotopic thermometry relies first on good measurement of the isotopic composition. In particular, the use of second order parameters, especially $^{17}O-excess$ requires 2 additional orders of magnitude of precision on the measurements. If new infrared spectrometer now measures $^{17}O-excess$, we will see in the next section that there still are some important bias to be corrected and therefore that mass spectrometry is still relevant. It is also necessary to have an efficient and relevant theoretical framework to describe the impact on isotopic composition of each step of the water cycles as described in Fig. 2.8. In this manuscript, we will mainly focus on the processes occurring at low temperature, from down to earth detailed physical studies of the isotopic thermodynamic to its impact in natural conditions.

Chapter 3

How to measure water stable isotopic composition ?

Since the first studies analysing the ratio between heavy and light water isotopes [Dole, 1935; Epstein and Mayeda, 1953], some evolutions took place into the analysis of the isotopic composition. The evolution of the methods and of their power of measurement enabled through the years to broaden the fields of applications of water isotopes. Nowadays, isotopic composition of water through the entire hydrological cycles is being measured. In glaciology, the main application is obviously for past climate reconstruction from the isotopic composition of the ice from Polar and Alpine ice cores.

Still, as we saw in the previous section, in order to understand the processes leading to the formation of the ice, measuring isotopic composition upstream to formation precipitation is really important. Measurements in the vapour has been done at the mid-latitudes since the fifties [Craig et al., 1955; Craig and Gordon, 1965] but remains challenging in Polar Regions where the humidity is lower. In the precipitation, with the expansion of the Polar Programs in the late fifties and in the sixties, a few precursor studies highlighted the importance of having reliable measurements techniques [Craig, 1961; Dansgaard, 1964; Lorius et al., 1969].

In this section, we will describe how to measure isotopic composition of water samples. These samples can be obtained from water directly but also from cryogenic trapping of the vapour or melting pieces of ice. First, we will describe mass spectrometry, the reference method to measure isotopic composition of a water sample. Then, we will describe how new developments in optical spectroscopy now enable measurements with similar precision than mass spectrometry and much simpler experimental protocols.

3.1 Mass spectrometry

3.1.1 General principle

The most commonly used mass spectrometry method for stable isotopes application uses momentum focusing to separate the different isotopes [Criss, 1999]. Using a high voltage source (tens of kilovolts), the molecules are split in ions of charge q and accelerated with a uniform distribution of energy. The kinetic energy of the particles in the beam is $mv^2/2 = qV$ where $\vec{v}$, m and q are the velocity, the mass and the charge of the particles respectively and V is the voltage of the source. The beam of molecules goes through an orthogonally oriented magnetic field $\vec{B}$ as illustrated on Fig. 3.1.

The moving ions are thus affected by the Lorentz force:

$$\vec{F} = q\left(\vec{E} + \vec{v} \times \vec{B}\right) \tag{3.1}$$

where $\vec{E}$ and $\vec{B}$ are the electric and magnetic fields respectively. The path followed by the ions is defined by a radius of curvature $r = mv/qB$. Using the kinetic energy given to the ion by the source, the radius of curvature can be expressed as:

$$r = \sqrt{\frac{2mV}{qB^2}} \tag{3.2}$$

If the charge remains the same for all the particles, the beam is split into several beams by particles mass. All the isotopes of the same mass share the same radius of curvature. By collecting the ions with collectors at the end of the different paths, one can count the relative quantity of ions with the same mass-to-charge ratio.

In the case of the water molecule, it is not possible to analyse the water itself. Water's highly adsorbing behaviour prevents this from being an efficient measurement method. Chemical transfer lines have been developed in order to transfer the atomic constituents of water into less "sticky" molecules, such as O_2, H_2, or CO_2.

3.1.2 Preparation of water samples

The measurement of δD of water was conventionally realised by converting water to dihydrogen by pyrolysis or reduction. Different reducing agents have been used such as uranium, zinc, carbon, magnesium, tungsten, or chromium, as listed in the review of Wong and Klein [1986]. In all cases, the samples are completely reduced into dihydrogen

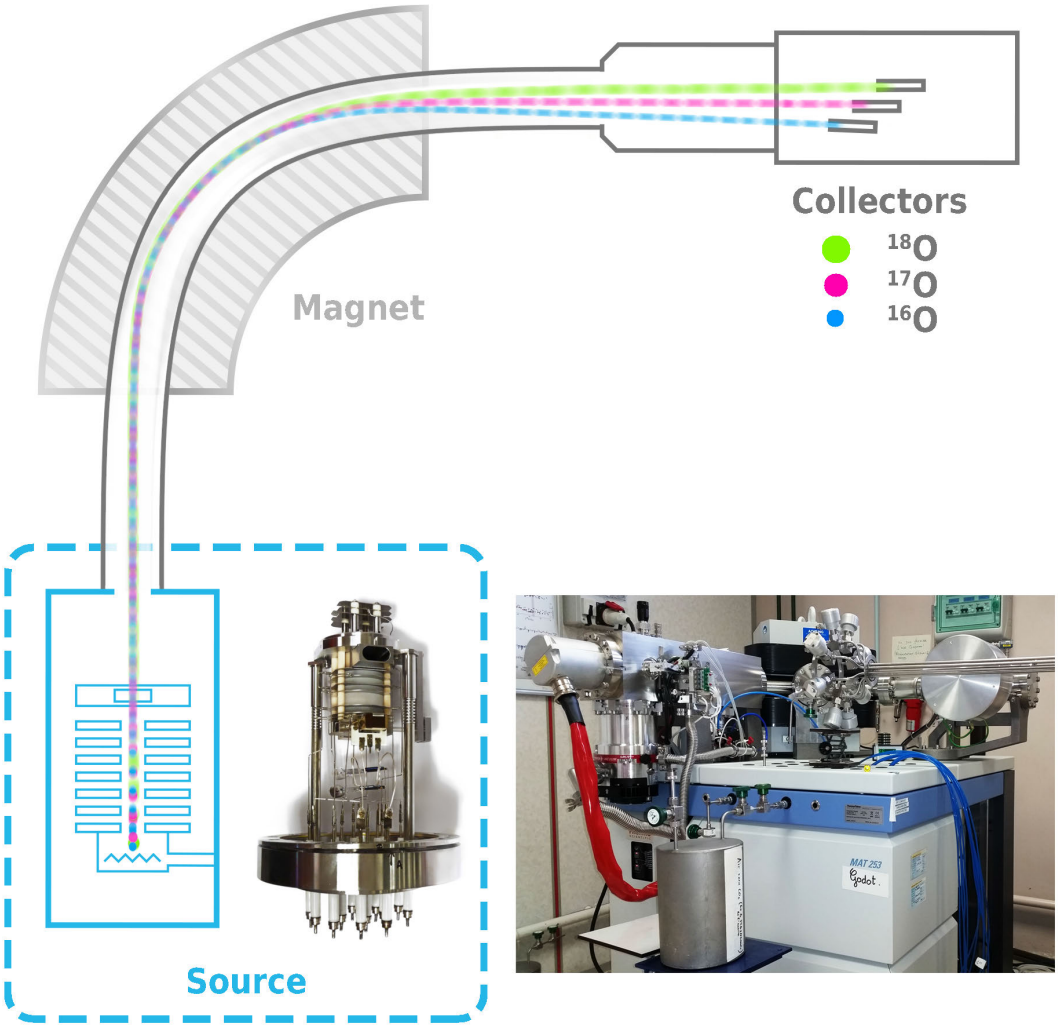

Figure 3.1: Schematic of a mass spectrometer such as a MAT 253 used to measure the isotopic composition of oxygen isotopes at LSCE. A magnet deflects the beam of ions toward cups, the heavier ions are less deflected and therefore, it is possible to count the ions by ratio mass over charge.

preventing any fractionation to occur. For instance, the reduction over hot chromium powder (around 1080°C) proceeds according to the chemical equation:

$$Cr + 2H_2O(HDO) \rightarrow CrO_2 + 2H_2(HD) \tag{3.3}$$

This method provides a precision better than 0.5‰ and a linear response from +23‰ to -428‰ [Donnelly et al., 2001]. At the LSCE, the measurement of δD was realised using a reduction over Uranium plates in an oven at 600°C. The apparatus developped by Nief and Botter [1958] could measure relative variations of δD with a precision of

0.6‰, which is very close to the best performances still obtained nowadays by infrared spectroscopy (see section 3.2).

The measurement of $\delta^{18}O$ has classically been realised by equilibration of water with CO_2 [Epstein and Mayeda, 1953] and can reach a precision of 0.05‰. The method is rather slow (from several hours to several days depending on the catalyst) and cannot usually be used to measure the $H_2^{17}O$ composition: indeed $^{17}O^{12}C^{16}O$ has the same weight $^{16}O^{13}C^{16}O$ but is much more abundant. Note that by using CO_2 of known isotopic composition, Uemura et al. [2010a] were able to measure $^{17}O-excess$ by equilibration with a limited precision of 184 ppm.

Accurate measurements of both $\delta^{18}O$ and $\delta^{17}O$ can be achieved by a reaction of fluorination at 370°C [Barkan and Luz, 2005] :

$$4CoF_3 + 2H_2O \rightarrow 4CoF_2 + 4HF + O_2 \tag{3.4}$$

The reaction is proceeded to completion, HF is trapped with liquid nitrogen at the exit of the reactor and the produced O_2 is trapped to be analysed later on a dual inlet mass spectrometer. Precision of this method have been estimated to be 0.13‰ for $\delta^{18}O$ and 5 ppm for $^{17}O-excess$ [Landais et al., 2006]. Note that in the case of fluorination, the same line is used for preparing and measuring the sample for both the measurement of $\delta^{18}O$ and $\delta^{17}O$, the associated errors are therefore not independent. This allows a precision on the $^{17}O-excess$ two orders of magnitude lower than for $\delta^{18}O$ and $\delta^{17}O$ individually. In the case of the determination of $d-excess$ by mass spectrometry, different independent methods are used for measuring δD and $\delta^{18}O$, resulting in the errors of both measurements cumulating.

In addition to the chemical transfers mentioned above, in the case of water vapour, cryogenic trapping is necessary to measure the water vapour isotopic composition by mass spectrometry [Craig and Gordon, 1965]. Such methods transfer a significant amount of the vapour toward ice (less than 13 ppm of the vapour is lost [Helliker et al., 2002]), and therefore produce ice samples with the same isotopic composition as the vapour. This method has been proven reliable in both temperate regions and polar regions [Craig and Gordon, 1965; Angert et al., 2008; Uemura et al., 2010b; Steen-Larsen et al., 2013]. For a more precise description of cryogenic trapping, refer to section 6.2 .

3.1.3 Calibration

Mass spectrometry measurements can be biased due to different experimental artefacts. First, drift of the environmental conditions, mainly the temperature of the laboratory, impacts directly the measurements. Indeed, mass spectrometers rely on counting the number of molecules at selected mass-to-charge ratios, as the ionisation efficiency is highly sensitive to the environmental conditions, drift of the instrument can occur. The use of Dual Inlet methods brings a first correction to the data: along with the gas sample, a gas of known isotopic composition is systematically analysed, such that environmental changes will affect roughly equally the measurement of these two samples. The relative difference in isotopic composition between the two samples will therefore be free of the influence of the drift.

If this method enables to cancel short term environmental conditions variations, it does not account for (1) preparation of the gas sample through the extraction line, (2) daily variations of the linearity of the mass spectrometer, and (3) the zero enrichment of the mass spectrometer. To solve points (1) and (2), it is necessary to realise daily calibration of the spectrometer with water samples of known isotopic composition, which are prepared the same way as the sample, against the SMOW-SLAP scale. For the calibration to be efficient, it is important to have a standard of similar isotopic composition in $\delta^{18}O$: a big difference in isotopic composition creates memory effects that can lead to important artefacts in the excess values. For this reason, LSCE has developed a large collection of working standards as described in Table 3.1.

Table 3.1: Values of working standards at LSCE reported against V-SMOW, respective analytical uncertainties ± 0.05 ‰, ± 0.1 ‰ and $\pm 6\,ppm$ for $\delta^{18}O$, δD and $^{17}O-excess$.

Standard	$\delta^{18}O$ (‰)	δD (‰)	$^{17}O-excess$ (ppm)
ORSMOW 3	$+0.4$	$+2.4$	0
EPB 7	-7.44	-50.4	18
ROSS 5	-18.64	-144.3	40
D57 1	-32.68	-286	38
NEEM 4	-33.56	-310.6	40
Talos 2	-39.15	-310.6	25
OC 3	-54.05	-424.1	18
SLAP 2	-55.5	-427.5	0

In the case of $^{17}O-excess$, the absolute offset of the mass spectrometer is crucial because of the very small signals (of the order of tenth of ppm). Figure 3.2 shows the differ-

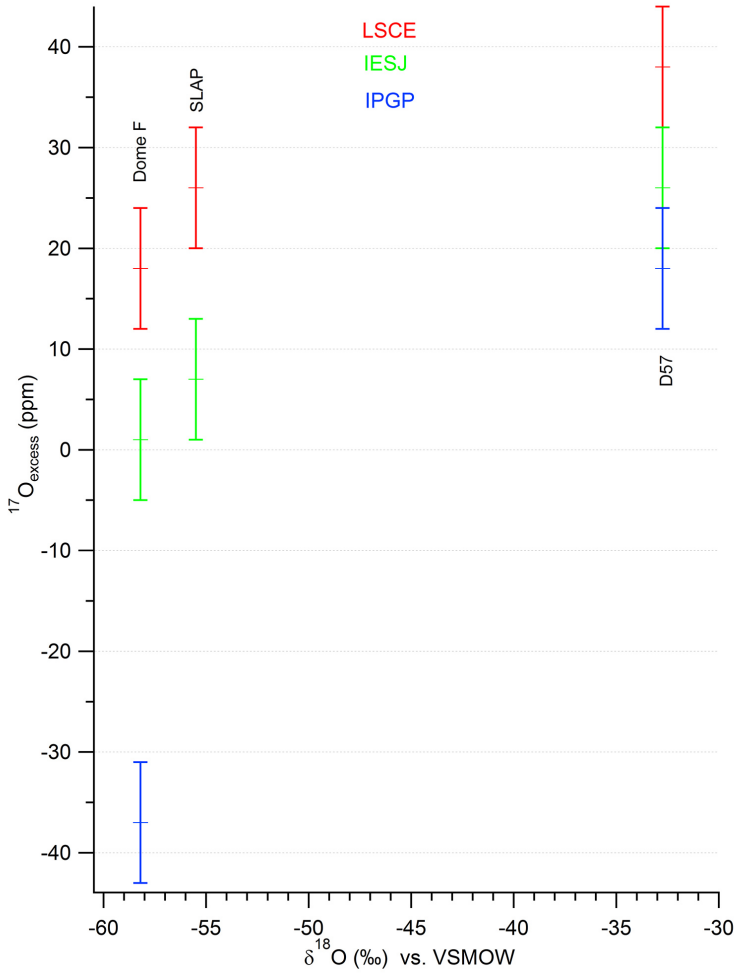

Figure 3.2: $^{17}O-excess$ values vs $\delta^{18}O$ for water standards measured at LSCE, IESJ and IPGP for intercalibration (Winkler, 2012)

ence between three mass spectrometers measuring the same water samples at the LSCE, IESJ (Institute of Earth Science of Jerusalem, Israel), and IPGP (Institut de Physique du Globe de Paris, France). For low $\delta^{18}O$ samples, we observe a large spread of values found for the same standard through the different spectrometers. Landais et al. [2014] show that assigning the $^{17}O-excess$ value of SLAP to $0\,ppm$ provides a second point for the calibration between spectrometers leading to an agreement between the different spectrometers and thus, enabling to obtain an absolute measurement relevant comparison between isotopic modelling and measurements [Schoenemann et al., 2013].

3.2 Infrared spectroscopy

The main alternative to mass spectrometry is optical spectroscopy. There are several techniques but all methods are based on the light/matter interactions at the microscopic level. In the case of atmospheric science, most of the instruments analysing isotopes use a transparent window of the atmosphere in the near-infrared region. Here, after an overview of the main principles of infrared spectroscopy, we will first describe the physical principle of light absorption. Then, we will describe 2 of the state of the art methods nowadays used to realise trace detection, and in particular in the case of water isotopes: Optical Feedback Cavity Enhanced Absorption Spectroscopy (OFCEAS), developed in LIPHY, and Cavity Ring Down Spectroscopy (CRDS), a technique typically used by Picarro instruments. These developments will serve as an technical introduction for next chapter. Finally, we will describe why calibration is as important for infrared spectroscopy as for mass spectrometry.

3.2.1 Overview

In this section, we provide a general overview of infrared spectroscopy in order to understand the scaling of the different variables involved in the technique, the physical point of view how infrared spectroscopy works will be detailed in the next section. Optical spectroscopy relies on light being absorbed by the molecules or the atoms. This measurement method is non-destructive (no chemical transfer required and the measurement is in theory not affecting the measurement; practically, adsorption of water still affects the samples).

This light absorption is characterised by absorption peaks at different wavelengths as illustrated in Fig. 3.3. For trace detection in general and water isotope measurement in particular, the measured elements are diluted in an air matrix. In the case of water, the concentration of water molecules is from a few ppm (Polar Region, stratosphere) to a few $\%$ (tropics). As we saw in section 2.1.2, natural abundances of heavy isotopes in water are of the order of hundreds of ppm. These concentrations result in the need of (1) a very sensitive method able to detect molecules at concentration down to 10^{-10} of the total number of molecules ($1/10^4$ of the water molecules themselves $1/10^6$ of the total number of molecules), (2) with a very high dynamic as the abundance of different isotopes can be different with a factor of 10^4, (3) in a spectral range where the air (nitrogen) matrix is transparent but also all other trace elements and (4) with a precision of the order of the ppm on each concentration to provide a relevant $^{17}O-excess$ estimate. To estimate the concentration of a specie using optical spectroscopy, we use the light extinction for one

absorption peak. This light extinction is directly linked to the number of molecule of the specie. As described in detail in section 3.2.2.1, the absorption peak presents a lineshape, which is not a pure Dirac distribution but a Gaussian distribution spanning, in the infrared region, over several MHz. This is due to the distribution of energy of the molecules of each specie. For each absorption peak, the concentration of each specie is related to the surface under this lineshape and not only the height, in order to take into account the entire distribution of molecules. This requires a spectral resolution much better than the linewidth and high enough to have a relevant number of data points per peak to fit complex profiles.

These are incredibly high requirements and justify the use of sophisticated measurement techniques. Two of the different available techniques described in sections 3.2.4.2 and 3.2.4.3 will provide examples of the current state-of-the-art. For all infrared spectroscopy techniques, if very high levels of sensitivity are needed, what will finally matter the most is how precisely the frequency scale can be determined and at which level of stability. Still, to keep the acquisition rate high, the bare minimum of spectral points is generally used (compared to the most adapted to fit the lineshape profile of each absorption peak at the condition of temperature and pressure). Small variations of the measurement conditions will have a strong impact on the molecular absorption line profile and, given the high requirements, these variations can yield important systematic errors in the measurements, and therewith a need for regular calibration (see section 3.2.6).

Despite these potential difficulties, infrared spectroscopy nowadays can provide a level of performances equivalent to mass spectrometry. We postulate, however, that it has not yet reached its full potential. The interests of infrared spectroscopy compared to mass spectroscopy are numerous and important: (1) direct sampling of the vapour enables one to easily analyse vapour samples but also liquid or ice samples with a vaporiser; this enabled for instance following in the field the isotopic composition of the ice of the Aurora Basin ice core (ABN project) and to insure to have at least 2000 years of temperature reconstruction [Moy et al., unpublished results], (2) it is crucial for the development of Continuous Flow Analysis for isotopes but also other trace elements as only infrared spectroscopy can measure the samples as soon as the ice is melted, (3) in laboratory, as no chemical transfer is required, it enables much faster measurements (even though the accuracy and reliability of mass spectrometry are yet still necessary in parallel) and (4) it provides new possibilities for understanding the processes involved in isotopic composition changes.

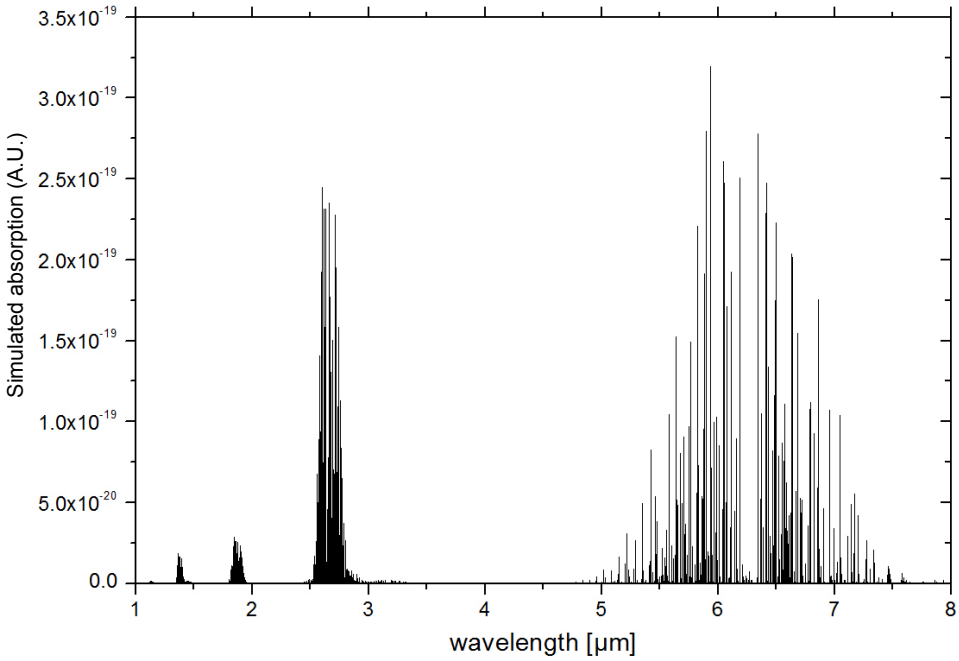

Figure 3.3: Simulated absorption spectrum of water in the infrared region based on the HITRAN 2012 database [Rothman et al., 2013]

3.2.2 Physical background

In this section, we will focus on the physical background needed to explain the spectroscopic point of view of this manuscript. First, we will provide a simple physical explanation of molecular absorption. Subsequently, we will discuss the spectral broadening of the absorption profiles due to the Doppler effect (temperature) and collisions (pressure). Then, we will provide a brief discussion about resonant cavities, which are classically used in infrared spectroscopy. Finally, we will address the conversion of the spectra to concentration, and thus, the necessity of calibrating infrared spectroscopy data.

3.2.2.1 Molecular absorption

Optical spectroscopy takes advantage of the absorption of light by the molecules. Water molecules behave as electric dipoles and interact with the electromagnetic field of light. The electromagnetic field can couple with the molecule through an interaction potential (we will not detail here the interaction Hamiltonian, see Weissbluth [2012] for more detailed theoretical developments). At the macroscopic level, with many molecules, these interactions result in absorption and refraction of the light by a medium formed by the molecules themselves, caused by a density of microscopic electric dipole interacting with

the electromagnetic field. This leads to a macroscopic polarisation such as:

$$\vec{P} = \varepsilon_0 \chi \vec{E} \tag{3.5}$$

where $\vec{E}$ is the electric field, ε_0 the dielectric constant of vacuum and $\chi = \varepsilon_r - 1$ the electric susceptibility of the medium. This complex susceptibility influences the propagation of the electromagnetic wave in the Maxwell equations, leading to:

$$\left(\Delta - \varepsilon_0 \varepsilon_r \mu_0 \mu_r \frac{\partial^2}{\partial t^2}\right) \vec{E}(\vec{r},t) = 0 \tag{3.6}$$

where μ_0 and μ_r are the magnetic permeability of vacuum and of the medium, respectively. In the case of a laser beam, the light can be represented as a coherent polarised plane wave propagating in the dielectric, which leads to a solution:

$$\vec{E}(\vec{r},t) = \vec{E_0} \underbrace{e^{-n_i \vec{k_0}.\vec{r}}}_{Absorption} \underbrace{e^{i(n_r \vec{k_0}.\vec{r} - \omega t)}}_{Refraction} \tag{3.7}$$

where $n = n_r + i\,n_i = \sqrt{\varepsilon_r}$ is the complex refractive index in the electric dipole approximation ($\mu_r \approx 1$) and $\vec{k_0}$ is the wave vector in vacuum defined by a dispersion in vacuum such as $\omega = c|\vec{k_0}|$. Eq. (3.7) highlights the two different effects of light matter interactions: refraction and absorption through both the real and imaginary part of the refractive index n. Calculation of the refractive index can easily be done in the case of the transition between two energy levels for an isolated atom. In the case of a polyatomic molecule such as water, numerous transitions associated with the pairs of the energy states may interact. In first approximation though, we will consider the case where each two levels transition is not under any influence from another transition. In this case, we can express the refraction index from the optical Bloch equation.

First, the real part of the refractive index n_r which affects the dispersion relation in the medium, thus reducing the speed of light in the medium and the wavelength of the light. The real component of the refractive index for a 2 levels transition as given by Loudon [2000] is:

$$n_r = 1 + \frac{N}{V} \frac{\mu_{eg}^2}{2\varepsilon_0 \hbar} \frac{\Delta}{\gamma} \frac{\gamma/2}{\Delta^2 + \gamma^2/4 + \Omega^2/2} \tag{3.8}$$

where $\frac{N}{V}$ is the density of the medium in molecules, $\vec{\mu_{eg}}$ is the transition dipole moment, $\Delta = \omega - \omega_t$ is difference between the laser frequency with the frequency associated with the idealistic two level transitions responsible for the absorption with a characteristic energy $\hbar\omega_t$, $\gamma = \frac{\mu_{eg}^2 \omega_t^3}{6\pi\hbar\varepsilon_0 c^3}$ is the spontaneous emission rate of the transition and $\Omega = \frac{\vec{\mu_{eq}}.\vec{E}}{\hbar}$

is the optical Rabi frequency. Second, the imaginary part of the refractive index n_i is responsible in Eq. 3.7 for the absorption term as the exponential term directly affects the amplitude of the electromagnetic field. This brings a definition of the molecular absorption coefficient α_{abs} (not to be confused with the isotopic fractionation coefficient):

$$\alpha_{abs} = -n_i k_0 \tag{3.9}$$

As for the real part of the refractive index n_r, we can express the imaginary part in the case of a 2 levels transition, which leads for the absorption coefficient to:

$$\alpha_{abs} = \frac{N}{V} \frac{\mu_{eg}^2 \omega}{\varepsilon_0 \hbar c} \frac{\gamma/2}{\Delta^2 + \gamma^2/4 + \Omega^2/2} \tag{3.10}$$

In the case of N levels of energy, the dielectric susceptibility and therefore, the refractive index and the absorption will be combining the transitions linked to all pairs of levels of energy:

$$\alpha_{abs} = \sum_{<i,j>} \alpha_{abs\, i \to j} \tag{3.11}$$

In the case where the transitions are not independent, the lineshape widens (see the next section for broadening effects).

This expression describes the Lorentzian distribution of the absorption coefficient associated with one two-level transition for non-interacting molecules at rest, which can only be observed at low pressures and low intensity. To observe this distribution, the other broadening effects (such as described in the next sections) can be reduced by different methods (cooling, low pressure,...). The minimum width of this Lorentzian distribution is determined by the spontaneous emission rate of a molecule. For this reason, the linewidth associated with spontaneous emission is called the *natural* width of the spectral line [Loudon, 2000]. Practically, in the case of infrared spectroscopy, the natural width of spectral line is negligible at standard temperature and pressure conditions and realised at conditions of temperature and pressure where other additional broadening processes will hide this effect.

3.2.2.2 Doppler Broadening

We measure the absorption of a gas with a temperature $T > 0\,K$, hence the velocity of the molecules follows a Boltzmann thermal probability distribution. For a molecule with velocity $\vec{u}$, the apparent frequency of the light is affected and becomes $\omega_{ap} = \omega - \vec{k}.\vec{u}$. The light is absorbed by the molecule only when its frequency ω is shifted by the Doppler

effects to the characteristic frequency of the transition ω_t:

$$\omega = \frac{\omega_t}{1-u/c} \approx \omega_t \left(1+\frac{u}{c}\right) \tag{3.12}$$

where c is the celerity of light. Therefore, the distribution of velocities of the molecules imposes the distribution of frequencies that can be absorbed. This results in an apparent broadening of the transition lineshape called Doppler Broadening. The typical order of magnitude of u/c at ambient conditions is 10^{-6}, therefore in the case of water in the infrared region, this is much larger than the natural linewidth. The distribution of velocities follows the Maxwell-Boltzmann speed distribution [Landau and Lifshitz, 1958]:

$$f(u)du = \sqrt{\frac{m}{2\pi k_B T}} e^{-\frac{Mu^2}{2k_B T}} du \tag{3.13}$$

where k_B is the Boltzmann constant, M the atomic mass and T the temperature. This results in normalised Gaussian lineshape of the Doppler-broadened absorption line such as:

$$F_G(\omega) = \frac{1}{\sqrt{2\pi\Delta^2}} e^{-(\omega-\omega_t)^2/2\Delta^2} \tag{3.14}$$

where Δ^2 is the variance of the Gaussian distribution such as $\Delta = \omega_t \sqrt{\frac{k_B T}{Mc^2}}$. Figure 3.4 presents the comparison of the normalised Gaussian lineshape with the respective Lorentzian lineshape defined by:

$$F_L(\omega) = \frac{\gamma/\pi}{(\omega-\omega_t)^2+\gamma^2} \tag{3.15}$$

The Lorentzian lineshape is characterised by tails extending larger away from the peak than in the case of the Gaussian lineshape where most of the distribution is sharply centred around the peak. The very fine Lorentzian distribution due to the natural width of the transition can be considered as a Dirac in the case of infrared spectroscopy, still, collisions of the molecules together also create broadening with a Lorentzian shape with a width typically equivalent to the Doppler broadening for the range of pressure we work at.

3.2.2.3 Collisional Broadening

Collisions between the atoms or molecules in a gas is a random process. During a collision, the interaction forces between the colliding particles shift the energy levels in a linear combination of the unperturbed molecules. Because the collision itself lasts a very short amount of time, we will here consider no emission and absorption occur during the

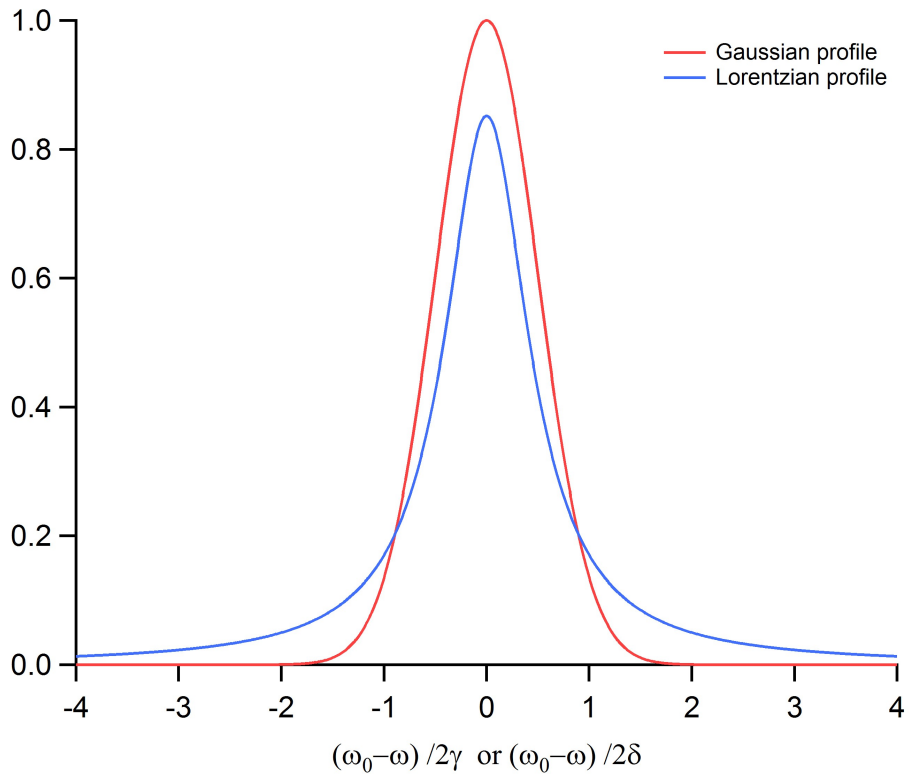

Figure 3.4: Comparison of the normalised Gaussian and Lorentzian lineshapes as a function of the frequency normalised by their respective integrals Loudon [2000]

collision itself. Then, the collisions affect the interaction between the molecules and the light only via the changes in the energy levels available [Loudon, 2000]. This results in an additional term in the Lorentzian lineshape of the dielectric susceptibility leading to γ in the expression of the Lorentzian lineshape being equal to $\gamma = \frac{f_c}{2\pi}$, f_c being the frequency of collisions (i.e. the number of collisions experienced by one molecule per second). This frequency is derived from the kinetic theory of an ideal gas by:

$$f_c = \sigma n \sqrt{\frac{8kT}{\pi\mu}} = \sigma p \sqrt{\frac{8}{\pi\mu kT}} \tag{3.16}$$

where σ represents the collision cross-section (m^2), n the density of molecules (m^{-3}), p the pressure (Pa), μ the reduced mass (kg) and T the temperature (K). Because of the dependency to pressure, collisional broadening is also referred to as pressure broadening.

In general cases, several broadening effects are going to influence the lineshape of the transitions, for instance for the Voigt profile: collision and doppler broadening [Voigt, 1912]. When the absorption is subject to two (or more) different processes affecting the

lineshape, it is necessary to determine the combination of the different mechanisms. For instance, in the case of two broadening effects centred on the same frequency ω_0, the composite lineshape is determined by:

$$F_{comp}(\omega) = \int_{-\infty}^{\infty} F_1(\nu)\, F_2(\omega + \omega_0 - \nu) d\nu \tag{3.17}$$

3.2.3 Application to spectroscopy

In infrared spectroscopy, the determination of the shape of the profile characterising the linewidth is crucial. Indeed, to infer quantitatively the quantity of molecule accountable for the transition absorbing the light, it is necessary to obtain the whole surface of the linewidth. Because integrating the dataset would create a lot of noise, it is necessary to fit the datapoint and integrate the area from the fit function which prerequisites (1) a good knowledge of the baseline and (2) an adapted profile to fit the datapoint. This justifies a dire need to understand precisely infrared spectroscopy. Here we detailed the basic equations explaining the light and matter interactions. Still more sophisticated theories are used nowadays and a rapid overview will be given in section 3.2.5. Before, we need to focus on how the spectrum is obtained.

The water vapour spectrum has a significant amount of rotational-vibrational transitions in the near and mid infrared region (Fig. 3.3). Furthermore, a large part of the absorption lines can be attributed to one single isotopic specie. At low pressures, the lineshapes are narrow enough to distinguish the transitions from one another and therefore enable determination of the isotopic composition of the gas sample. Because of the sensitivity of the different broadening effects to the environmental parameters such as temperature, pressure and partial pressure, it is very important to monitor or/and control them precisely. Rapid scans enable one to limit the possible variations of environmental conditions during the spectrum acquisition but limit the number of points. As we saw, the lineshape profiles are dependent to an important number of parameters and therefore require an important number of datapoints per transition to be able to fit the profile. The competition between rapid scans and important number of points in the profile calls for powerful optical techniques to realise spectra.

Building on the exponential decrease of the amplitude of the electromagnetic field along the propagation in the medium, the Beer-Lambert law states that the direct absorption of the medium is:

$$I(e) = I_0 e^{-\alpha_{abs}\ell} \tag{3.18}$$

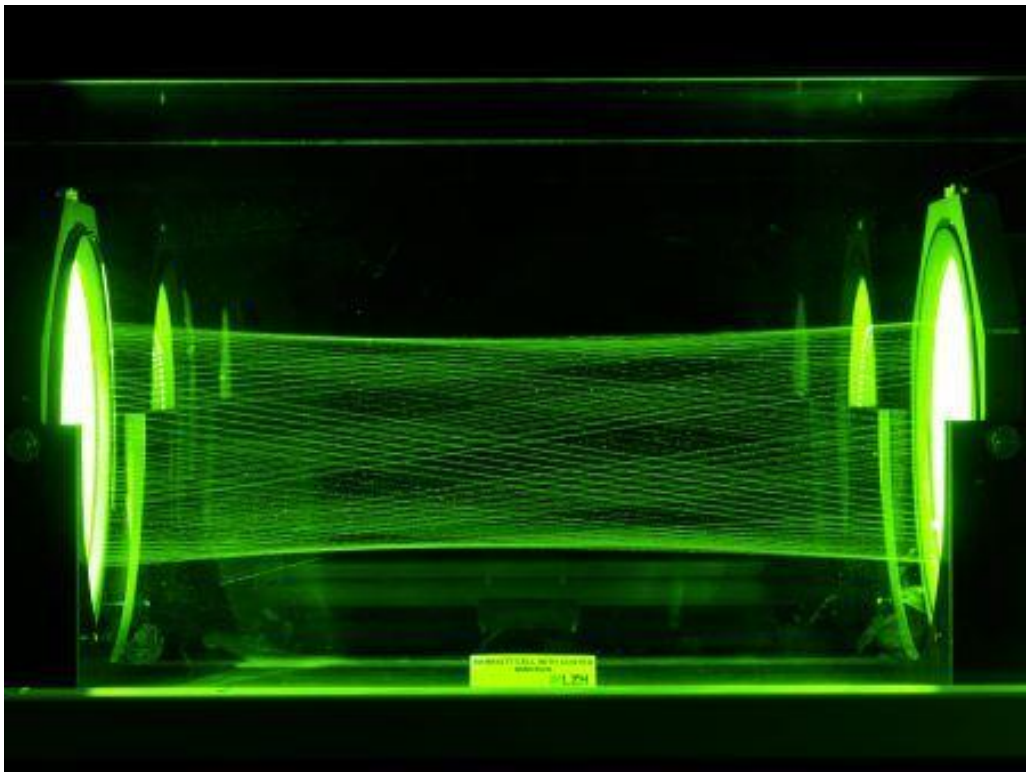

Figure 3.5: The Herriot cell is a type of multipass cell enabling important number of passes to increase the optical path without increasing the volume of the sample (source : lzh.de)

where ℓ is the optical path in the medium. By measuring the extinction of light through a sample, one can directly measure its composition. This method, which is still nowadays used in several commercial instrument, presents important limitation in sensitivity resulting in either important sampling volumes or low signal to noise ratio. In order to increase the optical path without increasing the volume, multipass cells use mirrors on both side on which the beam is reflected several times before leaving the cavity (for instance, a Herriot cell as illustrated in Fig. 3.5).

3.2.4 Resonant cavities

In this section, we detail how the use of resonant cavities enables a reduction of the amount of gas necessary and an increase of the optical path at the same time. This section gives a rapid overview of the different techniques of spectroscopy based on resonant cavities that have been studied during my PhD. The major asset of these methods is the high dynamic enabling precise measurements in a wide range of conditions and more importantly, enabling measurements of the concentration of different species whose concentrations differ by factors up to 10^4. First, we will describe the physical background of

resonant cavities, and then we will detail the principle of two methods: the Optical Feedback Cavity Enhanced Absorption Spectroscopy (OFCEAS) and the Cavity Ring Down Spectroscopy (CRDS).

3.2.4.1 Resonant cavity physical background

In order to increase even more the optical path, one can use "semi-transparent" mirrors and match them for the light beam to fold back on itself and therefore create an optical resonator. This set-up is called a Fabry-Perrot interferometer and was initially used to determine the thickness of a glass plate. Here, we apply the same method to determine the absorption after a very important number of passes [Kastler, 1962].

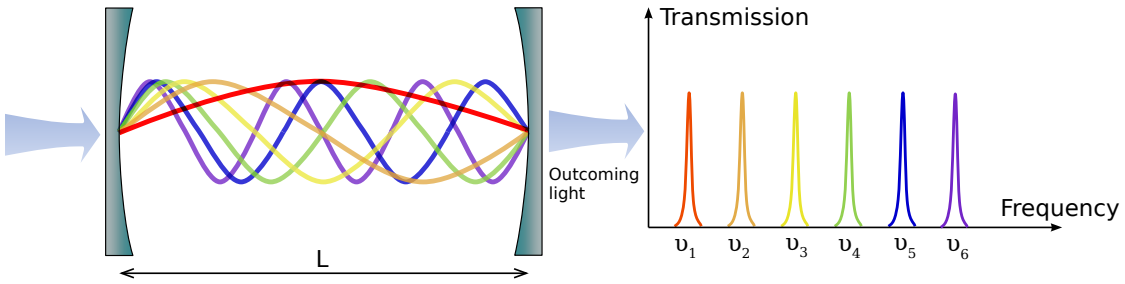

Figure 3.6: Schematic of an linear optical cavity, only modes with wavelength proportional to $L/2$ creates constructive interferences and can build up light in the cavity

A cavity with two mirrors of reflectivity R and transmission T (as on the schematic in Fig. 3.6) is injected with a coherent light source I_i. If R is important, each time the light hits a mirror, an important fraction is reflected and a small fraction is transmitted. After one roundtrip in the cavity, the remaining light (roughly $R^2 I_i$) is coherently summed up with new light, resulting in an accumulation of light in the cavity. The total transmitted light is the sum of the contributions due to the successive reflections, as for the reflected light and the energy stored inside the cavity. In a steady state, we obtain for the transmission:

$$\frac{E_t}{E_i} = t^2 e^{i\Phi/2}\left(1 + r^2 e^{i\phi} + ...\right) \tag{3.19}$$

where $r = \sqrt{R}$ and $t = \sqrt{T} = \sqrt{1-r^2}$ are the reflection and transmission coefficients of the electric field on the mirrors respectively and Φ is the phase shift associated with one round trip. This is equivalent to the sum of a geometric series, therefore:

$$\frac{E_t}{E_i} = \frac{t^2 e^{i\Phi/2}}{1 - r^2 e^{i\phi}} = \frac{(1-r^2)e^{i\Phi/2}}{1 - r^2 e^{i\phi}} \tag{3.20}$$

Alternatively for the reflected beam E_r and the internal power E:

$$\frac{E_r}{E_i} = r - \frac{r(1-r^2)e^{i\Phi}}{1-r^2e^{i\phi}} \tag{3.21}$$

$$\frac{E}{E_i} = i\frac{t+rte^{i\Phi}}{1-r^2e^{i\phi}} \tag{3.22}$$

The cavity transmission is maximal at resonance (when $\Phi = 0$ or 2π). The transmission of the cavity is given by the Airy function:

$$T_{cav} = \frac{(1-R)^2}{1-2Rcos\Phi+R^2} = \frac{(1-R)^2}{(1-R)^2+4Rsin^2\Phi/2} \tag{3.23}$$

The transmission is maximum when $sin^2\phi/2 = 0$ which is equivalent to $\frac{2\pi}{c}L\nu = m\pi$ with m an integer. Depending on the value of the reflectivity R, the cavity transmission will show characteristic peaks more or less sharp (Fig. 3.7). For low values of R, it is not possible to extinguish the transmission completely and the observed pattern is simply fringes. For high values of R, the signal is completely erased in between the resonances which occur at the frequency:

$$\nu_m = m\frac{c}{2L} = m\Delta\nu_{FSR} \tag{3.24}$$

where L is the distance between the mirrors and $\Delta\nu_{FSR} = \frac{c}{2L}$ is called the Free Spectral Range (FSR) of the cavity. The width of each resonance is defined by the Full Width Half Maximum (FWHM) such as:

$$\Delta\nu_w = \frac{c}{2\pi L}\frac{1-R}{\sqrt{R}} \tag{3.25}$$

The finesse $\mathscr{F}$ is defined as the ratio of the FSR by the width of the cavity mode and estimates the relative sharpness of the resonance:

$$\mathscr{F} = \frac{\Delta\nu_{FSR}}{\Delta\nu_w} = \pi\frac{\sqrt{R}}{1-R} \tag{3.26}$$

High finesse cavities are particularly interesting for spectroscopy for different reasons. First, the average time spent in the cavity by a photon is $<\tau>= \mathscr{F} * \frac{2L}{\pi c}$, therefore the mean optical path increases linearly with the finesse and can reach values of several hundreds kilometres. Second, the range of frequency at which photons are able to build up in such a cavity is very narrow, therefore it gives the possibility to sample at high frequency resolution. Third, the power inside the cavity $P_{IC} = 2\frac{F}{\pi}P_i$ is determined by the finesse and the input power P_i. Thus, even with a weak power input, it is possible to build up high

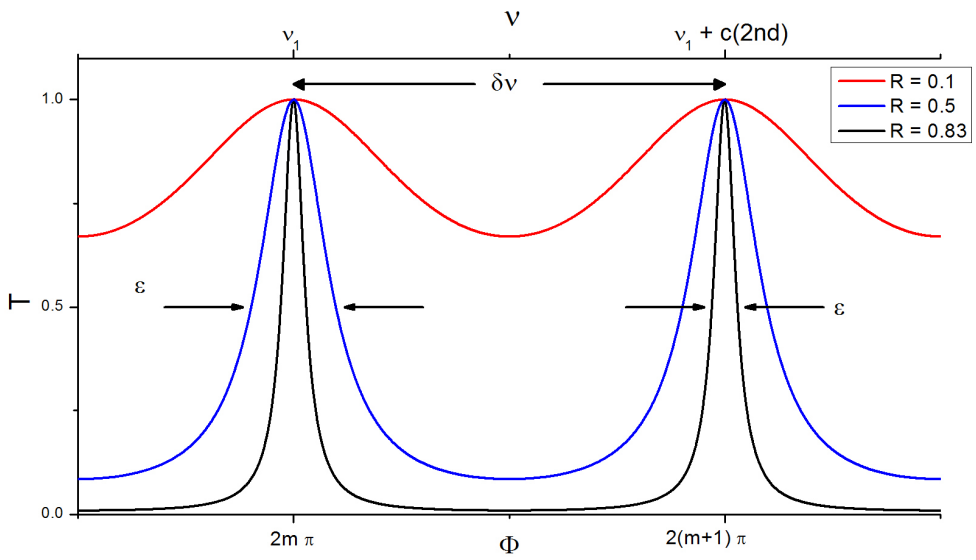

Figure 3.7: Cavity transmission for reflectivities ranging from 0.1 to 0.83

quantity of energy inside the cavity. Finally, if the cavity is built within a solid stable material and its length remains constant, the resonant frequencies are precisely determined and the cavity itself can provide a frequency reference.

Cavities with more than 2 mirrors can also be realised and have similar behaviour. In the case of a V-shaped cavity (3 mirrors), similar behaviour occurs with 4 possible exits for the light. For such cavities, the free spectral range is slightly different : $\Delta\nu_{FSR} = \frac{c}{4L}$ and the finesse is defined by : $\mathscr{F}_V = \pi\frac{R}{1-R^2}$. We will see in the next section the interest of such a cavity compared to a linear cavity.

3.2.4.2 Optical Feedback Cavity Enhanced Absorption Spectroscopy (OFCEAS)

OFCEAS is a method developed and patented by LIPHY to measure trace elements in gas phase [Morville et al., 2005]. It relies on V-shaped resonant cavity as presented in figure 3.8 made from a stainless steel. A PID (Proportional, Integral and Differential) comparator additionally insures the temperature stability of the cavity creating a stable frequency reference for the instrument. Building up on this, a portion of the light from the cavity is sent back to the laser source, resulting in a stabilisation of the frequency of the diode laser (optical feedback). A detailed framework of the optical feedback theory has been developed by Laurent et al. [1989]. An essential property of optical feedback on frequency locking is the suppression of frequency excursion to a frequency width $\Delta\nu_{OF}$ even narrower than the FWHM of the cavity.

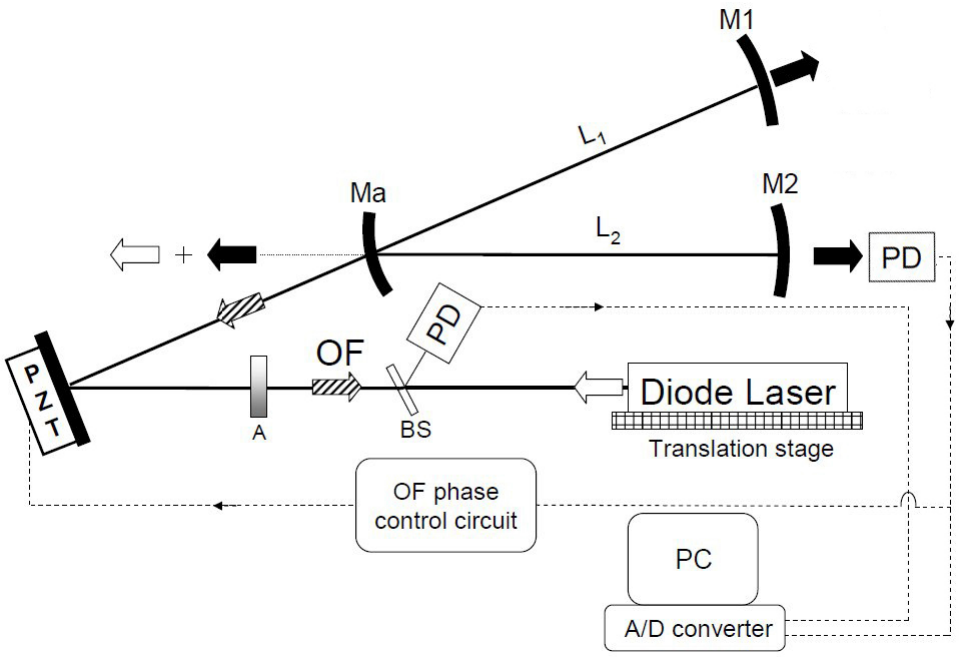

Figure 3.8: OFCEAS principle schematics as described by Morville et al. [2005]

The main advantage to use a V-shaped cavity in this instrument is to avoid direct reflection from the mirror labelled M_a in the Fig. 3.8 back to the laser. This reflection would create another "cavity" on which the laser could lock and would perturb the frequency locking. The optical feedback light still goes back to the laser. The beamsplitter (BS on the schematic) splits the beam toward both the cavity and a reference diode.

When the frequency of the laser is scanned, it will get locked successively on the resonance frequency of the cavity (see Fig. 3.9) and will remain locked until it can get locked to the next resonance. How long the laser stays locked can be set by adjusting the feedback rate with a linear polariser (attenuator A in Fig. 3.8). If an important feedback rate is interesting to improve the statistics of the laser getting/staying locked, it is crucial not to have a feedback rate too high for the cavity to be able to delock but relock instantaneously to the next mode.

During my Ph-D, I have been working on an instrument based on the OFCEAS technique named HiFI developed by Landsberg et al. [2014]. In this instrument, the lasers are DFB (distributed feedback) laser diodes with a typical maximal output of 10 mW around 7200 cm^{-1}. These diodes are particularly suited to optical feedback. The cavity is composed of 3 mirrors from Layertec GmbH with a radius of curvature of 1 m and a wedge

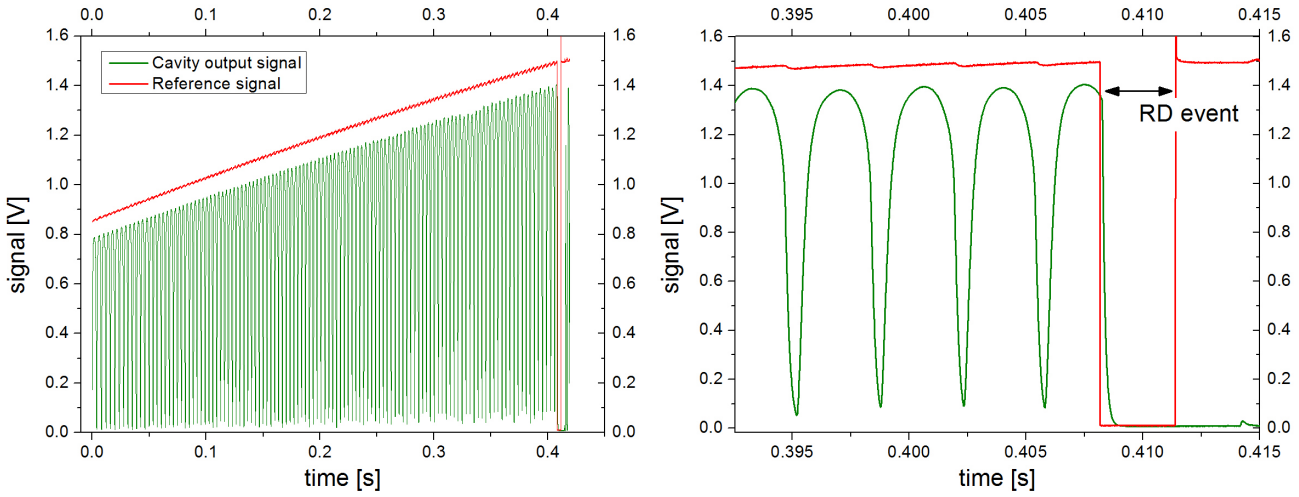

Figure 3.9: Example of OFCEAS signal during a full scan and zoom over the last resonance and the Ring-Down measurement used to convert the spectrum into an absorption scale [Landsberg, 2014]

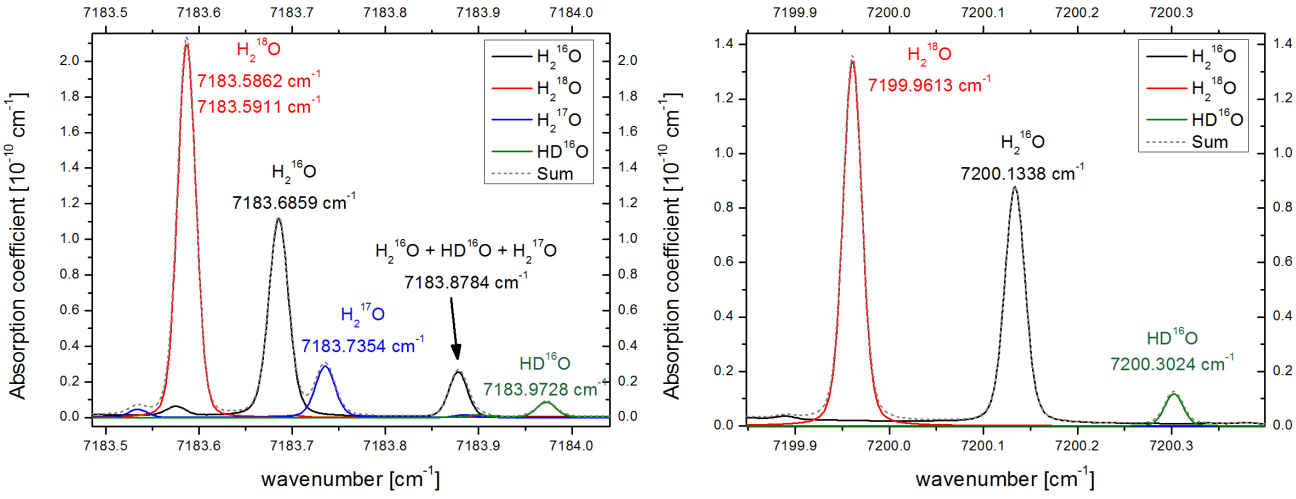

Figure 3.10: Simulated spectrum for 1 ppm of water vapour at natural concentration at 7184 cm^{-1} on the left and 7200 cm^{-1} on the right from the Hitran database [Rothman et al., 2013]

of 1°. The maximum ring-down time observed with an empty cavity at 7184 cm^{-1} was 150 μs which is equivalent to a reflectivity of 99.9989% or a finesse of roughly 144000 (see next section for the definition of ring-down and a comparison with last generations of commercial instruments). The instrument is housed in a 1.5U heigh 19" rack and has a weight of 20 kg. The working pressure inside the cavity is 35 $mBar$ and the air carrier

gas flows at approximately 150 *sccm* (the flow is adjusted for the gas cell pressure to remain constant). The volume of the cavity is approximately 20 *mL*. The instrument can be used at different wavelengths by changing the laser diode: we used two lasers of which the first operates at 7184 cm^{-1} where all three isotopic ratios $\delta^{18}O$, $\delta^{17}O$ and δD can be obtained (see Fig. 3.10a), and the second at 7200 cm^{-1} where only $\delta^{18}O$ and δD can be determined but where the transitions associated with each isotope are better separated (see Fig. 3.10b).

This instrument has been especially developed by Landsberg et al. [2014] to work at low humidity, and in particular, lower than all the commercial instruments that were available at the time. It can measure water vapour isotopic composition down to humidities of 200 *ppmv* with a precision better than 0.1‰ for $\delta^{18}O$, 0.15‰ for $\delta^{17}O$ and 0.8‰ for δD. This instrument has been involved in several campaigns carried out by Janek Landsberg including on a field trip campaign to Troll Station in Antarctica, the Cloud Chamber experiment described in section 5.2.2 and by me during the first field campaign to Concordia Station in Antarctica (see section 6.2).

3.2.4.3 Cavity Ring Down Spectroscopy

Cavity Ring Down Spectroscopy (CRDS) is another alternative to realise spectroscopy with a long effective optical path length. It also relies on a resonant cavity but in this case, the laser is not locked to the cavity. Indeed, in this case, the optical feedback is not the purpose of the resonant cavity but measuring the decay rate of the light going out of the cavity once the laser has been stopped. As a laser is injected in the cavity in a resonant situation (by adjusting the length of the cavity with a piezzo for instance), some energy will build up in it. Because of the energy conservation, the relation between the reflectance R, the transmittance T and the loss L due to scattering or absorption on the mirror at each reflection is:

$$R + T + L = 1 \tag{3.27}$$

Note that in this situation, it is not possible to neglect the impact of the loss contrary to section 3.6. If the light input is suddenly stopped for whichever reason, the intensity inside the cavity shows an exponential decay which is directly transferred to the intensity leaving the cavity:

$$I(t) = I_0 \, e^{-\frac{t}{\tau_{RD}}} \tag{3.28}$$

where I_0 is the intensity when the light input has been stopped and τ_{RD} is the ring-down time which does not depend on I_0, the initial intensity of the decay. After n round trips in the cavity, the intensity decays because of (1) the transmitted and the lost part of the light

at each reflection on the mirrors and (2) the molecular absorption during the trip from one mirror to the other, such as :

$$I(t) = I_0 e^{-2n(-lnR+\alpha_{abs}L)} \tag{3.29}$$

Each round trip in the cavity corresponds for the photons to a time $t = \frac{2nL}{c}$ spent in the cavity, thus, Eq. 3.29 can be written as:

$$I(t) = I_0 e^{-\frac{ct}{L}(-lnR+\alpha_{abs}L)} \tag{3.30}$$

The presence of molecule absorbing the light will reduce the ring down time. The exponential decrease of the light intensity is illustrated in Fig. 3.11. The decay time constant in Eq. (3.30) can be expressed as:

$$\tau = \frac{1}{c(-lnR+\alpha L)} \tag{3.31}$$

This decay is also called ring down time. To obtain the absorption coefficient, the subtraction with the ring down time of an empty cavity can simplify previous equation and leads to:

$$\alpha_{abs} = \frac{1}{c}\left(\frac{1}{\tau} - \frac{1}{\tau_0}\right) \tag{3.32}$$

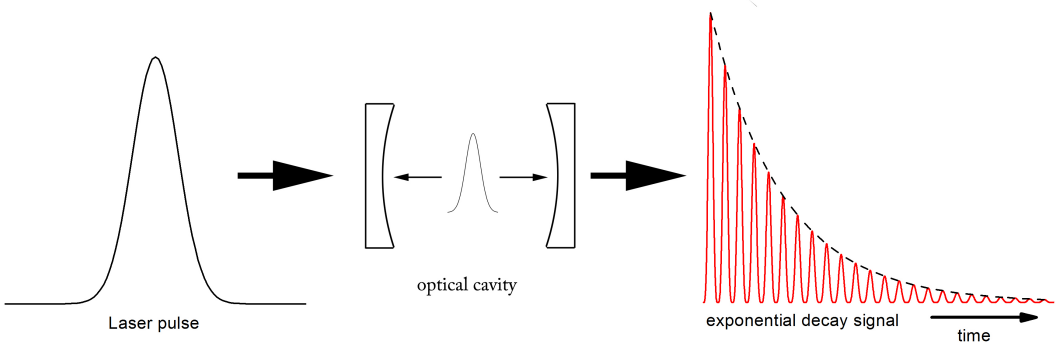

Figure 3.11: CRDS principle schematics as described by Paldus and Zare [1999] representing the exponential decay out of the optical cavity. The decay time is extremely short, a few μs but still measurable with satisfactory precision.

This is a simplified theoretical approach to describe the link between ring-down time and the absorption coefficient α_{abs} and a more complete theoretical description can be found in Romanini et al. [2014] and Burkart [2015] and will not be described here. This method presents several features of interest: first, the measurement is completely independent of everything occurring before the cavity as the incident light is off when the

measurement happens, this removes all uncertainties linked to phase noise, power fluctuations and locking between the laser and the cavity and is an enormous advantage; second, to infer precisely the time constant of an exponential decay is a rather precise measurement technique. Most of the instrument based on CRDS are actually building on Continuous-Wave Cavity Ring-Down spectrometry technique (CW-CRDS) developped by Romanini et al. [1997] for which the laser and the cavity mode are jointly tuned to scan a whole spectral ensemble with high resolution without relying on the free spectral range of the cavity.

During the time of my Ph-D, I used a couple of instruments based on this technique from the company Picarro: the L2120-i, the L2130-i and the L2140-i. Only the last one can measure all 3 isotopic compositions. These spectrometers are composed of a high finesse ring cavity with a empty ring-down time of $22\,\mu s$ which is equivalent to a finesse of 44 000 or an effective optical path length of $6.7\,km$ and a typical sensitivity of $2.3\,10^{-11}\ cm^{-1}Hz^{-1/2}$ [Crosson, 2008]. The working pressure inside the cavity is $66.7\,mbar$ and the flow approximately $40\,sccm$. In the case of the previous generation of water vapour isotope Picarro analysers (up to the L2130-i), one of the mirror is mounted on a piezoelectric actuator which enables changing the size of the cavity and therefore tune the cavity modes to whatever wavelength the laser is set (one method enabling CW-CRDS). For the latest version of the water vapour isotope analyser, the L2140-i, the length of the cavity is kept constant during measurements and the laser is locked to successive FSR of the cavity [Steig et al., 2014]. If this results in less freedom in the spectral sampling but enables to use the cavity as a frequency reference, as for OFCEAS: the cavity in the Picarro instruments is made a special steel which has a very small thermal expansion coefficient, this cavity provides a rather good frequency reference (see Table 4.3 in section 4.2.1 for comparison).

An additional modification of the Picarro L2140-i is a second laser at $7193\,cm^{-1}$ (see Fig. 3.12) allowing to obtain the composition in $H_2^{17}O$. The spectral window used is different than in the case of the HiFI (OFCEAS instrument, see section 3.2.4.2)for purely logistical reasons and theoretically, no difference of precision should occur from this difference. The ring-down and the finesse of Picarro's analysers are lower than the one of the HiFI which results in smaller optical path length and therefore an instruments less sensitive at low humidities. As important efforts have been made by Picarro to provide their analysers with efficient temperature, pressure and flux regulations (housekeeping), it is possible to average over long time period the data without being affected by drift of the instruments and Picarro analysers have been used successfully down to 100 ppmv.

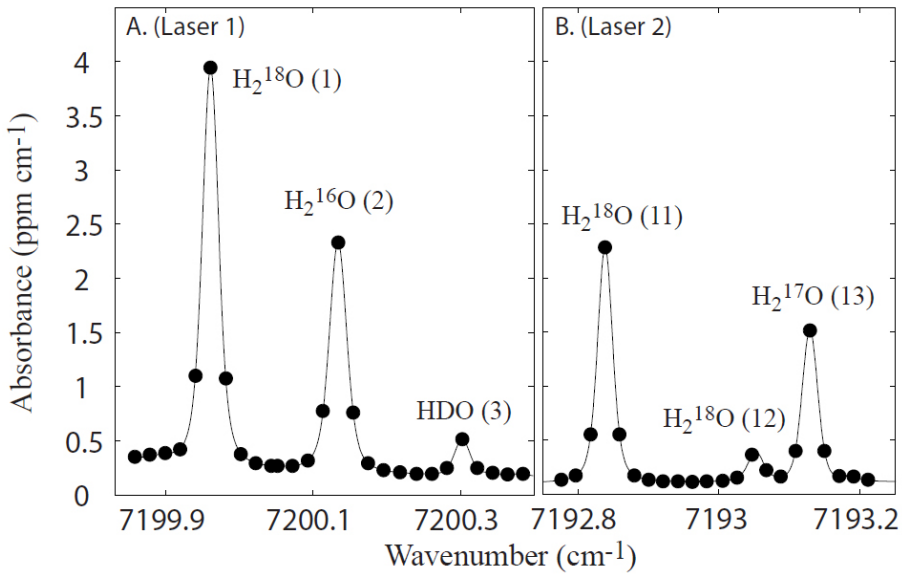

Figure 3.12: Measured absorption spectrum for 20000 ppm of water vapour in dry air at 7200 cm^{-1} on the left and 7193 cm^{-1} on the right, the lines are a least mean squares fit of the datapoint by Galatry profiles [Steig et al., 2014]

Picarro's analysers are not the only CRDS instruments available nor the only ones used in my Ph-D, as demonstrated in section 4.1.2.

3.2.5 From a spectrum to a concentration

The different kinds of spectrometers above will not provide directly a concentration. In the case of OFCEAS for instance, the ratio of powers received by the two photodiodes has to be converted into a molecular absorption. To calculate the molecular absorption from the cavity transmission obtained from the ratio of the powers of the two photodiodes, it is necessary to invert the Airy-shaped cavity transmission transfer function as detailed by Kerstel et al. [2006]. In the case of CRDS also, the molecular absorption is not directly obtained: it is necessary to fit the exponential decrease of power out of the cavity to obtain the ring-down time and calculate the absorption as described in section 3.2.4.3. Even, in some rare case of saturated absorption, non-exponential ring-down profiles have been reported [Burkart et al., 2015]. Once an absorption spectrum is obtained from an infrared spectrometer, an important amount of calculation is still required to obtain a concentration.

As we saw, the concentration of species associated with a transition is proportional

to the surface between the transition lineshape and the baseline. To estimate this concentration, it is possible to simply integrate points to points the surface. Still, this method is rather noisy, especially when the number of points is low (as to increase the number of spectral points decreases the sampling rate). By fitting the spectrum with the physical parameters upon which the broadening effects of each transition are based, the measurement of only a few spectral points per transition can already provide a satisfactory estimate of the concentration of the element associated with a transition. To be efficient, this method requires a lineshape profile which encompasses all the physical processes affecting the molecular absorption in the experiment conditions and precise fit parameters which are based on a set of reference spectra realised with an important amount of spectral points and laboratory controlled experimental conditions. Considering the precision needed to provide a relevant determination of isotopic composition, the choices in the profile and the fit parameters are crucial. Reducing the number of points decreases the time of the scans, therefore limits the risks of the environmental conditions (such as pressure, temperature and flux) changing during the measurement, but it is also a trade-off because with few spectral points, all the noises of the frequency and amplitude determinations create important biases or noises on the final concentration. Figure 3.13 presents the use of different profiles to fit one absorption line of water vapour around $1.4\,\mu m$ [Lisak et al., 2009].

The Voigt profile is the simplest, it is obtained by combining the Gaussian profile of the Doppler Broadening and the Lorentzian profile of hard-collisional broadening. The Galatry Profile is the one used on Picarro instruments to fit the spectra, it integrates soft-collision between molecules introducing collisional narrowing. The Speed-Dependent Voigt Profile takes into account the speed of the molecules in the collisions to introduce collisional broadening and shifting effect of the profile. Finally, the Speed-Dependent Nelkin-Ghatak profile uses hard-collision and takes into account collisional narrowing and the speed-dependence of collisional broadening and shifting. We will not go into details on the theoretical differences between these profiles, a description of the line shape models can be found in Ciurylo [1998]. All of these profiles have been widely used in spectroscopy and numerous studies attest whether they are relevant at the different experimental conditions. Figure 3.13 illustrates the typical $W - shape$ expected with a maladapted profile. In the case of the Voigt Profile, very important residuals occur due to the lack of line narrowing. If Galatry Profile greatly improves the fit, only when speed-dependence and line narrowing are taken into account together, are the residuals completely removed from the fit [Lisak et al., 2009].

In the case of the transition detailed in Fig 3.13 for instance, the absorption lineshape

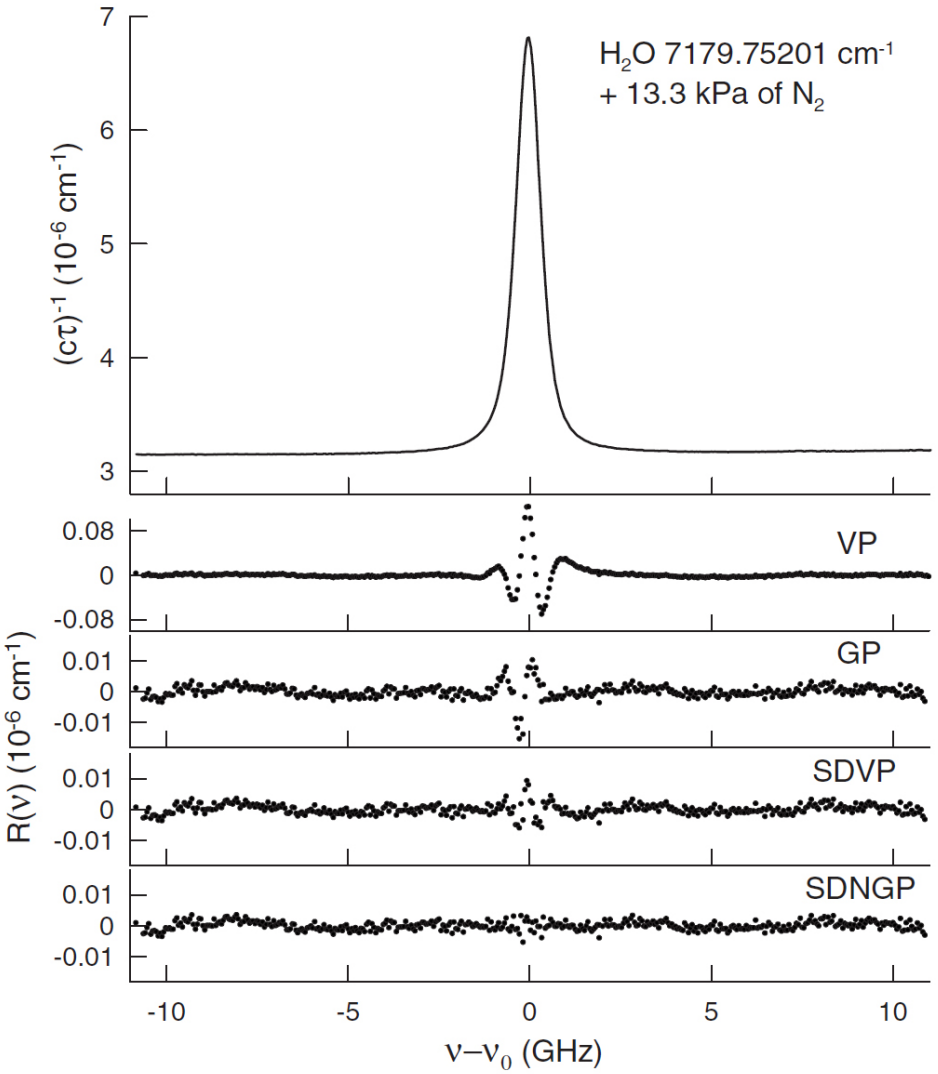

Figure 3.13: Measured absorption line of water vapour in Nitrogen carrier at 133 *mbar* at 7179.75201 cm^{-1} and residuals from fit with four commonly used profiles: *VP* Voigt Profile, *GP* Galatry Profile, *SDVP* Speed-Dependent Voigt Profile and *SDNGP* Speed-dependent Nelkin-Ghatak profile [Lisak et al., 2009]

is dependent of the experimental conditions as illustrated for instance by Eq. (3.10). The parameters that can fit the absorption profile from only physical experimental conditions are the fit parameters. Each profile requires a certain number of fit parameters as thoroughly described by the technical report of Tennyson et al. [2014]. For spectroscopy of water vapour, they recommend to use the Hartmann-Tran profile (HTP) [Tran et al., 2013]. This profile includes the speed dependence, hard velocity changes due to collision and that modification of the velocity is correlated with rotational state changing at the collision and requires up to 7 parameters to fully characterise the line shape for one transition at one temperature and in one matrix of ambient gases.

If spectroscopy experiments aim at measuring directly the fit parameters to understand the physics lying behind these, for trace detection application, the fit parameters are implemented with values from the literature. A strong effort has been lead to obtain the most relevant spectroscopic parameters, and the HITRAN database keeps a regularly updated list of the state of the art spectroscopy experiments [Rothman et al., 2013]. Still, as the final precision of the fit is directly influenced by these parameters, in order to obtain the best precision in the trace detection, it is important to constrain the fit parameters precisely. In section 4.1.2, we will present a set of spectra realised in laboratory experiments. They provide us with robust fit parameters that can be included in the next generations of infrared spectrometers. By characterising the dependency of the fit parameters with environmental conditions such as temperature or pressure, it is possible not to entirely fit them and to use instead parametrisation with temperature or pressure for instance. This enables to reduce the number of spectral points necessary to obtain precise concentration measurements.

3.2.6 Calibration

In this section, we will rapidly review the reasons why it is necessary to calibrate infrared spectroscopy measurements. 3 types of calibration are realised in infrared spectroscopy. Type (1) calibration estimates the drift of the instrument. As for mass spectrometry, it is mainly because of unaccounted evolutions of the environmental conditions. The calibration protocol for type (1) calibration relies on the measurement of one isotopic standard at one humidity level. The regularity of this calibration is given by the Allan-Variance diagnostic (See section 6.2 for an example on the Picarro L2130i at low humidities). It is calculated as the variance of one long steady measurement with different running average of the data (see Fig. 3.14 for an example in the case of a Picarro L2140-i). As we realise longer running average of the dataset, the white noise is being cancelled and the variance decreases (illustrated by the monotonous slope for all isotopic composition measurements in Fig 3.14). After a while though, the drift of the instrument can be larger than the noise of the instrument, creating variance that is characterised on an Allan deviation plot by an increase. The drift of infrared spectrometers is most of the time due to fringes in the optical setup due to parasite reflections on mirrors, windows or lenses. Because of small variations of temperature of the entire setup, small variations of the distance between the different optical elements will affect the fringes and therefore create biases. The drift can also be related in drift in the frequency of the laser or small variations of the temperature or the pressure of the gas. In the case of the Picarro L2140-i illustrated in Fig. 3.14, the Allan deviation of the measurement of δD stops decreasing earlier than $\delta^{18}O$ and $\delta^{17}O$

but rises less than $\delta^{18}O$ and $\delta^{17}O$ at longer time scale. In order to benefit from the best performances of the spectrometer (toward $10^{-2}‰$ for $\delta^{18}O$), it is necessary to realise type (1) calibrations every 10 000 seconds, so roughly every 3 hours.

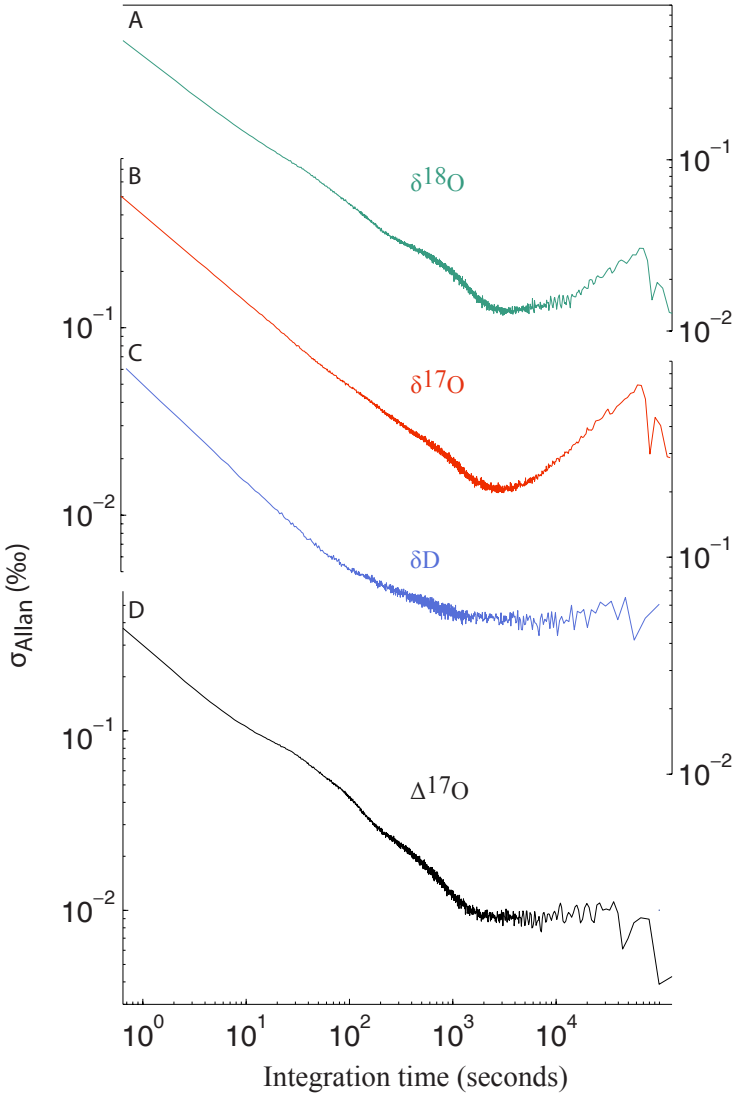

Figure 3.14: Allan standard deviation for water isotopic composition measured of a Picarro L2140-i: (A) $\delta^{18}O$: green, (B) $\delta^{17}O$: red, (C) δD: blue and (D) $^{17}O-excess$: black. Modified from Steig et al. [2014].

Type (2) calibration estimates the isotope-isotope response of the instrument. Because the absolute amplitudes of the transitions associated with the different isotopes are not referenced against the SMOW with enough precision, the estimatation of the isotopic composition from infrared spectrometers is not naturally referenced against the SMOW-

SLAP line. In order to account for this bias, two standards whose isotopic compositions bracket the isotopic composition being monitored are successively measured providing the response of the infrared spectrometer compared to the SMOW-SLAP scale. Typical isotope-isotope slope is between 0.95‰/‰ and 1.05‰/‰ for Picarro's analysers for instance. This type of calibration can be realised once a week provided type (1) calibration accounted for the drift.

Type (3) calibration estimates the isotope-humidity response of the instrument. This type of calibration is necessary if the collisional broadening is not properly estimating the impact of water vapour partial pressure changes on the lineshape. Because most spectrometers take too few spectral points to implement more sophisticated absorption profiles, it is necessary to correct this bias directly on the isotopic composition and on the humidity. Type (3) calibration is realised by measuring 1 standard at different levels of humidity in order to account for the response of the infrared spectrometer to humidity.

3.3 Optical frequency combs

Here, we introduce quickly optical frequency combs and how they can be used as an absolute frequency reference. Optical frequency combs have been used directly to realise spectroscopy, as highlighted for instance by the recent work of Millot et al. [2015]. Still, due to the price of an optical frequency comb (around $100\,k€$), alternative methods are often chosen. During my PhD, we used an optical frequency comb as an absolute frequency reference to characterise a very stable cavity (see next chapter).

An optical frequency comb is the representation in the frequency domain of stable train femto-second laser pulses ($femto = 10^{-15}$), the light is characterised by a large spread of discrete optical frequency separated evenly. Each frequency has a fine linewidth (around $100\,kHz$) and an important stability potential. The use of this kind of laser has opened a new era in spectroscopy and precision measurements in general and led to a Nobel price for John Hall and Theodor Hänsch [Hall, 2006; Hänsch, 2006].

Frequency combs are a train of short light pulses emitted at regular interval as presented in Fig. 3.15. Because of the short duration of these pulses of light, they can be considered like a comb of Dirac functions in the time domain with a repetition rate f_{rep}. As the Fourier transform of a comb of Dirac functions is also a comb of Dirac functions, the free spectral range between two successive frequencies is equal to the repetition rate

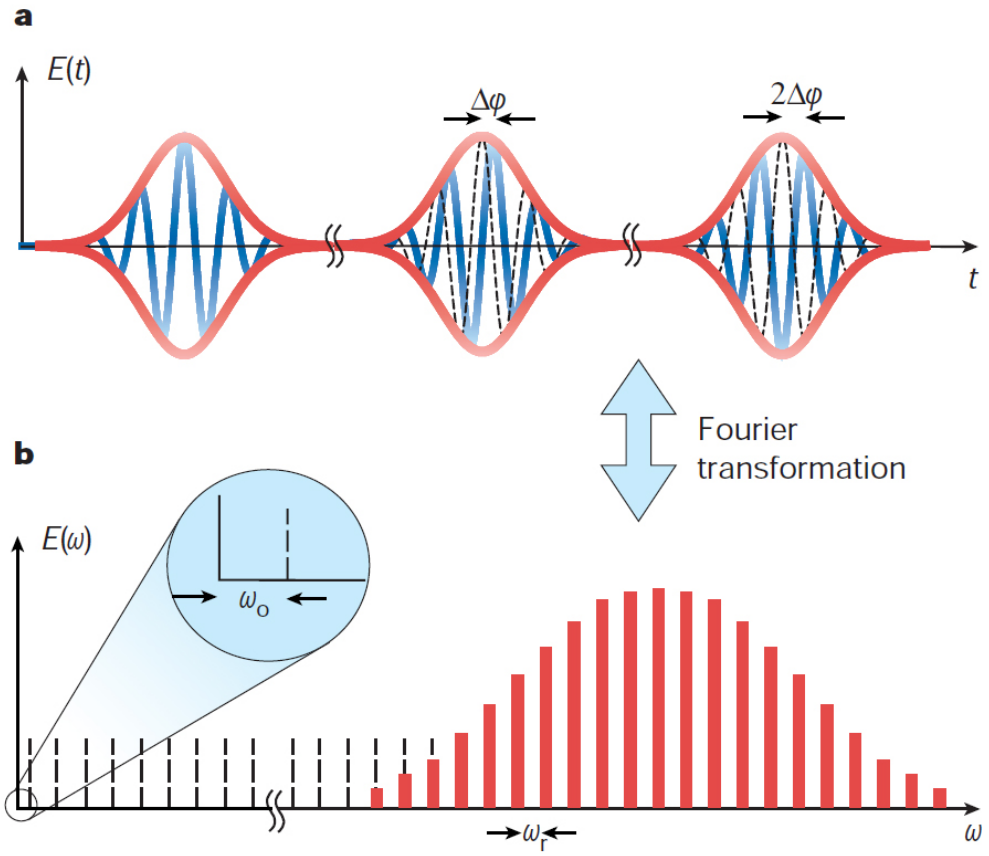

Figure 3.15: Representation of an optical frequency comb in the time domain a) by consecutive pulses emitted by a mode-locked laser and in the frequency domain b) with the corresponding spectrum [Udem et al., 2002]

$f_{FSR} = f_{rep}$ and the frequency of the mode n is defined by:

$$\omega_n = n \times \omega_{rep} + \omega_0 \tag{3.33}$$

where $\omega_{rep} = 2\pi f_{rep}$ and $\omega_0 = 2\pi f_0$ is a frequency offset resulting of the shift of the carrier wave (blue curve in Fig. 3.15a) with respect to the pulse envelope (red curve in Fig. 3.15a). Indeed, the carrier wave is moving with the phase velocity $v_p = \omega/k$ and the envelope is moving with the group velocity $v_g = d\omega/dk$ and in a dispersive medium, the phase and the group velocities are not equal. This leads to an expression of the frequency zero-offset:

$$\omega_0 = 2\omega_c L \left(\frac{1}{v_g} - \frac{1}{v_p} \right) f_{rep} \tag{3.34}$$

where L is the length of the cavity and ω_c is the frequency of the carrier wave.

In the frequency domain, a frequency comb displays an important number of discrete

frequency peaks completely determined from Eq. (3.33) by the repetition rate f_{rep} and the zero-offset frequency f_0. Using a fast photodiode, it is possible to detect the pulses and therefore measure the repetition rate f_{rep}. By an active control of the cavity length and using the expression of the free spectral range, it is possible to keep the repetition rate locked by controlling the cavity length using for instance a piezo-electric actuator (as for the continuous wave cavity ring down for example in section 3.2.4.2).

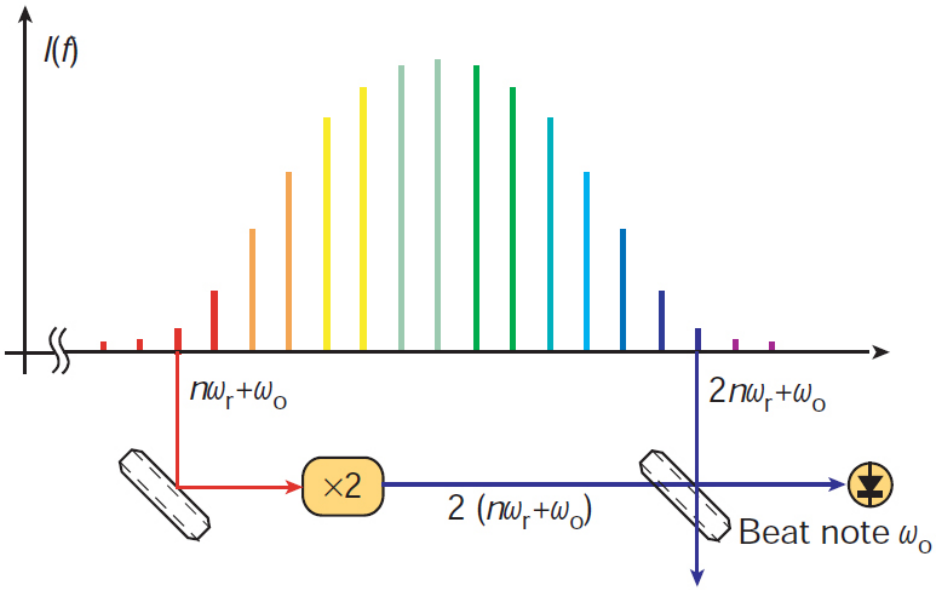

Figure 3.16: Determination of the zero-offset frequency by doubling the frequency of the mode n in a non-linear crystal and making it interfere with the mode $2n$ [Udem et al., 2002]

The measurement of ω_0 is much harder because the measurement of an optical frequency around $10^{14}\,Hz$ is not possible with a precision at the Hz level without a referenced optical frequency comb. The solution to this issue is the self referencing and is based on an interferometric measurement. If the comb spans over at least an octave (meaning the highest accessible frequency is higher than twice the lowest accessible frequency), it is possible to determine this frequency by simply doubling the frequency of the mode n as illustrated in Fig. 3.16: $2\omega_n = 2(n\omega_r + \omega_0)$ and overlapping it on a fast photodiode with the mode $2n$ of frequency $\omega_{2n} = 2n\omega_r + \omega_0$. The beatnote between the two frequencies (see section 4.2.4.1 for more detail on beatnote) is directly the offset frequency ω_0. Using this measurement, through a servo loop on the pump laser power, allows to control the value of ω_0 and to lock it to a reference radiofrequency, for instance against a rubidium clock. Because the first octave-spanning combs have only been realised recently [Jones et al., 2000; Diddams et al., 2000], only recently have we been able to build an absolute

frequency comb.

This method enables building a femto-second optical frequency comb that produces known absolute frequencies over a large range of wavelengths. Optical frequency combs can be used to do spectroscopy directly. If the different teeth of the comb can be injected in a resonant cavity, an entire spectrum can be realised within a few milliseconds and several species scanned at once [Bernhardt et al., 2010]. In this case, the main challenge is to analyse efficiently the light after the cavity. The beatnote obtained by combining the signal of two combs with a small offset in the repetition rate (Δf_r) provides another frequency comb in the radio-frequency domain which can be measured directly and can be scaled to produce the optical spectrum (see Fig. 3.17). With such a method, Rieker et al. [2014] has been able to use dual-comb spectroscopy to measure greenhouse gases remotely over several kilometres paths, including lines of different water isotopes. These methods can provide interesting opportunities to monitor atmospheric trace detection but are rather expensive.

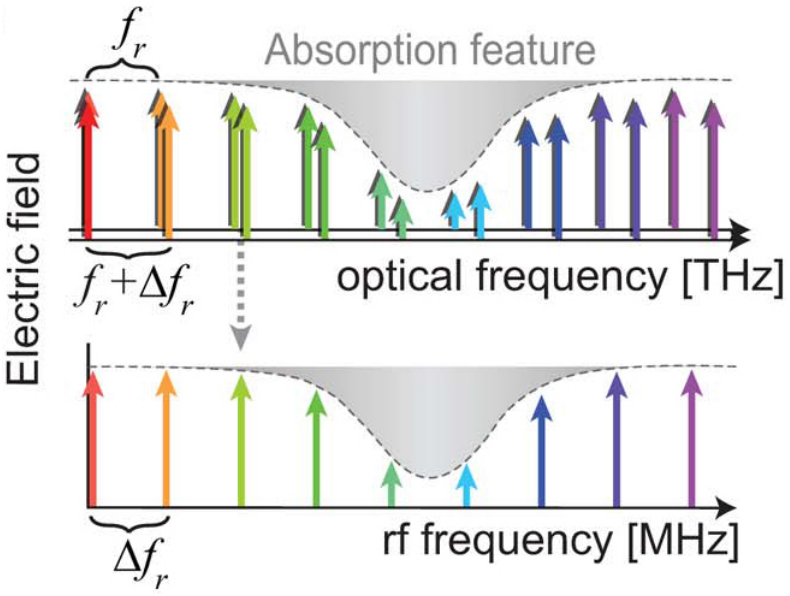

Figure 3.17: Conversion of the dual comb absorption feature into a radiofrequency signal for trace detection measurement [Rieker et al., 2014]

Chapter 4

Development of new spectrometry tools

> Le principe du Biglemoi que Monsieur connait sans doute, repose sur la production d'interférences par deux sources animées d'un mouvement oscillatoire rigoureusement synchrone. *

L'écume des jours
BORIS VIAN

Previous chapter detailed the state-of-the-art in term of mass and infrared spectrometry. In this chapter, we will describe the new developments in infrared spectroscopy that have been realised in the framework of my PhD. Even though commercial instruments are getting more and more powerful, in particular at low humidities, there remains important limitations. Therefore, we need to push the limits of what infrared spectroscopy can achieve. As described in section 3.2.5, infrared spectroscopy relies on both a good absorption measurement and a precise frequency determination. This motivated the development of a water isotope infrared spectrometer based on optical feedback to stabilise the frequency (as for OFCEAS, section 3.2.4.2) and on CRDS to measure the absorption (see section 3.2.4.3).

In this chapter, we will first describe the classical CRDS setup at LIPHY, which already has a sensitivity two orders of magnitude better than most commercial instruments. We describe the first experiments using this setup under a flow of water vapour of known isotopic composition and not for a static vapour as classically done. This was realised with a custom-made humidity generator that is described at the beginning of the section.

∗. The principle of *Biglemoi*, which you sir know for sure, relies on the production of interferences by two sources driven by a rigorously synchronous oscillatory movement.

This humidity generator was involved in laboratory experiments for spectroscopy of water vapour and also in several field campaigns that will be described in the next chapters. We will highlight that even for this powerful setup, one of the main limitation is the frequency noise. This justifies the development of a laser source stabilised by optical feedback from a highly stable V-shaped cavity based on the work of Burkart et al. [2013].

4.1 Water vapour infrared spectroscopy

As detailed in section 3.2.5, evaluation of the isotopic composition from a spectrum is realised by fitting the data with a lineshape and fit parameters. During my Ph-D, several experiments on the spectroscopy of water vapour were realised to evaluate the lineshapes of the transitions commonly used by infrared spectrometers. This was realised using a new generation of humidity generator, especially conceived for low humidities. We will first describe this generator and then a first use of this generator to produce stable water vapour fluxes in a spectroscopy experiment. This will finally be converted in a new set of fit parameters.

4.1.1 Humidity generator

This new generation of humidity generator is inspired from the prototype developed by Landsberg [2014]. The humidity levels at which we aim to measure, are very low (from 1 to 1000 ppm in volume mixing ratio), justifying the need to build a dedicated humidity generator able to provide moisture at these levels. Indeed, commercial calibration devices cannot be used to produce humidity levels that low.

4.1.1.1 Physical principle

The humidity generator is based on undersaturated evaporation of a small droplet at the tip of a needle (see Fig. 4.1a). Liquid water is pushed through a needle around which a flow of dry air is generated. The flux of water f_L is maintained low compared to the air flow f_A so the humidity h of the moist air flow is small ($h << 1$). Therefore, the air stays undersaturated and its humidity is limited only by both flows (liquid water in the needle and dry air around it). The specific humidity of the air is determined by:

$$HS = \frac{d_{H_2O}\, f_L\, R\, T_{st}}{f_A\, P_{st}\, M_{H_2O}} \tag{4.1}$$

where $d_{H_2O} = 1000\, kg\, m^{-3}$ is the density of water, $R = 8.314\, J\, mol^{-1}\, K^{-1}$ is the gas constant, $T_{st} = 293.16\, K$ and $P_{st} = 1.01\, 10^5\, Pa$ are the standard conditions of temperature and

pressure, respectively and $M_{H_2O} = 18\,10^{-3}\,kg\,mol^{-1}$. Note that the flux of water f_L needs to be expressed in $m^3\,min^{-1}$ if the air flow f_A is expressed in $s\,m^3\,min^{-1}$ (standard cubic meter per minute).

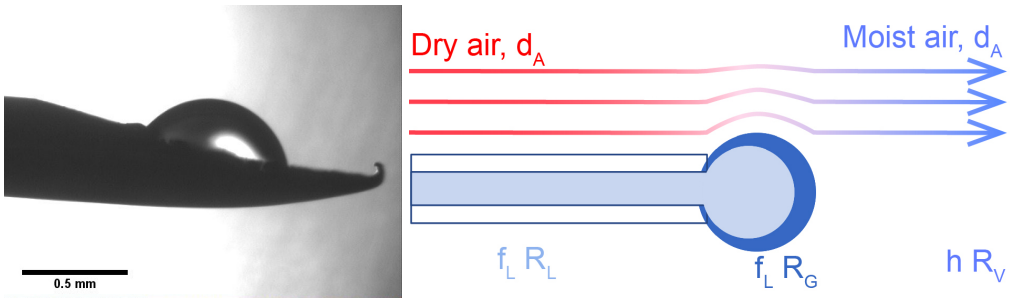

(a) (b)

Figure 4.1: Evporation of the droplet in the chamber of the humidity generator: left, picture from the prototype from Landsberg [2014]; right, schematics of the water molecules being transfered to the air flow.

Physically, when the flux of water or air is changed, there is first a transient regime during which the radius of the droplet changes, modifying the evaporative surface and therefore the humidity of the produced air. Once a permanent regime is reached, the radius of the droplet is stabilised and the humidity fixed by Eq. (4.1). As the stationary regime is reached, there is no accumulation of molecules in the system and therefore the isotopic composition of the vapour produced is equal to the isotopic composition of the water injected in the needle: $R^i_v = R^i_L$ (note that because of the fractionation during the phase transition, the isotopic composition of the droplet R^i_G is necessarily different from R^i_L and R^i_V). Each flux of water evaporating corresponds to a specific size of the evaporation surface and therefore a radius of the drop. The evolution of the radius of the drop can be modelled by a non-linear differential equation on the volume of the drop:

$$\frac{dV}{dt} = f_L - f_{evap} \tag{4.2}$$

where V is the volume of the drop and $f_{evap} = k_e\,S$ is the evaporation flux depending of k_e the evaporation rate and S the surface of the drop exposed to the dry air. The calculation of this surface is not so straightforward: it is the surface of a sphere of variable radius intercepted by the surface of a disk of constant radius (the syringe tip). This system has been numerically modelled by Janek Landsberg and Erik Kerstel. By solving numerically this differential equation, they obtain the simulation in Fig. 4.2. The isotopic composition is computed by the introduction of an evaporation fractionation factor following

Cappa et al. [2003]. This numerical approach validates the theoretical explanation of the undersaturated evaporation of the droplet.

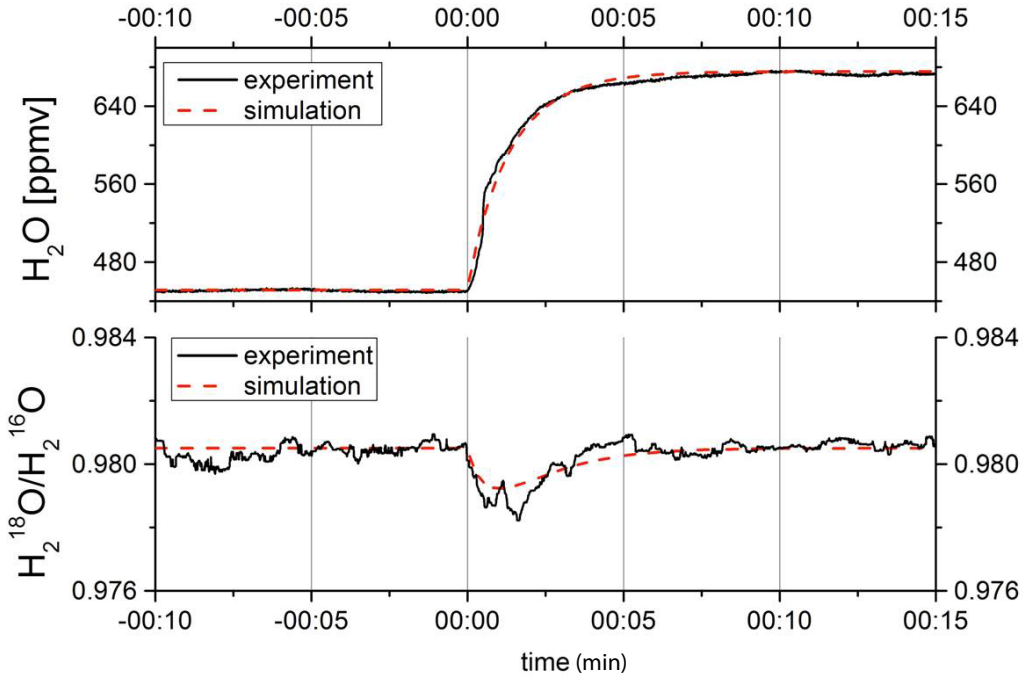

Figure 4.2: Simulation of the humidity and the isotopic composition of the water vapour during a transient event during which the water injected in the needle was doubled [Data and model from J. Landsberg and E. Kerstel, personal communications].

4.1.1.2 Technical realisation of the generator

As the instrument relies on operating on a stationary regime, it is important that the dry air input and the water input are steady. The dry air flux is controlled by a Bronkhorst mass flow controller IQF-200C-AAD-11-V-S from 0 to 500 *sccm* with a precision of 4 *sccm*. The water flux is controlled by a Harvard Apparatus Pump 11 Pico Plus Elite that can produce a water flow down to 3.66 $pL\,min^{-1}$ with an accuracy of 0.5 % using syringes from 10 to 250 μL. The same pump is equipped with two syringes that provides two water flows into two evaporation chambers in parallel (see Fig. 4.3). Each syringe is connected to a water reservoir and to the evaporation chamber by a double 3-ways liquid valve switching from an infuse mode to a pushing mode. The double 3-ways valve is a Rheodyne MXX777603 with leak tight connections and an internal volume 1.9 μL. This modification is a major improvement to the instrument designed by Landsberg [2014] as it enables automatic handling of the standards from a reservoir to the evaporation chamber with a robust connexion avoiding in particular potential air bubbles in the water flow.

Indeed, as we have had amble opportunity to observe, the system relies on a permanent regime, therefore all air bubbles trapped in the water flow will break the steady state and create artefacts in the humidity and isotopic composition, reducing the performance of the calibration device. In addition, this provides with the opportunity of a "refill" mode in which the syringes draw standard water from a reservoir. The 100 μL volume of the syringes suffices for operation over several hours, up to one day. With the addition of the refill option, the instrument can be used unattended for many months (such as demanded for an Antarctic campaign).

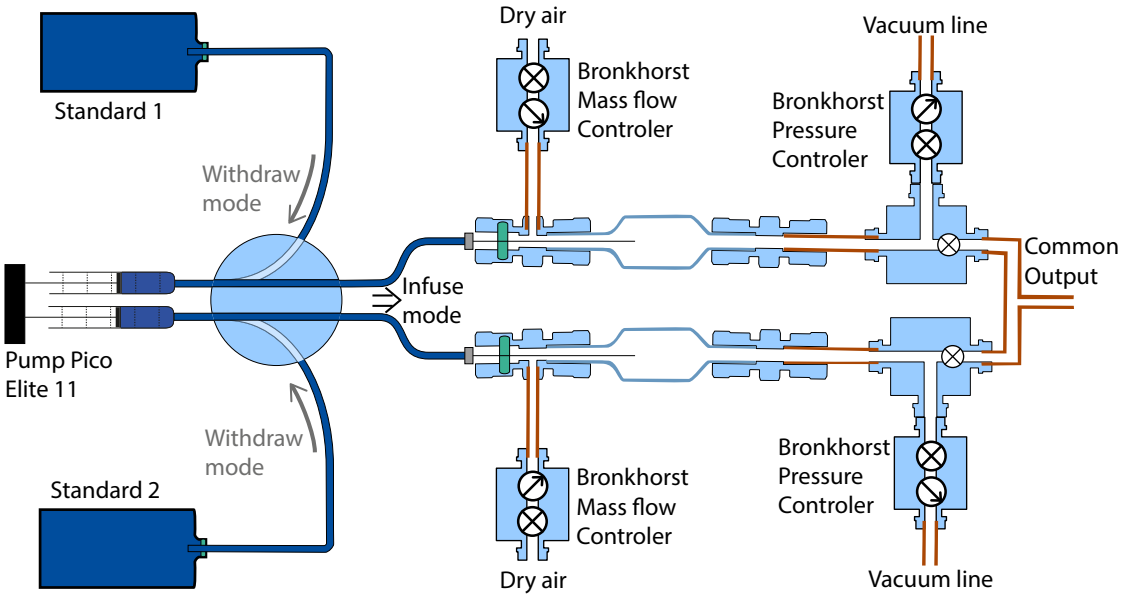

Figure 4.3: Humidity generator schematic drawing in the infuse mode. Note that on the schematic appear two pressure controllers. In reality only one single controller controls the pressure on both lines at the same time.

The evaporation chambers are made from stainless steel swagelok cylinders on which ultratorr connectors are holding viton septa in which needles are inserted toward the middle of the chamber. The pressure of both chambers is regulated by a single Bronkhorst P-702CV pressure controler with a precision of 3 *mbar* from 0 to 1000 *mbar*. This common pressurisation of the two chambers and the relatively high flow (higher than needed by the infrared spectrometers) allow to maintain a steady state whether or not the infrared spectrometer is connected, and increases the time efficiency of calibration procedures.

This humidity generator relies on the same principle than the one developed by Landsberg [2014] of steady undersaturated evaporation of a drop at the tip of a needle. Still, here, the entire instrument has been remodelled including:

- A new system to handle liquid samples without manual intervention with a liquid double 3-ways valve as described above.

- All the gas handling has been made with copper tubes and ultra-torr connectors to obtain the best performances in term of memory effects and airtightness.

- The injection chambers were redesigned: the chambers of the generator of Landsberg [2014] were home-made aluminium blocks in which the internal diameter was only 4 mm, this created issues if the needle was not perfectly straight, the tip could touch the walls of the injection chamber, resulting in variable surfaces of the aspherical drops and therefore important variations of the air/water interface which directly influences the humidity generated. Here, we used commercial stainless steel chambers Swagelok SS-4CD-TW-10 with an internal diameter of 21.8 mm and ultra-torr connectors holding the septum modified as on schematic 4.3 with an air inlet welded in the central part.

- A stand-alone electronic control which insures both power supply and communication between the different valves and pump and a computer on which a user-friendly software was developed using Labview.

- A new function for the pressure inside the cavity to mimic the atmospheric pressure: we use a differential pressure gauge to monitor the difference of pressure inside the evaporation chamber and of the outside air; this function can be used in the field to insure that the calibration is not affected by the evolution of the atmospheric pressure.

This humidity generator has been used several times during my Ph-D: in laboratory experiments to record spectrum of water vapour under continuous flow conditions and to measure the equilibrium fractionation, and during two field campaigns at Dome C in 2014/15 and 2015/16. It has been tested during long term measurements of the humidity. Unfortunately, at the noise level of the isotope analyser (Picarro L2130i), it was not clear whether the humidity generator or the Picarro was responsible for the noise at a level around 4 $ppmv$ on the humidity level.

4.1.2 Water isotope calibrated spectrum

Before realising new developments in infrared spectroscopy, we used an existing setup consisting of a CRDS cavity of 1.4 m optimised to measure absorptions of traces of water vapour similar to Kassi and Campargue [2012] injected by the humidity generator described in the previous section. These experiments aimed to realise reference spectra of water vapour at different isotopic compositions found in natural water. The purpose of this experiment is: (1) to characterise the spectral area where most of commercial infrared spectrometers are working and (2) to evaluate the performances that can be reached with an optimised CRDS system. These spectra are among the first to be realised in a flux of water vapour of known isotopic composition and therefore will provide information about the relative peak intensities of the transitions present in the spectrum for a precise referenced isotopic composition.

4.1.2.1 General set-up

These water spectra are realised for a steady flow of water vapour molecules. In order to realise these, we used the setup described in Kassi and Campargue [2012]. The frame of the CRDS is a 1.42 m long electro-polished stainless steel cell with an inner diameter of 11.5 mm equipped with two high reflectivity mirrors Layertec ($R = 0.99998$ at 1390 nm) with an empty cell ring down time up to 494 μs at 7200 cm^{-1}. The cavity is injected with a fibred DFB laser NEL 1392 nm emitting around 20 mW intensity power and with a 2 MHz linewidth. The DFB laser is powered with a custom made current source and temperature controller. This custom electronic control allows to scan the frequency of the laser by controlling the laser chip temperature from -10 to 60°C with a resolution of 1 mK equivalent to $sub-MHz$ potential resolution.

Even though the fibred laser is equipped with an optical isolator, a second optical isolator is protecting the DFB diode from optical feedback as illustrated in Fig. 4.4. A splitter sends a fraction of the light (10 %) to a wavemeter HighFinesse WSU7-IR: a commercial Fizeau type wavemeter with a 5 MHz resolution, a 20 MHz accuracy over 10 hours and a typical refresh rate of 20 Hz. The remaining light is sent to the CRDS cavity through an acousto-optic switch with a response time of 20 ns and an isolation of 100 dB.

A fibre port (FL in Fig. 4.4) consisting in a FC/APC fibre adapter is used to focus the light and to mode-match the laser to the TEM_{00} cavity mode with two steering mirrors (not shown in Fig. 4.4). The cavity relies on CW-CRDS as presented in section 3.2.4.3. The cavity temperature is monitored by a calibrated TSIC 501 sensor with an

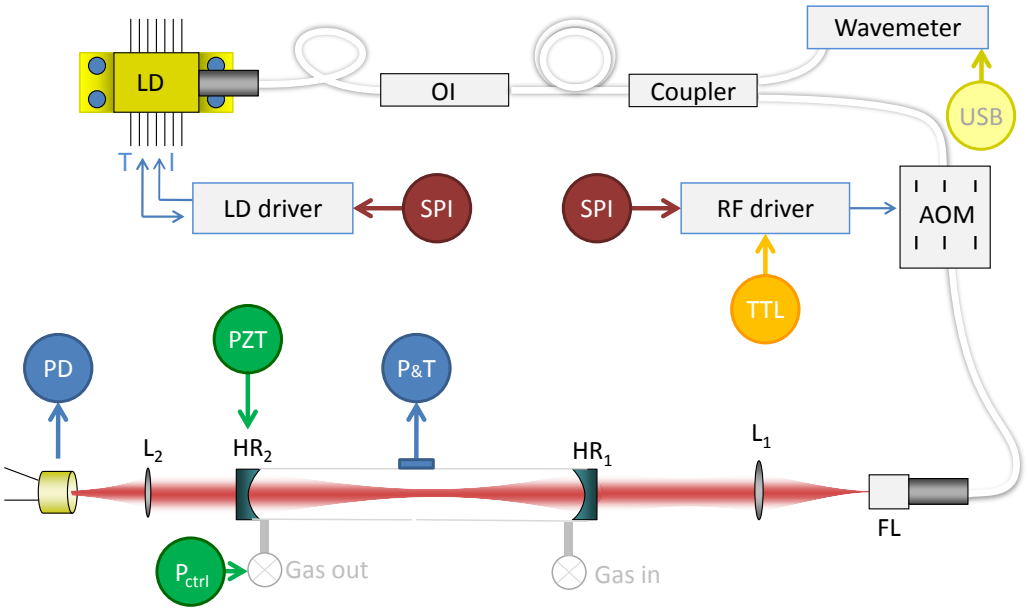

Figure 4.4: Schematic of the optical part of the setup used to realise the spectra of water vapour under a steady flow: the light of a fibred laser diode (LD) is sent through an optical isolator (OI) and split by a coupler. 10% of the light is sent to a wavemeter and 90% to an acousto-optic modulator (AOM) and then to the CRDS cavity. SPI communications enable to control the temperature and the current of the laser diode (modified from Kassi and Campargue [2012]).

accuracy of 0.1°C and by an uncalibrated PT1000 probe on a Wheatstone bridge with a precision of 10^{-4}°C. The cavity pressure is monitored by a pressure transducer Baratron 100 *Torr* and regulated by a Bronkhorst Pressure Controler P-702CV downstream of the cavity. After the cavity, on the optical path, a lens focuses the transmitted light onto an InGaAs avalanche photodiode (PD). The ring-downs are triggered once a computer controlled threshold is reached on the photodiode signal by activating the acousto-optic driver TTL switch. The transmission of the cavity signal on the photodiode is recorded by an acquisition board (NI-PCIe6351, 16 bits resolution, 2 *MHz* acquisition rate) and fitted to an exponential decay with a fast Newton method based C routine.

The flow was generated by the humidity generator described in the section 4.1.1 using three different water standards: EPB, NEEM and UL5 (see Table 3.1 for their isotopic compositions) for humidity ranging from 75 to 600 *ppmv* in an air matrix. A commercial infrared spectrometer (Picarro *L*2140*i*) was installed in parallel of the CRDS cavity previously described providing a validation of the stability of the vapour content (both humidity and isotopic composition) for the duration of the spectrum. We recorded spectra of the water mixture of isotopes for all three standards between 7199.33 and 7202.04 cm^{-1} for a large range of pressure (10 to 80 *mbar*) and water partial pressure (5 to 50 μbar).

These spectra will ultimately be used to constrain the fit parameter of a few transitions with known isotopic compositions with a multifit approach in order to be able to express their dependency to the pressure and the partial pressure.

4.1.2.2 Results

in Fig. 4.5, we present one spectrum realised by the flow CRDS setup described in the previous section, the three transitions measured by the Picarro analyser to infer water isotopic composition (see Fig. 3.12). The transition at 7199.96 cm^{-1} is attributed to $H_2^{18}O$, the one at 7200.13 cm^{-1} to $H_2^{16}O$ and the one at 7200.3 cm^{-1} to HDO. This spectrum is realised for a water vapour of known isotopic composition (NEEM in Table 3.1) at a pressure of 39.98 $mbar$, a temperature of 23.53°C, with a humidity of 603 $ppmv$. The spectrum is fitted using a Nelkin-Ghatak lineshape which takes into account the Doppler Broadening and Dicke narrowing (hard collisions with a change of the velocity distribution of the molecules associated with the increased collision rate). Several additional transitions, all belonging to $H_2^{16}O$ (626 in HITRAN nomenclature), have been included to realise the spectrum due to their non-negligible impact on the baseline, they have been modelled with the same type of profile. The intensities, Lorentzian broadening and Dicke narrowing paremeters, were taken from the HITRAN database. The Doppler Broadening was fixed to its theoretical values according to the gas temperature and the mass species. For these spectra, we included transitions at 7199.32, 7199.37, 7199.87, 7200.05, 7200.33 and 7200.38 cm^{-1}.

The complete spectrum covers roughly 2 cm^{-1} with a baseline RMS absorption noise around $2\,10^{-11}$ cm^{-1} per ring-down (by comparison, Picarro's analyser need to average 100 datapoints to reach this level [Crosson, 2008]). Despite the very high performances of the CRDS measurements, important residuals are noticeable in Fig. 4.5. These residuals are due first to the lack of frequency stabilisation and second to the lineshape. During the realisation of these spectra, the noise on the frequency of the laser diode was 4.7 MHz, this jittering creates important residuals particularly on the wings of the transition because variations of frequency are associated with important variations of absorption. We have identified the source of the noise to the current card driving the laser and the bug has been fixed since then. The second source of noise is the lack of speed-dependence in the physical model that creates additional residuals. This is visible thanks to the typical of the asymmetry of the residuals on the wings of the transitions. Nevertheless, we decided not to use a lineshape including the speed-dependence because the frequency noise had the same order of magnitude than these residuals and therefore prevented from a precise and meaningful determination of the fit parameters.

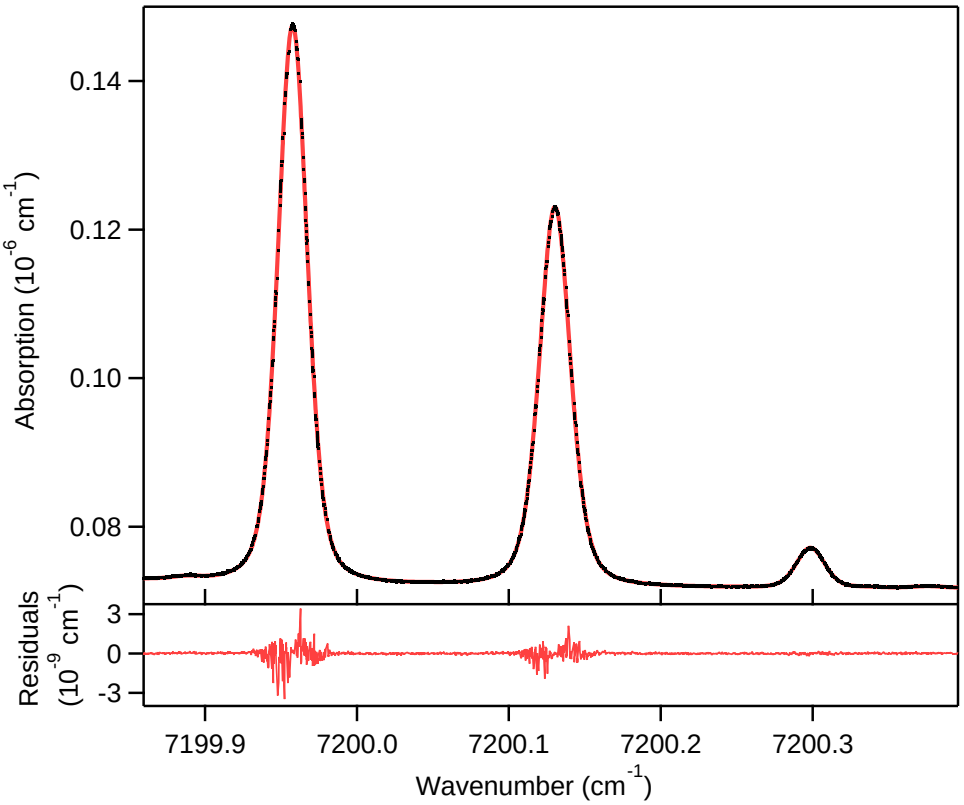

Figure 4.5: Spectrum of 24.12 μbar of water vapour in 39.98 *mbar* synthetic air at 23.53°C at 7200 cm^{-1} by the flow CRDS setup fitted with a Nelkin-Ghatak line profile.

We realised almost 100 spectra at different conditions of pressure and water partial pressure. The covered range for each type of water isotopic composition is presented in Fig. 4.7. Using precise pressure measurements and 27 of these spectra, in Fig. 4.6, we estimated the pressure dependency of the Lorentzian pressure broadening γ parameter and of the Dicke narrowing β parameter. For the pressure broadening, we observe a linear dependency of the Lorentzian parameter in agreement with the values from the literature from HITRAN database for the transitions at 7200.3 cm^{-1} as presented in Table 4.1, but not for the transition at 7199.96 and 7200.13 cm^{-1} where we found small differences. Note that the transition at 7200.3 cm^{-1} is weaker than at 7199.96 and 7200.13 cm^{-1} and therefore the signal to noise ratio is not as good, which might be the reason of the apparent agreement between our results and the one from the HITRAN database.

For the Dicke narrowing parameter, we obtained values as presented in Table 4.2. These curves are very powerful tool. Indeed, we can use the temperature to infer the Doppler Broadening and the pressure to directly infer the beta and the Lorentzian broad-

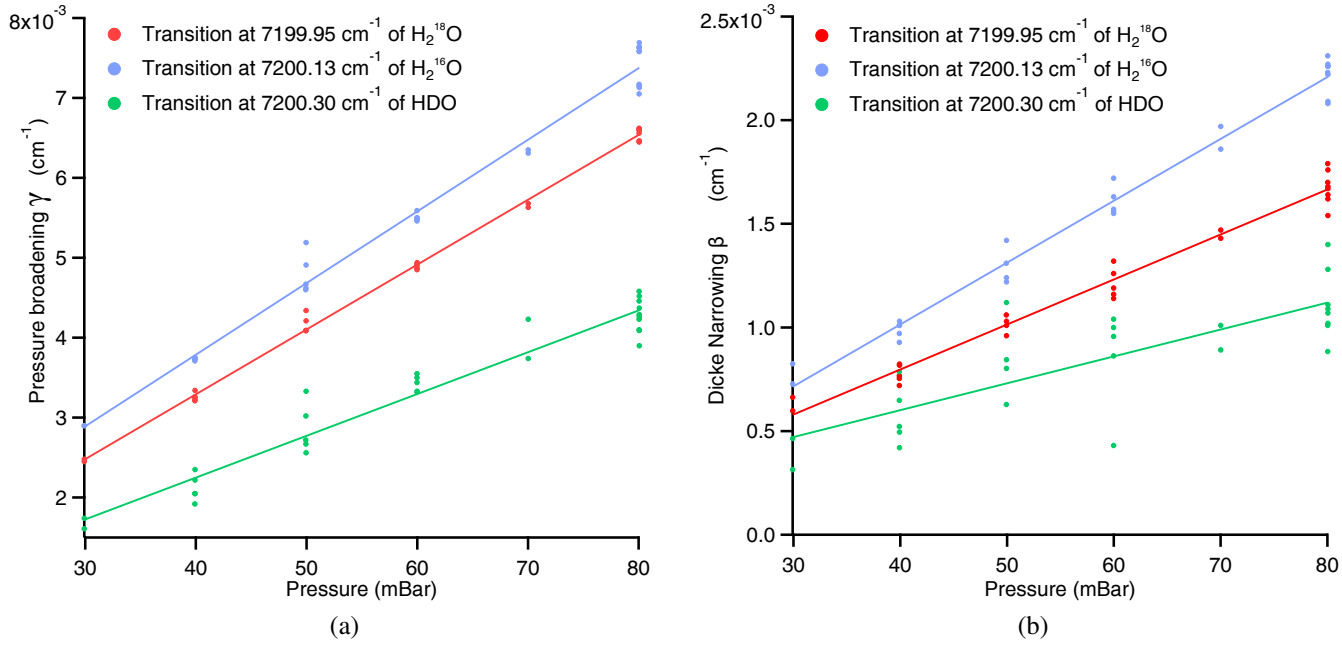

Figure 4.6: Determination of the fit parameters from 27 spectra realised at different conditions of pressure of a) the pressure broadening Lorentzian parameter and b) the beta Dicke narrowing parameter included in the Nelkin-Ghatak Humlicek profile for the three transitions at 7199.96, 7200.13 and 7200.3 cm^{-1}

Table 4.1: Dependency of the Lorentzian parameter with the pressure for the transitions at 7199.96, 7200.13 and 7200.3 cm^{-1}

Transition's wavelength (cm^{-1})	Estimated slope (cm^{-1}/atm)	Slope from the literature (cm^{-1}/atm)
7199.96	$8.38\,10^{-2}$	$8.29\,10^{-2}$
7200.13	$9.61\,10^{-2}$	$9.39\,10^{-2}$
7200.30	$5.54\,10^{-2}$	$5.54\,10^{-2}$

ening parameters without fitting them from the spectra. Each parameter fitted requires more datapoints per transition. Therefore, by providing robust parametrisation of the temperature and pressure dependencies of these parameters, we can optimise the sampling rate by reducing the number of points in the spectra. These parameters were successfully used to fit all the 100 spectra, attesting their relevance no matter the temperature, humidity or isotopic composition. To our knowledge, this is the first determination of the Dicke narrowing beta parameters of those water transitions.

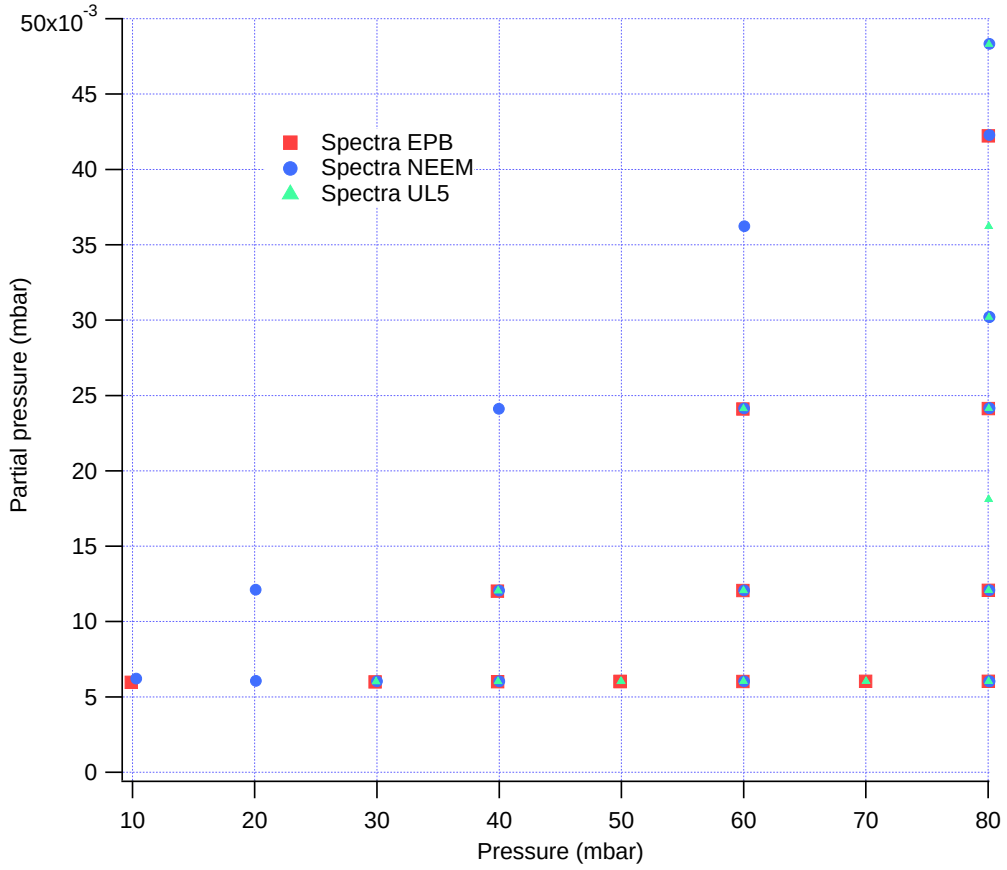

Figure 4.7: Summary of the range of pressure and water vapour partial pressure covered by the set of spectra presented here.

Table 4.2: Dependency of the beta parameter with the pressure for the transitions at 7199.96, 7200.13 and 7200.3 cm^{-1}

Transition's wavelength (cm^{-1})	Estimated slope (cm^{-1}/atm)
7199.96	$2.09\,10^{-2}$
7200.13	$2.74\,10^{-2}$
7200.30	$1.44\,10^{-2}$

Several sensitivity tests have been realised. In particular, we estimated the stability of the isotopic composition in the cell. We observed that there was an important outgasing of the cell itself which affects over several hours the isotopic composition. This created

large uncertainties on the isotopic composition of the vapour in the cell and limited the interpretation of the data for the absolute determination of the intensity of the transition per molecule. The important outgasing was attributed to the low temperature of the cell (around 20°C). Still, this is the first experiment of spectroscopy of water vapour with known isotopic composition. Indeed, previous realisations of spectra were realised by vaporising a water sample at natural abundance (presumably local tap water) in uncontrolled temperature conditions. Thus, the isotopic composition of the vapour formed was only weakly constrained because of (1) the variations of the equilibrium fractionation coefficients with the temperature and (2) the unknown initial liquid composition. Here, because we generate the moisture with a calibration device, the isotopic composition is known within 0.1‰ for $\delta^{18}O$ for instance. We estimate that the outgasing of the cell adds up a limited uncertainty of 3‰. These results show biases up to 40‰ on $\delta^{18}O$ on the absolute intensities of the transition of the heavy isotopes compared to the light isotope. These preliminary results justify to realise spectra of water vapour of precisely known isotopic composition in order to indicate the intensity of the transition per molecule of the *SMOW*. The precision of this value is crucial to obtain better interpretation of spectra in the future.

4.1.3 Conclusion

We realised the first spectra of water vapour of known isotopic composition in the near-infrared region. So far, we focused on the three transitions used by Picarro's analysers (such as the L2130i) and the HiFI. The spectra were realised at different conditions of pressure and water vapour partial pressure. We estimated the Lorentzian pressure broadening parameter and the Dicke narrowing parameter dependency with the pressure (see Tables 4.1 and 4.2). In addition, we show that the absolute intensities of the transitions of the different isotopes are not precisely referenced compared to the SMOW. For application in infrared spectroscopy, these biases in absolute intensities lead to important isotope-isotope correction to apply to the data.

The main limitation to obtain more information from these spectra is the laser frequency noise. Because of this limitation, we decided not to extend the analysis to the entire range of wavelength we covered and rather to fix the frequency issue to realise new set of spectra. In order to improve the precision of the frequency, we used optical feedback to stabilise the frequency of the laser.

4.2 Optical feedback frequency stabilisation

To infer the frequency more precisely during the realisation of the spectra, we can either measure with a precise wavemeter the frequency or stabilise the laser source, for instance with optical feedback frequency stabilisation. The only absolute and precise method to measure an optical frequency relies on the beatnote with a frequency comb (see section 3.3). Considering the price of an optical frequency comb and the complexity of the method, the frequency stabilisation by an external cavity was chosen.

The method of optical feedback frequency stabilisation we use here is based on the work of Burkart et al. [2013] (for more details, also see Burkart [2015]). In their work, Burkart et al. [2013] used Distributed-Feedback Diode laser (DFB) with a typical linewidth of several MHz locked on a V-shape cavity to create $sub-kHz$ very stable laser. DFB lasers in the infrared region build on important efforts to create cheap and efficient lasers for telecommunication purpose (more information about the DFB lasers we use here can be found in annex C.2). Indeed, optical fibres have a minimal absorption in this region. The initial purpose was to create a tunable laser source with a very fine linewidth for metrological purposes. First, we will describe the work of Burkart et al. [2013] and the first generation of V-shaped Cavity Optical-Feedback-stabilised laser source (VCOF), then we will focus on the second generation of VCOF developed during my Ph-D and finally, the performances of the last generation of VCOF compared to an optical frequency comb.

4.2.1 V-shaped Cavity Optical-Feedback-stabilised laser source

As in the case of OFCEAS (section 3.2.4.2), the VCOF relies on optical feedback from a very stable Fabry-Perot resonator to lock and stabilise the frequency of a jittering and relatively broadband laser, here a DFB laser. Nevertheless, in the case of a VCOF, the point of the cavity is not to acquire a spectrum for a gas but only to stabilise the laser. This stabilisation is thus several order of magnitude more precise than in the case of the OFCEAS instruments (no impact of the gas on the finesse of the cavity). Ultrastable cavity for metrology applications are usually built using linear cavities composed of two ultrapolished mirrors are optically contacted on the two faces of a Ultra-Low Expansion (ULE) glass spacer [Ludlow et al., 2007; Alnis et al., 2008]. In the case of this first VCOF, because of the V-shape, the mirrors were not optically contacted on the cavity but hold tightly by low-expansion mirror holders in super-INVAR as illustrated in Fig. 4.8. Indeed, the optical contacting of the mirror is rather complicated to achieve with a V-shaped cavity.

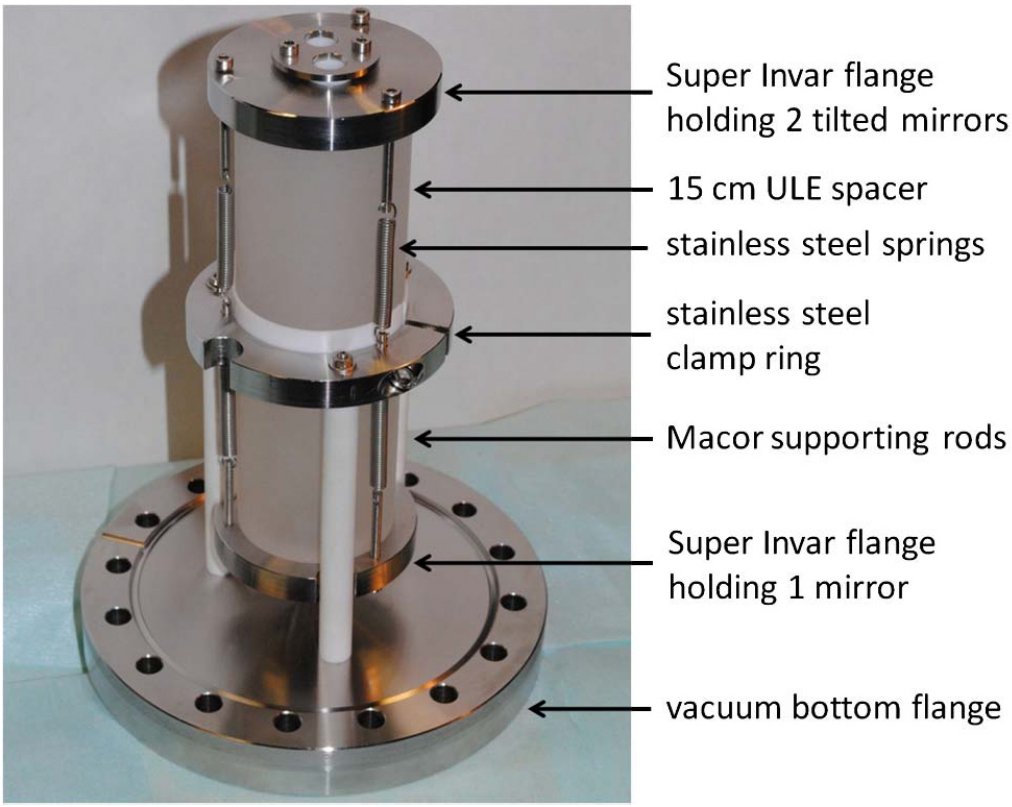

Figure 4.8: Picture of the first highly-stable V-shaped cavity on a stainless steel flange [Burkart et al., 2013]

This VCOF was therefore a hybrid between classical ultrastable cavities made only of ULE glass and OFCEAS cavities made from stainless steel (see Table 4.3 for thermal expansion coefficients). The choice of super-invar to hold the mirrors was the best compromise between a low thermal expansion, a high specific heat (in order to increase thermal inertia) and the possibility of machining at the laboratory's workshop. Machining a mirror holder requires high standards of precision for the relative position of the mirrors: the two mirrors on the top have a tilt of 2.50° which should be precisely respected in order to have the cavity aligned by construction. The mirror holders are fixed to the cavity by springs connected to the central stainless steel clamp ring. The whole cavity is mounted in a vacuum chamber made of stainless steel and closed by CF100 flanges to obtain high vacuum (down to $2.10^{-7} mbar$). High vacuum is important to reduce the refractive index fluctuations impact on frequency drift. In this version, in order to reduce temperature gradient inside the chamber, aluminium sheets were installed around the cavity. The cavity is hold by Macor glass ceramic legs, a material with low thermal conductivity ($1.46 W.m^{-1}.K^{-1}$) but good vacuum properties. Temperature was actively stabilised using a supercool sys-

tem to a temperature of 23°C with root mean square (RMS) temperature fluctuations of 250 μK and temperature difference between the two opposite ends of the chamber always smaller than 8 mK.

Table 4.3: Physical properties of several materials used in the conception of the different generations of VCOF

	ULE	Zerodur	Super Invar	Aluminium	Copper
Thermal conductivity ($W.m^{-1}.K^{-1}$)	1.31	1.46	10.5	237	401
Specific heat capacity ($J.kg^{-1}.K^{-1}$)	767	800	515	897	385
Density ($kg.m^{-3}$)	2210	2530	8150	2700	8960
Thermal expansion ($ppm.K^{-1}$)	0.03	0.007-0.1	0.6	23.1	16.5

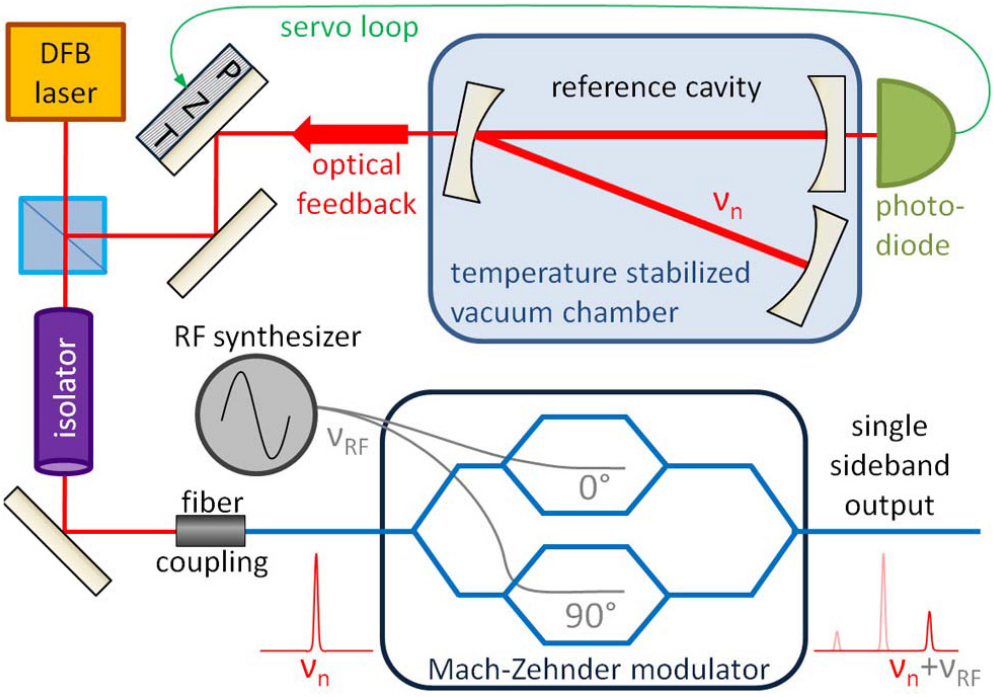

Figure 4.9: Schematic of the first VCOF experimental setup, PZT stands for piezoelectric transducer, ν_n is the reference cavity resonance frequency and ν_{RF} is the radiofrequency driving the Mach Zehnder Modulator [Burkart et al., 2013]

Typical time response of the cavity to a temperature step is approximately 12 hours [Burkart et al., 2013]. This means that the flange, the aluminium sheet and the vacuum are filtering low frequency temperature variations. The total frequency drift associated with the temperature jump would correspond to a thermal expansion coefficient of

$6.0\,10^{-7}K^{-1}$, this corresponds to the thermal expansion of the super invar.

Figure 4.9 illustrates the experimental setup around the cavity. The DFB laser light is separated in 2 arms by a Glan-Taylor Polariser (light blue cube). Part of the light (around $1\,mW$ out of the $20\,mW$ produced by the laser) is sent to the cavity. The phase of this part of the light is actively adjusted by a piezo transducer controlling the distance between the laser and the cavity for the light incoming the cavity to always be in phase with the resonant light in the cavity. The rest of the light is sent through an optical isolator to a fibred Mach-Zehnder modulator (MZM).

The Mach-Zender modulator is used here as an optical frequency shifter. This modulator can shift the frequency of the light from virtually DC to $20\,GHz$ using sideband modulation by a radiofrequence [Kawanishi et al., 2006]; detailed explanation can be found in [Burkart, 2015]. In this application, this device enables tuning the frequency of the laser without losing the coherence and altering the frequency stabilisation up to $6\,GHz$ on both sides of the carrier.

In order to characterise the setup, Burkart et al. [2013] used another Fabry-Perot cavity as an optical spectrum analyser. The secondary cavity was a linear cavity (two mirrors) made of super-invar with a finesse of $5.5\,10^5$ and a free spectral range (FSR) of $4.8\,GHz$. Using the MZM, they first scanned the etalon frequency response in transmission. Then, using this response function, they could estimate the drift of the laser around the centre of the resonance frequency of the etalon. This method provided with the power spectral density of the frequency noise as presented in Fig. 4.10. Important low frequency contribution from seismic noise affects the measurement. At higher frequency, two important peaks are visible: at $1.1\,kHz$ which is attributed to a mechanical resonance of the setup and at $5.9\,kHz$ due to the laser current modulation. Using the β-*separation line technique* [Di Domenico et al., 2010], Burkart et al. [2013] evaluated the full width half maximum (FWHM) of the laser $\Delta\nu < 530\,Hz$. This corresponds to a narrowing of at least 4 orders of magnitude of the laser width. Unfortunately, at this point, they were not able to estimate a more precise FWHM of the laser. The drift of this laser stabilised by this first generation of VCOF is estimated at $20\,Hz/s$.

This VCOF has been built to produce highly coherent light at $1590\,nm$ and has been used for absorption line metrology of CO_2 [Burkart et al., 2014; Burkart and Kassi, 2015]. At these wavelengths, water vapour is completely transparent and therefore this is not directly applicable to water vapour spectroscopy. During my Ph-D, I have assembled two

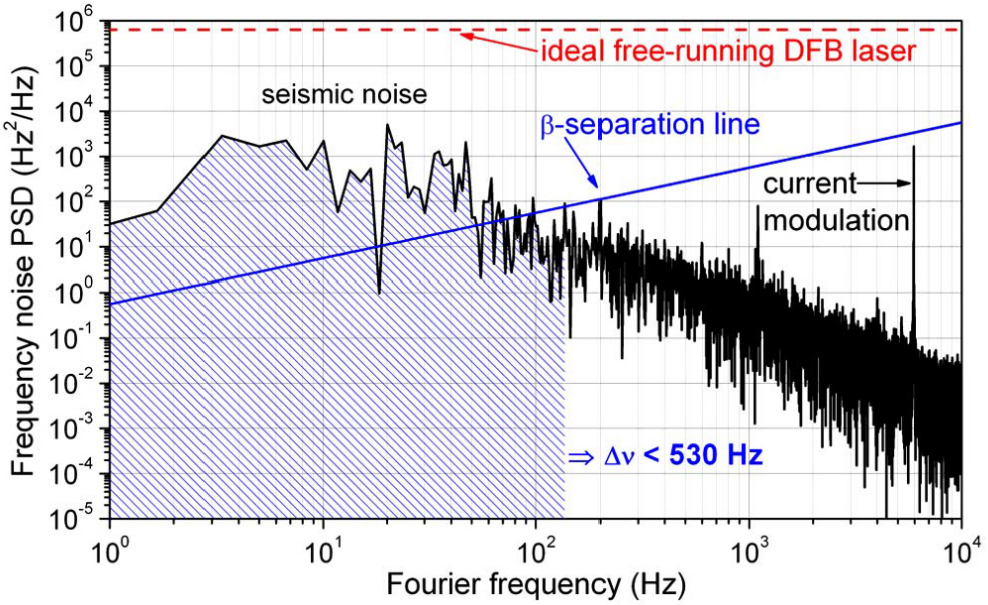

Figure 4.10: Frequency noise PSD of the single-sideband light measured using a Supar Invar etalon. [Burkart et al., 2013]

new generations of VCOF with the help of Johannes Burkart, trying to compensate for the flaw of this first VCOF. In particular, this first VCOF was characterised by a thermal expansion coefficient completely dominated by the super-invar whereas the holders correspond to a relatively low contribution of the length of the cavity. In order to reduce the high thermal expansion coefficient of this first VCOF, I have assembled a second prototype replacing the spring by threaded bars (see Fig. 4.11). Indeed, it was feared that the $1.1\,kHz$ highlighted above was due to the spring resonance on the bottom mirror and that this variations lead to the high thermal expansion.

The first attempt was realised with the bolts directly tightening the holders on the bars as on the picture 4.11. It quickly appears that even without putting an important torque on the bolts, we were compressing the ULE-glass spacers when changing the temperature, losing all the interests of such a glass. We introduce belleville washers between the bolts and the holders to reduce the stress on the spacer. These washers are not flat but have a conic shape and can be deformed. They act here as a spring, holding tight the holders on the spacer without creating stress on the glass. The second addition to this new VCOF was the addition of a massive copper shield around the cavity. This setup had a typical time response to a temperature step of approximately 18 hours, slightly better that the one presented by Burkart et al. [2013]. Finally, the vacuum system was optimised by the introduction of an ion pump to the flange: previously the system was only relying on active

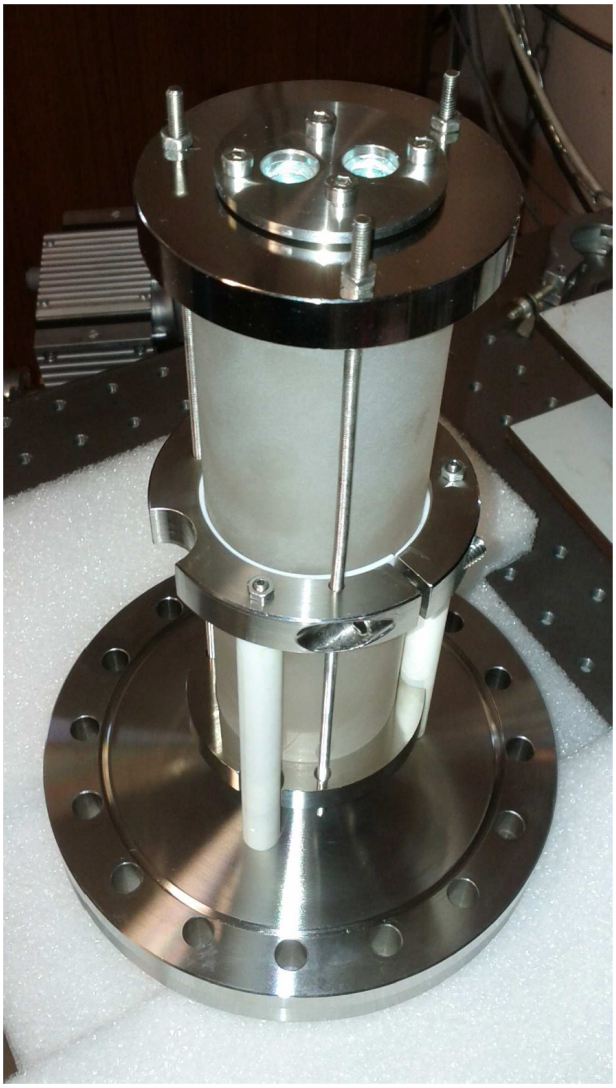

Figure 4.11: Picture of the second highly-stable V-shaped cavity on a stainless steel flange

turbo pumping which created vibration and perturbed the system, therefore pumping had to be stopped during measurement, relying only on passive vacuum inside the cell. The addition of a vibration-free ion pump enables to maintain condition on a long term basis. If the drift of the cell remains similar ($20\,Hz/s$), the FWHM has been determined to be lower than $670\,Hz$, similar results than the previous one. The main improvements for this cell are therefore not coming from replacing the springs by threaded bars but only by the shields and pressure control which are more efficient and therefore increase the duration during which the cavity is remaining stable for a measurement without any intervention.

If the performances of these cavities are perfectly fine for most of spectroscopy applications (a *sub-kilohertz* laser source can fully resolve absorption lines roughly $1\,GHz$

large), the drift of the cavities hampers their possible use on the field where the environmental conditions are not as stable as in the laboratory and therefore could quickly impact the datasets.

4.2.2 Realisation of a second generation VCOF

This motivated for the development of a new generation of VCOF with improved drift and stabilisation which could be used as a frequency reference. Following the classical designs of ultrastable cavity, we realised a new cavity made solely of ULE glass on which the mirrors would be fixed by optical contacting. This concept was challenging to realise given the V-shape geometry of our cavity (to our knownledge, all the ultrastable cavities are linear): indeed, installing the two top mirrors would require two arms in the spacer (V shape) which is fairly complicated to machine in glass. Instead, it was decided to create one big common aperture for both beams and mirrors and to only contact the mirrors on a small surface (see Fig. 4.12 and 4.13). The top mirrors were finally only hold by half the outer $1\,mm$ ring of the $1\,inch$ concave mirror which was chamfered and polished. Machining of the spacer and optical contacting were realised by Winlight Optics from the selected design in *Zerodur Extrem* 7 glass, which has a typical thermal expansion coefficient of $7\,10^{-9}\,K^{-1}$ (see Table 4.3).

The choice of materials (aside from the spacer) was realised to obtain the best vacuum qualities of the cavity, we therefore reduced to a minimum the use of hydrophilic materials and all metal parts have been electro-polished. The cavity was installed in the shield and in the flange in a white room class 100 to limit the impact of dust. Two pumping devices were used to put the cavity under vacuum. First, a turbo pump connected through the KF25 flange (T) in Fig. 4.12 to bring the whole system down to $10^{-6}\,mbar$. As we were forced to glue the windows to the flanges, it was not possible to heat the flange to more than 40°C to enhance the water outgasing from the surface. After 2 weeks of secondary vacuum, the copper tube (C) was crushed to seal the cavity and the ion pump, a GammaVacuum 3S-CV-1V-5K (I), was turned on. The ion pump is plugged on a uninterruptible power supply (UPS) and has been maintaining the cavity under vacuum for the last year at a level of $10^{-7}\,mbar$.

The mirrors are provided by Layertec with a nominal reflectivity at $1390\,nm$ of 0.99997 and a transmittance of 0.00002. We characterised these mirrors in a $27\,cm$ linear cavity. At $1390\,nm$, the ring-down of the empty cavity went up to $39\,\mu s$ which is equivalent to a finesse of 140000 and a reflectivity of the mirrors of 0.999977 therefore slightly better than the specifications.

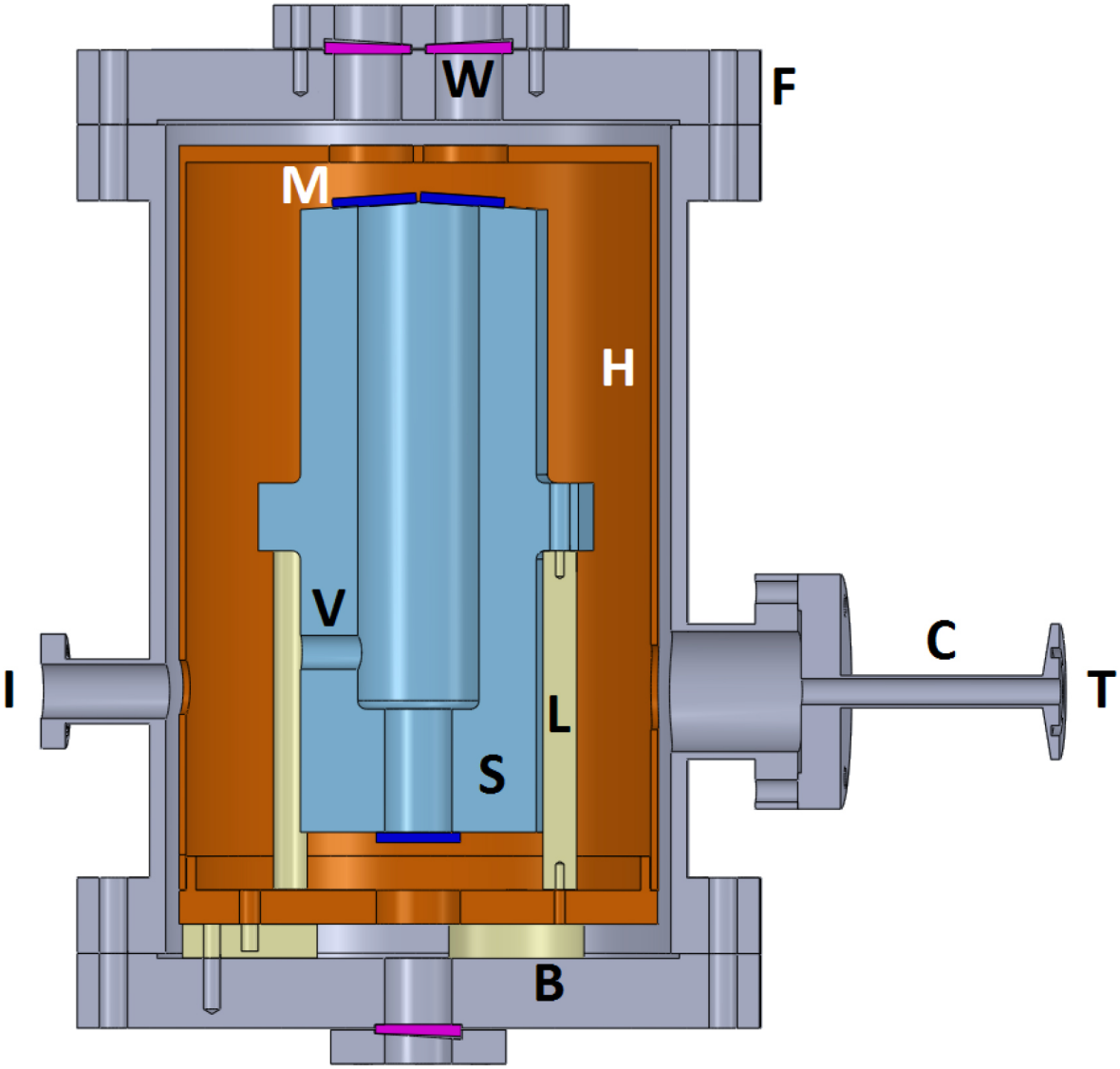

Figure 4.12: Computer assisted design of the second generation VCOF setup. Three high reflectivity silicium mirrors (M) are optically contacted on a Zerodur Extrem 7 spacer (S). Even though an important hole remains on the top of the cavity, a lateral vent (V) has been machined in front of the ion pump CF16 flange (I) to efficiently empty the inside of the cavity. The cavity is supported by 3 macor ceramic glass legs (L) inside a massive copper shield (H) itself supported by 3 macor ceramic glass sockets. Opposite to the ion pump flange is a copper tube (C) connecting to the turbo pump (T). The light is injected in the cavity by three wedged windows (W) glued on the CF160 ultra-vacuum flanges (F).

One major concern before the cavity was put under vacuum was intrusion of dusts over the mirrors which would hamper the performances of the cavity. Optical contacting was realised in Winlight facilities in April 2015. We built an optical setup to control directly

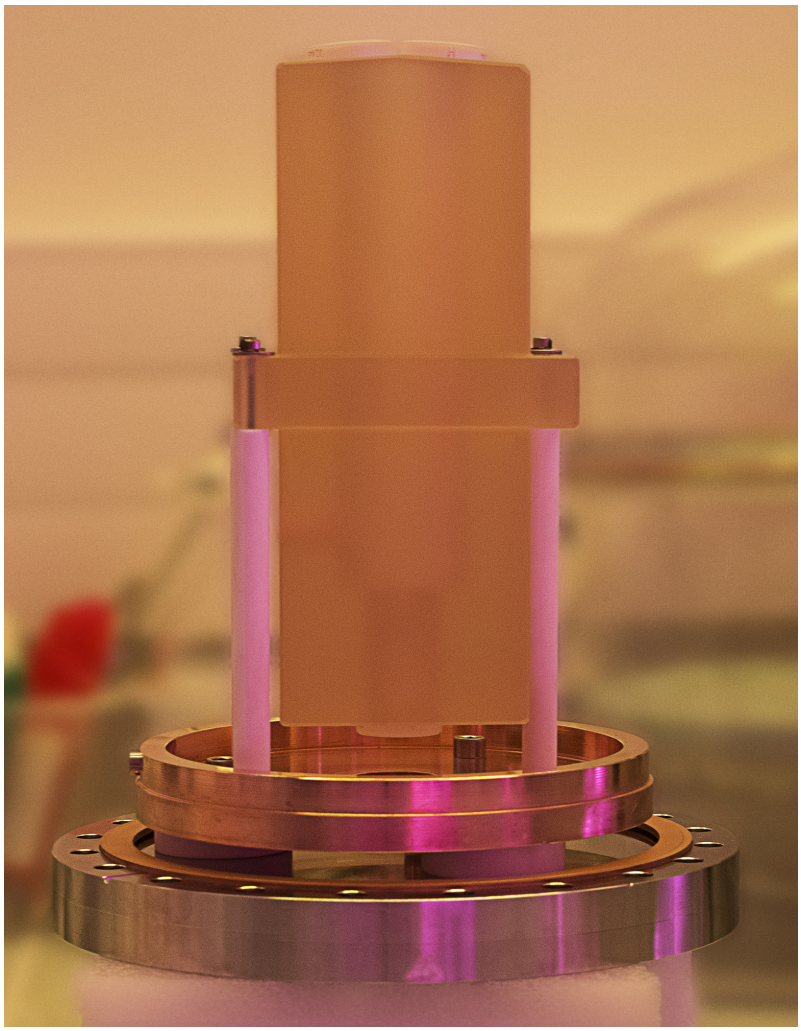

Figure 4.13: Picture of the second generation VCOF on the bottom part of the copper shield on a flange CF160 in the white room of LIPHY

the finesse of the cavity (see Fig. 4.14) right after the optical contacting was made. This enabled us to optimise the cleaning of the mirrors up to a ring-down of 18.6 μs of the cavity filled with air. Under vacuum back in LIPHY, we obtained a ring-down of 24.1 μs at 1392 nm, close to the optimal values at 27 μs according to our mirror characterisation (lower than in the linear cavity used for the characterisation as the shape and the length of the cavities were different). These ring-down times are rather small compared to the other V-shaped cavities and ultra-stable cavities in general, which means that the finesse is not very high (only 131000), but it will still be enough for optical feedback to narrow the FWHM of the diode laser down to *sub-kilohertz* levels. It also enhances the feedback efficiency as it is easier for the laser to lock in the cavity because more light comes back.

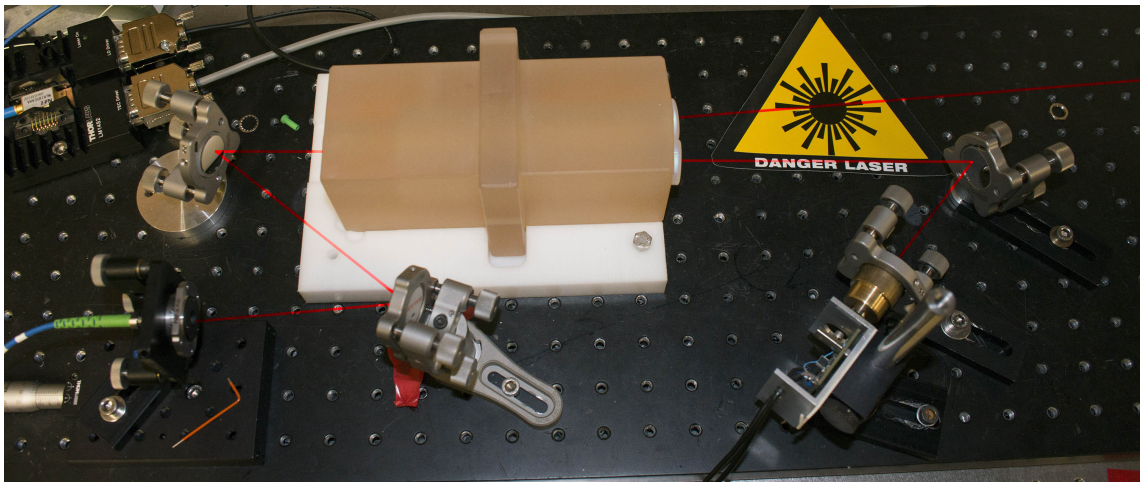

Figure 4.14: Picture of the optical setup deployed at Winlight facilities to characterise the ring-down of the cavity during optical contacting, indicative path of the laser beam in red.

4.2.3 Injection of the VCOF by a DFB laser

Once the light laser is injected in the VCOF, its frequency is narrowed and power accumulates inside the cavity. Despite very high reflectivity mirrors, it is possible to measure the transmission of the cavity with a InGaS photodiode. Even though the frequency of the laser is locked on the resonance frequency of the cavity by optical feedback, it does not naturally stay locked to the cavity. Indeed, the locking of the laser on the cavity (or of the cavity on the laser light) requires that the light entering the cavity is in phase with the light inside the cavity.

Figure 4.15 presents an example of an experimental transmission of the cavity obtain during a scan of the laser. A small modulation is applied on the current of the laser (in black) with a frequency of $1.4\,kHz$. It introduces a modulation of the emission frequency of the laser which results in a modulation of the transmission of the cavity. The signal of the transmission of the cavity is multiplied with the high passed filtered of the modulation signal at $200\,Hz$. Once filtered by a low pass filter at $200\,Hz$ as presented in Fig. 4.15 by the dark blue curve, the results of this multiplication provides us with an excellent error signal which equals 0 when cavity transmission is maximal. We built a home-made analog PID to use this error signal to maintain the laser locked inside the cavity by adjusting the phase of the light entering the cavity by modifying the distance between the laser and the cavity. Practically, one of the steering mirror is mounted on a piezoelectric-actuator which enable playing on the distance between the laser and the cavity. To summarise what is presented in Fig. 4.15, the current of the DFB laser is scanned by the laser current modulation (black). At first, the laser frequency is too far from the resonant frequency of

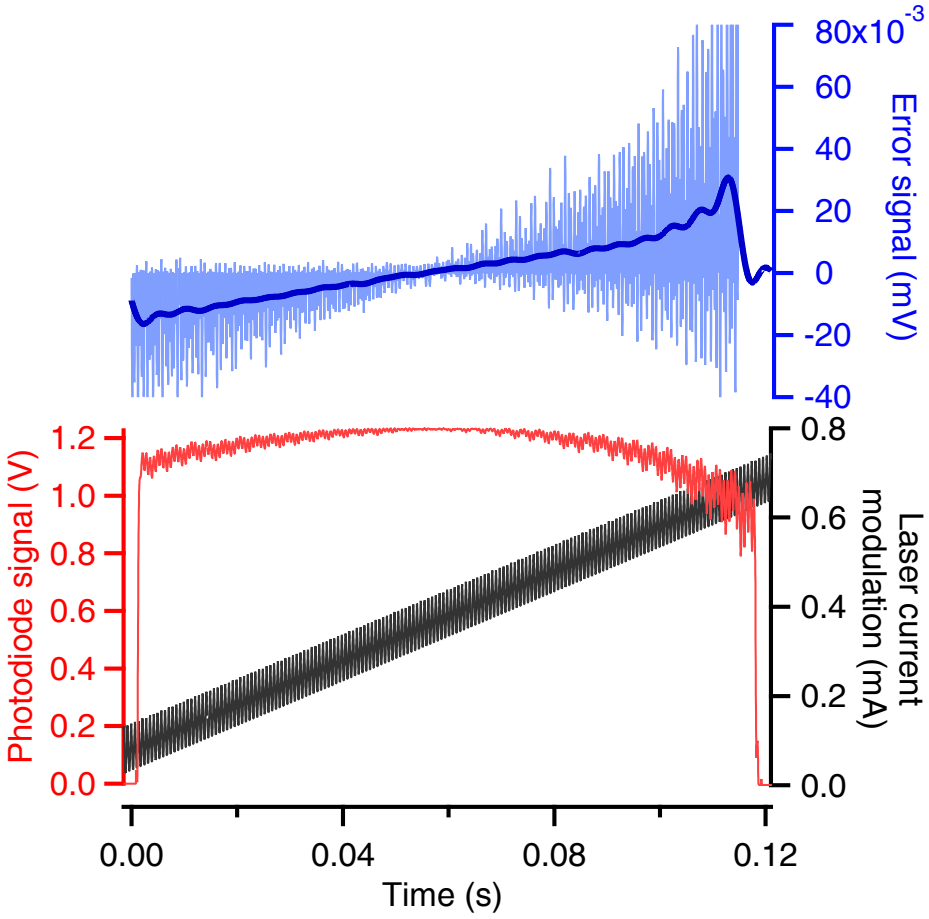

Figure 4.15: Transmission of the cavity measured on the photodiode signal (red) when the DFB laser is injected and error signal (light blue) created by the multiplication of the transmission signal with the modulation of the current of the laser (black). Dark blue, low pass filtered error signal.

the cavity, no light can accumulate in the cavity and the laser is not locked. At the instant 0, we observe a rapid increase of the cavity transmission associated with building up of the intra-cavity power. The laser is locked. We keep scanning the frequency of the laser (slope of the laser current modulation) and pass by the maximum of the transmission, the emission of the laser is centred with the resonance of the cavity. Then, shortly before $0.12\,s$, the frequency of the laser has been swept too far and the lock is not possible anymore.

For the purpose of this figure, we artificially set high laser modulation amplitude and decreased the frequency of the modulation $1.4\,kHz$. In normal conditions, the modulation frequency is $9\,kHz$, the multiplication and filtering are realised by an analog lock-in amplifier SRS SR510. The optical feedback of the cavity on the laser narrows its linewidth.

The typical linewidth of DFB laser diode is around $2\,MHz$, as we saw in section 4.1.2, this is one of the limiting factor to realise very fine spectra of water vapour (see section C.2 for more details on the characterisation of the DFB laser). We estimate the lineshape of the resonance of the cavity using Eq. (3.23) with the reflectivity inferred from the ring-down measurement at section 4.2.2 of $24\,\mu s$. The full width half maximum of the resonance is $3.103\,kHz$ which is already almost 1000 times smaller than the linewidth of the laser diode.

4.2.4 Performances of the new VCOF

Even though this mono-bloc zerodur VCOF should be less sensitive to temperature changes than the previous generation ULE/Invar hybrids, an important effort was realised to control the temperature conditions of the whole system. In addition to the full-coverage massive copper shield around the cavity inside the flange, an active temperature controlled box was built around the cavity. This box of $50x50x82\,cm$ is composed of two layers: a passive external $1\,cm$ thick plywood box around an actively heated $1\,mm$ thick copper box. Each face of the copper box is independently heated by heating bands from Omega up to a power of $120\,W$, controlled by 6 independent PID loops controlled by an Arduino Mega 2560. The PID loop was developed in the joint frame of LITOS and COMBINISO projects in collaboration with Tim Stoltmann, see section C.1 for more detail.

Measurement of the frequency of the laser stabilised by optical feedback on the V-shaped cavity using a high-finesse wavemeter HighFinesse WSU7-IR immediately showed the limit of the wavemeter itself. We observed important drift of the frequency completely decorrelated with the temperature variations of the cavity. This drift was actually the drift of the wavemeter, which was not temperature stabilised. In order to evaluate the frequency variations of the newly designed VCOF, we had to use comb-assisted frequency measurements. Indeed, the tooth of frequency combs can be used as an absolute frequency reference against which compare the frequency of the VCOF (see section 3.3). In the next section, we will explain how the measure of the frequency using a comb is realised, this method is called an optical beatnote.

Following [Burkart et al., 2015], we make use of a commercial optical frequency comb as an absolute frequency reference to measure the performances and the stability of the V-shaped cavity.

4.2.4.1 Beatnote of the frequency stabilised laser with a comb

We used a self-reference frequency comb Toptica FFS1550 to evaluate the frequency stability of the V-shape monobloc cavity. A DFB laser Eblana at 1.392 μm was injected in the V-shaped cavity and locked in with a servo-loop controlling the phase of the incoming light by actioning one of the injection mirrors through a piezoelectric actuator as illustrated in Fig. 4.16. Part of the light is coupled into an optical fibre. The wavelength is roughly monitored with a wavemeter HighFinesse WSU7-IR with an accuracy of 20 MHz in order to evaluate which peak of the comb is actually beating.

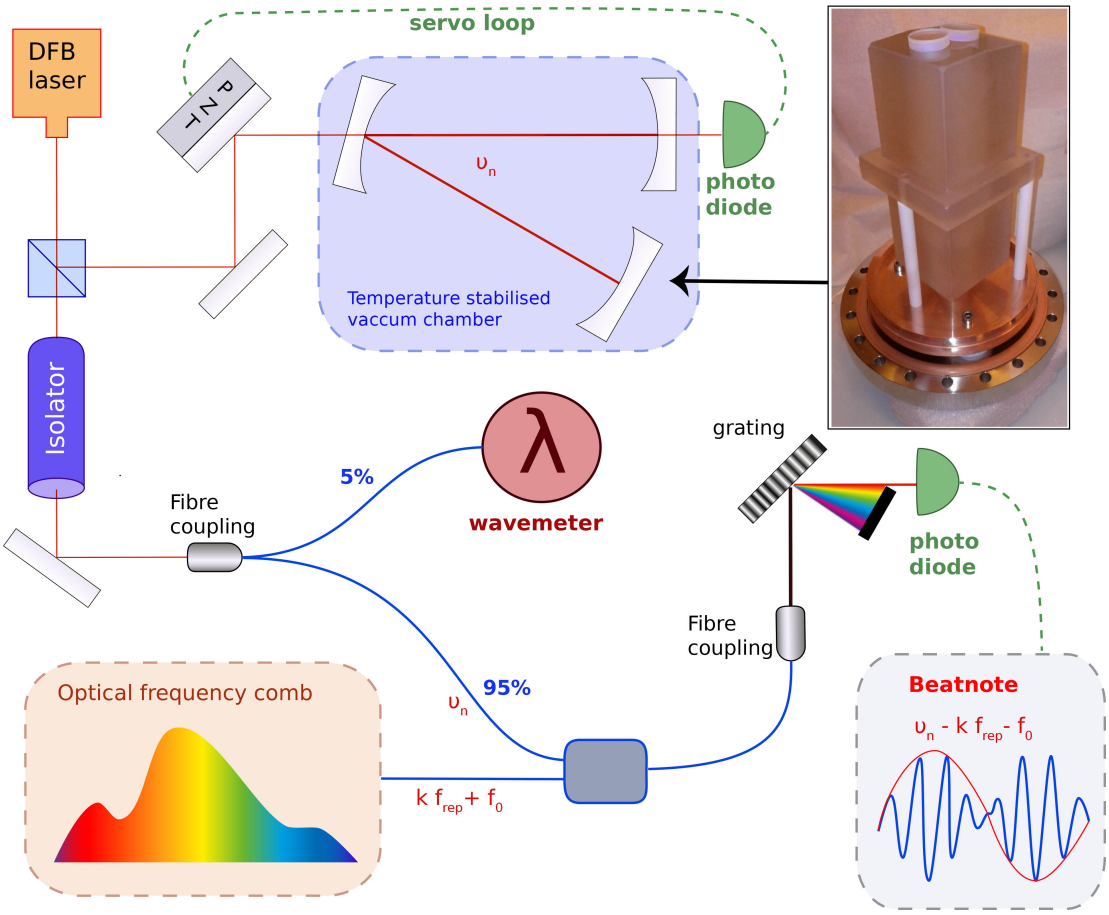

Figure 4.16: Experimental setup to realise the beatnote between the new monobloc VCOF and an optical frequency comb in order to evaluate the frequency drift and the absolute FSR of the VCOF

Using a fibre coupler, we combine the light of the optical frequency comb with the light from the laser stabilised with the VCOF. The light is diffracted using a grating and a fast photodiode is used to measure the so-called beatnote of the two combined pulsations. The physical principle of the beatnote is based on the interference of the superposition of

two pulsations with different frequencies. Their respective electric fields are written:

$$\vec{E}_1(\vec{r},t) = \vec{E}_0\, cos\,(\vec{k_1}.\vec{r} - \omega_1 t) \tag{4.3}$$

$$\vec{E}_2(\vec{r},t) = \vec{E}_0\, cos\,(\vec{k_2}.\vec{r} - \omega_2 t + \phi) \tag{4.4}$$

supposing their amplitude are the same (not necessarily the case but irrelevant for now). The total electric field is the sum of the two electric fields of the two waves:

$$\vec{E}(\vec{r},t) = \vec{E}_0 \left(cos\left[\omega_1 \left(\frac{z}{c} - t\right)\right] + cos\left[\omega_2 \left(\frac{z}{c} - t\right) + \phi\right]\right) \tag{4.5}$$

This equation can be re-written into:

$$\vec{E}(\vec{r},t) = 2\vec{E}_0 \underbrace{cos\left[\frac{\omega_1 + \omega_2}{2c}(z - ct)\right]}_{carrier} \underbrace{cos\left[\frac{\omega_1 - \omega_2}{2c}(z - ct)\right]}_{envelope} \tag{4.6}$$

The frequencies of the two waves $f_1 = \omega_1/2\pi$ and $f_2 = \omega_2/2\pi$ and of the carrier $f_{carrier} = f_1 + f_2$ are about $10^{14} - 10^{15}\,Hz$. Photoreceptors are not able to measure at rates above $20\,GHz$, therefore it is not possible to observe directly the evolution electric field with a detector. On the other hand, the frequency of the envelope $f_{enveloppe} = f_1 - f_2$ can be relatively small if the two waves have similar frequencies. With a measurement of the frequency of the envelope and of a known locking reference, it is possible to estimate the frequency of a laser. This is the beatnote measurement. By using a comb, it is always possible to find a peak of the comb whose frequency is around the frequency we want to characterise, but more importantly, the frequency of this peak is absolutely determined as we saw in section 3.3. This creates an absolute reference of frequency spanning over a large range of optical frequencies .

Here, when we combine the light from the VCOF to the appropriate peak of the optical frequency comb, it is possible to observe the oscillations of the envelope on a fast photodiode (red curve in Fig. 4.16). As previously stated, the carrier frequency around $10^{14}\,Hz$ is way too fast to be directly observed even with the fastest photodiodes to date. The teeth of the combs are separated by $250\,MHz$. We use the high-finesse wavemeter to evaluate roughly the frequency of VCOF and select the closest tooth of the comb. The difference $\nu_n - kf_{rep} - f_0$ is therefore necessary below $125\,MHz$ by construction, therefore measurable on a fast photodiode. This setup provides with an absolute determination of the frequency of the resonance n of the VCOF.

Two experiments were carried out to evaluate the performances of the cavity: first, we estimated the drift of the cavity by measuring for a period of several days the evolution of the frequency of the cavity compared to the comb, because of the extremely low level of drift, even with an absolute frequency reference like a comb, this requires integration over 20 minutes and an important number of points to obtain a robust statistic; second, we realised a ramp on the temperature of the DFB laser and injected the successive resonance of the V-shaped cavity, this enables us to evaluate with a very high precision the free spectral range of the cavity, and therefore to determine its size precisely. This information is very important to evaluate the long term drift of the cavity.

4.2.4.2 Estimation of the drift of the cavity

We realised the beat note of the VCOF with the comb for several days using the setup described in the previous section. The temperature of the VCOF was stabilised at roughly $10\,mK$ using the wood box as described in C.1. We observe various drifts of the frequency of the beat note. Among them, it is still not clear yet which ones can be attributed to the VCOF frequency variations as presented in Fig. 4.17. Indeed, at the hertz level, we are reaching the limits of the lock of the comb and therefore, the interpretation of the signal is more complicated because not all variations of frequency can be attributed to the VCOF. Here, we observe drifts lasting over several hours from 0.3 to $2.7\,Hz.s^{-1}$. Around the hour 60, the wood box was opened to optimise the injection of the laser in the V-shaped cavity. This leads to the important variations of temperature and to a gap in the beatnote measurement.

The temperature around the flange was monitored during the experiment. It is not possible to monitor directly the temperature of the cavity because it would lead to the insertion of materials not suited for high-vacuum applications. We estimate that the variations of temperature outside the flange should encompass the variations of temperature of the cavity because of (1) the inertia of the 15 kilos stainless-steel flange, (2) the isolation of the vacuum inside the flange, (3) the isolation from the massive copper shield around the cavity and (4) the inertia of the glass cavity. We observe that the drift of the frequency is completely decorrelated with the temperature variations of the flange. This limits the characterisation of the behaviour of the cavity toward temperature. An additional experiment consisting in a step of temperature should be realised soon in order to evaluate the thermal expansion of the cavity. Nevertheless, this shows that the worst performances of this new cavity are already 10 times better than the previous hybrid VCOF (which has a drift of $20\,Hz.s^{-1}$) and validates its relevance.

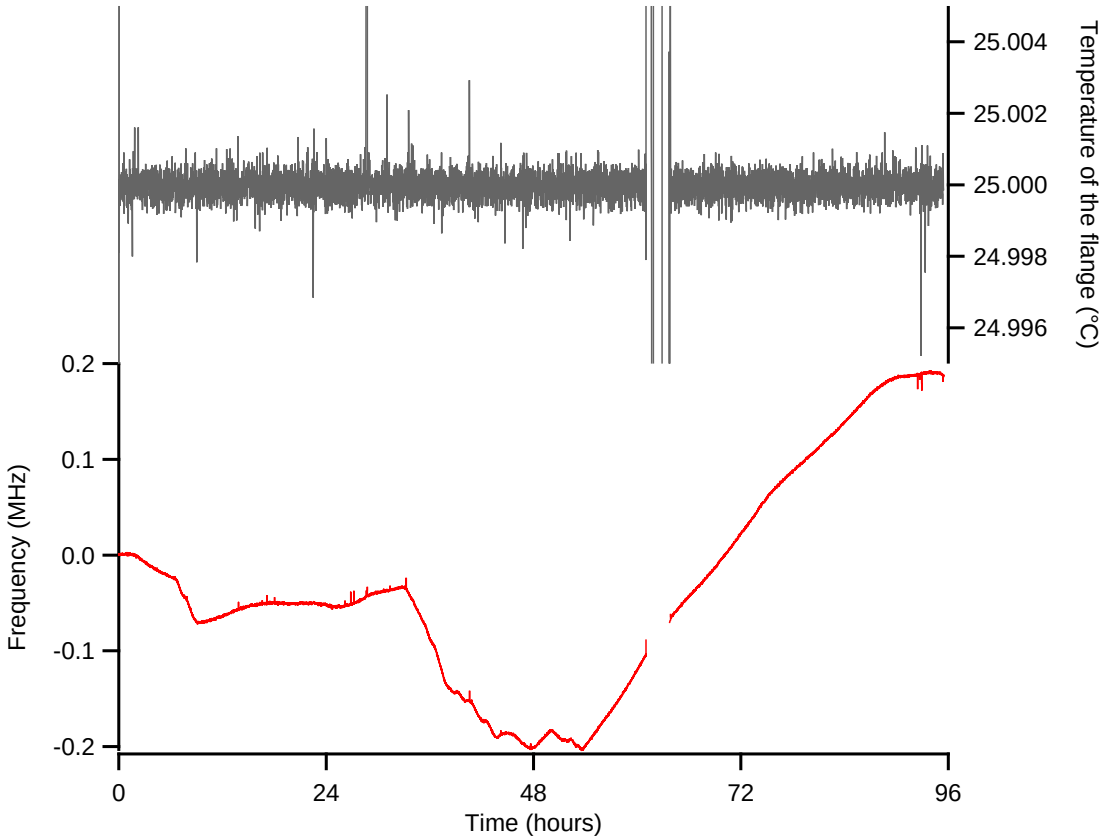

Figure 4.17: Variations of the frequency of the VCOF monitored by the beatnote with the comb for 96 hours and monitoring of the temperature of the flange inside which lies the VCOF

Another way to estimate the drift of the cavity is to measure the evolution of its size over several weeks/months.

4.2.4.3 Estimation of the size of the cavity

In order to evaluate the size of the cavity, we measured the free spectral range of the V-shaped cavity. Because of the principle of resonant cavities (see section 3.2.4.1), the laser can only get locked to the VCOF when the frequency is a multiple of $c/4L$. Because of the extreme accuracy of the frequency measurement from the beatnote with the comb, measuring a high number of FSR provides with an extremely precise and accurate estimation of the length of the cavity as illustrated in Fig. 4.18.

This estimation has been realised by scanning of the laser diode from $-10°$C to $+60°$C which is equivalent to scan from $7159.26611\,cm^{-1}$ to $7195.32520\,cm^{-1}$ with steps around $0.0001°$C. This scans revealed 2658 modes of the VCOF associated with a total relative frequency variation (sums of the 2658 FSR) of $1.08005\,THz$ with a standard de-

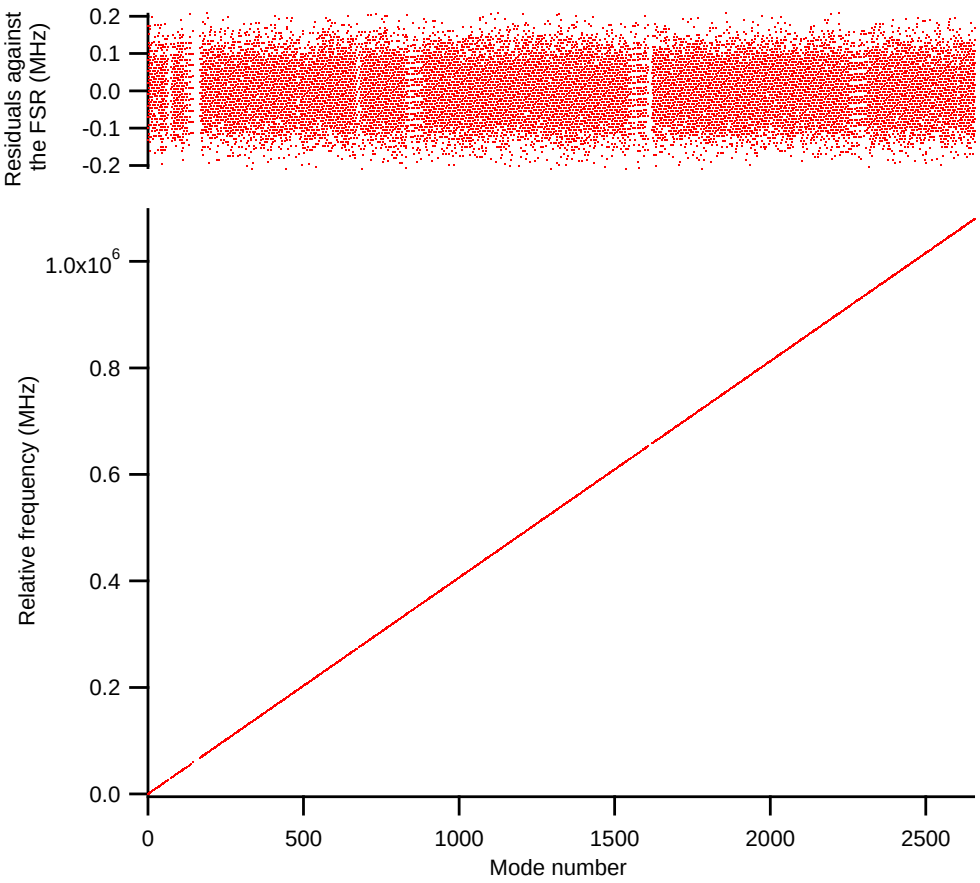

Figure 4.18: Relative frequency variations of 2568 modes of the monobloc VCOF, the DFB laser is locked in the successive modes with a spacing of exactly 406 337 674.5 Hz. The residuals observed here corresponds to the noise of the optical frequency comb.

viation of 5.5 10^4 Hz. These important residuals (observed in Fig. 4.18) are associated with the noise of the optical frequency comb. Here, a precision measurement of the FSR has been realised by successively locking the laser to the 2658 modes. The slope of the absolute frequency from the beatnote compared the mode number is exactly the FSR and we obtain a value of $406\,337\,674.5 \pm 0.3\,Hz$ with a perfect correlation (r^2 virtually equals 1). Using the expression of the FSR for a V-shape cavity $\Delta\nu_{FSR} = \frac{c}{4L}$, we obtain a size of V-shaped cavity of $0.1844478500\,m$ with an extreme level of precision of $1.4\,10^{-10}m$. Considering the drift of the cavity is around $1.5\,Hz.s^{-1}$, it means we know the size of this cavity at the atomic level and the variations of this length are around $10^{-14}m$ and should not be observable. The measurement of the size of the cavity by Winlight Optics given at $0.1843 \pm 0.0002\,m$ for the cavity is confirmed by this measurement.

Other determinations will be realised on regular occasions in order to estimate the

dilatation of the cavity with temperature and to evaluate the long term drift of the cavity. Still, considering the drift of the cavity below $3\,Hz.s^{-1}$, we need to wait several months to be able to realise this measurement and obtain a change of the FSR above $1Hz$. Combining the FSR and the finesse of the cavity, it is possible to obtain the cavity mode-width using Eq. (3.26). Here, we obtain cavity modes of $3101.8\,Hz$.

4.2.5 Overall comparison with other lasers

To estimate the performances of this source, we realise an Allan deviation of the frequency stabilisation of (1) a stand-alone DFB laser, (2) an External-Cavity Diode Lasers (ECDL) and (3) a DFB laser locked on the VCOF. The results of the Allan deviation are presented in Fig. 4.19. This measurement provides with an estimate of the accuracy on the frequency of the different lasers at different scales from a single point to several seconds.

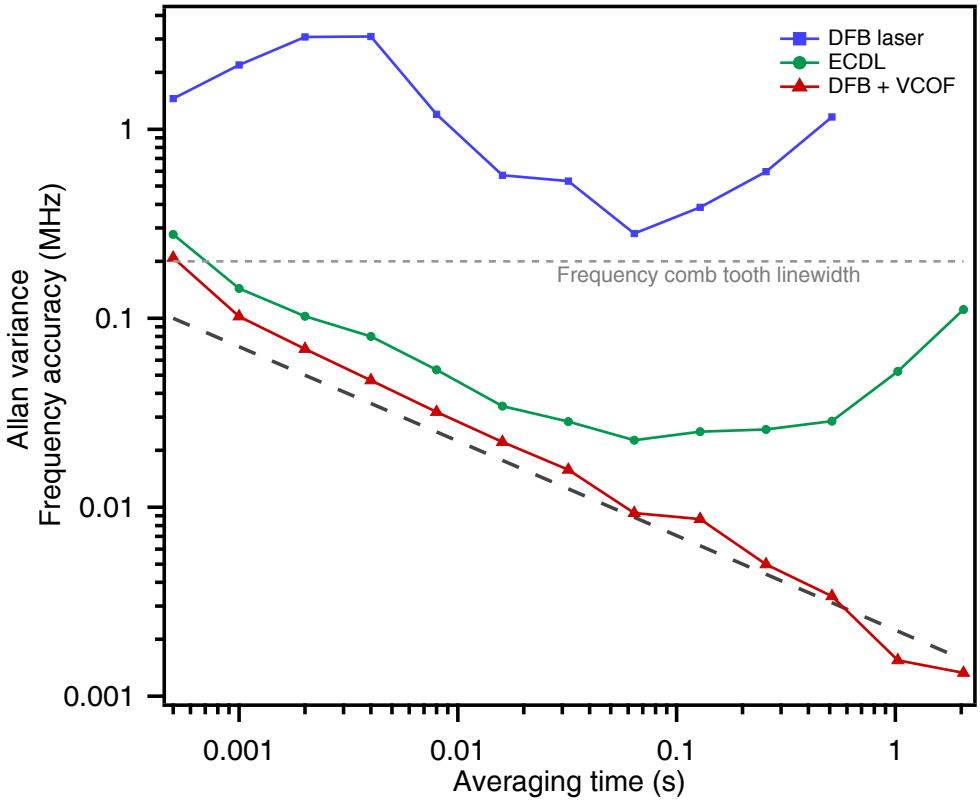

Figure 4.19: Comparison of the Allan variance of the frequency of a stand alone DFB laser (blue squares), an ECDL (green circles) and a DFB locked on the VCOF (red triangles) measured by the beatnote with a tooth of the comb. Dark grey dashed line represents the erasing of white noise over the line in $N^{-1/2}$.

First, at the sampling rate of the measurement ($2\,kHz$), we observe the instantaneous linewidth of the different lasers: slightly below $2\,MHz$ for a stand-alone DFB laser and around $200\,kHz$ for an ECDL. In the case of the DFB locked on the VCOF, we actually observe the linewidth of the frequency comb. This is the first indication that the measurement is limited by the comb and not by the VCOF. For the VCOF, independent measurement shows a linewidth below $300\,Hz$, therefore several orders of magnitude below the $100\,kHz$ presented here.

We observe that the stand-alone DFB laser frequency is not improved when the signal is averaged. This is due to important instantaneous drift of several MHz which leads the Allan Variance to increase. For the ECDL, we observe that the frequency goes down following a slope of $N^{-1/2}$ up to almost $0.1\,s$. Here, we show that the VCOF/comb stability goes beyond $1\,s$ with a slope of roughly $N^{-1/2}$. Once again, as we have not reached the values of the drift of the VCOF as estimated in previous section, here, we are limited by the frequency comb.

4.3 Design of a new OFFS-CRDS spectrometer

In this chapter, we have shown that the limits of infrared spectroscopy are not reached yet. In the first section, we have detailed a CRDS cavity with a detection limit at $5.10^{-13}\,Hz^{-1}$ which can be used to realise precise isotopic composition measurements down to below the *ppm* level. Still, we showed that the main limit of this setup is the frequency jittering which creates an important amount of noise on the wings of the transitions and hamper the determination of the concentration. In the second section, we have detailed a VCOF cavity that can be used to stabilise the laser frequency down the Hz level with frequency drift as low as $1.5\,Hz.s^{-1}$. The combination of the two methods could unfortunately not be achieved during the time frame of my Ph-D. Here, we detail the proof of concept of this kind of spectrometer for trace detection applications as already described by Burkart et al. [2014] for CO_2 and illustrated in Fig. 4.20.

The new spectrometer is based on a VCOF to stabilise a laser. We showed that it is possible to obtain a frequency reference with a precision at the Hz level which would correspond to a precision on the wavenumbers of $10^{-11}cm^{-1}$ (to be compared with the width of the transitions around $0.1\,cm^{-1}$ shown in Fig. 4.21). Compared to the experiment described in section 4.1.2, the linewidth and the frequency drift are known 6 orders of magnitude better.

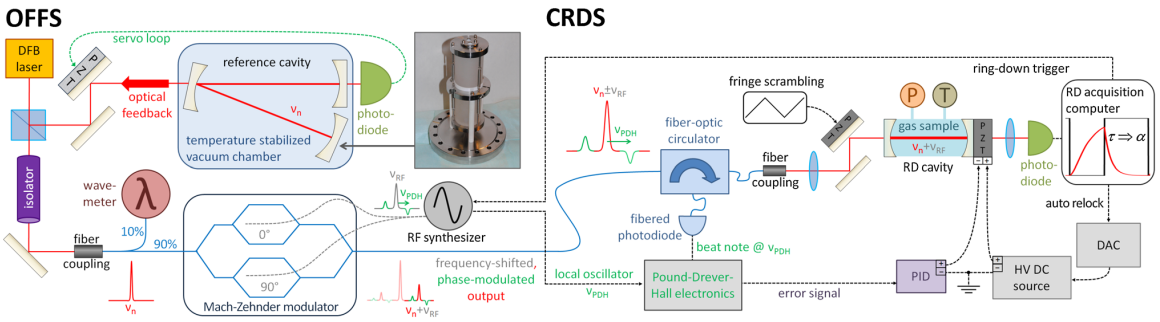

Figure 4.20: Schematic of the experimental setup for optical feedback frequency stabilised cavity ring down spectroscopy (OFFS-CRDS) including the stabilisation of a DFB laser by a VCOF, tuning of the frequency by an MZM and injection of the light into a CRDS cavity to measure samples [Burkart et al., 2014].

A second very important element is to be able to scan with fine spectral resolution. In Fig. 4.22, we present the comparison of the spectra realised by a Picarro L2140i with the spectra of a CRDS setup realised in LIPHY similar to the one we are realising for the OFFS-CRDS spectrometer such as described in section 4.1.2.1. This highlights the very small number of points on the spectra taken by commercial infrared spectrometers. As discussed in section 3.2.5, a small number of points still permits to obtain a precise

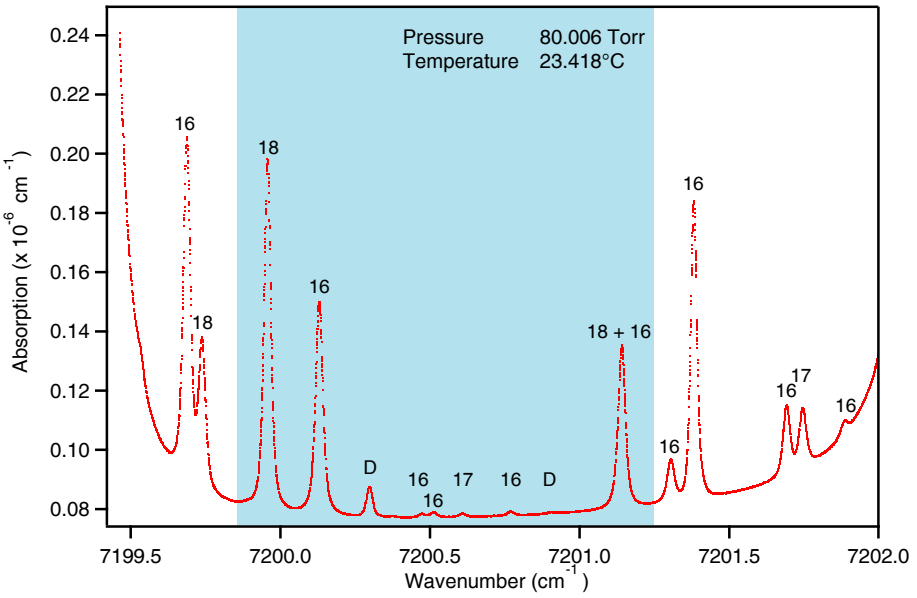

Figure 4.21: Experimental spectrum of water vapour at 23.42°C and 80.006 *mbar*, isotopic composition of EPB. Each transition is assigned to the isotopic species: 16 corresponds to $H_2{}^{16}O$, 17 corresponds to $H_2{}^{17}O$, 18 corresponds to $H_2{}^{18}O$, D corresponds to HDO . The blue area is the area available by the new infrared spectrometer based on OFFS-CRDS using only the Mach-Zender Modulator to scan the frequency.

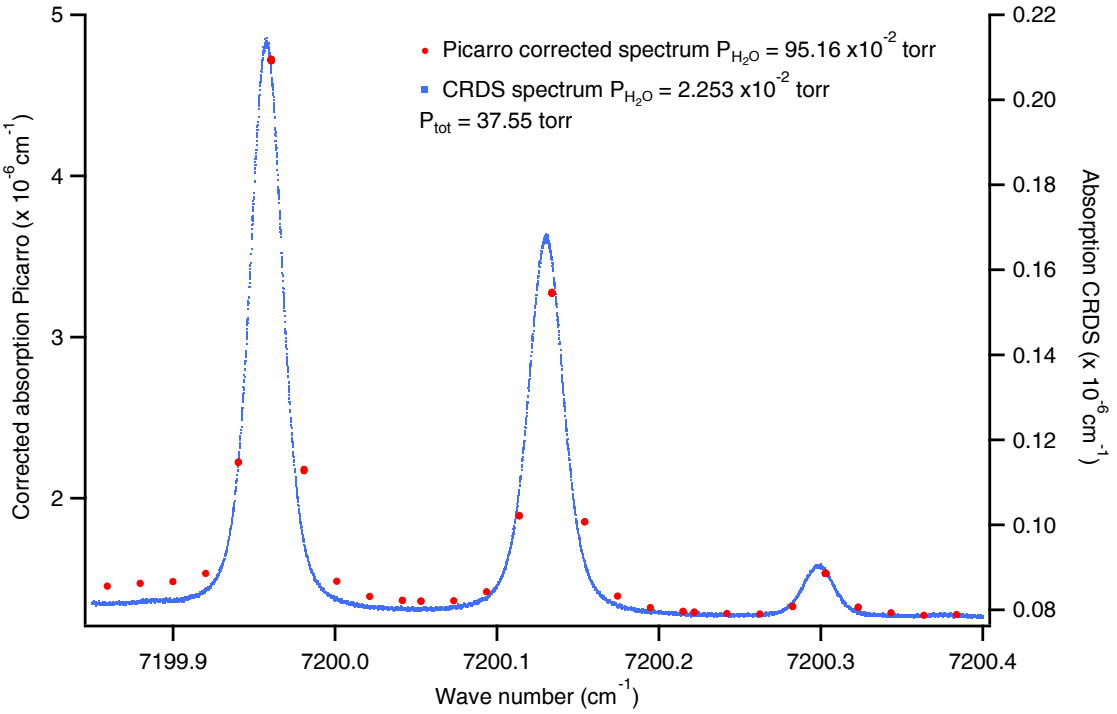

Figure 4.22: Spectra from a Picarro L2140i (red dots) measuring a water standard at 21150 *ppmv* compared to a spectra realised with the setup described in section 4.1.2.1 with the same standard at 500 *ppmv* (blue squares).

concentration of the elements associated with each transition provided the fit relies on a relevant lineshape and fit parameters. Nevertheless, as shown in section 4.1.2.2, jitter in the frequency of the laser can create important uncertainties on the surface of the transition (and therefore on the concentration), thus an important number of points on the wings of the transition is recommended to precisely obtain the frequency. This requires a very precise stabilisation of the frequency of the laser and the possibility to scan at finer resolution. In the case of spectrometers as the Picarro's, the laser frequencies scan the successive resonance of the spectrometer, therefore the resolution is limited by the FSR of the cavity.

Here, we want to be able to scan at finer resolution than the FSR of the CRDS cavity. Using an Mach-Zehnder Modulator (MZM), we are able to scan over an area equivalent to 40 GHz or 1.33 cm^{-1} as illustrated in Fig. 4.21 by the blue area. Because of the impressive performances of the CRDS to a level around $10^{-13} Hz^{-1}$, this can provide water isotopic composition in $H_2{}^{18}O$ and HDO with a precision 2 to 3 orders of magnitude better than present state-of-the-art. For the measurement of $^{17}O - excess$, the very small transition at 7200.6 cm^{-1} does not have a signal to noise ratio high enough for a precise

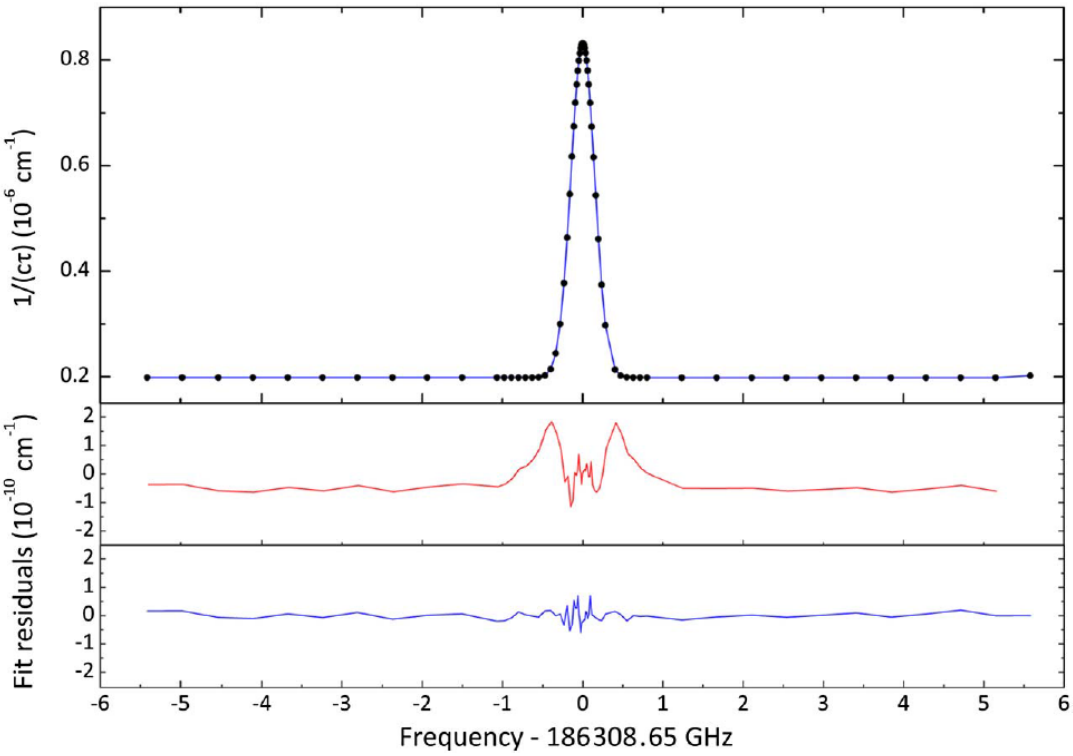

Figure 4.23: Isolated absorption line of 2 Pa of CO_2 recorded with an adaptive resolution using a MZM to control the frequency of the light and a VCOF to stabilise the laser frequency, residuals with a Gaussian (red) and a Voigt profile (blue) [Burkart et al., 2014]

determination. To access a transition of $H_2{}^{17}O$ such as the one at 7201.8 cm^{-1}, this would require to scan the laser itself and jump of several FSR of the VCOF cavity. Because of the impressive stability of the VCOF, this technique can be realised without any loss of stability and within a small amount of time.

The new spectrometer is able to significantly increase the spectral resolution on the areas of interest in order to gain both a good precision and a good sampling rate as illustrated in Fig. 4.23. A single scan with an adaptive resolution gradually increases from 435 MHz on the baseline to 10 MHz at the top of the line [Burkart et al., 2014]. This technique aims at providing fast and precise measurement of isotopic composition of water vapour. Considering the sensibility of the CRDS and the precision of the frequency measurement, from a spectroscopic point of view, the precision of this instrument for all three isotopic compositions ($\delta^{18}O$, $\delta^{17}O$ and δD) is at the level of 1 ppm. Provided the gas is handled properly, we expect measurement of isotopic composition and second order parameter efficiently using this system for humidity between 1 and 1500 $ppmv$.

4.4 Synthesis

Infrared spectroscopy has been a ground breaking advance in the measurement of water isotopic composition. It provides scientists with non-destructive, direct measurements of the water vapour isotopic composition. Infrared spectrometers can thus be used to monitor in the field directly the variations of water vapour isotopic composition and to measure the isotopic composition of liquid or ice samples without any chemical transfer within minutes. This technique is now widely spread in geosciences laboratory with large range of applications. Mainly, it provides an time efficient measurement technique compared to mass spectrometry for which time consuming chemical transfers are necessary. It also opens the possibility for Continuous Flow Analysis (CFA): the measurement of isotopic composition of the ice occurs continuously while the ice is being melted and thus, can increase highly the spatial resolution of the ice core measurements [Gkinis et al., 2011]. Even further, an infrared spectrometer has been included inside a drill (Subglacior project) and will be able to measure in-situ the ice isotopic composition [Grilli et al., 2014]. This opens new possibility for the time efficiency of deep ice core drilling: a 3000 m deep ice core such as the Dome C EPICA ice core can take up to 9 years to drill, with the Subglacior probe, an entire profile of ice isotopic composition and methane content can be realised within a summer season.

Yet, there are still limitations to what infrared spectrometers can achieve. On one hand, the precision of the different commercial instruments available are still overall below mass spectrometers, in particular for the measurements of $d-excess$ and $^{17}O-excess$ [Landais et al., 2014; Steig et al., 2014]. On the other hand, most of the commercial infrared spectrometers are limited at low humidities in their power of measurements. These two limitations are mainly due to (1) the spectroscopic lineshapes used to fit the spectrum and (2) frequency jitter of the lasers. In the case of commercial instruments for which high sampling rates limit the number of points in the spectra, these two effects are even more problematic and requires to average out the results over several minutes to obtain results at the same level of precision than mass spectrometry.

Here, we used high-performance CRDS experiment to evaluate the fit parameters of the absorption lines used by most commercial infrared spectrometers. We were able to evaluate the pressure dependency of the Lorentzian pressure broadening parameter and of the Dicke narrowing parameter for different lines. Still, important noise level on the wing of the absorption lines in the spectra highlighted how important the stabilisation of the laser frequency is. This justified the development of an Optical Feedback Frequency Stabilisation Cavity Ring Down Spectrometer (OFFS-CRDS) in which the issue of the

frequency jitter is dealt with by an additional high-finesse cavity serving as a frequency etalon. The comparison of this new laser with an optical frequency comb validated the approach with a reduction of the linewidth and of the drift of the laser of at least 5 orders of magnitude.

Chapter 5

Experimental investigations on fractionation processes

> Here comes the sun, here comes the sun
> (...) I feel that ice is slowly melting
>
> *Here comes the sun*
> THE BEATLES

As we saw in section 2.3.2, the interpretation of the isotopic signal from ice core is limited by important discrepancies in the fractionation coefficients determination, either equilibrium or kinetic fractionation. First, as described briefly in section 2.1.4, the important differences between the determinations of ice-vapour equilibrium fractionation coefficients impose important uncertainty on fractionation linked to phase transition. We therefore realised a laboratory experiment to measure once more the ice-vapour equilibrium fractionation coefficients in perspective in particular with Merlivat and Nief [1967], Majoube [1971a] and Ellehøj et al. [2013] works. Preliminary results show that it is important to realise new processes studies to better characterise the equilibrium fractionation.

Second, we followed the suggestion of Jouzel and Merlivat [1984] to realise cloud chamber experiments to investigate the impact of diffusion on kinetic fractionation. First, we realised an open air preliminary experiment highlighting the influence of kinetic fractionation on $^{17}O - excess$ linked with less efficient transport by diffusion of heavy isotopes in a gradient of humidity. Then, we measured the profile of isotopic composition in a water vapour gradient to identify the relevance of Jouzel and Merlivat [1984] approach.

5.1 Ice-vapour equilibrium fractionation coefficient

In this section, we focus on fractionation associated to the phase transition between ice and vapour. Commonly, as we saw in section 2.1.4, fractionation between ice and vapour is described using the framework of *equilibrium fractionation* which imply that the system satisfies thermodynamic equilibrium (or at least, quasi-equilibrium) conditions. We will first evaluate the impact of this hypothesis on experiments from Ellehøj et al. [2013] and then see how can this impact their results. Then, we will describe the new setup being realised to measure once more the isotopic fractionation during the phase transition.

5.1.1 Thermal equilibrium

As defined by Dansgaard [1964], equilibrium fractionation corresponds to thermodynamic equilibrium conditions between two phases, therefore to a closed box in which the net fluxes between both phases of every type of molecules are null. Quasi-thermodynamic equilibrium situation corresponds to the case when the net flux of molecules condensing or sublimating is very low compared to the number of molecules hitting the interface by thermal agitation:

$$\Delta N << N_{col} = \frac{P \Delta t S}{\sqrt{2\pi m k_B T}} \tag{5.1}$$

Merlivat and Nief [1967] claim their experiment corresponds to a quasi-thermodynamic equilibrium situation. In the case of Ellehøj et al. [2013], we test if this condition is validated at the lowest temperatures. We computed the number of molecules hitting the ice/vapour interface in Ellehoj set-up using the formulation in Eq. (5.1) for a surface of $1\,cm^2$ of ice. The number of molecules condensing is estimated by:

$$\Delta N = \frac{f_0 N_a (P_{vap} - P_{sat})}{RT} \tag{5.2}$$

where $f_0 = 150\,sccm$ is the air flow going through the trap, N_a is the Avogadro Number, P_{vap} is the incoming vapour partial pressure, P_{sat} is the saturated vapour pressure in the trap, and R and T are the gas constant and the temperature.

Figure 5.1 presents the ratio of molecules condensing by molecules hitting the surface compared to an arbitrary threshold of $1/10$ (note that here the threshold and the surface where ice is being formed are scaled together). In Ellehoj's experiment, the incoming fluxes have a constant humidity generated by a liquid water bath at a constant temperature of $274.7\,K$. But when the equilibration chamber is cooled down to lower temperature, more water vapour is transferred to ice, therefore the net flux of water molecules

from the vapour phase to the ice phase is increasing with decreasing temperature. On the other hand, when the temperature decreases, the number of molecules of water hitting the ice surface by thermal agitation also decreases. The ratio of the number of molecules condensing by the number of water molecules hitting the ice/vapour interface is therefore increasing when temperature decreases, probably creating out of thermal equilibrium conditions at low temperature, when results of Ellehøj et al. [2013] and Merlivat and Nief [1967] differ the most (see Fig. 2.3 in section 2.1.4).

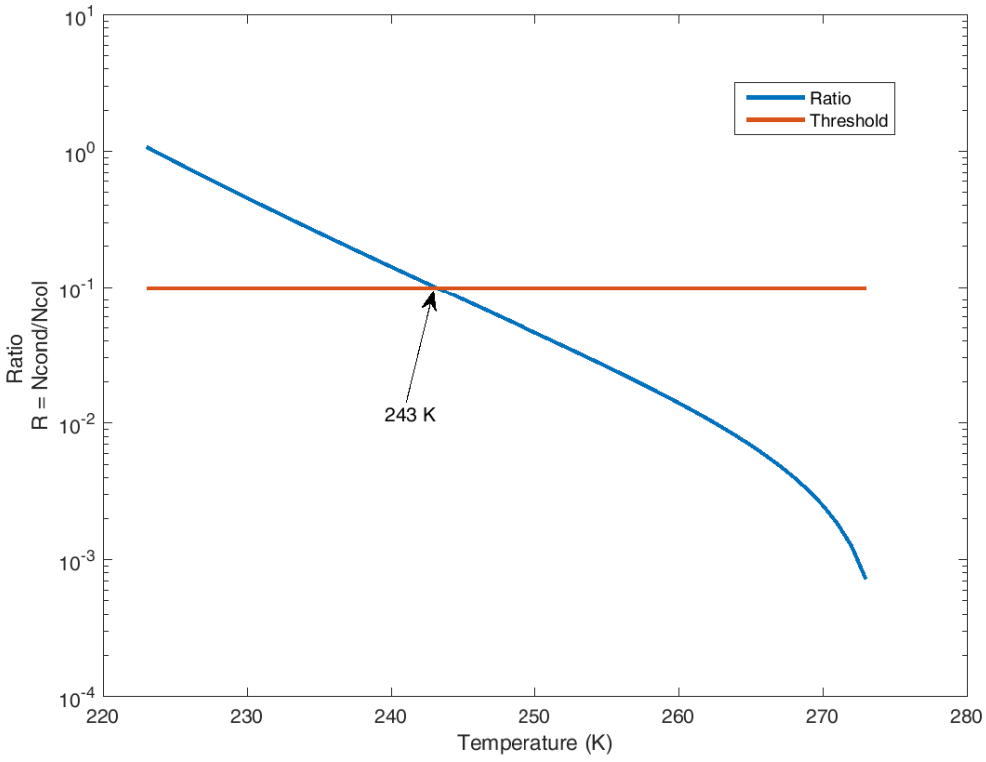

Figure 5.1: Ratio of the number of molecules condensing by number of molecules of water hitting the ice surface due to thermal agitation in Ellehoj experiment

Additionally, experiments during which we condensate water vapour on a cold plate in a cloud chamber (see section 5.2.1) do not support Ellehoj's measurements. In these experiments, we used the coefficients of Majoube/Merlivat to model the exchanges between the ice and the vapour because they lead to a slightly better agreement than the ones of Ellehoj. Another cloud chamber experiment realised by Moyer et al. [2013] seems to even validate the coefficients of Majoube/Merlivat over Ellehoj for equilibrium fractionation.

If these studies bring doubt on the relevance of Ellehoj's measurements to estimate equilibrium fractionation, it does not discredit these data. Indeed, measurements in the

field of water vapour and snow isotopic composition seem to agree better with coefficients of Ellehøj et al. [2013] to estimate the link between the water vapour isotopic composition and the snow surface isotopic composition [Casado et al., 2016b; Ritter et al., 2016]. In the field, the net flux of water molecule at vapour/ice interface is difficult to estimate. We believe that Ellehoj measurements could correspond to an isotopic fractionation at the vapour/ice phase transition out of thermodynamic equilibrium. Equilibrium fractionation requires a closed box model whose application is limited for field conditions where the boundary layer is actively mixed by turbulence.

5.1.2 Perspectives

This motivates to realise new laboratory experiments measuring fractionation at the phase transition taking into account both the temperature (as classically realised) but also the net flux of water molecules condensing (or sublimating), and trying to possibly impose a threshold in which thermodynamic equilibrium can be considered for isotopes. We use custom-made glass traps, that we immerse in a bath of ethanol regulated in temperature by a cryocooler, as a reactor for the phase transition to occur. We create a circulation of moist air through the trap, with the humidity generator described in section 4.1.1 set to generate a humidity level above the saturated vapour pressure. We use a Picarro L2140i to measure the vapour isotopic composition out of the trap.

Preliminary results show fractionation during condensation in the traps but we have not been able to realise quantitative analysis yet due to important drifts of the infrared spectrometer on one hand and too small ice deposition on the other hand.

This experiment could not be finished within the framework of my PhD but is being carried on. These measurements will be compared with an open box model using vapour and snow isotopic composition at Dome C (see section 6.2). We believe this is a very important experiment in particular because we will be able to evaluate the impact of the amount of water being condensed and therefore evaluate our hypothesis about Ellehøj et al. [2013] results.

5.2 Diffusion lead kinetic fractionation

In this section we focus on the impact of molecular diffusion on kinetic fractionation. Molecular diffusion coefficients of water vapour different isotopes have been poorly studied and for now, only two studies estimate theses coefficients from laboratory experi-

ments: Merlivat [1978b] and Cappa et al. [2003]. As discussed in section 2.2.4, the results from these two studies are contradictory. This creates important uncertainties in estimations of fractionation during the snow formation in remote Polar Regions. Indeed, in remote Polar Regions, the density of condensation nuclei is very low therefore the impact of diffusion is important during the formation of snow. This low density of condensation nuclei is also associated with supersaturated conditions on the East Antarctic Plateau. Jouzel and Merlivat [1984] estimates the impact of kinetic fractionation during the formation of snow in supersaturated conditions as we saw in section 2.2.6. Their equation is still nowadays used in all climatic models including water isotopes [Ciais and Jouzel, 1994; Kavanaugh and Cuffey, 2003; Schmidt et al., 2005; Risi et al., 2010; Werner et al., 2011]. Supersaturation is a parameter very weakly constrained in Antarctica, therefore in Jouzel and Merlivat [1984] formulation, uncertainty on supersaturation is subject to important issues. It is generally tuned by using data from a transect [Petit et al., 1982; Winkler et al., 2012].

This motivated to revisit laboratory experiments to estimate the impact of diffusion in supersaturated conditions over isotopic fractionation. First, we describe the different experimental setups, then we challenge the Jouzel and Merlivat [1984] formulation with new quantitative estimations.

5.2.1 Experimental setup

A first preliminary experiment was realised in 2010 by Alexandre Cauquoin. As in the experiment of Jouzel and Merlivat [1984], a cold plate was cooled to different temperatures in the laboratory ambient air. The results highlighted important impact of kinetic fractionation on $^{17}O-excess$, similarly to $d-excess$, as presented in next section. Still, the ambient conditions were not well constrained preventing from quantitative interpretation, therefore a similar experiment in a the cloud chamber CESAME at the Laboratoire Interuniversitaire des Systemes Atmospheriques (LISA) at Creteil near Paris was realised.

The cloud chamber is $5.2\,m^3$ and equipped with flanges from all sides. Temperature, pressure, humidity and concentration in aerosols are monitored by built-in instruments. The entire chamber can be cooled down to $-5°C$ and used at a large range of pressure. A clone of the chamber enable rapid adiabatic decompressions. If most of the applications are the atmospheric chemistry of aerosols, we used this chamber to realise experiments in controlled conditions. A copper was inserted at the bottom of the cloud chamber from a KF 40 flange as illustrated in Fig. 5.3. A circulation of ethanol inside the plate controls the temperature of the plate with a response time inferior to 1 minute. The isotopic

Figure 5.2: Picture of the cloud chamber CESAM

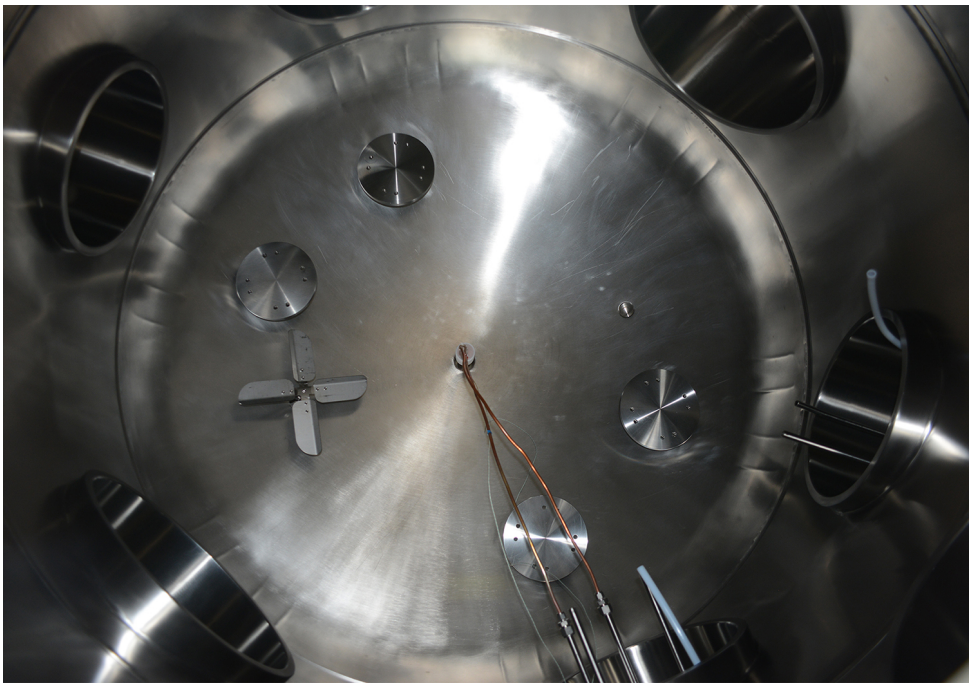

Figure 5.3: Picture inside the cloud chamber CESAM: two copper inlets pump air at different heights of the cold plate here covered with frost. No other sign of condensation is visible on the rest of the cloud chamber.

composition of the vapour is measured by two infrared spectrometers: a Picarro L2120i (CRDS instrument) and the SARA H_2Oi HiFI from LIPHY (OFCEAS instrument). Two copper inlets extract the air from right above the cold plate as illustrated in Fig. 5.3.

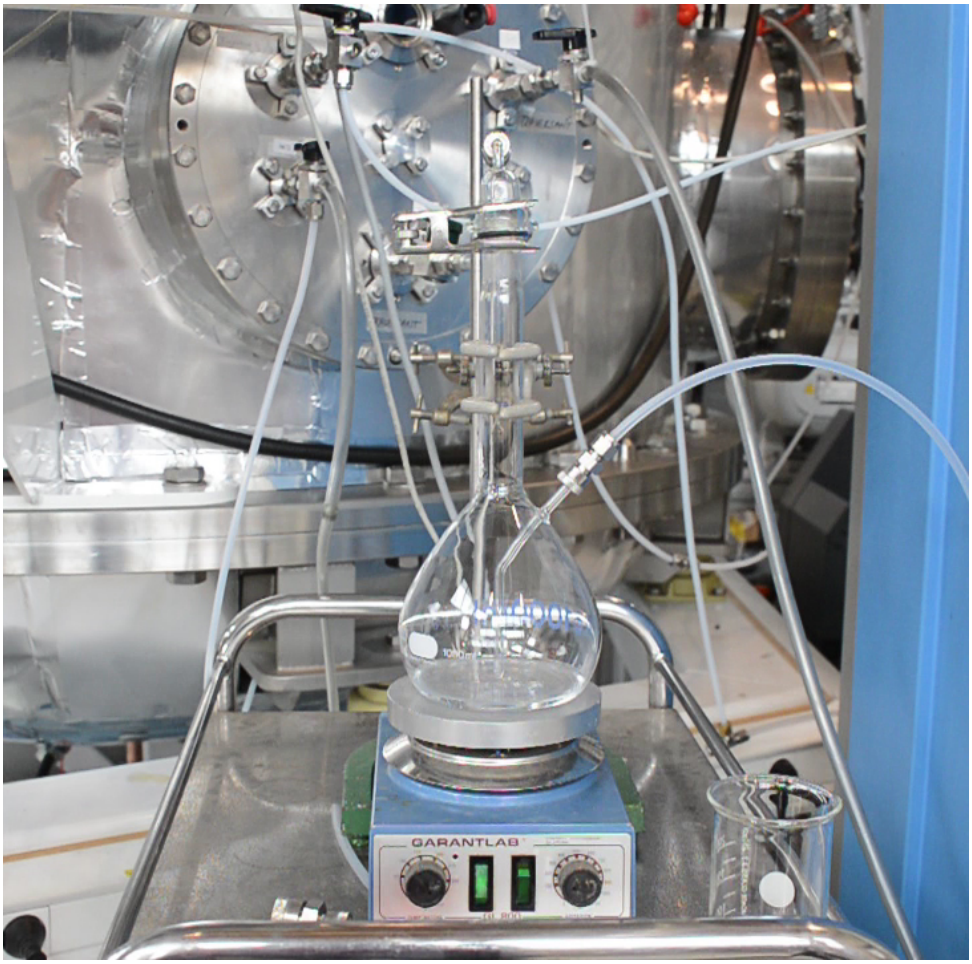

Figure 5.4: Picture of the volumetric flask used to generated the water vapour of known isotopic composition.

In order to fill the cloud chamber with water vapour of known isotopic composition, we used a volumetric flask of 1 L which was heated up to 120°C. An additional inlet was added to the flask in order to be able to flush it as illustrated in Fig.5.4. The protocol to fill the chamber was : (1) filling the chamber to 900 $mbar$ with a nitrogen/oxygen mix with roughly 20% of oxygen, (2) filling the volumetric flask with the amount of water necessary to reach the wished humidity in the volume of the chamber, (3) heating up the flask isolated from the chamber to 120°C filled with 1 atm of pure nitrogen, (4) once all the water is evaporated, opening the valve between the cloud chamber and the flask and transferring the vapour under a flux of hot dry nitrogen, (5) filling the cloud chamber up to

1 atm with nitrogen to reach a mix of 20/80 % of oxygen/nitrogen with a known humidity and isotopic composition of water vapour.

Each experiment lasted between 1 and 2 hours during which the cold plate relative position to the copper inlets was changed in order to realise a profile of isotopic composition. Each step lasted 15 minutes once a permanent regime was reached. Once the experiment was finished, the cold plate was extracted from the cloud chamber and the ice deposed on top of it gathered to be analysed a posteriori in the laboratory by both infrared and mass spectrometry.

5.2.2 Article 1: Experimental determination and theoretical framework of kinetic fractionation at the water vapour-ice interface at low temperature

In this section, we describe the results from the two experiments revisiting the Jouzel and Merlivat [1984] experiments. First, using an open air experiment, we compare the different impact of kinetic fractionation on both $d-excess$ and $^{17}O-excess$. Because we observe similar difference of diffusivities between $H_2^{17}O$ and $H_2^{18}O$ than between HDO and $H_2^{18}O$, it seems logical that kinetic fractionation directly affects $^{17}O-excess$ as it does for $d-excess$. Nevertheless it was never directly observed. The results of the open air experiment already differ from the one obtained by Jouzel and Merlivat [1984].

In order to infer a more quantitative point of view, a similar experiment has been realised in a cloud chamber as previously described. Here, solving the diffusion equation for the different isotopes in cylindrical coordinates, we manage to reproduce the profiles of isotopic composition with different hypothesis on the flux of heavy isotopes at the ice/air interface. We highlight important flaws in the Jouzel and Merlivat model which can be easily solved by the diffusion equation. More importantly, this model is completely independent of supersaturation which is a complicated parameter to evaluate.

Available online at www.sciencedirect.com

ScienceDirect

Geochimica et Cosmochimica Acta 174 (2016) 54–69

Geochimica et Cosmochimica Acta

www.elsevier.com/locate/gca

Experimental determination and theoretical framework of kinetic fractionation at the water vapour–ice interface at low temperature

Mathieu Casado [a,c,*], Alexandre Cauquoin [a,d], Amaelle Landais [a], Dan Israel [e,f], Anaïs Orsi [a], Edouard Pangui [g], Janek Landsberg [b], Erik Kerstel [b,c], Frederic Prie [a], Jean-François Doussin [g]

[a] *Laboratoire des Sciences du Climat et de l'Environnement – IPSL, UMR 8212, CEA-CNRS-UVSQ, Gif sur Yvette, France*
[b] *Univ. Grenoble Alpes, LIPHY, F-38000 Grenoble, France*
[c] *CNRS, LIPHY, F-38000 Grenoble, France*
[d] *LMD/IPSL, UPMC, Paris, France*
[e] *Sorbonne Universités, UPMC Univ Paris 06, UMR 7589, LPTHE, F-75005 Paris, France*
[f] *CNRS, UMR 7589, LPTHE, F-75005 Paris, France*
[g] *Laboratoire Inter-Universitaire des Systèmes Atmosphériques (LISA), UMR CNRS 7583, Université Paris Est Créteil et Université Paris Diderot, Institut Pierre Simon Laplace, Créteil, France*

Received 8 April 2015; accepted in revised form 4 November 2015; Available online 12 November 2015

Abstract

Water isotopes are commonly used for climate reconstruction from ice cores. The different heavy isotopes of water such as $H_2{}^{18}O$, $H_2{}^{17}O$ or HDO give information about local temperature but also temperature and humidity of water vapour sources. Quantification of these parameters relies on the good knowledge of equilibrium and kinetic isotopic fractionation at each step of the water cycle. One of the strongest limitations when interpreting water isotopes in remote Antarctic ice cores is the formulation of the isotopic fractionation at solid condensation (vapour to ice). This classical formulation also implies a good knowledge of coefficients for equilibrium fractionation and water vapour diffusion in air as well as supersaturation in clouds. The uncertainties associated with these different parameters make the formulation of isotopic fractionation at solid condensation only empirical.

Here, we make use (1) of recent development in the measurements of water isotopes in the water vapour through infra-red spectroscopy and (2) of the possibility to measure accurately ^{17}O-excess of water to test the classical formulation and parameterization of isotopic fractionation at solid condensation. A first experiment involving very strong supersaturation evidences a strong kinetic effect on ^{17}O-excess at solid condensation, similar to d-excess. It also shows the limits of the classical formulation of water isotopic fractionation during solid condensation estimation at very low temperature. A second experiment performed in a cloud chamber under controlled conditions uses cavity ring down spectrometers (CRDS) to determine the spatial variability of water vapour isotopic composition due to diffusion (kinetic effect) during solid condensation. The spatial variability of water vapour isotopic composition can be relatively well reproduced by the resolution of diffusion toward a cold plate. This preliminary study opens new perspectives to revisit the classical formulation of water isotopic fractionation during solid condensation at very low temperature.

* Corresponding author at: Laboratoire des Sciences du Climat et de l'Environnement – IPSL, UMR 8212, CEA-CNRS-UVSQ, Gif sur Yvette, France.
E-mail address: mathieu.casado@gmail.com (M. Casado).

http://dx.doi.org/10.1016/j.gca.2015.11.009
0016-7037/

1. INTRODUCTION

As the cold trap of the global water cycle, Antarctica is a unique archive of Earth's past climate and water cycle. On long timescales (up to 800,000 years), climate changes are retrieved from the water isotopic records of deep ice cores (Petit et al., 1999; EPICA, 2004; Jouzel et al., 2007). Indeed, water isotopic records ($\delta^{18}O$ or δD) are linked to condensation temperature through the Rayleigh distillation effect (the cooler the air, the less water it can hold).

Still, important limitations prevent us from obtaining a quantitative temperature record from $\delta^{18}O$ and δD profiles in polar ice cores. In Greenland, variations in the moisture source (Charles et al., 1994), seasonality of the precipitation (Fawcett et al., 1997; Krinner et al., 1997), and the link between condensation and surface temperature (existence of an inversion layer) (Loewe, 1936) can bias by a factor of two the temperature reconstructions from ice cores. In Antarctica, the same effects are at play (Sime et al., 2009; Laepple et al., 2011) but other factors should be considered too because the mean annual temperature is lower than in Greenland (less than −55 °C today on the East Antarctic plateau). Indeed, reconstructing polar temperature from isotopic composition of the snow is generally based on models describing the physics of isotope fractionation (either simple isotopic models describing water fractionation following Rayleigh distillation (Ciais and Jouzel, 1994), or Atmospheric General Circulation Models – AGCM – including the description of the water isotopes (Hoffmann et al., 1998; Schmidt et al., 2005; Risi et al., 2010; Werner et al., 2011)). These models, developed over the last decades, rely on the knowledge of the fractionation coefficients associated with each phase transition and on simple assumptions concerning cloud microphysics. Indeed, all mass dependent and symmetry dependent physical processes involve fractionation: the different isotopes do not have the same saturated vapour pressure or diffusivity in air. At low temperature, both vapour–solid equilibrium fractionation and the different diffusivities of water isotopes in air should be considered (Jouzel and Merlivat, 1984). A recent effort was made to determine the temperature dependence of the fractionation coefficients associated with δD and $\delta^{18}O$ (Ellehøj, 2011). The results turned out to be significantly different from the previous determination (Majoube, 1971a,b). Moreover, the evolution of diffusivities of water isotopes in air has never been studied at temperatures lower than 10 °C (Merlivat, 1978; Cappa et al., 2003; Luz et al., 2009). Using diffusivity values measured at 20 °C, as is commonly done, limits the quantitative interpretation of water isotopes in remote Polar Regions. In the classical formulation of the fractionation during ice/snow condensation, the ratio between kinetic (diffusivity) and equilibrium fractionation is only controlled by the degree of supersaturation of water vapour over ice. From available observations, it is expected that supersaturation increases with decreasing temperature and thus has a very strong influence at the very low temperatures encountered in central Antarctica. Even if recent studies have shown high supersaturation levels near the ground level, in the lower atmospheric boundary layer (Style and Worster, 2009; Genthon et al., 2013; Gallet et al., 2014) and in the higher atmosphere (Gettelman et al., 2006), the supersaturation in Antarctica remains poorly documented, and is thus very crudely tuned in isotopic models (Ciais and Jouzel, 1994). This further limits the models' ability to provide a quantitative link between water isotopic ratios and temperature. To progress on these issues, controlled laboratory experiments are needed to test the values of the fractionation coefficients, as well as the models describing water fractionation at snow formation.

In addition to the primary temperature information provided by δD and $\delta^{18}O$, the combination of δD and $\delta^{18}O$ in the form of the deuterium excess (d-excess = $\delta D - 8 \times \delta^{18}O$ (Dansgaard, 1964)) has been used over the last decades and provides information related to relative humidity during evaporation over the ocean (Gat, 1996) and re-evaporation in the convective zones (Risi et al., 2008) It also has an important added value in polar regions since d-excess has been shown (1) to help tuning the supersaturation spatial evolution (Ciais and Jouzel, 1994; Werner et al., 2011) and (2) to provide information on past changes of moisture source temperature. Vimeux et al. (1999) have indeed first used this tracer in the remote East Antarctica Vostok ice core over a timespan from present to 150 kiloyears before present (kyrs BP) to evidence a change in the moisture source temperature associated with Earth's obliquity. Unfortunately, this second order parameter of isotopic composition is not yet used widely in Polar Regions. One reason for the relatively little use that has been made of this tracer is probably that d-excess in polar ice cores is not as simple to interpret as previously thought since it also varies with relative humidity of the source, local temperature in polar regions (Jouzel et al., 2007), and the precise trajectory of the water masses (Bonne et al., 2015).

Recently, the increased precision provided by new analytical approaches has permitted the measurements of a new complementary tracer of the hydrological cycle: ^{17}O-excess, defined as $^{17}O\text{-excess} = \ln(\delta^{17}O + 1) - 0.528 \times \ln(\delta^{18}O + 1)$ (Barkan and Luz, 2005; Landais et al., 2008). Like d-excess, ^{17}O-excess shows variations in the hydrological cycle because the different fractionation processes, equilibrium and kinetic (diffusion), modify $\delta^{18}O$ and $\delta^{17}O$ in different ways. At low latitudes, ^{17}O-excess, like d-excess, is controlled by relative humidity that imposes the relative importance of equilibrium to kinetic fractionation during evaporation and re-evaporation. Consequently, both ^{17}O-excess and d-excess increase when relative humidity decreases. At higher latitudes, ^{17}O-excess and d-excess show different evolutions. d-excess is affected by local temperature, because the relationship between the fractionation coefficients associated with δD and $\delta^{18}O$ is temperature dependent (Luz et al., 2009; Majoube, 1971a,b). ^{17}O-excess is much less affected by changes in local temperature and keeps the signature of relative humidity acquired at low latitudes (this is so because the relationship between the fractionation coefficients associated with $\delta^{17}O$ and $\delta^{18}O$ is independent of temperature). Still, this does not seem to hold true in very isolated regions of East Antarctica where ^{17}O-excess is also influenced by condensation temperature through the increasing influence of kinetic fractionation

when temperature decreases (Landais et al., 2012; Winkler et al., 2012). In these regions, characterized by a $\delta^{18}O$ of precipitation less than -50‰, the quantitative interpretation of ^{17}O-excess is hampered by the same limitations expressed above: insufficient constraints of the fractionation coefficients at very low temperature, strong influence of supersaturation, and thus an inaccurate description of cloud microphysics. Still, this very strong sensitivity of ^{17}O-excess to supersaturation could also be seen as an advantage for interpretation of polar ice core isotopic records because it provides a stringent test for relative quantification of equilibrium and kinetic effects during solid condensation (Schoenemann et al., 2013).

Here, we combine $\delta^{18}O$, d-excess, and ^{17}O-excess in different laboratory experiments to test the current formulation of isotopic fractionation during solid condensation. With the exception of the recent experiment of Ellehøj et al. (2013), focusing only on equilibrium solid condensation and without ^{17}O-excess measurements, no laboratory experiments have been reported since the early work of Merlivat, Majoube and Jouzel in the 70's to better constrain our knowledge of water isotopic fractionation at solid condensation, even though this is essential for a quantitative interpretation of polar ice core records of water isotopes. Moreover, the recent development of (1) laser spectroscopy for continuous measurements of water isotopes in water vapour and (2) high resolution measurements of the new tracer ^{17}O-excess makes it timely to revisit the conventional formulation of isotopic fractionation of water at solid condensation. Also, a preliminary analysis reported by Moyer et al. (2013) of cloud chamber experiments determined fractionation factors for HDO and $H_2{}^{18}O$ down to 190 K. Interestingly, the results agree with an extrapolation of the 70's data to lower temperatures and appear to disagree with the experiments by Ellehoj and colleagues. However, a detailed analysis has so far not been published.

In a first section, we will present the by now classical formulation of Jouzel and Merlivat for water isotopic fractionation at solid condensation (Jouzel and Merlivat, 1984). We repeat the laboratory experiments of this reference study, including ^{17}O-excess measurements, in addition to the δD and $\delta^{18}O$ measurements of the bulk water vapour and condensate. In a second section, we present a more sophisticated experimental study run in a cloud chamber with measurements of the water isotopic gradient in the water vapour near the condensation point. Such an improved experimental set-up also requires a more advanced model description of isotopic diffusion and condensation. These two studies permit to pinpoint the limits of the current model for water isotopic fractionation at solid condensation that so far has been used to interpret polar ice core records.

2. REVISITING JOUZEL AND MERLIVAT (1984) EXPERIMENT

2.1. The first evidence of kinetic fractionation at solid condensation of water vapour

In the first paper evidencing kinetic fractionation during snow formation, Jouzel and Merlivat analysed the isotopic composition of condensed ice on a cold plate (−20 °C) (Jouzel and Merlivat, 1984). The water vapour isotopic composition of the environment (20 °C) was also analysed. Water vapour saturation over ice was unnaturally high, because of the strong temperature gradient between the environment and the cold plate. Unfortunately, the degree of supersaturation could not be precisely inferred because neither the relative humidity of the surrounding air, nor the temperature at the surface was measured. Still, the combined measurements of $\delta^{18}O$ and δD both in the water vapour and in condensed ice on the cold plate showed a strong departure from the relation expected for isotopic fractionation at equilibrium conditions (Majoube, 1971a, b; Merlivat and Nief, 1967), which directly shed light on the existence of the kinetic effect during snow formation. To quantify this effect, a simple modelling approach was developed through the expression of the fluxes of the three molecules ($H_2{}^{16}O$, $H_2{}^{18}O$ and $HD^{16}O$) toward a plane surface in a molecular regime.

In this approach, Jouzel and Merlivat made the hypothesis of steady state diffusion in one dimension. Consequently, the first hypothesis is that the condensation plate is of infinite dimension so that the molar flux, F, toward the cold plate can be expressed through Fick's first law:

$$F = -D\frac{\partial \phi}{\partial z} \tag{1}$$

where D is the diffusion coefficient ($m^2\ s^{-1}$), ϕ the molar concentration of water in air (in mol m^{-3}) and z (m) the distance from the centre of the condensation plate. In the hypothesis of steady state, we can express the isotopic ratio of the condensate, R_s, as the ratio of the fluxes F^i/F, F^i and F being the fluxes associated with heavy ($H_2{}^{17}O$, $H_2{}^{18}O$ and $HD^{16}O$) and light ($H_2{}^{16}O$) molecules, respectively. Hence, we can express R_s as:

$$R_s = \frac{D^i(\phi^i(z) - \phi^i(z_0))}{D(\phi(z) - \phi(z_0))} \tag{2}$$

where D^i is the diffusion coefficient of water in air for heavy molecules, ϕ^i and ϕ are the concentration of heavy and light water molecules in air, and z_0 indicates the surface of the ice–air boundary. Because we work at constant atmospheric pressure, the water concentration in air can be expressed through the partial pressures, e_v^i and e_v respectively for heavy and light molecules. We finally get:

$$R_s = \frac{D^i(e_v^i(z) - e_v^i(z_0))}{D(e_v(z) - e_v(z_0))} \tag{3}$$

At the ice boundary (z_0), it is assumed that there is equilibrium between condensate and water vapour in the boundary layer (Fig. 1) and the partial pressure is equal to the saturation vapour pressure over ice, e_i. The saturation ratio with respect to ice, S_i is defined as $S_i = e_v/e_i$. Using the above definitions, Jouzel and Merlivat end up with:

$$1 + \delta_s = \alpha_k \times \alpha_s \times (1 + \delta_v) \tag{4}$$

where

$$\alpha_k = \frac{S_i}{\alpha_s D/D^i(S_i - 1) + 1} \tag{5}$$

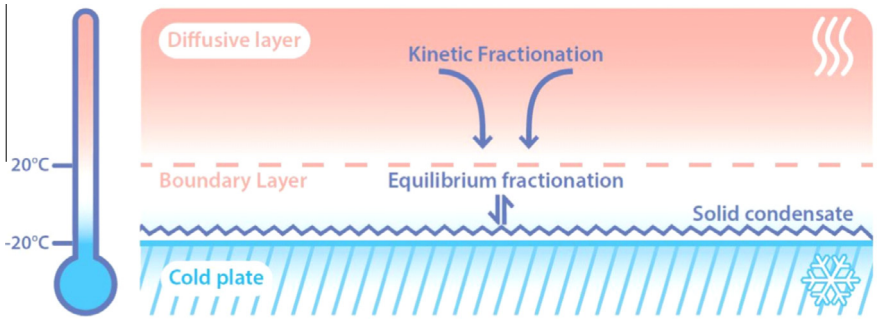

Fig. 1. Schematic representation of the solid condensation experiment and the associated concept of fractionation. At the solid vapour interface, it is classically assumed that equilibrium fractionation is occurring inside a boundary layer. More remotely, kinetic fractionation is at play.

with δ_s and δ_v, the isotopic composition (δD, $\delta^{17}O$ or $\delta^{18}O$) of the solid water and of the water vapour, respectively. S_i is the supersaturation of water over the cold point. α_s and α_k are the fractionation coefficients associated with solid condensation for respectively the equilibrium and the kinetic effects. D is the diffusion coefficient of $H_2{}^{16}O$ and D^i the diffusion coefficient of the heavy molecule ($H_2{}^{18}O$, $H_2{}^{17}O$, or $HD^{16}O$). The ratios D^i/D for $HD^{16}O$ and $H_2{}^{18}O$ were first determined by Merlivat (1978) through two independent experiments performed at a constant temperature of +20 °C. Later, different results were found for these ratios D^i/D (Cappa et al., 2003; Luz et al., 2009) placing an additional large uncertainty on the use of Eqs. (4) and (5).

In order to check the applicability of such a simple formulation and extend it to the new parameter ^{17}O-excess, we have first repeated the historic experiment, now also varying the temperature of the cold plate and measuring $\delta^{17}O$ in addition to δD and $\delta^{18}O$. Contrary to the case of D^{HDO}/D, $D^{H_2^{17}O}/D$ has been shown to be constant in laboratory experiments over a temperature range varying between 10 and 40 °C (Luz et al., 2009). If this result is also true for temperatures below 0 °C, the ^{17}O-excess provides an additional way to check the validity of the classical result of Jouzel and Merlivat.

2.2. A simple experimental set-up and its results

Our first experiment was carried out in the spring of 2010. The cold condensation plate was a 15 cm diameter copper disc attached to a 15 cm long cold finger immersed in ethanol or liquid nitrogen depending on the desired temperature of the condensing copper disc in the range from −2 °C to −42 °C. The humidity level in the room was almost constant over the series of experiments (11,000 ± 1000 ppm). Water vapour was continuously pumped during 4 h through a Pyrex cold trap immersed in ethanol at −70 °C at a flow rate of 2 L min^{-1}. The 4-h timespan corresponds to the time required to collect a sufficient amount of water for measurement of δD, $\delta^{18}O$ and $\delta^{17}O$. During these 4 h, the temperature of the cold plate was maintained constant and a sample of the condensing ice was collected every hour in order to check for any temporal evolution of its isotopic composition. Each 4-h condensation experiment was repeated once for each temperature level of the cold plate. By changing the duration of the second experiment, we were able to track the impact of the copper interaction with the water. No significant difference between the first and the second experiment condensate composition could be noticed even when the amount of condensate was doubled. The surface interaction between copper and ice is thus negligible in our experiments.

δD measurements of both the cryotrapped water vapour in the room and the ice collected on the cold plate were performed using an Isoprime isotope ratio mass spectrometer (IRMS). The method uses reduction of water in a chromium furnace followed by elemental analysis. The final precision of the δD measurements is 0.1‰. The same samples were analysed for $\delta^{17}O$ and $\delta^{18}O$ using a fluorination line to convert water to oxygen through chemical reaction with CoF_3. The oxygen is then measured on a dual-inlet IRMS and referenced to a pure commercial oxygen standard and the results are calibrated on the V-SMOW-SLAP scale. The details of the method are given in (Barkan and Luz, 2005; Landais et al., 2010; Schoenemann et al., 2013). The final precision on $\delta^{17}O$ and $\delta^{18}O$ is 0.1‰. Because measurements of $\delta^{17}O$ and $\delta^{18}O$ are performed on the same samples through the same fluorination line, experimental errors are not independent for $\delta^{17}O$ and $\delta^{18}O$ (Landais et al., 2006). This leads to a final precision on the ^{17}O-excess measurements of 7 ppm in this study. For d-excess, the final uncertainty is 1.6‰.

For the different experiments, we observe that the isotopic composition of the water vapour is rather constant, while $\delta^{18}O$ and δD of the solid condensate decrease with temperature. In parallel, d-excess and ^{17}O-excess generally increase with decreasing temperature (Fig. 2). Still, these tendencies are not constant and we notice a saturation effect below −26 °C: $\delta^{18}O$ of ice shows only a 0.85‰ decrease between the −26 °C and the −42 °C experiments; between −17 °C and −42 °C d-excess and ^{17}O-excess remain practically constant within the experimental error bars.

2.3. d-excess and ^{17}O-excess variations evidence a strong kinetic effect

As already noted by Jouzel and Merlivat (1984), large d-excess values are not unexpected for ice condensing at tem-

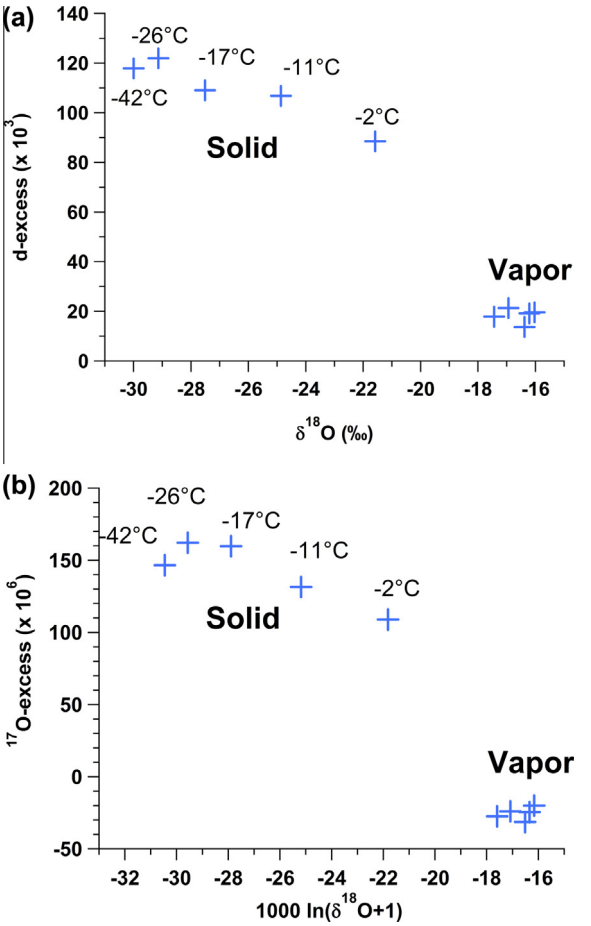

Fig. 2. (a) d-Excess vs $\delta^{18}O$ repartition for water vapour and solid ice for the different condensation experiments driven at different temperatures. (b) ^{17}O-excess vs $\delta^{18}O$ repartition for water vapour and solid ice for the different condensation experiments driven at different temperatures.

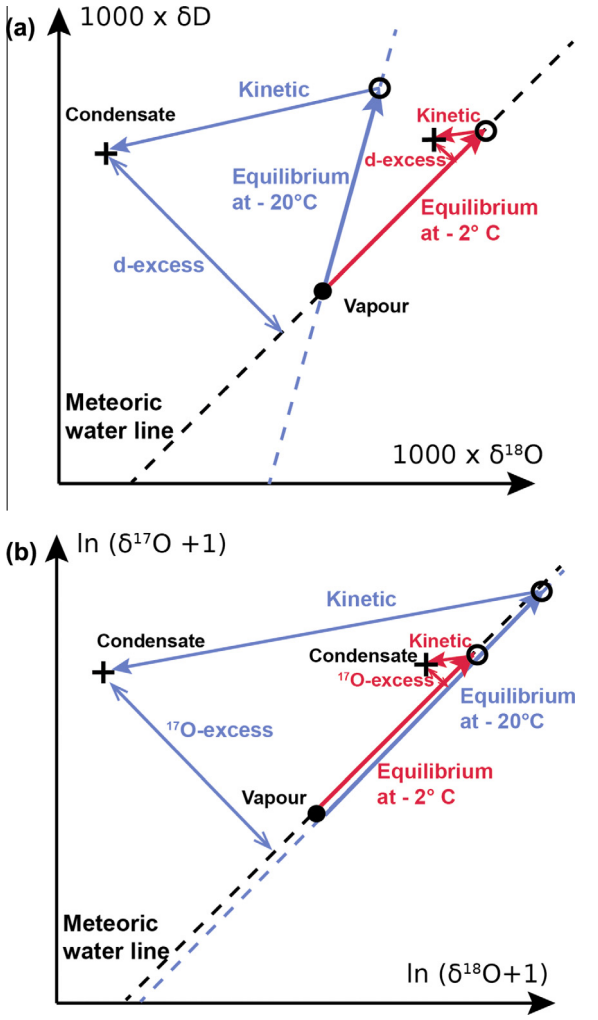

Fig. 3. (a) Theoretical evolutions of δD and $\delta^{18}O$ during solid condensation at different temperatures, the full circle is the vapour composition, the empty circles is the equilibrium condensate and the cross is the condensate. (b) Theoretical evolutions of $\delta^{17}O$ and $\delta^{18}O$ during solid condensation at different temperatures, the full circle is the vapour composition, the empty circles is the equilibrium condensate and the cross is the condensate.

perature below 0 °C in a room at 21 °C. This is the result of strong kinetic effects driven by the large temperature difference between the environment and the cold plate. As we will explain below, the same is true for ^{17}O-excess.

In a first schematic approach (Fig. 3), the δD ($\delta^{17}O$) vs $\delta^{18}O$ fractionation process at solid condensation can be summarised as follows. Equilibrium fractionation always results in the condensing phase being more enriched in heavier isotopes than the vapour phase. To first order and neglecting the temperature effect for δD vs $\delta^{18}O$, the ratio of fractionation coefficients at equilibrium is about 8 when comparing δD and $\delta^{18}O$ and 0.529 when comparing ln $(\delta^{17}O + 1)$ and $\ln(\delta^{18}O + 1)$. As a consequence, equilibrium fractionation during ice condensation drives the water isotopic composition very close to the slope of the meteoric water line (also equal to about 8 in the δD vs $\delta^{18}O$ plot and equal to 0.528 in a $\ln(\delta^{17}O + 1)$ vs $\ln(\delta^{18}O + 1)$ plot). d-excess and ^{17}O-excess are thus only very slightly modified during this process.

This schematic evolution of the isotope ratios in the case of equilibrium fractionation is, however, no longer true at very low temperature (below – 10 °C). In this case, the ratio of equilibrium fractionation coefficients for δD vs $\delta^{18}O$, $(\alpha^{D}_{eq} - 1)/(\alpha^{18}_{eq} - 1)$ increases to values higher than 10 (instead of 8 at +10 °C calculated from the experiment of (Majoube, 1971a)). As a result, the condensation at equilibrium does not follow the meteoric water line in the δD vs $\delta^{18}O$ plot (empty circles in Fig. 3). The resulting equilibrium condensate lies above the meteoric water line leading to the existence of a d-excess (Fig 3a.) (7‰ at −20 °C and 25‰ at −40 °C). Because temperature has no effect on the relationship between equilibrium fractionation coefficients for $\delta^{17}O$ and $\delta^{18}O$ (Van Hook, 1968), no ^{17}O-excess is associated with equilibrium fractionation even at very low temperature (Fig. 3b.).

Kinetic fractionation results from the fact that the lightest molecules diffuse faster toward the cold plate than the heavier molecules. Different experiments were performed

to determine the ratio of the diffusion coefficients and associated kinetic fractionation for water isotopes in air. Even if a large discrepancy (by a factor of 2) is observed between the different estimates, the ratios of kinetic fractionation coefficients are always lower than the associated ratios for equilibrium fractionation coefficients. To first order, the ratio of kinetic fractionation factors varies between 0.5 and 1 for the pair $\delta D/\delta^{18}O$ (Merlivat, 1978; Cappa et al., 2003; Luz et al., 2009) and is estimated at 0.518 for the pair $\delta^{17}O/\delta^{18}O$ (Barkan and Luz, 2007). Kinetic fractionation will thus move the isotopic composition of condensing ice toward lower $\delta^{18}O$ along a line of lower slope than the slope of the meteoric water line as illustrated on Fig. 3. The kinetic fractionation is thus responsible for a positive d-excess and ^{17}O-excess in condensing ice: the stronger the kinetic effect, the higher the d-excess or ^{17}O-excess. One simple way to increase the part of the kinetic fractionation in our experiment was to decrease the temperature of the cold plate and we indeed observe that down to −26 °C, we have a significant increase of d-excess and ^{17}O-excess with decreasing temperature.

2.4. Comparison between experimental data and the classical formulation of isotopic fractionation at solid condensation

In order to compare our data with the simple model proposed by Merlivat and Jouzel, we need an estimation of the supersaturation S_i and hence of the water vapour pressure e_v and the saturation pressure over ice e_i at the cold surface. The measured molar mixing ratio of 11,000ppmv of water vapour in the room air, together with the total pressure yields a value of 11 hPa for e_v. The formulation given by Wagner and Pruß (2002) relates the saturation vapour pressure over ice, e_i, to the temperature of the cold plate. A simple formula adapted to our case (maximum error of 0.052% for T between −70 °C and 0 °C) is:

$$e_i = A \times 10^{\frac{mT}{T+T_n}} \quad (6)$$

e_i is given in hPa, T is the temperature of the cold plate in °C. A, m and T_n are constant equal to 6.114742 hPa, 9.778707, and 273.1466 °C, respectively. It is now possible to use Eqs. (4) and (5) to link the isotopic composition of the water vapour to the isotopic composition of the ice condensate and compare this calculation to our experimental results. For this comparison (Fig. 4), we have chosen to use the measured isotopic composition of the ice δ_S and to compare measured and modelled δ_V (see Eq. (4)). Because different experimental values of D^i/D have been reported in the literature, we have calculated Eq. (5) with the different estimates given in Table 1. Luz et al. give the evolution of D^i/D over a temperature range of 10–40 °C (Luz et al., 2009). As we are interested in lower temperatures, we only took the values corresponding to $T = 10$ °C and $T = 20$ °C (the temperature at which D^i/D were estimated in (Merlivat, 1978; Cappa et al., 2003)). Note that the values of D^i/D for $\delta^{17}O$ are not given in Table 1 since only one estimate was made experimentally linking $D^{H_2^{17}O}/D$ and $D^{H_2^{18}O}/D$, such that: $\ln(D/D^{H_2^{17}O})/\ln(D/D^{H_2^{18}O}) = 0.5185 \pm 0.0003$ (Barkan and Luz, 2007; Luz et al., 2009).

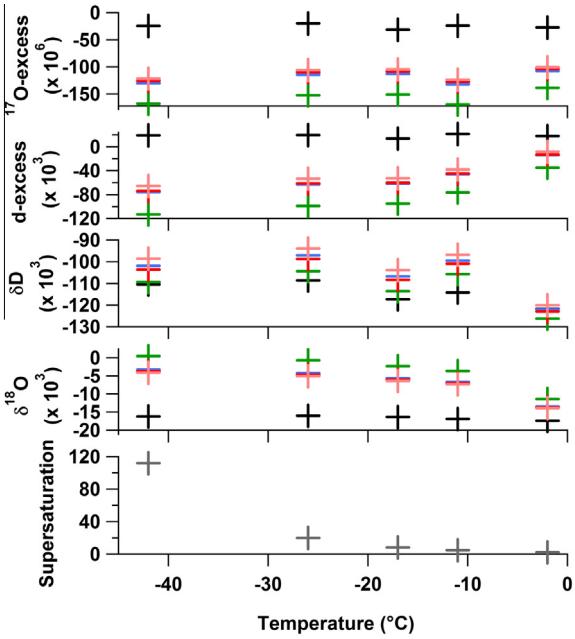

Fig. 4. Comparison of measured (black crosses) and modelled isotopic composition of the water vapour. Modelled isotopic composition of the water vapour is calculated using values of the isotopic composition of the condensate and Eqs. (4) and (5) using different values for D/D^i (Merlivat, 1978 – blue crosses; Cappa et al., 2003 – green crosses; pink crosses – Luz et al., 2009 for 10 °C; red crosses – Luz et al., 2009 for 20 °C). (For interpretation of the references to colour in this figure legend, the reader is referred to the web version of this article.)

Table 1
Different estimates of D/D^i.

	D/D^{HDO}	$D/D^{H_2^{18}O}$
Merlivat (1978)	1.025	1.028
Cappa et al. (2003)	1.016	1.032
Luz et al. (2009) ($T = 20$ °C)	1.023	1.028
Luz et al. (2009) ($T = 10$ °C)	1.029	1.027

Fig. 4 shows that we indeed worked in very extreme conditions with supersaturation reaching an extreme value of 112 at −42 °C, while values encountered in clouds of Polar Regions are of the order of 1.2. The lowest value for S_i in our experiments is 2 for a temperature of −2 °C on the cold plate. As for the isotopic values, we observe a generally good agreement between modelled and measured vapour δD, even for very low temperatures. On the contrary, for $\delta^{18}O$ and hence for d-excess and ^{17}O-excess, there is a clear difference between modelled and measured values, whatever the values chosen for D/D^i. The difference between experiment and modelled values for $\delta^{18}O$ and d-excess increases for decreasing condensation temperature, hence increasing supersaturation and kinetic fractionation. Interestingly, whereas the Cappa values for D/D^i give the best agreement in the case of δD, they show the worst agreement for $\delta^{18}O$.

The δD values are relatively less sensitive to kinetic fractionation than $\delta^{18}O$. Indeed, as explained above, vapour-ice equilibrium fractionation is about 8 times larger for δD

than for $\delta^{18}O$ ($\alpha_{eq}^{D} - 1 \approx 8 \times (\alpha_{eq}^{18} - 1)$), while fractionation associated with diffusion is of the same order of magnitude for δD and $\delta^{18}O$ ($D/D^{D} - 1 \approx D/D^{18} - 1$). Taking into account the temperature influence on α_{eq} (Majoube, 1971a; Ellehøj et al., 2013) it can be calculated that for δD, diffusive fractionation is less than the quarter of the magnitude of equilibrium fractionation, even at −42 °C; while the absolute value of this ratio is always larger than 1 in the case of $\delta^{18}O$. As a consequence, we believe that the fact that the Jouzel and Merlivat approach does not account properly for the isotopic fractionation during solid condensation at high supersaturation is due to an error in properly incorporating the kinetic fractionation in Eq. (5). This is obvious when looking at the $\delta^{18}O$, d-excess and ^{17}O-excess values strongly impacted by kinetic fractionation, especially at high supersaturation levels.

Several reasons can lead to a wrong estimate of the kinetic influence on the calculated fractionation factor through Eq. (5). First, the formulation of Eq. (5) may be correct but the input values of D/D^{i} may not. In fact, we never get a good agreement between measured and calculated $\delta^{18}O$ of the water vapour using any of the estimated D/D^{i} values reported in the literature (Merlivat, 1978; Cappa et al., 2003; Luz et al., 2009) (Fig. 4). Second, the formulation of Eq. (5) should be revised. Indeed, there are several hypotheses that are questionable in the approach that led to Eq. (5). On the one hand, it is assumed that vapour pressure e_V does not show any spatial variations, given that e_V has been measured far away from the cold plate to estimate water flux at the cold plate surface. On the other hand, the assumption was made of an infinite plate, which is also not the case in reality. In order to check these assumptions, we have developed a more sophisticated experimental set-up with spatial measurements of the isotopic composition of the water vapour that we discuss in the following sections.

3. CLOUD CHAMBER EXPERIMENTS AND DIFFUSION FRACTIONATION

3.1. Experimental set up

In order to perform more controlled experiments, we have used the national cloud simulation chamber facility CESAM (Wang et al., 2011) at the Laboratoire Inter-universitaire des Sciences Atmosphériques (LISA). This is a stainless steel chamber of 4.2 m^3, equipped with a vacuum pump facility enabling to reach a vacuum of the order of 10^{-4} mbar. The temperature of the chamber was controlled and set to 20 °C. For our experiments, it was first filled with an atmosphere composed with 80% N_2 and 20% O_2 at atmospheric pressure. We then introduced water vapour by connecting to the chamber a heated glass flask containing an amount of water that yielded the required level of humidity after complete evaporation. The water is heated to its boiling point, while a flux of dry nitrogen gas carries the water vapour into the chamber.

Condensation of water at low temperature occurs in the lower part of the chamber where we installed a cylindrical copper cold trap with a diameter of 3.9 cm. The trap temperature is controlled by internal circulation of cold ethanol at a controlled temperature. The surface temperature of the cold trap does not vary by more than 0.1 °C during a condensation experiment. The copper trap is kept at room temperature during the filling of the chamber and introduction of water vapour. Only after homogenization is achieved within the chamber, is the circulation of cold ethanol switched on, in order to reach a stable temperature of the copper surface in less than 2 min.

A near-infrared CRDS (cavity ring down spectroscopy) spectrometer (Picarro L2120) was used to analyse the isotopic composition of the water vapour (δD, $\delta^{18}O$) in the cloud chamber. A copper extraction tube was connected to the analyser enabling extraction of vapour from the centre of the cloud chamber. The inside surface of the tube was coated with a hydrophobic material and the tube was heated in order to prevent any condensation point, which could produce fractionation. Calibration of the CRDS instrument was performed 3 times a day at different humidity levels (from 2000 to 14,000 ppm) by 2 different homemade standards calibrated with respect to VSMOW and SLAP by repeated IRMS analyses: ODM ($\delta^{18}O = -7.6‰$, $\delta D = -49.0‰$) and ROSS ($\delta^{18}O = -18.71‰$, $\delta D = -144.7‰$). These calibrations were used to correct the raw $\delta^{18}O$ and δD of the water vapour measured by the CRDS instrument.

Humidity inside the cloud chamber was measured far from the cold point by a hygrometer Vaisala HMP234. In addition, the CRDS instrument continuously measured the concentration of water vapour. The calibration of the humidity measurements has been performed in the laboratory by a dew point generator, yielding a correction less than 0.5%. The extremity of the copper extraction tube, leading the air from the chamber to the spectrometer, was equipped with a thermocouple continuously measuring the temperature at the different levels above the cold trap. Except when the tube was in contact with the cold trap, the temperature given by the thermocouple was always 20 °C. Because of the thermal conduction of the tube, the measured temperature may not reflect the local temperature. Therefore, we are not confident that the temperature profile is really constant (Section 3.4.).

The isotopic composition of the water vapour is measured at varying vertical distances from the centre of the copper cold plate. Once the copper trap was cooled down, we noticed that the isotopic composition of the water vapour changed only for vertical distances less than 5 cm from the cold copper surface. We have thus measured the isotopic composition of the water vapour at different heights above the cold surface, decreasing the distance between the copper extraction tube and the surface of the cold plate in the sequence: 10 cm, 5 cm, 4 cm, 3 cm, 1 cm, 0.6 cm and 0.3 cm. Measurements at each step lasted 10–15 min with a stable concentration and isotopic composition of the water vapour, which enabled us to average the measurements and to increase the precision. Once the experiment finished (1h30 – 2 h), the condensed ice was removed from the cold trap and stored, to be later analysed by both IRMS and optical spectrometry (see Section 2.2). Even for low supersaturation, several grams of ice were produced on the cold trap surface. With this important

Table 2
Experimental results obtained in the controlled cloud chamber (Section 3, 2013) and in the simple room experiment (Section 2, 2011, grey highlights at the bottom of this table). A comparison is systematically displayed between the isotopic composition of the condensate and the predicted value as calculated from the vapour isotopic composition using Jouzel and Merlivat's theory with α_{eq} from Majoube (Majoube, 1971a) and D'/D from Merlivat (Merlivat, 1978). Note that when no measurements were available, ^{17}O-excess of the vapour is estimated at −20 ppm.

Date of sampling	Cold plate				Atmosphere (>10 cm from cold plate)				Predicted cold plate values from the vapour measurements			
	T (°C)	$\delta^{18}O$ (‰)	d-ex (‰)	^{17}O-ex (ppm)	T (°C)	RH (%)	$\delta^{18}O$ (‰)	d-ex (ppm)	S_i	$\delta^{18}O$ (‰)	d-ex (‰)	^{17}O-ex (ppm)
05/05/2011	−2	−21.6	88	109	17	55	−17.4	18	2.2	−25.5	119	186
19/04/13 morning	−5.3	−4.1	21	106	20.3	30	−8	12	1.8	−11.4	99	171
18/04/13 afternoon	−5.4	−4.4	51	117	20.4	17	−8.2	14	1.1	5.4	31	22
19/04/13 afternoon	−5.5	−11	69	140	20.2	52	−7.4	7	3.2	−21.3	139	226
25/04/13 afternoon	−7	−14	81	160	20.7	60	−6.9	7	4.3	−24.2	156	239
16/04/13 afternoon	−9.5	−15	84	131	17.5	32	−9.1	13	2.3	−17.8	125	206
06/05/2011	−11	−24.9	107	131	17	55	−16.9	21	4.8	−35	171	243
25/04/13 morning	−12.1	−14.4	83	146	21.3	62	−7	7	7.2	−28.1	173	250
17/04/13 afternoon	−15	−13.2	75	126	17.1	22	−11.9	27	2.5	−21.8	145	217
24/04/13 morning	−15	−15	85	159	20.3	35	−8	11	5	−26.5	166	246
10/05/2011	−17	−27.5	109	160	17	55	−16.4	14	8.3	−38	180	253
24/04/13 afternoon	−20	−15	84	163	20.3	40	−7.5	9	9.1	−29.8	181	254
23/04/13 afternoon	−20.8	−11.5	66	132	20.3	20	−8.4	13	5	−26.6	168	248
11/05/2011	−26	−29.1	122	162	17	55	−16	20	20	−40.6	200	257
12/05/2011	−42	−30	118	147	17	55	−16.2	19	111.9	−42.6	208	257

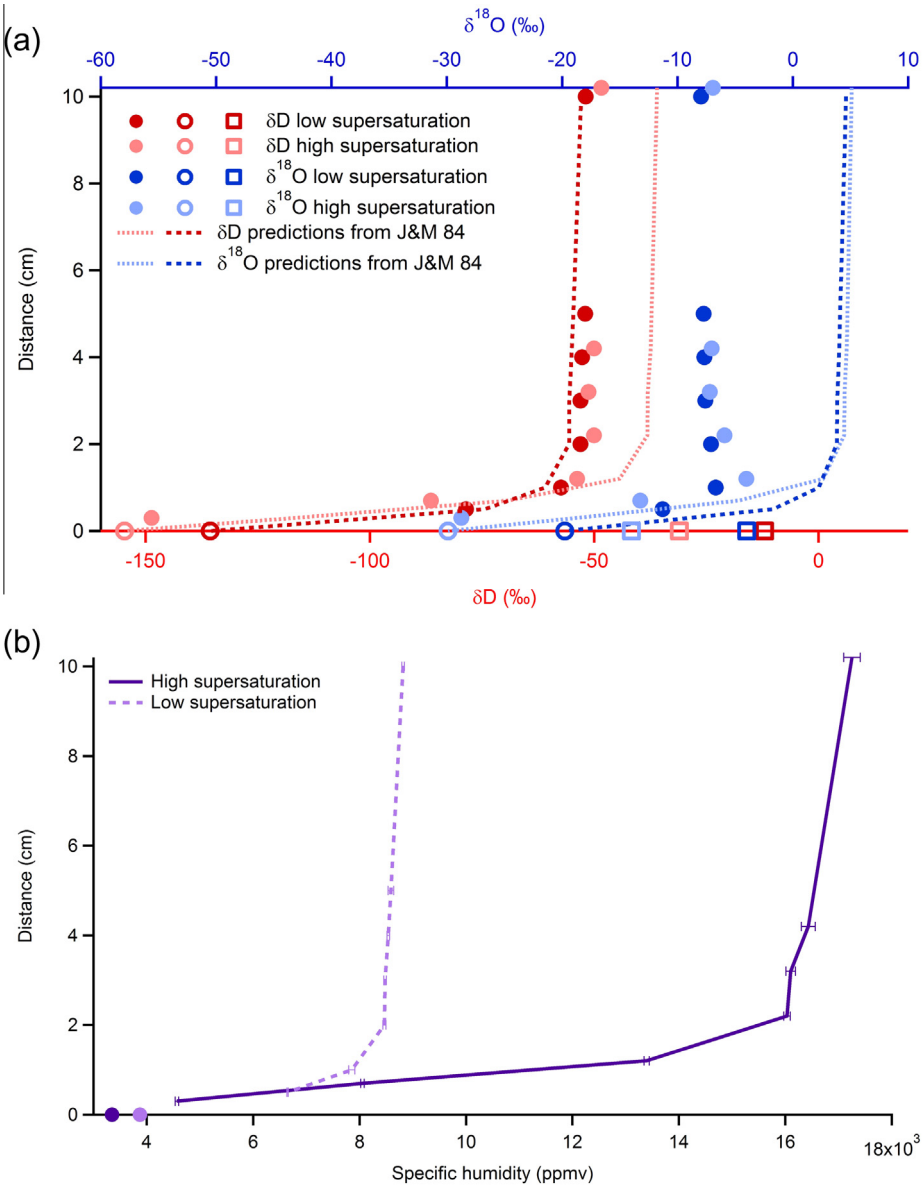

Fig. 5. (a) Comparison between the experiments of the afternoon of 25/04 with high supersaturation (light colours) and of the morning of 19/04 with low supersaturation (dark colours) of the evolution of $\delta^{18}O$ (blue) and δD (red): full circles are measured isotopic compositions of the vapour, empty squares are measured isotopic compositions of the ice, empty circles are calculated isotopic compositions of water vapour in isotopic equilibrium with the ice using the fractionation factors at the temperature of the cold plate (Majoube, 1971a), dotted lines are predictions for the isotopic composition of the vapour over the cold trap using Jouzel and Merlivat theory (J&M 84) and the isotopic composition of the vapour at the boundary layer predicted with the equilibrium fractionation (empty circles) (b) Comparison of the humidity levels between the experiments of the afternoon of 25/04 (full line, dark purple) and the one of the morning of 19/04 (dotted line, light purple) and the volume mixing ratios corresponding to the saturated vapour pressure at the cold trap temperature for both experiments (circles). (For interpretation of the references to colour in this figure legend, the reader is referred to the web version of this article.)

amount, all the effects linked to the interaction between the first layer of ice and the copper can be neglected.

3.2. Results and comparison with classical fractionation formulation

Ten experiments were run with different experimental conditions (temperature of the cold point, relative humidity far from the cold trap) as summarised in Table 2. We have explored relative humidity levels between 17% and 60% and temperatures of the cold point between −5 and −21 °C. Our aim was to explore supersaturation levels not as extreme as those presented in the non-controlled experiment of Section 2. Indeed, in the cloud chamber experiments, we could reach supersaturation level as low as 1.07 for the experiment of the afternoon of April 18.

For similar supersaturation levels, the isotopic compositions of the solid condensate are the same for both the

experiment ran in non-controlled conditions and the experiment ran in the cloud chamber. We also observe a similar increase in d-excess and ^{17}O-excess of the solid condensate by increasing supersaturation (the effect of temperature on d-excess is a second order one). As already discussed in the previous section, the model of Jouzel and Merlivat generally overestimates the change in d-excess and ^{17}O-excess between the water vapour and the solid condensate for supersaturation levels higher than 1.8. As noted above, one possible explanation for this discrepancy is that the spatial variations of the isotopic composition of water vapour were not taken into account. In the Jouzel and Merlivat approach and because of technical limitations, the flux toward the cold plate was indeed calculated with the humidity level and isotopic composition of the water vapour far away from the cold plate, but the isotopic composition of the water vapour and humidity strongly varies toward the cold plate, which may complicate the simple equation proposed by Jouzel and Merlivat. This is the reason why we now concentrate on the water vapour profile over the cold plate. We have selected two experiments to look at these profiles: first, an experiment with a rather low supersaturation $S_i = 1.8$ (19/04 morning) and one with a rather high supersaturation $S_i = 4.3$ (25/04 afternoon). Cold trap temperatures are similar in both experiments, only the humidity levels differ.

Fig. 5 shows the evolution of isotopic composition over the cold trap during the two experiments. Globally, the water mixing ratio, δ^{18}O, and δD decrease at distances less than 1 cm above the cold plate. Such a result is not unexpected. First, the decrease of water content toward the cold plate is due to the water trapping on this surface. Second, the diffusion toward the cold plate is associated with fractionation. Because lighter molecules diffuse more rapidly than heavier ones, the isotopic composition of the condensate is very depleted in heavy isotopes. Moreover it is expected that the condensate equilibrates with the water vapour in the boundary layer (Merlivat and Nief, 1967; Majoube, 1971a). The δ^{18}O and δD values observed at 0.3 cm above the cold plate should thus be influenced by both diffusion and equilibrium fractionation.

With the isotopic profiles in the water vapour, it is now possible to test the validity of the Jouzel and Merlivat formulation (Jouzel and Merlivat, 1984) at short spatial scale. For this, we have calculated the supersaturation profiles for our experiments from the measurements of the water mixing ratio and the temperature of the cold point. Then, as in Section 2, we have deduced the modelled isotopic composition of the water vapour at each level of our profile using the measured isotopic composition of the condensate, the value of supersaturation at each level and Eqs. (4) and (5). Fig. 5 shows that measured and modelled isotopic compositions of the water vapour already differ significantly at 1 cm above the cold point, i.e. for supersaturation levels higher than 2. For low supersaturation, the Jouzel and Merlivat model reproduces the profile of δD of the vapour, but fails for δ^{18}O as already observed in Section 2. For high supersaturation, both isotopic composition profiles are not reproduced by the model. The difficulty to obtain a good match between data and model even at short distances above the cold point is a strong limitation for quantitative interpretation of water isotopic fractionation at solid condensation.

We thus propose below an improved mathematical approach compared to the one of Jouzel and Merlivat to describe the spatial evolution of δ^{18}O and δD in the water vapour linked to equilibrium and diffusion fractionation processes. Our aim is thus to obtain a simple expression that will enable to fit the whole profile of δ^{18}O and δD in the water vapour based on physical processes. Such a model should enable us to test whether the values of diffusivity used for the water isotopes are valid for solid condensation at low temperature.

3.3. Formulation of fractionation associated with diffusion for a cloud chamber experiment

The cloud chamber experiment has been designed so that the main process controlling the spatial repartition of water isotopes in water vapour is diffusion toward the cold trap. In order to check this assumption, we estimated the stability toward convection through calculation of the Brunt Väisälä frequency and we obtained $N^2 = \frac{g}{\theta}\frac{d\theta}{dz} \approx 0$, $13s^{-2} > 0$, where g is the local acceleration of the gravity and θ the potential temperature. This indicates that the atmosphere is stable with respect to convective processes.

The second prerequisite for our problem is to be stationary. This assumption is not true for long experiments (longer than one day) because of continuous trapping of water vapour on the cold trap and extraction of water vapour for the optical analyser. Still the amount of water trapped during the 90 min condensation cycle is negligible compared to the large volume of the cloud chamber (in other words, the pressure difference between the beginning of one experiment and the end is less than 0.5%). We have also experimentally checked that the concentration profile was established very quickly at the beginning of the experiment to remain unchanged throughout the experiment. Real-time measurements of the isotopic composition of the water vapour have shown a rapid response to modifications of the temperature or height of the cold point. The transient periods are of the order of magnitude or smaller than the time response of the CRDS spectrometer (around 1 min). These transients are followed by a stationary water vapour isotopic composition with no further trend. Furthermore, at the spatial scale (centimetre) of our experiment, the characteristic time scale is small enough to consider only stationary effects of the diffusion.

From the above considerations, the problem we need to solve is the equation of diffusion with a flux through a disc at steady state. This system is similar to the one proposed by Jouzel and Merlivat and involves the same physical processes. Still, the assumption of an infinite plate for condensation is removed as it was leading to an unrealistic water vapour profile with a linear increase of water vapour concentration from the cold trap. The equation of diffusion in steady state in cylindrical coordinates with axial symmetry is given by:

$$\Delta e_v(r,z) = 0, \quad z > 0 \tag{7}$$

The boundary conditions for the cloud chamber experiments are:

1. The concentration far away from the cold trap: $\lim_{z\to\infty} e_v(r,z) = e_{v\infty}$
2. The vertical gradient of water isotopes at the cold plate surface is:

$$\left.\frac{\partial e_v}{\partial z}\right|_{z=0^+} = f_0$$

where e_v is the partial pressure of $H_2{}^{16}O$ in the air. The parameter f_0 is related to the flux density through Fick's law: $\vec{j} = -D\vec{\nabla}(e_v)$, hence $j_0 = -Df_0$. The total water flux going toward the cold trap is defined by $\Phi = \int\int_D j_z$ where j_z is the vertical component of the flux density $\vec{j}$ and D the domain of the $z = 0$ plane that the cold trap spans. We then obtain $\Phi = -\pi R^2 D f_0$ with R the radius of the cold trap and D the diffusion coefficient of water in air.

A similar set of equations can be written for the heavy isotopes:

$$\begin{cases} \Delta e_v^i(r,z) = 0, \quad z > 0 \\ \frac{\partial e_v^i}{\partial z}|_{z=0^+} = f_0^i \\ \lim_{z\to\infty} e_v^i(r,z) = e_{v\infty}^i \end{cases}$$

Without any temperature gradient (assumption discussed in Section 3.4), these sets of equations lead to the following solution along the central axis ($r = 0$):

$$e_v = f_0(\sqrt{R^2+z^2} - z) + e_{v\infty} \tag{8}$$

$$e_v^i = f_0^i(\sqrt{R^2+z^2} - z) + e_{v\infty}^i \tag{9}$$

The flux of the isotope i, f_0^i can be related to f_0, the flux of the main isotope $H_2{}^{16}O$ from the isotopic composition δ_B^i at the ice boundary layer, such that:

$$f_0^i = \left(\frac{\delta_B^i}{1000} + 1\right) R_{SMOW}^i \frac{D}{D^i} f_0 \tag{10}$$

Here, we first focus on the high supersaturation experiment during which the diffusion role should prevail. In a first step, we focus on the water vapour concentration profile e_v and evaluate how Eq. (8) is able to reproduce our experimental data. We forced $e_{v\infty}$ to be equal to the value of e_v at 10 cm from the cold trap. The experimental water partial pressure of the light isotopes in the vapour phase e_v is directly calculated from the relative humidity. Two parameters remain:

1. f_0 which mainly influences the shape of the profile close to the cold point. We thus adjust its value to fit the experimental value at the lowest level (0.3 cm).
2. The radius R of the cold trap. If we use the true value, the inflection of the concentration profile is too high (more than 3 cm from the cold trap). In order to reproduce an inflection point at 1–2 cm above the cold trap (Fig. 5b), we need to reduce the radius to 0.8 cm (deeper discussion in Section 3.4.).

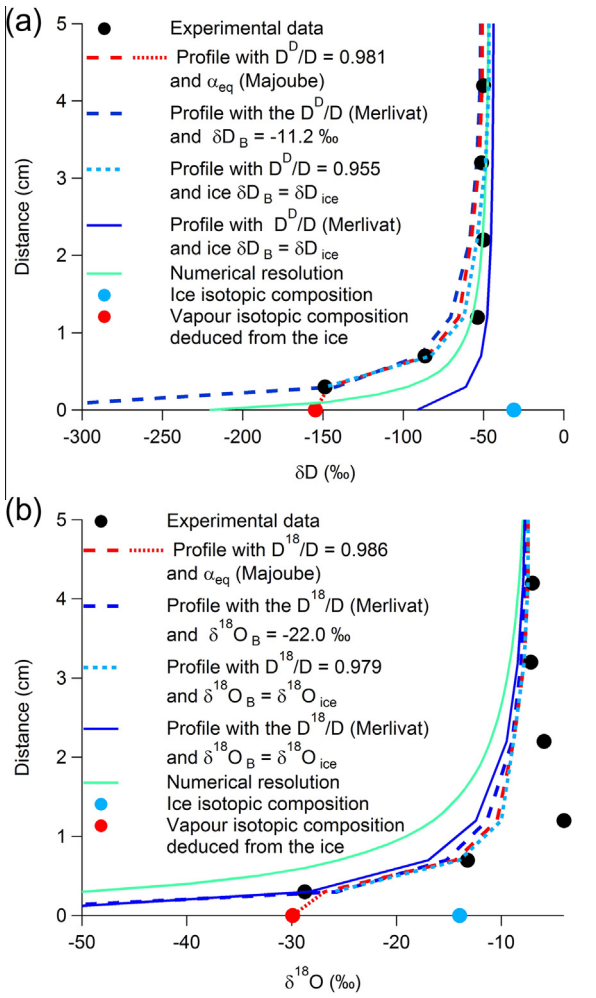

Fig. 6. Isotopic composition for (a) δD and (b) $\delta^{18}O$ for the high supersaturation experiment: black dots are the isotopic composition of the vapour during the high supersaturation experiment, dark blue line is the isotopic composition profile calculated from Eqs. (8) and (9) using the ice isotopic composition as a boundary layer and D^i/D from Merlivat, 1978, light blue dotted line is the isotopic composition profile using the ice composition as a boundary layer and adjusting D^i/D, dark blue dashed line represents the isotopic composition profile adjusting the boundary layer isotopic composition and using D^i/D from Merlivat, 1978, and red dashed line gives the isotopic composition using the equilibrium fractionation to predict the boundary layer isotopic composition and adjusting D^i/D; the blue dot is the isotopic composition of the ice and the red one is the isotopic composition of the vapour calculated with the Majoube equilibrium fractionation coefficient (Majoube, 1971a). (For interpretation of the references to colour in this figure legend, the reader is referred to the web version of this article.)

In a second step, we focus on the water isotopic composition profiles e_v^i. We adjust $e_{v\infty}^i$ to the value of e_v^i at 10 cm from the cold trap. f_0^i is calculated from Eq. (10) using $\delta_B^i = \delta_{ice}^i$. When we take D^i/D to be equal to the value given by Merlivat, 1978 ($D^{18}/D = 0.973$ and $D^D/D = 0.976$ full blue line on Fig. 6) a satisfactory agreement is observed between modelled and measured water vapour isotopic

Table 3
Summary of the hypotheses for the boundary layer flux values and literature values for D^i/D.

	Low supersaturation experiment		High supersaturation experiment	
δ^i_B (‰)	D^D/D	D^{18}/D	D^D/D	D^{18}/D
$\delta^i_B = \delta^i_{ice}$	0.928	0.984	0.955	0.979
$1+\delta^i_B = \alpha^i_{eq}(1+\delta^i_{ice})$	0.966	0.996	0.981	0.986
	Merlivat, 1978		Cappa et al. (2003)	
Literature coefficients	0.976	0.973	0.989	0.969

composition even though some discrepancies remain in particular in the case of δD as the isotopic composition does not go low enough. In order to fit the experimental data, we need to relax the constrain on one of the parameters involved in the expression of f^i_0. The value of D^i/D has been adjusted by root mean square minimization of the modelled δ^iX to best reproduce the measured δ^iX (Fig. 6). Small adjustments of D^i/D (see Table 3) to best fit the data provide a clear improvement in the agreement between theoretical profiles and experimental measurements (light blue dotted line on Fig. 6).

Our approach for solving Eq. (10) does not take into account any fractionation at the vapour/ice interface, therefore the flux of molecule brought by diffusion is directly transferred to the ice. In the case of a permanent regime, the thermodynamic equilibrium would prevent a complete transfer of molecule and involve a fractionation at the vapour/ice interface. This suggests another hypothesis for f^i_0 adjustment: rather than adjusting D^i/D, we keep the values of D^i/D from Merlivat, 1978 and adjust δ^i_B (dark blue dashed line on Fig. 6). In the case of the best fit for δ^{18}O, the isotopic composition of the boundary layer is compatible with the equilibrium fractionation with the ice ($\delta^{18}_B = -22.0‰$ instead of $\delta^{18}_B = -29.9‰$ in the case of equilibrium fractionation between the boundary layer and the condensate) whereas it is not for δD ($\delta^D_B = -11.2‰$ instead of $\delta^{18}_B = -154.1‰$ in the case of equilibrium fractionation).

Finally, imposing $1+\delta^i_B = \alpha^i_{eq}(1+\delta^i_{ice})$ at the boundary layer give an acceptable solution taking into accounts equilibrium fractionation and the diffusion is adjusted within a reasonable range (see Table 3). These values are in the range given in the literature, as shown in Fig. 6 by the blue dotted line (see Table 3). Still the fact that we do not end up with a unique D^i/D value for δ^{18}O and δD for the experiments performed at high and low supersaturation implies that the proposed model is not perfect. Using alternative values for α^i_{eq} such as the one of Ellehoj et al., 2013, does not improve the global shape of the modelled profiles: the calculated values for δ^{18}O and δD are only slightly modified by less than 2‰ and 5‰ respectively.

To conclude, the diffusion model that we developed here is mainly forced by f^i_0, the flux at the vapour-ice interface. We have tested different assumptions for the f^i_0 value and for each case, D^i/D remains within the range of values expected in the literature. In the case of HDO, D^D/D is lowest when no fractionation at the interface is implemented ($\delta^i_B = \delta^i_{ice}$). The values are even lower in the case of low supersaturation. This is not unexpected and shows that fractionation occurs at solid condensation. The depletion of HDO in the vapour associated with equilibrium fractionation at solid condensation is much more important than for $H_2{}^{18}O$. Without taking into account fractionation at the vapour–ice interface for the estimate of f^i_0 it is compensated by adjusting D^i/D to fit the water vapour isotopic profiles. This adjustment is therefore stronger for HDO/H_2O. The fact that this phenomenon is accentuated when the supersaturation is lower, hence when equilibrium fractionation dominates shows that it is important to consider equilibrium fractionation at the vapour–ice interface, even with strong supersaturation.

3.4. Limitations

Because of the strong supersaturation, our system is mainly controlled by diffusion toward the cold trap. Our approach is based on the classical formulation of diffusion toward a disc. Still some effects have been neglected in this approach: mainly the influence of temperature and the geometry of the cold trap (a cylinder, not a disc). To take into account the influence of temperature, we cannot solve the diffusion equation analytically and therefore we present a numerical resolution in the following.

Because of the lack of reliable temperature profile, we model the temperature diffusion over the cold trap. We solve the heat equation ($\Delta T = 0$) in 3D and integrate this profile in the thermodiffusion equation (Landau and Lifshitz, 1959). Taking into account the dependence of the diffusion coefficient of water on temperature (Hall and Pruppacher, 1976):

$$D = 0.211\left(\frac{T}{T_0}\right)^{1.94}\left(\frac{P_0}{P}\right) \tag{11}$$

where $T_0 = 273.15\,K$ and $P_0 = 1013.25\,mbar$, we end up with the following equation:

$$1.94\frac{\vec{\nabla}T}{T}.\vec{\nabla}e_v + \Delta e_v = 0 \tag{12}$$

As there is no analytical solution to Eq. (12), this final diffusion problem is numerically solved using Mathematica software with the geometry of a disc for the sink. As for the previous solution, we have to decrease the radius of the cold plate compared to the true value in order to best fit the concentration profile. Different temperature gradients have been tested ($\vec{\nabla}T = 0$ and $\vec{\nabla}T = constant$) but do not yield significantly different results (not shown).

As for the resolution of Eq. (8), to obtain the best fit to the data we need to adjust f_0 and f_0^i. Even if the fluxes (f_0 and f_0^i) are different when taking the temperature into account, the ratio of the fluxes f_0^i/f_0 remains the same as for the case with no temperature gradient, such that the conclusion of the previous section remains unchanged. We have chosen to keep D^i/D constant with temperature variations since we are not aware of any study evaluating the relative variations of the different water isotopes diffusion coefficients. Nevertheless, studies of thermal diffusion for nitrogen isotopes (Grachev and Severinghaus, 2003) highlighted a temperature dependence in the ratio of diffusion coefficients of different isotopes. This is another limitation of our approach that could only be explored with a much more controlled temperature profile.

A second limitation of our approach is the assumption that the whole flux of water was toward the disc surface, hence neglecting the fluxes toward the lateral cylinder surface. This effect could influence the diffusion profile and explain why we need to use a smaller effective radius to fit the water vapour profile. We thus solve Eq. (12) on a cylinder of radius 1.9 cm and height 8 cm instead of a flat disc. The numerical resolution of Eq. (12) was performed using the Mathematica software. Temperature influence could not be taken into account in this model because of numerical instabilities. However, even with this solution, we still need to decrease the radius (cf Fig. 7, blue curve) compared to the true value in order to fit the water vapour profile. We thus conclude that our system is not purely diffusive, especially at the edge of the trap with possible convective effects.

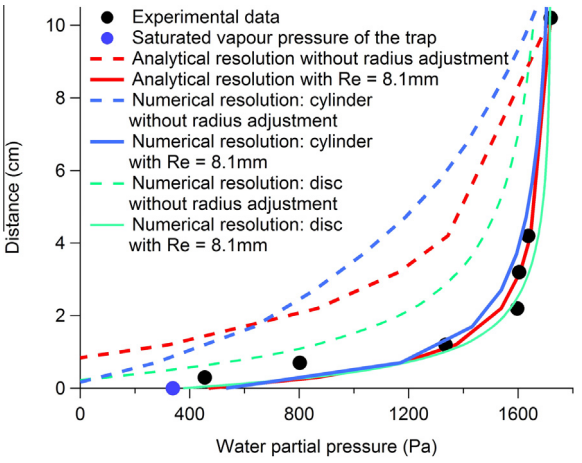

Fig. 7. $H_2{}^{16}O$ partial pressure of the vapour during the experiment of the 25th of April: the black dots are the experimental datapoints, the blue dot is the saturated vapour pressure over the cold trap and the red lines are the fit as described in Section 3.3. with an effective radius: $R_e = 0.81$ cm (full line) instead of 1.9 cm (dashed line), the blue lines are the numerical resolution in the case of a cylinder (Section 3.4) and the green lines are the numerical resolution in the case of a disc (Section 3.4); note that in the case of the disc, temperature profile has been modelled with the heat equation. (For interpretation of the references to colour in this figure legend, the reader is referred to the web version of this article.)

The existence of convective effects at the edge would explain why we need to use an effective radius smaller than the true radius to bring into agreement modelled and measured water vapour profiles.

Third, despite a relatively good agreement between the modelled and measured profiles, we still do not manage to reproduce the observed excursion or "bump" in the $\delta^{18}O$ profile. Whereas δD is continuously decreasing when approaching the cold plate, the $\delta^{18}O$ profile shows a bump at a distance of about 1 cm above the cold plate. This can be explained by the competition between equilibrium and diffusion fractionations. While equilibrium fractionation leads to low δD and $\delta^{18}O$ values in the water vapour just above the condensation plate, diffusion tends to deplete the water vapour in light isotopes because they move more easily toward the cold plate, leaving heavier molecules behind. Because of the relative values of the equilibrium and kinetic (diffusion) fractionation coefficients, the diffusion fractionation becomes visible in the water vapour $\delta^{18}O$ profile, whereas the δD profile remains mainly dominated by equilibrium fractionation. We therefore interpret the bump in the $\delta^{18}O$ profile at 1 cm above the cold plate as due to enrichment in $H_2{}^{18}O$ because of the relatively strong diffusion of light isotopes toward the cold plate. As for the δD profile, the isotopic enrichment due to diffusion is masked by the strong isotopic fractionation associated with the vapour-solid equilibrium. This competition is not included in our model in which diffusion and equilibrium act independently on different regions (boundary layer for equilibrium and free air for diffusion). Possible variations of D^i/D with the temperature (as mentioned above) and the addition of a vertical advection process may also contribute to the existence of this bump. Still, we decided not to include these effects at this stage. First, we do not have solid data on temperature variations in the cloud chamber. Second, we could not provide any explanation for the existence of a vertical advection flux toward the cold plate.

Finally, the inlet itself can impact the temperature, humidity and isotopic composition profiles. Copper was chosen as it is the material commonly used for isotopic composition measurements and has been shown to have a limited impact compared to a number of other materials on the isotopic composition of moist air in contact with it (Steen-Larsen et al., 2014). Still, as copper has a good thermic conductivity, it probably biased the temperature measurements, justifying a calculation of temperature profiles with the heat equation.

To summarize, the above mentioned issues, in combination with the design of this first cloud chamber experiment with its poorly defined temperature profile, a lack of measurements close enough to the cold trap and even the geometry of the cold trap itself hinder in the interpretation of the results. The measurement of temperature without advection is challenging: there is an impact of radiation on the sensor itself and heat conduction through the copper inlet homogenises on a large scale the temperature measured by our sensor. An additional challenge is to measure water isotopic composition very close to the cold plate. Such measurements require a smaller inlet than the one we used

(0.64 cm outer diameter). However, a smaller diameter tube could lead to a more turbulent flow towards the spectrometer. Finally, the size of the cold trap was limited by the aperture of a flange KF 40 through which the cold trap was inserted into the cloud chamber.

4. CONCLUSION AND PERSPECTIVES

In this study we presented two approaches to better understand the fractionation during solid condensation under very high supersaturation conditions. Under such conditions, both kinetic and equilibrium fractionation effects should be taken into account. First experiments (Section 2) show extremely supersaturated situations in which kinetic effects predominate. These experiments prove that ^{17}O-excess increases with the increasing importance of kinetic fractionation, as is the case for d-excess. This validates to first order the implementation of fractionation associated with ^{17}O-excess in the same manner as has been done for d-excess variations in isotopic models (Landais et al., 2008; Risi et al., 2013).

Using both simple and controlled experiments in a cloud chamber, we show that a parametrisation as proposed by Jouzel and Merlivat, 1984 is able to properly reproduce δD for low supersaturation level, but fails to reproduce δ^{18}O, d-excess and ^{17}O-excess, even for low supersaturation. Since the relative influence of kinetic vs equilibrium fractionation is much more important for δ^{18}O than for δD, this suggests that kinetic fractionation is not properly taken into account in the Jouzel and Merlivat approach.

We have proposed a more sophisticated model for the diffusion toward a cold trap than the one proposed by Jouzel and Merlivat. This approach aims to reproduce water vapour isotopic profiles measured by laser spectroscopy in a cloud chamber above a cold trap. Still, a match between modelled and observed values could not be obtained from the ratio of diffusivities of water isotopes in the air as classically used (Merlivat, 1978). Moreover, the lack of measurement of the water vapour isotopes very close to the cold trap prevents us from providing a correct description of the boundary layer. The bump in the δ^{18}O profile is the major unresolved issue in our model, but in the absence of (1) spatially better resolved data for the boundary layer description and (2) relevant profiles of other physical properties, we are unable to progress on this issue without further experiments.

To progress with the investigation of these processes, a more accurate description of the boundary layer near the condensing point is needed and would allow to improve the associated modelling. Also, our experiments were all performed at an ambient temperature of 20 °C, whereas a proper representation of isotopic processes in Polar Regions calls for laboratory experiments at temperatures below 0 °C. Working at temperatures below zero would require significant changes to the cloud chamber environment. Finally, the development of laser analysers and their improving performances at low temperature (Landsberg et al., 2014) now renders it possible to continuously measure water vapour isotopic composition at very remote sites in Antarctica where both temperature and humidity are very low. Such measurements, in parallel to precipitation and surface snow sampling, would permit to better constrain the isotopic fractionation between water vapour and snow in this region and hence complement our laboratory approach.

This study is preliminary and provides new perspectives to revisit the classical formulation of water isotopic fractionation during solid condensation at very low temperature. Compared to Jouzel and Merlivat's formulation, the kinetic fractionation is not imposed by the supersaturation but by the fluxes of the different isotopes (f_0 and f_0^i in the text). Our formulation is particularly adapted for the two following examples. The determination of moisture fluxes between the ice and the air at the surface in Polar Regions is an important open question (Frezzotti et al., 2004) that involves complex mechanisms. Using the isotopic composition of frost flowers, surface hoar and water vapour could give clues about the thermodynamic condition in which they occur. At the surface, important supersaturation can occur. They are linked with out of equilibrium phase transition (Style and Worster, 2009; Gallet et al., 2014). Field measurements of water vapour isotopic composition in Antarctica will allow further investigation of the impact of molecular diffusion in real conditions and the complete diffusion scheme we presented here should also be adapted to describe the very stratified polar night conditions.

In the sub-surface, our formulation is also well adapted. Exchanges between the snow and the interstitial air create snow metamorphism which is associated with isotopic fractionation and therefore post deposition effects on the isotopic composition of the archived snow (Town et al., 2008). On the first centimetres of the snow, important temperature gradients occur, leading to diffusion through the porous matrix. The integration of isotopic composition in snow models such as CROCUS (Touzeau et al., 2015) will need to take into account diffusion through robust parametrisation of kinetic fractionation.

As in Jouzel and Merlivat (1984), the design of our experiment does not correspond to cloud microphysics and the implementation of our new formulation for air-ice isotopic fractionation is not directly an application to isotopic fractionation in clouds. In cloud microphysics, diffusion of water molecules toward condensation nuclei creates kinetic fractionation. In the case of high density of condensate nuclei, equilibrium fractionation is important and therefore the impact of diffusion on the condensation fractionation is reduced. In remote Polar Regions, this density is low and sustainable supersaturation can occur. A good representation of the fractionation induced by the long diffusion path toward the condensation nuclei is important for models to predict the isotopic composition on a distillation path. To realise a cloud chamber experiment depicting more accurately what happens in cloud microphysics, there should not be a unique cold trap acting as a sink of water molecules. Instead, condensation should occur on a limited number of condensation nuclei while isotopic composition is monitored. The challenge for such an experiment is to create conditions in which condensation on the wall of the cloud chamber impact is moderate compared to the condensation on the nuclei. As a long term perspective,

isotope diffusion calculations could be integrated in the parametrisation of the physics of water distillation using a characteristic diffusion length deduced from the condensation nuclei density in clouds, for instance in models such as MAR (Gallée and Gorodetskaya, 2010) or MCIM (Ciais and Jouzel, 1994).

ACKNOWLEDGEMENTS

The research leading to these results has received funding from the European Research Council under the European Union's Seventh Framework Programme (FP7/2007-2013)/ERC grant agreement n°306045 and ANR Citronnier, we warmly thank all the staff of the LISA that really helped us for this experiment and for their patience during all the long process of building up the set up. We acknowledge Bernard Chelli for helping out during the preparation of the experiment. Finally we warmly acknowledge the helpful comments of Emmanuel Witrant, Samir Kassi and Guillaume Mejean; and Geoffrey Gourdet for his help with drawing the schematics. The authors want to thank CNRS-INSU for supporting CESAM as a National Instrument.

REFERENCES

Barkan E. and Luz B. (2005) High precision measurements of $^{17}O/^{16}O$ and $^{18}O/^{16}O$ ratios in H_2O. *Rapid Commun. Mass Spectrom.* **19**, 3737–3742.

Barkan E. and Luz B. (2007) Diffusivity fractionations of $H_2^{16}O/H_2^{17}O$ and $H_2^{16}O/H_2^{18}O$ in air and their implications for isotope hydrology. *Rapid Commun. Mass Spectrom.* **21**, 2999–3005.

Bonne J.-L., Steen-Larsen H. C., Risi C., Werner M., Sodemann H., Lacour J.-L., Fettweis X., Cesana G., Delmotte M., Cattani O., Vallelonga P., Kjær H. A., Clerbaux C., Sveinbjörnsdóttirffilmark Á. E. and Masson-Delmotte V. (2015) The summer 2012 Greenland heat wave: in situ and remote sensing observations of water vapour isotopic composition during an atmospheric river event. *J. Geophys. Res. Atmos.*, 2014JD022602.

Cappa C. D., Hendricks M. B., DePaolo D. J. and Cohen R. C. (2003) Isotopic fractionation of water during evaporation. *J. Geophys. Res. -Atmos.* **108**, 10.

Charles C. D., Rind D., Jouzel J., Koster R. D. and Fairbanks R. G. (1994) Glacial-interglacial changes in moisture sources for greenland: influences on the ice core record of climate. *Science* **263**, 508–511.

Ciais P. and Jouzel J. (1994) Deuterium and oxygen 18 in precipitation: Isotopic model, including mixed cloud processes. *J. Geophys. Res. Atmos.* **99**, 16793–16803.

Dansgaard W. (1964) Stable isotopes in precipitation. *Tellus* **16**, 436–468.

Ellehøj M. D. (2011) *Ice–VAPOR equilibrium fractionation factor*. University of Copenhagen, Faculty of Science.

Ellehøj M. D., Steen-Larsen H. C., Johnsen S. J. and Madsen M. B. (2013) Ice-vapor equilibrium fractionation factor of hydrogen and oxygen isotopes: experimental investigations and implications for stable water isotope studies. *Rapid Commun. Mass Spectrom.* **27**, 2149–2158.

EPICA (2004) Eight glacial cycles from an Antarctic ice core. *Nature* **429**, 623–628.

Fawcett P. J., Ágústsdóttir A. M., Alley R. B. and Shuman C. A. (1997) The Younger Dryas termination and north atlantic deep water formation: insights from climate model simulations and greenland ice cores. *Paleoceanography* **12**, 23–38.

Frezzotti M., Pourchet M., Flora O., Gandolfi S., Gay M., Urbini S., Vincent C., Becagli S., Gragnani R., Proposito M., Severi M., Traversi R., Udisti R. and Fily M. (2004) New estimations of precipitation and surface sublimation in East Antarctica from snow accumulation measurements. *Clim. Dyn.* **23**, 803–813.

Gallée H. and Gorodetskaya I. V. (2010) Validation of a limited area model over Dome C, Antarctic Plateau, during winter. *Clim. Dyn.* **34**, 61–72.

Gallet J. C., Domine F., Savarino J., Dumont M. and Brun E. (2014) The growth of sublimation crystals and surface hoar on the Antarctic plateau. *Cryosphere* **8**, 1205–1215.

Gat J. R. (1996) Oxygen and Hydrogen isotopes in the hydrologic cycle. *Annu. Rev. Earth Planet. Sci.* **24**, 225–262.

Genthon C., Six D., Gallée H., Grigioni P. and Pellegrini A. (2013) Two years of atmospheric boundary layer observations on a 45-m tower at Dome C on the Antarctic plateau. *J. Geophys. Res. Atmos.* **118**, 3218–3232.

Gettelman A., Walden V. P., Miloshevich L. M., Roth W. L. and Halter B. (2006) Relative humidity over Antarctica from radiosondes, satellites, and a general circulation model. *J. Geophys. Res. Atmos.* **111**, D09S13.

Grachev A. M. and Severinghaus J. P. (2003) Laboratory determination of thermal diffusion constants for 29 N 2/28 N 2 in air at temperatures from− 60 to 0 C for reconstruction of magnitudes of abrupt climate changes using the ice core fossil–air paleothermometer. *Geochim. Cosmochim. Acta* **67**, 345–360.

Hall W. D. and Pruppacher H. R. (1976) The survival of ice particles falling from cirrus clouds in subsaturated air. *J. Atmos. Sci.* **33**, 1995–2006.

Hoffmann G., Werner M. and Heimann M. (1998) Water isotope module of the ECHAM atmospheric general circulation model: a study on timescales from days to several years. *J. Geophys. Res. Atmos.* **103**, 16871–16896.

Jouzel J. and Merlivat L. (1984) Deuterium and oxygen 18 in precipitation: modeling of the isotopic effects during snow formation. *J. Geophys. Res. Atmos.* **89**, 11749–11757.

Jouzel J., Stievenard M., Johnsen S. J., Landais A., Masson-Delmotte V., Sveinbjornsdottir A., Vimeux F., von Grafenstein U. and White J. W. C. (2007) The GRIP deuterium-excess record. *Q. Sci. Rev.* **26**, 1–17.

Krinner G., Genthon C. and Jouzel J. (1997) GCM analysis of local influences on ice core δ signals. *Geophys. Res. Lett.* **24**, 2825–2828.

Laepple T., Werner M. and Lohmann G. (2011) Synchronicity of Antarctic temperatures and local solar insolation on orbital timescales. *Nature* **471**, 91–94.

Landais A., Barkan E. and Luz B. (2008) Record of $\delta^{18}O$ and ^{17}O-excess in ice from Vostok Antarctica during the last 150,000 years. *Geophys. Res. Lett.* **35**, L02709.

Landais A., Barkan E., Yakir D. and Luz B. (2006) The triple isotopic composition of oxygen in leaf water. *Geochim. Cosmochim. Acta* **70**, 4105–4115.

Landais A., Ekaykin A., Barkan E., Winkler R. and Luz B. (2012) Seasonal variations of ^{17}O-excess and d-excess in snow precipitation at Vostok station, East Antarctica. *J. Glaciol.* **58**, 725–733.

Landais A., Risi C., Bony S., Vimeux F., Descroix L., Falourd S. and Bouygues A. (2010) Combined measurements of ^{17}O excess and d-excess in African monsoon precipitation: Implications for evaluating convective parameterizations. *Earth Planet. Sci. Lett.* **298**, 104–112.

Landau L. D. and Lifshitz E. M. (1959) Fluid mechanics (eds. L. D. Landau and E. M. Lifshitz). Pergamon Press, London.

Landsberg J., Romanini D. and Kerstel E. (2014) Very high finesse optical-feedback cavity-enhanced absorption spectrometer for low concentration water vapor isotope analyses. *Opt. Lett.* **39**, 1795–1798.

Loewe F. (1936) The greenland Ice Cap as seen by A Meteorologist. *Q. J. R. Meteorol. Soc.* **62**, 359–378.

Luz B., Barkan E., Yam R. and Shemesh A. (2009) Fractionation of oxygen and hydrogen isotopes in evaporating water. *Geochim. Cosmochim. Acta* **73**, 6697–6703.

Majoube M. (1971a) Fractionation in O-18 between ice and water vapor. *J. Chim. Phys. -Chim. Biol.* **68**, 625-&.

Majoube M. (1971b) Oxygen-18 and deuterium fractionation between water and steam. *J. Chim. Phys. -Chim. Biol.* **68**, 1423-&.

Merlivat L. (1978) Molecular diffusivities of (H_2O)-O-1 6 HD16O, and (H_2O)-O-18 in gases. *J. Chem. Phys.* **69**, 2864–2871.

Merlivat L. and Nief G. (1967) Fractionnement isotopique lors des changements d'état solide-vapeur et liquide-vapeur de l'eau à des températures inférieures à 0 °C. *Tellus* **19**, 122–127.

Moyer E., Sarkozy L., Lamb K., Clouser B., Stutz E., Kuhnreich B., Landsberg J., Habig J., Hiranuma N., Wagner S., Ebert V., Kerstel E., Moehler O. and Saathoff H. (2013) Applications of absorption spectroscopy for water isotopic measurements in cold clouds, Goldschmidt. *Mineral. Mag.*, 1797.

Petit J. R., Jouzel J., Raynaud D., Barkov N. I., Barnola J. M., Basile I., Bender M., Chappellaz J., Davis M., Delaygue G., Delmotte M., Kotlyakov V. M., Legrand M., Lipenkov V. Y., Lorius C., Pepin L., Ritz C., Saltzman E. and Stievenard M. (1999) Climate and atmospheric history of the past 420,000 years from the Vostok ice core, Antarctica. *Nature* **399**, 429–436.

Risi C., Bony S. and Vimeux F. (2008) Influence of convective processes on the isotopic composition ($\delta^{18}O$ and δD) of precipitation and water vapor in the tropics: 2. Physical interpretation of the amount effect. *J. Geophys. Res. Atmos.* **113**, D19306.

Risi C., Bony S., Vimeux F. and Jouzel J. (2010) Water-stable isotopes in the LMDZ4 general circulation model: model evaluation for present-day and past climates and applications to climatic interpretations of tropical isotopic records. *J. Geophys. Res. Atmos.* **115**, D12118.

Risi C., Landais A., Winkler R. and Vimeux F. (2013) Can we determine what controls the spatio-temporal distribution of d-excess and 17O-excess in precipitation using the LMDZ general circulation model? *Clim. Past* **9**, 2173–2193.

Schmidt G. A., Hoffmann G., Shindell D. T. and Hu Y. (2005) Modeling atmospheric stable water isotopes and the potential for constraining cloud processes and stratosphere-troposphere water exchange. *J. Geophys. Res. Atmos.* **110**, D21314.

Schoenemann S. W., Schauer A. J. and Steig E. J. (2013) Measurement of SLAP2 and GISP $\delta^{17}O$ and proposed VSMOW-SLAP normalization for $\delta^{17}O$ and ^{17}O excess. *Rapid Commun. Mass Spectrom.* **27**, 582–590.

Sime L. C., Wolff E. W., Oliver K. I. C. and Tindall J. C. (2009) Evidence for warmer interglacials in East Antarctic ice cores. *Nature* **462**, 342–345.

Steen-Larsen H. C., Sveinbjörnsdottir A. E., Peters A. J., Masson-Delmotte V., Guishard M. P., Hsiao G., Jouzel J., Noone D., Warren J. K. and White J. W. C. (2014) Climatic controls on water vapor deuterium excess in the marine boundary layer of the North Atlantic based on 500 days of in situ, continuous measurements. *Atmos. Chem. Phys.* **14**, 7741–7756.

Style R. W. and Worster M. G. (2009) Frost flower formation on sea ice and lake ice. *Geophys. Res. Lett.* **36**, L11501.

Touzeau A., Casado M., Baroni M., Morin S., Ekaykin A., Magand O., Picard G., Arnaud L., Bard E. and Landais A. (2015) *Deciphering influences of temperature, moisture sources, post-deposition effects and stratospheric inputs in records of stable isotopes in East Antarctic snow*. IUGG, Prague, Czech Republic.

Town M. S., Warren S. G., Walden V. P. and Waddington E. D. (2008) Effect of atmospheric water vapor on modification of stable isotopes in near-surface snow on ice sheets. *J. Geophys. Res. Atmos.* **113**, n/a-n/a.

Van Hook W. A. (1968) Vapor pressures of the isotopic waters and ices. *J. Phys. Chem.* **72**, 1234–1244.

Vimeux F., Masson V., Jouzel J., Stievenard M. and Petit J. R. (1999) Glacial-interglacial changes in ocean surface conditions in the Southern Hemisphere. *Nature* **398**, 410–413.

Wagner W. and Pruß A. (2002) The IAPWS formulation 1995 for the thermodynamic properties of ordinary water substance for general and scientific use. *J. Phys. Chem. Ref. Data* **31**, 387–535.

Wang J., Doussin J. F., Perrier S., Perraudin E., Katrib Y., Pangui E. and Picquet-Varrault B. (2011) Design of a new multi-phase experimental simulation chamber for atmospheric photosmog, aerosol and cloud chemistry research. *Atmos. Meas. Tech.* **4**, 2465–2494.

Werner M., Langebroek P. M., Carlsen T., Herold M. and Lohmann G. (2011) Stable water isotopes in the ECHAM5 general circulation model: toward high-resolution isotope modeling on a global scale. *J. Geophys. Res. Atmos.* **116**, D15109.

Winkler R., Landais A., Sodemann H., Dümbgen L., Prié F., Masson-Delmotte V., Stenni B. and Jouzel J. (2012) Deglaciation records of ^{17}O-excess in East Antarctica: reliable reconstruction of oceanic normalized relative humidity from coastal sites. *Clim. Past* **8**, 1–16.

Associate editor: Hagit P. Affek

5.3 Perspectives

In this chapter, we study the processes affecting water isotopes at (1) the phase transition vapour and ice and (2) due to the diffusion in the vapour phase. In the processes study involving the measurement of water vapour, the new developments of infrared spectroscopy are crucial. First, to be able to measure isotopic composition of water vapour at very low humidity (down or even below 1 $ppmv$), it is necessary to evaluate fractionation associated with the vapour-ice phase transition (equilibrium or out of equilibrium) for the entire range of temperature encountered in Polar Regions (temperature down to $-90°C$ in winter on the East Antarctic Plateau). Second, the evaluation of the impact of kinetic fractionation quantitatively can be greatly improved by (1) reducing the response time of the infrared spectrometers in order to be able to observe the transient effect of diffusion (typical time scale for diffusion of water vapour in an air matrix over 10 cm is $1min30s$) and (2) by measuring at a finer scale the isotopic composition profile near the ice-vapour interface. We believe that the new instrument described in section 4.3 can provide solutions to improve laboratory experiments to constrain the isotopic fractionation (both equilibrium and kinetic). Presently, infrared spectroscopy has not been widely used in controlled laboratory experiments.

Nevertheless, we hope this use will be extended to more experiments. As we mentioned, we are actually using a commercial infrared spectrometer to infer fractionation associated to the phase transition in laboratory experiments. Many more processes affecting isotopic composition still need to be studied in controlled conditions and for which infrared spectroscopy would be a great aid such as metamorphism in temperature cycles, diffusivity of the different isotopes at low temperatures or even the impact of turbulence on kinetic fractionation.

An important effort is starting using ab-initio calculation to evaluate the thermodynamic and physical properties of the different isotopes as highlighted by Pinilla et al. [2014] for equilibrium fractionation for instance. Calculation of diffusivity can also be realised by using high-quality ab-initio intermolecular potentials [Tulegenov et al., 2007] as realised by Hellmann et al. [2014] for CH_4 in N_2. Once validated against dataset, the ab-initio calculations can easily be extended to large range of conditions. For instance, for diffusivity calculation, once the physics included in the calculation is validated for a small range of temperature or gas matrix, it can be used to physically extrapolate the data for other temperature or gas matrix. As mentioned in the introduction, it is necessary to have robust determination of the isotopic composition at low temperature and low humidity for modelling purposes.

Chapter 6

Exchanges between snow and vapour on the East Antarctic Plateau

Да воссияет солнце ночью
и падет снег в августе*

Ностальгия
Андрей Тарковский

Post-deposition processes affect the isotopic signal recorded by the snow. In order to address the impact of these processes, during my Ph-D were organised two campaigns at the French and Italian station Concordia near the top of the dome C to study the isotopic composition of the continuum vapour, precipitation, surface snow and buried snow in a French, Italian and Russian collaboration involving the LSCE, the LGGE (Grenoble), University of Venice, and the AARI (Saint-Petersbourg).

Dome C is located at 75° 06' S, 123° 21' E on the East Antarctic Plateau; it tops at 3233 m above sea level and the mean annual temperature and accumulations are -54.3°C and 27 $kg.m^{-2}.yr^{-1}$, respectively [Petit et al., 1982; Genthon et al., 2015; Röthlisberger et al., 2000]. After the EPICA ice core covering 800 000 years of climatic archives was drilled [EPICA, 2004], a permanent station jointly operated by French and Italian polar institutes was installed to study remote polar climate. This cooperation enables tens of programs to deploy perennial installations monitoring the atmospheric boundary layer conditions [Genthon et al., 2013], the troposphere structure with a LIDAR and a radiometer [Ricaud et al., 2012], the properties of the snow pack... This motivated us to install water vapour isotopic composition monitoring in summers 2014/15 and 2015/16 and I went to Concordia during the first campaign. If measurements of isotopic composition

∗. And the sun will shine all night and the snow will fall in August

of water vapour are routinely realised at the mid-latitudes and even in the high-latitudes of the Arctic, very few studies have been realised in Antarctica. Thanks to the important effort realised to monitor and understand atmospheric processes at Dome C, it is the perfect location to follow processes affecting the isotopic composition. In this section, we will first describe the first campaign including the first results obtained by comparing the water vapour isotopic composition to other boundary layer datasets. Then, we will also describe the second campaign which was led by Frederic Prie.

6.1 Field campaign

The monitoring of the water vapour at Dome C was part of the project NIVO (IPEV project 1110) which focuses on the snow metamorphism on the field and co-supported by the project GLACIO. Including isotopes in snow surface studies is a logical step as on one hand, they can be used as a tracer of the history of the snow and on the other hand, metamorphism is one of the key to understand post deposition impact on snow isotopic composition. Following a preliminary campaign in summer 2013/14 during which Ghislain Picard sampled snow to measure its isotopic composition in parallel with physical properties of surface snow, I went to Concordia in summer 2014/15 to monitor water vapour isotopic composition, sample snow surface and dig snow pits for further isotopic composition measurements.

6.1.1 Deployment of the instruments

We deployed at Dome C two infrared spectrometers and a cryogenic trapping device. Infrared spectrometry is a brand new method that has a lot of potentials for studying remote regions like Dome C but has not been proven reliable before the campaign. Hence a cryogenic trapping device has also been used to sample the vapour in parallel and obtain a replicate measurements with a reliable method. The instruments were deployed in the Snow Shelter, located 900 m east from the station, and therefore upwind of the station in order to avoid as much as possible contamination by the fumes emitted by the station. This shelter has been buried in the snow, removing all impacts of the shelter structure on the wind field. This is particularly important to study boundary layer processes: indeed boundary layer wind-driven turbulence would have been affected by the roughness from a large structure, for instance the atmospheric shelter on the right in Fig. 6.1. At the immediate proximity of this shelter are installed several thermometers, a hygrometer and an anemometer. About 300 m north from the shelter is the American tower where temperature, humidity and wind speed over 45 m are monitored [Genthon et al., 2013]. About

300 m south is the Atmospheric Shelter where chemical composition of the atmosphere is measured.

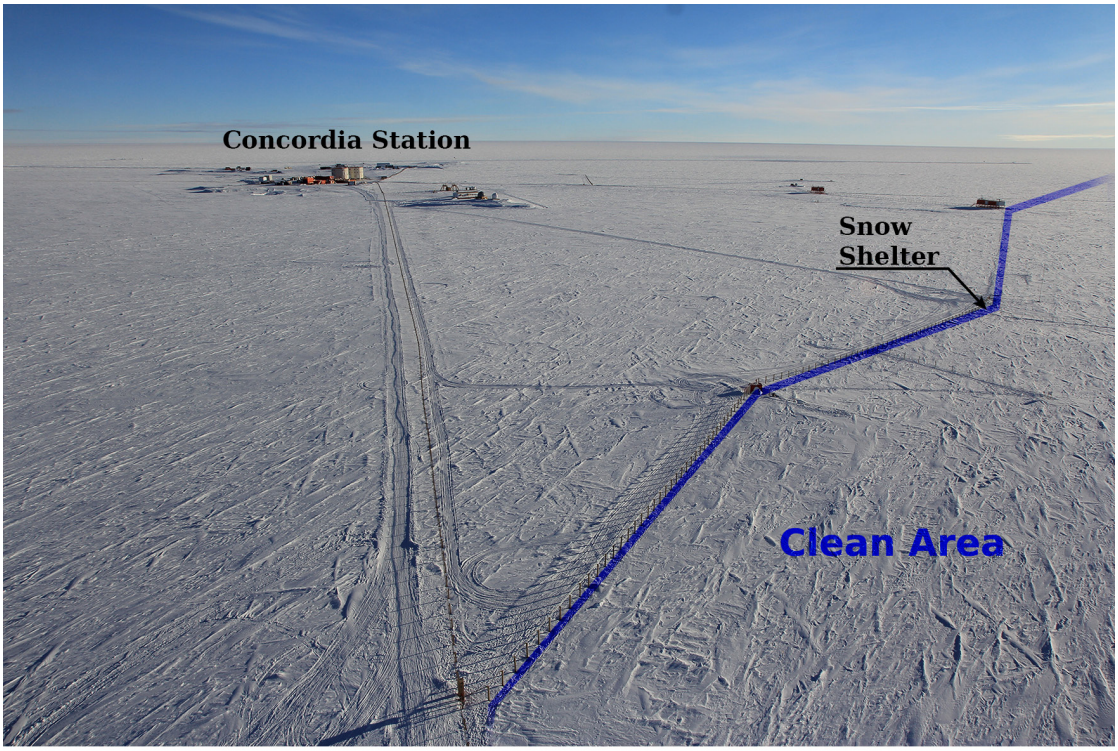

Figure 6.1: Picture of Concordia station and surrounding from the American tower. The instruments were deployed at the Snow Shelter at the edge of the Clean Area. Dominant winds blow from the clean area (Courtesy Bruno Jourdain).

Figure 6.2 shows the schematic of set-up deployed during the campaign of 2014/15. The two infrared spectrometers were installed in the Snow Shelter to provide them with a relative temperature stability and were sniffing outside air through a common copper inlet. A second inlet was installed for the cryogenic trapping system. Both inlets were heated with a self-regulated heating bands of roughly 29 $W.m^{-1}$ (Raychem 10BTV2-CT) and insulated by 30 mm thick insulation foam (see Fig. 6.3). During the whole campaign, no sign of condensation in the inlet was observed and the temperature was estimated around 10°C insuring that no water vapour would condensate in the inlet before being analysed. The inlets were hung at 2 m above the ground level and facing toward the clean area. A clean zone of 12 m^2 was protected around the inlets (the green poles in Fig. 6.3) in order to realise daily snow surface samples right under the inlet.

The cryogenic trapping was realised with 50 cL glass trap filled with glass balls in order to increase the surfaces where condensation could occur (see section C.4 for a pre-

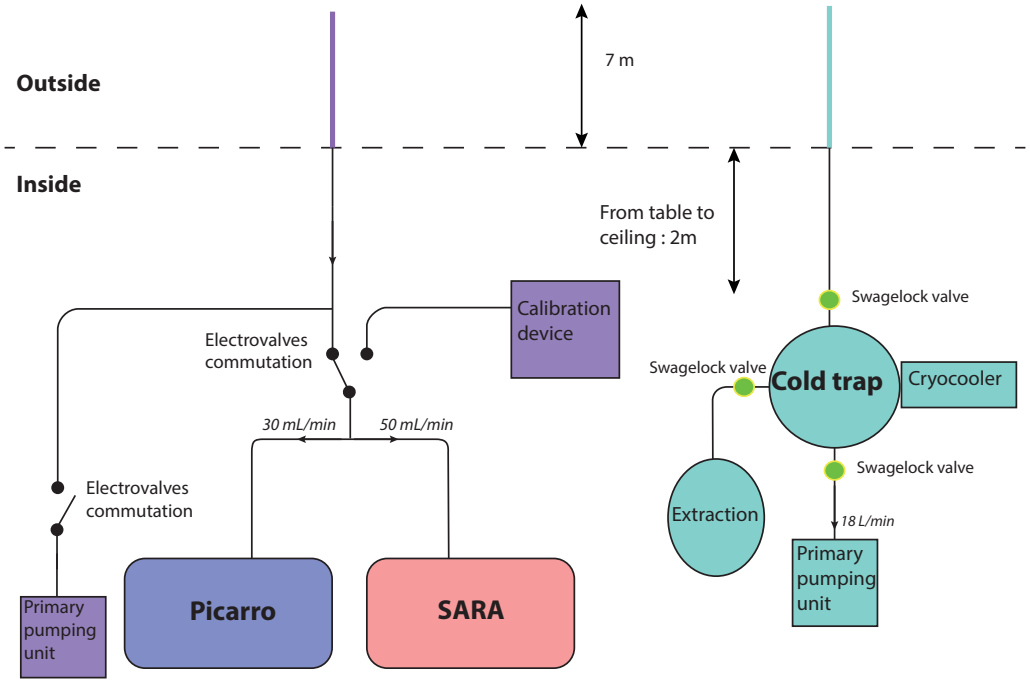

Figure 6.2: Schematic of the set up deployed at Dome C in 2014/15 including 2 infrared spectrometers: a Picarro L2130i and a SARA H_2Oi, with a cryogenic trapping system.

sentation of the different types of traps used at LSCE). The traps were immersed in 99% pure ethanol maintained at $-100°C$ by an immersion cooler Huber TC100. A flux of air of $18\,L.min^{-1}$ of air was pumped through the glass trap in order to obtain at least $2\,mL$ of water per period of 12 hours. The cryogenic system is shown in Fig. 6.4. Once the moisture of the air is trapped, it is necessary to extract the water from the glass balls. In order to do so, the traps are put under vacuum and heated up to 200°C. This fills the volume of pure water vapour. Once all the ice is vaporised, a valve connecting the trap to a phial immersed into the ethanol bath at $-100°C$ is opened. This phial being also under vacuum, the vapour is transferred from the hot trap to the cold phial to counter the pressure gradient which is maintained by the temperature difference. This method has been proven reliable to transfer the vapour [Steen-Larsen et al., 2013]. The liquid samples were stored in $8\,mL$ parafilmed plastic phials, shipped back to France for analysis on a mass spectrometer Thermofischer MAT253 (see section 3.1.1) and an infrared spectrometer Picarro L2140i (see section 3.2.4.3).

During this campaign, were also deployed a Picarro L2130i which is a CRDS instrument (see section 3.2.4.3) and a SARA H_2Oi, the HiFI developed by Janek Landsberg which is a OFCEAS instrument (see section 3.2.4.2). The two infrared spectrometers were calibrated by a common home-made humidity generator as described in section

4.1.1. During calibration, electrovalves were rerooting the inlet to a pumping unit in order to maintain a flux in the inlet, deleting stagnant moisture in the inlet and reducing memory effects after the calibrations. The calibration scheme is described in details in section 6.2.

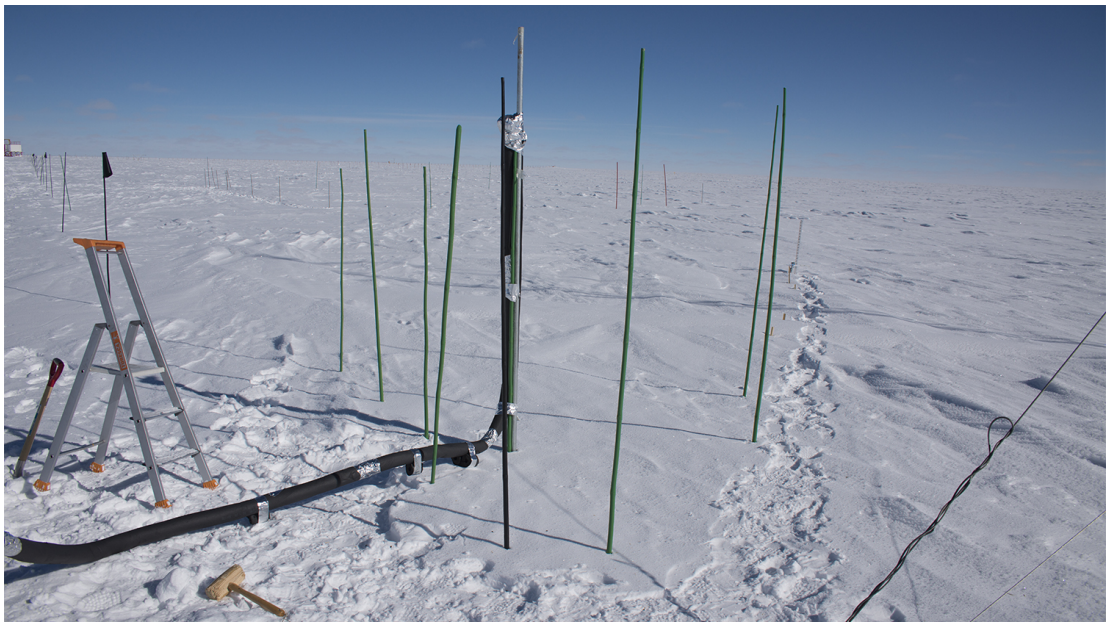

Figure 6.3: Picture of the two inlets in the insulation foam facing the Clean Area. A $12m^2$ area was cleared around the inlet to be able to sample the snow right under the inlet.

The structure of the shelter is made out a $22\,ft$ container inside which a wood structure was holding the tables and the instruments. Because of the light structure, important vibrations could build up inside the shelter and the vibration hampered the capacity of measuring of the HiFI. The data suffer from important noise and this leads to the decision of discarding the part of the dataset to focus on the data obtained from the Picarro.

6.1.2 Validation of the measurements

Because it was the first time infrared spectrometers were deployed at humidity as low as $100\,ppmv$, we had to validate the relevance of the measurement. The cryogenic trapping is the traditional method to measure water vapour isotopic composition and has been used in the next section to validate the accuracy of the isotopic composition monitoring. Before trying to analyse the content of the moisture, it is important to validate the humidity measurement itself.

Figure 6.4: Picture of the cryogenic trapping set up in the Snow Shelter at Dome C: while a trap is connected to the outside air, the previous one is heated to detrap the water from the glass balls and transfer it into a small phial

Measuring humidity at low temperature is very challenging and can lead to numerous artefacts. Indeed, because of the supersaturation, if the hygrometers are not heated, condensation occurs on every surface leading to depletion of the moisture content. On the other hand, by heating the instruments, because of large quantity of buoyant micro-droplets and micro-crystals, the aspiration can easily sample solid or liquid water content increasing the moisture content. In order to validate the measurement realised by the Picarro, they have been compared to the other humidity measurements realised by Christophe Genthon with a Vaisala HMP 155 hygrometer sensor measuring relative humidity compared to liquid water (see Fig. 6.5). The results of these hygrometers are calibrated and guaranteed down to $-60°C$. These data were converted in partial pressure using the Goff and Gratch formula [Goff and Gratch, 1945] (see section 2.1.1). After a calibration of the humidity measurement by the humidity generator as described in next section, we converted the humidity provided by the Picarro in *ppmv* to partial pressure using the formula:

$$P_{H_2O} = P_{atm} \frac{Hum_{ppmv} * 10^{-6}}{Hum_{ppmv} * 10^{-6} - 1} \tag{6.1}$$

The comparison between the partial pressure out of the Picarro measurements and the HMP measurements are displayed in Fig. 6.5. Apart from a few outliers, very good cor-

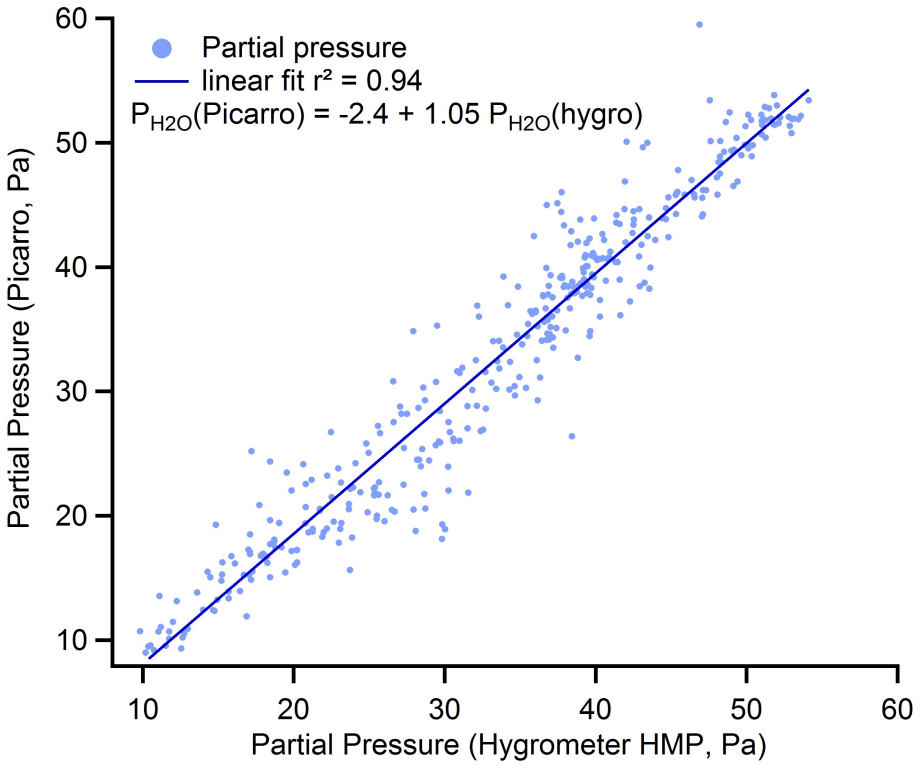

Figure 6.5: Partial pressure calculated from the measurements of the Picarro compared to the one calculated from the HMP155 of Vaisala at Dome C between the 1st of January 2015 to the 10th of January 2015.

relation is found between the two datasets with a linear fit with a correlation coefficient $r^2 = 0.94$ and a slope of 1.05. This indicates very satisfactory performances of the Picarro humidity measurements on the field down to partial pressure of $10\,Pa$. Note that the Picarro data were calibrated, see section C.3 for the comparison with the uncalibrated results.

More detailed comparisons of the diurnal datasets highlight that the Picarro over estimates supersaturation at night, in particular when relative humidity is over 120% as illustrated in Fig. 6.6. During the day, we observe that the humidity measured by the Picarro matches the relative humidity better when using the supersaturation definition against liquid water. This could indicate the presence of a layer of liquid water which the vapour equilibrates with. After, the temperature is cooling ("night" period) and the relative humidity matches better when using the ice definition of the saturated vapour pressure. Finally, for important supersaturation, the buoyant micro-crystals of ice composing the mist are sampled together with the vapour by the inlet because the inlet is heated and no filter is applied. This results in artificially high values of relative humidity up to 200%.

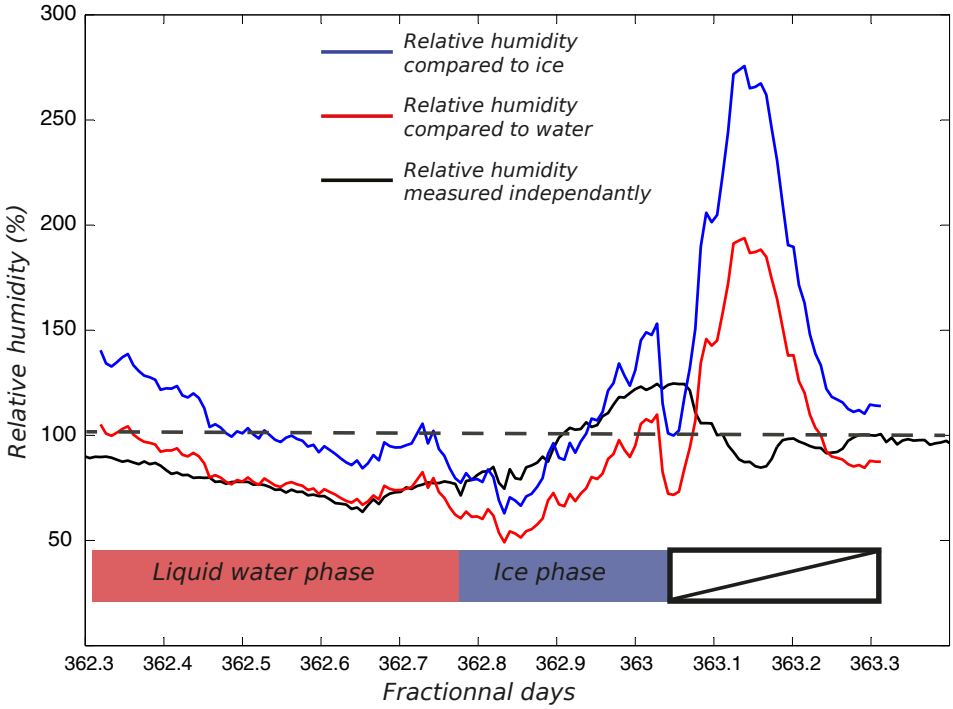

Figure 6.6: Relative humidity obtained from the Picarro humidity measurement by comparing with the saturated vapour pressure over ice (blue) and over liquid water (red) compared to independent calibrated relative humidity (black).

This artefact provides a clear indicator of misty, supersaturated conditions associated with frost deposition.

6.2 Article 2: Continuous measurements of isotopic composition of water vapour on the East Antarctic Plateau

In this section, we focus on the monitoring of the isotopic composition of the vapour. After a short introduction, we present the technical aspects of the monitoring of water vapour isotopic composition in a site like dome C: the installation of the spectrometers including the Allan Variance estimation and the calibration procedure but also the development of new standards at isotopic composition lower than the SLAP value necessary to bracket the vapour isotopic composition and calibrate the infrared spectrometers and finally references to validate the choice of the comparison with cryogenic trapping. This study includes additionally cryogenic trappings realised in 2006/07 by Olivier Catanni which have not been published before. Apart from these results, only two other attempts of measuring water vapour isotopic composition have been realised inland Antarctica: Janek Landsberg at Troll Station using the HiFI but due to calibrations issues, the results

could not be used; and Francois Ritter at Kohnen Station using a Los Gatos analyser (multipass cell, see section 3.2.3): Kohnen station is at a similar latitude than Dome C, but elevation is lower (2982 m a.s.l.) leading the important katabatic winds [Ritter et al., 2016], temperature, humidity and accumulation are also higher. The results will be compared in section 6.4.

Then, we analyse the results from the datasets. First, we compare the isotopic composition measured in situ by the Picarro and the isotopic composition of the cryogenic trapping samples measured in the laboratory by mass spectrometry and infrared spectroscopy. After validating the results, we focus on the impact of the turbulence in the boundary layer on the relationship between isotopic composition and temperature. Indeed, during this first campaign, several days occurred during which the isotopic composition signal was completed erased, leading to decorrelation between temperature and water vapour isotopic composition. We attribute this intermittent behaviour to weakly turbulent (or even stratified) conditions in the atmospheric boundary layers as described in section 6.3.1. Finally, we study the slope between δD and $\delta^{18}O$ in order to understand the origins of the vapour isotopic composition. Indeed, if the values of water vapour isotopic composition match values calculated from equilibrium fractionation from the snow with the literature coefficients, the slope obtained between δD and $\delta^{18}O$ from the calculation using equilibrium fractionation from the literature [Majoube, 1971a; Merlivat and Nief, 1967; Ellehøj et al., 2013] (from 5.7 to 7‰/‰) is very different from the slope obtained in the data (from 4.5 to 5.3‰/‰).

Atmos. Chem. Phys., 16, 8521–8538, 2016
www.atmos-chem-phys.net/16/8521/2016/
doi:10.5194/acp-16-8521-2016

Atmospheric Chemistry and Physics Open Access EGU

Continuous measurements of isotopic composition of water vapour on the East Antarctic Plateau

Mathieu Casado[1,2], Amaelle Landais[1], Valérie Masson-Delmotte[1], Christophe Genthon[4,5], Erik Kerstel[2,3], Samir Kassi[2], Laurent Arnaud[4,5], Ghislain Picard[4,5], Frederic Prie[1], Olivier Cattani[1], Hans-Christian Steen-Larsen[6], Etienne Vignon[4,5], and Peter Cermak[7]

[1]Laboratoire des Sciences du Climat et de l'Environnement – IPSL, UMR 8212, CEA-CNRS-UVSQ, Gif-sur-Yvette, France
[2]CNRS, LIPHY, 38000 Grenoble, France
[3]Université Grenoble Alpes, LIPHY, 38000 Grenoble, France
[4]Université Grenoble Alpes, LGGE, 38041 Grenoble, France
[5]CNRS, LGGE, 38041 Grenoble, France
[6]Centre for Ice and Climate, University of Copenhagen, Copenhagen, Denmark
[7]Department of Experimental Physics, Faculty of Mathematics, Physics and Informatics, Comenius University, Mlynska dolina F2, 842 48 Bratislava, Slovakia

Correspondence to: Mathieu Casado (mathieu.casado@gmail.com)

Received: 5 January 2016 – Published in Atmos. Chem. Phys. Discuss.: 21 March 2016
Revised: 24 May 2016 – Accepted: 21 June 2016 – Published: 13 July 2016

Abstract. Water stable isotopes in central Antarctic ice cores are critical to quantify past temperature changes. Accurate temperature reconstructions require one to understand the processes controlling surface snow isotopic composition. Isotopic fractionation processes occurring in the atmosphere and controlling snowfall isotopic composition are well understood theoretically and implemented in atmospheric models. However, post-deposition processes are poorly documented and understood. To quantitatively interpret the isotopic composition of water archived in ice cores, it is thus essential to study the continuum between surface water vapour, precipitation, surface snow and buried snow.

Here, we target the isotopic composition of water vapour at Concordia Station, where the oldest EPICA Dome C ice cores have been retrieved. While snowfall and surface snow sampling is routinely performed, accurate measurements of surface water vapour are challenging in such cold and dry conditions. New developments in infrared spectroscopy enable now the measurement of isotopic composition in water vapour traces. Two infrared spectrometers have been deployed at Concordia, allowing continuous, in situ measurements for 1 month in December 2014–January 2015. Comparison of the results from infrared spectroscopy with laboratory measurements of discrete samples trapped using cryogenic sampling validates the relevance of the method to measure isotopic composition in dry conditions. We observe very large diurnal cycles in isotopic composition well correlated with temperature diurnal cycles. Identification of different behaviours of isotopic composition in the water vapour associated with turbulent or stratified regime indicates a strong impact of meteorological processes in local vapour/snow interaction. Even if the vapour isotopic composition seems to be, at least part of the time, at equilibrium with the local snow, the slope of δD against δ^{18}O prevents us from identifying a unique origin leading to this isotopic composition.

1 Introduction

Ice cores from polar ice sheets provide exceptional archives of past variations in climate, aerosols and global atmospheric composition. Amongst the various measurements performed in ice cores, the stable isotopic composition of water (e.g. δ^{18}O or δD) provides key insights in past polar climate and atmospheric water cycle. The atmospheric processes controlling this signal have been explored throughout the past decades using present-day monitoring data. Based on the sampling of precipitation or surface snow, relationships be-

tween precipitation isotopic composition and local temperature have been identified since the 1960s and understood theoretically to reflect atmospheric distillation processes (Dansgaard, 1964; Lorius et al., 1969). Nevertheless, there is both observational and modelling evidence that the isotope–temperature relationship is not stable in time and space (Jouzel et al., 1997; Masson-Delmotte et al., 2008). The variation in the isotope–temperature relationship has been explained by the isotopic composition of precipitation being sensitive to changes in condensation vs. surface temperatures, to changes in evaporation condition and transport paths and to changes in precipitation intermittency (Charles et al., 1994; Fawcett et al., 1997; Krinner et al., 1997; LeGrande and Schmidt, 2006; Masson-Delmotte et al., 2011; Werner et al., 2011). While complex, these processes can be tracked using second-order isotopic parameters such as d-excess, which preserve information on evaporation conditions (Jouzel et al., 2013; Landais et al., 2008), and they are accounted for by atmospheric models equipped with water stable isotopes (Risi et al., 2010; Schmidt et al., 2005; Werner et al., 2011).

The variations of d-excess and some variations in $\delta^{18}O$ are due to the different influences of equilibrium fractionation and diffusion driven kinetic fractionation processes at each step of the water mass distillation trajectory. Specific limitations exist for the representation of the isotopic fractionation at very low temperature. Equilibrium fractionation coefficients have been determined either by spectroscopic calculations (Van Hook, 1968) or by laboratory experiments (Ellehøj et al., 2013; Majoube, 1971; Merlivat and Nief, 1967), with significant discrepancies at low temperatures. Molecular diffusivities have mainly been measured at 20 °C (Cappa et al., 2003; Merlivat, 1978), but recent experiments have shown that temperature can have a strong impact on these coefficients (Luz et al., 2009).

Another source of uncertainty for the climatic interpretation of ice core records arises from poorly understood post-deposition processes. Indeed, the isotopic signal of initial local snowfall can be altered through wind transport and erosion, which are strongly dependent on local and regional topography, and can produce artificial variations in ice core water stable isotopes caused by gradual snow dune movement (Ekaykin et al., 2002, 2004; Frezzotti et al., 2002). Moreover, it is well known that the initial isotopic signal associated with individual snowfall events is smoothed in firn, a process described as "diffusion" (Johnsen et al., 2000; Neumann and Waddington, 2004). This diffusion occurs through isotopic exchanges between surface water vapour and snow crystals during snow metamorphism (Waddington et al., 2002). "Diffusion lengths" have been identified based on spectral properties of ice core records and shown to depend on several processes: wind transport and erosion will alter the surface composition with a very strong influence of orography, and diffusion through the pores of the snow firn smooths the signal as does metamorphism of the crystals (Schneebeli and Sokratov, 2004). Finally, there are hints based on high-resolution isotopic measurements performed near snow surface of potential alteration of the initial precipitation isotopic composition (Hoshina et al., 2014; Sokratov and Golubev, 2009; Steen-Larsen et al., 2014a). This motivates investigations of the isotopic composition not only of precipitation and surface snow but also of surface water vapour.

Atmospheric monitoring in extreme polar climatic conditions remains challenging. Supersaturation generates frost deposition, which can bias temperature and humidity measurements, and low vapour contents are often outside of range of commercial instruments. As specific humidity is under 1000 ppmv on the central Antarctic plateau, measuring the isotopic composition of surface water vapour requires either very long cryogenic trapping (typically 10 h at 20 L min^{-1}) to collect enough material for offline (mass spectrometric or laser-based) isotopic analyses or very sensitive online (laser-based) instruments able to produce accurate in situ isotopic measurements.

Recent developments in infrared spectroscopy now enable direct measurements of isotopic composition of the vapour in the field, without time-consuming vapour trapping. With careful calibration methodologies, these devices provide accuracies comparable with those of mass spectrometers (Bailey et al., 2015; Tremoy et al., 2011) and have already been used for surface studies in the Arctic region (Bonne et al., 2015, 2014; Steen-Larsen et al., 2014a).

The goal of our study is first to demonstrate the capability to reliably measure the isotopic composition of central Antarctic surface water vapour during summer, second to investigate the magnitude of its diurnal variations, in comparison with the corresponding results from central Greenland (Steen-Larsen et al., 2013), and third to highlight the impact of a intermittently turbulent boundary layer on the isotopic composition variations.

We focus on Concordia station, at the Dome C site, where the oldest Antarctic ice core record, spanning the last 800 000 years, has been obtained (EPICA, 2004). During the last 20 years, the French–Italian Concordia station has been progressively equipped with a variety of meteorological monitoring tools, documenting vertical and temporal variations in atmospheric water vapour (Ricaud et al., 2012). During summer, meteorological data depict large diurnal cycles in both surface air temperature and humidity (Genthon et al., 2013), which may result from either boundary layer dynamics and/or air–snow sublimation/condensation exchanges.

During the Antarctic summer of 2006–2007, cold trap samplings of water vapour were performed. Here, we report for the first time the results of this preliminary study together with continuous measurements performed during the austral summer of 2014–2015 using laser instruments with a specific methodology for low-humidity calibration, as well as new cold trap sampling for laboratory measurements.

This manuscript is organized in two main sections to highlight the two different aspects of the study. First, Sect. 2 describes the technical aspect: the site, the material deployed

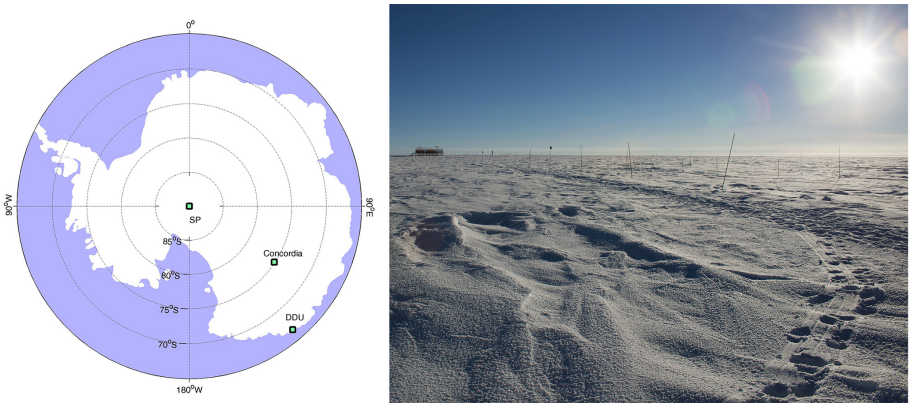

Figure 1. Left: map of Antarctica showing the location of Concordia, Dumont d'Urville station (DDU) and the South Pole (SP). Right: picture of the area from the top of the underground shelter where the instrument was located, looking toward the clean area.

and the applied methods, with a focus on calibration in order to assess the technical reliability of such methods for sites as cold as the Antarctic Plateau. Section 3 reports the scientific aspect of the results, with first a focus on the relevance of infrared spectroscopy compared to cryogenic trapping, second a description of the diurnal to intra-seasonal surface vapour isotopic variations and third an analysis of the origin of the vapour. We conclude and discuss outlooks for this work in Sect. 4.

2 Technical challenges

2.1 Sampling site

Concordia station is located near the top of Dome C at 75°06′06″ S–123°23′43″ E, 3233 m above sea level and 950 km from the coast. While the local mean temperature is −54.3 °C, it was −32.4 °C during the campaign of 2014/2015, reaching a maximum value of −24.5 °C. Ice core data suggest an average annual accumulation of $2.7 \pm 0.7\,\mathrm{g\,cm^{-2}\,yr^{-1}}$ (Genthon et al., 2015; Petit et al., 1982; Röthlisberger et al., 2000).

The first cold trap vapour sampling campaign was performed in summer 2006–2007. The second field campaign took place from 24 December 2014 to 17 January 2015.

The spectrometers for the 2014/2015 campaign were installed in an underground shelter located 800 m upwind from the station, therefore protected from the fumes of the power generator of the station (discussed in Sect. 2.5). Such underground shelter allows us to avoid any impact of the monitoring structure on the wind field and possible sampling artefacts. The area around the shelter is characterized by few sastrugi, none higher than 20 cm (Fig. 1). A clean area of $12\,\mathrm{m^2}$ with no sastrugi was marked around the inlets. We decided to point the inlets toward the dominant wind in order to prevent artefacts from condensation or evaporation from the protection of the inlet or the pole holding it. Indeed, frost formation was observed on the protective foam and pole.

Together with our water vapour isotopic data, we use meteorological observations from the lowest level of the 45 m meteorological profiling system at Dome C (Genthon et al., 2013). The profiling system was located at proximity with the spectrometers. The temperature observations on the 45 m profiling system are made in aspirated shields and thus not affected by radiation biases. Genthon et al. (2011) demonstrated that when the wind speed is below $5\,\mathrm{m\,s^{-1}}$, radiation biases are very significant and can reach more than 10 °C in conventional (non-wind-ventilated) shields. Temperature is measured using HMP155 thermohygrometers, while wind speed and direction are measured using Young 05103 and 05106 aerovanes. Elevation above the snow surface was 3.10 m for the wind and 2.58 m for temperature in 2014–2015. This will be henceforth commonly referred as the 3 m level. Further details on the observing system, instruments, sampling and results are available in previous publications (Genthon et al., 2013, 2010). Surface temperature is measured with a Campbell scientific IR120 infrared probe. The probe is located at 2 m height and uses upwelling infrared radiation and the temperature of the detector to compute the temperature of the surface of the snow. The uncertainty of the surface temperature measurement is around ±1 °C, which is mainly due to unknown and possibly varying emissivity of the snow (Salisbury et al., 1994).

2.2 Water vapour isotope monitoring

Two infrared spectrometers were used to measure continuously the isotopic composition of water vapour pumped 2 m above the snow surface: a cavity ring-down spectrometer (CRDS) from Picarro (L2130-i) and a high-finesse water isotope spectrometer (HiFI) based on the technique of optical feedback cavity-enhanced absorption spectroscopy (OFCEAS) developed in LIPhy (Laboratoire Interdisci-

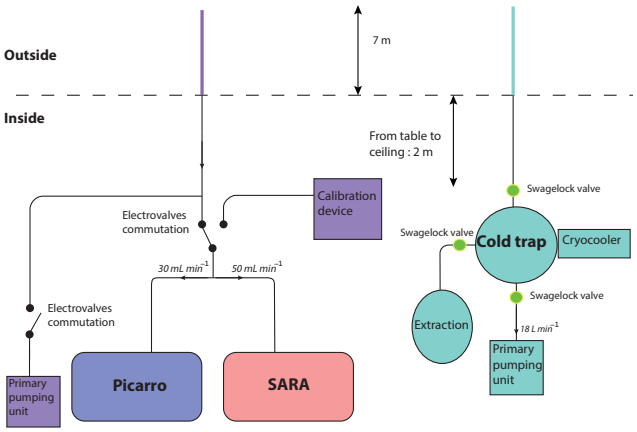

Figure 2. Schematics of the experimental set-up implied in the water vapour isotopic composition monitoring.

plinaire de Physique), Grenoble, France (Landsberg et al., 2014), as described on Fig. 2.

Both instruments are based on a general technique of cavity-enhanced absorption spectroscopy (Romanini et al., 2014). This is essentially a long-path-length optical detection technique that increases the sensitivity of detection of molecules in the optical cavity by folding the optical beam path between two (or three) highly reflective mirrors. The commercial Picarro spectrometer is based on near-infrared continuous-wave cavity ring-down spectroscopy (CW-CRDS) (Crosson, 2008). It has proven to be a fairly robust and reliable system, delivering good-precision isotopic measurements at concentration (water mixing ratio) values between 1000 and 25 000 ppmv.

The HiFI spectrometer also operates in the near-infrared region of the spectrum but uses OFCEAS (Romanini et al., 2014). In the case of the HiFI spectrometer, the optical path length was increased by about 1 order of magnitude to 45 km. This optimizes the spectrometer for oxygen-18 isotopic measurements with a precision better than 0.05 ‰ at a water mixing ratio around 500 ppmv (Landsberg et al., 2014). The HiFI spectrometer was shown to be able to reach this level of performance also in Antarctica during a 3-week campaign at the Norwegian station of Troll (Landsberg, 2014). Unfortunately, during the current campaign at Dome C the spectrometer had to operate in a noisy environment. The system was not isolated from vibrations of several vacuum pumps in the shelter and an accidental resonance did perturb the phase control. This resulted in a baseline noise level more than one order higher than normal, which created a corresponding increase of the error on the isotope ratio measurements. At this level of noise, the Picarro measurements turned out to be more precise than the HiFI measurements. It is for this reason that the latter were only used as an independent tool to check on the absolute values from Picarro measurements. All time series shown hereafter were obtained with the Picarro spectrometer.

The two instruments were connected through a common heated inlet consisting of a 1/4 in copper tube. The internal pumps of each instrument pumped the outside vapour through the common inlet and into the respective cavities. The fluxes generated by the instruments were small enough not to interact with one another, as attested by stable pressure in the cavities of both instruments. The length of this common inlet (approximately 10 m long) caused a response delay of approximately 2 min for the humidity signal. Memory effects caused by interactions between the water vapour and the inside of the tubes introduce different delays for different isotopes. In the case of high-resolution data, artificial d-excess can be produced as the memory effect of HDO is substantial larger than $H_2^{18}O$ (Steen-Larsen et al., 2014b). However, our measurements were averaged over 1 h thereby removing this effect. No sign of condensation in the inlet was observed during the whole campaign.

2.3 Allan variance analyses

The measurements of isotopic composition with an acquisition time of approximately 1 s have a standard deviation of 10 ‰ for δD and of 2 ‰ for δ^{18}O at approximately 500 ppmv (Fig. 3). Infrared spectrometers typically produce data perturbed by different kinds of noise: one is noise due to frequency instabilities of the laser, temperature and mechanical instabilities of the cavity, temperature and pressure of the sampled gas, electronic noise and residual optical interference fringes on the spectrum baseline. The noise, usually predominantly white noise, can be significantly reduced through time averaging; for instance, with an acquisition time of 2 min, we decrease the standard deviation to 1.3 ‰ for δD and 0.2 ‰ for δ^{18}O.

With increasing integration time, one expects the precision of the measurements to initially improve, due to the reduction of white noise, up to the point where instrumental drift becomes visible. The so-called Allan–Werle plot shows the overall expected precision as a function of integration time (Fig. 3).

Long-term laboratory measurement of a standard was carried out at a humidity of 506 ± 3 ppmv in order to reproduce the range of the expected humidity for Concordia station. Stable humidity production for 13 h was realized using the calibration device described in the next section and in the Supplement 1. The standard deviation of δD follows the optimum line almost up to 4 h integration time. The standard deviation of δ^{18}O does not follow the optimum profile after 100 s but still drops continuously over almost 2 h. These measurements confirm the reliability of the Picarro L2130i even at low humidity and justify the use of such an instrument in this campaign. The integration time providing the ultimate precision could not be achieved because of the lack of a vapour generator stable for more than 13 h. At other hu-

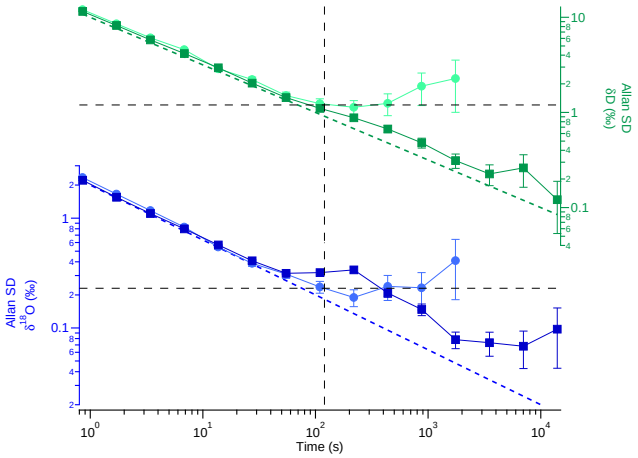

Figure 3. Allan variance plots for laboratory long-term standard measurement (dark squares) and for field long-term standard measurement (light circles) for δD (Top, green) and for δ^{18}O (bottom, blue). Dash lines correspond to the quantum limit on $N^{-1/2}$ for each composition.

midity levels, we observe similar profiles with an increasing initial precision as the moisture content increases (not shown).

In the field, we performed calibrations lasting up to 90 min, as a trade-off between instrument characterization and measurement time optimization. This, however, is not long enough to accurately estimate the rise of uncertainty due to instrumental drift but does allow us to assess the ultimate precision for the instruments under realistic field conditions. The Allan variance was thus calculated from field Picarro calibration data, at 450 ppmv. From this analysis, we conclude that 2 min appear to provide an optimal integration time, associated with an ultimate precision of the spectrometer of 0.2 ‰ for δ^{18}O and 1.1 ‰ for δD (black dashed lines on Fig. 3). This test could not be performed at other humidities.

2.4 Calibrations

Calibration of the spectrometer is crucial in order to be able to express the measurement results with confidence on the international VSMOW2–SLAP2 (Standard Mean Ocean Water 2 and Standard Low Antarctic Precipitation 2) isotope scale (IAEA, 2009). Calibrations have been reported to vary between instruments and calibration systems, as well as over time. Tremoy et al. (2011) highlighted the importance of calibration for Picarro analysers under 10 000 ppmv with biases up to 10 ‰ for δD and of 1 ‰ for δ^{18}O at volume mixing ratios (VMRs) down to 2000 ppmv. Protocols have been developed and adapted for calibration under Greenland ice sheet summer (Steen-Larsen et al., 2013) and south Greenland year-round conditions (Bonne et al., 2014) with good performance attested from parallel measurements of PICARRO and LGR analysers for humidity above 2000 ppmv. At VMRs below 2000 ppmv, much larger errors can be expected without calibrating the instruments.

For this field season, we have followed the classical calibration protocols with (1) a study of the drift of the instrument, (2) a linearity calibration using two working standards whose isotopic values were established in the laboratory vs. SMOW and SLAP and (3) a study of the influence of humidity on the isotopic value of the water vapour. At very low-humidity levels (below 2000 ppmv), standard calibration devices (such as the SDM from Picarro) are not able to generate stable constant humidity. Here, we expected humidity levels below 1000 ppmv and therefore we could not use standard water vapour generator and had to develop our own device inspired from the device developed by Landsberg (2014) and described in detail in the Supplement Sect. 1.

The calibration protocol for type (1) calibration relies on the measurement of one standard at one humidity level (the average of the expected measurement) twice a day for 30 min in order to evaluate the mean drift of the infrared spectrometer. Standard values of the drift on a daily basis should not exceed 0.3 ‰ in δ^{18}O and 2 ‰ in δD. The calibration protocol for type (2) calibration relies on the measurement of two standards whose isotopic compositions bracket the one measured in order to evaluate the response of the infrared spectrometer compared to the SMOW–SLAP scale (thereafter isotope–isotope response). Typical isotope–isotope slope is between 0.95 and 1.05 ‰‰$^{-1}$ for δ^{18}O and for δD. The calibration protocol for type (3) calibration relies on the measurements of one standard at different levels of humidity in order to evaluate the response of the infrared spectrometer to humidity (thereafter isotope–humidity response). Type (2) and type (3) calibration can only be realized once a week provided type (1) calibration has validated the drift of the instrument was within acceptable values (below excess 0.3 ‰ in δ^{18}O and 2 ‰ in δD). For temperate range where humidity is important (above 5000 ppmv), it is possible to consider a linear relationship for the isotope–humidity response; for dryer situations (below 5000 ppmv), the isotope–humidity response requires at least a quadratic relationship.

The three types of calibrations were performed in the field and in the laboratory prior and after field work. It was particularly important to add laboratory calibrations (especially for drift of the instrument) in addition to field calibrations because of the short season and lack of dry air at the beginning of the season, in particular to strengthen the results from type (2) and (3) calibrations as we will present in the following.

In order to evaluate the performances of our spectrometer, all type of calibrations were performed in the laboratory at different humidities (from 100 to 1000 ppmv) and repeated on five occasions in a time span of 4 weeks with two standards: UL1 (δ^{18}O = −54.30 ‰ and δD = −431.1 ‰) and NEEM (δ^{18}O = −33.56 ‰ and δD = −257.6 ‰). We estimate the mean drift for a period of 1 month (type 1) by com-

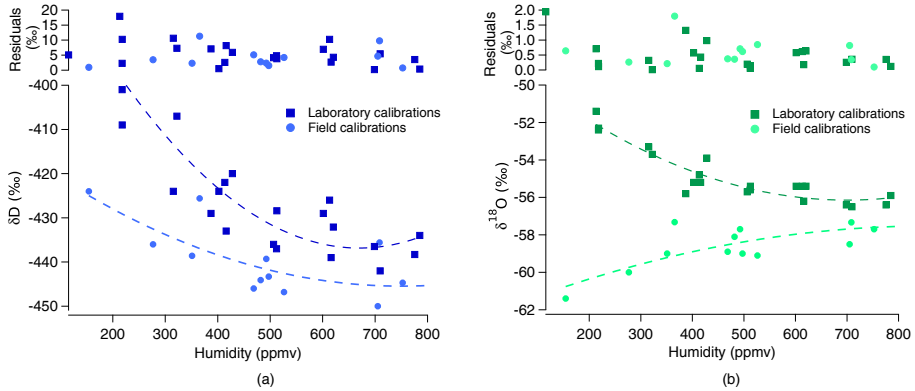

Figure 4. Measured isotopic composition for **(a)** δD and **(b)** δ^{18}O using the PICARRO spectrometer for a fixed humidity: light circles are field calibration points, dark squares are laboratory calibration points, the dashed lines are the fit with a quadratic function and at the top are the residuals compared to the fit for the entire series.

Table 1. Average residuals compared to the quadratic fit toward humidity of laboratory (five sets) and field calibrations for different humidity levels for the Picarro; cf. Fig. 4a and b.

Laboratory calibrations	Humidity (ppmv)	200	400	600	800
	δD residuals (‰)	10.1	4.9	6.0	3.1
	δ^{18}O residuals (‰)	0.3	0.7	0.5	0.3
Field calibrations	Humidity (ppmv)	150	350	480	710
	δD residuals (‰)	1.0	6.8	2.9	5.1
	δ^{18}O residuals (‰)	0.6	1.0	0.5	0.4

paring the offset of the isotopic composition over the five occurrences. For the isotope–isotope slope, we obtain standard values around 0.95 ‰ ‰$^{-1}$. We evaluate the laboratory isotope–humidity response by comparing the measured value of the isotopic composition to the value of humidity. Each independent set of calibrations (each week) can be fitted by a quadratic function with a small dispersion of the data points (inferior to 2 ‰ for δD and 0.2 ‰ for δ^{18}O). Different calibration sets performed over different days show dispersion due to the instrument drift. We observe a much larger dispersion for δD than for δ^{18}O, in particular at low concentration (200 ppmv) due to the combined action of the drift and of the noise of the instrument (see Table 1). Note that the low residuals for the field calibration at 150 ppmv are an artefact due to few measurements at this humidity. The average drift observed combining the offset isotopic composition over 1 month is slightly under 1 ‰ in δ^{18}O and reaches 8 ‰ in δD (type 1 calibration).

Field calibration could only be performed after 7 January when the dry air bottle was delivered to Concordia. Then, two calibrations per day were realized as follows: 30 min calibration, 30 min measurements of outside air and 30 min calibration. As the data are interpolated on an hourly resolution, this procedure prevents gaps in the data. Altogether, 20 calibrations were achieved from 7 to 17 January with two working standards. These logistical issues require adjustment to the calibration procedure described above. Because type (1) calibration could not be performed during the field campaign, we use the drift evaluated from the laboratory calibrations to bracket the maximum drift expected over a period of 1 month. This results in an important increase of the uncertainty of the measurement of δ^{18}O from 0.2 ‰ (optimal value from the Allan variance) to 1 ‰ (estimated from the drift of the instrument during the laboratory type (1) calibration) and in δD from 1.3 to 6 ‰.

Type (2) calibration was realized on the field using two working standards calibrated against VSMOW–SLAP: NEEM and UL1 at the end of the campaign. Because the vapour isotopic composition at Dome C was much lower than expected (well below the SLAP isotopic composition), in order to properly estimate the isotope–isotope response of the instrument it was necessary to evaluate the relevance of the correction obtained from the field calibration. This is described in Sect. 2.6 and required to produce new standards with isotopic composition below the SLAP value. As described in Sect. 2.6, we validated that even by calibrating the isotope–isotope response of the instrument above the SLAP composition, the linearity of the instrument was good enough to extend the calibration down at least to −80 ‰ in δ^{18}O.

As it was not possible to perform relevant ramps of humidity within 1 day, type (3) calibration was realized by merging all calibration realized on the field into one series (Fig. 4, light colour points). This merged field calibration set provides with an estimate of the linear correction to be applied on the measured humidity (cf. Supplement 2). The merged field calibration series also documents the nonlinearity of the instrument as a function of the background humidity level and is used to correct the values of δD and δ^{18}O measurements in water vapour. The laboratory and field calibrations do not match. Calibrations realized in the lab and in the field have been reported to differ (Aemisegger et al., 2012), which rules out the use of pre-campaign laboratory calibrations,

even though laboratory calibration is still useful for providing insight into the minimum error to be expected during the field campaign. There is no indication from Aemisegger et al. (2012) that opposite trends were obtained during the different calibrations. We checked the possibility that this behaviour could be linked with the remaining water content of the air carrier as it occurred for Bonne et al. (2014) e.g. at low humidities. For both field and laboratory calibrations, we used Air Liquid Alphagaz 1 air with a remaining water content below 3 ppmv. One possible explanation for the opposite trend on the field compared to laboratory calibrations could be an extraordinary isotopic composition of the air carrier from the dry air cylinder during the field campaign. However, we do not believe the air carrier is responsible for this opposite trend. First, we realized a calculation of the isotopic composition of the 3 ppmv of water remaining in the cylinder necessary to explain the difference between the field and the laboratory calibrations trends. The calculation is the average of the isotopic composition weighted by the water content between the remaining 3 ppmv (unknown isotopic composition to be determined) and the water vapour generated by the calibration device (known humidity and isotopic composition). It is not possible to find one unique value matching the system and the range of calculated values spans between $\delta^{18}O = -450\,‰$ and $\delta^{18}O = -650\,‰$. This range is beyond anything observed from regular use of air carrier cylinder. Second, the same cylinder was used during another campaign and a similar feature was not observed (not shown). Finally, we observe a very good agreement between the results from the Picarro and the cryogenic trapping data (see Sects. 2.6 and 3.1) with a difference of 1.16 ‰ for $\delta^{18}O$ using the field calibrations. If we use the laboratory calibrations, this would create a much larger difference (above 5 ‰ difference in $\delta^{18}O$) which validates the calibration procedure and the use of the field calibration. Here, we attribute this odd behaviour of the isotope–humidity response to the important amount of vibration in the shelter and therefore decided to use this isotope–humidity response to calibrate the dataset. Indeed, this response should be representative of the global behaviour of the Picarro measuring during this campaign.

To summarize, here we cannot estimate from these measurements the drift over the period of field measurement. However, we incorporate an uncertainty for this drift from the laboratory calibrations. These laboratory calibrations were realized on a period longer than the campaign and therefore should bracket the actual drift of our instrument during field deployment and decrease the accuracy of the measurement to 1 ‰ in $\delta^{18}O$ and 8 ‰ in δD.

The precision on the absolute value is calculated from the largest residuals of both the laboratory and field calibration fit. It rises up to 18 ‰ for δD at 200 ppmv and 1.7 ‰ for $\delta^{18}O$ at 400 ppmv, with better precision at higher humidity (Fig. 4). This highlights the need for regular calibrations to obtain the best performances, unfortunately with a very high cost for this study: the lack of regular calibrations hinders by a factor of 5 the precision of the measurements (1.3 ‰ for δD in the best conditions from the Allan variance against 6 ‰ for δD from the mean residuals of the calibration). Additional information about the linearity of Picarro infrared spectrometers against the SMOW–SLAP scales at isotopic composition below the SLAP values can be found in Sect. 2.6 with the description of the measurements of the cryogenic trapping samples.

2.5 Data post-treatment and performances

In addition to the calibration and averaging necessary to improve the accuracy and precision of the dataset, we had to correct our data from the introduction of condensate inside the inlet. Figure 5 illustrates two of such "snow-intake" events, providing typical examples of duration and shape. Indeed, our inlet was facing the dominant wind without any protection to prevent introduction of condensates. Such protection usually requires to be heated to prevent condensation of water vapour under supersaturated conditions; however, heating would lead to sublimation of all the precipitation falling into the inlet, which would then increase the vapour content. Moreover, micro-droplets or crystals are often floating in the air on the Antarctic Plateau and reduce the efficiency of any precipitation filter. We therefore decided to remove the effect of all sorts of precipitation events through a post-treatment of our datasets. This is justified by a small number of cases (fewer than 100), clearly identified as "snow-intake" events.

A manual post-treatment was thus realized following systematic rules. All data with a specific humidity higher than 1000 ppmv were discarded; this value was chosen as the maximum surface air temperature observed during the campaign (−24.6 °C) and implies a theoretical maximum saturated vapour content of 1030 ppmv. After this first post-treatment, the largest humidity measurements of 977 ppmv, slightly lower than the maximum saturated vapour content, suggested that we may have discarded only a few relevant high-humidity data in our post-processing.

All humidity peaks higher than natural variability were also discarded, using as a threshold 5 times the standard deviation in normal conditions (which is between 10 and 20 ppmv). In very few occasions (only twice during the entire campaign), a very high density of snowflakes could create a regular inflow of snow in the inlet, leading to an increase of the vapour content without peak shapes. In those cases, the amplitude and the frequency of the specific humidity variability still allowed us to distinguish precipitation introduction from the "background" vapour signal. These periods associated with important "snow-intakes" created gaps in the dataset (4 h in total). Gaps in our dataset mostly arise from calibration of the instruments and power shortages (30 to 60 min gaps) that could be filled by interpolating.

Two running averages were performed: first at 10 min resolution, without filling the gaps which correspond to approx-

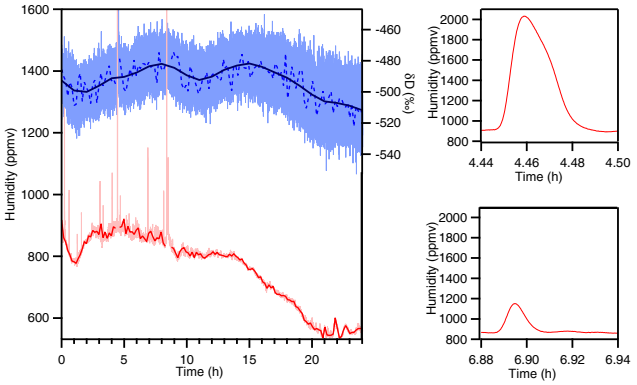

Figure 5. Left: example of raw data measured by the Picarro. Humidity (light red, ppmv) and δD (light blue, ‰), data averaged over 10 min for humidity (red, ppmv) and for δD (dashed line blue, ‰) and over 1 h for δD (dark blue, ‰). Right: zoom on two "precipitation events" identified in the humidity signal of the Picarro (top, snow flake; bottom, diamond dust).

imately 3 % of the dataset (Fig. 5), then an average at a resolution of the hour where the gaps were filled by linear interpolation (only 1 % of the whole datasets had gaps larger than an hour), apart from 13 January when 4 h in a raw were missing due to an intense precipitation event. Finally, 0.7 % of the dataset is missing at the 1 h resolution.

Even though the spectrometer was located at the border of the clean area of the station, we verified that the influence of the station did not contaminate the vapour by analysing wind direction. As mentioned earlier, the shelter is almost 1 km upstream the station against the dominant wind. Few events with wind direction pointing from the station were identified (21 h spread over 5 days during the whole campaign when the wind direction is pointing from the station plus or minus 20°). Most of these events match the period when the wind speed was very low ($< 2\,\mathrm{m\,s^{-1}}$). We used the methane measurements also provided by the Picarro L2130 in parallel with the vapour measurements to assess any potential anthropic contamination of the vapour at the shelter area. An anthropic contamination of the vapour could lead to artificial values of isotopic composition. Indeed, combustion of fossil fuels have been shown to produce d-excess, for instance (Gorski et al., 2015). Small spikes of methane were detected for only two occurrences: 28 December between 09:30 and 10:40 and 3 January between 06:00 and 07:00 (local time). They match events with wind direction pointing at the shelter. These two events were fairly short and no specific impact on either humidity or isotopic composition can be identified for these events.

2.6 Cryogenic trapping of the moisture

Water vapour was trapped with a cryogenic trapping device (Craig and Gordon, 1965) consisting of a glass trap immersed in cryogenic ethanol. Cryogenic trapping has been proven reliable to trap all the moisture contained in the air and therefore to store ice samples with the same isotopic composition as the initial vapour (He and Smith, 1999; Schoch-Fischer et al., 1983; Steen-Larsen et al., 2011; Uemura et al., 2008). Two different cryogenic trapping set-ups have been deployed. The first one, in 2006/2007, was based on traps without glass balls. These traps cannot be used with air flow above $6\,\mathrm{L\,min^{-1}}$ in order to trap all the moisture because the surface available for thermal transfer is rather small. In order to be certain of trapping all the moisture, two traps in series were installed. Because of the lack of glass balls, the absence of water in the trap at the end of the detrapping can be observed. This was a very important validation because detrapping efficiency is essential to obtain correct values of isotopic composition (Uemura et al., 2008). During the second campaign, we used traps filled with glass balls to increase the surface available for thermal transfer and therefore that can be used at higher flows. This cryogenic trapping set-up relies on extensive tests previous to the campaign, indicating that our custom-made glass traps filled with glass balls at $-100\,^{\circ}\mathrm{C}$ successfully condensate all the moisture, even for a flow up to $20\,\mathrm{L\,min^{-1}}$. These tests have been realized with (1) a Picarro (L2140i) to attest that the remaining humidity was below the measurement limit (around 30 ppmv) and (2) a second trap downstream to evaluate the presence of ice after a period of 12 h which would indicate a partial vapour trapping. These tests enable us to validate the system we used, similar to Steen-Larsen et al. (2011), and motivate its deployment for the second campaign at Dome C. Extensive tests have also proven that complete detrapping can be done with traps filled with glass balls despite no direct observation of possible remaining water. The results shown later on (Fig. 10) show that similar values are obtained from both types of set-up (with or without glass balls) and assess the reliability of both the methods.

Here, we present the results of two cryogenic trapping campaigns: one in 2006/2007 and one in 2014/2015. During the 2006/2007 campaign, 20 samples were gathered by cold traps (without glass balls) immersed in ethanol at $-77\,^{\circ}\mathrm{C}$, with a pump with a flow of $6\,\mathrm{L\,min^{-1}}$ and 36 h sampling periods. For the campaign of 2014/2015, 20 samples were gathered by cold traps (filled with glass balls) immersed in ethanol at $-100\,^{\circ}\mathrm{C}$ under a flow of $18\,\mathrm{L\,min^{-1}}$ and 10 to 14 h trapping periods. The samples were extracted from the traps by heating them up to 200 °C on a line under vacuum connected to a glass phial immersed in the cryogenic ethanol for 10 to 12 h. This process allows the total transfer of the water by forced diffusion and produces samples between 2 to 4 mL. On 8 January 2015, the high flux pump was damaged and was replaced by a membrane vacuum pump with only $8\,\mathrm{L\,min^{-1}}$ flow, increasing the trapping duration from 24 to 36 h.

As no particles filter was installed on the inlet (cf. Sect. 2.1), we trapped both the precipitation captured by the inlet and the surface vapour. This might lead to biases

when precipitation occurred, which must be taken into account when comparing the results between the spectrometers and the cold trap.

Samples from the 2014/2015 campaign were then shipped for laboratory analyses using a Picarro L2140i. The samples were injected through a syringe in a vaporizer and an auto-sampler. The classical calibration procedure to be analysed polar samples is using three internal standards calibrated against SMOW and SLAP: NEEM ($\delta^{18}O = -33.56‰$ and $\delta D = -257.6‰$), ROSS ($\delta^{18}O = -18.75‰$ and $\delta D = -144.6‰$) and OC3 ($\delta^{18}O = -54.05‰$ and $\delta D = -424.1‰$). The isotopic composition of the sample to analyse has to be surrounded by the isotopic composition of the standards for the calibration to be efficient. As the isotopic composition of the vapour in Concordia is well below SLAP ($\delta^{18}O = -55.50‰$ and $\delta D = -427.5‰$), i.e. $\delta^{18}O$ is around $-70‰$, no standard was available to bracket the sample isotopic composition. It was therefore important to check the linearity of the instruments for $\delta^{18}O$ values below $-55‰$.

In order to do so, we prepared new home-made standards: we diluted a known home-made standard EPB ($\delta^{18}O = -7.54 \pm 0.05‰$) with highly depleted water, Isotec water-^{16}O from Sigma-Aldrich (99.99 % of ^{16}O atoms, hereafter DW for depleted water). We first had to determine the absolute composition of the DW by realizing several dilutions of the water with isotopic composition in the range between SMOW and SLAP. The dilution was realized with a Sartorius ME215P scale, whose internal precision is certified at 0.02 mg. The water was injected through needles in a glass bottles covered by paraffin films to prevent evaporation. All the weights were measured four times in order to improve the precision of the measurements. From the different measurements, the accuracy is estimated at 0.1 mg after correcting for the weight of the air removed from the bottle by injecting the water. Four new home-made standards were realized in the range SMOW–SLAP and measured 15 times each with a Picarro L2140i (cf. Fig. 6, part 1). Their isotopic composition is scattered along the line from the EPB composition to the DW composition. Because we know the exact dilution of EPB with the DW, we can use the measured $\delta^{18}O$ values to precisely infer the isotopic composition of the DW: $\delta^{18}O_{DW}$ or $R^{18}_{DW} = (\delta^{18}O_{DW}/1000+1) \cdot R_{SMOW}$, where $R^{18}_{SMOW} = 2005.2$ is the absolute isotopic composition of the SMOW in $H_2^{18}O$.

The isotopic composition of the mix is given by

$$\delta^{18}O_{mix} = \delta^{18}O_{EPB} + \frac{R^{18}_{DW} - R^{18}_{EPB}}{R^{18}_{SMOW}} X_{DW} \quad (1)$$

where X_{DW} is the ratio of quantities of DW vs. EPB in the dilution. The slope of the linear regression of $\delta^{18}O_{mix}$ with X_{DW} provides directly an estimate of the isotopic composition of the DW. We find $R^{18}_{DW} = 128 \pm 2$ (equivalent to $\delta^{18}O_{DW} = -936.2 \pm 0.6‰$), which is slightly less depleted than the specifications given by the producer (purity of 99.99 %). Another determination can be done independently by using the Eq. (1) for one single dilution. Using independent dilutions done within the range SMOW–SLAP, we obtain $R^{18}_{DW} = 127$ and 130.

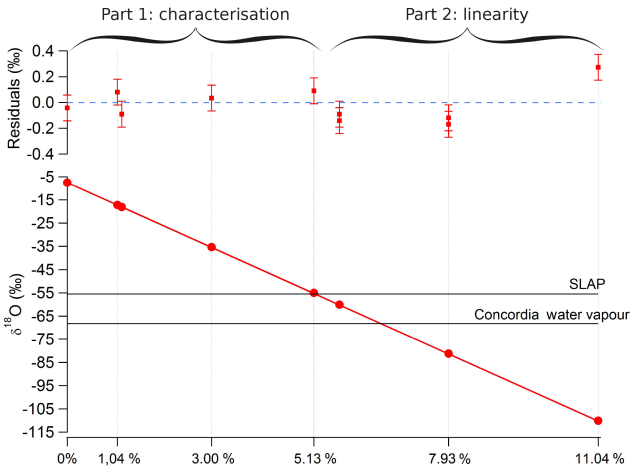

Figure 6. Isotopic composition measured by liquid injection in the Picarro L2140i for different samples prepared by dilution of EPB with "almost pure" water: the red dots are the measurements, the red line is the calculated isotopic composition and the red squares for residuals are the difference between the measurements and the theoretical composition.

In a second step, we produce three other water home-made standards by dilution of EPB with "almost pure" $H_2^{16}O$ to obtain $\delta^{18}O$ values below SLAP. Using the known dilution amount and the isotopic ratio of "almost pure" $H_2^{16}O$ determined above, we compare the measurements for these three home-made standards, i.e. placed on a SMOW–SLAP scale with classical calibration procedure to the values calculated using Eq. (1) (Fig. 6, part 2). Given the precision on the isotopic ratio of the "almost pure" $H_2^{16}O$, on the EPB and the precision of the scale, the precision of the calculation of $\delta^{18}O_{mix}$ is 0.05‰ (uncertainty propagation in Eq. 1).

Residuals between measured and calculated $\delta^{18}O$ are less than 0.2‰ for the home-made standards at -60 and $-80‰$ and less than 0.3 at $-110‰$. We thus conclude that the Picarro L2140i can be used safely to infer linearly $\delta^{18}O$ values down to $-80‰$, which encompasses the $\delta^{18}O$ range of our water vapour samples, and is close to linear for $\delta^{18}O$ values down to $-110‰$ (deviation of 0.3‰ slightly higher than the measurement uncertainty).

3 Results

3.1 Validation of infrared spectrometry data

The data gathered by the cold trap and the infrared spectrometers during the 2014/2015 campaign are displayed in Fig. 7.

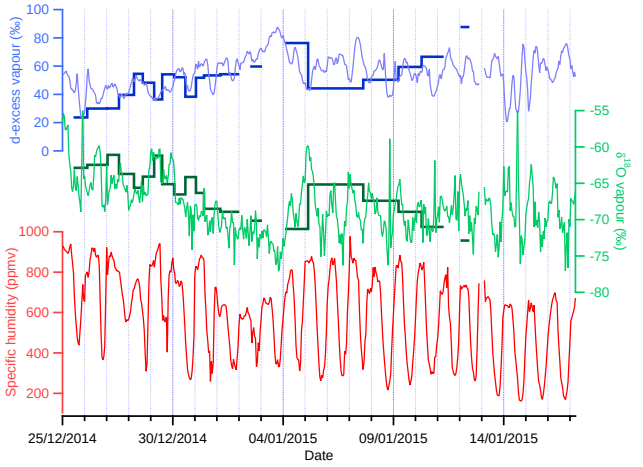

Figure 7. Hourly average δ^{18}O (‰) in green, raw d-excess (‰) in light blue (d-excess smoothed on a 3 h span in thick blue) and hourly average of the specific humidity (ppmv) in red during the campaign 2014/2015. Measurements by the Picarro are displayed as the thin light lines and measurements performed in the laboratory from the cold trap samples are displayed as dark bars.

The measurements performed by the Picarro (light lines) from 25 December to 4 January are marked by a 10 ‰ gradual decline in δ^{18}O and a 40 ‰ gradual increase in d-excess. By contrast, the second part of the measurements (performed after 4 January) does not show any long-term multi-day trend. We also observe a decrease in δ^{18}O and an increase in d-excess in the cold trap data from 25 December to 5 January. The decrease in δ^{18}O and increase in d-excess are also recorded in the period from 5 January to 13 January in the cold trap results, while they are not observed in the Picarro data.

During a similar campaign in Greenland (Steen-Larsen et al., 2011), differences between infrared spectrometry in situ and cryogenic trapping measurements were generally around 0.1 ‰ in δ^{18}O. In comparison, we observe that the cold trap δ^{18}O values are generally higher than the δ^{18}O measured by the Picarro. This can be explained by several factors. First, the isotopic composition sampled using the cold trap is weighted by humidity: the cold trap traps more moisture when the humidity is highest, which also corresponds to the moment when the isotopic composition is the highest. In order to take this into account, we weighted the isotopic composition from the Picarro by specific humidity (not shown). On average, the weighted isotopic composition has an offset of +1.1 ‰ in δ^{18}O compared with the original dataset, rising up to 7.2 ‰ on 31 December and down to −2.9 ‰ on 6 January. In this case, the cold trap δ^{18}O is still in average higher than the isotopic composition weighted by humidity, with an offset of +1.16‰ for δ^{18}O and −3 ‰ for d-excess, which lies within the error bar of our measurements. We thus conclude that, at first order, our cold trap measurements validate the laser spectrometer data.

Table 2. Average, minimum and maximum values over the whole campaign for air temperature ($T_{3\,m}$), snow surface temperature (T_{surf}), specific humidity (q), δD (‰), δ^{18}O (‰) and 3 h smoothed d-excess (‰).

	Average	Minimum	Maximum
$T_{3\,m}$ (°C)	−31.2	−42.6	−24.6
T_{surf} (°C)	−31.5	−46.1	−21.2
q (ppmv)	589	161	977
δD (‰)	−491	−558	−393
δ^{18}O (‰)	−68.2	−77.1	−53.9
d-ex (‰)	55.1	21	88

The cold trap measurements may also include snow-intake events that were captured by the inlet, whereas we removed such data in the spectrometer measurements. Because the isotopic composition of precipitation is enriched compared to the vapour, the introduction of snow crystals in the cold trap inlet could explain a small part of the positive offset of cold trap measurements compared to the infrared spectrometry. No quantitative estimation of this bias has been realized.

3.2 Two climatic regimes

Figure 8 presents the specific humidity and isotopic composition (δ^{18}O, δD and d-excess) measured by the Picarro. The data are continuous from 25 December 2014 to 17 January 2015, except for 4 h on 13 January due to a large snowfall event. These data are compared with the 3 m temperature and the 3 m wind speed (Sect. 2.1) and also to the surface temperature monitored by infrared sensing. Note that the different temperature measurements are not intercalibrated and may present a limited bias of 1 °C. Table 2 summarizes the average, minimum and maximum values for 3 m temperature, surface temperature, humidity and isotopic composition.

Even though the sun never actually passes below the horizon, when the zenithal angle is low, snow surface radiation deficit generates a strong radiative cooling of the surface, which leads to stratification of the atmospheric boundary layer. Daily cycles are clearly visible in all the variables. Greater diurnal temperature variations are observed at the surface than at 3 m even though average temperatures remain similar as already observed in Kohnen (van As et al., 2006). Day temperature at the surface rises up to 8 °C higher than at 3 m during the period from 26 December 2014 to 4 January 2015. After 4 January, differences remain small (less than 2 °C). This first difference will lead us to distinguish the two regimes to further investigate: the first one from 26 December 2014 to 4 January 2015, and the second one from 5 to 17 January 2015.

Table 3 compares the average values, the diurnal amplitudes and the trends within the different datasets. Temperature is higher during regime 1, probably due to the proxim-

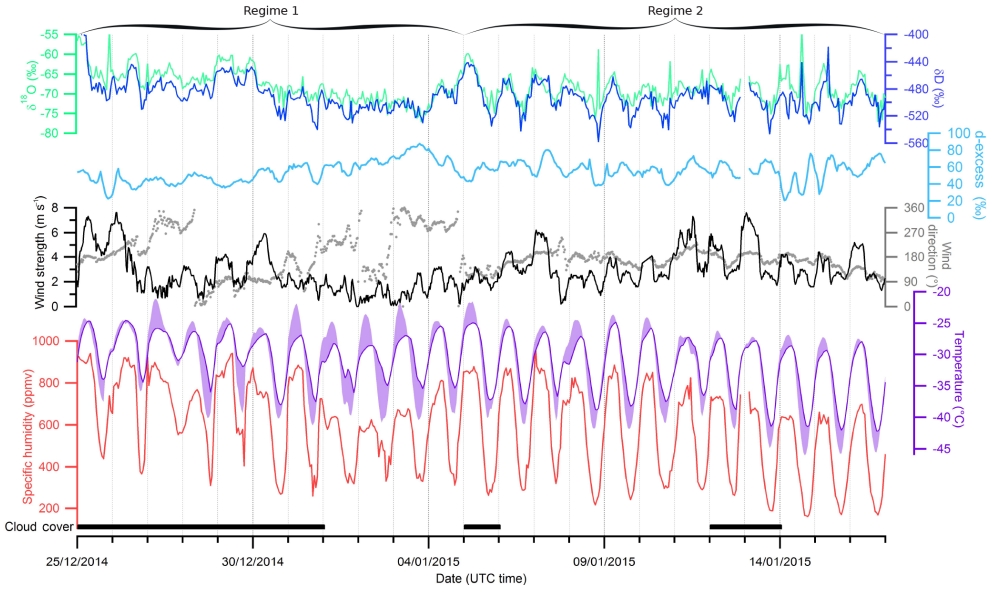

Figure 8. Hourly average δD (‰) in dark blue, hourly average δ^{18}O (‰) in green, d-excess (‰) smoothed on a 3 h span in light blue and hourly average of the specific humidity (ppmv) in red, measured by the Picarro during the campaign; comparison with 3 m temperature (purple, °C), difference between ground and 3 m temperature (purple shade, °C), wind direction (grey dots, °) and speed (black line).

ity to the solar solstice. Diurnal amplitudes in air temperature and humidity are significantly higher in regime 2 than in regime 1. In regime 1, isotopic daily cycles are dumped and completely erased from 1 to 3 January, whereas daily cycles are important for regime 2 (in phase with those of temperature); a significant day-to-day trend appears during regime 1 with almost $-1\,‰\,\mathrm{day}^{-1}$ for δ^{18}O and is not present in regime 2 ($0.07‰\,\mathrm{day}^{-1}$ for δ^{18}O).

We attribute the difference between the two regimes to changes in atmospheric stability, in particular during the "night". Indeed, during daytime, the convection enables strong mixing in both regime 1 and regime 2. However, significant differences are noticeable in the nocturnal stability between regime 1 and 2 which impact the night-time turbulent mixing.

Atmospheric static stability is further assessed using the Richardson number (Richardson, 1920), which is a ratio between the square of the Brunt–Väisälä frequency ($N = \sqrt{\frac{g}{\theta}\frac{\mathrm{d}\theta}{\mathrm{d}z}}$, where $\theta = T(P_0/P)^{R/C_P}$ is the potential temperature calculated from P_0 the standard reference pressure, R the gas constant of air and c_P the specific heat capacity) and the square of the horizontal wind gradient (see Supplement part 3). During regime 1, the Richardson number experiences important daily cycles, rising higher than 0.2 during night-time, indicating a stable and well-stratified boundary layer, and dropping lower than 0 during daytime, indicating a non-stable, convective atmosphere (King et al., 2006). The Richardson number is in particular really large for the nights from 1 to 3 January (rising up to 0.85) highlighting an enhanced night-time stratification during this period. Regime 1 is thus characterized by a well-marked diurnal cycle with a convective activity during the "day" and a stably stratified atmospheric boundary layer during the "night". By contrast, the Richardson number is lower during the night in regime 2, which leads to smaller diurnal cycles of stratification. This can be explained by stronger winds during the nights in regime 2 (Fig. 9), which enhance the turbulent mixing in the atmospheric boundary layer and tend to reduce the stratification.

We now investigate the mean daily cycle of all data during each regime. For this purpose, the trend is removed by subtracting the average value of the day from all data. We then produce a mean value for each hour of the day over the whole regime. The correlations between the average daily cycles of isotopic composition, 3 m temperature, 3 m wind speed and surface temperature are given on Table 4. Temperature of 3 m is less strongly correlated with surface temperature during regime 1 compared to regime 2. During night-time in regime 2, the atmosphere is more turbulent and therefore atmospheric mixing is more efficient. For a more stratified nocturnal atmosphere (regime 1), we expect surface temperature to be less correlated to 3 m temperature and also to isotopic composition.

We also observe that the correlation of surface isotopic composition and temperature, as well as between δ^{18}O and δD, is stronger for regime 2 (turbulent nocturnal atmosphere) than for regime 1 (stratified nocturnal atmosphere). An explanation for this correlation could be the temperature influence on the fractionation at the snow–air interface. In the case of regime 2, as the turbulence allows efficient air mass mixing, the isotopic composition at 2 m is directly related to what

Table 3. Average, daily amplitude and daily trend over the whole campaign for air temperature ($T_{3\,m}$, °C), snow surface temperature (T_{surf}, °C), specific humidity (q, ppmv), δD (‰), δ^{18}O (‰) and smoothed d-excess (‰).

	Regime 1: from 26 Dec to 4 Jan			Regime 2: from 5 to 17 Jan		
	Average	Amplitude	Trend (/day)	Average	Amplitude	Trend (/day)
$T_{3\,m}$ (°C)	−29.9	7.6 ± 0.2	-0.29 ± 0.02	−32.4	11.9 ± 0.2	-0.38 ± 0.02
T_{surf} (°C)	−30.2	14.2 ± 0.4	-0.34 ± 0.05	−32.6	16.2 ± 0.3	-0.47 ± 0.03
q (ppmv)	631	341 ± 20	-24 ± 3	541	521 ± 13	-39 ± 2
δD (‰)	−490	14 ± 3	-3.7 ± 0.4	−495	38 ± 2	-0.8 ± 0.3
δ^{18}O (‰)	−68.1	1.4 ± 0.6	-0.92 ± 0.06	−68.9	5.4 ± 0.4	-0.07 ± 0.04
d-ex (‰)	54.9	8 ± 1	3.7 ± 0.2	56.2	13 ± 2	-0.2 ± 0.2

Table 4. Slope and correlation coefficient between the different data average daily cycle: for each data, the average of the day was removed and a trend-free daily cycle for each regime was produced.

	Regime 1: from 26 Dec to 4 Jan		Regime 2: from 5 to 17 Jan	
	Slope	r^2	Slope	r^2
δD (‰) vs. q (ppmv)	0.043 ± 0.005	0.79	0.071 ± 0.003	0.96
δD (‰) vs. $T_{3\,m}$ (°C)	2.0 ± 0.2	0.74	3.2 ± 0.2	0.94
δD (‰) vs. T_{surf} (°C)	0.95 ± 0.2	0.58	2.3 ± 0.1	0.95
δD (‰) vs. δ^{18}O (‰)	6.0 ± 1.3	0.48	6.5 ± 0.6	0.85
q (ppmv) vs. $T_{3\,m}$ (°C)	45 ± 2	0.94	44 ± 2	0.96
q (ppmv) vs. T_{surf} (°C)	24 ± 2	0.89	32 ± 1	0.98
$T_{3\,m}$ (°C) vs. T_{surf} (°C)	0.49 ± 0.05	0.80	0.69 ± 0.04	0.92

is happening at the surface; hence the isotopic composition is strongly correlated to surface temperature. Such a situation was already described at the NEEM station in Greenland (Steen-Larsen et al., 2013), where similar temperature and water vapour isotopic composition cycles were observed during 10 days, leading to the conclusion that the snow surface was acting successively as a sink during the night and as a source during the day. They also hypothesized that the vapour isotopic composition could be at equilibrium with the snow one, at least during part of the day. Exchange with the vapour could also have strong impact on snow metamorphism in Concordia, as observed in NEEM (Steen-Larsen et al., 2014a).

In the case of regime 1, when atmosphere is at least part of the time stratified, the mixing of the first layers of the atmosphere is not efficiently done by turbulence. In these situations happening mostly at night, the ground is cooling faster than the air above it, creating vertical gradients in moisture content of the atmosphere (van As and van den Broeke, 2006).

We now investigate the timing of the average diurnal cycles (Fig. 9). By comparing the position of the maximal slope (which enables a more precise determination of dephasing than the maxima), we notice a shift of approximately 2 h between surface and 3 m temperature. Specific humidity average daily cycle is synchronized with 3 m temperature in both regimes 1 and 2. For regime 1, no diurnal cycle appears in surface vapour isotopic composition. For regime 2, the daily cycle of surface vapour isotopic composition is synchronized with surface temperature and therefore shifted 2 h earlier than 3 m temperature and humidity. This is consistent with the hypothesis of temperature-driven exchanges of molecules between the air and the snow surface in regime 2. This hypothesis will be discussed in more details in part 3.3.

The diurnal amplitude that we measured (38‰ for δD in average during regime 2) is within the range obtained in previous studies in Greenland. In NEEM, daily cycles up to 36‰ for δD were measured during summer campaigns (Steen-Larsen et al., 2013), much more important than those cycles on the coastal areas of Greenland with peak-to-peak amplitudes of variations of 1 ‰ for δ^{18}O in Ivittuut, Greenland (Bonne et al., 2014). A similar pattern is observed around Antarctica, near coastal areas, on a ship near Syowa station, where isotopic composition variations are dominated by day-to-day evolution and there are no diurnal cycles (Kurita et al., 2016).

3.3 Local water vapour δD–δ^{18}O relationship and snow surface interactions

Figure 10 presents the δD and δ^{18}O isotopic composition during the 2014/2015 campaign, for continuous measurements and cold trap data, and earlier cold trap data from

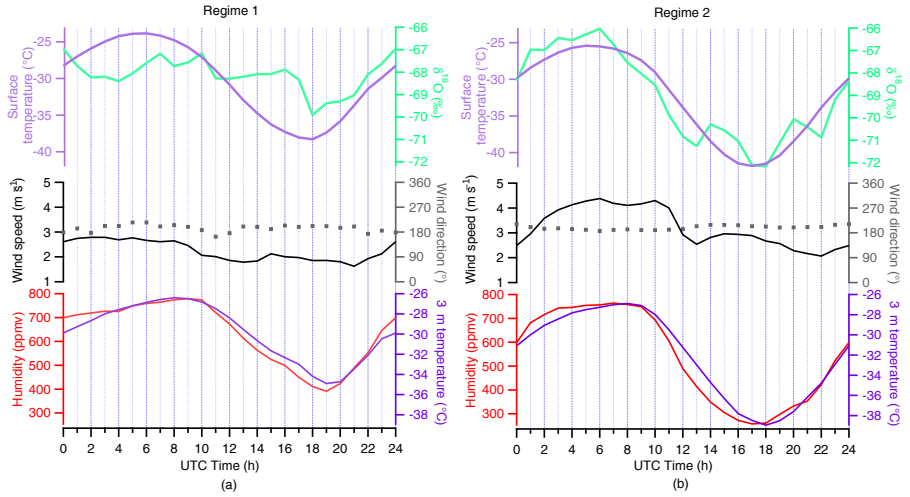

Figure 9. Comparison of average daily cycles (UTC time) of 3 m temperature (light purple, °C), surface temperature (dark purple), specific humidity (red, ppmv), wind speed (black line, $m\,s^{-1}$), wind direction (black dots, °) and $\delta^{18}O$ (green, ‰) for **(a)** regime 1 and **(b)** regime 2.

2006/2007. We observe that all these data depict a common range of isotopic composition and align on a similar slope. In this section, we focus on the slope between δD and $\delta^{18}O$ and not on the d-excess. Indeed, the high values of d-excess are related to the low value of the slope δD vs. $\delta^{18}O$ (around 5 compared to the value of 8 used in the d-excess calculation). Note that discussions of d-excess or of the slope between δD and $\delta^{18}O$ are strictly equivalent in this case.

We observe very low (around 5) δD and $\delta^{18}O$ slopes measured using on-site infrared spectroscopy and post-campaign mass spectrometry of the cryogenic trapping samples (Table 5). In fact, publication of the 2006/2007 cold trap data was postponed until an explanation for such low vapour line was identified due to the fear of sampling vapour from the station generator. As stated in Sect. 2.5, no such contamination occurred. This slope is much lower than observed in Greenland (Bonne et al., 2014; Steen-Larsen et al., 2013). A very low slope for δD vs. $\delta^{18}O$ in water vapour is not unexpected as Dome C is very far on the distillation path and air masses are very depleted in heavy isotopologues (Touzeau et al., 2016). Indeed, for a Rayleigh distillation, the local relative variations of the isotopic composition of δD and $\delta^{18}O$ are defined by

$$\frac{d\delta D}{d\delta^{18}O} = \frac{\alpha_D - 1}{\alpha_{18} - 1}\frac{1+\delta D}{1+\delta^{18}O}, \quad (2)$$

where α_D and α_{18} are respectively the equilibrium fractionation coefficients of HDO and $H_2^{18}O$ (Jouzel and Merlivat, 1984). In the average condition of the campaign ($T = -31.5$°C and isotopic composition from Table 2), even if $(\alpha_D - 1)/(\alpha_{18} - 1) = 9.71$, the very low value of δD (around -500 ‰) brings down the slope δD and $\delta^{18}O$ to 5.3 ‰‰$^{-1}$. Note that the important d-excess values obtained in Sect. 3.2. are due to the very low slope between δD and $\delta^{18}O$ and not necessarily to important kinetic effects in this case.

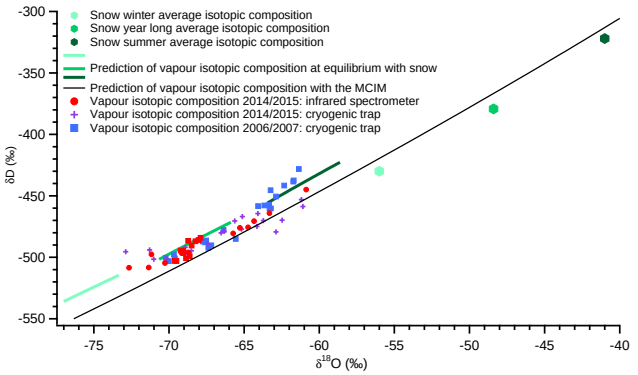

Figure 10. δD and $\delta^{18}O$ plots: red is the daily average isotopic composition from the Picarro (circles: regime 1; squares: regime 2), purple crosses are the cold trap isotopic composition from 2014/2015 campaign, blue squares are the cold trap isotopic composition from 2006/2007, green hexagons are the isotopic composition of the snow (Touzeau et al., 2015) (light tone is the average composition minus 1 standard deviation, mid-tone is the average composition and dark tone is the average composition plus 1 standard deviation), green lines are the respecting calculated equilibrium fractionation in the range of temperature observed during the campaign (Majoube, 1971) (local origin thereafter) and the black line is the curve established with a Rayleigh distillation in the MCIM (remote origin thereafter).

We now discuss in details the possible drivers of the isotopic composition of water vapour at Dome C following several hypotheses: the first being local origin (equilibrium between surface snow and water vapour), the second being remote origin (distillation of a water mass from the coast).

Table 5. Slope and correlation coefficients between the different datasets. Picarro and meteorological data are daily average data. Equilibrium fractionation slopes are calculated from the average values (average, ± 1 standard deviation) with Majoube fractionation coefficients (high M, med M, low M) or Ellehøj fractionation coefficients (med E).

		Data for all season	
		Slope	r^2
Picarro data	δD (‰) vs. q (ppmv)	0.12 ± 0.02	0.61
	δD (‰) vs. $T_{3\,m}$ (°C)	3.7 ± 1.5	0.22
	δD (‰) vs. T_{surf} (°C)	4.3 ± 1.2	0.30
	δD (‰) vs. δ^{18}O (‰)	5.3 ± 0.3	0.92
	q (ppmv) vs. $T_{3\,m}$ (°C)	43 ± 6	0.69
	q (ppmv) vs. T_{surf} (°C)	45 ± 5	0.79
Meteological data	$T_{3\,m}$ (°C) vs. T_{surf} (°C)	0.7 ± 0.1	0.63
Trapping 2006/2007	δD (‰) vs. δ^{18}O (‰)	4.6 ± 0.7	0.82
Trapping 2014/2015	δD (‰) vs. δ^{18}O (‰)	4.8 ± 0.4	0.90
Equilibrium fractionation	δD (‰) vs. δ^{18}O (‰) high M	7.02	Th.
	δD (‰) vs. δ^{18}O (‰) med M	6.50	Th.
	δD (‰) vs. δ^{18}O (‰) low M	5.99	Th.
	δD (‰) vs. δ^{18}O (‰) med E	5.65	Th.
MCIM	δD (‰) vs. δ^{18}O (‰) at −35 °C	6.11	Th.

For the first hypothesis, we used the range of annual isotopic composition of the snow at Dome C (Touzeau et al., 2016), represented by green hexagons (average value ± 1 standard deviation). The slope between δD and δ^{18}O of the snow annual isotopic composition is 7.2 ‰‰$^{-1}$, already lower than 8. From these values, we calculate the corresponding vapour isotopic composition in the range of summer temperature (−20 to −45 °C) using standard equilibrium fractionation coefficients (Majoube, 1971; Merlivat and Nief, 1967). The range of calculated vapour isotopic contents is consistent with observed vapour: from the average value of snow δ^{18}O = −48.4 ‰, we get a vapour predicted δ^{18}O = −68.2 ‰ at −35 °C, which lies within the values measured by the Picarro (on average over the campaign δ^{18}O = −68.9 ‰). The slope between δD and δ^{18}O, however, is higher than the one observed: 6.5 ‰‰$^{-1}$ vs. 5.3 ‰‰$^{-1}$ for the Picarro and even 4.8 ‰‰$^{-1}$ for the cold traps. The same calculation with the equilibrium fractionation coefficients from Ellehøj et al. (2013) can predict relevant δ^{18}O and δD values and more realistic slopes (5.7 ‰‰$^{-1}$).

We now analyse the effect of the distillation on the isotopic composition of the water vapour. For this test, we used the Mixed Cloud Isotopic Model (MCIM) to compute the isotopic composition of the vapour. The MCIM is a Rayleigh model taking into account microphysical properties of clouds and in particular accounting for mixed phases (Ciais and Jouzel, 1994). The model was tuned with snow isotopic composition of an Antarctic transect from Terra Nova Bay to Dome C to accurately reproduce the isotopic composition of the Antarctic Plateau (Winkler et al., 2012). For instance, the model predicts an average value of snow isotopic composition at Dome C of −51 ‰ for an average site temperature of −54.5 °C when the measurements indicated −50.7 ‰; note that the model takes into account an inversion temperature and that the condensation temperature T_{cond} is deduced from the surface temperature T_{surf} through (Ekaykin and Lipenkov, 2009)

$$T_{cond} = 0.67 \times T_{surf} - 1.2. \quad (3)$$

The prediction of average vapour isotopic composition by the MCIM is δ^{18}O = −51.6 ‰ at −35 °C, which is much higher than the average vapour measurements (δ^{18}O = −68.9 ‰). However, the MCIM manages to predict the isotopic composition of the summer precipitation (δ^{18}O = −37 ‰ at −35 °C for the model compared to values rising up to −39 ‰ for matching temperature in Dome C summer precipitation). Therefore, we conclude that the vapour isotopic composition seems to be principally influenced by local effects. Note that the slope between δD and δ^{18}O predicted by the MCIM is around 6.1 ‰‰$^{-1}$, which is also higher than the one observed during the campaign (between 4.6 and 5.3 for the different datasets).

The precipitation amount in Dome C is less than 10 cm per year (Genthon et al., 2015). Each precipitation event does not form a complete layer of snow and is mixed with earlier snowfall possibly deposited under the earlier winter conditions. The snow isotopic composition is therefore a mix of new snowfall and older snow. This phenomenon is amplified by drift and blowing snow (Libois et al., 2014). A mixing be-

tween a large range of source isotopic compositions should be considered to compute the local origin hypotheses, which could explain the bias of the slope predicted by equilibrium from a single snow composition compared to experimental data.

4 Conclusion

In this study, we assessed the relevance of infrared spectrometry to measure isotopic composition of water at concentrations as low as those encountered over the Antarctic Plateau. Apart from the logistic challenges involved in the installation of spectrometers in remote areas, humidity levels, very depleted samples and important local variability create a technical challenge that the new infrared spectroscopy techniques overcame.

Allan variance measurements in the laboratory indicated the possibility of using Picarro and HiFI spectrometers at humidity as low as 200 ppmv and with almost no loss of precision from 500 ppmv (limit of precision of 0.1 ‰ δ^{18}O and for 1.1 ‰ for δD). Identical measurements in the field showed it was possible to reach similar results in the field even though great care in the environment where the instruments are deployed should be addressed.

For such humidities, the linearity of the instruments is not guaranteed toward humidity and regular calibrations in the field are necessary. In this particular study, it was not possible to calibrate the instruments regularly in the field for logistical reasons, so we bracketed the drift of the instrument by series of calibration in the lab. This is not the optimal method and results in significant error bars compared to the performances of the instrument. The uncertainty of the isotopic composition measurement is therefore 6 ‰ for δD and 1 ‰ for δ^{18}O. We have further validated these measurements through (i) a comparison of the data acquired by infrared spectrometry with cryogenic trapping samples and (ii) a protocol to calibrate on the SMOW–SLAP scale at δ^{18}O lower than the SLAP δ^{18}O value (−55.5 ‰). This calibration demonstrated that our Picarro instrument is linear in δ^{18}O, down to −80 ‰ in δ^{18}O and stays almost linear down to −110 ‰. This is essential for our study since the mean δ^{18}O value was −68.2 ‰ at Concordia between 25 December 2014 and 17 January 2015.

Two different regimes have been identified during the campaign: the first from 26 December 2014 to 4 January 2015 and the second from 5 to 17 January 2015. The main difference between the two regimes on isotopic composition is the amplitude of the daily cycles: large and regular during regime 2, small and irregular in regime 1 and an almost erased one from 1 to 4 January 2015. For regime 1, correlation of humidity with surface temperature is lowered and isotopic composition is almost stable, whereas for regime 2 there is an almost perfect correlation for both humidity and isotopic composition with temperature. We attribute these differences to differences in the stability of the atmosphere. We explain the drop of correlation in regime 1 by a weakly turbulent boundary layer during which temperature, humidity and isotopic composition diurnal cycles are truncated in comparison to regime 2, which is characterized by efficient turbulence with important diurnal cycles and almost perfect correlation between the snow surface temperature and the first metres of the atmosphere. The second regime therefore appears to be characterized by equilibrium between the isotopic composition of vapour over the first metres and that of the snow, as already shown for Greenland (Steen-Larsen et al., 2013).

Temperature cycles seem to be directly responsible for isotopic composition cycles, at least in regime 2, through equilibrium fractionation in sublimation/condensation cycles. At first order, it seems the snow isotopic composition is influencing directly the vapour through fractionation at phase change. The vapour isotopic composition average value matches the one obtained by equilibrium fractionation of the local snow. However, the measured slope between δD and δ^{18}O still cannot be explained purely by equilibrium fractionation from local snow. We cannot rule out a contribution of horizontal air advection from inland locations, transported by southward winds and providing small amounts of very depleted moisture.

Finally, our study opens new perspectives on the influence of post-deposition effects and their importance for the water stable isotope signal recorded in deep ice cores. In particular, we have shown that the relationship between water vapour δ^{18}O and temperature can be erased by weakly turbulent regimes. Yearlong monitoring of the isotopic composition of the water vapour could help identify how often these conditions happen and also whether the snow isotopic composition could present a biased relationship toward seasonality, temperature or precipitation.

5 Data availability

The dataset used for this study is available as a Supplement.

The Supplement related to this article is available online at doi:10.5194/acp-16-8521-2016-supplement.

Author contributions. Mathieu Casado, Amaelle Landais, Frederic Prie, Samir Kassi and Peter Cermak prepared the field campaign; Mathieu Casado deployed the instruments on the field; Valérie Masson-Delmotte, Erik Kerstel and Samir Kassi provided the infrared spectrometers; Christophe Genthon, Laurent Arnaud, Ghislain Picard, Olivier Cattani and Etienne Vignon provided data; Mathieu Casado prepared the manuscript with contributions from all co-authors.

Acknowledgements. The research leading to these results has received funding from the European Research Council under the European Union's Seventh Framework Programme (FP7/2007-2013)/ERC grant agreement no. 306045. We acknowledge the programs NIVO and GLACIO and all the IPEV that made this campaign possible and LGGE and LIPHY for providing logistic advice and support. We thank Catherine Ritz, Anais Orsi and Xavier Fain for their help during the preparation of the mission. Many thanks to Philippe Ricaud, Doris Thuillier, Nicolas Caillon, Bruno Jourdain, Olivier Magand and all the 11th winter-over team for your support and your presence in Concordia. Thanks to Hubert Gallée for all the discussions about polar meteorology.

Edited by: Y. Balkanski

References

Aemisegger, F., Sturm, P., Graf, P., Sodemann, H., Pfahl, S., Knohl, A., and Wernli, H.: Measuring variations of δ^{18}O and δ^{2}H in atmospheric water vapour using two commercial laser-based spectrometers: an instrument characterisation study, Atmos. Meas. Tech., 5, 1491–1511, doi:10.5194/amt-5-1491-2012, 2012.

Bailey, A., Noone, D., Berkelhammer, M., Steen-Larsen, H. C., and Sato, P.: The stability and calibration of water vapor isotope ratio measurements during long-term deployments, Atmos. Meas. Tech., 8, 4521–4538, doi:10.5194/amt-8-4521-2015, 2015.

Bonne, J.-L., Masson-Delmotte, V., Cattani, O., Delmotte, M., Risi, C., Sodemann, H., and Steen-Larsen, H. C.: The isotopic composition of water vapour and precipitation in Ivittuut, southern Greenland, Atmos. Chem. Phys., 14, 4419–4439, doi:10.5194/acp-14-4419-2014, 2014.

Bonne, J.-L., Steen-Larsen, H. C., Risi, C., Werner, M., Sodemann, H., Lacour, J.-L., Fettweis, X., Cesana, G., Delmotte, M., Cattani, O., Vallelonga, P., Kjær, H. A., Clerbaux, C., Sveinbjörnsdóttirffilmark, Á. E., and Masson-Delmotte, V.: The summer 2012 Greenland heat wave: in situ and remote sensing observations of water vapour isotopic composition during an atmospheric river event, J. Geophys. Res.-Atmos., 120, 2970–2989, 2015.

Cappa, C. D., Hendricks, M. B., DePaolo, D. J., and Cohen, R. C.: Isotopic fractionation of water during evaporation, J. Geophys. Res.-Atmos., 108, 4525, doi:10.1029/2003JD003597, 2003.

Charles, C. D., Rind, D., Jouzel, J., Koster, R. D., and Fairbanks, R. G.: Glacial-Interglacial Changes in Moisture Sources for Greenland: Influences on the Ice Core Record of Climate, Science, 263, 508–511, 1994.

Ciais, P. and Jouzel, J.: Deuterium and oxygen 18 in precipitation: Isotopic model, including mixed cloud processes, J. Geophys. Res.-Atmos., 99, 16793–16803, 1994.

Craig, H. and Gordon, A.: Deuterium and oxygen 18 variations in the ocean and the marine atmosphere, Stable Isotopes in Oceanic Studies and Paleotemperatures, edited by: Tongiorgi, E., 9–130, Laboratorio di Geologia Nucleare, Pisa, 1965.

Crosson, E. R.: A cavity ring-down analyzer for measuring atmospheric levels of methane, carbon dioxide, and water vapor, Appl. Phys. B, 92, 403–408, 2008.

Dansgaard, W.: Stable isotopes in precipitation, Tellus, 16, 436–468, 1964.

Ekaykin, A. A. and Lipenkov, V. Y.: Formation of the ice core isotopic composition, Low Temperature Science, 68, 299–314, 2009.

Ekaykin, A. A., Lipenkov, V. Y., Barkov, N. I., Petit, J. R., and Masson-Delmotte, V.: Spatial and temporal variability in isotope composition of recent snow in the vicinity of Vostok station, Antarctica: implications for ice-core record interpretation, Ann. Glaciol., 35, 181–186, 2002.

Ekaykin, A. A., Lipenkov, V. Y., Kuzmina, I. N., Petit, J. R., Masson-Delmotte, V., and Johnsen, S. J.: The changes in isotope composition and accumulation of snow at Vostok station, East Antarctica, over the past 200 years, Ann. Glaciol., 39, 569–575, 2004.

Ellehøj, M. D., Steen-Larsen, H. C., Johnsen, S. J., and Madsen, M. B.: Ice-vapor equilibrium fractionation factor of hydrogen and oxygen isotopes: Experimental investigations and implications for stable water isotope studies, Rapid Commun. Mass Sp., 27, 2149–2158, 2013.

EPICA: Eight glacial cycles from an Antarctic ice core, Nature, 429, 623–628, 2004.

Fawcett, P. J., Ágústsdóttir, A. M., Alley, R. B., and Shuman, C. A.: The Younger Dryas Termination and North Atlantic Deep Water Formation: Insights from climate model simulations and Greenland Ice Cores, Paleoceanography, 12, 23–38, 1997.

Frezzotti, M., Gandolfi, S., La Marca, F., and Urbini, S.: Snow dunes and glazed surfaces in Antarctica: new field and remote-sensing data, Ann. Glaciol., 34, 81–88, 2002.

Genthon, C., Town, M. S., Six, D., Favier, V., Argentini, S., and Pellegrini, A.: Meteorological atmospheric boundary layer measurements and ECMWF analyses during summer at Dome C, Antarctica, J. Geophys. Res.-Atmos., 115, 2156–2202, doi:10.1029/2009JD012741, 2010.

Genthon, C., Six, D., Favier, V., Lazzara, M., and Keller, L.: Atmospheric Temperature Measurement Biases on the Antarctic Plateau, J. Atmos. Ocean. Tech., 28, 1598–1605, 2011.

Genthon, C., Six, D., Gallée, H., Grigioni, P., and Pellegrini, A.: Two years of atmospheric boundary layer observations on a 45-m tower at Dome C on the Antarctic plateau, J. Geophys. Res.-Atmos., 118, 3218–3232, 2013.

Genthon, C., Six, D., Scarchilli, C., Ciardini, V., and Frezzotti, M.: Meteorological and snow accumulation gradients across Dome C, East Antarctic plateau, Int. J. Climatol., 36, 455–466, 2015.

Gorski, G., Strong, C., Good, S. P., Bares, R., Ehleringer, J. R., and Bowen, G. J.: Vapor hydrogen and oxygen isotopes reflect water of combustion in the urban atmosphere, P. Natl. Acad. Sci. USA, 112, 3247–3252, 2015.

He, H. and Smith, R. B.: Stable isotope composition of water vapor in the atmospheric boundary layer above the forests of New England, J. Geophys. Res.-Atmos., 104, 11657–11673, 1999.

Hoshina, Y., Fujita, K., Nakazawa, F., Iizuka, Y., Miyake, T., Hirabayashi, M., Kuramoto, T., Fujita, S., and Motoyama, H.: Effect of accumulation rate on water stable isotopes of near-surface snow in inland Antarctica, J. Geophys. Res.-Atmos., 119, 274–283, 2014.

IAEA: Reference Sheet for VSMOW2 and SLAP2 international measurement standards. International Atomic Energy Agency, Vienna, 2009.

Johnsen, S. J., Clausen, H. B., Cuffey, K. M., Hoffmann, G., and Creyts, T. T.: Diffusion of stable isotopes in polar firn and ice:

the isotope effect in firn diffusion, Physics of ice core records, 159, 121–140, 2000.

Jouzel, J. and Merlivat, L.: Deuterium and oxygen 18 in precipitation: Modeling of the isotopic effects during snow formation, J. Geophys. Res.-Atmos., 89, 11749–11757, 1984.

Jouzel, J., Alley, R., Cuffey, K., Dansgaard, W., Grootes, P., Hoffmann, G., Johnsen, S., Koster, R., Peel, D., and Shuman, C.: Validity of the temperature reconstruction from water isotopes in ice cores, J. Geophys. Res., 102, 26471–26487, 1997.

Jouzel, J., Delaygue, G., Landais, A., Masson-Delmotte, V., Risi, C., and Vimeux, F.: Water isotopes as tools to document oceanic sources of precipitation, Water Resour. Res., 49, 7469–7486, 2013.

King, J. C., Argentini, S. A., and Anderson, P. S.: Contrasts between the summertime surface energy balance and boundary layer structure at Dome C and Halley stations, Antarctica, J. Geophys. Res.-Atmos., 111, D02105, doi:10.1029/2005JD006130, 2006.

Krinner, G., Genthon, C., and Jouzel, J.: GCM analysis of local influences on ice core δ signals, Geophys. Res. Lett., 24, 2825–2828, 1997.

Kurita, N., Hirasawa, N., Koga, S., Matsushita, J., Steen-Larsen, H. C., Masson-Delmotte, V., and Fujiyoshi, Y.: Influence of large-scale atmospheric circulation to marine air intrusion on the East Antarctic coast, Geophys. Res. Lett., under review, 2016.

Landais, A., Barkan, E., and Luz, B.: Record of δ^{18}O and ^{17}O-excess in ice from Vostok Antarctica during the last 150,000 years, Geophys. Res. Lett., 35, L02709, doi:10.1029/2007GL032096, 2008.

Landsberg, J.: Development of an OF-CEAS laser spectrometer for water vapor isotope measurements at low water concentrations, University of Groningen, 2014.

Landsberg, J., Romanini, D., and Kerstel, E.: Very high finesse optical-feedback cavity-enhanced absorption spectrometer for low concentration water vapor isotope analyses, Opt. Lett., 39, 1795–1798, 2014.

LeGrande, A. N. and Schmidt, G. A.: Global gridded data set of the oxygen isotopic composition in seawater, Geophys. Res. Lett., 33, L12604, doi:10.1029/2006GL026011, 2006.

Libois, Q., Picard, G., Arnaud, L., Morin, S., and Brun, E.: Modeling the impact of snow drift on the decameter-scale variability of snow properties on the Antarctic Plateau, J. Geophys. Res.-Atmos., 119, 11662–11681, 2014.

Lorius, C., Merlivat, L., and Hagemann, R.: Variation in the mean deuterium content of precipitations in Antarctica, J. Geophys. Res., 74, 7027–7031, 1969.

Luz, B., Barkan, E., Yam, R., and Shemesh, A.: Fractionation of oxygen and hydrogen isotopes in evaporating water, Geochim. Cosmochim. Ac., 73, 6697–6703, 2009.

Majoube, M.: Fractionation in O-18 between ice and water vapor, J. Chim. Phys. PCB, 68, 625–636, 1971.

Masson-Delmotte, V., Hou, S., Ekaykin, A., Jouzel, J., Aristarain, A., Bernardo, R. T., Bromwich, D., Cattani, O., Delmotte, M., Falourd, S., Frezzotti, M., Gallée, H., Genoni, L., Isaksson, E., Landais, A., Helsen, M. M., Hoffmann, G., Lopez, J., Morgan, V., Motoyama, H., Noone, D., Oerter, H., Petit, J. R., Royer, A., Uemura, R., Schmidt, G. A., Schlosser, E., Simões, J. C., Steig, E. J., Stenni, B., Stievenard, M., van den Broeke, M. R., van de Wal, R. S. W., van de Berg, W. J., Vimeux, F., and White, J. W. C.: A Review of Antarctic Surface Snow Isotopic Composition: Observations, Atmospheric Circulation, and Isotopic Modeling*, J. Climate, 21, 3359–3387, 2008.

Masson-Delmotte, V., Buiron, D., Ekaykin, A., Frezzotti, M., Gallée, H., Jouzel, J., Krinner, G., Landais, A., Motoyama, H., Oerter, H., Pol, K., Pollard, D., Ritz, C., Schlosser, E., Sime, L. C., Sodemann, H., Stenni, B., Uemura, R., and Vimeux, F.: A comparison of the present and last interglacial periods in six Antarctic ice cores, Clim. Past, 7, 397–423, doi:10.5194/cp-7-397-2011, 2011.

Merlivat, L.: Molecular diffusivities of (H_2O)-O^{16} $HD^{16}O$, and (H_2O)-O^{18} in gases, J. Chem. Phys., 69, 2864–2871, 1978.

Merlivat, L. and Nief, G.: Fractionnement isotopique lors des changements d'état solide-vapeur et liquide-vapeur de l'eau à des températures inférieures à 0 °C, Tellus, 19, 122–127, 1967.

Neumann, T. A. and Waddington, E. D.: Effects of firn ventilation on isotopic exchange, J. Glaciol., 50, 183–194, 2004.

Petit, J. R., Jouzel, J., Pourchet, M., and Merlivat, L.: A detailed study of snow accumulation and stable isotope content in Dome C (Antarctica), J. Geophys. Res.-Oceans, 87, 4301–4308, 1982.

Ricaud, P., Genthon, C., Durand, P., Attié, J. L., Carminati, F., Canut, G., Vanacker, J. F., Moggio, L., Courcoux, Y., Pellegrini, A., and Rose, T.: Summer to Winter Diurnal Variabilities of Temperature and Water Vapour in the Lowermost Troposphere as Observed by HAMSTRAD over Dome C, Antarctica, Bound.-Lay. Meteorol., 143, 227–259, 2012.

Richardson, L. F.: The Supply of Energy from and to Atmospheric Eddies, P. Roy. Soc. Lond. A, 97, 354–373, 1920.

Risi, C., Bony, S., Vimeux, F., and Jouzel, J.: Water-stable isotopes in the LMDZ4 general circulation model: Model evaluation for present-day and past climates and applications to climatic interpretations of tropical isotopic records, J. Geophys. Res.-Atmos., 115, D12118, doi:10.1029/2009JD013255, 2010.

Romanini, D., Ventrillard, I., Méjean, G., Morville, J., and Kerstel, E.: Introduction to Cavity Enhanced Absorption Spectroscopy, in: Cavity-Enhanced Spectroscopy and Sensing, edited by: Gagliardi, G. and Loock, H.-P., Springer Berlin Heidelberg, 1–60, 2014.

Röthlisberger, R., Hutterli, M. A., Sommer, S., Wolff, E. W., and Mulvaney, R.: Factors controlling nitrate in ice cores: Evidence from the Dome C deep ice core, J. Geophys. Res.-Atmos., 105, 20565–20572, 2000.

Salisbury, J. W., Wald, A., and D'Aria, D. M.: Thermal-infrared remote sensing and Kirchhoff's law: 1. Laboratory measurements, J. Geophysical Res.-Sol. Ea., 99, 11897–11911, 1994.

Schmidt, G. A., Hoffmann, G., Shindell, D. T., and Hu, Y.: Modeling atmospheric stable water isotopes and the potential for constraining cloud processes and stratosphere-troposphere water exchange, J. Geophys. Res.-Atmos., 110, D21314, doi:10.1029/2005JD005790, 2005.

Schneebeli, M. and Sokratov, S. A.: Tomography of temperature gradient metamorphism of snow and associated changes in heat conductivity, Hydrol. Process., 18, 3655–3665, 2004.

Schoch-Fischer, H., Rozanski, K., Jacob, H., Sonntag, C., Jouzel, I., Östlund, G., and Geyh, M.: Hydrometeorological factors controlling the time variation of D, ^{18}O and ^{3}H in atmospheric water vapour and precipitation in the northern westwind belt, IAEA, Isotope Hydrology, Vienna, IAEA, 3–30, 1983.

Sokratov, S. A. and Golubev, V. N.: Snow isotopic content change by sublimation, J. Glaciol., 55, 823–828, 2009.

Steen-Larsen, H. C., Masson-Delmotte, V., Sjolte, J., Johnsen, S. J., Vinther, B. M., Bréon, F. M., Clausen, H. B., Dahl-Jensen, D., Falourd, S., Fettweis, X., Gallée, H., Jouzel, J., Kageyama, M., Lerche, H., Minster, B., Picard, G., Punge, H. J., Risi, C., Salas, D., Schwander, J., Steffen, K., Sveinbjörnsdóttir, A. E., Svensson, A., and White, J.: Understanding the climatic signal in the water stable isotope records from the NEEM shallow firn/ice cores in northwest Greenland, J. Geophys. Res.-Atmos., 116, D06108, doi:10.1029/2010JD014311, 2011.

Steen-Larsen, H. C., Johnsen, S. J., Masson-Delmotte, V., Stenni, B., Risi, C., Sodemann, H., Balslev-Clausen, D., Blunier, T., Dahl-Jensen, D., Ellehøj, M. D., Falourd, S., Grindsted, A., Gkinis, V., Jouzel, J., Popp, T., Sheldon, S., Simonsen, S. B., Sjolte, J., Steffensen, J. P., Sperlich, P., Sveinbjörnsdóttir, A. E., Vinther, B. M., and White, J. W. C.: Continuous monitoring of summer surface water vapor isotopic composition above the Greenland Ice Sheet, Atmos. Chem. Phys., 13, 4815–4828, doi:10.5194/acp-13-4815-2013, 2013.

Steen-Larsen, H. C., Masson-Delmotte, V., Hirabayashi, M., Winkler, R., Satow, K., Prié, F., Bayou, N., Brun, E., Cuffey, K. M., Dahl-Jensen, D., Dumont, M., Guillevic, M., Kipfstuhl, S., Landais, A., Popp, T., Risi, C., Steffen, K., Stenni, B., and Sveinbjörnsdottír, A. E.: What controls the isotopic composition of Greenland surface snow?, Clim. Past, 10, 377–392, doi:10.5194/cp-10-377-2014, 2014a.

Steen-Larsen, H. C., Sveinbjörnsdottir, A. E., Peters, A. J., Masson-Delmotte, V., Guishard, M. P., Hsiao, G., Jouzel, J., Noone, D., Warren, J. K., and White, J. W. C.: Climatic controls on water vapor deuterium excess in the marine boundary layer of the North Atlantic based on 500 days of in situ, continuous measurements, Atmos. Chem. Phys., 14, 7741–7756, doi:10.5194/acp-14-7741-2014, 2014b.

Touzeau, A., Landais, A., Stenni, B., Uemura, R., Fukui, K., Fujita, S., Guilbaud, S., Ekaykin, A., Casado, M., Barkan, E., Luz, B., Magand, O., Teste, G., Le Meur, E., Baroni, M., Savarino, J., Bourgeois, I., and Risi, C.: Acquisition of isotopic composition for surface snow in East Antarctica and the links to climatic parameters, The Cryosphere Discuss., 9, 6275–6313, doi:10.5194/tcd-9-6275-2015, 2015.

Touzeau, A., Landais, A., Stenni, B., Uemura, R., Fukui, K., Fujita, S., Guilbaud, S., Ekaykin, A., Casado, M., Barkan, E., Luz, B., Magand, O., Teste, G., Le Meur, E., Baroni, M., Savarino, J., Bourgeois, I., and Risi, C.: Acquisition of isotopic composition for surface snow in East Antarctica and the links to climatic parameters, The Cryosphere, 10, 837–852, doi:10.5194/tc-10-837-2016, 2016.

Tremoy, G., Vimeux, F., Cattani, O., Mayaki, S., Souley, I., and Favreau, G.: Measurements of water vapor isotope ratios with wavelength-scanned cavity ring-down spectroscopy technology: new insights and important caveats for deuterium excess measurements in tropical areas in comparison with isotope-ratio mass spectrometry, Rapid Commun. Mass Sp., 25, 3469–3480, 2011.

Uemura, R., Matsui, Y., Yoshimura, K., Motoyama, H., and Yoshida, N.: Evidence of deuterium excess in water vapor as an indicator of ocean surface conditions, J. Geophys. Res.-Atmos., 113, D19114, doi:10.1029/2008JD010209, 2008.

van As, D. and van den Broeke, M. R.: Structure and dynamics of the summertime atmospheric boundary layer over the Antarctic Plateau: 2. Heat, moisture, and momentum budgets, J. Geophys. Res.-Atmos., 111, D07103, doi:10.1029/2005JD006956, 2006.

van As, D., van den Broeke, M. R., and Helsen, M. M.: Structure and dynamics of the summertime atmospheric boundary layer over the Antarctic Plateau: 1. Measurements and model validation, J. Geophys. Res.-Atmos., 111, D07102, doi:10.1029/2005JD005948, 2006.

Van Hook, W. A.: Vapor pressures of the isotopic waters and ices, J. Phys. Chem., 72, 1234–1244, 1968.

Waddington, E. D., Steig, E. J., and Neumann, T. A.: Using characteristic times to assess whether stable isotopes in polar snow can be reversibly deposited, Ann. Glaciol., 35, 118–124, 2002.

Werner, M., Langebroek, P. M., Carlsen, T., Herold, M., and Lohmann, G.: Stable water isotopes in the ECHAM5 general circulation model: Toward high-resolution isotope modeling on a global scale, J. Geophys. Res.-Atmos., 116, D15109, doi:10.1029/2011JD015681, 2011.

Winkler, R., Landais, A., Sodemann, H., Dümbgen, L., Prié, F., Masson-Delmotte, V., Stenni, B., and Jouzel, J.: Deglaciation records of ^{17}O-excess in East Antarctica: reliable reconstruction of oceanic normalized relative humidity from coastal sites, Clim. Past, 8, 1–16, doi:10.5194/cp-8-1-2012, 2012.

6.3 Study of the moisture origins

6.3.1 Impact of turbulence on the intermittency of the relationship between isotopic composition and temperature

In this section, we rapidly go back on the impact of turbulence on isotopic composition signal in the vapour mentioned in previous section. As indicated by the more important Richardson number during the Regime 1, in particular at night, the lower layers of the atmospheric boundary layer are stratified and a suppression of the diurnal cycle of water vapour isotopic composition is observed. Figure 6.7a shows a schematic of the processes involved in the suppression of the water vapour isotopic composition cycles in the boundary layer. Temperature diurnal cycles at the surface create variations in the fractionation at the phase transition between vapour and ice. Because of these temperature variations, snow still faces sublimation/condensation cycles and exchanges isotopes with the first layer of water vapour (layer 0 on the graph). But because of the stratified boundary layer, the signal is not able to be advected up. This also leads to a reduce reservoir of water vapour the snow can exchange with, therefore, in such a situation, we expect a smaller impact of post-deposition by sublimation/condensation cycles though we have not been able to confirm this hypothesis by observations yet. Even for a weakly-turbulent atmospheric boundary layer (such as described by Zilitinkevich et al. [2008]), we can expect to observe a weaker propagation of the surface signal in isotopic composition toward the boundary layer. Indeed, a lasting stratified boundary layer is unlikely to be observed in summer at Dome C, but our conclusions can be extended to an intermittently weakly turbulent boundary layer. At Summit, Berkelhammer et al. [2016] report similar stable atmospheric conditions during which the atmospheric vapour near the surface is apparently isolated from the free troposphere. In these stable conditions, we still expect to observe diffusion of moisture in the boundary layer (especially because of the gradient of temperature and of humidity). Even though molecular diffusion is less efficient than eddy diffusion, this might lead to a net flux of moisture. As shown by Casado et al. [2016a], the diffusion of water in the air creates fractionation, therefore we expect that even in stratified conditions, the moisture exchanges can alter the vapour isotopic composition, still it has not been observed yet in Antarctica.

During the regime 2, we observe full complete diurnal cycles in water vapour isotopic composition. Indeed, during this regime, strong winds and a more turbulent boundary layer mixed more efficiently the first layers of the boundary layer, in particular, lifting the signal of water vapour isotopic composition from the surface to higher up in the boundary layer. This probably enables more exchanges of isotopes between the snow and water

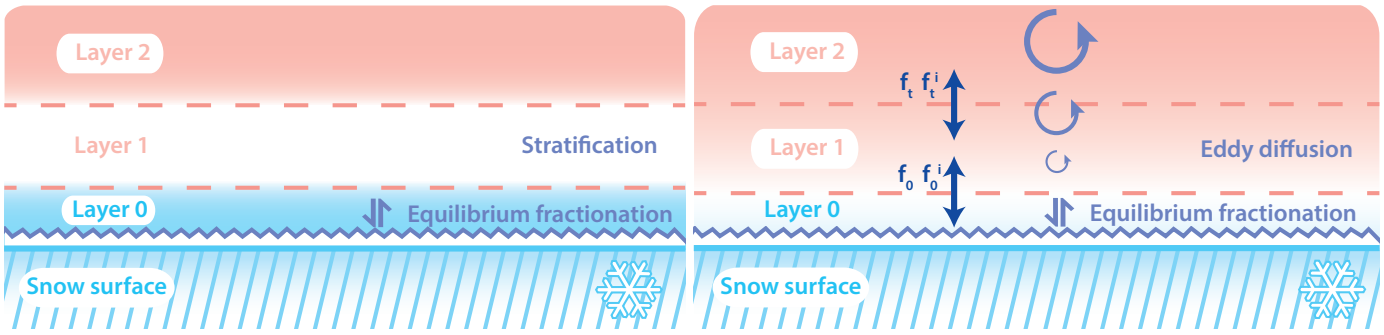

Figure 6.7: Schematic of the impact of turbulence on the water vapour isotopic composition: left, stratified regime, exchanges between vapour and snow still occur but the vapour is not mixed efficiently, right, turbulent regime, vapour and snow can exchange freely because eddy diffusion provides a large reservoir of water vapour.

vapour and should trigger post deposition effects of sublimation/condensation cycles on snow isotopic composition. This will be discussed more thoroughly in section **??**.

6.3.2 Source of moisture

In both cases, the first hypothesis is that the main source of vapour is from exchanges with the snow pack which is not validated. Indeed, if the mean water vapour isotopic composition matches the values predicted by equilibrium fractionation with the snow, as described in section 6.2, the slope between δD and $\delta^{18}O$ cannot be properly predicted, no matter which fractionation coefficients are used. If Ellehoj's fractionation coefficients seem more appropriate to predict both the values of isotopic composition and the slope between the isotopic compositions, they still fail to predict it precisely.

In section 6.2, we showed that the "remote origin" hypothesis was not compatible with the slope between δD and $\delta^{18}O$. We used the MCIM (a Rayleigh model) tuned with a transect from Terra Nova Bay to Dome C to evaluate the slope between δD and $\delta^{18}O$ and found a slope higher than the one of the vapour at Dome C (6.1 ‰/‰ for the Rayleigh distillation against roughly 5‰/‰ for the measurements). The "remote origin" hypothesis, defined by a Rayleigh distillation from a unique source was therefore rejected. Still, the slope obtained for the vapour created only from local sublimation of snow using equilibrium fractionation is not equal to the one found in the vapour. To explain this difference, we propose two hypothesis: (1) the vapour has been formed from an extreme Rayleigh distillation followed by a refill of moisture near the surface in a nearby location (within $100\,km$) where the isotopic composition is not necessarily equal to the one found at Dome

C or (2) the parametrisation of the exchanges with the local snow through equilibrium fractionation is not relevant or badly parametrised.

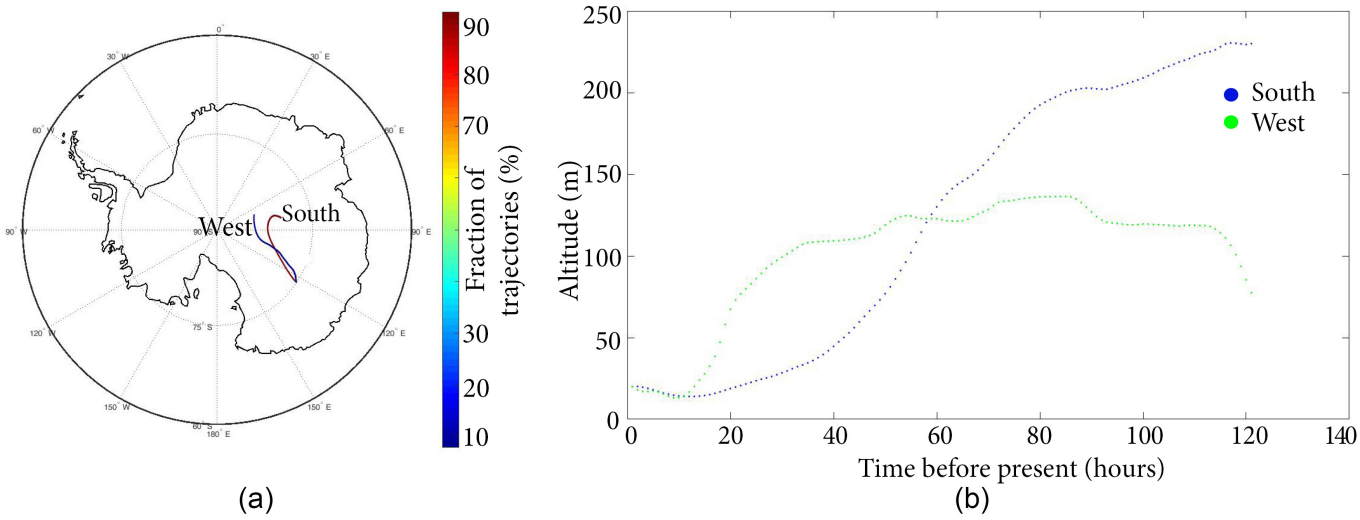

Figure 6.8: Backtrajectories of the air masses to Concordia from the 5th of January 2015 to the 17th of January 2015 realised using the software HYSPLIT: a) average backtrajectories on a map of Antarctica of clusters of the direction of transport of the air masses of the last 2 steps, only trajectories from the South are really visible, b) altitude of the air parcel along the backtrajectory

First, we test the "refill" hypothesis. Back trajectory analyses indicate that all the air masses are originating from further inland mostly from the south (figure 6.8). These analyses indicate that air parcels have been near the ground level for more than 30 km (in the dataset used to compute the backtrajectory, the first layer is from 0 to 20 m), which enable important exchanges between the moisture of these parcels and the snow surface for tens of kilometres before reaching Dome C in particular considering the low windspeed encountered at Dome C (below 5 $m.s^{-1}$), this range of distance corresponds to several hours. In this case, the dry air masses could get refilled with moisture near the surface which is not included in the MCIM. This refill would lead to isotopic composition of the vapour close to equilibrium fractionation with the snow. In this case, the air masses are coming from further south. The classical trajectory computed in the MCIM is not going by 30 km further South Dome C. It could be modelled by integrating an extreme distillation down to 30 km South of Dome C and then computing a refill by sublimation of the snow.

It is expected that snow from further inland would be more depleted in heavy isotopes because it is further away on the Rayleigh distillation path. Indeed, a recent publication by Genthon et al. [2015] indicates that over the 25 km North and South of Dome C,

there is a gradient of accumulation of 10% (lowest value 25 km South of Dome C). This indicates that the region farther South Dome C is further away on the Rayleigh distillation path, and that the snow is more depleted than in Dome C. Still, preliminary results of isotopic composition of snow from 25 km South Dome C does not support this hypothesis.

Still, if the snow is more depleted, the vapour formed would also be more depleted, in addition of the slope between δD and $\delta^{18}O$ being lower. The "refill" hypothesis further south is therefore not completely satisfactory. This suggests the second hypothesis: the temperature dependency of the equilibrium fractionation at low temperature is perhaps not well estimated. We additionally tested to include kinetic fractionation, with a similar formulation than Jouzel and Merlivat [1984] and it was not possible to match the value of the slope (the slope obtain for the vapour isotopic composition was then below 2‰/‰, not shown). A complete understanding of the origin of the moisture would require a model including isotopes and able to evaluate several sources and mixing of air masses. We believe the regional model MARiso will be perfectly suited for this kind of study.

6.4 Comparison with other measurements from East Antarctica

A similar campaign was realised at Kohnen station (located at 75° 00' S, 00° 04' E, 2892 m above see level, see the map in Fig. 1.2) in 2013/14 by Francois Ritter [Ritter et al., 2016] where important diurnal oscillations were also intermittently observed. Kohnen station is located lower on a slight slope which enables katabatic winds. Additionally, Kohnen site is warmer with an average temperature of -44.5°C and the accumulation is higher: 64 $kg.m^{-2}.yr^{-1}$. Despite the presence of katabatic winds, Ritter et al. [2016] found that the diurnal variability is predominant in the variations of water vapour isotopic composition and they attribute it to the exchanges between snow and vapour (see Fig. 6.9b).

Figure 6.9 presents the comparison of the mean diurnal cycle of turbulent regime at Dome C with the mean diurnal cycle of a sample of large amplitude days in Kohnen. Despite temperature being higher at Kohnen, similar temperature diurnal cycles characterise both sites. The wind speed is more important at Kohnen except at night when it falls to almost 0 $m.s^{-1}$, this is a typical feature of katabatic winds. Water vapour isotopic composition at Dome C is more depleted than in Kohnen due to its more remote location on the Rayleigh distillation path. Still, we observe similar amplitudes of water vapour isotopic composition cycles in Dome C (38‰ for δD) and in Kohnen (36‰ for δD).

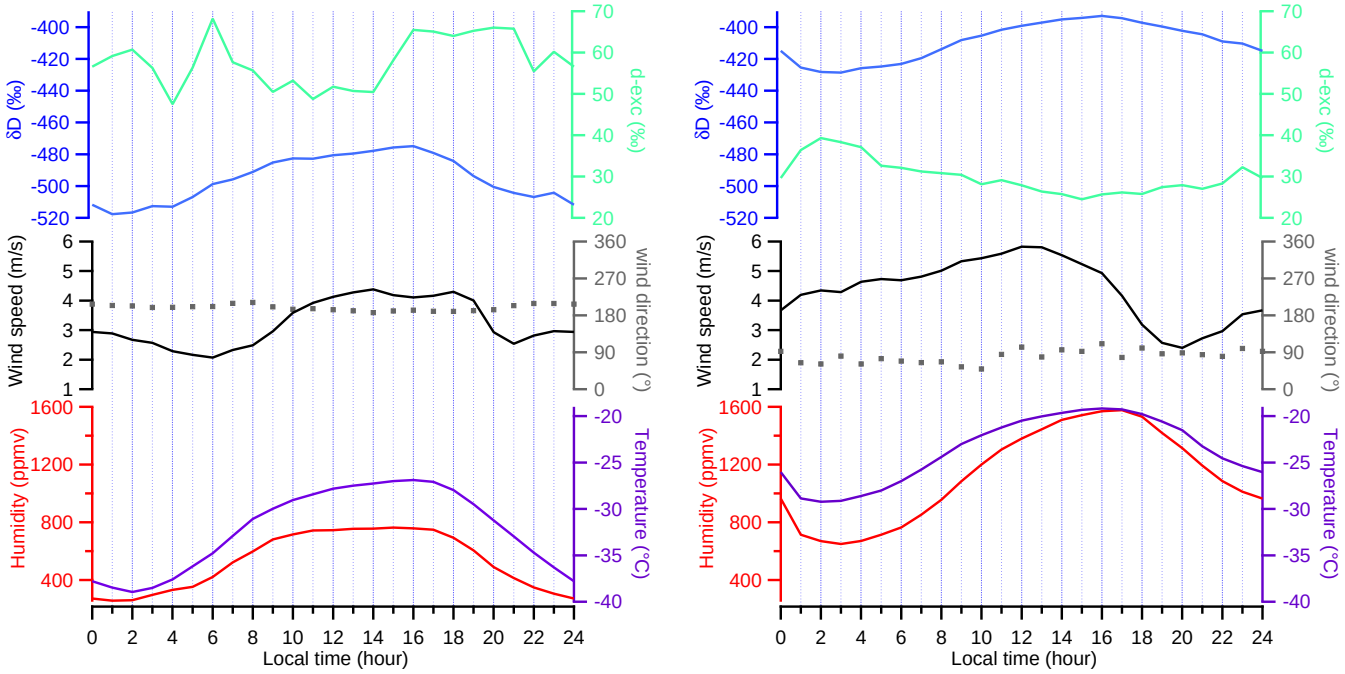

Figure 6.9: Comparison of the measurements of water vapour isotopic composition mean diurnal cycles in (a) Dome C and in (b) Kohnen for in both cases days with important diurnal cycles: regime 2 in the case of Dome C and 18 days scattered in the dataset for Kohnen [Ritter et al., 2016]

Keeping the hypothesis that the first contribution to the isotopic composition of the vapour are the vertical fluxes of moisture from/to the snow, the results from Kohnen generalise our results from Dome C to a large range of places over the East Antarctic Plateau. Indeed, the amplitude of variations of humidity and isotopic composition of the vapour at Kohnen and Dome C are similar. To conserve a neutral mass budget, this requires amplitudes of variations of snow isotopic composition of the same order of magnitude, and thus that the post deposition due to condensation/sublimation should be of the same order of magnitude. As accumulation is 3 times larger in Kohnen than at Dome C, we expect a smaller impact in Kohnen than at Dome C. More studies inland Antarctica would strengthen our knowledge of the processes affecting water vapour isotopic composition. Additionally, these results only focus on the diurnal scale and extension to seasonal scale requires year long water vapour isotopic composition monitoring.

To our knowledge, these two sites (Dome C and Kohnen) are the only two inland sites in Antarctica where water isotopes in the vapour have been measured. Still, in Green-

land, Steen-Larsen et al. [2013] has monitored water vapour isotopic composition and compared it to snow. Climatic conditions at NEEM are warmer than in Dome C and in Kohnen and the distillation path is much shorter and therefore, the water vapour isotopic composition is enriched at NEEM compared to Dome C. This is clearly visible in the slopes between δD and $\delta^{18}O$. At NEEM, the slope was estimated by Steen-Larsen et al. [2013] around 6.5‰/‰, this is higher that in Kohnen where it was estimated by Ritter et al. [2016] around 6.0‰/‰ which is also higher than at Dome C where it is only 5.3‰/‰ [Casado et al., 2016b]. This reflects the impact of continentality over the slope between δD and $\delta^{18}O$, and it is associated with an artificial increase of $d-excess$. Still, already at NEEM, Steen-Larsen et al. [2014a] found that the exchanges between water vapour and snow surface were impacting the isotopic composition not only of the vapour but also of the snow. Because of the very low precipitation rate at Dome C, it is the perfect location to estimate the impact of the exchanges between water vapour and snow on the snow isotopic composition.

The amount of sublimated/condensed snow required for this range of modification of the vapour isotopic composition is difficult to estimate as we are not in a closed box system, and therefore, a large part of the flux influences layers higher than the measurement height or even than the atmospheric boundary layer most likely. Ritter et al. [2016] realised a closed box model to estimate the variations of vapour isotopic composition computing only thermodynamic properties at equilibrium during an average diurnal cycle. They show that a snow reservoir of 5 mm provides enough vapour to observe variations of the vapour isotopic composition 2 times larger than observed. This overestimation is most likely due to closed system. In section 7.2.3, we will show in experimental data that the amount of water involved in one frost deposition event during a normal night at Dome C can reach amounts larger than what would be necessary to justify the range of evolution of the water vapour content observed here.

6.5 Perspective for new water vapour measurements

In 2015/16, Frederic Prie went to Concordia station to realise a second study, the first preliminary results are presented in Fig. 6.10. During this campaign, issues with the calibration device drivers prevented from calibrating during the first three weeks of the campaign and therefore from obtaining the best possible precision from in situ infrared spectrometry. Still, cryogenic trapping and in situ measurements from the Picarro are in agreement. During 2015/16 campaign, it is not possible to separate easily two clear turbulent or stratified regimes of several days as it was for 2014/15 and it seems that turbulent

and stratified conditions tend to successively occur. Additionally, several precipitation events create gaps in the dataset that we were not able to fill by interpolation. Finally, issues with the gas handling seems to have impacted the $\delta^{18}O$ of the water vapour in the inlet of the Picarro. Indeed, if the values of the calibration are normal, the values of outside air $\delta^{18}O$ are completely out of range of what is expected for the East Antarctica Plateau (around $-30‰$, not shown). We expect that $d-excess$ will be not available for this dataset.

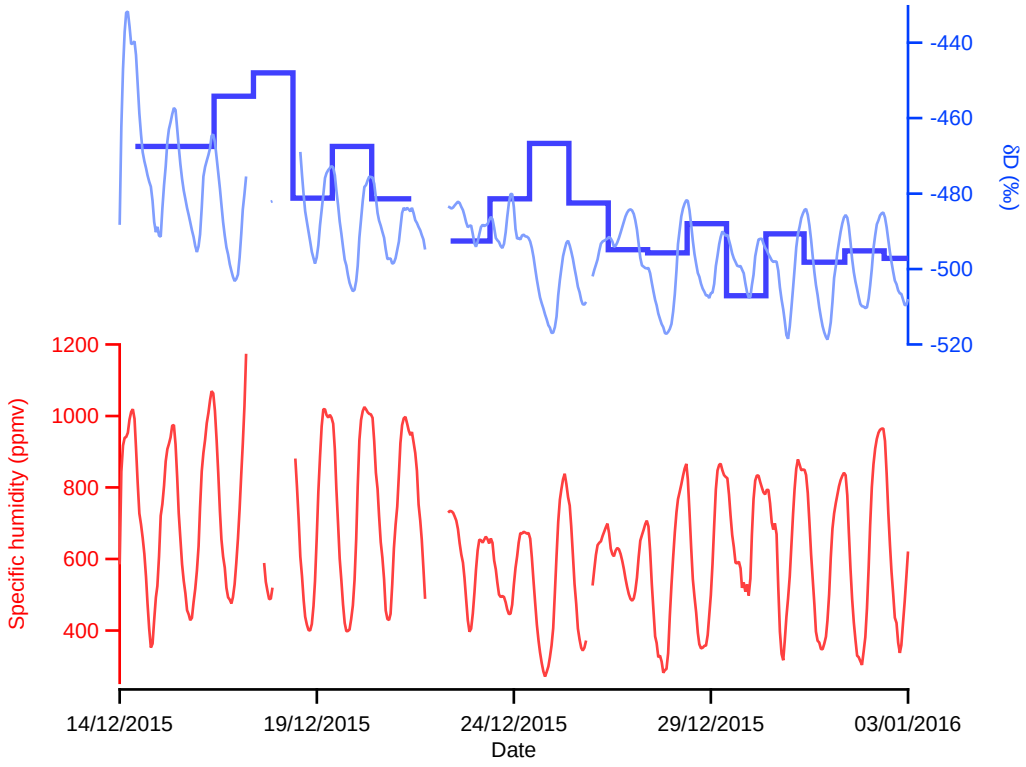

Figure 6.10: Specific humidity and water vapour isotopic composition during the campaign of 2015/16 from the Picarro (light lines) and the cryogenic trapping (dark bars)

This 2015/16 campaign benefited from the participation of Alexey Ekaykin from the AARI (Saint Petersburg) and it was possible to realise extensive snow pits studies to complete the one realised at Vostok and compare them with the vapour. The measurements of these snow pits could not be realised within the framework of my PhD.

The development of a field deployable instrument to measure water vapour isotopic composition as described in section 4.3 would enable one to measure down to humidity and temperature never measured yet. In particular, this instrument would be able to monitor the isotopic composition all year long at Dome C. This would be an extraordi-

nary opportunity to improve the constrain on physical processes affecting water stable isotopes.

Chapter 7

Archival of the water stable isotope signal in East Antarctic ice cores

This section was realised using material from a manuscript submitted to The Cryosphere

Ice is a natural archive of past climate variations. The chemical and physical compositions of the ice and of the air bubbles trapped inside are used as paleoclimate proxies [Jouzel and Masson-Delmotte, 2010]. In Greenland, ice cores provide reconstructions of past temperature from greenhouse gas concentrations and water isotopes back to the last interglacial period, 120 000 years ago [North Greenland Ice Core Project members, 2004; NEEM community members, 2013]. In Antarctica, low accumulation rates enable the reconstruction of past climate over several interglacial periods, e.g. 420 000 years at Vostok [Petit et al., 1999b] and 800 000 years at Dome C [EPICA, 2004, 2006]. Even though reconstructions from ice cores from Greenland do not extend as far back as from Antarctic's ice cores, high resolution analyses of the cores from Greenland provide very fine temporal resolution and can even resolve the seasonal cycle [Vinther et al., 2010]. Seasonal variations are also imprinted in the snow isotopic composition of high accumulation sites of coastal areas of Antarctica [Morgan, 1985; Masson-Delmotte et al., 2003; Küttel et al., 2012]. For low accumulation sites as found on the East Antarctic Plateau, there is no consensus whether ice core records can reveal the climatic signal at resolutions finer than multidecadal [Baroni et al., 2011] or not [Ekaykin et al., 2002; Pol et al., 2014]. Ekaykin et al. [2002] analysed multiple pits from Vostok and identified large spatio-temporal variations caused by post-deposition associated with surface topography and wind interactions. These non-climatic phenomena creates high frequency signal in single cores, which calls for stacking isotopic composition profiles from several snow pits to distinguish the common climatic signal from this post-deposition noise. Still, on the East Antarctic Plateau, a significant seasonal cycle is depicted in the isotopic composition

of the precipitation [Fujita and Abe, 2006; Landais et al., 2012a; Stenni et al., 2016] and of the surface snow [Touzeau et al., 2016]. So far, whether this seasonal cycle is archived or not in buried snow, and thus, whether stacking an array of snow pits permits to increase the signal to noise ratio and depict a climatic record at the seasonal scale from water isotopic signal remain unclear [Ekaykin et al., 2014; Altnau et al., 2015; Münch et al., 2016].

Several studies have focused on understanding how is the climatic signal archived in the isotopic composition of snow and ice on the East Antarctic Plateau. Since the early works of Dansgaard [1964] and Lorius et al. [1969], the relationship between ice isotopic composition and local temperature has been attributed to the distillation associated with the successive condensation events on the path from the initial evaporation site to the deposition site. Nevertheless, the relationship between isotopic composition and surface temperature is not constant through time and space, due notably to processes within the boundary layer [Krinner et al., 1997], the seasonality of the precipitation between glacial and interglacial periods [Sime et al., 2009], variations in the air masses transport trajectories [Delaygue et al., 2000; Schlosser et al., 2004] and evaporation conditions [Vimeux et al., 1999]. For Central East Antarctica, the glacial-interglacial isotope-temperature relationship appears quite close to the spatial gradient (Werner et al., in prep), but its validity for inter-annual variations [Schmidt et al., 2007] and warmer than present-day conditions [Sime et al., 2009] is challenged.

In addition, under the exceptionally cold and dry conditions of the East Antarctic drilling sites, the contribution of post-deposition processes to the isotopic composition of the surface snow cannot be neglected [Town et al., 2008; Sokratov and Golubev, 2009]. It has been recently evidenced that summer exchanges between snow and water vapour at the surface significantly affect the isotopic composition of the snow both in Greenland [Steen-Larsen et al., 2014a] and on the East Antarctic Plateau [Ritter et al., 2016]. In the first top metres of the snowpack, isotope exchanges involved during the snow metamorphism and the diffusion within the porous matrix additionally affect the isotopic composition of the snow [Langway, 1970; Johnsen, 1977; Whillans and Grootes, 1985]. The diffusion length associated with these processes depends on the firn ventilation, the snow density and the exchange rate between the atmospheric water vapour and the surface snow [Waddington et al., 2002; Schneebeli and Sokratov, 2004; Sokratov and Golubev, 2009]. This wide range of processes hampers the interpretation of the isotopic signal, in particular it is not clear how much of the original signal acquired during the formation of the precipitation is conserved during the burial of the snow.

Due to the extreme conditions on the East Antarctic Plateau, the general understanding of the processes involved in the hydrological cycle (out of any isotopic consideration) is not straightforward, and there remains open questions such as the definition of the accumulation, the estimation of the mass balance or the impact of snow metamorphism on the albedo feedback loop. In the case of accumulation, the low amount of precipitation [Petit et al., 1982; Frezzotti et al., 2007; Genthon et al., 2015] and the important contribution of blowing snow in the total deposition [Groot Zwaaftink et al., 2013; Picard et al., 2016a] creates patchiness in the accumulation, resulting in large uncertainties in the determination of the real precipitation amounts. Snow metamorphism is difficult to quantify due to the large noise created by the spatial variability, requiring a large number of samples every day. Using passive microwave satellite data, Picard et al. [2012] argue that the grain index is an indicator of the coarsening of snow grains and show its increase in summer to be anti-correlated with the integrated summer precipitation amount. Supersaturation is estimated from the combined measurements of humidity and temperature, both of which are complexified by the extreme conditions in Antarctica [Genthon et al., 2016]. Including water isotopic composition as a tracer of the interactions between the snow pack and the atmospheric boundary layer could help refine our knowledge of the processes involved in the hydrological cycle in these regions.

Recent studies have focused either on the monitoring of the isotopic composition of the snow pack on the East Antarctic Plateau [Touzeau et al., 2016], of the precipitation [Fujita and Abe, 2006; Landais et al., 2012a; Stenni et al., 2016], or of the atmospheric water vapour [Casado et al., 2016b; Ritter et al., 2016]; exploring their links to climatic parameters and the implications for post-deposition processes during the archival of the climatic signal by the snow isotopic composition. Here, we study the isotopic composition of the continuum between atmospheric vapour, precipitation, surface and buried snow. To do so, we combine different datasets from the East Antarctic Plateau, based on published studies and new results, in order to qualitatively characterise the different processes affecting surface snow isotope composition at different time scales. We first report and compare the different methodologies applied for sampling surface snow, snow pits, precipitation and water vapour in the atmosphere (Section 2). Then, we present the results from these different studies including surface snow measurements over several years, precipitation measurements, vapour and snow measurements and snow pits sampling (Section 3). Finally, we discuss the impact of post-deposition processes at the snow surface through the exchanges between the snow and the vapour and within the firn (Section 4) before summarising our key conclusions.

7.1 Sampling of snow on the East Antarctic Plateau

7.1.1 Sites

The East Antarctic Plateau is a high elevation area, over 2500 metres above sea level ($m\,a.s.l.$) covered with snow and ice spreading on most of the eastern continental part of Antarctica (Fig. 7.1). The East Antarctic Plateau is characterised by mean annual temperatures below $-30°C$ and accumulation below $80 kg.m^{-2}.yr^{-1}$, as illustrated in Fig. 7.1.

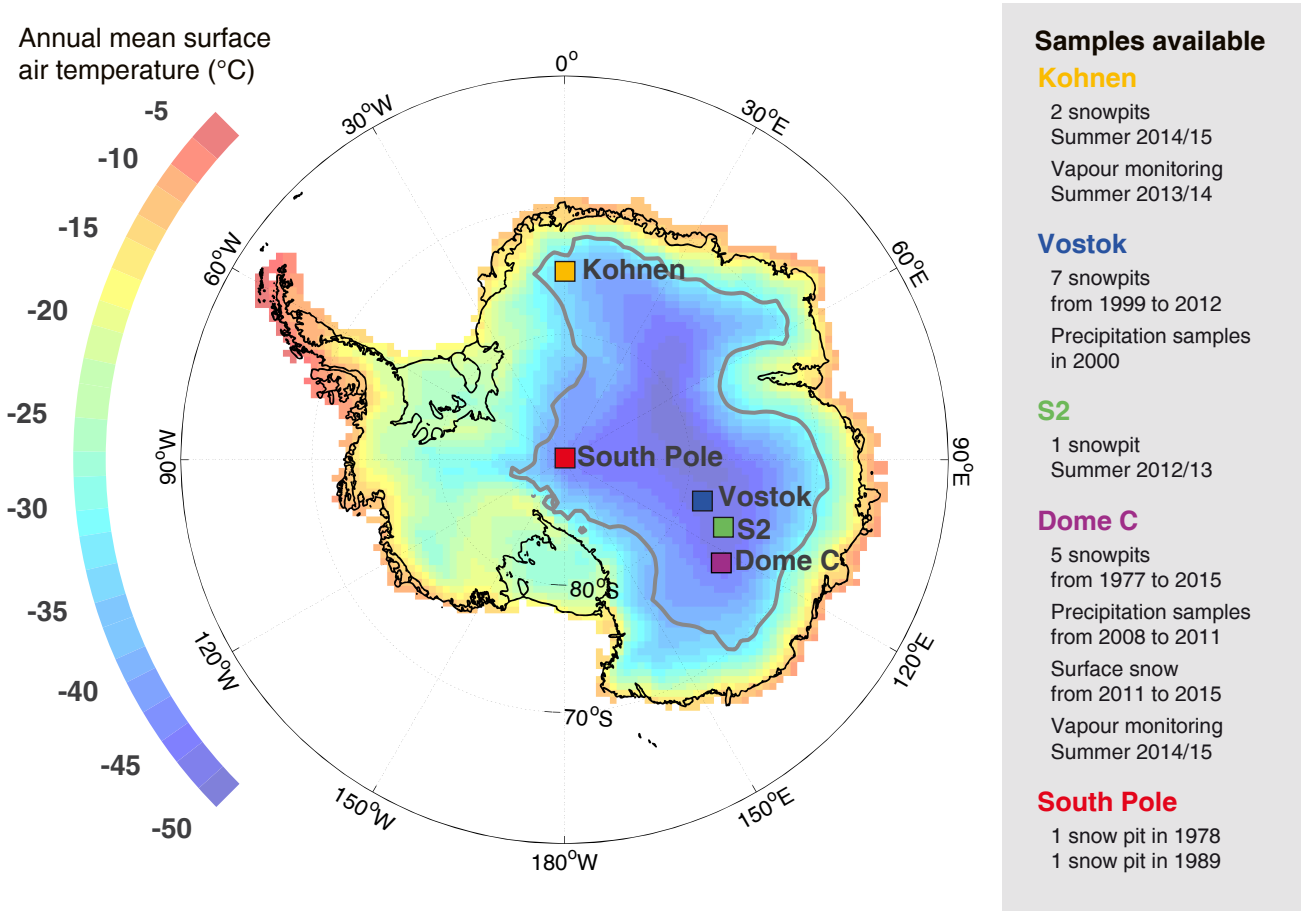

Figure 7.1: Map of Antarctica highlighting the East Antarctic Plateau (grey line = contour of 2500 m a.s.l. elevation) indicating the location of the sampling sites (solid squares) included in this work. Colours indicate the annual mean surface air temperature at 2 m modified from the ERA-interim dataset from 1979 to 2009 [Nicolas and Bromwich, 2014].

This study mainly focuses on Dome C, the site of the Concordia overwintering station, enabling year-long operations and thus giving the rare opportunity to study the entire seasonal cycle of isotopic composition. We extend the results to the entire East Antarctic Plateau by comparing the data from Dome C to observations from the Kohnen, Vostok and

Amundsen-Scott South-Pole stations and from the point S2 which is one of the drilling sites of the campaign Explore-Vanish joining Dome C and Vostok (see Fig. 7.1). These locations span a large range of climatic conditions of the East Antarctic Plateau as illustrated on Table 7.1.

Table 7.1: Climatic conditions at the different sites used in this study [Alley, 1980; Petit et al., 1982; Wendler and Kodama, 1984; Oerter et al., 2000; Ekaykin et al., 2002; van As et al., 2007; Lazzara et al., 2012; Casey et al., 2014; Genthon et al., 2015; Touzeau et al., 2016; Laepple et al., 2016]

Site	Location	Altitude (m a.s.l.)	AWS mean temperature (°C)	10 m firn temperature (°C)	Accumulation ($kg.m^{-2}.yr^{-1}$)	Mean wind speed ($m.s^{-1}$)
Kohnen	75.0°S - 0.1°E	2892	-42.2	-44.5	62 - 73	4.5
Vostok	78.5°S - 106.8°E	3488	-55.2	-57	21	5.1
S2	76.3°S - 120°E	3229	NA	-55.1	21	NA
Dome C	75.1°S - 123.3°E	3233	-52.4	-54.3	27	3.3
South Pole	90°S - 0°E	2835	-49.3	-50.8	69	4.1

7.1.2 Surface snow and precipitation sampling

Precipitation and surface snow have been sampled at Dome C regularly by different teams since 2008. Here, we report new measurements of precipitation and surface snow together with previously published data from Stenni et al. [2016] and Touzeau et al. [2016] (see Table 7.2). Because different teams were in charge of the different sampling activities, the protocols differ between the years (Table 7.2).

The sampling protocol of the 2011 campaign (SUNITEDC) has been precisely described by Touzeau et al. [2016]: the upper first millimetres of snow (1 to 5 mm) were gathered every 1-2 weeks using a metallic blade over a surface of 20 per 20 cm. This leads to samples of approximately 20 mL. The sampling areas were randomly picked provided the surface was flat.

During the NIVO project (from 2013 to 2015), the surface snow was gathered by sampling roughly 15 mm of snow with a corning flask over a surface of 20 per 10 cm. This led to samples of approximately 50 mL. The sampling areas of 2013/14 were chosen randomly in a 100 per 100 m "clean area" near the Atmospheric Shelter in parallel with density and specific surface area (SSA) measurements (see section 7.1.4). Two samples were collected during each collect and we present here the average value of the two sam-

Figure 7.2: Impact of the surface snow sampling, approximately 20 per 10 *cm* of snow are gathered. The surface conditions vary a lot at the meter scale with the presence or not of frost hoar.

ples. In addition, during summer 2013/14, regular samplings of surface and sub-surface snow were performed for almost 2 months. The surface samples were gathered using a corning flask from 0 to 3 *cm* depth. The sub-surface samples were gathered by the same tool from 3 to 6 *cm* depth. In 2014/15, an additional sampling took place within the GLACIO project twice a day from December 2014 to January 2015 near the location of the inlet used for water vapour monitoring (See section 7.1.4 and Casado et al. [2016b]) following the same protocol.

Sampling of surface snow and precipitation isotopic composition were carried out in parallel by the Italian winterover crews (program PRE-REC). Precipitation samples have been collected all year round on a 80 per 120 *cm* wooden table standing 1 *m* above the ground level 800 *m* from Concordia Station from 2008 to 2011. The samples were collected at 1 a.m. every day if the amount was sufficient. The surface snow samples were gathered from an adjacent wooden plate of 80 per 120 *cm* at ground level. If the amount of snow on this second table was sufficient, snow samples were collected. Both precipitation and surface snow samples were sealed into date-labelled plastic bags and preserved in frozen state until delivery and measurement in Italy. For the precipitation samples, the protocol is detailed by Stenni et al. [2016]. It is important to note that the protocol of sur-

face snow sampling from the PRE-REC campaign differ greatly from the protocols from the NIVO and SUNITEDC programs due to the presence of the wood plate.

Table 7.2: Summary of the different campaigns of surface snow and precipitation samplings presented here.

Project	Location	Years	Resolution (days)	Reference
SUNITEDC (French)	Surface snow	2011	7	[Touzeau et al., 2016]
PRE-REC (Italian)	Precipitation Surface snow	2008 to 2011 2012 and 2014	1 7	Partially in [Stenni et al., 2016] This study
NIVO (French)	Surface snow Sub-surface	2013 to 2016 11/2013 to 01/2014	3 1	This study
GLACIO (French)	Surface snow	12/2014 to 01/2015	1	This study

7.1.3 Snow pits sampling

We present profiles of isotopic composition sampled in snow pits at Dome C : two unpublished profiles from the first preliminary campaigns at Dome C in 1978 and two new snow pit profiles obtained in 2014/15, dug 50 m apart in parallel with surface snow sampling and vapour monitoring. For one of them, snow temperature and density profiles were established. The samples were taken in plastic flasks and analysed later on in the laboratory. To extend the results to other sites of the East Antarctic Plateau, we additionally present snow pit samplings performed through several campaigns over different sites of East Antarctica which were realised and analysed by different teams. An example of a snow pit being dug is shown of figure 7.3.

Two new isotopic composition profiles from Kohnen are extracted from trenches, following the methodology reported in Münch et al. [2016] but down to 3.6 m depth sampled at a 3 cm vertical resolution. The two profiles are separated by approximately 500 m. A large number of snow pits from Vostok station are presented here, they have been previously described in Ekaykin et al. [2002, 2004] and Ekaykin and Lipenkov [2009]. We combine the results from six snow pits with depths varying from 2.5 m to 12 m and a minimum resolution of 5 cm. In addition, snow pits from the Explore-Vanish campaign are included comprising one 3.5 m deep snow pit from Vostok, one 2.6 m deep from S2 and one 2 m deep from Dome C, all of them including triple isotopic compositions ($\delta^{18}O$,

Figure 7.3: Picture of the realisation of a snow pit realised at Dome C in January 2015

$\delta^{17}O$ and δD) published in Touzeau et al. [2016]. Finally, we include two snow pits from South Pole [Jouzel et al., 1983; Whitlow et al., 1992].

7.1.4 Atmospheric and snow surface monitoring

Water vapour isotopic composition has been measured at Kohnen station in 2013/14 [Ritter et al., 2016] and at Dome C in 2014/15 [Casado et al., 2016b]. In both cases, to reduce the noise, the dataset were averaged to hourly resolution and cover approximately one month. In parallel to water vapour isotopic composition monitoring, surface snow was sampled once to twice a day. For a period from 27 hours to 72 hours, the surface snow

Table 7.3: Summary of the different snow pits presented in this study.

Station	Years	Resolution (cm)	Number of pits	Reference
Vostok	2001 to 2015	2 to 5	6	Ekaykin et al. (2002, 2004, 2009)
	2012/13	3	1	Touzeau et al. [2016]
Kohnen	2012/13	3	2	Münch et al. [2016]
Dome C	1977/78	1 to 3	2	This study
	2012/13	3	1	Touzeau et al. [2016]
	2014/15	1.5 to 5	2	This study
S2	2012/13	3	1	Touzeau et al. [2016]
South Pole	1978	2	1	Jouzel et al. [1983]
	1989/90	1.1	1	Whitlow et al. [1992]

was sampled every hour to evaluate the diurnal cycle of both the vapour and the snow isotopic composition (see section 7.1.2).

Dome C hosts a large set of instruments probing the troposphere and the firn justifying to focus this study on this site. Here, we make use of temperature, wind speed and humidity measurements from the 45m meteorological profiling system described by Genthon et al. [2013]. The temperature and humidity observations are performed using ventilated thermohygrometers HMP155 and are therefore free of radiation biases [Genthon et al., 2011]. The temperature reanalysis product (ERA interim) has been compared to ventilated automatic weather station data (AWS) from Genthon et al. [2013] and we found a good agreement at the seasonal scale and fairly good agreement at the event scale (not shown here). Depending on data availability (as the ventilated AWS were installed at Dome C in 2009), we will use either ERA-interim or measurements from AWS. An intercomparison when the two datasets are overlapping reveals that most of the variability from the day-to-day to the seasonal and inter-annual scales in captured by ERA-interim and major differences appear only for the evaluation of the diurnal cycle (not shown). Wind speed and direction are measured using Young 05103 and 05106 aerovanes. Snow surface temperature is measured with a Campbell scientific IR120 infrared probe located $2\,m$ above ground level.

Finally, we include grain index observations [Picard et al., 2012] obtained by satellite measurements. The grain index is used as an indicator of the evolution of the size of the snow grains, and provides a qualitative evaluation of metamorphism. When available,

we include Surface Sensitive Area (SSA) measurements also as an indicator of metamorphism [Libois et al., 2015]. These optical methods are completed with snow surface observations. Frost deposition was monitored with a time lapse of the growth of hoar at the surface (see the video at https://vimeo.com/170463778). An image processing script was used to characterise the growth of a few crystals at the surface of the sastruga.

7.1.5 Modelling approaches

To highlight the impact of post-deposition processes, it is necessary to present how the surface snow isotopic composition differs from the initial precipitation signal formed during the Rayleigh distillation. Here, we make use of the Rayleigh-type Mixed Cloud Isotope Model (MCIM) developed by Ciais and Jouzel [1994] which computes the Rayleigh distillation along the air masses trajectories. The model includes microphysical properties of clouds and in particular takes into account mixed phase conditions. It is tuned with triple snow isotopic composition measured along a transect from Terra Nova Bay to Dome C [Landais et al., 2008]. This tuning has been proven suitable to evaluate the variations of isotopic composition at Dome C [Winkler, 2012]. This will provide a comparison between the spatial and the temporal slope of precipitation isotopic composition at the seasonal scale.

7.2 Results

In this section, we review the results from the different datasets, illustrating the different steps of the archival of climatic signal by the snow isotopic composition, from the precipitation to the buried snow (see Fig. 7.4).

We first present precipitation isotopic composition variations based on data from Stenni et al. [2016] and additional new data. We then present our new data of surface snow isotopic composition compared to the variations in $2\,m$ surface air temperature, the grain size index and the precipitation isotopic composition, in order to evaluate at the day-to-day and at the seasonal scales the difference between surface snow and precipitation isotopic signals. We then report short time scale parallel measurements of vapour and surface snow isotopic composition, providing inputs on one of the major component of summer metamorphism on surface snow isotopic composition: the diurnal cycles of sublimation/condensation. We finally compare the isotopic composition of the surface, sub-surface and buried snow to evaluate the processes involved during the archival of the isotopic composition signal.

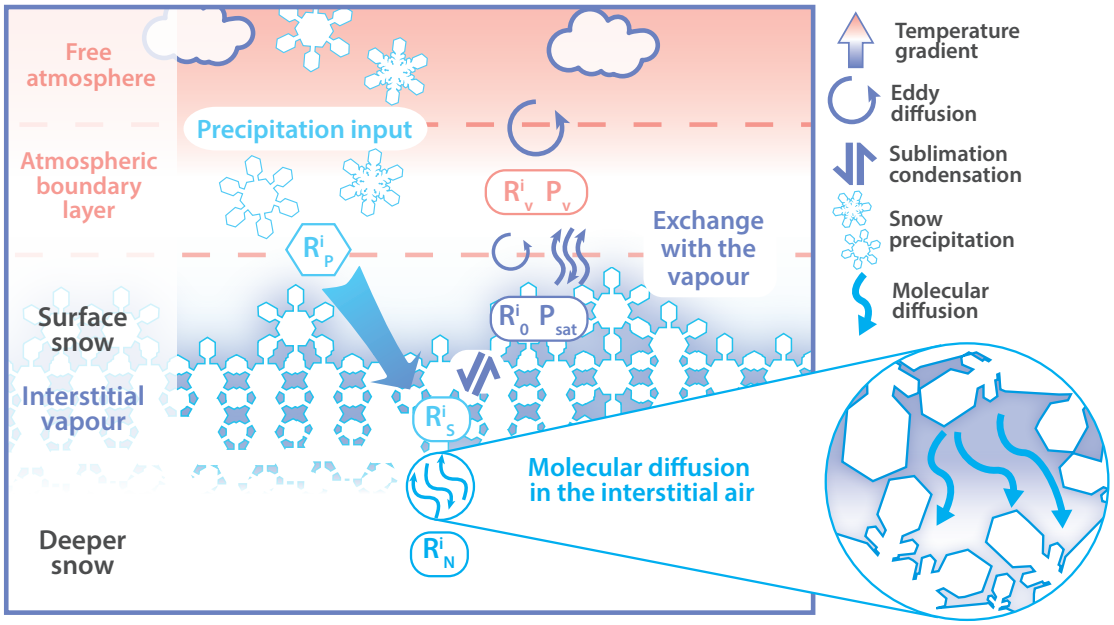

Figure 7.4: Schematic of the different contributions to the snow isotopic composition (R^i_X stands for the composition of isotope i in the phase X) in remote Polar Regions: above the surface, both the precipitation and the sublimation/condensation cycles can contribute to the surface composition; in the open-porous firn below the surface, the snow can exchange with the air below the surface, enhanced or not by wind pumping. Deeper in the firn, molecular diffusion in the interstitial air affects the snow isotopic composition.

7.2.1 Precipitation isotopic composition

In this section, we present precipitation isotopic composition data at Dome C from Stenni et al. [2016] depicting 3 complete annual cycles from 2008 to 2010, completed by new, unpublished data from 2011 (Fig. 7.5).

At Dome C, the precipitation isotopic composition presents a large variability at the day-to-day scale and a regular seasonal cycle. At the seasonal scale, precipitation isotopic composition is relatively well correlated to local temperature with a slope of 0.49 ± 0.02 ‰/ °C ($R^2 = 0.63$, $n = 500$) [Stenni et al., 2016] and no apparent lag between temperature and isotopic composition variations. Compared to other year-long precipitation sampling on the East Antarctic Plateau, this slope is lower than at Dome F (0.78 ‰/°C with $R^2 = 0.78$ [Fujita and Abe, 2006]) and higher than at Vostok (0.26 ‰/°C with $R^2 = 0.58$ [Touzeau et al., 2016]). In summer, we systematically observe precipitation $\delta^{18}O$ above -40 ‰ at Dome C, whereas in winter, $\delta^{18}O$ values below -65 ‰ are systematically observed.

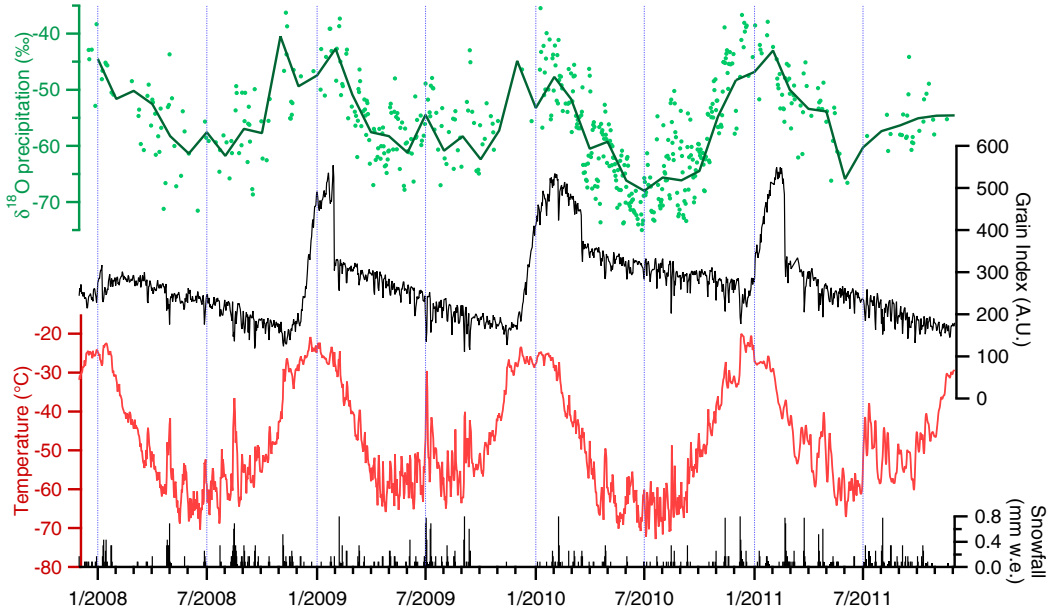

Figure 7.5: Four years (2008 to 2011) of monitoring at Dome C of the variations of precipitation isotopic composition from the PRE-REC campaign [Stenni et al., 2016] ($\delta^{18}O$, green, dots: raw data, line: monthly average) in surface air temperature from the reanalysis ERA-interim (red line), grain index from satellite observations (black line) and snowfall amount calculated from the reanalysis ERA-interim (black bars).

7.2.2 Surface snow isotopic composition

Here, we present measurements of surface snow isotopic composition at Dome C from December 2010 to January 2016 (Fig. 7.6) combining results from Touzeau et al. [2016] with new data presented for the first time in this study from the PRE-REC, NIVO and GLACIO projects. The dataset includes three complete annual cycles of surface snow isotopic composition (in 2011, 2014 and 2015) and part of the 2012 cycle, with the respective temperature variations from AWS [Genthon et al., 2013] and the precipitation events (from reanalysis products). Note here that we use the available data from AWS in this section and not reanalysis products as in section 7.2.1 (see section 7.1.4).

First, we focus on the spatial variability impact on the measurements. To disentangle the local (below 1 km) spatial variability from the temporal variations of the surface snow isotopic composition (Fig. 7.6), we compare the duplicate measurements realised during the year 2014 (Fig. 7.7). Indeed, for this year, several sets of measurements are available: one sampled at a fixed location on a wood surface (PRE-REC, blue dots) and one sampled randomly from the snow surface in a large field (NIVO, red line) as described in section 7.1.2. For the NIVO datapoints, we additionally present the raw maximum

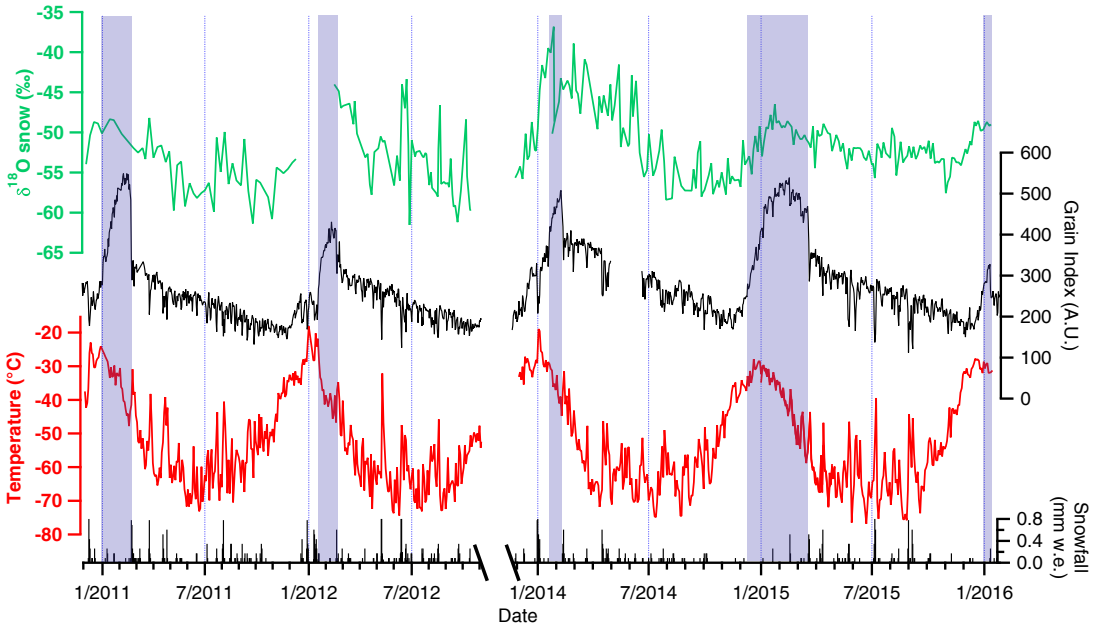

Figure 7.6: Surface snow isotopic composition ($\delta^{18}O$, green lines) sampling from December 2010 to 2015: Dec 2010 to Dec 2011, data from the project SUNITEDC [Touzeau et al., 2016]; Feb 2012 to Oct 2012, data from the project PRE-REC (this study); Nov 2013 to Jan 2016, data from the project NIVO (This study). For comparison: AWS $2\,m$ temperature measurements [Genthon et al., 2013] (red line), grain index [Picard et al., 2012] (black fine line) and precipitation (black bars) from ERA-interim reanalysis product. The blue shaded areas highlight the high grain index values (arbitrary threshold).

and minimum values obtained from duplicates. Strong differences are visible at the event scale, in particular during some events in March May and June. During these events, the very low values of the PRE-REC sampling reflect the isotopic composition of precipitation (not shown, Dreossi et al., in prep). This indicates that the sampling directly on the surface snow is a mixture of newly accumulated and existing snow and thus shows smaller variations than the wood surface and the precipitation itself. Also, when comparing the PRE-REC results to the NIVO results, there is an average difference of 4‰, which we attribute here to spatial variability. At the event scale (synoptic event of typically a couple of days), the variations of the surface snow isotopic composition exhibit an important small scale spatial variability (meter scale) due to the patchiness of the accumulation and of the frost deposition. Caution in interpretation of variations of surface snow isotopic composition at short time scale is therefore necessary. Larger statistics would be necessary to distinguish the climatic signal from the sampling variability. Still, the overall trends of the different datasets (and therefore representing different locations) are similar and demonstrate that the temporal variations are larger than the spatial variations. We estimate the spatial uncertainty of the surface snow isotopic composition measurements

to be 1.7‰ for $\delta^{18}O$ from the standard deviation calculated with the duplicates on the NIVO samples (randomly picked within 50 m).

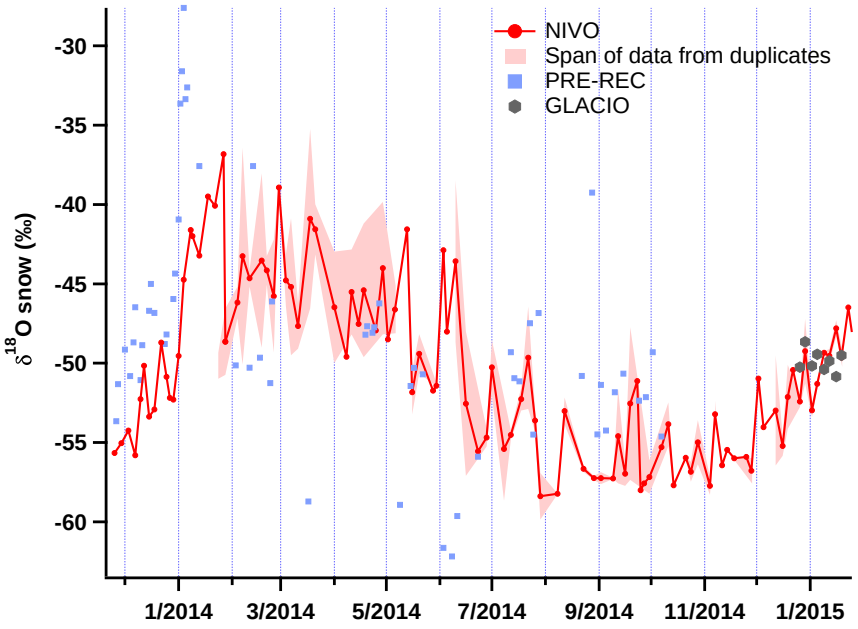

Figure 7.7: Reproducibility of surface snow isotopic composition measured in 2014. The NIVO dataset (red dots and line, duplicate span represented by the red shade, also presented in green in Fig. 7.6) is compared to measurements obtained by independent teams (PRE-REC, blue dots; GLACIO, grey hexagon) and independent methods: PRE-REC snow samples were collected from a wood table whereas NIVO and GLACIO snow samples were collected directly from the surface snow;

Second, we focus on the temporal variability at different time scales. The three years (2011, 2014 and 2015) present the typical temperature variations for the East Antarctic Plateau: a short, "warm" summer before a long, rather constant, winter as described by Van Den Broeke [1998]. Over this cycle are imprinted short warm events often associated with advection of warmer air masses and precipitation events; these warms events are particularly visible in winter. We observe a similar pattern for $\delta^{18}O$ of the surface snow: annual cycles with a steep maximum centred on January (roughly a month after the temperature maximum) and a gradual decrease along most of the winter delayed by several months when compared to local temperature. Over these annual cycles, peaks of $\delta^{18}O$ of surface snow occur and some of them might be related to warm precipitation events as previously suggested by Touzeau et al. [2016].

The winter values of the surface snow isotopic composition are similar between all

observed years but the summer values show strong inter-annual variations, resulting in variable amplitudes of the annual cycles of $\delta^{18}O$. In 2011 and 2015, the amplitude of the annual cycle is below 10‰ in $\delta^{18}O$, whereas it is above 20‰ in 2014. In 2012, despite missing data at the beginning of the year, we observe variations of $\delta^{18}O$ more similar to the ones of 2014 than to the one of 2011 and 2015 with a difference of 15‰ in $\delta^{18}O$ between the maximum at the beginning of February and the minimum in September. These differences are significant with respect to the results obtained from replicate samples.

Third, in Fig. 7.6, we present the grain index estimated from satellite data [Picard et al., 2012] to evaluate the impact of metamorphism on the surface snow. Periods of strong metamorphism identified during the summer are highlighted (blue shaded areas) using an arbitrary level on the summer grain index increase. We observe a link between summer grain index highs and the amplitude of the seasonal variation of $\delta^{18}O$ of the surface snow: in 2011 and 2015, small cycles of $\delta^{18}O$ are associated with a large grain index starting to increase in December; whereas in 2014 (and partially in 2012), the large summer increase of $\delta^{18}O$ is associated with small summer increase of grain index, in this case delayed after mid-January. Such a pattern is not observed for precipitation (Fig. 7.5) whose isotopic composition seasonal variations appear more regular and in phase with temperature.

Finally, we focus on the slope between surface snow isotopic composition and temperature to evaluate if the slope between isotopic composition and temperature observed in precipitation is conserved in surface snow after being impacted by post-deposition processes. Because the timeseries of surface snow $\delta^{18}O$ and of temperature are not in phase, it is not possible to directly estimate the corresponding temporal slope by linear regression. This is particularly important in 2014 when the amplitude of the isotopic composition cycle is maximal. We therefore estimate the relationship by comparing the peak to peak range in temperatures and isotopic composition. As the phase lag is smaller in 2011, we use this year to compare the peak-to-peak slope to the linear regression. For 2011, during which the amplitude of the isotopic composition seasonal cycle is greatly reduced with respect to 2014, the slope between $\delta^{18}O$ and temperature is 0.14‰°C [Touzeau et al., 2016] rising up to 0.22‰°C if considering the difference between maximum summer values and minimum winter values. For 2014, we obtain a slope of 0.49‰°C, lower than the prediction of the MCIM of almost 1‰°C but closer to the value of the slope between $\delta^{18}O$ and temperature reported by Touzeau et al. [2016] of 0.46‰°C in precipitation at Dome C (see Table 7.5).

This illustrates that, at the seasonal scale, the seasonal amplitude of variations in surface snow isotopic composition is greatly reduced compared to that of precipitation.

7.2.3 Exchanges between atmospheric water vapour and snow isotopic composition

In this section, we focus on the isotope exchanges between the surface snow and the atmospheric vapour at the diurnal to day-to-day scales by comparing measurements of vapour isotopic composition from Casado et al. [2016b] with new results of surface snow isotopic composition from samples obtained in parallel with the vapour monitoring. To evaluate the impact of sublimation/condensation cycles on the snow isotopic composition, we performed hourly samplings of the snow isotopic composition during 24 hours at Dome C in parallel with vapour isotopic composition monitoring. In Fig. 7.8, we present the simultaneous evolution of snow and vapour isotopic compositions over 24 hours on the 7th of January 2015.

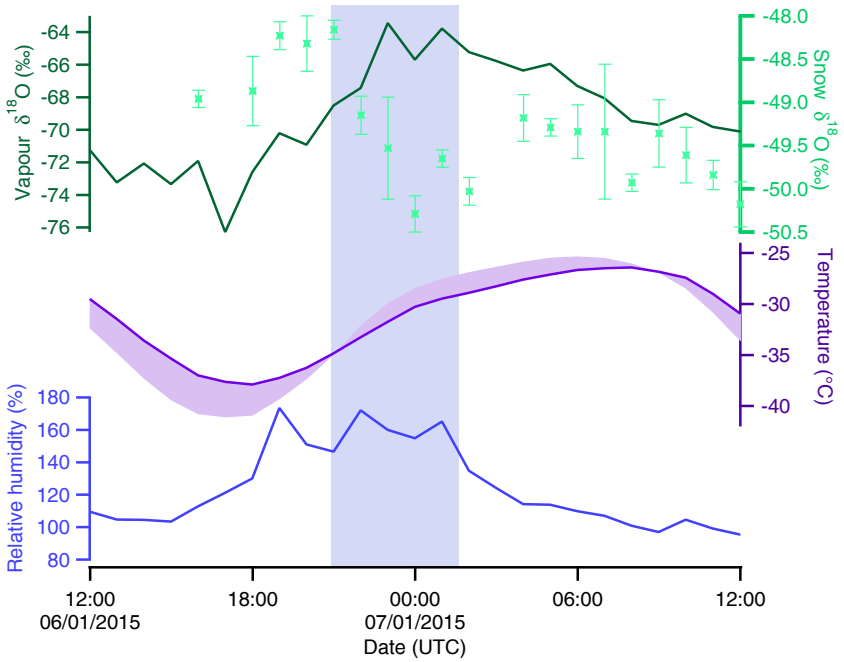

Figure 7.8: Isotopic composition of surface snow (light green dots, error bars are obtained from replicates) compared with isotopic composition of water vapour (dark green line) during one typical summer day at Come C , with 3m-temperature (purple line) compared to the surface temperature (light purple shade) and with the relative humidity (blue line) during the same period from Casado et al. [2016b]. The blue shaded area marks the time-period when frost deposition was observed (see the time-lapse video: https://vimeo.com/170463778)

To evaluate the impact exchanges between snow and vapour on surface snow isotopic composition, we chose the 7th of January as a case study. Indeed, it was characterised by a large diurnal cycle in water vapour isotopic composition, humidity and temperature associated with a turbulent and convective atmospheric boundary layer enabling important exchanges of moisture between snow and vapour [Casado et al., 2016b]. This is a common situation in summer at Dome C due to weak katabatic winds. The afternoon was perturbed by the advection of a frontal perturbation (not shown) which affected the value of the vapour isotopic composition from 06:00 on the 7th of January (the maximum of $\delta^{18}O$ is typically reached around 06:00 UTC). To study the exchanges between snow and vapour free of the impact of meteorological events, we therefore focus on the night from 18:00 on the 6th of January to 5:00 on the 7th of January. In addition to the isotopic composition of the vapour and of the surface snow are presented in Fig. 7.8 the 3m-temperature measured by AWS, the surface temperature measured by infrared sensing [Casado et al., 2016b] and the relative humidity calculated from the specific humidity measured by the Picarro laser instruments and the saturated vapour pressure at the ground temperature [Goff and Gratch, 1945]. Note that due to intake of snow crystals in the inlet of the Picarro, relative humidity is overestimated in very supersaturated conditions, still other hygrometers installed at Dome C indicated supersaturated conditions with relative humidity ranging between 105% and 125% between 19:00 on the 6th of January and 06:00 on the 7th of January. Measurements of supersaturation are complicated by the loss of water vapour at the condensation on the surface of instruments for non-heated instruments and sampling of floating microcrystals for heated instruments [Genthon et al., 2016].

During this five hours period, water vapour $\delta^{18}O$ increased from -73‰ to -64‰ . The evolution of water vapour isotopic composition is synchronous to observations of mist and frost deposition due to local large supersaturation (which are visible on the time-lapse video: https://vimeo.com/170463778). This situation is typical for the "night" at Dome C in summer, and thus is an typical illustration of the "night" deposition of frost.

During this event of frost deposition, snow $\delta^{18}O$ decreased by roughly 2‰. From 21:30 on the 6th of January (UTC time) to 01:40 on the 7th of January (UTC time), the volumes of three snow crystals have been monitored by a script transferring the size in pixels of each crystals from the video on this link (https://vimeo.com/170463778) to surfaces using a length etalon and estimating the volume variations using a power law from the surface variations. This shows an increase by a factor from 1.5 to 3.9. The growth of the crystals observed in the time-lapse can be interpreted as the deposition

of an amount of ice large enough to significantly affect the isotopic composition. The frost deposition occurs simultaneously with the modification of the isotopic composition of the snow and of the vapour. These observations can be explained by an exchange of molecules between the snow and the vapour affecting significantly the snow isotopic composition leading to an enrichment of the isotopic composition of the vapour and a depletion of the isotopic composition of the snow. While this new line of evidence clearly shows vapour-snow isotopic variations associated with frost deposition, it remains to be confirmed by an extended monitoring over several days.

7.2.4 Surface and sub-surface snow isotopic exchanges

In this section we investigate the difference in isotopic composition between surface and sub-surface (5 *cm* below the surface) snow. First, we want to test if the delay observed between the variations of surface snow isotopic composition and temperature is due to the sampling procedure (see section 7.2.2). Second, we want to investigate how is the isotopic signal propagated inside the firn, from the surface to the sub-surface.

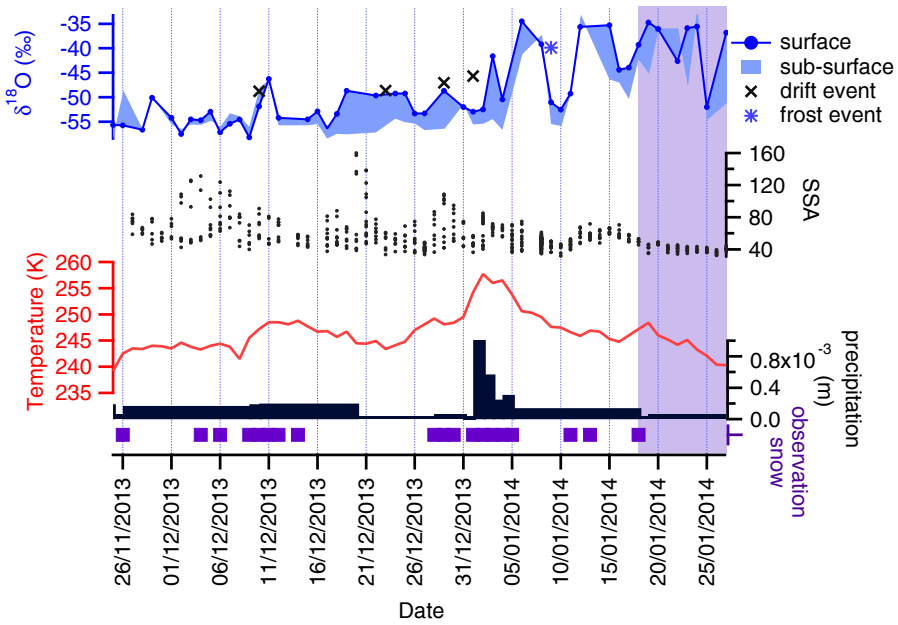

Figure 7.9: Isotopic composition of the snow at the surface (blue line) and difference between surface and the sub-surface (blue shade) during 2 months at Dome C in 2013/14, compared with SSA measurements (black dots), temperature (red line) and precipitation (black bars) from ERA-interim, and precipitation observations (purple squares). The shaded area corresponds to the period during which the grain index changes reflect large metamorphism (see section 7.2.2).

During the summer 2013/14, regular samplings of surface (0 to 3 *cm*) and sub-surface

(3 to 6 cm) snow have been realised at Dome C. Once a day, 2 samples of snow at each level have been taken along with specific surface area (SSA) measurements to evaluate the size of the grains and therefore, how much metamorphism has taken place [Picard et al., 2016b]. These data are presented in Fig. 7.9 with the temperature and the precipitation from reanalysis products and in-situ observations of precipitation. We observe that overall, during these two summer months, the sub-surface isotopic composition is almost systematically lower than the surface isotopic composition. This is found as well in most of the snow pits presented in this manuscript (see section 7.2.5).

From the end of November to the 15th of December, we observe similar values of surface and sub-surface snow isotopic composition. This is a period during which metamorphism has not started yet as indicated by the large values of SSA (Fig. 7.9). The surface snow isotopic composition is low (around -55‰) and the SSA is high which is typical of winter snow. From the 16th of December, we observe large differences between the surface and the sub-surface snow isotopic composition (up to 5‰ higher at the surface) and the SSA decreases indicating the metamorphism is effective. Until the 31st of December, numerous drift events mix the snow and therefore cause strong spatial variability. Finally, due to a large episode of precipitation around the 2nd of January, we observe a significant increase of snow $\delta^{18}O$ of 18 ‰ at the surface first and at the subsurface no more than two days later. The accumulation of snow associated with this event cannot account for enough snow to create a layer of 5 cm as the annual accumulation at Dome C is barely 8 cm. If the surface snow isotopic composition seems to be directly affected by this precipitation event, it seems that the subsurface snow isotopic composition is less sensitive to this impact and that it only changes as a reaction of the surface changes.

As illustrated in Fig. 7.6, the grain index shows that strong metamorphism only starts in the middle of January (high grain index increase is indicating strong metamorphism, in the case of SSA, accumulation of metamorphism results in a small SSA). During this period, we observe a large variability of both the surface and the sub-surface snow isotopic composition. It is important to note here that the variations of isotopic composition include both spatial and temporal variations as only one sample per day was realised, therefore some of the variability might be spatial variability.

A single frost event, on the 9th of January, seems to have depleted strongly the snow in heavy isotopes, but any robust analysis would require more events to discriminate the impact of the frost event from the spatial variability.

7.2.5 Signal in the snow pits

At the annual or seasonal scale, there is no consensus whether or not snow isotopic composition archives the climatic conditions on the East Antarctic Plateau. Ekaykin et al. [2002] observed 20 to 30 cm cycles in the isotopic composition of the snow at Vostok. Here, we compare the oscillations of the snow isotopic composition of five sites on the East Antarctic Plateau (Dome C, Kohnen, S2, South Pole and Vostok) which are characterised by different meteorological and glaciological parameters such as mean annual temperature, elevation, wind speed and direction, accumulation or sastrugi height. A representative subsection of the profiles of isotopic composition from the different sites is presented in Fig. 7.10.

We analyse the typical varriations observed in the snow pits by manual counting of the successive local extrema with a threshold of minimum 1.5‰ for $\delta^{18}O$ and 10‰ for δD for the difference between a minimum and a maximum (in both cases, the thresholds are chosen higher than the measurement precision and lower than the annual variations of surface snow isotopic composition; sensitivity tests have been realised that show insignificant impacts). For each snow pit, the mean cycle length is estimated by counting the number of maxima over the length of the pit. We present the average of the cycle length of the different pits for each site (Table 7.4).

Table 7.4: Mean cycle length obtained by manual counting of maxima from the isotopic composition profiles from the pits. Sites are sorted by accumulation in snow equivalent (calculated using an average snow density of 350 $kg.m^{-3}$).

Site	Accumulation (cm snow equivalent)	$\delta^{18}O$ cycles (cm)	δD cycles (cm)	Number of pits	Length of the pits (m)	Finest Resolution (cm)
S2	6.0	24	20	1	2.6	3
Vostok	6.9	22	22	6	From 2 to 12	2
Dome C	7.7	18	19	4	From 1 to 3	1
Kohnen	18.3	19	NA	2	3	3
South Pole	19.7	20	20	2	From 6 to 10	1.1

Manual counting shows recurrent 20 cm 'cycles' across most of the Antarctic Plateau (Table 7.4). This signal is particularly robust for sites such as Vostok with seven snowpits with cycle lengths between 19 and 26 cm and for Kohnen with 2 snowpits with cycle lengths between 17 and 23 cm. Similar cycle lengths are generally observed for δD and $\delta^{18}O$, but our manual counting method applied on a limited number of pits with a rela-

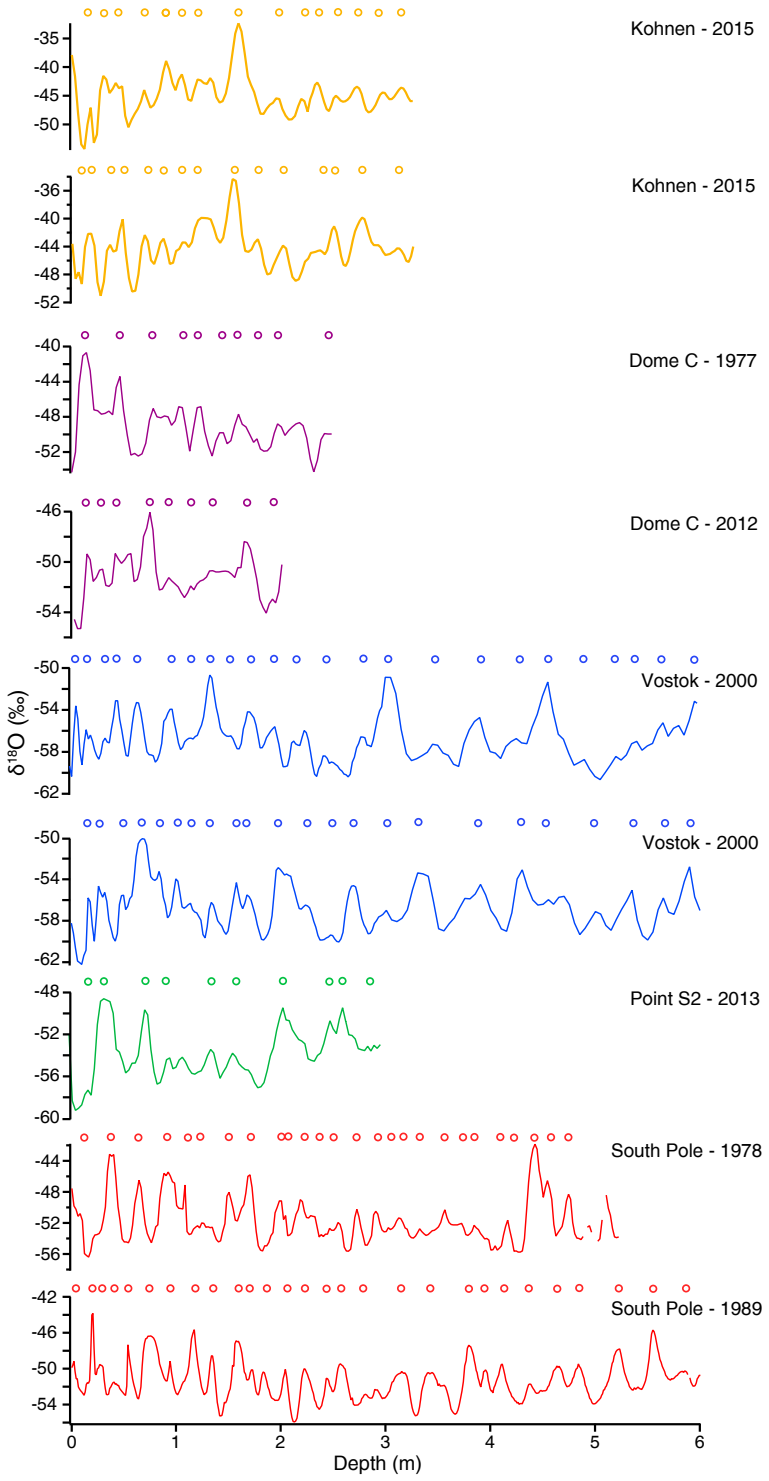

Figure 7.10: Isotopic composition profiles from 2 pits from Kohnen (Yellow), 2 pits from Dome C (Purple), 2 pits from Vostok (Blue), one pit from S2 (Green) and two pits from South pole (Red) and counting of cycles (circles) for each profile with a threshold of 1.5‰ in $\delta^{18}O$ between the successive local minima/maxima to prevent noise from artificially being counted as cycles.

tively low resolution would not allow to detect small differences. Still, for one pit at S2 where we observe a difference of 4 cm between the length of the cycle in δD and in $\delta^{18}O$. This difference is due to one skipped local maximum in the case of $\delta^{18}O$ compared to δD and shows the limits of the counting of successive maximum for a limited number of pits with relatively low resolution.

The cycle lengths are longer than expected with the annual accumulation rates for the lowest accumulation sites such as S2, Vostok and Dome C. For these sites, in order to observe the seasonal cycles (with a length of the order of the accumulation between 6 and 7 cm), a resolution finer than 3 cm is necessary to avoid aliasing according to the theorem of Shannon-Nyquist [Nyquist, 1924; Shannon, 1949]. Due to the interannual variability of the snow accumulation, the snow isotopic composition will not necessary capture the seasonal variations of temperature and precipitation isotopic composition. The limited resolution of the S2 profile may explain why no seasonal cycle of isotopic composition is visible. In the case of Vostok and Dome C, the vertical resolution of the isotopic composition profile is fine enough to establish the lack of seasonal cycle. Once the resolution is finer than the frequency of Shannon-Nyquist, we do not observe differences in the cycle length with the resolution of the pits. For sites with higher accumulation such as South Pole and Kohnen (around 20 cm of snow equivalent accumulation), it is expected to be able to identify seasonal cycles in snow isotopic composition [Jouzel et al., 1983]. In this case, the observed depth cycles could simply reflect the preservation of seasonal variations in annual layers, as commonly observed in Greenland [Vinther et al., 2010]. The profiles are highly variable, exhibiting significant differences in between sites and as well in between pits from a single site, even if sampled the same year, and even for the pits from relatively high accumulation. This can be attributed to the mixture of the potential climate signal and non-climate noise [Fisher et al., 1985; Münch et al., 2016; Laepple et al., 2016].

We observe meaningful differences of the cycle lengths between the top of the pits (typically 20 cm for the first 3 m) and the bottom of the pits (typically 30 cm 10 m deep) for Vostok and South Pole. The amplitude of the cycles is clearly not reduced at the bottom part of the pits compared to the top part as could be expected from diffusion. We note that for Dome C, Kohnen and S2, the profiles are not long enough to evaluate the cycle length-depth dependency.

7.3 Discussion

In this section, we discuss how the results presented above can constrain the different contributions to the snow isotopic composition and the implications for the archival of a climatic isotopic composition signal. First, we evaluate the contribution of precipitation to the surface snow isotopic composition budget. Then, we focus on the post-deposition contribution to the surface snow isotopic composition from exchanges with the atmospheric water vapour. Finally, we discuss how the surface signal is modified during snow burial, and if this affects the archival of the signal. The different processes contributing to the isotopic budget of the snow evaluated in this study are summarised in Fig. 7.4.

7.3.1 Contribution of the precipitation to the surface snow isotopic composition

Annual records of precipitation isotopic composition at Dome C highlight a regular cycle in isotopic composition (Fig. 7.5 and Stenni et al. [2016]) in agreement with the classical modelling of isotopic effects during the distillation along the moisture path and the formation of the snow [Dansgaard, 1964; Jouzel and Merlivat, 1984]. As shown in section 7.2.2, this is not the case for surface snow isotopic composition variations: the seasonal cycle of surface snow isotopic composition is not in phase with the temperature cycle and the precipitation cycle, and the slope between the surface snow isotopic composition and the temperature is reduced compared to the one between the precipitation isotopic composition and the temperature. In this section, we explore whether or not this feature can be explained by (1) the patchiness of the accumulation and the spatial variability due to redistribution and mixing/diffusion in the top centimetres of the snowpack and (2) precipitation intermittency.

First, we evaluate model-data comparison of the climatic signal in the precipitation isotopic composition. Figure 7.11a presents the isotopic composition - temperature relationship in the dataset of precipitation isotopic composition and computed by the Mixed Cloud Isotopic Model (MCIM). Except in summer (December, January, and February), the MCIM is able to faithfully simulate the precipitation isotopic composition. The simulated relationship between $\delta^{18}O$ and the temperature in the model of 0.95‰/°C (see Table 7.5) is similar to the one found from the data from the transect between Terra Nova Bay and Dome C which is not unexpected as these data were used to tune the model [Winkler et al., 2012]. For the entire seasonal cycle, we observe for the precipitation isotopic composition a slope below 0.46‰/°C. Important differences are not unexpected between temporal and spatial slope of precipitation [Ekaykin, 2003; Landais et al., 2012a; Touzeau

et al., 2016]. It is interesting to note here that the winter temporal slope of precipitation isotopic composition (0.76 ‰/°C) matches the spatial slope of isotopic composition for the East Antarctic Plateau (0.77 ‰/°Cfor low isotopic composition area). Here, the low slope of the entire seasonal cycle is associated to the deviation of the summer isotopic composition to a slope of 0.41‰/°C. One way to explain such a low slope would be to introduce an additional fractionation linked with re-evaporation during the precipitation events which can affect the snow flakes isotopic composition [Koster et al., 1992] and therefore decrease the slope with temperature. This may also result from changes in air masses trajectory and thus, in the Rayleigh distillation. Backtrajectory calculations for the East Antarctic Plateau indicate strong asymmetry of the moisture sources for austral summer and winter [Sodemann and Stohl, 2009; Winkler et al., 2012]. Finally, in the MCIM, the condensation temperature is estimated through a linear relationship with the local surface temperature [Ciais and Jouzel, 1994]. The reduced summer temperature inversion at Dome C [Ricaud et al., 2014] is thus not taken into account in the MCIM which could also lead to a reduced slope.

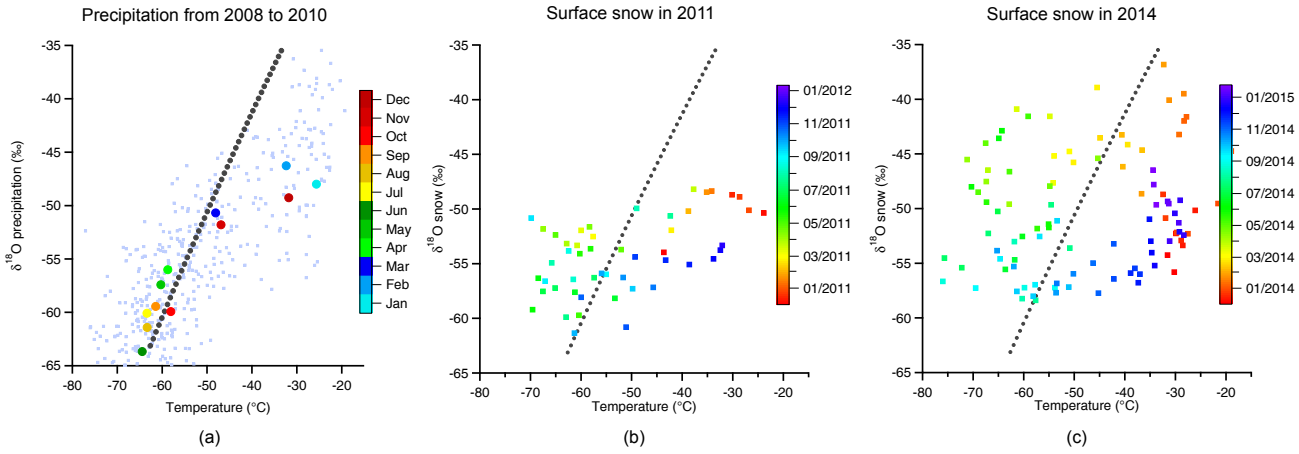

Figure 7.11: a) Isotopic composition of precipitation versus 3m temperature from 2008 to 2010 (light blue squares) and mean monthly values over these three years (coloured circles) from our datasets, compared with outputs of the MCIM for the same range of temperature tuned for Dome C (black dots); b) and c) respectively isotopic composition of surface snow in 2011 and 2014 versus 3m temperature.

This indicates that at least during winter, this model is able to predict the value of snow isotopic composition from mixed phase Rayleigh distillation. The tuning of supersaturation for the site of Dome C from Winkler et al. [2012] such as $S = 1 - 0.003T$, appears valid, at least for winter conditions. This tuning of the supersaturation implies supersaturation up to 115% in summer conditions at Concordia, in the range of measure-

ments obtained by Genthon et al. [2016].

By contrast, links between temperature and surface snow isotopic composition are more complex (Fig. 7.6) and we do not observe a linear relationship between surface snow and precipitation isotopic compositions. The range of values spanned by the surface snow isotopic composition cycle is sometime coherent with the precipitation cycle (2014) and sometimes not (2011, 2015; see also Fig. 7.11). The difference of methods to sample the surface snow through the year does not explain this behaviour as for instance, the same protocol was applied to both 2014 and 2015. The surface snow isotopic composition is compared with the output of the MCIM model (Fig 7.11). These results confirm that in 2014, the snow isotopic composition spans all the range predicted by the model for this range of temperature, as for precipitation isotopic composition; whereas for 2011 (and 2015, not shown), the surface snow isotopic composition does not rise above -45‰ and does not reflect the enriched summer values. The differences in the maximal summer values between 2014 and 2011 reported here are not linked to the precipitation isotopic composition. Indeed, precipitation events with values of isotopic composition higher than -40 ‰ have been reported during all these summers and the isotopic composition of precipitation is in phase with the temperature.

The loop shape of the data for year 2014 (Fig. 7.11c) suggests that variations of snow isotopic composition are delayed compared to temperature variations. This feature can be attributed to the sampling of 15 mm of snow which implies mixing of fresh snow with older snow, considering the mean accumulation rate at Dome C below 8 cm per year. Nevertheless, the high isotopic compositions of the 2014 summer have been recorded almost simultaneously at the surface and at the sub-surface (section 7.2.4 and Fig. 7.9) and do not exhibit the 2 months phasing between change in precipitation $\delta^{18}O$ due to temperature and change in surface snow $\delta^{18}O$.

During an episode of precipitation, for "high-accumulation" sites, the isotopic composition of the precipitation is stored in the surface snow, and contributes to archiving the local temperature signal through the isotopic fractionation during the formation of the snowflakes [Jouzel and Merlivat, 1984]. For a low accumulation site such as Dome C, each precipitation event is not necessarily captured by the surface snow isotopic composition because the snow deposition is patchy and strongly dependant of the surface roughness [Groot Zwaaftink et al., 2013; Libois et al., 2014; Picard et al., 2016a]. In Fig. 7.6, we also present the isotopic composition with ERA-interim snowfall product to illustrate this patchiness of the snow deposition at the event scale. If ERA-interim does not provide

Table 7.5: Summary of the isotope temperature relationships observed for the different datasets. For the surface, because of the 2 months shift, the slopes are calculated using the difference between the extrema of isotopic composition and temperature as detailed in section 7.2.2. For 2012, the summer maxima of isotopic composition were not sampled leading to an underestimation of the slope. For 2011, the dephasing is small enough to perform a linear regression, the result is indicated inside parenthesis. For the precipitation, the vapour and the MCIM output, we ran a linear regression. All the correlations are significant ($p - values < 0.05$).

Type of sample	Period	Slope $\delta^{18}O$ vs T (‰/°C)	r^2
Surface	2011	0.22 (0.14)	0.29
	2012	> 0.27	NA
	2014	0.49	NA
	2015	0.27	NA
Precipitation	All years	0.46	0.65
	Summer	0.41	0.54
	Winter	0.76	0.56
Vapour	Summer 2015	0.46	0.26
MCIM	Multiyear	0.95	0.99
Transect to Dome C	Multiyear	1.20	0.69
	$\delta^{18}O$ < -40 ‰	0.77	0.90

reliable quantitative estimates of the amount of snowfall on the East Antarctic Plateau, it has been shown to be relevant to predict at least the temporality of most snowfall events at Dome C [Libois et al., 2015]. At Dome C, as described by Touzeau et al. [2016], we can see that warm winter precipitation events are often associated with significant variations of surface snow isotopic composition (up to 5‰), nevertheless, we still observe a large number of precipitation events not associated with any variations of surface snow isotopic composition.

At the seasonal scale, the patchiness of the accumulation cannot explain why the surface snow does not systematically record the precipitation signal, and thus, why we observe missing summer values in the surface snow isotopic composition. Indeed, in 2014, we obtained several time-series of surface snow isotopic composition and at the seasonal scale, we observe a strong agreement between the time-series. Additionally, for the NIVO and the SUNITEDC campaigns, the samples were randomly taken, thus, they should not be systematically affected by the erasing of the precipitation signal in the surface snow isotopic composition.

Finally, while the slope between precipitation isotopic composition versus temperature is also stable over the different years, it is not the case for the surface snow. The slope between surface snow $\delta^{18}O$ and temperature of 2014 (0.49 ‰/°C) is similar to the one observed in precipitation (0.46 ‰/°C), as shown in Table 7.5, indicating a probable link. The slopes of 2011 and 2015 are much lower. In the case of 2015, we observe a rather low cumulative precipitation amount (see Fig. 7.6) which could explain the small values of summer $\delta^{18}O$, but it is not the case for 2011. Because both the average values of $\delta^{18}O$ and the slopes of surface snow $\delta^{18}O$ against temperature differ from the ones of precipitation in 2011 and 2015, the lack of a summer signal in 2011 and 2015 surface snow isotopic composition cannot only be due to the intermittency of precipitation, and requires to involve post-deposition processes.

7.3.2 Contribution of sublimation/condensation cycles to the surface snow isotopic composition

Another possible factor affecting the surface snow isotopic composition is post-deposition, in particular exchange with atmospheric water vapour associated with metamorphism. At the seasonal scale, the significance of the contribution of the post-deposition is supported by the comparison of the isotopic composition of the surface snow to the grain index (see Fig. 7.6).

The high values of grain index in the summer can be attributed to intense metamorphism [Picard et al., 2012; Libois et al., 2015], the rise usually starts during the first week of December. Rapid falls of the grain index result from important precipitation events and the input of small snow grains from precipitation. Finally, the slow decrease during winter is explained by the accumulation of new small snow flakes by precipitation onto the coarse grains formed during the summer. Winter metamorphism is too slow to impact the snow structure.

For the surface snow isotopic composition variations, two features of interests are visible in Fig. 7.6. We observe inter-annual variability of the summer surface snow isotopic composition. This inter-annual variability seems to be directly related to the strength of the metamorphism: we obtain a strong negative correlation between the amplitude of the grain-index increase in summer and the maximum $\delta^{18}O$. The summer increase of $\delta^{18}O$ seems to be very sensitive to the date at which the intense summer metamorphism starts. The large values of $\delta^{18}O$ observed in 2014 (and maybe for the year 2012, but the max-

imum of $\delta^{18}O$ was reached before the sampling started) are associated with a small and delayed increase of grain index (in both case, the main increase of grain index happens after the 15th of January, whereas for normal years, it starts the first week of December). This delayed start of the metamorphism enables the surface snow to capture the enriched precipitation isotopic composition of summer. Second, in winter, we observe a mixing of new income of precipitation on the top of already deposited snow as illustrated by the slow decrease of the $\delta^{18}O$ during the entire winter. This is similar to what is observed for the grain index. By contrast, there is no apparent relationship between precipitation isotopic composition and grain index from 2008 to 2011 (see Fig. 7.5).

This indicates the importance of metamorphism in the formation of the surface snow isotopic signal as a post-deposition process. If Picard et al. [2012] highlight a direct link between the summer intensity of metamorphism and the integrated amount of accumulation over the summer, we do not observe a link with the summer amplitude of the surface snow isotopic composition variations (even though more years are necessary to attest the lack of link). In order to disentangle the different fractionation processes involved in the metamorphism, we evaluate the formation of this $\delta^{18}O$ signal during snow metamorphism by studying in parallel the vapour and the snow isotopic composition at the diurnal time scale in summer.

Metamorphism can affect the surface snow isotopic composition through exchanges of water molecules between the snow and the moisture: either the atmospheric water vapour or the interstitial air water vapour. Here, we focus on the coarsening of the grains due to the exchanges with the atmospheric vapour under the influence of the diurnal cycle of temperature. Exchanges between snow and atmospheric vapour during sublimation/condensation cycles can significantly affect the surface snow isotopic composition. Indeed, it has been shown in Greenland that the mass balance was set by both sublimation/condensation cycles and synoptic storm events [Steen-Larsen et al., 2014a; Berkelhammer et al., 2016]. In between precipitation events, moisture exchanges significantly affect the snow isotopic composition over several days and a parallel evolution of the snow and vapour isotopic compositions is observed in NEEM [Steen-Larsen et al., 2014a]. Similar observations have been made in Kohnen in Antarctica by Ritter et al. [2016] during summer 2013/2014. Dome C is a colder site than NEEM or Kohnen, thus we expect a less efficient metamorphism. Still, because the accumulation rate at Dome C ($2.3\,cm.yr^{-1}\,w.e.$) is lower than at NEEM ($20\,cm.yr^{-1}\,w.e.$) and than at Kohnen ($6.4\,cm.yr^{-1}\,w.e.$), we expect to observe a stronger relative impact of the interplay between vapour and snow.

At Dome C, we also observe that the surface snow isotopic composition is significantly affected by the exchanges of molecules with the vapour in between precipitation events. However, at the diurnal scale (see section 7.2.3), no parallel evolution is observed in snow and vapour isotopic compositions contrasting with results from NEEM and Kohnen. Our observations are coherent with exchanges in a closed box system: the vapour is enriched in heavy isotopes while snow is depleted during frost deposition events. This is consistent with equilibrium fractionation in a closed box where the vapour isotopic composition is predicted by equilibrium fractionation with the snow [Casado et al., 2016b]. We attribute the difference of behaviour compared to Kohnen [Ritter et al., 2016] and NEEM [Steen-Larsen et al., 2014a] to the position of the station on the top of a dome. Indeed, at Dome C, the weakness of the katabatic winds decreases the renewal of air masses long enough for the exchanges with the snow to be detected. At Kohnen and NEEM, stronger winds are observed leading to a more efficient renewal of air masses able to exchange with the surface. Preliminary results from back trajectory analyses indicate that most of the air masses arriving at Dome C have been loaded with moisture within the last 50km before Dome C. It is important to note that the humidity content at Dome C is lower than at Kohnen and NEEM, resulting in a smaller reservoir of water vapour with which the snow can exchange. Despite these low humidity levels, a significant impact of the sublimation/condensation cycles on the snow isotopic composition is observed. Similar studies measuring isotopic composition of vapour and snow at sites with similar temperatures but larger wind speeds (such as at Vostok), could provide more robust insights on the impact of wind on renewal of air masses compared to humidity levels. This study relies on one event of attested frost deposition and the monitoring of more events is necessary to be able to quantitatively evaluate the fractionation processes involved.

7.4 Conclusions

In this study, we explored the post-deposition processes affecting the archival of water isotopic composition from precipitation to the snow pack for low accumulation sites of the East Antarctic Plateau. We focused in particular on the exchanges between the vapour and the snow occurring during snow metamorphism and on how the accumulation and the burial of the snow layers affect the isotopic composition signals found in the precipitation, the surface snow and the buried snow. We combined a comprehensive dataset from precipitation, surface snow, buried snow and atmospheric vapour isotopic compositions to assess the impact of theses two post-deposition processes compared to the original climatic signal captured by precipitation isotopic composition. Figure 7.12 presents the histogram of the isotopic composition of the precipitation, the surface snow, in 2011 and

in 2014, and in the snow pits. Additionally, we present the average value of each distribution as well with the standard deviation of the distributions.

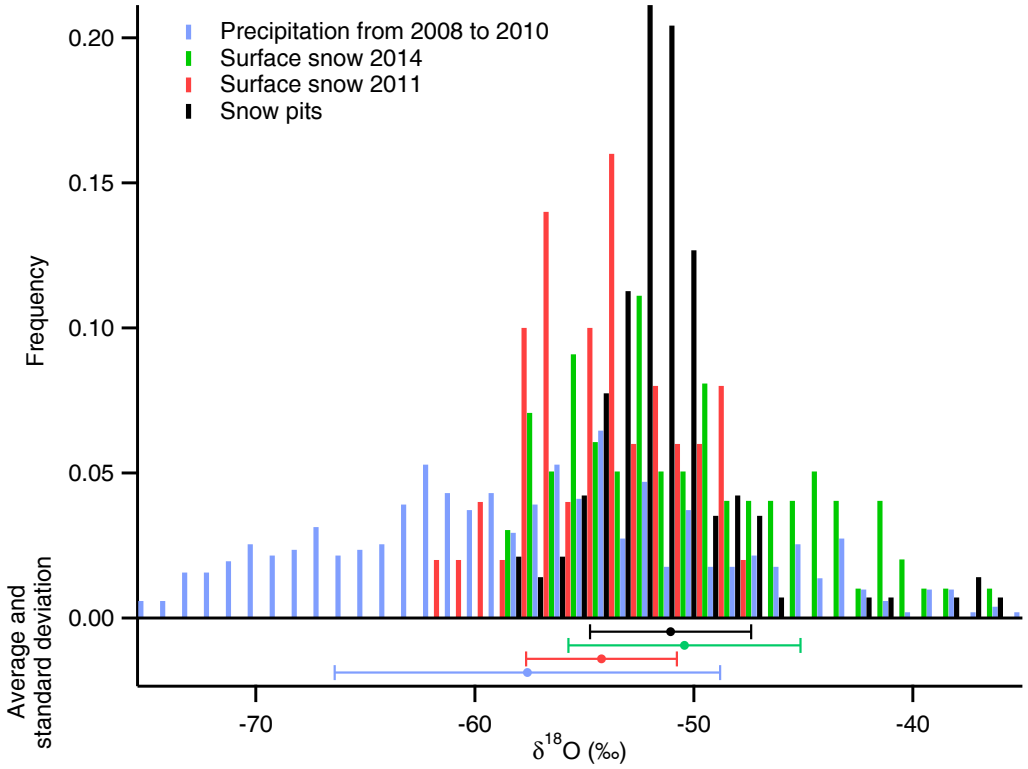

Figure 7.12: Top: Histogram of the isotopic composition at Dome C of precipitation (blue), of surface snow in 2014 (green) and in 2011 (red) and of four snow pits stacked together (black). Bottom: dots: average value for each distribution and, error bars: standard deviation of the ensemble.

The distribution of isotopic composition in the precipitation is much larger than the distribution of the surface snow isotopic composition. As discussed in section 7.2.2, a large range of depleted precipitation isotopic composition, mostly observed in winter, are not represented in the surface snow isotopic composition. Below the surface, apart from a few isolated enriched samples with $\delta^{18}O$ values above -45‰, the distribution of isotopic composition is even narrower than at the surface (both the red and the green points). The narrowing of the distributions of the isotopic composition from the surface to the buried snow (Fig. 7.12) could be explained by isotopic diffusion in the snow [Langway, 1970; Johnsen, 1977; Johnsen et al., 2000; Gkinis et al., 2014]. These large differences of the signals in the isotopic composition of the precipitation, the surface snow and the buried snow document the various processes involved in the archival of the climatic signal in the snow isotopic composition on the East Antarctic Plateau.

First, we evaluated at the seasonal scale the different contributions to the snow isotopic composition between the precipitation on one hand and the exchanges with the atmosphere on the other hand. We compared the seasonal variations of precipitation and surface snow isotopic composition. We observed an inter-annual variability in the seasonal cycle of surface snow isotopic composition which deviates from the regular seasonal cycle of precipitation isotopic composition. The large differences between the average isotopic composition of surface snow and precipitation might indicate a significant impact of post-deposition processes in the site of Dome C. This is supported by a clear link between the surface snow isotopic composition and both the intensity and the temporality of summer metamorphism. Furthermore, post depositions effects are not limited to summer: in winter, a large range of very depleted precipitation isotopic compositions is not observed at all in the surface snow isotopic composition.

Second, we focused on the impact of the exchanges between the vapour and the snow at the diurnal scale. With simultaneous hourly measurements of atmospheric vapour and surface snow isotopic composition, we evaluated one part of the metamorphism component: exchanges between atmosphere and snow pack through sublimation/condensation cycles. We showed that for a place like Dome C with low wind speed, it is possible to have a closed system where the vapour is enriched while the snow is depleted. This one case is the first field observation of a potentially closed system in Antarctica and differs from NEEM and Kohnen where the vapour and the snow evolve in parallel, probably due to stronger katabatic winds which renew the vapour reservoir.

Finally, we evaluated the evolution of the isotopic signal while the snow is being buried. We highlighted that there are recurrent $20\,cm$ cycles in the isotopic composition profiles in the snow pack in five sites from East Antarctica: Dome C, Kohnen, S2, South Pole and Vostok. This finding raises doubts on the interpretation of high resolution variations from such sites. A detailed investigations of these cycles is out of the scope of this study, but will ,be presented in a follow up publication (Laepple et al., in prep).

Despite combining different types of data (precipitation, vapour surface snow and snow pits isotopic compositions) from five different sites, some elements are still lacking to robustly quantify the different contributions to the snow isotopic composition budget due to diverse limitations: the lack of winter measurement of the vapour isotopic composition prevented us to evaluate the complete annual cycle of exchanges between vapour and snow, especially considering that the atmospheric boundary layer has a different struc-

ture in winter than in summer; the differences of resolution and of depth of the snow pits depending of the sites limited the interpretation of the cycles through robust spectral methods; and finally the small number of locations where precipitation and surface snow were sampled all year long on the East Antarctic Plateau (only Dome C) hindered a generalisation of the results for the link between metamorphism and surface snow isotopic composition to the entire East Antarctic Plateau. This study was limited to the impact of post-deposition processes on the first order of variations of isotopic composition (δ values). Still, excesses ($d-excess$ and $^{17}O-excess$) are expected to provide further insights to understand processes due to their different sensitivity to kinetic fractionation [Casado et al., 2016a]. This will be explored in another independent study.

Our study covers different contributions to the snow isotopic signal during the archival in Antarctica and demonstrates that the climatic signal initially acquired in the precipitation isotopic composition is not necessarily stored in the surface snow and in the buried snow. These results yield for a more quantitative evaluation of the impact of post-deposition processes on the isotopic composition, in particular of snow metamorphism and interstitial diffusion; through controlled laboratory experiments, field studies and using snow models. The link between snow isotopic composition and temperature in Polar ice cores appear strongly affected by all these post-deposition processes at the intra to inter-annual scale. The interpretation of ice core records is today most limited by the lack of understanding of these post-deposition processes. Progress in this direction is needed to strengthen a physically based interpretation of water stable isotope records for quantitative paleoclimate reconstructions.

Chapter 8

Conclusions and perspectives

During the time frame of my Ph-D, important efforts have been done to measure and understand water stable isotopes content. The geoscience part of this project has been mainly carried on at the Laboratoire des Sciences du Climat et de l'Environnement (LSCE) and the instrumental development part at the Laboratoire Interdisciplinaire de Physique (LIPhy). This project involved an important amount of collaborations, including principally the Laboratoire de Glaciologie et de Geophysique de l'Environnement (LGGE), the French Polar Institue (IPEV), the Centre National de Recherche Meteorologique (CNRM), the Laboratoire Inter-universitaire des Sciences Atmospheriques (LISA) and also several foreign collaborations with Italy, Russia, Denmark and Germany. In this section, we will go back to the scientific questions of the PhD (as detailed in the introduction) and summarise the new analytical possibilities we foresee and the implications of our results for paleoclimate reconstructions.

What is the primary contribution to snow isotopic composition on the East Antarctic Plateau ?

This is the main question of the manuscript and is mainly treated in section 7. Since the early works of Dansgaard [1964] and Lorius et al. [1969], variations of snow isotopic composition are used to infer the past variations of temperature. Still, all processes involved during the archival of the snow isotopic composition are not well known and there remain uncertainties on the relative contribution of the precipitation, the sublimation/condensation cycles, the metamorphism and the blowing snows. In the framework of the NIVO project, I have participated to one campaign and organised two to sample surface and sub-surface snow, excavate snow pits and monitor the vapour isotopic composition in order to understand the formation of the snow isotopic signal. This work was completed by some additional results from the sites of Vostok, Kohnen,S2 and South Pole

and enabled to explore the different contributions to the snow isotopic composition budget from the diurnal to the seasonal time scale at the surface and also in the first metres of the snowpack.

First, at the surface, we showed that the precipitation signal can be erased by important metamorphism at the diurnal and at the seasonal scale. This creates variability of the surface snow isotopic composition summer highs and therefore different isotope-temperature slope at the seasonal scale for the different years. The origin of the intermittency of the linear relationship between isotopic composition and temperature seems to be linked with the temporality of summer metamorphism, and requires further studies comparing the impact of metamorphism on the snow isotopic composition such as what the amount of water exchanged for a given temperature cycle, what overall depth is affected for a given temperature gradient, and the relative contribution of kinetic fractionation. We recommend several approaches to characterise this impact: through snowpack models including isotopes (Touzeau et al., in prep), laboratory controlled experiments and field studies. In particular, it is important to characterise the exchanges between the surface and the local atmospheric water vapour and between the surface and the layers of snow underneath in the snowpack. All of our studies have been realised in summer and a lot is still to be learnt when we are able to measure water vapour isotopic composition in winter on the East Antarctic Plateau.

We also observed rapid propagation (within a few days) of the surface snow signal toward the sub-surface. This propagation is much faster than what is expected by the accumulation and could be associated with isotopic diffusion. In thi case, because the temperature gradient can be oriented upward or downward, we expect this propagation to be also bi-directional, in particular with a lasting upward transport in winter conditions. To test this hypothesis, the winterover crew at Dome C is currently realising snowpits in winter to analyse if an opposite phase can be found in winter.

Finally, we showed that a generalised 20 cm cycle is found in snow isotopic composition at the low accumulation sites of the East Antarctic Plateau. Considering the large differences in climatic conditions (mean average temperature, accumulation, insulation, mean wind speed, height of sastrugi...) of the different sites we analysed, it is not obvious how to explain these recurrent cycles. These conclusions call for a more comprehensive approach of how the isotopic composition signal is archived at low accumulation sites.

How do equilibrium and kinetic fractionation processes affect the isotopic composition at low temperature and low humidity ?

The measurements of vapour isotopic composition at Dome C highlight that there remains discrepancies in the parametrisation of kinetic and equilibrium fractionation for the formation of snow at low temperature. In addition to the field campaign, we realised several processes studies to evaluate equilibrium and kinetic fractionation at low temperature and low humidity. All the uncertainties on the coefficients used to parametrise these different types of fractionation directly affect the ability to model isotopic composition of snow and vapour, and therefore the precision of the climate reconstruction.

In section 5.1, we presented preliminary results on equilibrium fractionation. Using our experience to measure water vapour isotopic composition on the field (see section 6.2), we wanted to evaluate the equilibrium fractionation coefficients at temperature lower than that reached by Ellehøj et al. [2013] and Merlivat and Nief [1967]. We believe that equilibrium fractionation at low temperature needs to be better constrained but also that it is important to evaluate out-of-equilibrium fractionation associated with the ice-vapour phase transition.

Additionally, in section 5.2 we investigated the fractionation due to the difference of diffusivities of the different isotopes. We realised two experiments where this type of kinetic fractionation was at play by condensing vapour over a cold plate in a humidity (and temperature) gradient. First, we demonstrated that kinetic fractionation affects $^{17}O-excess$ similarly to $d-excess$ in very supersaturated conditions in a qualitative laboratory experiment. Then we realised profiles of water vapour isotopic composition to quantitatively infer the diffusion in controlled cloud-chamber experiments. These results show that the Jouzel and Merlivat [1984] model fails to represent the impact of kinetic fractionation on the vapour isotopic composition. We introduced a classical diffusion framework to model the impact of the difference of diffusivity on the isotopic composition, independent of any parametrisation of supersaturation.

How to measure water vapour isotopic composition on the East Antarctic Plateau ?

As we saw, the exchanges between the local vapour and the surface is very important in the isotopic budget on the East Antarctic Plateau and still poorly characterised. Improving this characterisation requires robust measurements of water vapour isotopic composition at low temperature and low humidity. In section 6.2, we explored different methods of

measurements: cryogenic trapping, an OFCEAS instrument and a CRDS instrument.

First, we demonstrated the ability of two types of custom-made cryogenic trappings to sample water vapour isotopic composition at low humidity such as encountered on the East Antarctic Plateau. For both trap designs, we showed that a careful detrapping protocol is essential in order to obtain a relevant isotopic composition (in particular for $d-excess$). In low humidity conditions, the design with glass balls enables one to reduce the duration of the trapping from 36 hours to 12 hours for summer conditions at Dome C for instance.

Second, we successfully deployed two infrared spectrometers at Dome C: an OFCEAS instrument (HiFI, home-made in LIPHY) and a CRDS instrument (Commercial Picarro L2130i). The data from the OFCEAS were very noisy and therefore not exploited in this manuscript, we still learned from this experiment that extra-care is necessary with this instrument to protect it from the vibrations to obtain precise results. Still, this method shows the best potential with measurements of $\delta^{18}O$ with precision better than 0.5‰ at 20 $ppmv$. We also showed that commercial CRDS instrument can provide measurements of water vapour isotopic composition with precision better than 0.3‰ down to 200 $ppmv$ but requires a robust calibration protocol. At this range of humidity, we had to build a new humidity generator able to serve as a calibration device below 1000 $ppmv$.

Still, these performances would barely be sufficient to monitor water vapour isotopic composition in winter on the East Antarctic Plateau where the humidity goes down to 1 $ppmv$. This level of humidity would require to push the limits of the state-of-the-art in term of infrared spectroscopy but it is essential to measure in such dry conditions if we want to understand air/snow exchanges on the East Antarctic Plateau.

What are the limits of the measurements of water stable isotope content by infrared spectroscopy ?

We believe that the limits of infrared spectroscopy are still not reached yet, as presented in section 4. We developed a new kind of infrared spectrometer based on Optical Feedback Frequency Stabilisation (OFFS) and Cavity Ring-Down Spectroscopy (CRDS) to attempt to push the limits further by using the benefits of both methods. Because infrared spectroscopy relies on the integrated absorption profile of the transition to infer the concentration of each compound, both the absorption and the frequency need to be precisely measured. Here, we conceived the first V-shaped cavity in ultra-low expansion

glass (ULE) and we use optical feedback frequency stabilisation to stabilise a DFB laser diode down to the hertz level (10^{-14} precision on the determination and the stabilisation of the frequency) and a high-performances CRDS cavity to measure the absorption with a sensitivity of $10^{-13}\,cm^{-1}.Hz^{-1/2}$, almost 100 time better than standard commercial infrared spectrometers.

If this instrument will never be able to go on the field because of its size and fragility, this is the first step toward the development of a new type of infrared spectrometers able to measure isotopic composition at humidity down to the *ppm* level. The performances of this instrument even exceed what is needed for isotopic composition and application in Doppler thermometry are foreseen. For water isotopes monitoring, we expect to be able to measure triple isotopic composition of water vapour down to the *ppm* level. These performances would enable to evaluate the equilibrium fractionation down to -90 °C, to develop instruments able to monitor the isotopic composition of the vapour on the East Antarctic Plateau in winter, both in the atmosphere and in the snow.

Applications to atmospheric dynamics and modelling

The results from the field campaign showed that water vapour isotopic composition can be used as a tracer for boundary layer atmospheric processes. Indeed, because of the important impact of turbulence (and of stratification) on water vapour isotopic composition, it is a very powerful tool to evaluate the turbulence of the low atmospheric boundary layer.

As we saw, isotopic composition has been used to infer the supersaturation parametrisation against temperature and the data of precipitation presented here tends to confirm the parametrisation found in a mixed phase Rayleigh distillation model at the seasonal scale. Previous tuning of supersaturation were realised using transect across the East Antarctic Plateau. Here, we show that the parametrisation of supersaturation obtain from the spatial variations of snow isotopic composition is validated with temporal variations of the precipitation isotopic composition.

In perspectives, preliminary results from the 2014/15 campaigns highlight an important $d-excess$ anomaly ahead of an advection of humid air and an important precipitation events. Indeed, during the campaign of 2014/15, we observed an important increase of $d-excess$ before the arrival of a cloud system larger than usually observed at Dome C. These results have not been completely studied yet unfortunately, but they show similarities with results of Aemisegger et al. [2015] at the mid-latitudes.

Perspectives

This thesis covers several aspects of the physics of water stable isotopes. If water isotopes are a very powerful tool due to the direct link between temperature and fractionation at the phase transition, we showed that on the East Antarctic Plateau, the interpretation is not as straightforward as once expected. The understanding of how the climatic signal is actually archived by the snow isotopic composition is crucial. Indeed, for now, the relationship linking the water stable isotopic composition to the temperature is empirically deduced from data. As we saw, important variations on this relationship occur in time and space. The main limitation to theoretically infer this link is due to the lack of a robust framework of the physical processes affecting the water isotopic composition at low temperature.

Here, we present with OFFS-CRDS the first analytical tool able to measure water vapour isotopic composition down to volume mixing ratios of 1 ppm. The setup described here provides the proof of concept and will be further used to realise reference spectra to constrain the broadening parameters in perfect experimental conditions with an important number of points. This work will be pursued by combining CRDS measurement of water standard of known isotopic composition under flow using a stabilised diode laser. These measurements should also improve the infrared spectrometry performances for all instruments by generating physically robust lineshape profiles for different conditions of pressure, temperature and humidity. The performances of this type of instrument also enable studies beyond trace detection, for instance the study of saturated absorption line or also Doppler thermometry. Additionally, this type of instrument has been developed for water vapour but the principle can be easily transferred for other gas such as CO_2 or O_2.

Both OFCEAS and OFFS-CRDS techniques provide an incredible opportunity to study the physical processes affecting isotopes in conditions as cold as in winter on the East Antarctic Plateau, and therefore fully study the formation of the snow in Antarctica. The first application these techniques can be used for, is to estimate directly the equilibrium fractionation for sublimation/condensation for temperatures down to $-90°C$. As we saw, this is an important limitation for the interpretation of isotopic composition signal. Second, we plan on developing of a second type of CRDS cavities able to measure at atmospheric pressure, therefore not requiring any pumping. These high-pressure CRDS cavities coupled with ultra-stable laser source will provide the opportunity to measure the isotopic composition of the vapour in interstitial air in the snow pack without sublimating the snow with an external pumping. The deployment of such a cavity in a snow meta-

morphism chamber can help to constrain the impact of metamorphism on snow isotopic composition in controlled laboratory experiments.

Additionally, these analytical tools can also be used to pursue the effort of monitoring water vapour isotopic composition on the East Antarctic Plateau and obtain year-long time series. It would be the first measurement of water vapour isotopic composition below 100 *ppmv* on the field providing the first observations of the impact of stratification (mostly observed in winter) on the exchanges between snow and vapour in Antarctica. The measurement of water vapour isotopic composition at several heights could bring additional features about (1) the net flux of moisture and of heavy isotopes in the boundary layer, and (2) the molecular diffusion characterisation over the first meter of the snow surface. It would also be the opportunity to deploy a high pressure CRDS cavity buried in the snow to evaluate all at once the snow, the interstitial vapour (at different depths) and the atmospheric vapour isotopic compositions.

A better understanding of the formation of the snow is not only crucial for paleoclimate purposes but also for the study of climate change: as we saw, water stable isotopes can be used as a tool to trace atmospheric processes, and therefore to understand large scale atmospheric dynamics in Polar Region; or metamorphism which plays a predominant role in the albedo of the snow.

Annexe A

Résumé

La composition des isotopes stables de l'eau sur le plateau Est Antarctique : mesure à basse température de la composition de la vapeur, utilisation comme un traceur atmosphérique et implication pour les études paléoclimatiques

Introduction

Les carottes de glaces permettent de reconstruire le climat du passé, à partir entre autre de la composition isotopique de l'eau ($\delta^{18}O$, $\delta^{17}O$ et δD) [Petit et al., 1999a; EPICA, 2004; Jouzel et al., 2007]. Sur le plateau Est Antarctique, les températures très froides et les faibles accumulations ont permis de remonter jusqu'à 800 000 ans sur le site de Dôme C et 400 000 ans sur le site de Vostok. Cela dit, des limitations importantes bloquent l'interprétation quantitative en terme de variation de temperature des signaux de compositions isotopiques dans les carottes de glace. Au Groenland, les variations de sources d'humidité [Charles et al., 1994], de saisonalité de précipitation [Fawcett et al., 1997; Krinner et al., 1997], de liens entre température de condensation et température de surface dûs à l'existence d'une couche d'inversion [Loewe, 1936] peuvent biaiser d'un facteur 2 les estimations de variations de température entre période glaciaire et interglaciaire. En Antarctique, des effets similaires vont affecter les performances des reconstructions de température [Sime et al., 2009; Laepple et al., 2011]. De plus, à cause des températures plus basses en Antarctique qu'au Groenland, d'autres facteurs doivent être considérés. Premièrement, les reconstructions des variations de température dans les carottes de glace à partir des isotopes de l'eau se basent sur des modèles pour décrire la physique tout au long du cycle de l'eau, en particulier associé aux différents fractionnements isotopiques. Ces modèles peuvent aller de simples modèles décrivants la distillation successive des masses d'air humide (dits modèles de Rayleigh) [Ciais and Jouzel, 1994] ou des modèles de circu-

lation atmosphérique incluant les isotopes de l'eau [Hoffmann et al., 1998; Schmidt et al., 2005; Risi et al., 2010; Werner et al., 2011]. Ces modèles, qui ont été développés au cours des dernières décénnies, reposent sur la connaissance de coefficients du fractionnement isotopique associé à chaque transition de phase et sur des hypothèses pour représenter la micro-physique des nuages. En effet, chaque processus physique dépendant de la masse ou de la symétrie de la molécule d'eau va résulter en un fractionnement isotopique.

Ainsi, lors de la formation de flocons de neige à basse température, le fractionnement isotopique associé à la transition de phase vapeur-glace mais aussi aux différentes diffusivités des différents isotopes doivent être pris en compte [Jouzel and Merlivat, 1984]. A basse température, les déterminations des coefficients du fractionnement isotopique associés à la transition de phase vapeur-glace présentent d'importantes différences [Merlivat and Nief, 1967; Majoube, 1971a; Ellehøj et al., 2013] et n'ont jamais pu être mesurées à des températures inférieures à $-40°C$. Or, la température moyenne annuelle à Dome C est de $-54°C$ atteignant jusqu'à $-85°C$ l'hiver. Les diffusivités des différents isotopes quant à elles n'ont jamais été mesurées à des températures inférieures à $10°C$ [Merlivat, 1978a; Cappa et al., 2003; Luz et al., 2009] et seuls des modèles permettent d'estimer les variations des différentes diffusivités des différents isotopes [Lu and DePaolo, 2016].

En plus de l'information principale de température enregistrée par $\delta^{18}O$, $\delta^{17}O$ et δD, les combinaisons des différentes compositions isotopiques en paramètres de second ordre appelés *excès* fournissent des informations supplémentaires. L'excès en deutérium ($d-excess = \delta D - 8 \times \delta^{18}O$ [Dansgaard, 1964]) fournit des informations sur l'humidité relative pendant l'évaporation au niveau des océans [Gat, 1996], pendant la ré-évaporation dans les zones convectives [Risi et al., 2008]. Le *d-excess* a aussi été utilisé pour paramétriser l'évolution spatiale de la sursaturation en régions polaires [Ciais and Jouzel, 1994; Werner et al., 2011] ou encore mettre en évidence les changements de température à la source des masses d'air humide associés aux changements d'obliquité sur les 150 000 dernières années [Vimeux et al., 1999]. L'utilisation du *d-excess* dans les carottes de glace polaires reste limité car il est aussi affecté par l'humidité de la région source et la température locale [Jouzel et al., 2007] ou encore la trajectoire suivie par la masse d'air [Bonne et al., 2015].

Récemment, l'amélioration des techniques de mesure a permis la mesure d'un second paramètre de second ordre, l'excès en ^{17}O ($^{17}O-excess = ln\left(\delta^{17}O+1\right) - 0.528\, ln\left(\delta^{18}O+1\right)$ [Barkan and Luz, 2005; Landais et al., 2008]). Comme pour le *d-excess*, le $^{17}O-excess$ est affecté au cours du cycle hydrologique par différents processus de fractionnement

qui affectent le $\delta^{18}O$ et le $\delta^{17}O$ différemment. Aux basses latitudes, le $^{17}O-excess$ est affecté par l'humidité relative qui impose l'importance relative du fractionnement à l'équilibre par rapport au fractionnement cinétique dans les processus d'évaporation et de ré-évaporation comme l'est le *d-excess*. Il en découle que *d-excess* et le $^{17}O-excess$ augmentent tous deux quand l'humidité relative diminuent. Aux hautes latitudes en revanche, contrairement au d-excess, le $^{17}O-excess$ n'est que peu affecté par les changements de température locale car les fractionnements à l'équilibre associés au $\delta^{18}O$ et le $\delta^{17}O$ ont la même dépendance en température. Pour les régions les plus froides cela dit, l'impact croissant du fractionnement cinétique a pu induire la signature de la température de condensation dans le $^{17}O-excess$ [Landais et al., 2012a; Winkler et al., 2012].

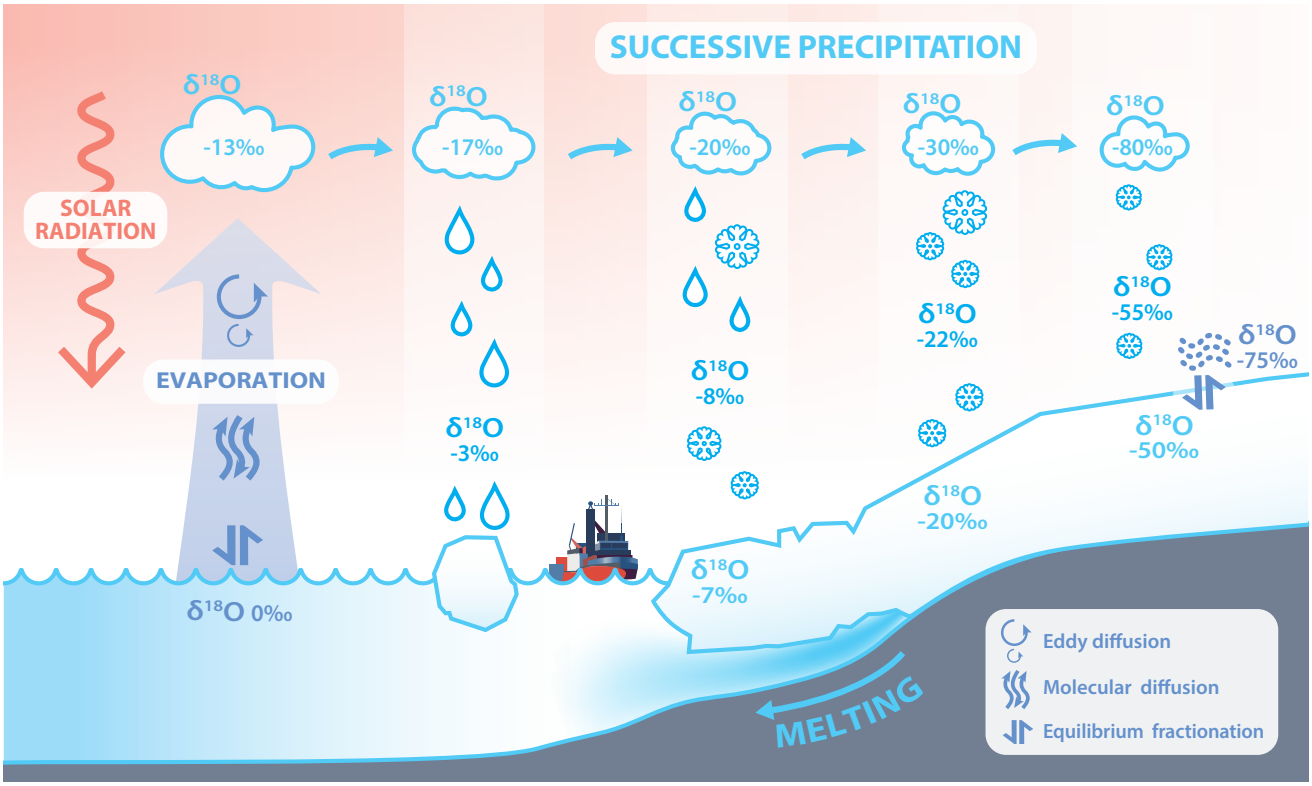

FIGURE A.1 – Description des différents processus affectants la composition isotopique dans le cycle de l'eau en régions polaires.

Afin d'améliorer les performances du paléothermomètre isotopique, l'étude des processus affectant la composition isotopique de la glace est primordiale. Dans cette optique, ma thèse a été à l'interface entre les études de processus au laboratoire et en Antarctique et le développement instrumental afin de pouvoir réaliser des mesures encore inédites. Ainsi, afin de pouvoir réaliser des études de processus avec des méthodes analytiques poussées, j'ai d'abord approfondi les recherches sur les différentes techniques de mesure

existantes avant ma thèse, ce qui a conduit au développement d'un nouveau spectromètre infrarouge aux performances bien au delà des instruments commerciaux. En Parallèle, des expériences au laboratoire ont permis de renforcer les connaissances sur les processus affectant les isotopes de l'eau, en particulier le fractionnement lié à la transition de phase vapeur - glace et le fractionnement cinétique lié aux différentes diffusivités des différents isotopes. Enfin, durant une campagne en Antarctique, j'ai pu réaliser parmi les premières mesures de la composition isotopique de la vapeur et de la glace en Antarctique et appliquer les modèles physiques des processus à des données de terrain.

Méthodes de mesure

Afin d'être à même d'étudier les processus affectant les isotopes de l'eau dans les meilleures conditions, il est important d'avoir des protocoles de mesure de la glace et de la vapeur aussi performants que possible. Dans cette optique, un grand volet de ma thèse a été de travailler avec les différentes méthodes de mesure des isotopes de l'eau. En particulier, j'ai pu travailler en parallèle avec des méthodes de spectrométrie de masse, la référence, et des méthodes de spectroscopie infrarouge. Si la spectrométrie de masse permet des mesures précises et robustes, les méthodes d'extraction chimiques sont longues et permettent seulement la mesure de 8 échantillons par jour. Les mesures de $\delta^{18}O$ et le $\delta^{17}O$ au LSCE ont été réalisées sur une ligne de fluorination sur le modèle de la méthode développée par Barkan and Luz [2005] avec une précision d'environ 5 ppm sur le $^{17}O-excess$. La spectroscopie infrarouge permet maintenant de mesurer les trois compositions isotopiques de manière moins précise (environ 15 ppm [Steig et al., 2014]) mais beaucoup plus rapide (jusqu'à 20 échantillons par jour).

Afin de pousser plus loin, en collaboration avec le LIPHY, j'ai travaillé sur un instrument de type OFCEAS qui permet de mesurer les isotopes de l'eau jusqu'à des humidités de l'ordre de quelques ppm. Cela dit, la véritable évolution provient du développement d'un spectromètre infrarouge de nouvelle génération basé sur deux cavités : une pour stabiliser la fréquence du laser et obtenir une source ultra-stable et très fine (largeur inférieure à 300 Hz avec une drift d'environ 1.5 $Hz.s^{-1}$) et une cavité de mesure de très haute performance avec une rapport signal sur bruit allant jusqu'à 700 000. Ces nouveaux développements instrumentaux promettent des mesures d'une précision incomparable des isotopes de l'eau au laboratoire et sur le terrain. Ce nouvel instrument a aussi pu être utilisé pour des mesures d'optique appliquées à la détermination des paramètres de spectroscopie de l'eau et à la stabilisation d'un laser télécom par une cavité ultra-stable.

Etude du fractionnement isotopique en laboratoire

Pendant ma thèse, j'ai réalisé des expériences de laboratoire pour étudier le fractionnement isotopique, à la fois cinétique et à l'équilibre. En effet, les nouvelles méthodes de spectroscopie infrarouge permettent de mesurer directement la vapeur sans passer par un transfert chimique vers le spectromètre de masse. En particulier, celles-ci ont permis de revisiter l'expérience de Jouzel and Merlivat [1984] afin de mesurer l'impact du fractionnement cinétique sur le $d-excess$ et le $^{17}O-excess$. Une expérience préliminaire a montré que l'impact du fractionnement cinétique lié aux différences de diffusivité avait le même impact sur le $^{17}O-excess$ que sur le $d-excess$. Une seconde expérience en chambre à nuage a permis d'analyser de manière quantitative les profils de compositions isotopiques dans un gradient d'humidité et de température, mettant en évidence les lacunes de la représentation de Jouzel and Merlivat [1984].

Suivant l'approche débutée par Ellehøj et al. [2013] d'utiliser un spectromètre infrarouge pour analyser la vapeur après une chambre de condensation, l'étude du fractionnement à l'équilibre solide-vapeur a pu aussi être abordé. Si les mesures de laboratoire n'ont pas pu être réalisées de manière répétées dans le cadre de ma thèse, une comparaison avec des données de terrain et un modèle en boite permet une comparaison d'étude de processus en laboratoire et sur le terrain et fournit une explication sur la différence entre les mesures d'Ellehøj et al. [2013] d'une part et de Merlivat and Nief [1967] et Majoube [1971a] d'autre part.

Etude de la composition isotopique sur le Plateau Antarctique

Durant le cadre de ma thèse, j'ai pu prendre part à une campagne de mesure de la composition isotopique de la vapeur et de la neige à Dome C. Cette étude est la première à mesurer la composition isotopique de la vapeur d'eau à si basse humidité et une des premières en Antarctique. Afin de réaliser cette campagne, nous avons dû porter spécialement soin aux calibrations des instruments qui fonctionnaient hors de leur gamme linéaire. L'installation simultannée de deux spectromètres infrarouge (un Picarro L2130i et un OFCEAS H_2Oi) ainsi qu'un piège cryogénique a permis de valider une série de mesures continues de la vapeur d'eau de 25 jours consécutifs. L'intérêt de mesurer la composition isotopique de la vapeur d'eau à Dome C pour étudier les processus réside dans la multitude d'installations de mesure de la couche limite atmosphérique (température, humidité, vent), de la troposphère entière (un LIDAR et un radiomètre mesurants la température, l'humidité, la

présence d'eau sous forme liquide ou solide...), de la surface de la neige (température, chimie, SSA)... En combinant nos résultats à des mesures de la couche limite, nous avons mis en évidence l'impact de la turbulence sur le lien entre la composition isotopique de la vapeur et la température à l'échelle diurnale. Dans les régimes turbulents ou non, d'importants cycles de condensation/sublimation résultent en d'importants échanges entre la vapeur et la neige. Dans le cas d'un régime turbulent, la vapeur de la couche limite est bien mélangée et la neige échange avec un important réservoir de vapeur. Dans le cas d'un régime stratifié ou faiblement turbulent, la composition isotopique de la vapeur à deux mètres n'affiche plus aucun cycle diurnal.

La pente entre δD et $\delta^{18}O$ est néanmoins beaucoup plus basse que prédite par le fractionnement à l'équilibre (5.3‰/ ‰ au lieu de 6.5‰/ ‰), ce qui pose des questions sur l'hypothèse d'une source principale de la vapeur par les échanges avec la neige locale.

Dans un second temps, la comparaison entre la composition isotopique de la vapeur, de la précipitation, de la neige de surface et de la neige plus profonde a permis de mieux comprendre comment le signal climatique est archivé. Suivant les bases posées par Touzeau et al. [2016], j'ai pu réaliser une étude quantitative de données de neige, de vapeur et de précipitation autour du plateau Antarctique. Les données de Dome C mettent en évidence une intermittence du lien entre la composition isotopique de la neige et la température à l'échelle saisonnière. Ces résultats viennent altérer l'interprétentation des reconstructions à l'échelle annuelle à partir de la composition isotopique de la neige/glace en Antarctique de l'Est. Finalement, tous ces résultats sont utilisés pour approfondir l'utilisation des isotopes de l'eau comme proxy paléoclimatique et aussi comme traceur atmosphérique.

Conclusions et perspectives

Cette thèse m'a permis de couvrir plusieurs aspects de la physique des isotopes stables de l'eau. Les isotopes de l'eau peuvent fournir énormément d'informations grâce au lien direct entre le fractionnement isotopique pendant un changement d'état et la température. Cependant, sur le plateau Est Antarctique, leur interprétation n'est pas si directe. La compréhension de la manière dont le signal climatique est archivé par la composition isotopique de la neige est cruciale. En effet, pour le moment, la relation liant la composition isotopique de l'eau à la température est seulement empirique. Comme nous l'avons vu, d'importantes variations de cette relation ont lieu selon les lieux et les époques. La principale limite pour pouvoir théoriser ce lien est le manque d'un cadre robuste des processus

physiques affectant la composition isotopique de l'eau à basse température.

Ici, nous avons présenté le premier instrument capable de mesurer la composition isotopique de la vapeur d'eau à des concentrations de l'ordre du *ppm*. Cet instrument procurera des opportunités exceptionnelles dans l'étude des processus physiques affectant les isotopes de l'eau dans les conditions qui règnent sur le Plateau Est Antarctique, même en hiver et permettra de repousser les limites de notre compréhension de la formation de la neige en Antarctique. Il n'est pas seulement crucial d'améliorer notre appréhension de la formation de la neige pour les études de paléoclimatologie mais aussi pour les études des climats actuels : en effet, les isotopes stables de l'eau peuvent être utilisé comme traceur des processus atmosphériques à différentes échelles : de la turbulence dans la couche limite à des circulations de grande échelle ; mais aussi comme traceur du métamorphisme qui joue un rôle prédominant par exemple dans les variations d'albédo de la neige.

Appendix B

My Ph-D from a non-scientific perspective

During my Ph-D, I was involved into several initiative to bring my research and research in general to a broader audience. I think this enables research to be more transparent to a larger public which is fundamental to fight scepticism and obscurantism.

B.1 Opening research to highschoolers: building a 3D scanner

During my campaign to Dome C, I realised a time lapse of the evolution of the frost hoar at the surface of the snow. This idea just meant to be a fun video to show to my folks once back home finally provided interesting scientific estimates of the deposition of frost during the daily cycle. In order to realise a more quantitative estimate of the mass budget associated to the frost deposition, I decided to build a 3D-scanner building on the Do-It-Yourself trend (DIY). The small project has been awarded at the Flash Freeze event of the Cryosphere division of the American Geophysicist Union (AGU) and is supported by APECS France logistically.

B.1.1 The 3D-scanner project

The analysis of the time lapse images has highlighted important evolution of the size of the ice crystals as illustrated on figure B.2. Using a ruler as a reference, it was possible to highlight that within a couple of hours, the length and the width of a series of crystals was multiplied by 2. This growth is simultaneous with opposite evolutions of the isotopic composition of the snow surface and of the vapour, a supersaturation higher than 120% and observations of mist. Still, because the third dimension is missing, it is not possible

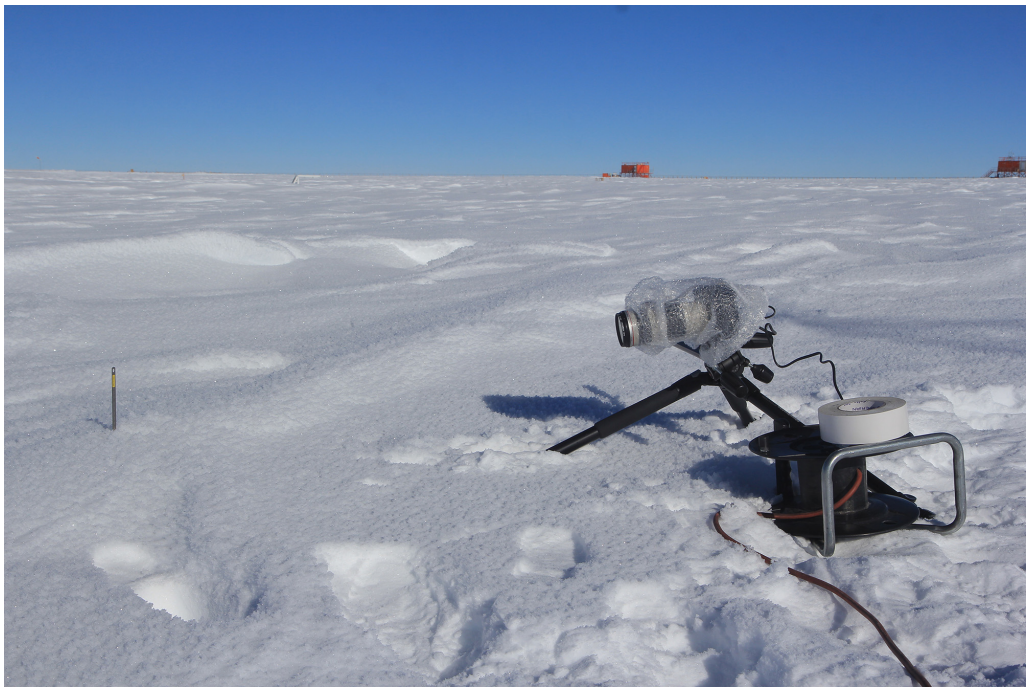

Figure B.1: Picture of the camera realising the time lapse of the frost deposition during 24 hours at Dome C (Courtesy Bruno Jourdain)

to realise a complete mass budget.

Nevertheless, these submillimetric frost deposition can have a significant contribution to the global mass budget of the snow surface. Indeed, because accumulation is lower than 8 *cm* every year at Dome C, these small depositions can add up and significantly contribute. This motivated a plan to build a 3D-scanner able to measure frost deposition by realising time lapse all year long. The new developments of powerful micro-controllers is also an additional motivation to develop such a system. Indeed, numerous projects build on the DIY trend using Arduino's or Raspberries' micro-controllers to realise small project from 3D-scanner to 3D-printers or automatic samplers. The initial plan of the 3D-scanner is illustrated on figure B.3. A camera equipped with a macro-lens would be positioned above the snow surface. The third dimension would be reconstructed using a laser beam with an angle and measuring the position where it hit the snow crystals using Thales law. To improve the efficiency of the scanning, 4 laser slits with different colors can be used and separated with the Bayer matrix of the camera. This method would still require more than a minute to realise one 3D-image. Extra care has to be addressed for temperature stabilisation of the instrument enabling mechanical part and electronic part to work properly but preserving the radiation from sublimating the snow artificially.

Figure B.2: Picture of the small ice crystals at Dome C durinng the time lapse of the frost deposition during 24 hours

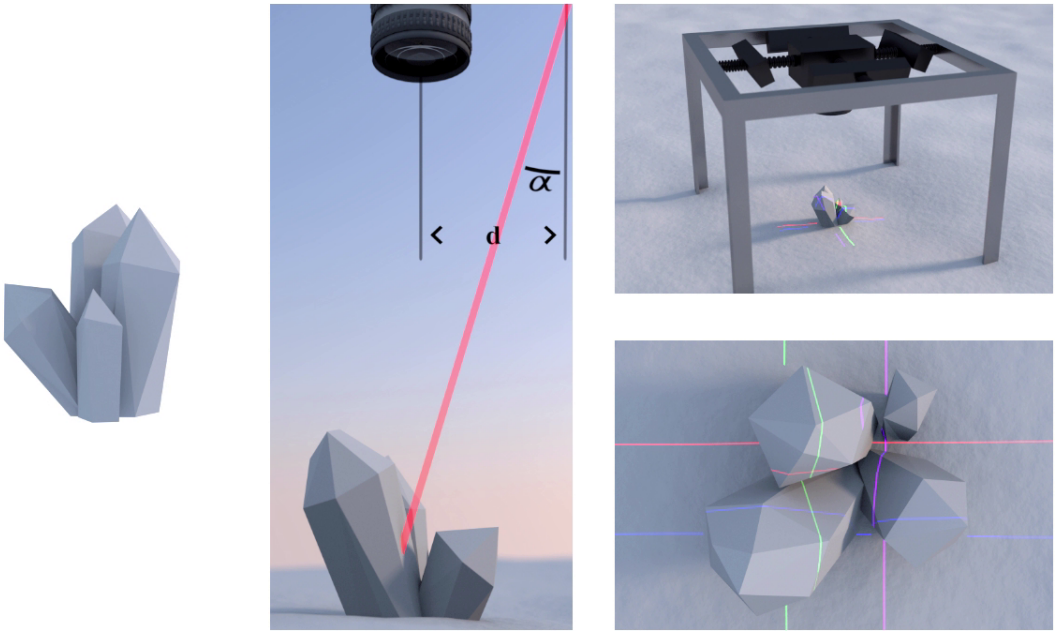

Figure B.3: 3D-schematics of a crystal (left), the principle of measurement using a laser beam with an angle to estimate the vertical dimension (middle), a large view of the scanner (right top) and a representation of what kind of picture the camera should shoot (right bottom)

The *MPS* 2^{nd} highschool class from Jacques Decour (Paris, France) has participated in the project with the help of Juliette Dumas and of the association APECS France. Unfortunately, schedules issues prevented from actually building the 3D-scanner during the scholar year, but the highschoolers were involved in the project with 3 discussion sessions during which they could learn how building a research project can be done. The original plan to involve a class in testing the instrument and even maybe deploying the instrument in the Alps will be tried again in 2017.

B.1.2 Pedagogic content

Attached bellow are the slides used during the discussions with the students:

- On the 9th of May, how to realise a 3D image
- On the 23rd of May, on the formation of the snow in Antarctica

Comment acquérir une image en 3D ?

Mathieu Casado
Laboratoire des sciences du climat et de l'environnement (LSCE)
Institut Pierre Simon Laplace, CEA, CNRS, UVSQ
Gif Sur Yvette France

La glace : une archive

A. Orsi

Comprendre sa formation

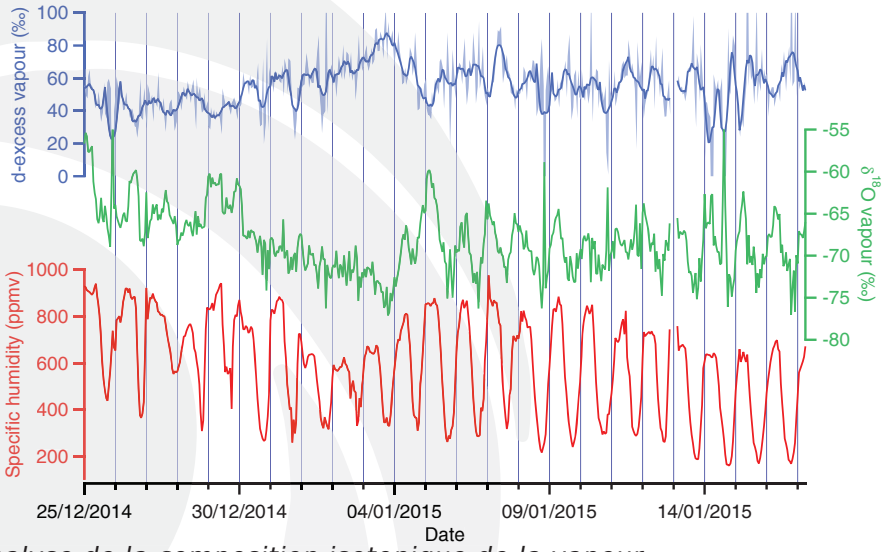

Analyse de la composition isotopique de la vapeur en parallèle du dépot de givre

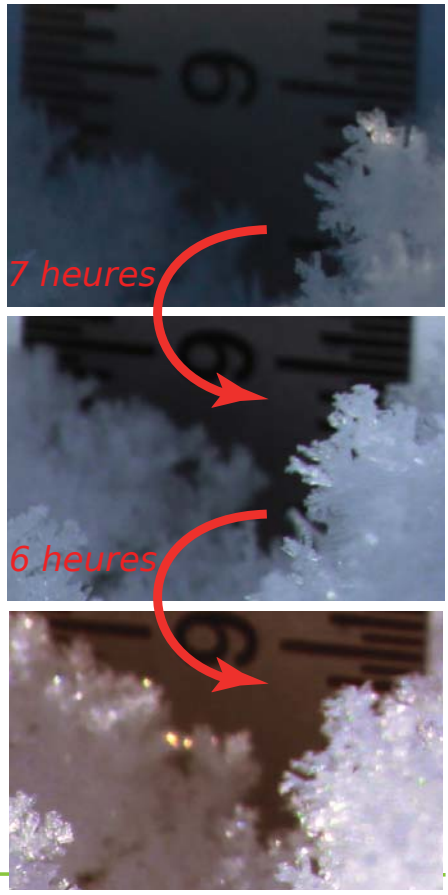

- L'accumulation annuelle à Concordia est de moins de 8 cm par an
- Avec une accumulation si faible, même des dépots qui sont inférieurs au mm vont contribuer de manière significative au budget annuel

Realisation d'un scanner 3D

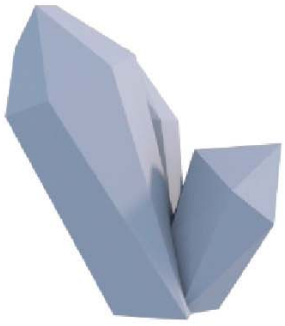

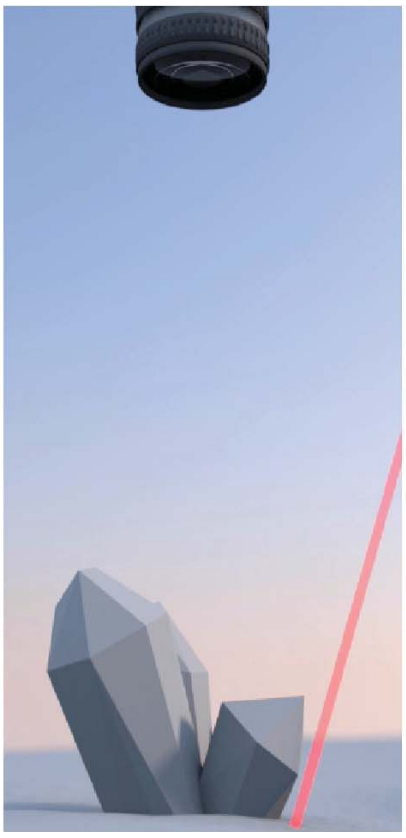

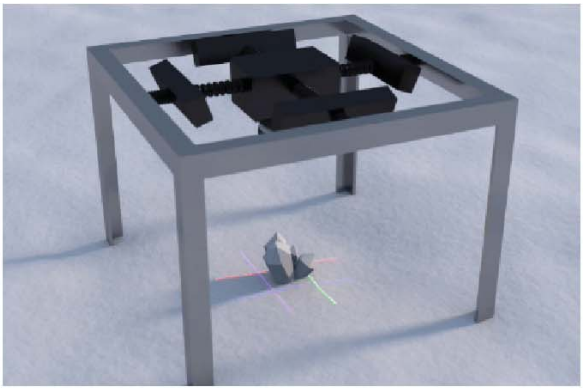

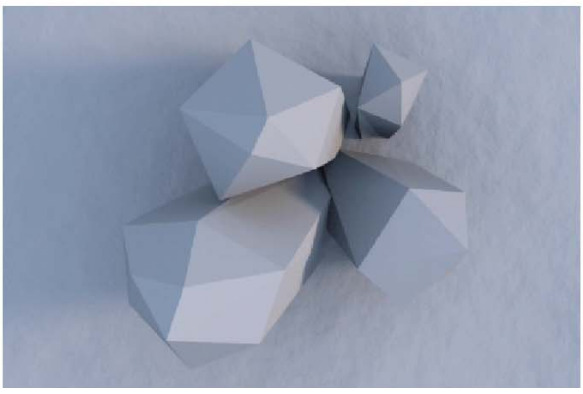

Acquisition d'une image

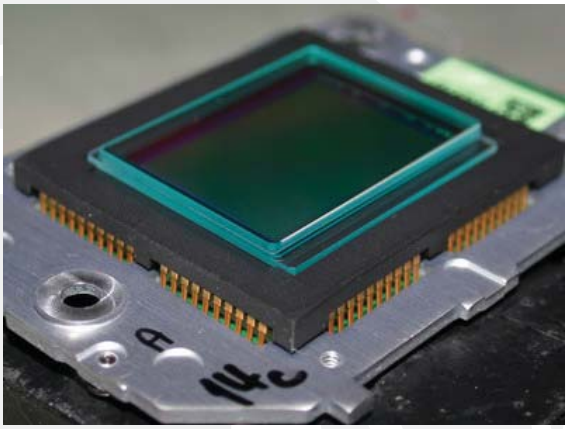

Capteur d'appareil photo numérique

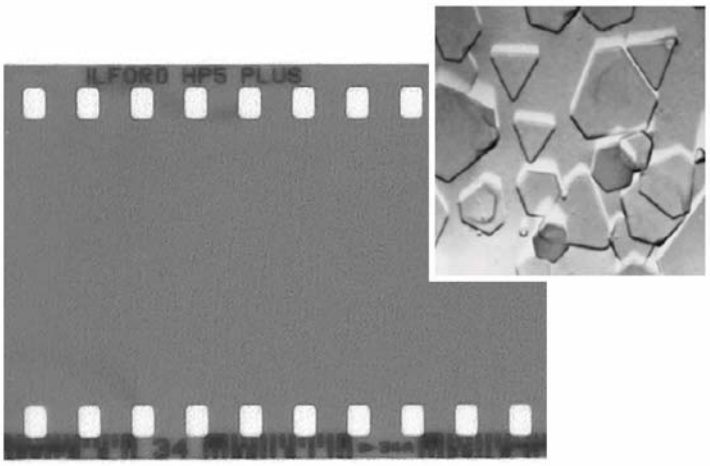

Pellicule photographique et détail de cristaux de bromure d'argent

La photographie permet d'acquérir le signal lumineux et de reconstruire une image en 2D, que la technologie soit numérique ou argentique

Acquisition d'une image

$$Br^- + h\upsilon \longrightarrow Br^0 + e^-$$

Les cristaux sont sensibles à la lumière visible car l'énergie correspond à celui de la réaction chimique

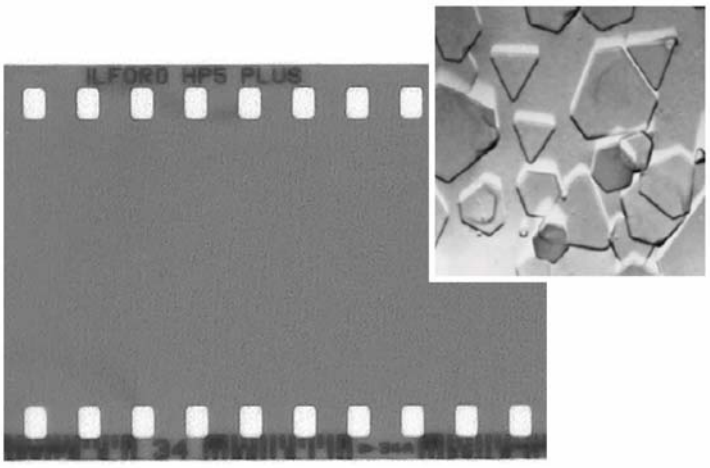

Pellicule photographique et détail de cristaux de bromure d'argent

Acquisition d'une image

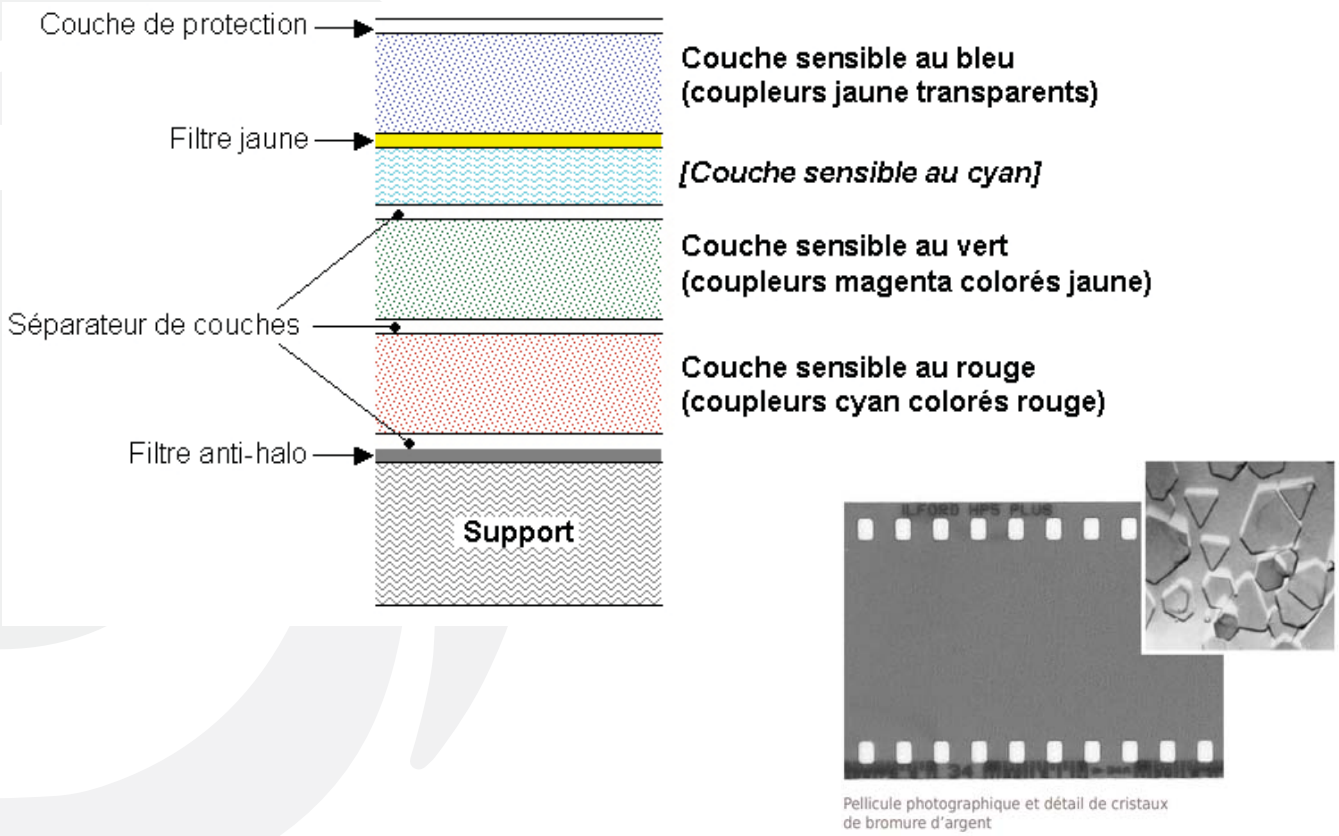

Pellicule photographique et détail de cristaux de bromure d'argent

Acquisition d'une image

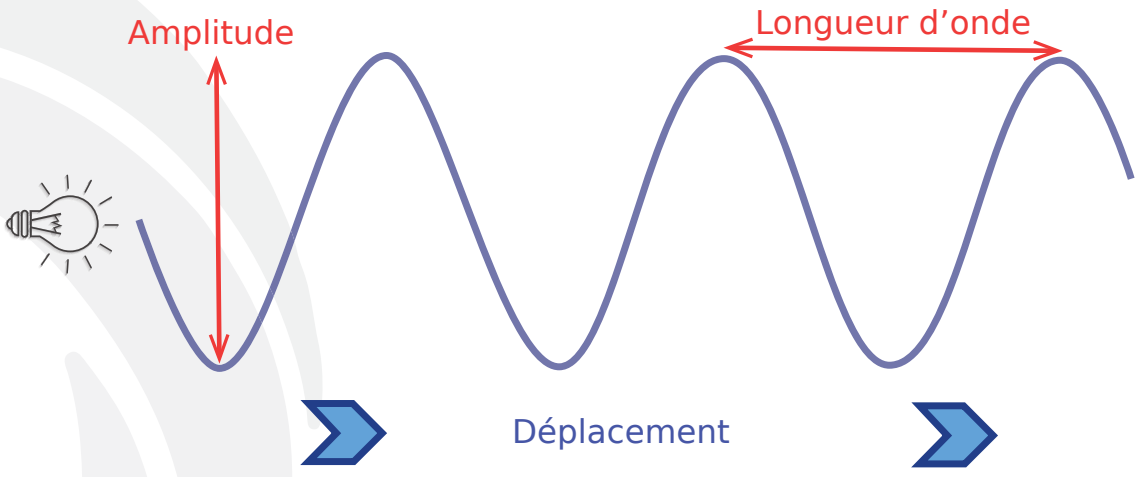

L'amplitude est égale au nombre de photons

La longueur d'onde donne la couleur

Acquisition d'une image

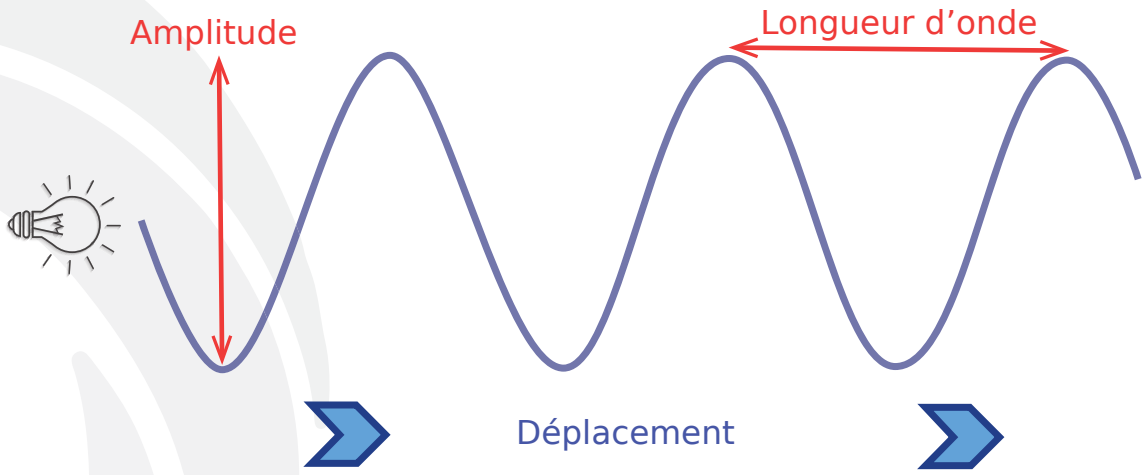

Troisième information:

la phase du faisceau lumineux

Acquisition d'une image

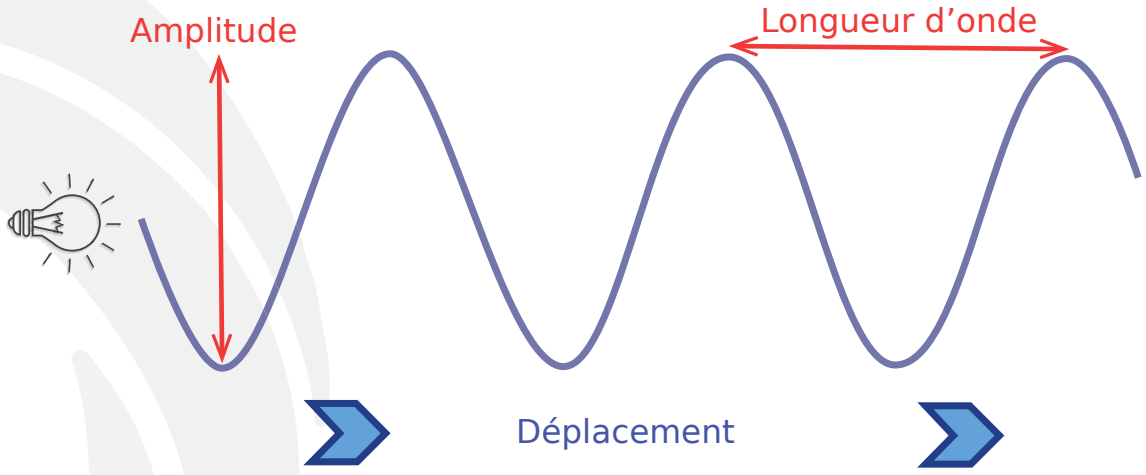

Troisième information:

la phase du faisceau lumineux
Pour la lumière visible, l'échelle est bien trop petite pour être mesurée avec des fréquences typiques de 10^{14}Hz

Comment récupérer la phase

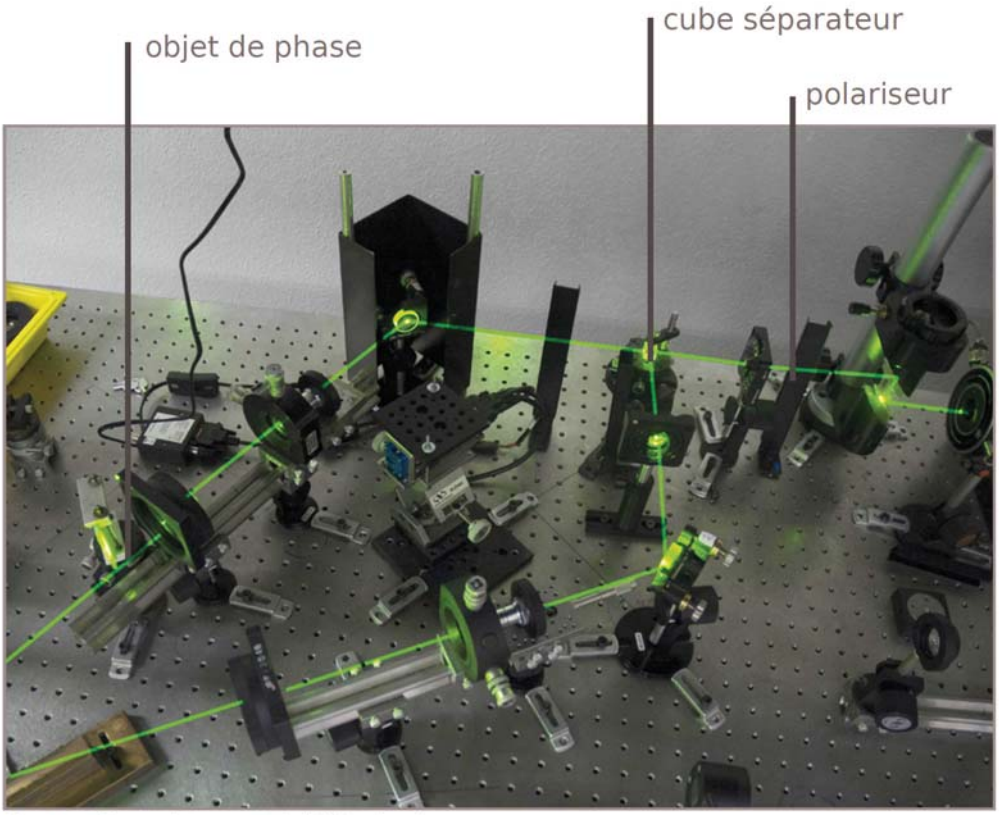

Montage d'enregistrement de l'objet de phase

Interférences lumineuses

Interférences d'ondes électromagnétiques cohérentes :

- Quand les ondes sont en phase, les signaux s'additionnent

- Quand les ondes sont en opposition de phase, elles s'annulent

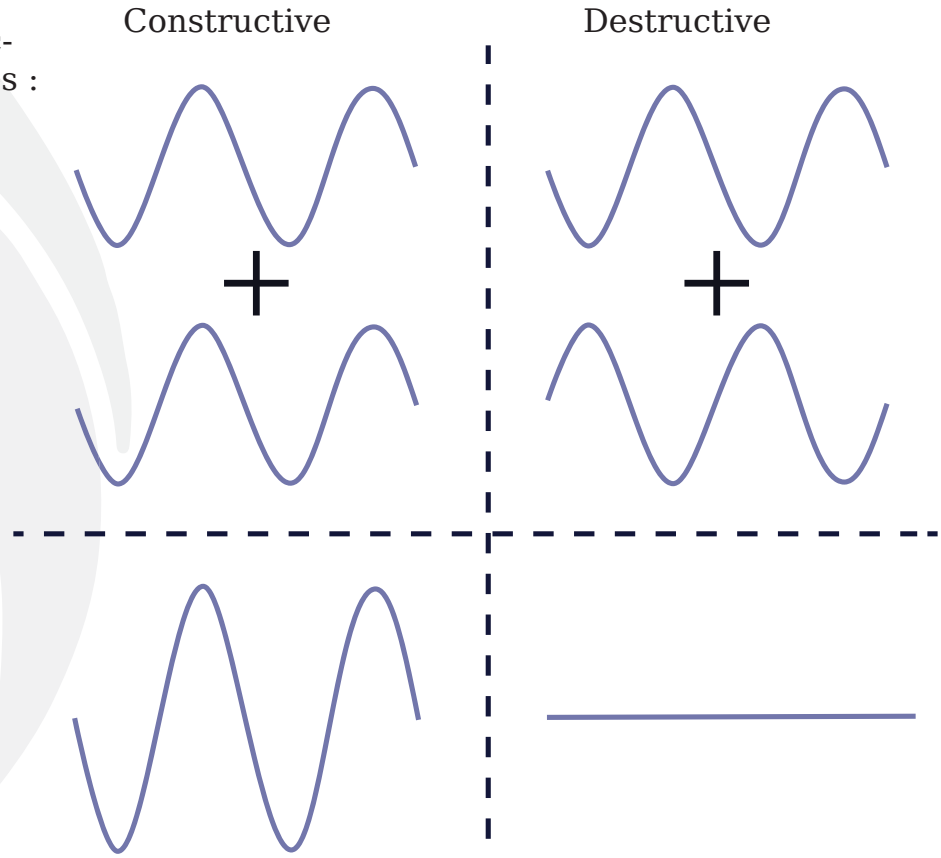

Interférences lumineuses

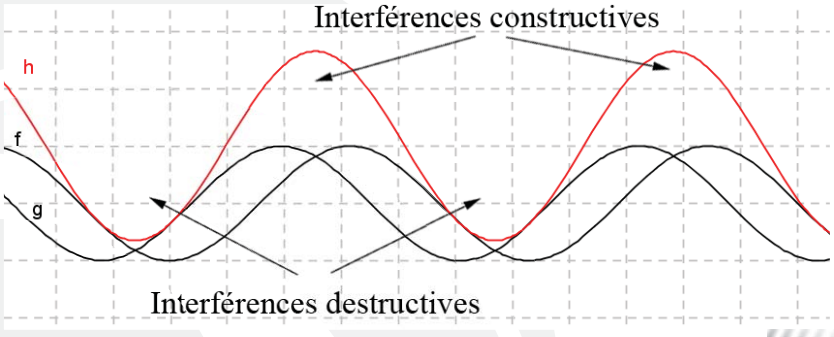

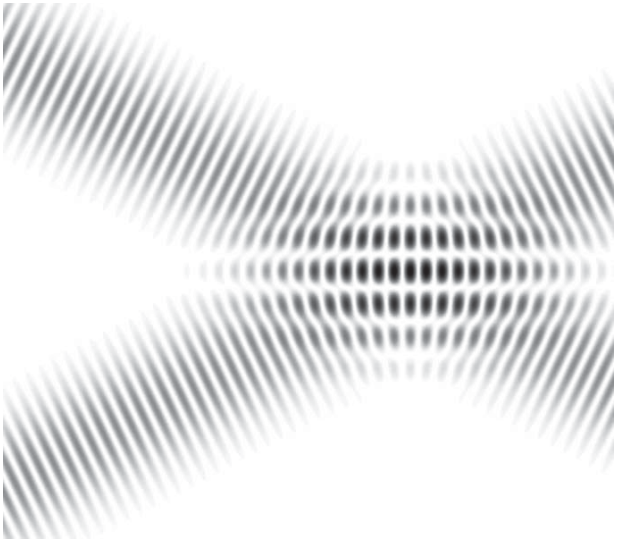

Source: wikipedia

Reconstruction de la 3D

Un objet homogène :

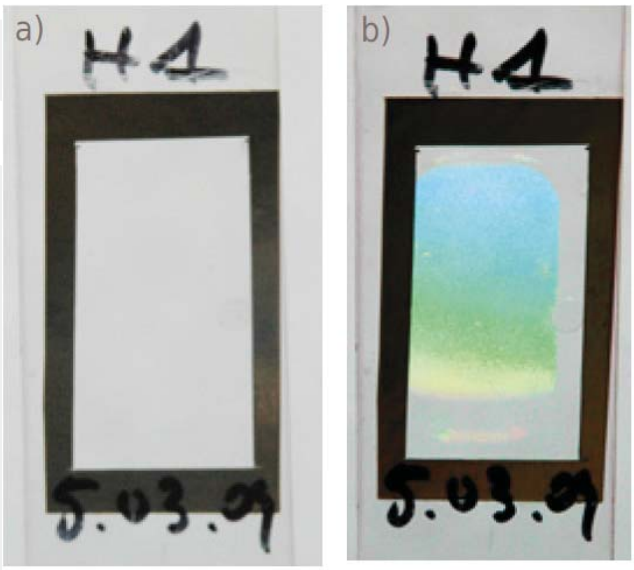

a) à un angle quelconque
b) à l'angle de Bragg(1)

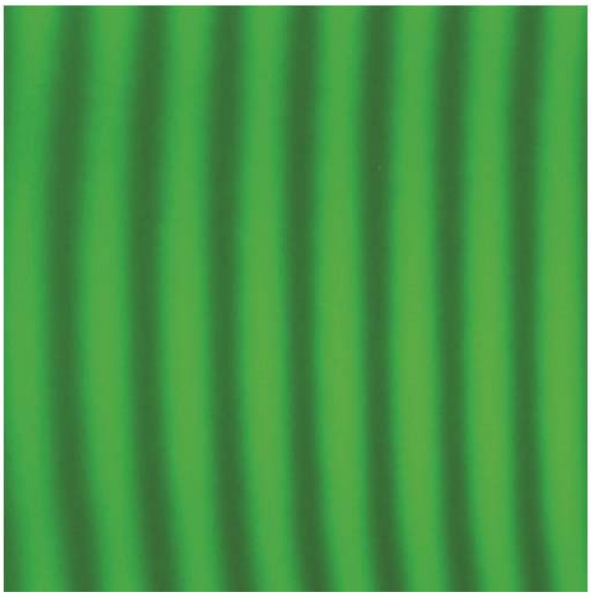

Observation des franges sans objet de phase à l'aide d'un microscope interférentiel.

Reconstruction de la 3D

La mire :

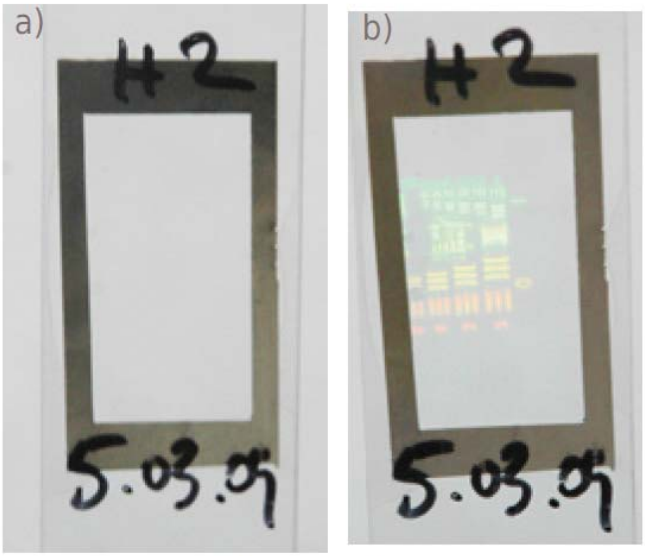

a) à un angle quelconque
b) à l'angle de Bragg(1)

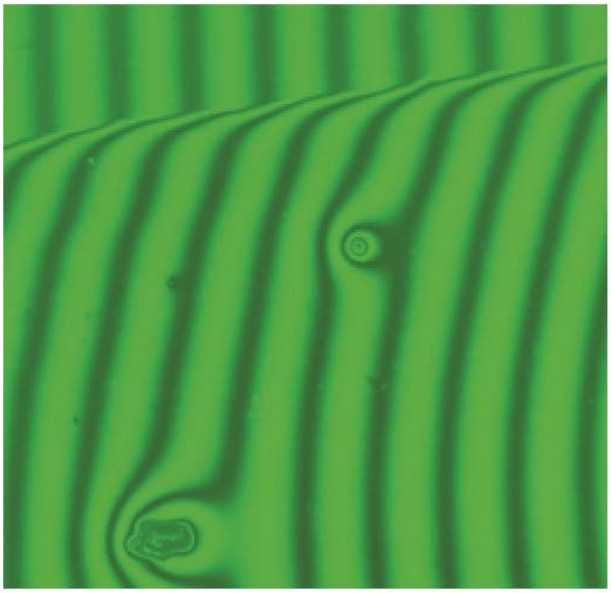

Observation des franges déformées par la phase de l'objet à l'aide d'un microscope interférentiel.

Reconstruction de la 3D

Fabrication d'un hologramme

En utilisant une référence lumineuse, on obtient une information sur la profondeur

Les hologrammes numériques ne sont pas encore répandus.

Pour une expérience de terrain, on ne peut pas encore se baser sur cette technique

Hologramme réalisé par Yves Gentet

Comment obtenir la 3D ?

Le but de l'expérience :

Fabriquer un scanner 3D déployable sur le terrain pour scanner des cristaux de glace d'une taille de 0.1 à 1mm

Nécessite:

- Un système robuste (Froid, vent, peu d'attention à lui donner)

- Précision < 0.1 mm

- Temps de mesure : moins d'une minute

- Equipement informatique minimal

- Automatisé

La vision

La vision humaine utilise la stéréoscopie pour reconstruire la 3D

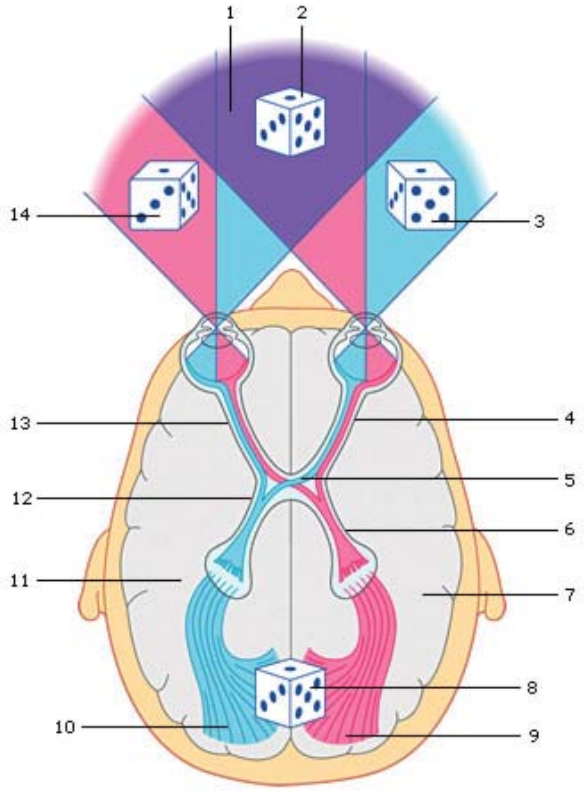

Exemples de stéréoscopie

Source: E. Lucas

Exemples de stéréoscopie

b/d = 0.02

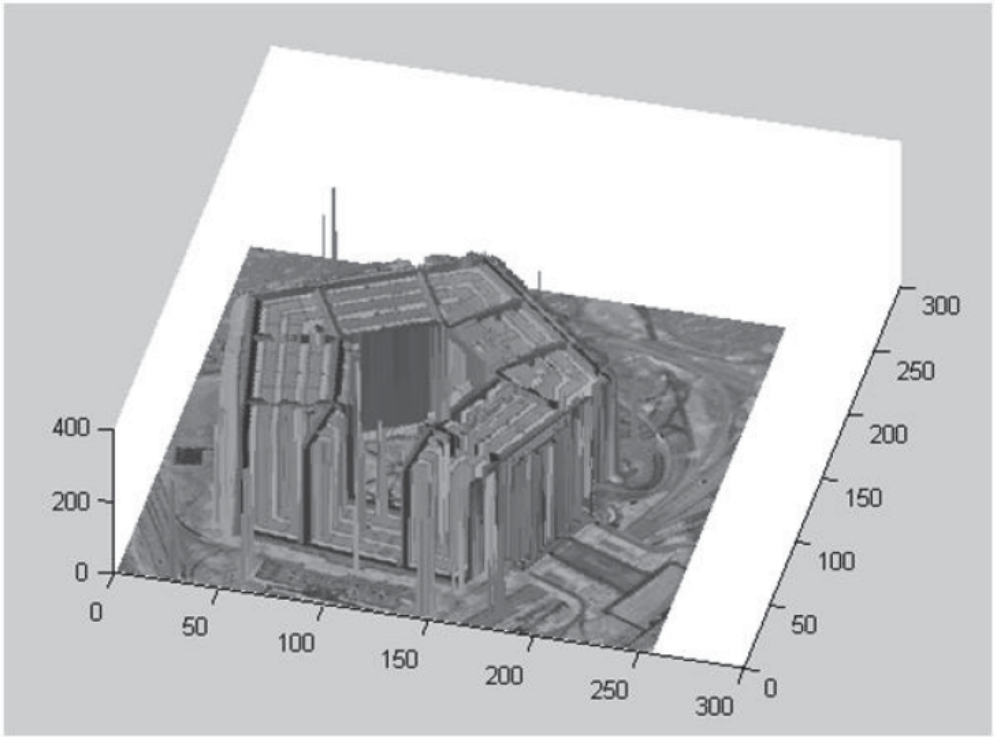

Source: E. Lucas

Faisceau laser

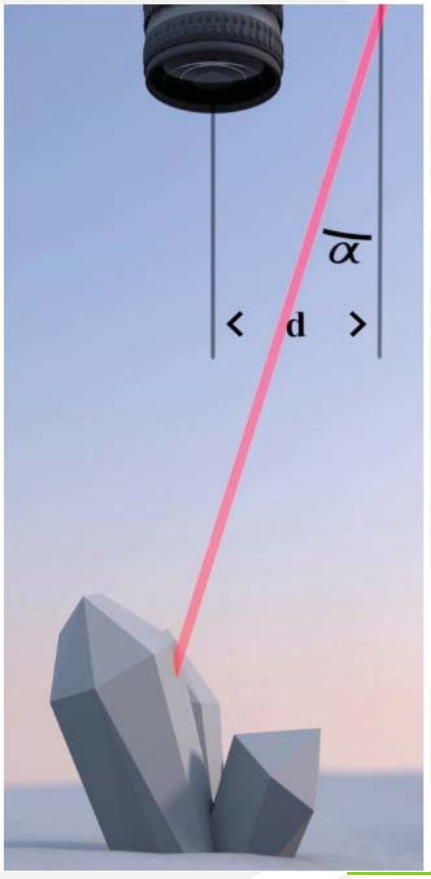

Précision limitée par la taille du faisceau laser

Comment se forme la neige de l'Antarctique ?

Mathieu Casado
Laboratoire des sciences du climat et de l'environnement (LSCE)
Institut Pierre Simon Laplace, CEA, CNRS, UVSQ
Gif Sur Yvette France

La glace garde en mémoire le climat du passé

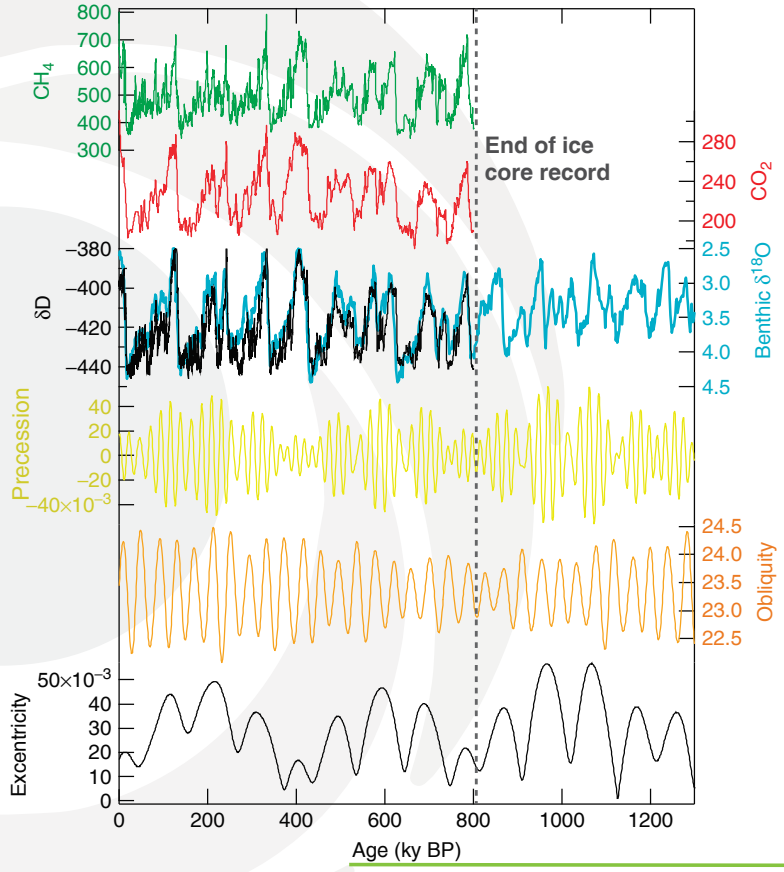

- La composition de la glace (isotopes)
- Les bulles d'air piégées dans la glace (CO_2 et CH_4...)
- La temperature dans les trous de forage
- Les cendres et les poussières

Jouzel et Masson-Delmotte 2010

La glace garde en mémoire le climat du passé

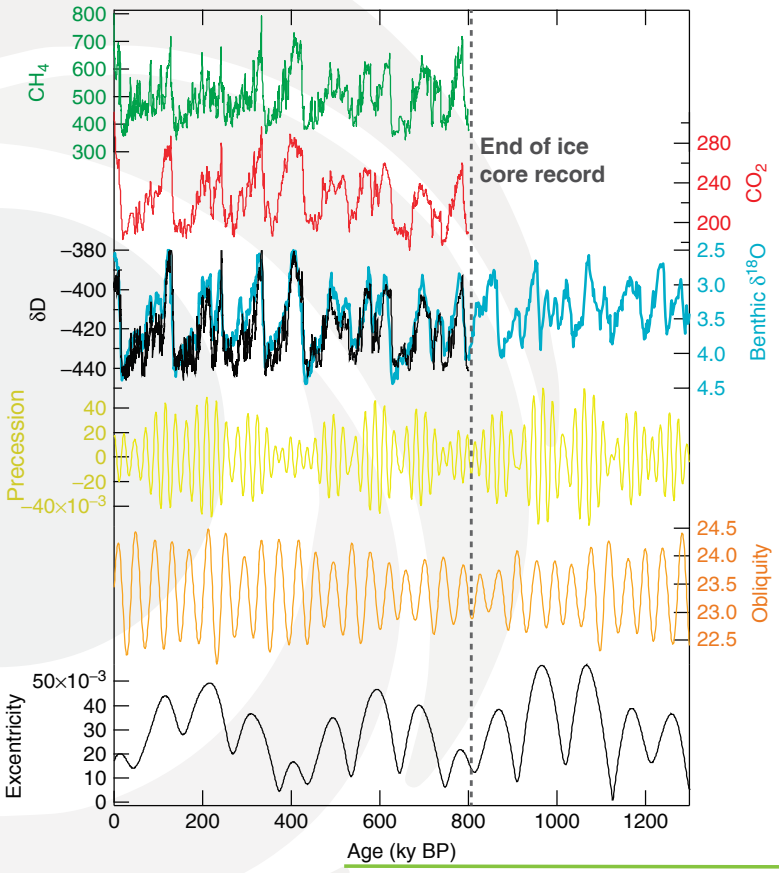

- Ces cycles sont liés aux variations des paramètres de l'orbite de la terre :

  - l'excentricité E

  - l'obliquité T

  - la précession P

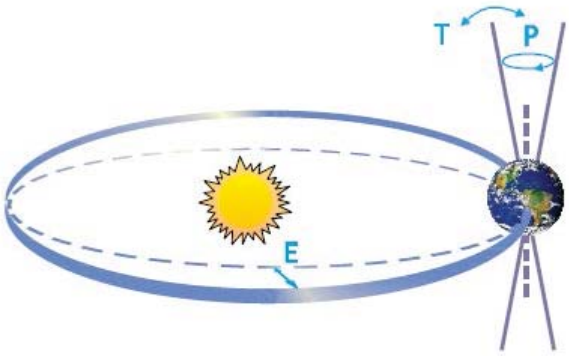

Jouzel et Masson-Delmotte 2010

Archivage du signal climatique

Des bulles d'air sont piégées dans la glace avec la composition de l'atmosphère de l'époque.

Comme la neige est poreuse sur les 100 premiers mètre, des échanges entre l'atmosphère et l'air dans la neige peuvent avoir lieu.

Pour des sites de faible accumulation, 100 mètres de neige correspondent à plusieurs milliers d'années et donc, l'air piégé est plus jeune que la glace qui l'entoure.

Pour reconstruire le climat, il est important de comprendre les méchanismes qui assurent la formation de la glace.

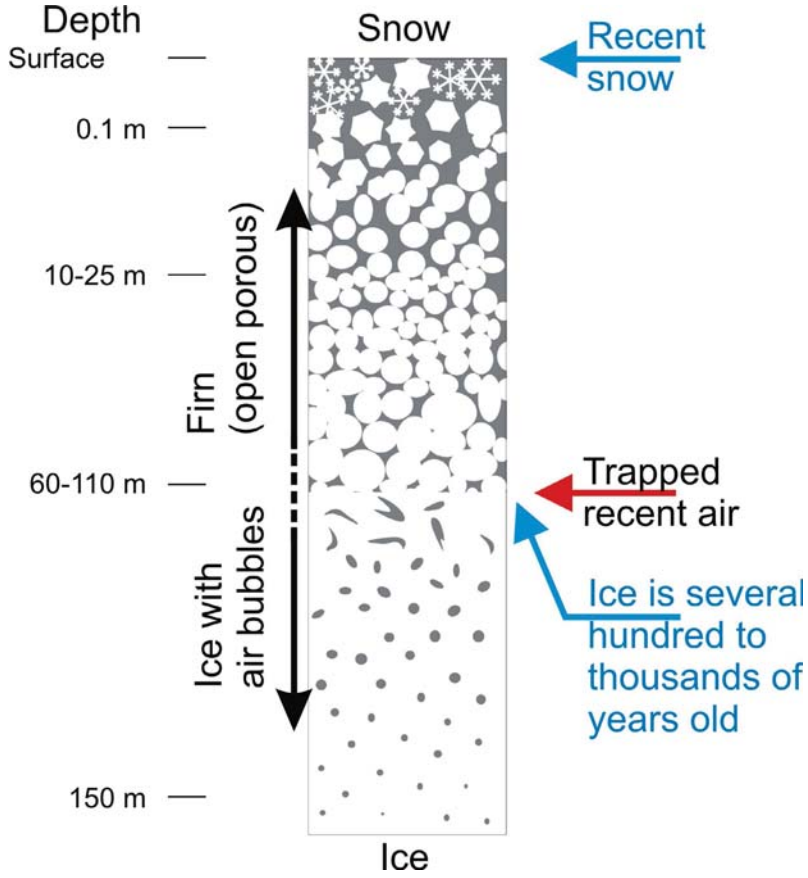

Source T. Blunier
http://www.iceandclimate.nbi.ku.dk

La neige n'est pas une archive passive

Evolution de la structure de la neige dans un gradient de temperature de 50°C/m pendant 3 semaines

La vidéo est réalisée à l'aide d'un micro scanner CT.

La matière est redistribuée et donc il y a un mélange entre flocons dont la composition isotopique n'est pas forcément la même.

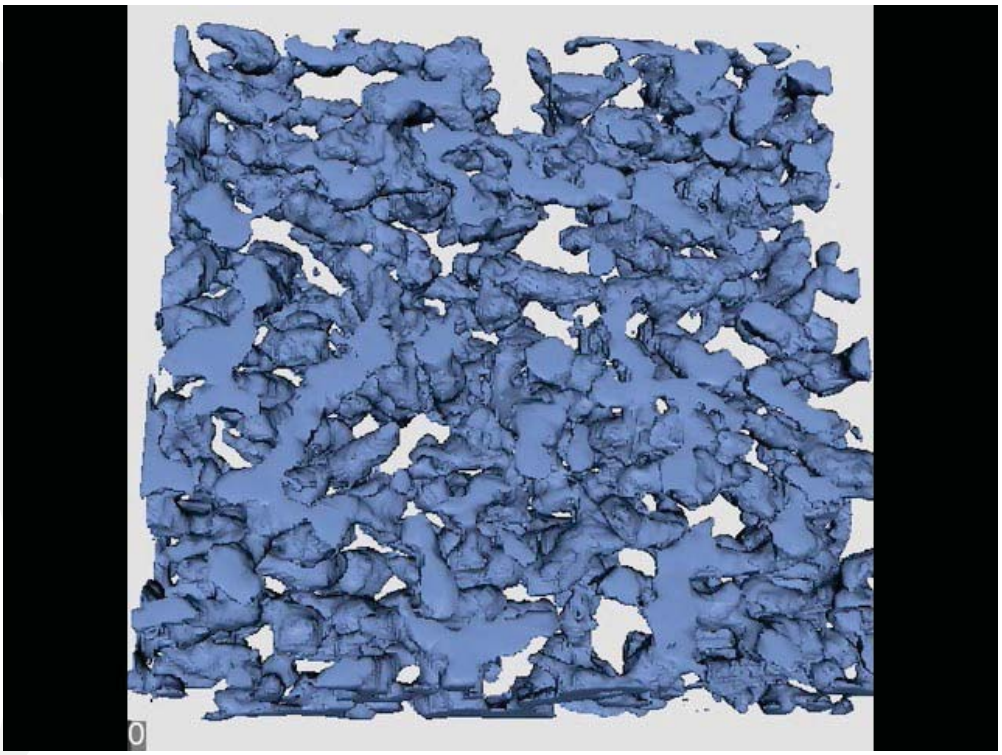

Pinzer et al, 2012

La neige se sublime

Et se recondense

Comprendre sa formation

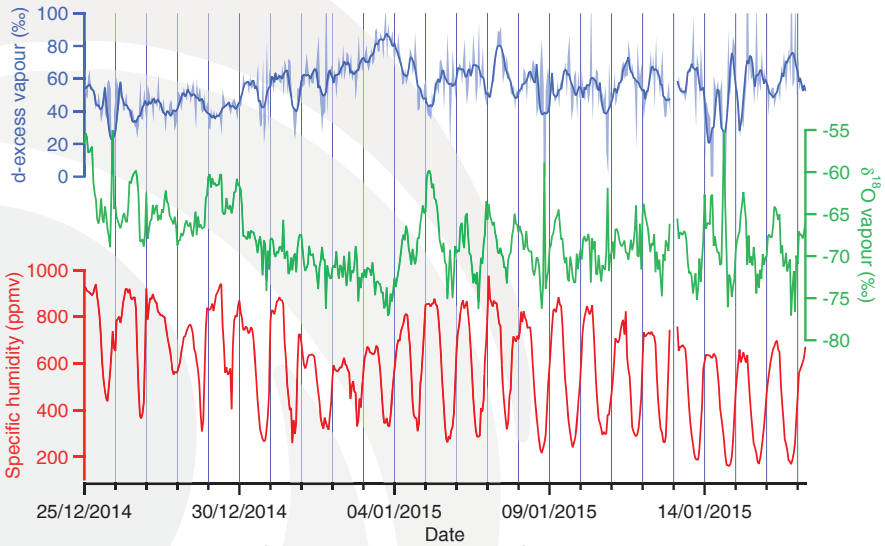

Analyse de la composition isotopique de la vapeur en parallèle du dépot de givre

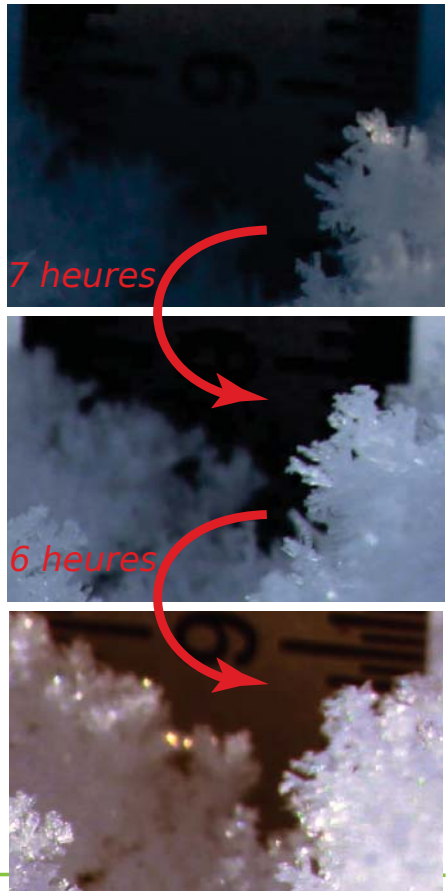

- L'accumulation annuelle à Concordia est de moins de 8 cm par an
- Avec une accumulation si faible, même des dépots qui sont inférieurs au mm vont contribuer de manière significative au budget annuel

Quelques autres flocons

Impact sur l'albédo

L'albédo est la quantité d'énergie reflechie par la surface.

La neige fraiche est très blance et très claire, elle refechie une grosse partie de la lumière :

Son albédo est entre 0.8 et 0.9.

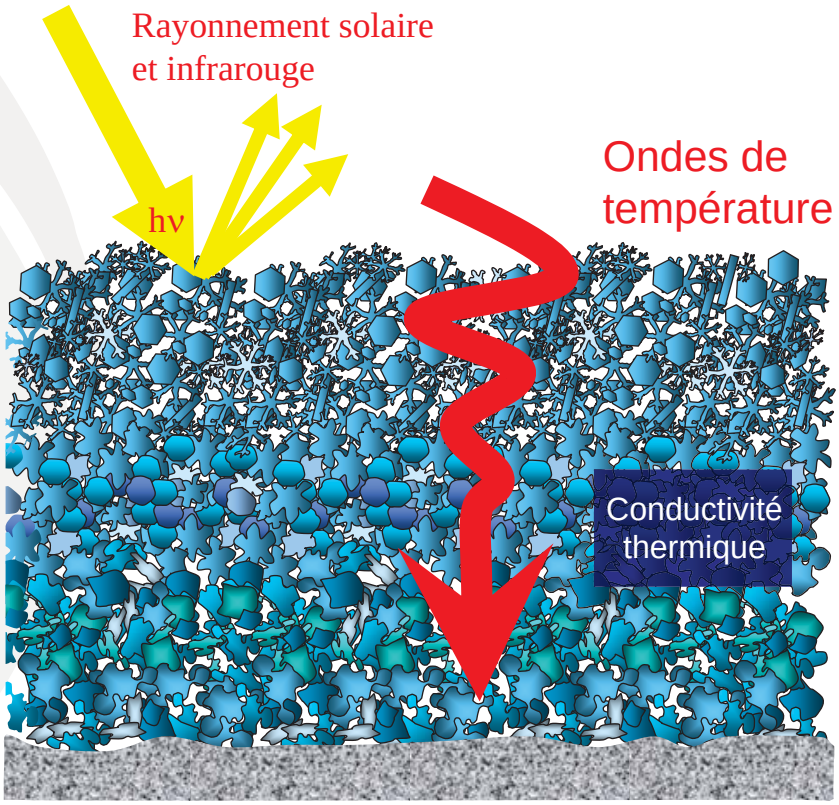

Source : Cours Neige
F. Domine

Différents types de cristaux

Albédo = 0.90

Conductivité thermique
0.05 $W.m^{-1}.K^{-1}$

Albédo = 0.84

Conductivité
thermique
0.08 $W.m^{-1}.K^{-1}$

Albédo = 0.79

Conductivité
thermique
0.53 $W.m^{-1}.K^{-1}$

Albédo = 0.86

Conductivité
thermique
0.23 $W.m^{-1}.K^{-1}$

Albédo = 0.82

Conductivité
thermique
0.04 $W.m^{-1}.K^{-1}$

Source : Cours Neige
F. Domine

Impact d'un changement de type de neige

Flux de rayonnement solaire incident: 100 $W.m^{-2}$

Un changement d'albédo de 0.79 à 0.75 du par exemple au métamorphisme de surface entraine un changement de quantité d'énergie absorbée 4 $W.m^{-2}$

A droite, un exemple d'un changement de 0.16 $W.m^{-2}$ entraine déjà des changements de température très importants

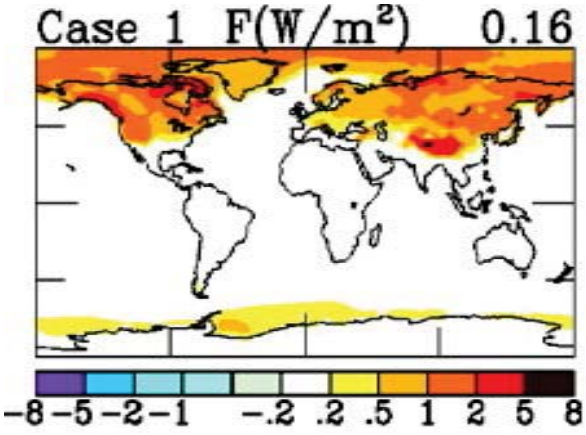

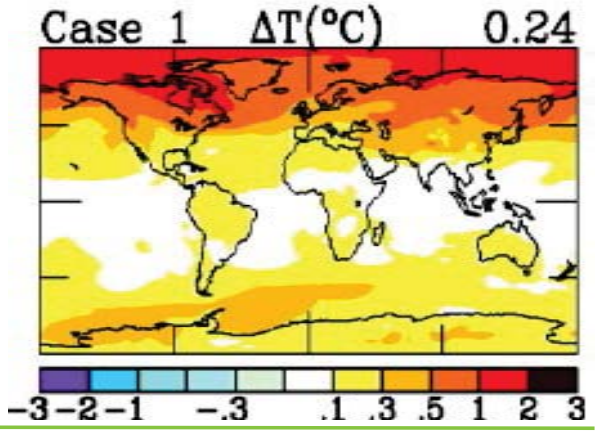

Source : Cours Neige
F. Domine

Hansen et al., 2004

Un autre exemple de boucle de rétroaction

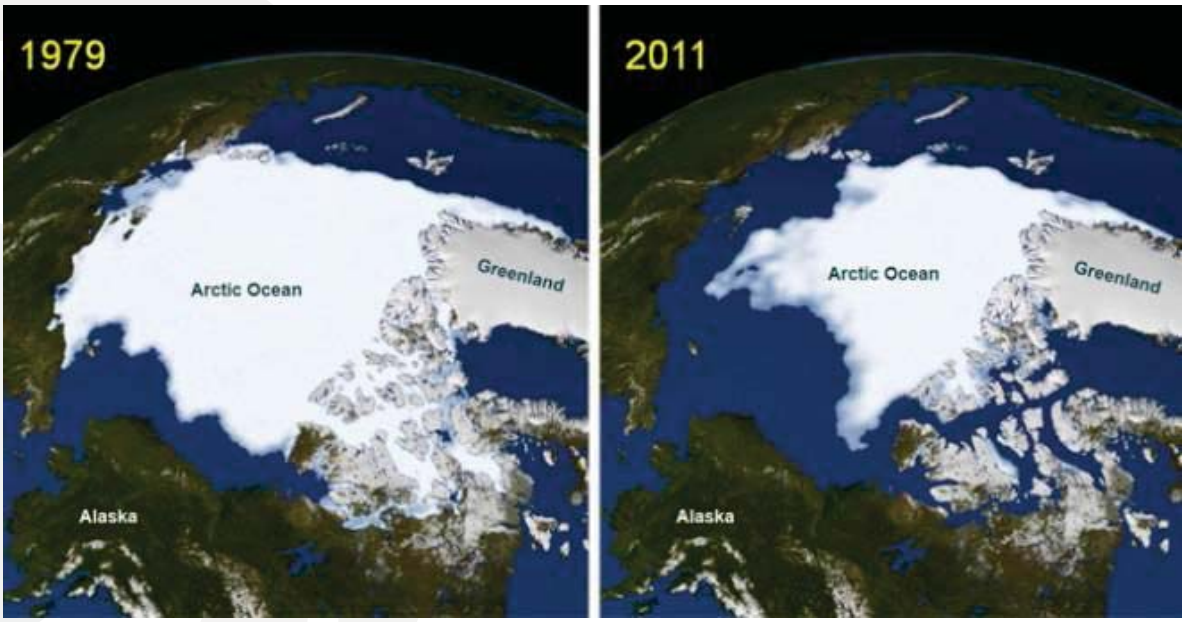

Albédo glace de mer : 0.6 à 0.7

Albédo océan : 0.05 à 0.15

Source : NASA

B.2 Acquired skills

During my Ph-D, I have spent an important amount of time on experimental aspects, both in LSCE and in LIPHY. First, in LSCE, as a part of measuring triple isotopic composition of water, I have been using both mass spectrometry and infrared spectroscopy. I have followed the days advanced training class about Dual Inlet Isotope Ratio Mass Spectrometry at Thermo Fischer factory in Bremen (Germany). I have been using regularly the fluorination technique to transfer water to dioxygen, which involves manipulation of high-vacuum and cryogenic liquid handling (helium and nitrogen). Between LSCE and LIPHY, I have been using a wide range of infrared spectrometers from commercial Picarro analysers (L2120,L2130 and L2140) to homemade analysers from LIPHY (HiFI, an OFCEAS instrument for water triple isotopic composition) that I learned to assemble completely and even to building a new generation of infrared spectrometer based on optical feedback frequency stabilisation.

During my time in LIPHY, I had to face a large range of new challenges and got basic skills in electronics, instrument interfacing and data acquisition. I took a two days training class about machine tools at the workshop of LIPHY getting an independent level in milling, lathing and crafting of small components that require to be custom made during the realisation of the spectrometer. For high complexity machinery usage, I also learned how computer-aided design techniques. Finally, obviously, I learned a wide range of techniques related to the optical setups in infrared spectrometry: cavity injection, fiber injection, laser techniques and phase control. Finally, I designed a new range of humidity generator adapted for very low humidity levels as required for field and laboratory experiments.

During the field work at Dome C (Antarctica), I was in charge of running a commercial analyser Picarro (L2130), the HiFI, including the calibration scheme of the two instruments on a daily basis, a cryogenic trapping setup, surface snow sampling and snowpits sampling. A mission in a location as remote as Dome C requires careful planning and packing and I was in charge of the organisation of my campaign. I also realised the protocol for the 2015/16 campaign and helped Frederic Prie in the packing and the organisation of the campaign. Finally, I realised the protocols for the winterover crew for snowpits and surface sampling in 2015 and 2016.

For the analyses of the data, I have been using different levels of complexity of modelling. First, I have been developing a serie of tools analysing the data and the calibration, statistical evaluation of the quality of the data and uncertainty evaluation using mainly

Matlab. I have been using models such as the MCIM (intermediate complexity model to compute Rayleigh distillation in mixed phase conditions) and handling model outputs from GCM including isotopes and reanalyses products.

Being part of an Antarctic expedition is an exceptional opportunity and it has taught me a lot outside the frame of scientific knowledge: from team work to improvising without the necessary equipment due to the isolation. It is primarily in these situations that you see how much relying on a team means and how important are the services provided by the IPEV.

B.3 Courses, summer schools, and scientific conferences

B.3.1 Courses

- Thermo Fisher Scientific advanced training course, 3 days, Thermo Fisher factory, Bremen Germany, course in analytical techniques, specialized operation and maintenance for Delta V and MAT 253 Dual Inlet Isotope Ratio Mass Spectrometry.
- University Joseph Fourier, 24 hours (scientific) of Optical Spectroscopy by Prof. Erik Kerstel, Jan. 2014.
- International French-German Summer School SPECMO 2014, 5 days (scientific) of New experimental and theoretical developments in molecular spectroscopy - pushing the limits organised by Dr. Isabelle Kleiner, September 2014.
- University Versailles Saint Quentin: 24 hours (scientific) of Arctic Climate: science, society and geography by Prof. Alain Sarkissian, July 2015.
- University Pierre and Marie Curie: 26 hours (non-scientific) of Russian classes by Prof. Svetlana Trouve, December 2015.

B.3.2 Scientific Conferences and seminars

- Société Francaise des Isotopes Stables 2013, Dunkerque, oral presentation.
- European Geophysicist Union 2014, Vienna, poster.
- 5^{th} workshop of the International Collaboration and Education in Ice Core Science 2015, Grenoble, poster.
- American Geophysical Union 2015, San Francisco, posters + flash freeze presentation (awarded).

- 2^{nd} open science conference of the International Partnerships in Ice Core Sciences 2016, Hobart, poster.
- Invited seminar at the Ice and Climate Center 2016, Copenhagen, oral presentation
- First thematic workshop Panoply 2016, LSCE, oral presentation
- Field Laser Applications in Industry and Research 2016, Aix-les-Bains, oral presentation + posters.

Appendix C

Technical parts

Instrumentation requires an important amount of technical work which does not necessary belong in the main text of a thesis. Still, this part of every day work is important because without it, no experiment would actually be working.

C.1 Thermal regulation of the VCOF

In order to regulate the temperature of the VCOF around 1 mK, we build a multi-layer active temperature regulated box. Indeed, even though the cavity is not sensitive to temperature variations, in order to obtain the best of performances, it is important for it to remain absolutely regulated. The box is composed of a 10 mm thick plywood outer box of 420x420x570mm, inside which is a 1 mm thick copper inner box of 370x370x540mm. On each face of the copper box are Omega SRFR-12 silicon heat bands covering more than 60% of each face. Because failure in temperature regulation can always happen, a multi-layer box enables to obtain already interesting passive properties as illustrated on figure C.1 which justified the choice of plywood. The important amount of air between the inner copper box and the massive stainless steel flange is also acting as a secondary isolation. The wood and copper box combined passive isolation erase 90% of the AC temperature cycles of roughly 30 minutes. With the inertia of the flange and the air acting as a secondary isolation, the 30 minutes cycles are completely erased even at the mK level in the temperature of the flange. Still, this isolation is not able to erase a diurnal cycle of 1°C as illustrated by the important trend on the flange temperature.

In order to erase all temperature variations as well as the gradient, we integrate a PID (Proportional, Integrate and Differential) control on the power supply of the heat bands. The PID, realised by Tim Stoltman and Samir Kassi, is a digital PID running on a Arduino Mega 2560. Temperature is read independently on each face of the copper

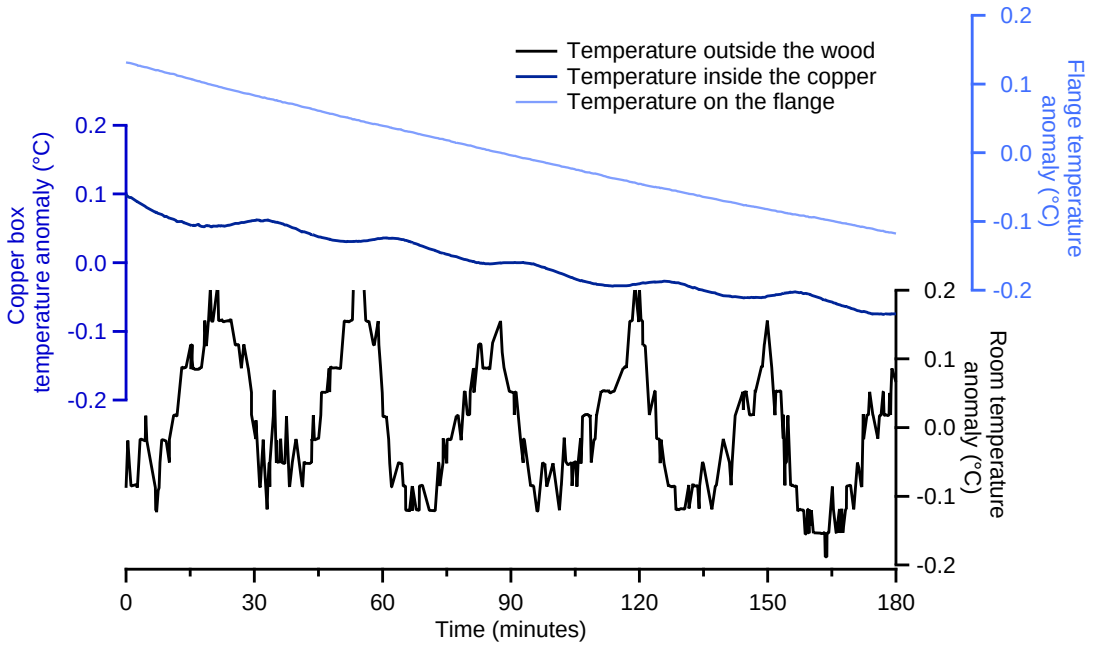

Figure C.1: Impact of the passive temperature cycles under 0.3°C peak-to-peak AC cycles.

box by a PT1000 sensor read with a Wheatstone bridge by an ARM communicating in SPI. Two multiplexers MC14051BDG enable the arduino to communicate to 8 SPI driven temperature probes. One digital to analog convertor DAC8568C enables the arduino to address individually 6 operational amplifiers. After an inter-calibration of 16 PT1000 sensors, this setup can control individually the temperature of the 6 faces of the copper box with a precision of 1 mK and absolute differences between faces below 10 mK.

C.2 Characterisation of the DFB laser

We use diode laser Eblana EP1392 which includes a Peltier temperature regulation. The specifications of the laser diode from Eblana photonics are presented in figure C.2. At 25°C, we observe that the laser emits light around 1392.5 nm. There is a current threshold at 15 mA and the maximum power is around 20 mW. We characterised the diode laser we have been using slightly beyond the specifications in order to obtain quantitatively the behaviour of our laser diode.

We scanned the temperature of the laser diode from 20°C to 60°C. We estimate the temperature tuning coefficient of the diode at 0.0872 $nm.°C^{-1}$, slightly lower than the specifications at 0.1 $nm.°C^{-1}$. During the scan, it was possible to actually observe the absorption of the water in the air over the 50 cm of open optical path between the laser

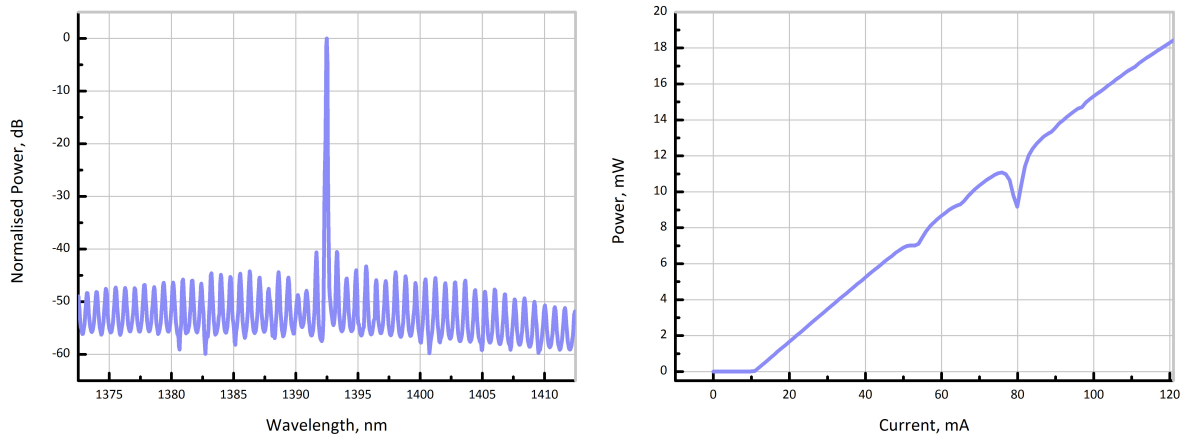

Figure C.2: Specifications of the Eblana EP1392 laser diode: C.2a power at the different wavelength at 25°C normalised against the maximum of power and C.2b scan of power for different current of the laser diode (Source: Eblana documentations http://www.eblanaphotonics.com)

diode and the wavemeter as illustrated on figure C.3.

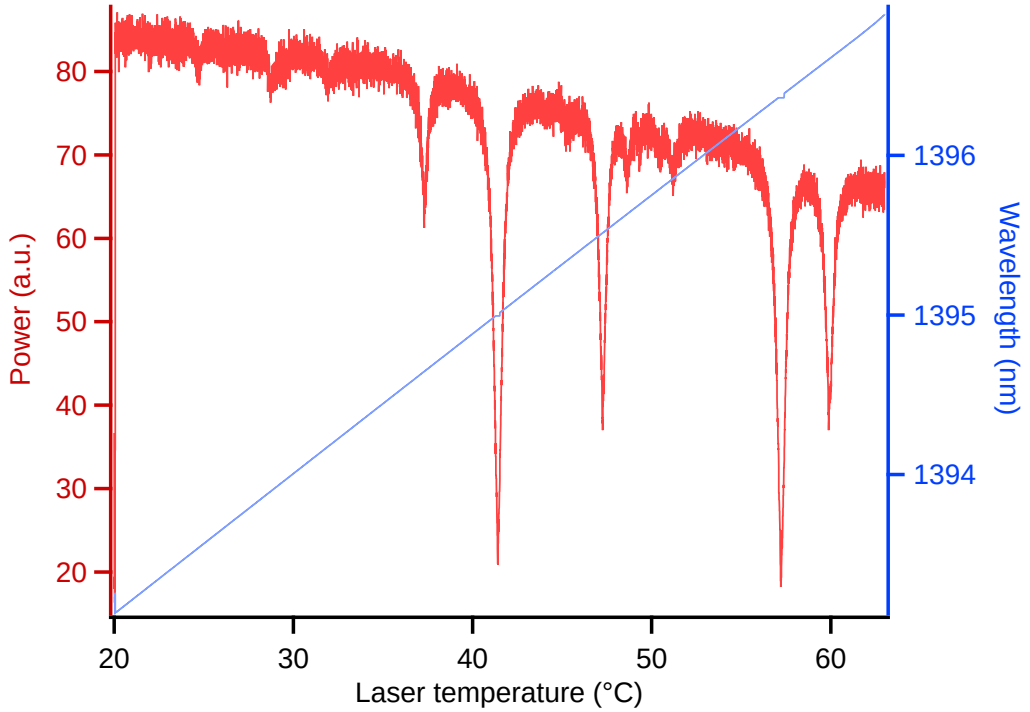

Figure C.3: Wavelength (in blue) and power (in red) measured by the High-Finesse WSU7-IR during a scan of the temperature of the laser diode.

We measured the waist of the laser beam along the propagation direction using both the knife-edge technique and measurement of intensity on a CCD sensor. We found a beam slightly elliptic with an eccentricity of 0.19. We optimised the focus of the beam by measuring the waist when positioning the lens in front of the laser. The final waist of the beam with the lens mounted on is respectively 150 μm and 219 μm on the X and Y axes at 22.1 cm of the laser.

C.3 Utilisation of Picarro analysers

We have mentioned in this manuscript that Picarro's analysers require calibration to accurately estimate the isotopic composition. An internal report from Guillaume Tremoy showed that it is also necessary to calibrate the humidity measurements of the Picarro's analysers. Here, we present the comparison of the not calibrated humidity from the field campaign at Dome C compared to the data from the calibration hygrometer HMP.

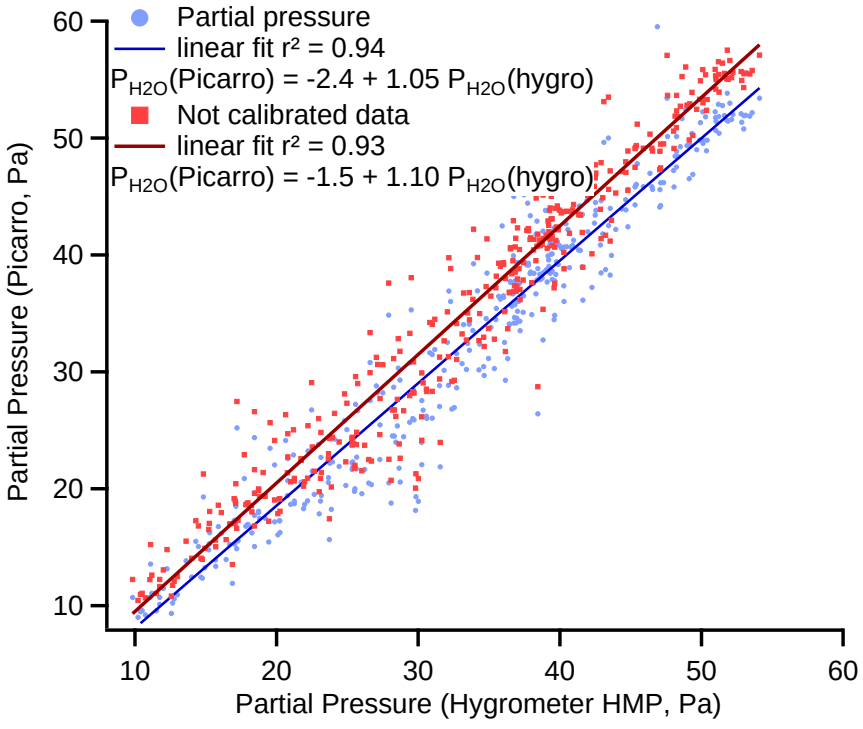

Figure C.4: Humidity calibrated (in blue) and not calibrated (in red) from the Picarro L2130i at Dome C compared to the one calculated from the HMP155 of Vaisala at Dome C between the 1st of January 2015 and the 10th of January 2015.

This justify the need of calibration of the humidity product from Picarro instruments. Traditional method at LSCE uses a dew point generator Licor LI-610 to generate a fixed

moisture content. It is not possible to set the dew point generator below 0°C, therefore for low concentration, we usually dilute the moist air generated by the LICOR with dry air using 2 mass flow controllers. For the range of humidity encountered at Dome C, the dilution between the moist air generated by the LICOR (roughly 6000 $ppmv$) is large so the accuracy of the mass flow controllers we used is not enough to precisely generated a known humidity. We used the humidity generator described in section 4.1.1 to realise the calibration of the humidity presented on figure C.5.

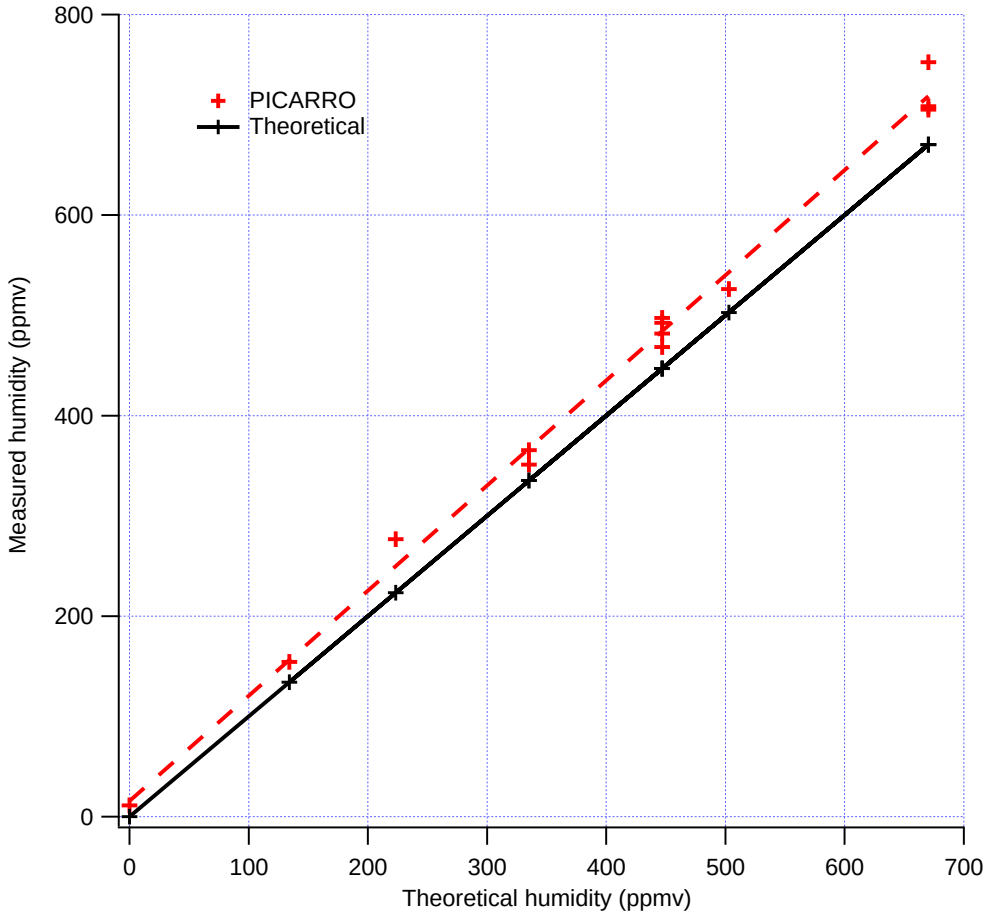

Figure C.5: Measured humidity by the Picarro L2130i (red crosses, data and dashed lined, fit) in the field compared to the theoretical produced humidity by the calibration device (black line).

We obtain a linear function $Hum(Picarro) = 15.7 + 1.049 \times Hum(Th)$ with $r^2 = 0.99$. This function was used to correct the raw data and provide for the blue curve on figure C.4.

C.4 Glass traps for cryogenic trapping

Several architectures of traps for cryogenic trapping have been used through the years at LSCE. The two most efficient designs are presented on figure C.6. On the left, we present traps filled with glass balls. This kind of traps can be used at high flow because the balls create only very small interstitial canals where the moist air flows by, and therefore successively traps all of the moisture for flows up to $20\,L.min^{-1}$. The second type of trap, on the right, is not filled with glass balls but is composed of two traps and of long tubes connecting the traps. It has been proven reliable to trap the moisture for flows up to $6\,L.min^{-1}$. Both systems require detrapping, though the traps without glass balls are singularly more convenient for detrapping. This is a crucial step because an incomplete detrapping creates fractionation and therefore a large uncertainty on the isotopic composition of the vapour.

(a) (b)

Figure C.6: Pictures of the two type of cryogenic traps deployed in Antarctica and used at LSCE: C.6a single trap filled with glass balls to increase the surface where the vapour can condensed and C.6b double trap without glass balls but with an efficient architecture still totally traps the moisture for flow below $6\,L.min^{-1}$.

Both types of traps have been deployed at Concordia with satisfactory performances. For both traps, an important number of interns have been characterising the performances for different flows and isotopic composition.

Appendix D

Article : Acquisition of isotopic composition for surface snow in East Antarctica and the links to climatic parameters

The Cryosphere, 10, 837–852, 2016
www.the-cryosphere.net/10/837/2016/
doi:10.5194/tc-10-837-2016

The Cryosphere Open Access EGU

Acquisition of isotopic composition for surface snow in East Antarctica and the links to climatic parameters

Alexandra Touzeau[1], Amaëlle Landais[1], Barbara Stenni[2], Ryu Uemura[3], Kotaro Fukui[4], Shuji Fujita[5,6], Sarah Guilbaud[7], Alexey Ekaykin[8,9], Mathieu Casado[1], Eugeni Barkan[10], Boaz Luz[10], Olivier Magand[11], Grégory Teste[11], Emmanuel Le Meur[11], Mélanie Baroni[12], Joël Savarino[11], Ilann Bourgeois[13], and Camille Risi[14]

[1]LSCE – UMR CEA-CNRS-UVSQ-Université Paris Saclay, 8212-IPSL, Gif-sur-Yvette, France
[2]DAIS, Ca'Foscari University of Venice, Venice, Italy
[3]Faculty of Science, University of the Ryukyus, Okinawa, Japan
[4]Tateyama Caldera Sabo Museum, Toyama, Japan
[5]National Institute of Polar Research, Research Organization of Information and Systems, Tokyo, Japan
[6]Department of Polar Science, The Graduate University for Advanced Studies (SOKENDAI), Tokyo, Japan
[7]LPCA, Université du Littoral Côte d'Opale, Dunkirk, France
[8]Arctic and Antarctic Research Institute, St. Petersburg, Russia
[9]Saint Petersburg State University, St. Petersburg, Russia
[10]Institute of Earth Sciences, Hebrew University of Jerusalem, Jerusalem, Israel
[11]Univ. Grenoble Alpes/CNRS, Laboratoire de Glaciologie et Géophysique de l'Environnement (LGGE), 38041 Grenoble, France
[12]LECA, UMR5553 – CNRS-UJF, Université Joseph Fourier, Grenoble, France
[13]Aix-Marseille Université, CNRS, IRD, CEREGE – UM34, 13545 Aix-en-Provence, France
[14]Laboratoire de Météorologie Dynamique, Paris, France

Correspondence to: Alexandra Touzeau (alexandra.touzeau@lsce.ipsl.fr)

Received: 19 October 2015 – Published in The Cryosphere Discuss.: 18 November 2015
Revised: 1 March 2016 – Accepted: 30 March 2016 – Published: 15 April 2016

Abstract. The isotopic compositions of oxygen and hydrogen in ice cores are invaluable tools for the reconstruction of past climate variations. Used alone, they give insights into the variations of the local temperature, whereas taken together they can provide information on the climatic conditions at the point of origin of the moisture. However, recent analyses of snow from shallow pits indicate that the climatic signal can become erased in very low accumulation regions, due to local processes of snow reworking. The signal-to-noise ratio decreases and the climatic signal can then only be retrieved using stacks of several snow pits. Obviously, the signal is not completely lost at this stage, otherwise it would be impossible to extract valuable climate information from ice cores as has been done, for instance, for the last glaciation. To better understand how the climatic signal is passed from the precipitation to the snow, we present here results from varied snow samples from East Antarctica. First, we look at the relationship between isotopes and temperature from a geographical point of view, using results from three traverses across Antarctica, to see how the relationship is built up through the distillation process. We also take advantage of these measures to see how second-order parameters (d-excess and ^{17}O-excess) are related to δ^{18}O and how they are controlled. d-excess increases in the interior of the continent (i.e., when δ^{18}O decreases), due to the distillation process, whereas ^{17}O-excess decreases in remote areas, due to kinetic fractionation at low temperature. In both cases, these changes are associated with the loss of original information regarding the source. Then, we look at the same relationships in precipitation samples collected over 1 year at Dome C and Vostok, as well as in surface snow at Dome C. We note that the slope of the δ^{18}O vs. temperature (T) relationship decreases in these samples compared to those from the traverses, and thus caution is advocated when using spatial slopes for past

climate reconstruction. The second-order parameters behave in the same way in the precipitation as in the surface snow from traverses, indicating that similar processes are active and that their interpretation in terms of source climatic parameters is strongly complicated by local temperature effects in East Antarctica. Finally we check if the same relationships between δ^{18}O and second-order parameters are also found in the snow from four snow pits. While the d-excess remains opposed to δ^{18}O in most snow pits, the ^{17}O-excess is no longer positively correlated to δ^{18}O and even shows anti-correlation to δ^{18}O at Vostok. This may be due to a stratospheric influence at this site and/or to post-deposition processes.

1 Introduction

Water isotopic composition of shallow and deep ice cores has long been used for reconstructing past climatic conditions in polar regions (Jouzel et al., 2007; Küttel et al., 2012; Schneider et al., 2006). The correlation between temperature and δ^{18}O in polar regions is explained by the progressive relative loss of heavy isotopes with respect to the light ones during distillation of the water mass along its trajectory from warm to cold regions. However, more and more recent studies are evidencing that the water isotopic composition (δ^{18}O or δD) in shallow snow pits in Antarctica does not follow the recent (last 50 years) temporal evolution of temperature, especially in regions of very low accumulation like the East Antarctic plateau (Ekaykin et al., 2002, 2004; Hoshina et al., 2014; Winkler et al., 2013). Post-depositional effects at the snow surface (Sokratov and Golubev, 2009) are responsible for a large noise, i.e., a non-climatic signal, in water isotopic records. This non-climatic signal can be shaped by many local effects such as surface relief, accumulation rate (Ekaykin et al., 2004) or temperature gradient in surface snow (Town et al., 2008). The situation is however improved when working on stacks of several shallow pits from which a climatic signal can be extracted (Altnau et al., 2015; Ekaykin et al., 2014; Schneider et al., 2006). In addition, the fact that δ^{18}O or δD records in deep ice cores have been providing robust and high-resolution records of past temperature over the last glacial period clearly confirms the direct link between temperature and water isotopic composition of surface snow. Accordingly, either the post-depositional noise is not strong enough to entirely erase the original climatic signal, or some of the post-deposition processes are under the control of local temperature and thus reinstate a link between δ^{18}O and temperature.

In addition to δD and δ^{18}O records bringing information on temperature at first order, additional climatic information can be retrieved from second-order parameters like d-excess (d-excess $= \delta\mathrm{D} - 8 \cdot \delta^{18}\mathrm{O}$) and ^{17}O-excess (^{17}O-excess $= \ln(\delta^{17}\mathrm{O}+1) - 0.528 \cdot \ln(\delta^{18}\mathrm{O}+1)$) (Dansgaard, 1964; Barkan and Luz, 2007; Landais et al., 2008). These parameters represent the y intercepts of two straight lines, one relating δD and δ^{18}O with a slope of 8, and the other relating $\ln(\delta^{17}\mathrm{O}+1)$ and $\ln(\delta^{18}\mathrm{O}+1)$ with a slope of 0.528. Most meteoric and surface waters over the globe fall on a line with a slope of 8 and a y intercept of 10 in the δD/δ^{18}O diagram, called the Global Meteoric Water Line (Craig, 1961). However, variations of d-excess values have been observed in waters from various regions around the globe, and have been attributed, in the middle to low latitudes, to regional hydrological conditions (importance of evaporation and precipitation amount). When plotting the isotopic compositions of meteoric waters in a $\ln(\delta^{17}\mathrm{O}+1)/\ln(\delta^{18}\mathrm{O}+1)$ diagram, they fall on a straight line with a slope of 0.528 (Barkan and Luz, 2007; Landais et al., 2008; Luz and Barkan, 2010; Meijer and Li, 1998). Following the model of the d-excess definition, Barkan and Luz (2007) defined the ^{17}O-excess in this diagram, and proposed that it was a tracer of climatic conditions at evaporation. The fact that δ^{18}O, d-excess and ^{17}O-excess bear slightly different climatic information is due to influences of both equilibrium and kinetic fractionation processes on the water isotopic composition. Equilibrium and kinetic fractionation effects are induced by differences in saturation vapor pressure and diffusivities among isotopes, respectively. The different water isotopes exhibit different sensitivities to equilibrium and kinetic fractionation leading to variations in d-excess and ^{17}O-excess. At low latitudes, both d-excess and ^{17}O-excess will be sensitive to relative humidity during evaporation because of large variations in kinetic fractionation (Gat, 1996; Uemura et al., 2008, 2010). However, along the distillation process, the influence of relative humidity on d-excess is fading away to the benefit of the temperature gradient between the source and the precipitation site through equilibrium fractionation (Petit et al., 1991; Vimeux et al., 1999).

For coastal stations of Antarctica, ^{17}O-excess and d-excess are markers of water origin, mainly temperature for d-excess (Delmotte et al., 2000; Kurita, 2011; Schlosser et al., 2008) and relative humidity for ^{17}O-excess (Winkler et al., 2012). Presence of sea ice at the oceanic water evaporative regions may also contribute to the d-excess and ^{17}O-excess signal (Gao et al., 2011; Schoenemann et al., 2014). However, at very low temperatures, and therefore in the central regions of Antarctica, the d-excess and ^{17}O-excess in the precipitation become much more sensitive to the temperature of condensation than in the coastal regions. By using the different isotopic parameters, it remains possible to separate the influence of the source temperature from the influence of the local temperature, as was done in central Greenland (Masson-Delmotte et al., 2005; Jouzel et al., 2005) and more recently in East Antarctica (Uemura et al., 2012) with a sensitivity of polar d-excess to source temperature of $1.5\,‰\,^{\circ}\mathrm{C}^{-1}$ (Risi et al., 2010) and a sensitivity of polar ^{17}O-excess to source relative humidity of $-0.9\,\mathrm{ppm}\,\%^{-1}$ (Landais et al., 2009). Because ^{17}O-excess is less sensitive to temperature than d-

excess, the site temperature influence on ^{17}O-excess is only perceptible in very remote sites of East Antarctica (Winkler et al., 2012). Finally, ^{17}O-excess may also bear the signature of stratospheric input since photochemical reactions involving ozone can affect the triple isotopic composition of oxygen in water in the stratosphere (Franz and Röckmann, 2005; Lin et al., 2013; Winkler et al., 2013; Zahn et al., 2006). This effect is generally marginal since the amount of water vapor in the stratosphere is very small (a few ppm only). However, it can become significant in East Antarctica where surface humidity is very low (i.e., at Vostok, the average specific humidity value is ~ 112 ppmv and decreases to almost 0 ppmv in winter; Ekaykin, 2003).

The goal of this study is to understand how a climatic and environmental signature can be imprinted in the water isotopic composition of surface snow in remote East Antarctica. Our strategy is to make an optimal use of the combination of all water stable isotopes (δD, δ^{17}O, δ^{18}O) in different types of snow on the Antarctic plateau (precipitation, surface snow, buried snow) to disentangle temperature, water cycle and stratospheric influences.

The outline of our study is the following. In Sect. 2, we present the spatial distribution of water isotopic composition averaged in the top 30 cm of surface snow in East Antarctica with a focus on the remote East Antarctic plateau. In Sect. 3, we present variations of isotopic composition of precipitation and surface snow on two drilling sites in East Antarctica (Dome C, Vostok). Section 4 is a multi-isotope compilation of new data on several snow pits in East Antarctica. Each section is organized in three subsections: a review of current knowledge, a description of new measurements and results and a discussion. The final discussion shows that the multi-isotopes approach at different sites with similar temperature and accumulation rate characteristics is a useful tool to identify the main drivers for the water isotopic variations observed on shallow ice cores and to test the origin of the δ^{18}O variations classically interpreted in terms of past temperature changes.

2 Spatial variations of d-excess vs. δ^{18}O and ^{17}O-excess vs. δ^{18}O in Antarctic transects

2.1 Review of current knowledge

The measurements of water isotopic composition in Antarctic transects have first provided a spatial relationship of 0.8 ‰ °C^{-1} between surface temperature and δ^{18}O in snow (Lorius and Merlivat, 1977; Masson-Delmotte et al., 2008). Applications of this relationship for reconstructing past temperature from records of δ^{18}O in ice cores have however revealed some limitations because of combined influences of the seasonality of precipitations, origin of moisture, variations in elevation or post-deposition effects (e.g., Charles et al., 1994; Fawcett et al., 1997; Hoshina et al., 2014; Jouzel et al., 2003; Krinner et al., 1997; Masson-Delmotte et al., 2012; Neumann et al., 2005). Changes in moisture source, post-deposition effects and ice condensation are associated with kinetic fractionation effects. As a consequence, ^{17}O-excess and d-excess are useful tools to disentangle the different influences on water isotopic composition in ice cores and hence improve our knowledge of the δ^{18}O vs. temperature relationship.

For quantitative interpretations, the isotopic measurements are also classically combined with simple isotopic models (such as Mixed Cloud Isotope Model, i.e., MCIM, Ciais and Jouzel, 1994) or more sophisticated general circulation models (GCMs) equipped with water isotopes (such as the model LMDZ-iso from the Laboratoire de Météorologie Dynamique of Paris, where Z stands for the zoom function of the model; Risi et al., 2010, 2013). The aim of such a model–data approach is twofold. First, the comparison of data and a model on the present-day spatial repartition of water isotopic composition in Antarctica is essential for the validation of the implementation of water isotopes in the model. Second, the use of isotopic models is essential to quantitatively interpret the water isotopic records in deep ice cores and translate them into records of climatic parameters (e.g., local temperature).

The model–data comparison over polar transects enables the correct implementation of the relative influences of kinetic vs. equilibrium fractionation processes during snow formation. These different influences are balanced through the expression of the supersaturation function, S, in the formulation of the fractionation coefficient (α_{V-S}) during snow formation so that

$$\alpha_{V-S} = \frac{S}{(S-1)D/D^* + 1/\alpha_{\mathrm{eq}}}, \quad (1)$$

where α_{eq} is the fractionation coefficient at equilibrium between vapor and solid; D and D^* are the diffusion coefficients of the light and heavy water isotopes in air. In the classical approach, S is related to inversion temperature, T in °C, at which precipitation is assumed to form, so that $S = 1 - a\,T$ (Ciais and Jouzel, 1994; Jouzel and Merlivat, 1984). The relationship between supersaturation and temperature is not well constrained from atmospheric data. The classical way to adjust the slope a in the different models is to compare water isotopes data and model outputs in polar regions. More precisely, because d-excess is very sensitive to kinetic effects at condensation in cold polar regions, the tuning of the supersaturation relationship to temperature is performed so that the observed relationship between δ^{18}O and d-excess in Antarctica can be reproduced by the model (Ciais and Jouzel, 1994; Risi et al., 2013; Schmidt et al., 2007). In GCMs, this tuning leads to values for a between 0.003 and 0.005, with recent models (Risi et al., 2010; Lee et al., 2007; Schmidt et al., 2005; Tindall et al., 2009; Werner et al., 2011) favoring values equal to or greater than 0.004. Using the link between ^{17}O-excess and δ^{18}O on polar transects is an additional con-

straint (Landais et al., 2008; Pang et al., 2015). The best fit of an MCIM model to the isotopic compositions (d-excess and ^{17}O-excess) measured on the Terra Nova Bay–Dome C traverse, is obtained with a value for a of 0.0033 (Winkler et al., 2012). Pang et al. (2015) used the same value to fit to the Zhongshan–Dome A traverse. Adequate tuning of supersaturation is the key to quantitatively interpret the influence of temperature and moisture origin on δ^{18}O, d-excess and ^{17}O-excess, especially in deep ice core records (Masson-Delmotte et al., 2005; Stenni et al., 2010; Winkler et al., 2012).

The longest ice core records (Dome C, Dome F, and Vostok) are located in the cold and dry regions of East Antarctica (EPICA comm. members, 2004; Kawamura et al., 2007; Petit et al., 1999). In these cold regions, the kinetic fractionation is very strong because of a high supersaturation level. The influence of kinetic fractionation on water isotopic composition is even stronger in glacial climatic conditions. In order to quantitatively interpret these glacial isotopic records, the expression of kinetic fractionation during snow formation should be known precisely at very low temperatures. Unfortunately, there are barely any present-day analogs for the glacial conditions encountered at Dome F, Vostok and Dome C. To better document the water isotopic composition of snow in extremely cold regions of Antarctica, and to improve the tuning of the supersaturation function, recent transects have been performed toward remote regions of the East Antarctic plateau (e.g., Becagli et al., 2004; Fujita et al., 2011; Masson-Delmotte et al., 2008; Mayewski and Goodwin, 1999; Pang et al., 2015).

2.2 Measurements and results

We present here a compilation of existing and new transect data combining the measurements of all water stable isotopes (δ^{18}O, d-excess and ^{17}O-excess). The first transect combining these surface measurements was obtained within the ITASE project (Magand et al., 2004; Mayewski and Goodwin, 1999; Mayewski et al., 2005) between Terra Nova Bay and Dome C (Fig. 1), and water isotopic data were already published (Landais et al., 2008; Proposito et al., 2002). The second transect was performed between Zhongshan station and Dome A (Fig. 1) during the CHINARE expedition and water isotopic data were published in Pang et al. (2015). Finally, we present new water isotopic records from a transect obtained between Syowa, Dome Fuji and the site of the Drönning Maud Land ice core (EPICA DML, obtained within the European Project for Ice Coring in Antarctica, EPICA) (Fig. 1) through a Swedish–Japanese project (Fujita et al., 2011).

The surface snow samples were obtained from shallow pits on which the average water isotopic composition was measured. These pits had a depth of 1 m for the Terra Nova Bay–Dome C traverse (Proposito et al., 2002; Magand et al., 2004), 10 cm for the Zhongshang–Dome A traverse (Pang et al., 2015) and 10 to 30 cm for the Syowa–Dome F traverse.

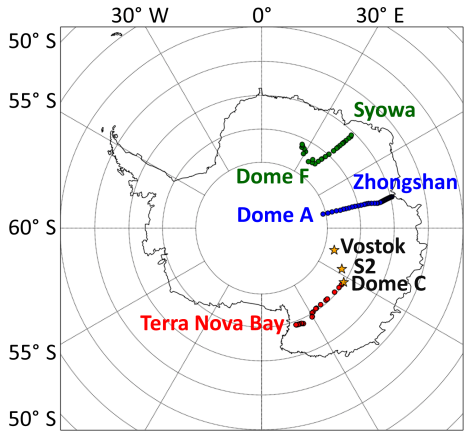

Figure 1. Map of the sites discussed in this manuscript.

Because the accumulation decreases from the coast towards the inland sites, the recorded period, for the first transect, varies from 2 years near the coast to 12 years at Dome C. For the Chinese traverse, the recorded period varies from 1 year in inland areas to 3 months in coastal areas. For the Syowa–Dome F traverse, the pits were shallower at inland sites (10 cm) and deeper at coastal sites in order to record at least 1 year in each sample. For the three transects presented here, ^{17}O-excess measurements were obtained by fluorination method of water to oxygen (Barkan and Luz, 2005) followed by dual inlet measurements of produced oxygen vs. a reference oxygen standard. Measurements of the Terra Nova Bay–Dome C transect were performed at the Hebrew University of Jerusalem Israël (HUJI) using a Delta V mass spectrometer. Measurements of the two other transects were performed in France at the Climate and Environment Sciences Laboratory (LSCE) on a MAT 253 instrument. The measurements were calibrated vs. VSMOW (Vienna Standard Mean Ocean Water) and SLAP (Standard Light Antarctic Precipitation), taking reference values for δ^{18}O and ^{17}O-excess of respectively 0 ‰ and 0 ppm (or per meg) and −55.5 ‰ and 0 ppm (Pang et al., 2015; Schoenemann et al., 2013; Winkler et al., 2012). The pooled standard deviation (1σ) was computed from duplicate injection, fluorination and isotope ratio mass spectrometry (IRMS) measurements of the same sample, and is on average of 5–6 ppm for ^{17}O-excess. The δ^{18}O and d-excess measurements for the Syowa–Dome Fuji transect were performed using an equilibration method (Uemura et al., 2007) at the National Institute of Polar Research, Japan.

All three transects show similar evolutions for the relationships between d-excess and δ^{18}O on the one hand, and ^{17}O-excess vs. δ^{18}O on the other hand (Fig. 2, Table 2). For δ^{18}O level lower than −40 ‰, d-excess decreases for increasing δ^{18}O with a slope of -0.95 ‰ ‰$^{-1}$. ^{17}O-excess does not exhibit a significant trend if we restrict the data in the range of $\delta^{18}\mathrm{O} > -50$ ‰ as in the Terra Nova Bay–Dome C transect

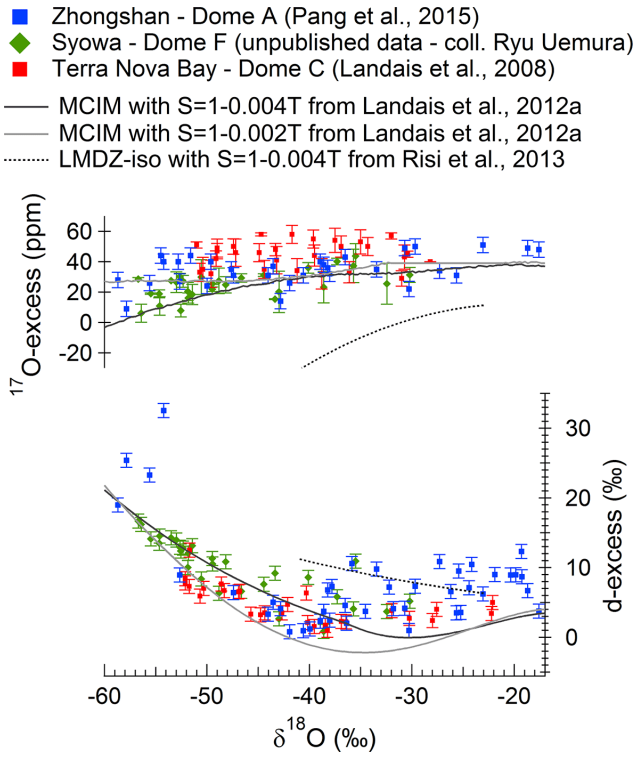

Figure 2. Water isotopic composition along Antarctic transects (blue: Zhongshan–Dome A transect; green: Syowa–Dome F transect; red: Terra Nova Bay–Dome C transect) and comparison with modeling outputs (black and grey line: MCIM with $S = 1–0.004T$ and $S = 1–0.002T$ respectively, from Landais et al., 2012a; dotted line: LMDZ-iso with $S = 1–0.004T$; Risi et al., 2013).

(Fig. 2, Table 2). For δ^{18}O values lower than −40 ‰, ^{17}O-excess increases with δ^{18}O with a slope of 0.91 ppm ‰$^{-1}$ (Table 2).

2.3 Discussion

For δ^{18}O values between −20 and −40 ‰, there is a large scattering of the d-excess values, with no clear trend. This can be due to a variability of the climatic conditions (temperature and relative humidity) at the source. For δ^{18}O values below −40 ‰, d-excess values are clearly anti-correlated with the δ^{18}O values and change from ∼ 4 ‰ to about 25 ‰. Such a change cannot be due to a change of the relative humidity of the source nor to a change of the source temperature that could explain only a few per mil changes. Thus, the increase of d-excess for decreasing δ^{18}O values is probably caused by the fractionation at condensation during the distillation. This increase of d-excess is directly related to a decrease of the slope (dδD/dδ^{18}O) of the distillation line towards low δ^{18}O values (i.e., low temperatures). Indeed, in the case of simple Rayleigh distillation, when the precipitated snow is immediately removed from the air mass and when only equilibrium fractionation occurs, we can express the local slope of the Rayleigh's distillation line at a given point as

$$\frac{\mathrm{d}\delta\mathrm{D}}{\mathrm{d}\delta^{18}\mathrm{O}} = \frac{\left(\alpha^{D}_{V-S} - 1\right)}{\left(\alpha^{18}_{V-S} - 1\right)} \times \frac{(1+\delta\mathrm{D})}{\left(1+\delta^{18}\mathrm{O}\right)}. \quad (2)$$

This slope expression comes from a simple mass balance associated with a condensation step, with a small amount of snow precipitated at equilibrium and thus removed from the vapor. No assumption is made on the previous distillation path. When considering only equilibrium, $(\alpha^{D}_{V-S} - 1)/(\alpha^{18}_{V-S} - 1)$ equals 8.7 at 0 °C and then increases for lower temperature (it equals 10.1 at −40 °C). However, when distillation increases, the ratio $(1+\delta\mathrm{D})/(1+\delta^{18}\mathrm{O})$ no longer equals 1, and $1+\delta\mathrm{D}$ reaches values lower than 0.6 (corresponding to δD lower than −400 ‰) in East Antarctica. The combined effect of distillation and equilibrium fractionation at low temperature leads to a slope of the meteoric water line smaller than 8 at about −40 °C (i.e., 0.6×10.1 is smaller than 8). The distillation effect is thus responsible for the decrease of the slope of the meteoric water line and hence the increase of d-excess for cold regions. Still, as explained in Jouzel and Merlivat (1984), the anti-correlation between d-excess and δ^{18}O is muted by the existence of the kinetic effect. Indeed, when considering also kinetic effects in addition to equilibrium during solid precipitation, $(\alpha^{D}_{V-S} - 1)/(\alpha^{18}_{V-S} - 1)$ equals 11.4 at −40 °C. Still, the distillation effect dominates over the effect of both equilibrium and kinetic fractionation (0.6×11.4 still remains smaller than 8) and the d-excess tends to increase toward low temperature.

The decrease of ^{17}O-excess with decreasing temperature is not linked to distillation effect. Pure equilibrium fractionation in a Rayleigh distillation with similar dependencies of $\alpha^{17}_{V-S}$and α^{18}_{V-S} to temperature (with $\ln(\alpha^{17}_{V-S}/\alpha^{18}_{V-S}) = 0.528$) would lead to an increase of ^{17}O-excess toward low temperatures (Landais et al., 2012b; Van Hook, 1968). Actually, the decrease of the ^{17}O-excess toward low temperature is due to the kinetic effect at condensation. Indeed, the ratio $\ln(D/D^{17})/\ln(D/D^{18})$ is significantly lower (0.518) than the corresponding ratio between equilibrium fractionation factors and it results in a decrease of the ^{17}O-excess in a Rayleigh distillation system when kinetic effect at condensation is significant.

When the temperature decreases, the supersaturation in the air mass increases. This enhances the kinetic effect at condensation and leads to a decrease of both ^{17}O-excess and d-excess compared to their evolutions at pure equilibrium. In turn, the evolution of d-excess and ^{17}O-excess at low temperature can help tuning the kinetic effect (Eq. 1) and especially the dependency of supersaturation to temperature. A change in the source region of the water vapor also influences ^{17}O-excess and d-excess at low temperature, but cannot by itself explain the observed decrease in ^{17}O-excess from about 30 ppm to about 10 ppm between δ^{18}O values of −50 and

−60 ‰ (Fig. 2). Following Winkler et al. (2012) we estimate that the effect of relative humidity would not be more than 10 ppm and the effect of a change of temperature, not more than 3 ppm.

The three transect data sets are of primary interest to constrain the fractionation formulation between vapor and snow in remote regions of Antarctica, as has already be done in previous publications (Landais et al., 2008; Pang et al., 2015; Winkler et al., 2012). We give here two examples for this tuning using published modeling experiments incorporating all stable water isotopes. Figure 2 shows that a good agreement can be obtained between isotopic data and modeling results when using a simple model of water trajectory (MCIM, Ciais and Jouzel, 1994; Landais et al., 2008) with an appropriate tuning of the supersaturation function ($S = 1 - 0.0033T$ or $S = 1 - 0.004T$ according to the tuning of other parameters such as the temperature of solid condensation) (Landais et al., 2012a; Pang et al., 2015; Winkler et al., 2012). Winkler et al. (2012) discussed in details the tuning of the different parameters of the MCIM to be able to fit together δ^{18}O, d-excess and ^{17}O-excess in central Antarctica and showed that supersaturation is indeed the key parameter to fit the relative evolution of ^{17}O-excess vs. δ^{18}O and d-excess vs. δ^{18}O. When supersaturation is too low (e.g., $S = 1 - 0.002T$), equilibrium fractionation dominates and modeled ^{17}O-excess and d-excess are too high at low temperature (Fig. 2).

Things are more complicated when using AGCM equipped with water isotopes. Figure 2 shows that a d-excess increase and ^{17}O-excess decrease for decreasing δ^{18}O are also predicted by the LMDZ-iso model with an appropriate supersaturation function ($S = 1 - 0.004T$, Risi et al., 2013). However, the modeled δ^{18}O values are not low enough in Antarctica, thus leading to a strong discrepancy between the East Antarctica data sets and the modeling outputs. One of the main reasons for this disagreement is that temperatures in Antarctica are not cold enough in the LMDZ model. The overestimation of polar temperature is a common bias of CMIP5–PMIP3 simulations (e.g., Cauquoin et al., 2015b; Risi et al., 2010; Werner, 2011). This problem might be linked to the generally poor representation of the polar atmospheric boundary layer and related atmospheric inversion temperatures in GCMs (e.g., Krinner et al., 1997). Future improvements in the incorporation of the water isotopes in AGCM should take advantage of the transect data presented here.

Finally, the combined measurements of water isotopes along the three transects are essential to quantify the temperature influence on δ^{18}O, d-excess and ^{17}O-excess. Using the supersaturation tuning on the transect data, Winkler et al. (2012) and Pang et al. (2015) found the following influences of temperature on δ^{18}O, d-excess and ^{17}O-excess in the remote drilling stations of East Antarctica (Dome A, Vostok, Dome C): 1 ‰ °C^{-1}, −1.8 ‰ °C^{-1} and 0.3 ppm °C^{-1}. These determinations are in agreement with the recent estimates by Uemura et al. (2012) for the Dome F d-excess and δ^{18}O sensitivity to temperature.

3 Temporal variation of the water isotopic composition on the East Antarctic plateau

3.1 Introduction

While the spatial relationship between δ^{18}O and temperature has long been the reference to link δ^{18}O records in ice cores to past temperature variations (Jouzel et al., 2013), numerous studies have shown the limitations of such an approach because climate influences δ^{18}O in a complex way (see Sect. 2.1). One way to capture the uncertainty associated with such reconstruction is to evaluate the temporal dependency of δ^{18}O to temperature. In this section, we thus estimate the relationship between temperature and water isotopes in precipitating snow over 1 year and the relationship between temperature and water isotopes in the surface snow on the same site. Because isotopic composition archived in ice core probably results both from the isotopic composition of the precipitation and from post-deposition effects, we study the annual relationship between the isotopic composition of snow and the temperature, both on precipitation samples and on surface snow sampled every week.

3.2 Method

Precipitation and surface snow samples come from two stations located on the East Antarctica plateau: Vostok and Dome C (Fig. 1). Climatological characteristics for these stations are listed in Table 1. Vostok and Dome C are both located on the East Antarctica plateau in low accumulation regions (2–3 cm ice eq yr^{-1}, Table 1). Vostok station is the most remote and highest station. In terms of temperature, Vostok experiences the coldest conditions, and the wind speed is greater at Vostok relative to Dome C (Table 1).

At Vostok, precipitation occurs in three forms: snow from clouds, diamond dust and rime. The durations of precipitation events vary from a few hours to a few days (the latter is typical for diamond dust). The Vostok precipitation sampling has been performed immediately after each precipitation event from December 1999 to December 2000 and can be separated into two data sets. The first one (series A) corresponds to sampling from a precipitation trap placed at 1 m above the snow surface and at ∼ 50 m windward from the station (Landais et al., 2012a). Samples collected in this trap consist of pure precipitation as ascertained by the calm weather conditions and absence of blowing snow at the time of collection. Sublimation in the trap is unlikely for two reasons. First, the high walls of the trap shaded the precipitation within it. Second, most of the samples were collected in winter, when insolation is minimal. The second series (B) corresponds to sampling from a lower precipitation trap buried with its upper edge at the snow surface. Thus the flow of

Table 1. Main characteristics of the snow pits drilled in East Antarctica at three different stations. Meteorological data for Vostok from http://www.aari.ru. Data indicated by a * correspond to the snow pit Vostok_winkler (Winkler et al., 2013). Accumulation rate (S2) from E. Le Meur et al. (2016). Temperature at S2: L. Arnaud, personal communication, 2015, 10 m temperature at Dome C: J. Schwander, unpublished data, 2001. Wind speed at Dome C from the IPEV/PNRA project "Routine Meteorological Observations" at Concordia station http://www.climantartide.it.

	Vostok	S2	Dome C
Latitude	−78.5° S	−76.3° S	−75.1° S
Elevation	3488 m	3229 m	3233 m
Mean annual air T (2 m)	−55.2 °C	NA	−51.7 °C
Air T coldest month	−68.0 °C (Aug)	NA	−63.5 °C (Jul.)
Air T hottest month	−31.8 °C (Dec)	NA	−31.3 °C (Jan)
10 m borehole T	−57 °C	−55.1 °C	−54.9 °C
Acc. rate (ice eq.)	2.4 cm yr^{-1}	2.1 cm yr^{-1}	2.7 cm yr^{-1}
Wind speed	5.1 m s^{-1}	NA	3.3 m s^{-1}
Average $\delta^{18}O$	−57.13 ‰*; −57.06 ‰	−53.81 ‰	−51.14 ‰
Average d-excess	15.3 ‰*; 16.1 ‰	12.3 ‰	9.1 ‰
Average ^{17}O-excess	10 ppm*; 26 ppm	32 ppm	31 ppm

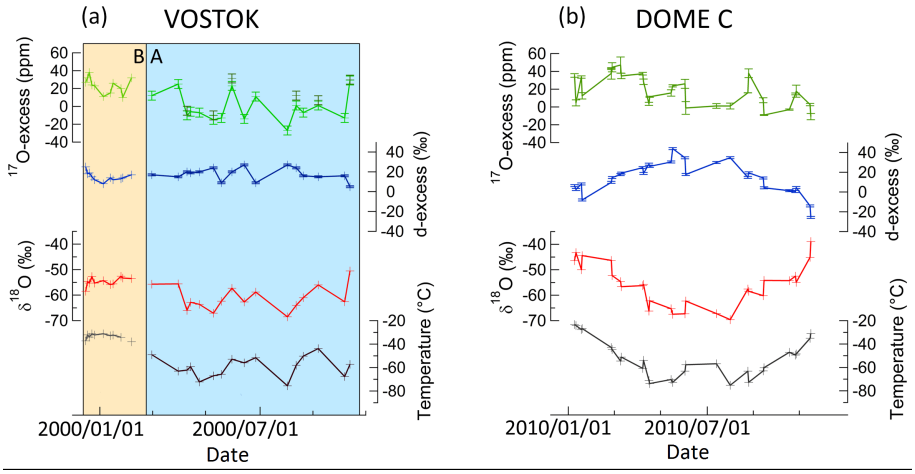

Figure 3. (a) Isotopic composition of the precipitation at Vostok over 1 year. A: samples from the upper trap (pure precipitation); B: samples from the lower trap (precipitation mixed with blowing snow). For the ^{17}O-excess, dark green points were measured at LSCE, whereas light green points were measured at HUJI. **(b)** Isotopic composition of the precipitation at Dome C over 1 year.

blowing snow around the trap was unimpeded and the snow collected consists of a mixture of precipitation and blowing snow. After the collection, the samples from the two series were melted, poured into special plastic bottles and frozen again. This procedure was followed to avoid alteration of the initial isotopic composition of precipitation due to sublimation and exchange with the atmospheric water vapor. Sample volume varied between 1 mL (diamond dust) and 10–20 mL (heavy precipitation).

The δD, δ^8O and ^{17}O-excess measurements for the 16 samples of series A (Fig. 3a, blue panel: February 2000–September 2000) have been published in Landais et al. (2012a). $\delta^{18}O$ and d-excess measurements were performed at Geophysics department, Niels Bohr Institute, University of Copenhagen, while ^{17}O-excess was measured at HUJI using a Delta V instrument (duplicate measurements of ^{17}O-excess were also realized at LSCE for six samples). The 11 samples of series B were measured in the same institutions as the samples of series A (Fig. 3a, yellow panel: December 1999–February 2000).

The Dome C precipitation sampling has been continuously performed since December 2007 in the framework of the Italian glaciology program at Concordia station. Almost 100 samples are collected every year and analyzed for δD and $\delta^{18}O$. Here, we present only a subset of this sample collection from January to December 2010 (Fig. 3b). Unfortunately, samples from the year 2011 (period when the surface snow was sampled, see the last paragraph of this section) were not available. The ^{17}O-excess was measured at LSCE using the fluorination method followed by dual inlet analy-

sis on a MAT 253 as for the transect samples of the previous section (Sect. 2) and Vostok precipitation samples.

It should be noted that some $\delta^{18}O$ values presented on Fig. 3 are significantly lower than the $\delta^{18}O$ value of the SLAP (−55.5 ‰). The classical two-point calibration VSMOW–SLAP is thus possibly not valid here. We have addressed the $\delta^{18}O$ calibration issue for very low $\delta^{18}O$ values by diluting well-characterized standards with almost pure $H_2^{16}O$ (Isotec Water-16O from Sigma-Aldrich; Casado et al., 2016). These dilutions and associated measurements have shown that the VSMOW–SLAP calibration for $\delta^{18}O$ on our instrument can be extrapolated down to −90 ‰. It was not possible to do the same exercise with ^{17}O-excess because the water with almost pure $H_2^{16}O$ (99.98 %, Casado et al., 2016) was not characterized in $H_2^{17}O$ content. Still, measurements of much depleted $\delta^{18}O$ samples on different mass spectrometers suggest that we may create biases of up to 10 ppm in the ^{17}O-excess values expressed in a VSMOW–SLAP scale. Mean ^{17}O-excess values associated with $\delta^{18}O < -55.5$ ‰ and performed on different mass spectrometers may therefore not be directly comparable.

The sampling of surface snow at Dome C was performed between December 2010 and December 2011, in the clean area, about 1 km away from Concordia station, according to the following procedure. Each day of collection, an area of approximatively 5 m^2 was chosen (different from the previous one) and snow is scraped from 5 to 10 spots (∼ 0.04 m^2) within this area. This variability is due to the necessity to collect enough snow for later analysis. Only the first 1–2 mm of snow was collected, using a metal blade. The snow collected was homogenized and melted, and a fraction destined for isotopic analysis transferred into a 20 mL vial and then kept frozen until analysis. In every 5 m^2 area, sastrugi were avoided, but otherwise (i.e., in flat areas) the sampling was performed randomly and no distinction was made between snow types; drifted snow, wind crust, soft, hard and hoar snow are sampled indiscriminately. The aim was to sample all types of snow present during the day of sampling to access the average composition of the surface snow in direct contact with the atmosphere. On this set of samples, $\delta^{18}O$ and δD were measured by a wavelength scanned cavity ring-down spectroscopy instrument (Picarro L2130i) with a resulting uncertainty of $1\sigma = 0.05$ ‰ for $\delta^{18}O$ and 0.5 ‰ for δD. As for the other new ^{17}O-excess data presented in this manuscript, we used here the fluorination method coupled with dual inlet mass spectrometry (MAT 253) with a resulting uncertainty $1\sigma = 5$ ppm.

3.3 Discussion

As already observed for other Antarctic sites where $\delta^{18}O$ measurements on precipitation samples have been performed, $\delta^{18}O$ of falling snow is strongly related to temperature both at Dome C ($R = 0.88$, $p < 0.05$, Table 2) and at Vostok ($R = 0.77$, $p < 0.05$, Table 2). The annual slope of

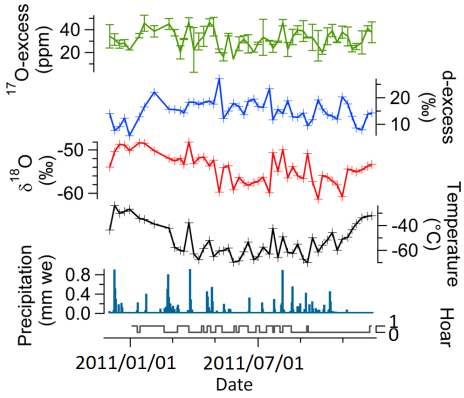

Figure 4. Isotopic composition of surface snow sampled every 1–2 weeks at Dome C.

$\delta^{18}O$ vs. temperature is 0.46 and 0.26 ‰ °C^{-1} at Dome C and Vostok respectively (Table 2). The annual slope at Dome C is comparable to the one observed at Dome F for a similar temperature level (0.47 to 0.78 ‰ °C^{-1}, Fujita and Abe, 2006; Motoyama et al., 2005), while the Vostok seasonal $\delta^{18}O$ vs. temperature slope is significantly lower. Using only the samples of series A (instead of A + B) increases the annual slope at Vostok slightly (0.35 ‰ °C^{-1}), suggesting that this low slope can result from post-deposition noise (i.e., blowing snow with an isotopic composition different from the one of the falling snow). Several other possible explanations have already been evoked to explain this low slope (Ekaykin, 2003; Landais et al., 2012a), such as a strong gradient between condensation and surface temperature at Vostok when precipitation occurred, or a change in the type of precipitation at Vostok (possible high contribution of diamond dust in precipitation). However, we should also note that at Vostok, we have only a small number of water samples corresponding to precipitation events associated with the largest amount of snow. These large precipitation events are associated with relatively high temperature in winter. Such a selection of particular precipitation events may also have an influence on the final $\delta^{18}O$ vs. temperature slope; therefore we avoid speculating on this particular value with so few data points (26 at Vostok).

As for the surface snow at Dome C, there is a rather good correlation between $\delta^{18}O$ and 2 m air temperature (Fig. 4) with a global slope of 0.14 ‰ °C^{-1} ($R = 0.54$, $p < 0.05$, Table 2). This slope is lower than the annual slope in the precipitation at Dome C (0.46 ‰ °C^{-1}, $R = 0.88$, $p < 0.05$, Table 2) and hence much lower than the spatial slope. The fact that temporal slopes are smaller than the spatial ones has to be kept in mind when applying these slopes to past temperature reconstructions. When looking in more detail at the evolution of $\delta^{18}O$ over 1 year, two observations can be made. First, between December 2010 and March 2011, we observe a long-term decreasing trend of both temperature and surface snow $\delta^{18}O$, in a period associated with only rare precipita-

Table 2. Correlation coefficients and slopes of the linear regression between δ^{18}O and temperature, deuterium excess and δ^{18}O and ^{17}O-excess and δ^{18}O, for various sample types (traverse: see Sect. 2; precipitation and surface snow: see Sect. 3; snow pits: see Sect. 4). The slopes between parameters are only indicated when the correlation coefficient is significant at the 95 % level (p value < 0.05). SD denotes standard deviation. (NB: correlation coefficients: Pearson's R for traverse, precipitation, surf. snow; Spearman's R for the snow pits.)

	δ^{18}O/temp.					d-excess/δ^{18}O					^{17}O-excess/δ^{18}O				
	N	R	p value	Slope	SD	N	R	p value	Slope	SD	N	R	p value	Slope	SD
Traverses															
All points															
Dome A	42	0.897	8.9×10^{-16}	0.92	0.07	42	−0.406	7.6×10^{-3}	−0.24	0.08	31	0.456	9.9×10^{-3}	0.40	0.15
Dome F	13	0.950	7.1×10^{-7}	0.91	0.09	29	−0.809	1.1×10^{-7}	−0.45	0.06	29	0.575	1.1×10^{-3}	0.67	0.18
Dome C	29	0.833	2.1×10^{-3}	1.20	0.15	29	−0.609	4.6×10^{-4}	−0.18	0.04	29	0.056	0.775	na	na
δ^{18}O < −40 ‰															
Dome A	11	0.911	9.3×10^{-5}	0.75	0.11	11	−0.868	5.2×10^{-4}	−1.41	0.27	17	−0.018	0.946	na	na
Dome F	8	0.799	1.7×10^{-2}	0.64	0.20	23	−0.834	7.5×10^{-7}	−0.64	0.09	23	0.396	0.061	na	na
Dome C	16	0.951	1.5×10^{-8}	0.77	0.07	18	−0.711	9.4×10^{-4}	−0.43	0.11	16	0.219	0.416	na	na
All transects	35	0.858	4.2×10^{-11}	0.71	0.07	52	−0.777	1.3×10^{-11}	−0.95	0.11	56	0.355	7.2×10^{-3}	0.91	0.01
Precipitation															
Dome C	28	0.877	9.2×10^{-10}	0.46	0.05	28	−0.884	4.7×10^{-10}	−1.61	0.16	28	0.105	0.596	na	na
Vostok (A)	16	0.625	9.6×10^{-6}	0.35	0.12	16	−0.698	2.6×10^{-3}	−0.91	0.25	16	0.884	5.7×10^{-6}	2.95	0.42
Vostok (A & B)	26	0.765	5.4×10^{-6}	0.26	0.04	27	−0.635	3.8×10^{-4}	−0.73	0.17	27	0.854	1.5×10^{-8}	3.12	0.38
Surf. snow															
Dome C	50	0.542	4.8×10^{-5}	0.14	0.03	50	−0.398	4.3×10^{-3}	−0.47	0.16	50	0.320	2.3×10^{-2}	0.76	0.32
Snow pits															
Dome C	na	na	na	na	na	67	−0.157	0.205	na	na	66	0.026	0.834	na	na
S2	na	na	na	na	na	102	−0.804	$< 5 \times 10^{-16}$	−1.03	0.07	101	0.002	0.986	na	na
Vostok	na	na	na	na	na	123	−0.436	4.5×10^{-7}	−0.46	0.09	112	−0.079	0.412	na	na
Vostok_winkler	na	na	na	na	na	115	−0.335	2.5×10^{-4}	−0.49	0.14	116	−0.396	1.1×10^{-5}	−3.95	0.73

tions events. Here the number of points is limited and this correlation should be checked by a higher resolution study. A possible explanation for the joint evolution of these two parameters (between precipitation events) would be surface snow metamorphism and exchange with the atmospheric water vapor, as already evidenced in Greenland (Casado et al., 2016; Ritter et al., 2016; Steen-Larsen et al., 2013). This mechanism is supported by the synchronous prolonged period of hoar formation (Fig. 4), surface hoar crystals being the product of water vapor condensation (Champollion et al., 2013). Besides, the porous surface hoar could also act as a trap for the rare snow particles and diamond dust (Champollion et al., 2013), therefore facilitating the evolution of the isotopic composition of the snow in the absence of precipitation events. Second, several short warming events during winter 2011 are also clearly imprinted in the δ^{18}O signal. Because warm events are often associated with precipitation events (Fig. 4), the temperature-δ^{18}O link during these events can result from fresh snow deposition. Note that the warm event of mid-June (17 June) is not reflected in the δ^{18}O signal. This may be due to wind erosion and redeposition of the snow.

The relationship between d-excess or ^{17}O-excess and δ^{18}O can also help us to understand the annual variation of the isotopic composition of the snow. Here the annual amplitude of variation (10–20 ‰ for d-excess and 30–40 ppm for ^{17}O-excess) suggests that the main control is the site temperature, because other parameters such as source temperature and relative humidity would not account for more than a few per mil for d-excess or more than 10 ppm for ^{17}O-excess (Winkler et al., 2012). Both for Vostok and Dome C precipitation, d-excess and δ^{18}O are anti-correlated with a slope of $-1.61\,‰\,‰^{-1}$ ($R = -0.88$, $p < 0.05$, Table 2) at Dome C and -0.7 at Vostok ($R = -0.64$, $p < 0.05$, Table 2). Even if there is a large difference between the two slopes, this anti-correlation is expected and has already been observed with similar values (1 to $2\,‰\,‰^{-1}$) on the transect data: for δ^{18}O level below -40 ‰, we observe a clear anti-correlation between δ^{18}O and d-excess linked to the effect of distillation. In the surface snow at Dome C, d-excess is also globally anti-correlated with δ^{18}O over the whole year 2011 with a slope of $-0.47\,‰\,‰^{-1}$ ($R = -0.4$, $p < 0.05$, Table 2), indicating that the effect of the distillation process is still perceptible in the surface snow but somehow obscured by another process.

^{17}O-excess of precipitation is significantly correlated with δ^{18}O at Vostok ($2.95\,\text{ppm}\,‰^{-1}$, $R = 0.88$, $p < 0.05$, Table 2) with a higher slope and correlation coefficient compared to the transect data set with $\delta^{18}\text{O} < -40$ ‰ ($0.91\,\text{ppm}\,‰^{-1}$, $R = 0.36$, $p < 0.05$, Table 2). On the opposite, no clear relationship can be drawn from the ^{17}O-excess vs. δ^{18}O values in the precipitation at Dome C, even if sampling at both sites encompasses the same range of δ^{18}O values down to -70 ‰ and surface temperature down to -75 °C. Such a result suggests that the kinetic effect during condensation is not the only driver for ^{17}O-excess variations in East Antarctica. The analysis of the surface snow at Dome C, however, shows a small (but significant) correlation between ^{17}O-excess and δ^{18}O. How can this correlation exist in the surface snow and not (significantly) in the precipitation at the same site? We propose two hypotheses regarding this phenomenon. First, at Dome C the annual cycle of temperature in 2010 is very well defined and does not show the frequent warming events (up to -50 °C) observed during the winter of 2011 at Dome C and in 2000 at Vostok. In other words, natural variability may be the cause of these differences, with winter 2010 experiencing more stable (and therefore colder) conditions than winter 2000 and 2011, and thus reduced correlation between ^{17}O-excess and δ^{18}O. Alternatively, the post-deposition processes within the snow could be responsible for a renewed correlation between ^{17}O-excess and δ^{18}O.

4 Variability of water isotopic composition in snow pits

4.1 Description of the sampling sites

The next step to understand the archiving of the water isotopic composition is to look at the combined water isotopes on short snow pits at different places in Antarctica. The isotopic composition on snow pits will indeed be influenced by the isotopic composition of snow precipitation, diamond dust deposition and post-deposition effects, involving exchanges with atmospheric water vapor. Many isotopic measurements have been performed on snow pits in Antarctica (e.g., Altnau et al., 2015; Ekaykin et al., 2014) but except the study from Winkler et al. (2013) focusing on one shallow pit only in Vostok, none of the previous studies have combined measurements of all stable water isotopes.

Here, we compare the results obtained from snow pits from three localities: Vostok, S2 and Dome C (Fig. 1). The main characteristics of the sampling sites are described in Table 1. From Dome C to S2, and then to Vostok, the temperature decreases, while the altitude increases. Thus the combination of the continental effect and of the altitudinal effect should lead to decreasing δ^{18}O values, because of a more advanced distillation at the most remote sites. Interestingly, results from modeling of air parcel trajectories (Reijmer et al., 2002) indicate that air parcels moving toward Vostok pass over Dome C, thus confirming the pathway of the distillation.

To see if the distillation is indeed the main process controlling the isotopic composition in the snow pits, we first compare the average values between the pits, and then look at the evolution of isotopic parameters. Given the accumulation rate, several decades are probably recorded (about 60 years). However, we avoid discussing any precise age scale for these shallow pits drilled in East Antarctica. Indeed, because of the low accumulation rate and redeposition effects in this region, the precise chronology is uncertain (possibility of gaps or snow layer repetition). This prevents a proper interpretation of isotopic variations in terms of interannual variability and

we only discuss in the following the average isotopic values and correlation between the different isotopic parameters. If distillation is the main driver, we expect low δ^{18}O values to be associated with high d-excess values, because they would be symptomatic of a more pronounced distillation, and with lower ^{17}O-excess values, because of the kinetic effect at very low temperature.

4.2 Isotopic measurements

Here, we have analyzed the isotopic composition of the first (2 to 4) meters of snow at three localities: Vostok, S2 and Dome C (Fig. 1). At Vostok, we can compare new data from the snow pit obtained for this study to a snow pit previously analyzed in δD, δ^{18}O and δ^{17}O (Winkler et al., 2013) that was dated to 1951 at 3.46 m. In the following, this snow pit will be called Vostok_winkler. For the different snow pits, the snow was sampled every 3 cm from the top to the bottom. The new δ^{18}O, δD and ^{17}O-excess measurements presented here were performed following the analytical methods of Sect. 2.2 with a MAT253, while the data from Vostok_winkler were measured on a Delta V.

4.3 Results

The average values for δ^{18}O (Table 1) decrease from Dome C to Vostok. The average d-excess values have an opposite trend relative to the δ^{18}O values (they increase from 9.1 ‰ at Dome C to 12.3 ‰ at S2 and to 16.1 ‰ at Vostok). Finally, the average ^{17}O-excess values measured on the same instrument are similar at Dome C, S2 and Vostok ($\sim$ 30 ppm). Correlations between variations of δ^{18}O, d-excess and ^{17}O-excess were inferred first for the whole isotopic series of the snow pits and then, for the couple δ^{18}O/^{17}O-excess for subsections of 20 points, corresponding to 60 cm, or about 10 years. The Spearman's correlations performed over a shifting window of 20 points are significant (with $\alpha = 0.05$) if the absolute value of the correlation coefficient ρ is higher than 0.443.

The results of Spearman's correlations for the whole series are presented in Table 2. For the d-excess/δ^{18}O couple of parameters, the correlation is negative in all the pits, and strongest at S2. We note that the correlation at Dome C is also negative but not significant at the 0.05 level. Regarding the ^{17}O-excess/δ^{18}O couple of parameters, the correlation is significant only in the Vostok_winkler snow pit. At this site, the correlation is negative.

The shifting window correlation coefficients between ^{17}O-excess and δ^{18}O are overall negative at Vostok and S2 (Fig. 5a–c). They are significant in most of the core (70 % of cases) for Vostok_winkler, and also in a large part of the core for the second snow pit at Vostok (30 % of cases) and at S2 (40 % of cases). At Dome C, the correlation coefficients are small, and oscillate between positive and negative values (Fig. 5d). They only reach significant values in 4 % of cases.

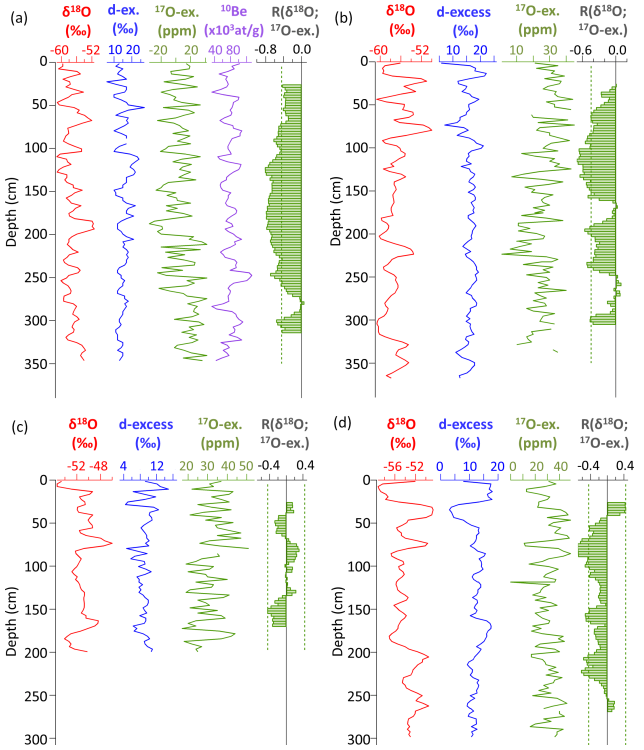

Figure 5. Water isotopic data from snow pits and correlation between δ^{18}O and ^{17}O-excess for Vostok_winkler (**(a)**; Winkler et al., 2013), Vostok **(b)**, Dome C **(c)** and S2 **(d)**. Each correlation coefficient R between δ^{18}O and ^{17}O-excess corresponds to a correlation realized over 20 points (see Sect. 4.3). The correlation coefficients are significant when they are larger than 0.443 in absolute values. The limit of significance is displayed as a green dotted line.

4.4 Interpretation of the results and discussion of processes

The comparison of the average values between sites is coherent with the distillation process, with δ^{18}O values decreasing and d-excess values increasing from Dome C to Vostok. However, the kinetic effect at condensation is not clearly apparent, as the ^{17}O-excess values remain more or less the same between the sites.

Global Spearman's correlations led to significant negative correlations between δ^{18}O and d-excess for S2, Vostok and Vostok_winkler. These negative correlations are consistent with those already detected in the snow from transects and in the precipitation, and therefore with a distillation process. An effect of the source is also possible, but not sufficient to explain the large amplitude of variations in d-excess and ^{17}O-excess (10–20 ‰ for d-excess and 30–40 ppm for ^{17}O-excess). At Dome C, the absence of significant correlation in the snow pit is unexpected, considering the anti-correlation observed at this site both in the precipitation and in the surface snow. Thus the distillation process at this site appears somehow obliterated by post-deposition processes

(erosion, transport and redepositing of snow, diffusion of isotopes within the firn) affecting the isotopic compositions and their relationships.

The overall negative relationship between δ^{18}O and ^{17}O-excess at Vostok and S2 (considering not only the whole series values but also the subsections values) is rather intriguing. In effect, this is opposed to what has been observed on transects and at the seasonal scale for precipitation samples. The anti-correlation between ^{17}O-excess and δ^{18}O in these two sites definitively shows that distillation is not the driver of the ^{17}O-excess variations in the East Antarctica snow pits. Other mechanisms must then be considered to account for such negative correlation. Winkler et al. (2013) have explored different possible explanations for the relationships between ^{17}O-excess, δ^{18}O and δD. Using additional ^{10}Be measurements in the same pit at Vostok and the good correlation between ^{10}Be and ^{17}O-excess, they have concluded that stratospheric input may be a good candidate for explaining the high ^{17}O-excess values concomitant with high ^{10}Be and low δ^{18}O. Indeed, mass-independent fractionation associated with reaction with ozone in the stratosphere may lead to strong ^{17}O-excess in the stratosphere (Zahn et al., 2006). Even if the amount of water vapor is very small there (2 ppm), East Antarctica is very dry (30 ppm at Vostok) and located under the influence of the polar vortex hence with significant stratospheric input (e.g., Cauquoin et al., 2015a; Stohl and Sodemann, 2010). We propose here that the more frequent anti-correlation between ^{17}O-excess and δ^{18}O observed at Vostok relative to S2, and also at Vostok and S2 with respect to Dome C, is linked to a stronger influence of stratospheric input in areas that are more remote (i.e., Vostok and S2). This is supported by the highest level of natural tritium observed at Vostok (100 TU) compared to Dome C (30 TU) (Becagli et al., 2004; Fourré et al., 2006; Proposito et al., 2002). Natural tritium is indeed mainly produced by the interaction of cosmic radiations with the upper atmosphere (Craig and Lal, 1961; Masarik and Beer, 2009) and is thus a good marker of stratospheric water input when measured in surface snow. Unfortunately, no tritium measurement is available at S2 now.

Finally, note that post-deposition could also have an effect on the relationship between δ^{18}O, d-excess and ^{17}O-excess. This effect has been studied in Winkler et al. (2013) who showed by simple calculations at steady state that this effect could be important. Still, this calculation could not explain the observed relationship at Vostok_winkler and particularly how the seasonal correlation between δ^{18}O and ^{17}O-excess observed in precipitation at Vostok can be changed to an anti-correlation in the snow. To better quantify this effect in East Antarctica, modeling of post-deposition effect should be improved by using a dynamic model as in Town et al. (2008) and by using field measurements and experiments to tune it to the East Antarctic plateau.

5 Conclusions

We presented a compilation of new water stable isotopic data in East Antarctica on surface snow, precipitation and snow pits. The comparison of the different stable isotope parameters δ^{18}O, d-excess and ^{17}O-excess is very useful to decipher the various influences on the water isotopic composition in ice cores that is further archived in deep ice cores. We selected sites in East Antarctica with extreme climatic and isotopic values (δ^{18}O down to -70 ‰ in winter) in order to obtain a present-day equivalent to the glacial period archived in deep ice cores. These sites are located at the very end of the distillation trajectory with possible significant input of stratospheric water vapor that has an influence on water isotopic ratios.

Table 2 presents the compilation of the relationships between the different isotopic parameters and temperature for the different types of snow and different locations. Measurements of water isotopes in average surface snow and precipitations show a systematic anti-correlation between d-excess and δ^{18}O for δ^{18}O lower than -40 ‰ and, except at Dome C, a systematic correlation between ^{17}O-excess and δ^{18}O for δ^{18}O lower than -40 ‰. Even if the low δ^{18}O values encountered in East Antarctica cannot yet be reproduced by AGCM equipped with water isotopes, the (anti-)correlation between water isotopic parameters can be explained well. The anti-correlation between d-excess and δ^{18}O results from the distillation and the correlation between ^{17}O-excess and δ^{18}O at very low temperatures; this is the result of kinetic effects at condensation in a strongly supersaturated environment.

The links between isotopic parameters are however different in snow pits of East Antarctica. Especially, the positive relationship between δ^{18}O and ^{17}O-excess, associated with kinetic effects at low temperatures, is not visible, and an anti-correlation between δ^{18}O and ^{17}O-excess appears at Vostok and S2 that could be explained by a stratospheric input of water vapor. ^{10}Be values, measured in the same snow pit at S2, show a positive correlation with ^{17}O-excess values (M. Baroni, personal communication, 2015), and thus give weight to this explanation. Such an effect is not visible at Dome C where no particular relationship between ^{17}O-excess and δ^{18}O is visible.

From the different types of snow in East Antarctica, we always observe a positive relationship between changes in surface temperature and change in δ^{18}O of snow, even in the absence of precipitation. If confirmed by future studies, the correlation between δ^{18}O of surface snow and temperature in the absence of precipitation in East Antarctica has strong importance for the interpretation of water isotopes in deep ice cores. Indeed, East Antarctica is characterized by a very small accumulation rate (even smaller during glacial periods); therefore post-deposition effects are expected to have a significant effect. Our findings suggest that post-deposition effects lead to a correlation between δ^{18}O and temperature. To better understand the exchanges between surface snow

and atmospheric vapor, and to assess their impact on the isotopic compositions, detailed models focusing on these interactions are needed. In the future, the development of models of post-deposition processes equipped with water isotopes may become the key to the quantitative interpretation of isotopes in ice cores.

Finally, from our data, we calculated a wide range of temporal slopes between δ^{18}O and temperature (0.14 to 0.46 ‰ °C^{-1}, Table 2). They are in general significantly lower than the spatial slope of the δ^{18}O vs. temperature relationship over Antarctica (0.8 ‰, Lorius and Merlivat, 1977; Masson-Delmotte et al., 2008). Such results have important implications for the temperature reconstructions from deep ice cores in central Antarctica. Indeed, with a smaller δ^{18}O vs. temperature slope, the δ^{18}O-inferred amplitude of past temperature changes is larger. This is in agreement with outputs of experiments performed with AGCM equipped with water isotopes. Indeed, the modeled temporal slopes between δ^{18}O and temperature over the East Antarctic plateau, both at annual and glacial–interglacial scales, are generally smaller by up to a factor of 2 compared to the present-day spatial slope over Antarctica (Cauquoin et al., 2015b; Lee et al., 2008; Risi et al., 2010; Schmidt et al., 2007; Sime et al., 2008, 2009).

The Supplement related to this article is available online at doi:10.5194/tc-10-837-2016-supplement.

Acknowledgements. The research leading to these results has received funding from the European Research Council under the European Union's Seventh Framework Programme (FP7/2007-2013)/ERC grant agreement no. 306045. We are indebted to Michel Fily and Laurent Arnaud who organized the VANISH expedition and provided samples for this study. We would like to thank the ANR VANISH (ANR-07-VULN-013) for their support, as well as the IPEV programme SUNITEDC (1011). We also acknowledge the contribution of the PRIDE project funded by PNRA-MIUR and of the Russian Antarctic Expeditions. The snow samples from the transects including Syowa–Dome F were sampled by the Japanese Antarctic Research Expedition and the National Institute of Polar Research (NIPR), Tokyo, in the framework of the joint Japanese-Swedish IPY traverse. This research was partly supported by JSPS Postdoctoral Fellowships for Research Abroad and by JSPS KAKENHI grant number 26550013.

Edited by: M. Schneebeli

References

Altnau, S., Schlosser, E., Isaksson, E., and Divine, D.: Climatic signals from 76 shallow firn cores in Dronning Maud Land, East Antarctica, The Cryosphere, 9, 925–944, doi:10.5194/tc-9-925-2015, 2015.

Barkan, E. and Luz, B.: Diffusivity fractionations of H_2 $^{16}O/H_2^{17}O$ and $H_2^{16}O/H_2^{18}O$ in air and their implications for isotope hydrology, Rapid Commun. Mass Spectrom., 21, 2999–3005, 2007.

Barkan, E. and Luz, B.: High precision measurements of $^{17}O/^{16}O$ and $^{18}O/^{16}O$ ratios in H_2O, Rapid Commun. Mass Spectrom., 19, 3737–3742, 2005.

Becagli, S., Proposito, M., Benassai, S., Flora, O., Genoni, L., Gragnani, R., Largiuni, O., Pili, S. L., Severi, M., Stenni, B., Traversi, R., Udisti, R., and Frezzotti, M.: Chemical and isotopic snow variability in East Antarctica along the 2001/02 ITASE traverse, Ann. Glaciol., 39, 473–482, 2004.

Casado, M., Landais, A., Masson-Delmotte, V., Genthon, C., Kerstel, E., Kassi, S., Arnaud, L., Picard, G., Prie, F., Cattani, O., Steen-Larsen, H.-C., Vignon, E., and Cermak, P.: Continuous measurements of isotopic composition of water vapour on the East Antarctic Plateau, Atmos. Chem. Phys. Discuss., doi:10.5194/acp-2016-8, in review, 2016.

Cauquoin, A., Jean-Baptiste, P., Risi, C., Fourré, E., Stenni, B., and Landais, A.: The global distribution of natural tritium in precipitation simulated with an Atmospheric General Circulation Model and comparison with observations, Earth Planetary Sc. Lett., 427, 160–170, 2015a.

Cauquoin, A., Landais, A., Raisbeck, G. M., Jouzel, J., Bazin, L., Kageyama, M., Peterschmitt, J.-Y., Werner, M., Bard, E., and Team, ASTER: Comparing past accumulation rate reconstructions in East Antarctic ice cores using ^{10}Be, water isotopes and CMIP5-PMIP3 models, Clim. Past, 11, 355–367, doi:10.5194/cp-11-355-2015, 2015b.

Champollion, N., Picard, G., Arnaud, L., Lefebvre, E., and Fily, M.: Hoar crystal development and disappearance at Dome C, Antarctica: observation by near-infrared photography and passive microwave satellite, The Cryosphere, 7, 1247–1262, doi:10.5194/tc-7-1247-2013, 2013.

Charles, C. D., Rind, D., Jouzel, J., Koster, R. D., and Fairbanks, R. G.: Glacial-Interglacial changes in moisture sources for Greenland: Influences on the ice core record of climate, Science, 263, 508–511, 1994.

Ciais, P. and Jouzel, J.: Deuterium and oxygen 18 in precipitation: Isotopic model, including mixed cloud processes, J. Geophys. Res.-Atmos., 99, 16793–16803, 1994.

Craig, H.: Isotopic variations in meteoric waters, Science, 133, 1702–1703, 1961.

Craig, H. and Lal, D.: The production rate of natural tritium, Tellus, 13, 85–105, 1961.

Dansgaard, W.: Stable isotopes in precipitation, Tellus, 16, 436–468, 1964.

Delmotte, M., Masson, V., Jouzel, J., and Morgan, V. I.: A seasonal deuterium excess signal at Law Dome, coastal eastern Antarctica: A Southern Ocean signature, J. Geophys. Res.-Atmos., 105, 7187–7197, 2000.

Ekaykin, A. A.: Meteorological regime of central Antarctica and its role in the formation of isotope composition of snow thickness,

Glaciology, Faculté de Géographie de Saint Pétersbourg, Saint Pétersbourg, 137 pp., 2003.

Ekaykin, A. A., Lipenkov, V. Y., Barkov, N. I., Petit, J. R., and Masson-Delmotte, V.: Spatial and temporal variability in isotope composition of recent snow in the vicinity of Vostok station, Antarctica: implications for ice-core record interpretation, Ann. Glaciol., 35, 181–186, 2002.

Ekaykin, A. A., Lipenkov, V. Y., Kuzmina, I. N., Petit, J. R., Masson-Delmotte, V., and Johnsen, S. J.: The changes in isotope composition and accumulation of snow at Vostok station, East Antarctica, over the past 200 years, Ann. Glaciol., 39, 569–575, 2004.

Ekaykin, A. A., Kozachek, A. V., Lipenkov, V. Y., and Shibaev, Y. A.: Multiple climate shifts in the Southern hemisphere over the past three centuries based on central Antarctic snow pits and core studies, Ann. Glaciol., 55, 259–266, 2014.

EPICA comm. members: Eight glacial cycles from an Antarctic ice core, Nature, 429, 623–628, 2004.

Fawcett, P. J., Ágústsdóttir, A. M., Alley, R. B., and Shuman, C. A.: The Younger Dryas termination and North Atlantic Deep Water formation: Insights from climate model simulations and Greenland ice cores, Paleoceanography, 12, 23–38, 1997.

Fourré, E., Jean-Baptiste, P., Dapoigny, A., Baumier, D., Petit, J.-R., and Jouzel, J.: Past and recent tritium levels in Arctic and Antarctic polar caps, Earth Planet. Sc. Lett., 245, 56–64, 2006.

Franz, P. and Röckmann, T.: High-precision isotope measurements of $H_2^{16}O$, $H_2^{17}O$, $H_2^{18}O$, and the $\Delta^{17}O$-anomaly of water vapor in the southern lowermost stratosphere, Atmos. Chem. Phys., 5, 2949–2959, doi:10.5194/acp-5-2949-2005, 2005.

Fujita, K. and Abe, O.: Stable isotopes in daily precipitation at Dome Fuji, East Antarctica, Geophys. Res. Lett., 33, L18503, doi:10.1029/2006GL026936, 2006.

Fujita, S., Holmlund, P., Andersson, I., Brown, I., Enomoto, H., Fujii, Y., Fujita, K., Fukui, K., Furukawa, T., Hansson, M., Hara, K., Hoshina, Y., Igarashi, M., Iizuka, Y., Imura, S., Ingvander, S., Karlin, T., Motoyama, H., Nakazawa, F., Oerter, H., Sjöberg, L. E., Sugiyama, S., Surdyk, S., Ström, J., Uemura, R., and Wilhelms, F.: Spatial and temporal variability of snow accumulation rate on the East Antarctic ice divide between Dome Fuji and EPICA DML, The Cryosphere, 5, 1057–1081, doi:10.5194/tc-5-1057-2011, 2011.

Gao, J., Masson-Delmotte, V., Yao, T., Tian, L., Risi, C., and Hoffmann, G.: Precipitation water stable isotopes in the South Tibetan Plateau: observation and modeling, J. Climate, 24, 3161–3178, 2011.

Gat, J. R.: Oxygen and hydrogen isotopes in the hydrologic cycle, Annu. Rev. Earth Planet. Sci., 24, 225–262, 1996.

Hoshina, Y., Fujita, K., Nakazawa, F., Iizuka, Y., Miyake, T., Hirabayashi, M., Kuramoto, T., Fujita, S., and Motoyama, H.: Effect of accumulation rate on water stable isotopes of near-surface snow in inland Antarctica, J. Geophys. Res., 119, 274–283, 2014.

Jouzel, J. and Merlivat, L.: Deuterium and oxygen 18 in precipitation: modeling of the isotopic effects during snow formation, J. Geophys. Res., 89, 11749–11757, 1984.

Jouzel, J., Vimeux, F., Caillon, N., Delaygue, G., Hoffmann, G., Masson-Delmotte, V., and Parrenin, F.: Magnitude of isotope/temperature scaling for interpretation of central Antarctic ice cores, J. Geophys. Res.-Atmos., 108, 4361, doi:10.1029/2002JD002677, 2003.

Jouzel, J., Masson-Delmotte, V., Stiévenard, M., Landais, A., Vimeux, F., Johnsen, S. J., Sveinbjörnsdottir, A. E., and White, J. W. C.: Rapid deuterium-excess changes in Greenland ice cores: a link between the ocean and the atmosphere, Compt. Rendus Geosci., 337, 957–969, 2005.

Jouzel, J., Masson-Delmotte, V., Cattani, O., Dreyfus, G., Falourd, S., Hoffmann, G., Minster, B., Nouet, J., Barnola, J. M., Chappellaz, J., Fischer, H., Gallet, J. C., Johnsen, S., Leuenberger, M., Loulergue, L., Luethi, D., Oerter, H., Parrenin, F., Raisbeck, G., Raynaud, D., Schilt, A., Schwander, J., Selmo, E., Souchez, R., Spahni, R., Stauffer, B., Steffensen, J. P., Stenni, B., Stocker, T. F., Tison, J. L., Werner, M., and Wolff, E. W.: Orbital and millennial Antarctic climate variability over the past 800,000 years, Science, 317, 793–796, 2007.

Jouzel, J., Delaygue, G., Landais, A., Masson-Delmotte, V., Risi, C., and Vimeux, F.: Water isotopes as tools to document oceanic sources of precipitation, Water Resour. Res., 49, 7469–7486, 2013.

Kawamura, K., Parrenin, F., Lisiecki, L., Uemura, R., Vimeux, F., Severinghaus, J. P., Hutterli, M. A., Nakazawa, T., Aoki, S., Jouzel, J., Raymo, M. E., Matsumoto, K., Nakata, H., Motoyama, H., Fujita, S., Goto-Azuma, K., Fujii, Y., and Watanabe, O.: Northern Hemisphere forcing of climatic cycles in Antarctica over the past 360,000 years, Nature, 448, 912–916, 2007.

Krinner, G., Genthon, C., Li, Z.-X., and Le Van, P.: Studies of the Antarctic climate with a stretched-grid general circulation model, J. Geophys. Res.-Atmos., 102, 13731–13745, 1997.

Kurita, N.: Origin of Arctic water vapor during the ice-growth season, Geophys. Res. Lett., 38, L02709, doi:10.1029/2010GL046064, 2011.

Küttel, M., Steig, E., Ding, Q., Monaghan, A., and Battisti, D.: Seasonal climate information preserved in West Antarctic ice core water isotopes: relationships to temperature, large-scale circulation, and sea ice, Clim. Dynam., 39, 1841–1857, 2012.

Landais, A., Barkan, E., and Luz, B.: Record of $\delta^{18}O$ and ^{17}O-excess in ice from Vostok Antarctica during the last 150,000 years, Geophys. Res. Lett., 35, L02709, doi:10.1029/2007GL032096, 2008.

Landais, A., Barkan, E., Vimeux, F., Masson-Delmotte, V., and Luz, B.: Combined analysis of water stable isotopes ($H_2^{16}O$, $H_2^{17}O$, $H_2^{18}O$, $HD^{16}O$) in ice cores, Physics of Ice Core Records II, Supplement Issue of Low Temperature Science, 2009.

Landais, A., Ekaykin, A., Barkan, E., Winkler, R., and Luz, B.: Seasonal variations of ^{17}O-excess and d-excess in snow precipitation at Vostok station, East Antarctica, J. Glaciol., 58, 725–733, 2012a.

Landais, A., Steen-Larsen, H. C., Guillevic, M., Masson-Delmotte, V., Vinther, B., and Winkler, R.: Triple isotopic composition of oxygen in surface snow and water vapor at NEEM (Greenland), Geochim. Cosmochim. Acta, 77, 304–316, 2012b.

Lee, J.-E., Fung, I., DePaolo, D. J., and Henning, C. C.: Analysis of the global distribution of water isotopes using the NCAR atmospheric general circulation model, J. Geophys. Res.-Atmos., 112, D16306, doi:10.1029/2006JD007657, 2007.

Lee, J.-E., Fung, I., DePaolo, D. J., and Otto-Bliesner, B.: Water isotopes during the Last Glacial Maximum: New general circulation model calculations, J. Geophys. Res., 113, D19109, doi:10.1029/2008JD009859, 2008.

Le Meur, E., Magand, O., Arnaud, L., Fily, M., Frezzotti, M., Mulvaney, R., Erbland, J., and Cavitte, M.. Snow accumulation pattern over the East Antarctic plateau from combined Ground Penetrating Radar measurements and shallow core analysis, The Cryosphere, in preparation, 2016.

Lin, Y., Clayton, R. N., Huang, L., Nakamura, N., and Lyons, J. R.: Oxygen isotope anomaly observed in water vapor from Alert, Canada and the implication for the stratosphere, P. Natl. Acad. Sci., 110, 15608–15613, 2013.

Lorius, C. and Merlivat, L.: Distribution of mean surface stable isotopes values in East Antarctica; observed changes with depth in coastal area, General assembly of the International Union of Geodesy and Geophysics, Grenoble, France, 1–18, 1977.

Luz, B. and Barkan, E.: Variations of $^{17}O/^{16}O$ and $^{18}O/^{16}O$ in meteoric waters, Geochim. Cosmochim. Acta, 74, 6276–6286, 2010.

Magand, O., Frezzotti, M., Pourchet, M., Stenni, B., Genoni, L., and Fily, M.: Climate variability along latitudinal and longitudinal transects in East Antarctica, Ann. Glaciol., 39, 351–358, 2004.

Masarik, J. and Beer, J.: An updated simulation of particle fluxes and cosmogenic nuclide production in the Earth's atmosphere, J. Geophys. Res., 114, D11103, doi:10.1029/2008JD010557, 2009.

Masson-Delmotte, V., Landais, A., Stievenard, M., Cattani, O., Falourd, S., Jouzel, J., Johnsen, S. J., Dahl-Jensen, D., Sveinsbjornsdottir, A., White, J. W. C., Popp, T., and Fischer, H.: Holocene climatic changes in Greenland: Different deuterium excess signals at Greenland Ice Core Project (GRIP) and NorthGRIP, J. Geophys. Res.-Atmos., 110, D14102, doi:10.1029/2004JD005575, 2005.

Masson-Delmotte, V., Hou, S., Ekaykin, A., Jouzel, J., Aristarain, A., Bernardo, R., Bromwich, D., Cattani, O., Delmotte, M., and Falourd, S.: A review of Antarctic surface snow isotopic composition: Observations, atmospheric circulation, and isotopic modeling, J. Climate, 21, 3359–3387, 2008.

Masson-Delmotte, V., Swingedouw, D., Landais, A., Seidenkrantz, M.-S., Gauthier, E., Bichet, V., Massa, C., Perren, B., Jomelli, V., Adalgeirsdottir, G., Hesselbjerg Christensen, J., Arneborg, J., Bhatt, U., Walker, D. A., Elberling, B., Gillet-Chaulet, F., Ritz, C., Gallée, H., van den Broeke, M., Fettweis, X., de Vernal, A., and Vinther, B.: Greenland climate change: from the past to the future, Wiley Interdisciplinary Reviews: Climate Change, 3, 427–449, 2012.

Mayewski, P. A. and Goodwin, I.: Antarctic's role pursued in global climate change, Eos T. Am. Geophys. Union, 80, 398–400, 1999.

Mayewski, P. A., Frezzotti, M., Bertler, N., van Ommen, T., Hamilton, G., Jacka, T. H., Welch, B., Frey, M., Dahe, Q., Jiawen, R., Simoes, J., Fily, M., Oerter, H., Nishio, F., Isaksson, E., Mulvaney, R., Holmund, P., Lipenkov, V., and Goodwin, I.: The International Trans-Antarctic Scientific Expedition (ITASE): an overview, Ann. Glaciol., 41, 180–185, 2005.

Meijer, H. A. J. and Li, W. J.: The use of electrolysis for accurate $\delta^{17}O$ and $\delta^{18}O$ isotope measurements in water, Isotop. Environ. Health Stud., 34, 349–369, 1998.

Motoyama, H., Hirasawa, N., Satow, K., and Watanabe, O.: Seasonal variations in oxygen isotope ratios of daily collected precipitation and wind drift samples and in the final snow over at Dome Fuji Station, Antarctica, J. Geophys. Res., 110, D11106, doi:10.1029/2004JD004953, 2005.

Neumann, T. A., Waddington, E. D., Steig, E. J., and Grootes, P. M.: Non-climate influences on stable isotopes at Taylor Mouth, Antarctica, J. Glaciol., 51, 248–258, 2005.

Pang, H., Hou, S., Landais, A., Masson-Delmotte, V., Prie, F., Steen-Larsen, H. C., Risi, C., Li, Y., Jouzel, J., Wang, Y., He, J., Minster, B., and Falourd, S.: Spatial distribution of ^{17}O-excess in surface snow along a traverse from Zhongshan station to Dome A, East Antarctica, Earth Planet. Sc. Lett., 414, 126–133, 2015.

Petit, J. R., White, J. W. C., Young, N. W., Jouzel, J., and Korotkevich, Y. S.: Deuterium excess in recent Antarctic snow, J. Geophys. Res.-Atmos., 96, 5113–5122, 1991.

Petit, J. R., Jouzel, J., Raynaud, D., Barkov, N. I., Barnola, J. M., Basile, I., Bender, M., Chappellaz, J., Davis, M., Delaygue, G., Delmotte, M., Kotlyakov, V. M., Legrand, M., Lipenkov, V. Y., Lorius, C., Pepin, L., Ritz, C., Saltzman, E., and Stievenard, M.: Climate and atmospheric history of the past 420,000 years from the Vostok ice core, Antarctica, Nature, 399, 429–436, 1999.

Proposito, M., Becagli, S., Castellano, E., Flora, O., Genoni, L., Gragnani, R., Stenni, B., Traversi, R., Udisti, R., and Frezzotti, M.: Chemical and isotopic snow variability along the 1998 ITASE traverse from Terra Nova Bay to Dome C, East Antarctica, Ann. Glaciol., 35, 187–194, 2002.

Reijmer, C. H., van den Broeke, M. R., and Scheele, M. P.: Air parcel trajectories and snowfall related to five deep drilling locations in Antarctica based on the ERA-15 dataset, J. Climate, 15, 1957–1968, 2002.

Risi, C., Bony, S., Vimeux, F., and Jouzel, J.: Water-stable isotopes in the LMDZ4 general circulation model: Model evaluation for present-day and past climates and applications to climatic interpretations of tropical isotopic records, J. Geophys. Res.-Atmos., 115, D12118, doi:10.1029/2009JD013255, 2010.

Risi, C., Landais, A., Winkler, R., and Vimeux, F.: Can we determine what controls the spatio-temporal distribution of d-excess and ^{17}O-excess in precipitation using the LMDZ general circulation model?, Clim. Past, 9, 2173–2193, doi:10.5194/cp-9-2173-2013, 2013.

Ritter, F., Steen-Larsen, H. C., Werner, M., Masson-Delmotte, V., Orsi, A., Behrens, M., Birnbaum, G., Freitag, J., Risi, C., and Kipfstuhl, S.: Isotopic exchange on the diurnal scale between near-surface snow and lower atmospheric water vapor at Kohnen station, East Antarctica, The Cryosphere Discuss., doi:10.5194/tc-2016-4, in review, 2016.

Schlosser, E., Oerter, H., Masson-Delmotte, V., and Reijmer, C.: Atmospheric influence on the deuterium excess signal in polar firn: implications for ice core interpretation, J. Glaciol., 54, 117–124, 2008.

Schmidt, G. A., Hoffmann, G., Shindell, D. T., and Hu, Y.: Modeling atmospheric stable water isotopes and the potential for constraining cloud processes and stratosphere-troposphere water exchange, J. Geophys. Res.-Atmos., 110, D21314, doi:10.1029/2005JD005790, 2005.

Schmidt, G. A., LeGrande, A. N., and Hoffmann, G.: Water isotope expressions of intrinsic and forced variability in a coupled ocean-atmosphere model, J. Geophys. Res.-Atmos., 112, D10103, doi:10.1029/2006JD007781, 2007.

Schneider, D. P., Steig, E. J., Ommen, T. D. v., Dixon, D. A., Mayewski, P. A., Jones, J. M., and Bitz, C. M.: Antarctic tem-

peratures over the past two centuries from ice cores, Geophys. Res. Lett., 33, L16707, doi:10.1029/2006GL027057, 2006.

Schoenemann, S. W., Schauer, A. J., and Steig, E. J.: Measurement of SLAP2 and GISP δ^{17}O and proposed VSMOW-SLAP normalization for δ^{17}O and ^{17}Oexcess, Rapid Commun. Mass Spectrom., 27, 582–590, 2013.

Schoenemann, S. W., Steig, E. J., Ding, Q., Markle, B. R., and Schauer, A. J.: Triple water-isotopologue record from WAIS Divide, Antarctica: Controls on glacial-interglacial changes in ^{17}O excess of precipitation, J. Geophys. Res.-Atmos., 119, 8741–8763, 2014.

Sime, L. C., Tindall, J. C., Wolff, E. W., Connolley, W. M., and Valdes, P. J.: Antarctic isotopic thermometer during a CO_2 forced warming event, J. Geophys. Res., 113, D24119, doi:10.1029/2008JD010395, 2008.

Sime, L. C., Wolff, E. W., Oliver, K. I. C., and Tindall, J. C.: Evidence for warmer interglacials in East Antarctic ice cores, Nature, 462, 342–345, 2009.

Sokratov, S. A. and Golubev, V. N.: Snow isotopic content change by sublimation, J. Glaciol. 55, 823–828, 2009.

Steen-Larsen, H. C., Johnsen, S. J., Masson-Delmotte, V., Stenni, B., Risi, C., Sodemann, H., Balslev-Clausen, D., Blunier, T., Dahl-Jensen, D., Ellehøj, M. D., Falourd, S., Grindsted, A., Gkinis, V., Jouzel, J., Popp, T., Sheldon, S., Simonsen, S. B., Sjolte, J., Steffensen, J. P., Sperlich, P., Sveinbjörnsdóttir, A. E., Vinther, B. M., and White, J. W. C.: Continuous monitoring of summer surface water vapor isotopic composition above the Greenland Ice Sheet, Atmos. Chem. Phys., 13, 4815–4828, doi:10.5194/acp-13-4815-2013, 2013.

Stenni, B., Masson-Delmotte, V., Selmo, E., Oerter, H., Meyer, H., Röthlisberger, R., Jouzel, J., Cattani, O., Falourd, S., Fischer, H., Hoffmann, G., Iacumin, P., Johnsen, S. J., Minster, B., and Udisti, R.: The deuterium excess records of EPICA Dome C and Dronning Maud Land ice cores (East Antarctica), Quaternary Sci. Rev., 29, 146–159, 2010.

Stohl, A. and Sodemann, H.: Characteristics of atmospheric transport into the Antarctic troposphere, J. Geophys. Res., 115, D02305, doi:10.1029/2009JD012536, 2010.

Tindall, J. C., Valdes, P. J., and Sime, L. C.: Stable water isotopes in HadCM3: Isotopic signature of El Niño–Southern Oscillation and the tropical amount effect, J. Geophys. Res.-Atmos., 114, D04111, doi:10.1029/2008JD010825, 2009.

Town, M. S., Warren, S. G., Walden, V. P., and Waddington, E. D.: Effect of atmospheric water vapor on modification of stable isotopes in near-surface snow on ice-sheets, J. Geophys. Res., 113, D24303, doi:10.1029/2008JD009852, 2008.

Uemura, R., Matsui, Y., Motoyama, H., and Yoshida, N.: Deuterium and oxygen-18 determination of microliter quantities of a water sample using an automated equilibrator, Rapid Commun. Mass Spectrom., 21, 1783–1790, 2007.

Uemura, R., Matsui, Y., Yoshimura, K., Motoyama, H., and Yoshida, N.: Evidence of deuterium excess in water vapor as an indicator of ocean surface conditions, J. Geophys. Res.-Atmos., 113, D19114, doi:10.1029/2008JD010209, 2008.

Uemura, R., Barkan, E., Abe, O., and Luz, B.: Triple isotope composition of oxygen in atmospheric water vapor, Geophys. Res. Lett., 37, L04402, doi:10.1029/2009GL041960, 2010.

Uemura, R., Masson-Delmotte, V., Jouzel, J., Landais, A., Motoyama, H., and Stenni, B.: Ranges of moisture-source temperature estimated from Antarctic ice cores stable isotope records over glacial–interglacial cycles, Clim. Past, 8, 1109–1125, doi:10.5194/cp-8-1109-2012, 2012.

Van Hook, W. A.: Vapor pressures of the isotopic waters and ices, J. Phys. Chem., 72, 1234–1244, 1968.

Vimeux, F., Masson, V., Jouzel, J., Stievenard, M., and Petit, J. R.: Glacial-interglacial changes in ocean surface conditions in the Southern Hemisphere, Nature, 398, 410–413, 1999.

Werner, A. T.: BCSD Downscaled Transient Climate Projections for Eight Select GCM's over British Columbia, Canada, Victoria, BC, 63 pp., 2011.

Werner, M., Langebroek, P. M., Carlsen, T., Herold, M., and Lohmann, G.: Stable water isotopes in the ECHAM5 general circulation model: Toward high-resolution isotope modeling on a global scale, J. Geophys. Res.-Atmos., 116, D15109, doi:10.1029/2011JD015681, 2011.

Winkler, R., Landais, A., Sodemann, H., Dümbgen, L., Prié, F., Masson-Delmotte, V., Stenni, B., and Jouzel, J.: Deglaciation records of ^{17}O-excess in East Antarctica: reliable reconstruction of oceanic normalized relative humidity from coastal sites, Clim. Past, 8, 1–16, doi:10.5194/cp-8-1-2012, 2012.

Winkler, R., Landais, A., Risi, C., Baroni, M., Ekaykin, A., Jouzel, J., Petit, J. R., Prié, F., Minster, B., and Falourd, S.: Interannual variation of water isotopologues at Vostok indicates a contribution from stratospheric water vapor, P. Natl. Acad. Sci., 110, 17674–17679, 2013.

Zahn, A., Franz, P., Bechtel, C., Grooß, J.-U., and Röckmann, T.: Modelling the budget of middle atmospheric water vapour isotopes, Atmos. Chem. Phys., 6, 2073–2090, doi:10.5194/acp-6-2073-2006, 2006.

Appendix E

Article : Atmospheric moisture supersaturation in the near-surface atmosphere at Dome C, Antarctic Plateau

Atmos. Chem. Phys. Discuss., doi:10.5194/acp-2016-670, 2016
Manuscript under review for journal Atmos. Chem. Phys.
Published: 18 August 2016

Atmospheric Chemistry and Physics Discussions

Atmospheric moisture supersaturation in the near-surface atmosphere at Dome C, antarctic plateau

Christophe Genthon[1], Luc Piard[1], Etienne Vignon[2], Jean-Baptiste Madeleine[3], Mathieu Casado[4], Hubert Gallée[1]

[1] CNRS, LGGE, Grenoble, France

[2] Université Grenoble Alpes, LGGE, Grenoble, France

[3] LMD – IPSL, UP6 – CNRS, Paris, France

[4] LSCE – IPSL, CEA-CNRS-UVSQ-U. paris-Saclay, Gif-sur-Yvette, France

Corresponding authors: Christophe Genthon, Laboratoire de Glaciologie et Géophysique de l'Environnement, 54 Rue Molière, BP96, 38402 Saint Martin d'Hère Cedex, France. Email: Christophe.genthon@univ-grenoble-alpes.fr.

Atmos. Chem. Phys. Discuss., doi:10.5194/acp-2016-670, 2016
Manuscript under review for journal Atmos. Chem. Phys.
Published: 18 August 2016

Atmospheric Chemistry and Physics Discussions

Abstract. Supersaturations in the natural atmosphere are frequent at the top of the troposphere where cirrus clouds form, but are very infrequent near the surface where the air is generally warmer and laden with liquid and/or ice condensation nuclei. An exception is the surface of the high antarctic plateau. One year of atmospheric moisture measurement at the surface of Dome C on the East Antarctic plateau is presented and compared with results from 2 models implementing cold microphysics parametrizations: the European Center for Medium-range Weather Forecasts through its operational analyzes, and the Model Atmosphérique Régional. The measurements are obtained using commercial hygrometry sensors modified to allow air sampling without affecting the moisture content even in case of supersaturation. Supersaturations are very frequent in the observations and in the models, but the statistical distribution differs both between models and observations and between the 2 models, living much room for improvements in both models. Unadapted hygrometry sensors generally fail to report supersaturations, and most reports of atmospheric moisture on the antarctic plateau are thus likely biased low. This is unlikely to strongly affect estimations of surface sublimation because supersaturations are more frequent as temperature is lower, and moisture quantities and thus water fluxes are very small anyway. Ignoring supersaturation may be a more serious issue when considering water isotopes, a tracer of phase change and temperature, largely used to interpret snow and ice samples from the antarctic plateau and reconstruct past climates and environments from ice cores. Longer and more continuous in situ observation series to test parameterizations of cold microphysics, such as those used in the formation of cirrus clouds in climate models, can be obtained at surface levels than higher in the atmosphere.

Keywords:

Antarctic plateau

Atmospheric supersaturation

Atmos. Chem. Phys. Discuss., doi:10.5194/acp-2016-670, 2016
Manuscript under review for journal Atmos. Chem. Phys.
Published: 18 August 2016

Atmospheric Chemistry and Physics Discussions

Atmospheric modeling

Cold microphysics

Hygrometer

In situ measurement

Atmos. Chem. Phys. Discuss., doi:10.5194/acp-2016-670, 2016
Manuscript under review for journal Atmos. Chem. Phys.
Published: 18 August 2016

Atmospheric Chemistry and Physics Discussions

1. Introduction

Ice supersaturation is frequently found in the upper troposphere [Spichtinger et al. 2003] and specific cloud microphysics parameterizations are developed to represent this process in meteorological and climate models. These models have to be validated against the observations to reproduce cirrus and other clouds including contrails which develop at altitudes where supersaturations occur (e.g. Rädel and Shine [2010]). Radiosondes provide snapshot information but obtaining in situ observation series to calibrate and validate such parameterizations is a challenge because it requires flying and operating instruments on high altitude aircrafts or balloons. Sampling supersaturated air parcels without affecting the air moisture content is also a challenge, as the excess moisture with respect to saturation tends to condensate on any surfaces including those of the sampling device and the sensor itself. There are thus not many in situ observations available to characterize and quantify natural supersaturations and their evolution in time, and evaluate and validate microphysics parameterizations in such conditions.

While they are frequent at high altitude, ice supersaturations do not generally occur in the surface atmosphere, where operating instruments is obviously much easier. Conditions close to the tropopause are however found over the antarctic ice sheet both in terms of temperature and humidity levels. Because of the distance from the nearest coasts and the high elevation, the antarctic plateau is also particularly secluded from sources of aerosols. This is the most likely place on Earth to observe ice supersaturation in the near surface atmosphere. For instance, Schwerdtfeger [1970] reports on observations of relative humidity with respect to ice exceeding 120% at Vostok station in the heart of Antarctica.

The possibility of surface atmospheric supersaturation on the antarctic plateau raises an important

Atmos. Chem. Phys. Discuss., doi:10.5194/acp-2016-670, 2016
Manuscript under review for journal Atmos. Chem. Phys.
Published: 18 August 2016

issue, that of the relative contribution of the different terms of the surface mass balance of the antarctic ice sheet. The terms are precipitation (positive for the surface) and evaporation/sublimation (negative or positive), and possibly blowing snow (positive or negative as blown snow redeposits, but generally negative because of enhanced snow evaporation). Melting and runoff do not occur on the antarctic plateau and can be excluded. The net surface mass balance, observed using glaciological methods, is very small on the antarctic plateau. It is typically a few cm water equivalent per year [Arthern et al., 2006]: the antarctic plateau is one of the driest places on Earth. This is because it is so cold, and thermodynamics imply that the various terms of the surface mass balance are bound to be correspondingly small. Because they are so small, and because of a harsh environment, the direct determination of precipitation and evaporation/sublimation on the antarctic plateau is not conclusive. Their relative contribution to the surface mass balance of the antarctic plateau is still poorly quantified, using indirect approaches [Frezzotti et al., 2004]. In most places on continents, precipitation largely dominates. This is not necessarily the case on the antarctic plateau. In particular, if atmospheric supersaturation occurs near the surface, then moisture concentration is likely larger in the surface atmosphere than at the snow surface and the turbulent moisture flux is thus directed towards the surface (surface condensation). Unlike most other regions of the Earth, this turbulent flux could contribute positively to the surface water budget and thus, here, on the surface mass balance.

Another potential issue with ice supersaturation on the antarctic plateau is that of the impact on the water isotopic composition of snow. Supersaturation leads to kinetic fractionation of the stable isotopic composition of water when it condensates. Since the 1980's [Jouzel et al. 1987], the longest ice core records of past climate and environment are obtained from drilling operations on the antarctic plateau. Past atmospheric temperatures are deduced from the variations of the concentration of stable water isotopes along the core. Variations in supersaturation levels may

Atmos. Chem. Phys. Discuss., doi:10.5194/acp-2016-670, 2016
Manuscript under review for journal Atmos. Chem. Phys.
Published: 18 August 2016

impact on this reconstruction. Supersaturations thus involve not only meteorological (clouds, precipitation, surface evaporation / sublimation) but also climate and paleoclimate reconstruction issues. It is therefore important to measure and assess supersaturations on the Antarctic plateau.

95

However, as already mentioned, measuring atmospheric supersaturation is a challenge because sampling a supersaturated air mass can affect its moisture content. Schwerdtfeger [1970] expresses concerns about the reliability of reports of supersaturation at Vostok station. On the other hand, many reports of relative humidity with respect to ice (RHi) on the antarctic plateau reach but seem
100 to be capped at 100% [King et al., 1999]. Genthon et al. [2013] compare RHi observed at Dome C on the antarctic plateau using conventional solid state sensors with results from the ECMWF (European Center for Medium-range Weather forecasts) meteorological analyzes and from the MAR (Modèle Atmosphérique Régional, Gallée and Gorodetskaya [2010]) meteorological model. In both models, cold microphysics parameterizations are used which, depending on local
105 conditions, allow for supersaturations. More often than not, when ~100% RHi is observed at Dome C with conventional instruments (not adapted to sample supersaturation), both models produce significant supersaturation, occasionally reaching more than 150% [Genthon et al., 2013]. The cold microphysics parameterizations differ in the 2 models (see Genthon et al. [2013] for references), and other aspects such as the vertical resolution also differ: if both model produce significant
110 supersaturations, they do not quantitatively agree as to the amplitude of the supersaturations.

To verify such numbers and decide between models, using direct is situ measurements, instruments must be designed and/or adapted so as to bring the air mass to the moisture sensor without affecting its moisture content. This can be done by warming the air above its condensation temperature
115 before ushering it to the sensor. Here, after the present general introduction (Section 1) , Section 2 presents 2 instruments which are adaptations of commercial sensors to perform in very cold

Atmos. Chem. Phys. Discuss., doi:10.5194/acp-2016-670, 2016
Manuscript under review for journal Atmos. Chem. Phys.
Published: 18 August 2016

conditions and to enable the measurement of atmospheric supersaturation at Dome C. The measurement site and deployment are also described in Section 2, and previous atmospheric humidity reports from this site are reminded. In Section 3, results from the older instruments are compared with the reports by the 2 adapted instruments. In this Section the models are shown to agree with the observations from the adapted instruments, of frequent occurrences of supersaturation at all time in the year including in summer. It is also shown that details of the climatology and the statistics of occurrence of supersaturation differ between the models and the observations and between the 2 models. Section 4 discusses the results, provides an outlook of research to follow, and finally concludes the paper.

2. Measurement site, instruments and methods

Dome C (Figure 1) is one of the main domes on the east antarctic plateau. Since 2005, the summit of the dome (75° 06' S, 123° 20' E, 3233 m a.s.l.) hosts a permanently manned station, Concordia, jointly operated by the French and Italian polar institutes (IPEV and PNRA). One of the first Antarctic Meteorological Research Center automatic weather station (AMRC AWS, https://amrc.ssec.wisc.edu/) deployed in Antarctica, back in the 1980s, was at Dome C. When the actual location of the summit of the dome was later more accurately determined using satellite and aircraft radar altimeters in the 1990s, the AWS was moved about 50 km to its present position. This induced a 30 m rise and correspondingly slight mean surface pressure change but otherwise little impacted the series consistency because the local environment is very homogeneous. The AWS provides one of the longest quasi-continuous meteorological reporting on the high antarctic plateau. The station measures pressure, temperature and wind, but not moisture. Additional meteorological reports are available since the construction of Concordia station, including an other AWS closer to the station and a daily radiosonde. Both the new station and the radiosondes report atmospheric

Atmos. Chem. Phys. Discuss., doi:10.5194/acp-2016-670, 2016
Manuscript under review for journal Atmos. Chem. Phys.
Published: 18 August 2016

humidity using solid state film capacitive sensors [Kämpfer et al., 2013], . In early 2008, a system to vertically profile the lower part of the atmosphere was deployed along an ~45 m high tower. Temperature, wind and moisture are measured, the latter again using solid state film capacitive sensors. This profiling system is fully described in Genthon et al. [2010], Genthon et al. [2011] and Genthon et al. [2013].

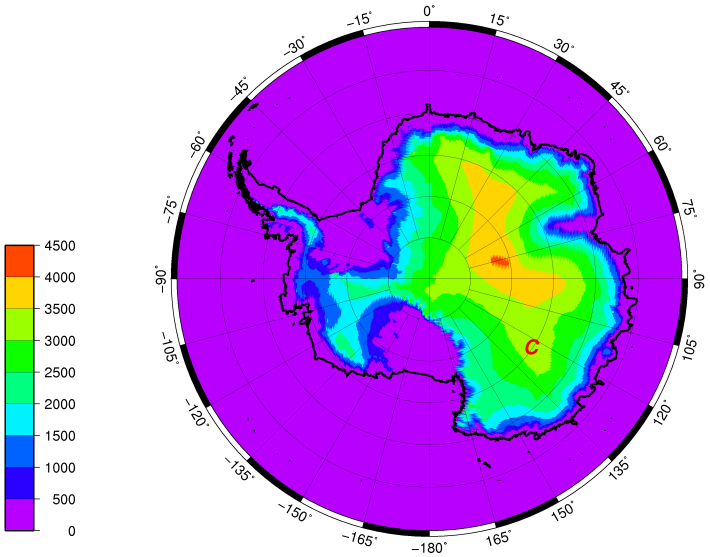

Figure 1: Topographic map of Antarctica, showing the location of Dome C (red C). Altitude" is in m.

Genthon et al. [2013] evaluate and compare 2 contrasted years, 2009 and 2010, respectively the warmest and coldest in a 10-year period. They report measuring humidity up to ~100% with respect to ice but also observing frequent frost deposition, a hint that supersaturation occurs but is missed by standard hygrometers without an adaption. Occurrences of supersaturation are further supported by a comparison with models that implement cold microphysics parameterizations: the

Atmos. Chem. Phys. Discuss., doi:10.5194/acp-2016-670, 2016
Manuscript under review for journal Atmos. Chem. Phys.
Published: 18 August 2016

models often simulate supersaturation when the hygrometers hit the 100% RHi ceiling. That raw solid state hygrometers cannot measure supersaturation is understandable: a supersaturated air mass will deposit its excess moisture on any hard surface that serves as a condensation surface. The hygrometer body itself will condensate the excess moisture before it can be measured. One way to overcome this problem is to aspirate and warm the air above its thermodynamic saturation temperature at the intake.

There are several techniques to measure atmospheric moisture [Kämpfer, 2013]. The traditional wet bulb thermometer is not very practical, particularly when measuring well below freezing temperature. The dew-point hygrometer provides a direct physical measure of the saturation temperature. This is done by progressively cooling from ambient temperature a surface until atmospheric moisture condensation is detected on the surface. The cooled surface is generally a mirror and condensation is optically detected when the reflection of a light beam is observed to be diffused and diffracted. The device also works below freezing temperature but should then be referred as frost-point hygrometer [King and Anderson, 1999]. Dew and frost-point hygrometers are accurate but bulky, complex and expensive. They require significant amounts of energy, and they have moving parts as the mirror must be periodically cleaned. They are thus comparatively prone to dysfunction and failures, and they cannot be used in remote unattended places or in radiosondes. On the other hand, they mechanically aspirate air to the sensing mirror, and if the aspiration intake is heated significantly above ambient temperature the measured air is sampled without affecting its moisture content even if supersaturated. Some commercial instruments ensure this such as the Meteolobor VTP6 Thygan described below.

In the 1970s, Vaisala Oy (Finland) developed a very different, very compact humidity sensor, the Humicap thin film capacitive sensor[1]. The dielectric properties and capacitance of a

1 http://www.vaisala.com/Vaisala%20Documents/Technology%20Descriptions/HUMICAP-Technology-description-

Atmos. Chem. Phys. Discuss., doi:10.5194/acp-2016-670, 2016
Manuscript under review for journal Atmos. Chem. Phys.
Published: 18 August 2016

polymer film vary with the relative humidity of the ambient air. Although the physical processes for dependence have been described (e.g. Anderson [1994]), the relationship between capacitance and atmospheric moisture is an empirical one. The sensor needs calibration and a small but significant uncertainty affects the measurement. The uncertainty increases as temperature decreases. On the other hand, the Humicap is convenient, very compact, comparatively inexpensive, robust, and its use can be automated and deployed even in remote places and on radiosondes. It is thus currently widely used for such purposes. Thin film capacitive sensors are used in all automatic weather stations in Antarctica that report moisture as well as on the 45-m profiling system at Dome C mentioned above, in the latter case bundled in Vaisala HMP155 thermometers – hygrometers (thermohygrometers) [Genthon et al 2013]. According to the manufacturer, the uncertainty is +/- 1.4% of the reading in the -60°C to -20°C temperature range. It may be expected to be larger below -60°C. However, then, the absolute moisture content of the atmosphere is smaller and absolute measurement errors are correspondingly smaller.

To tentatively confirm and quantify supersaturations at Dome C, both frost-point and thin film capacitive hygrometers were deployed at a height of 3 m and adapted as necessary to operate in the general Dome C conditions and to sample the air without altering its moisture content even when above saturation. In both systems, the hygrometer aspirated intake is heated so that the temperature of the sampled air parcel is raised above condensation level and condensation is avoided. The frost-point hygrometer is a Meteolabor VTP6 Thygan chilled mirror instrument. It was selected because it is factory-designed to perform to cold temperatures and correspondingly low specific humidities. According to manufacturer the lowest measurable frost point temperature is -65°C. The fact that the air intake is heated (see below) does not improve the temperature range of the instrument as the actual limitation is due to the ability to cool the mirror to the condensation temperature. A -65°C

B210781EN-C.pdf?utm_campaign=CEN-TIA-G-Humidity%20Nurturing%202015&utm_medium=email&utm_source=Eloqua&utm_content=CEN-TIA-G-HUMICAP%20Technology%20Promotion

Atmos. Chem. Phys. Discuss., doi:10.5194/acp-2016-670, 2016
Manuscript under review for journal Atmos. Chem. Phys.
Published: 18 August 2016

temperature limit is not quite low enough to consistently operate at Dome C, where the surface atmospheric temperature can occasionally fall below -80°C. However, data from the vertical profiling system show that from 2009 to 2015, the air temperature ~3 m above the snow surface was warmer than -55°C more than 50% of the time, and almost consistently (more than 99.5% of the time) warmer than -55°C during the local summer (Dec – Jan – Feb). Assuming near saturation, the instrument can nominally operate a large fraction of the time at Dome C. For our application, the frost-point hygrometer (noted FP from now on) is hosted in a heated box so that the electronics and mechanics are not affected by the extreme cold temperatures in winter. By factory design, the outside air is aspirated inside the instrument through a heated intake which prevents frost deposition. This design is not modified, the intake being simply made to protrude out of the heated box to sample the outside air. This is the only part of the instrument kept outside the heated box and, because it is itself heated, loss of moisture along the way to the mirror is consistently prevented. Visual inspection confirms that even when frost deposition occurs on other instruments on the tower, no frost deposition is observed in the vicinity of the instrument intake. Each measurement cycle lasts 10 minutes: heating and defrosting the mirror from the previous measurement, cleaning, then cooling until frost point is reached. The sensor thus reports measurements of frost point temperature, and conversion to relative humidity, on a 10' time step basis. The manufacturer claims a very high accuracy: 0.1% expressed in term of relative humidity. Dew and frost point hygrometers are indeed often used to calibrate other types of hygrometers. Here the FP is used as a reference against which other sensors may be adjusted and are evaluated, at least down to temperatures where the FP performs well.

For the other type of hygrometer used here, the manufacturer (Vaisala Oy) guaranties its HMP155 sensor down to -80°C for the measurement of temperature, but only to -60°C for the measurement of moisture. However, the main issue with colder temperatures for this instrument is that the time

Atmos. Chem. Phys. Discuss., doi:10.5194/acp-2016-670, 2016
Manuscript under review for journal Atmos. Chem. Phys.
Published: 18 August 2016

response increases. Yet, unlike in a radiosonde for which the environment quickly varies during ascent, variations are comparatively slow for fixed instruments and the operational limit is actually much below -60°C [Genthon et al., 2013]. In addition, to avoid frost deposition and preserve the air moisture content, for our application, the instrument aspirates the air through an inlet consistently heated ~5°C above the ambient temperature (Figure 2). The ambient temperature itself is measured by a separate PT100 platinum resistance thermometer in an unheated derivation of the system. A comparison with the frost point hygrometer shows that this simple and low cost innovative design succeeds to measure even highly supersaturated air, up to 200% with respect to ice or even more. In addition, the fact that the air reaching the hygrometer sensor is 5°C above ambient temperature correspondingly extends the actual nominal temperature range of the instrument with respect to ambient temperature. The sensor reports relative humidity. According to manufacturer, the accuracy in the low temperature range (-60° to -40°C) is +/-1.4 % of the reading. Accuracy improves at warmer temperature, and may conversely be expected to deteriorate for even colder temperatures. The temperature range -40° to -60°C is typical at Dome C although temperatures as cold as -80°C and as warm as -15°C may be encountered. Note that, in accordance with meteorological conventions, all sensors report relative humidity with respect to liquid water rather than ice even when the air temperature is below 0°C. Here the Goff-Gratch formulas [Goff and Gratch, 1946] are used to convert between RH with respect to liquid, water vapor partial pressure and RHi.

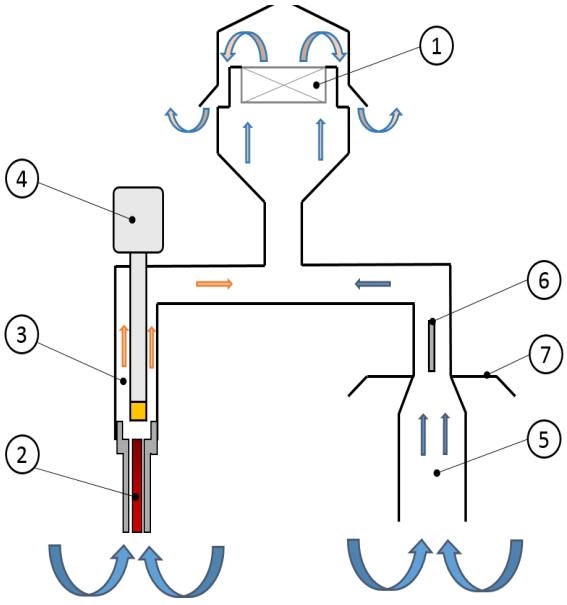

Atmos. Chem. Phys. Discuss., doi:10.5194/acp-2016-670, 2016
Manuscript under review for journal Atmos. Chem. Phys.
Published: 18 August 2016

260

Figure 2: Schematic drawing of the modified (HMPmod) hygrometer. The air is aspirated by the fan (1) and heated through an inlet (2). The temperature and the moisture content of the heated air (3) is measured by the HMP155 (4). The ambient air temperature (5) is measured by a separate PT100 (6) located in the unheated aspirated inlet shaded from sun radiation (7).

265

The 2 adapted instruments are deployed side by side ~3 m above the snow surface on the ~45-m tower. At the same level, hosted in an aspirated but unheated radiation shield (see Figure 1 of Genthon et al. [2011]), an unmodified HMP155 allows for comparison with a traditional design –

270 and to exhibit biases of the latter. From now on, the original and modified HMP155 will be referred to as "HMP" and "HMPmod", respectively. Table 1 lists the instruments and adaptations. The various instruments performed over the duration of 2015 except for limited periods due to datalogging failures or servicing in summer. The results are presented and analyzed in the next section.

275

Short name	Instrument / sensor	Housing
HMP	Vaisala HMP155 tehermohymeter / thin film polymer hygrometer	Aspirated radiation shield
HMPmod	Modified Vaisala HMP155 thermohygrometer / thin film polymer	Aspirated radiation shield + heated intake (Figure 2)

Atmos. Chem. Phys. Discuss., doi:10.5194/acp-2016-670, 2016
Manuscript under review for journal Atmos. Chem. Phys.
Published: 18 August 2016

	hygrometer	
FP	Meteolabor Thygan VPT6 mirror frost-point hygrometer	Heated enclosure, heated intake

Table 1: List of hygrometers and adaptation. See text for details

280

3. Data, results and comparison with meteorological analyses and model simulation

3.1. Summer

285 Figure 3 displays the mean diurnal cycle of atmospheric moisture and temperature in January, February and December 2015 according to the various instruments. During this period, the FP is consistently running within its nominal manufacturer-stated temperature range and can serve as a moisture measurement reference for the other instruments. The sun never really sets at this time of the year, however its changing elevation above the horizon induces a strong temperature cycle near 290 the surface (figure 3.d). Here, “night” will broadly refer to the local hours during which sun elevation is lower at Dome C and sets at lower latitudes. Figure 3a shows the mean cycle of partial pressure of water vapor from FP. The numbers are low due to the cold temperature: the water partial pressure ranges on average between ~15 Pa in the early morning and slightly over 35 Pa in the early afternoon. This cycle demonstrates that surface evaporation occurs during the day, followed by 295 deposition at night, resulting in surface (3-m) atmospheric moisture diurnally changing by a factor of more than 2. Figure 3.b shows small differences and consistent agreement between the HMPmod and FP instruments. Note here that HMPmod is slightly calibrated for moisture report against the FP instrument for agreement in the early afternoon at the warmest of the day. This calibration does not exceed manufacturer stated accuracy for HMP155 (Section 2). The calibration proves robust and

Atmos. Chem. Phys. Discuss., doi:10.5194/acp-2016-670, 2016
Manuscript under review for journal Atmos. Chem. Phys.
Published: 18 August 2016

valid at all time during the day in this period. Results from (unmodified) HMP significantly depart from those of the FP, and thus HMPmod instruments: the agreement is good in the afternoon only but quite poor the rest of the day and at night. Figure 3c displays the calculated RHi for the 3 instruments, using the independent moisture measurements by each instrument ,but all finally reported to the atmospheric temperatures of the (unmodified) HMP. This is likely the most accurate estimation of temperature, i. e. the least likely affected by radiation and other biases because it is unheated and efficiently ventilated [Genthon et al. ,2011]. Temperature differences of as much as 2°C are occasionally observed with the other instruments in low wind conditions.

RHi differs markedly between the unmodified HMP and the 2 other instruments. The latters both report RHi significantly exceeding 100% while the unmodified instrument hardly reaches saturation. All instruments agree well in the early afternoon at the warmest of the day but HMP disagrees at night. The FP and HMPmod instruments consistently agree with each other, including when reporting supersaturations reaching 120 % at night, confirming the high levels of supersaturation hinted by Genthon et al. [2013] from models.

Atmos. Chem. Phys. Discuss., doi:10.5194/acp-2016-670, 2016
Manuscript under review for journal Atmos. Chem. Phys.
Published: 18 August 2016

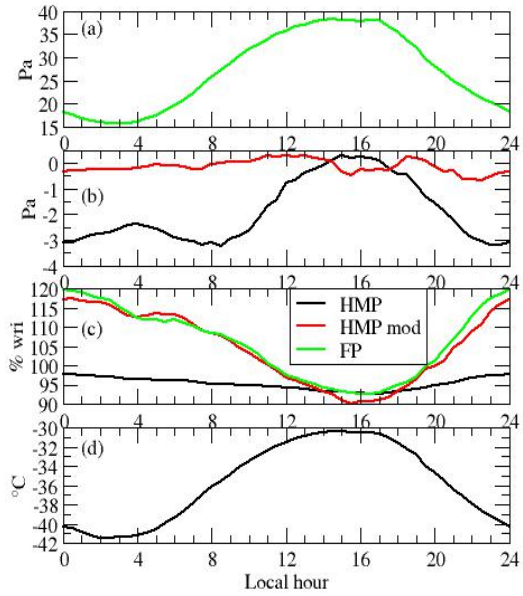

Figure 3: Mean Dec-Jan-Feb diurnal cycle of: (a) water vapor partial pressure from FP instrument ; (b) difference with respect to FP of water vapor partial pressure from original (HMP, black) and modified (HMPmod, red) thin rilm polymer sensors ; (c) RHi from the 3 instruments; (d) air temperature.

Figure 4 compares the observed diurnal cycles of temperature and moisture with ECMWF analyses of temperature and moisture at the 1st model level and at the standard 2 m level. The mean elevation of the 1st model level in summer is 8.2 m. Thus the elevations of the 2-m and 1st level data bracket that of the observations. While at the 1st model level, temperature and moisture are prognostic variables of the general circulation equations (the integration of which alternates with a diagnostic resolution of the diabatic and hydrological processes), the 2-m variables are interpolations between the 1st level and the surface using gradient equations of the surface layer (Section 3.2 of Part IV, physical processes of ECMWF IFS Cyc41r1 documentation). Vignon et al. [2016] show that the

Atmos. Chem. Phys. Discuss., doi:10.5194/acp-2016-670, 2016
Manuscript under review for journal Atmos. Chem. Phys.
Published: 18 August 2016

surface layer where classical interpolation relationships are valid is often much shallower than 8 m in stable conditions at Dome C. The 2 m interpolated values probably encompass biases due to the interpolation formula and have to be considered carefully. The physics parameterizations for cold water condensation in the ECMWF model allow supersaturation to occur [Tompkins et al., 2007].

335 There are only 4 analyses steps per day, so ECMWF data are shown as dots on Figure 4 when the observations (48 data per day) are shown as continuous curves.

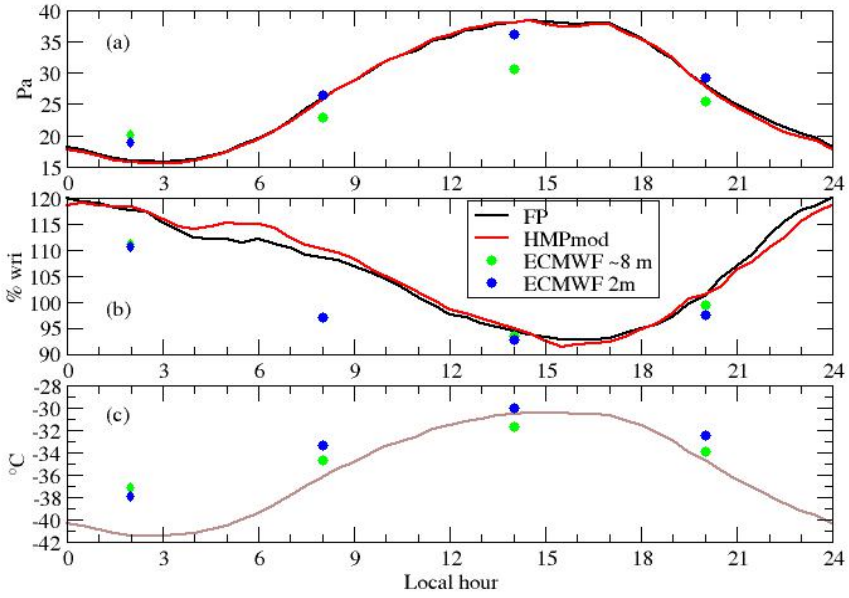

Figure 4: Mean Dec-Jan-Feb diurnal cycle of observed (FP and HMPmod) and analyzed (ECMWF,

340 *2 m and 1st model level at ~8 m) water vapor partial pressure (a), relative humidity with respect to ice (b) and temperature (c). The reference temperature is that from the unmodified HMP (brown curve on plot (c)).*

The ECMWF analyses overestimate nigh-time temperature and consequently underestimate the

Atmos. Chem. Phys. Discuss., doi:10.5194/acp-2016-670, 2016
Manuscript under review for journal Atmos. Chem. Phys.
Published: 18 August 2016

345 amplitude of the diurnal cycle. The amplitude of the cycle of moisture partial pressure is also underestimated but not as badly as could be expected considering a non linear relation between temperature and saturation humidity. The model thus confirms a large diurnal change of magnitude and sign of the surface turbulent flux of moisture. The surface atmosphere is expectedly moister, and the vertical gradient and turbulent flux directed upward (surface sublimation) in the early
350 afternoon. It is downward (deposition) and very weak at night. Because of the temperature errors, RHi is less than observed at night, yet it is significantly larger than 100%. The analyzes reproduce supersaturation at night and minimum RH in the early afternoon. While there are only 4 ECMWF analyses per day, at synoptic times (dots on Figure 4), the time step of the MAR model is 6 minutes only, which allows for a much more continuous comparison with the observations (Figure 5). Here,
355 a more recent version of the MAR model is used than in Genthon et al. [2013]. The model still uses a parameterization for cold microphysics [Meyer et al. [1992] and produces large supersaturations, actually too large compared to the observations in summer (Figure 5a). However, the model is now significantly and consistently too warm (Figure 5b). It will be shown that the MAR model significantly differs from the observations and ECMWF analyses in the rest of the year.

360

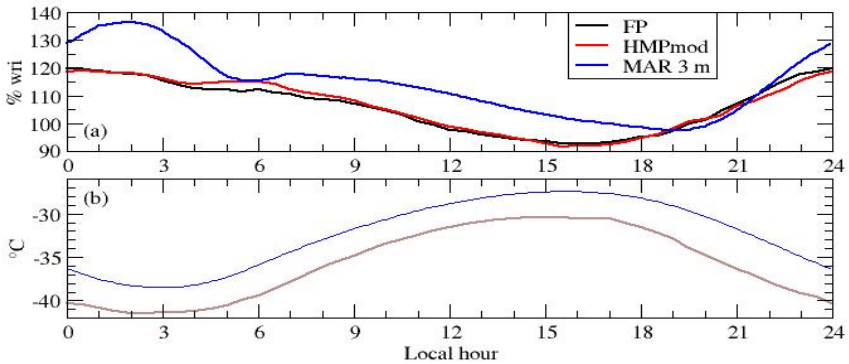

Atmos. Chem. Phys. Discuss., doi:10.5194/acp-2016-670, 2016
Manuscript under review for journal Atmos. Chem. Phys.
Published: 18 August 2016

Atmospheric Chemistry and Physics Discussions

Figure 5: Mean Dec-Jan-Feb diurnal cycle of observed (FP and HMPmod for moisture, HMP for temperature) and MAR simulated RHi (a) and air temperature (b), the brown curve being the observed as on Figure 4.

365

Figure 6 displays correlation plots of moisture reports from the unmodified (HMP) and modified (HMPmod) thin film capacitive sensors with respect to FP in summer. The direct correlations between water vapor pressures would be very high because humidity is largely controlled by temperature. Plotting deviations to the saturation vapor pressure, rather than the vapor pressure

370 itself, removes much of the temperature codependence effect and concentrates on the relative ability of the instruments to correctly measure moisture. The correlation between the regular HMP and FP is good below saturation but is obviously very poor above since the HMP fails to capture supersaturations. The correlation between HMPmod and FP reports is very high, above 0.97. The regression constant (the intercept) is 0.1 but the standard error on the constant is larger than 0.1. The

375 linear regression is thus not statistically different from a 1/1 one.

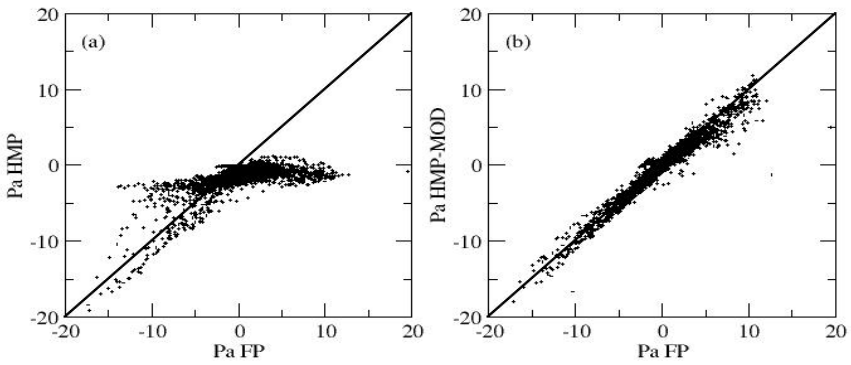

Figure 6: regression of anomaly to saturation vapor pressure from HMP ((a) and HMPmod (b) instruments against FP.

Atmos. Chem. Phys. Discuss., doi:10.5194/acp-2016-670, 2016
Manuscript under review for journal Atmos. Chem. Phys.
Published: 18 August 2016

Atmospheric Chemistry and Physics Discussions

380 **3.2 Annual variations and statistics**

According to instrument reports, a strong diurnal cycle dominates the variability of atmospheric moisture in summer. The partial pressure is maximum in the early afternoon while RHi peaks near local midnight (Figure 3) when it occasionally reach more than 150% (not shown). As the diurnal
385 cycle variability progressively vanishes and is replaced by synoptic variability in the colder months, RHi occasionally reaches values above 200%. Limiting the range to values between 50 – 150 % (more than 99% of HMPmod reports), Figure 7 displays the distribution functions of observed, ECMWF analyzed and MAR modeled RHi.

390

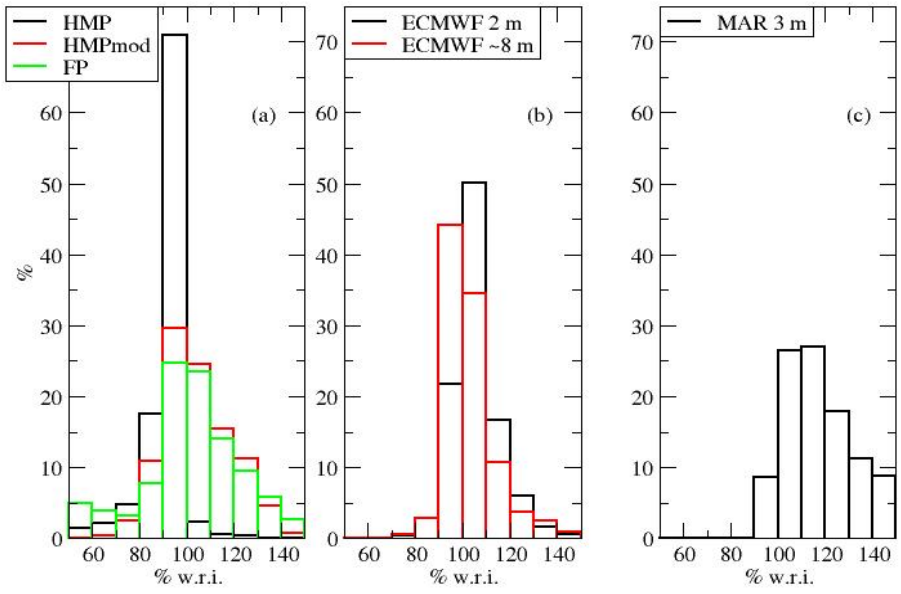

Figure 7: Observed (a), ECMWF analyzed (b) and MAR (c) distributions of Hi in 2015 for csases

Atmos. Chem. Phys. Discuss., doi:10.5194/acp-2016-670, 2016
Manuscript under review for journal Atmos. Chem. Phys.
Published: 18 August 2016

of Rhi between 50 and 150%.

Although measurement uncertainties and uncertainties on conversions from relative humidity with respect to liquid to RHi allow some occurrences above 100%, as expected the reports from HMP peak near and hardly exceed the 100% ceiling. More than 50% of all reports between 50% and 150% are above 100% for HMPmod and FP, with a similar distribution for the 2 instruments. The 2 models are successful at reproducing very frequent occurrences of supersaturation, however their distributions differ both with the observations and with each other. The MAR model is much more often supersaturated than the observations report, and also than the ECMWF analyses. Further analyzes of these differences, comparing the respective cold physics parameterizations, tracking possible contributions of temperature biases, is beyond the scope of the present study. However, this result illustrates that because long series of consistent in situ observations are feasible at Dome C, not only short term chronology but also the statistics of supersaturation can be observed and used to exhibit differences in behavior of models and parameterizations of natural atmospheric supersaturation.

Differences between models and between one or the other model and the observations are beyond observation uncertainties. However, there are also significant differences between observations by even the 2 modified hygrometers. There are more differences between the HMPmod and FP below 100% than above. Both the HMP155 and frost point hygrometer loose accuracy and sensitivity as temperature is colder and/or water vapor partial pressure is less. Below -55°C, FP occasionally, and more and more frequently as temperature gets colder, reports unrealistically low moisture content. Figure 8 displays the regressions of water vapor partial pressure differences with saturation, separately for partial pressure ranging between 2 and 5, 5 and 10, 10 and 20, and exceeding 20 Pa. The correlation deteriorates, and the regression line increasingly deviates from 1 to 1, as the

Atmos. Chem. Phys. Discuss., doi:10.5194/acp-2016-670, 2016
Manuscript under review for journal Atmos. Chem. Phys.
Published: 18 August 2016

moisture content decreases.

Obviously, the smallest moisture partial pressures occur when the temperature is coldest. The instruments show their limits during the coldest of the winter. Figure 9 displays the annual cycle of monthly averaged temperature and RHi. HMP displays weak seasonal variability of RHi compared to the other instruments. On the other hand, FP displays extreme seasonal variability with values reaching below 30% (beyond the plot scale on Figure 9) in winter. Such unrealistically low values, at odd with the other instruments, reflect instrument limitation with very low moisture content. Limiting the analysis to cases of partial pressure of moisture above 2 Pa (dashed curves on Figure 9) excludes significant portions of the coldest parts of the winter records. This is reflected by monthly winter temperature more than 20°C warmer (Figure 9a). The fact that HMPmod reports are strongly increased suggests that this sensor also does not perform well at very low moisture levels. Both HMPmod and FP show strong seasonal variability with monthly mean RHi reaching 120% for HMPmod and exceeding 130% for FP. In both cases, the maximum monthly supersaturation is reached in early winter (April) and remains above 100% all year long, except in October for HMPmod when it is slightly below. Figure 10, same as Figure 7 but for partial pressure of moisture above 2 Pa only, confirms that in the surface atmosphere of Dome C, supersaturation is the norm rather than an exception.

Atmos. Chem. Phys. Discuss., doi:10.5194/acp-2016-670, 2016
Manuscript under review for journal Atmos. Chem. Phys.
Published: 18 August 2016

Atmospheric Chemistry and Physics Discussions

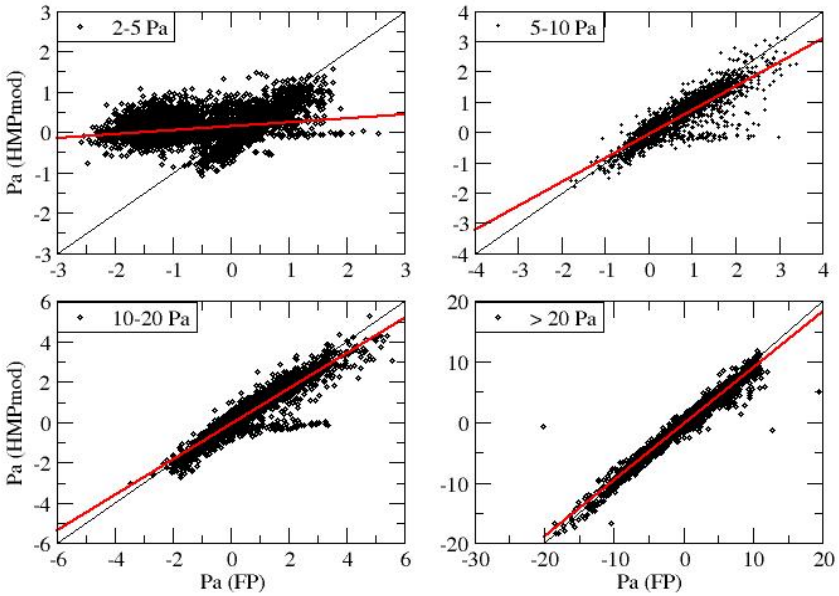

Figure 8: Regressions of partial pressure difference with saturation from HMPmod against FP, depending on partial pressure range as indicated on the upper left corner of each plot. The black line is the 1st bisector, the red line shows the linear regression.

Atmos. Chem. Phys. Discuss., doi:10.5194/acp-2016-670, 2016
Manuscript under review for journal Atmos. Chem. Phys.
Published: 18 August 2016

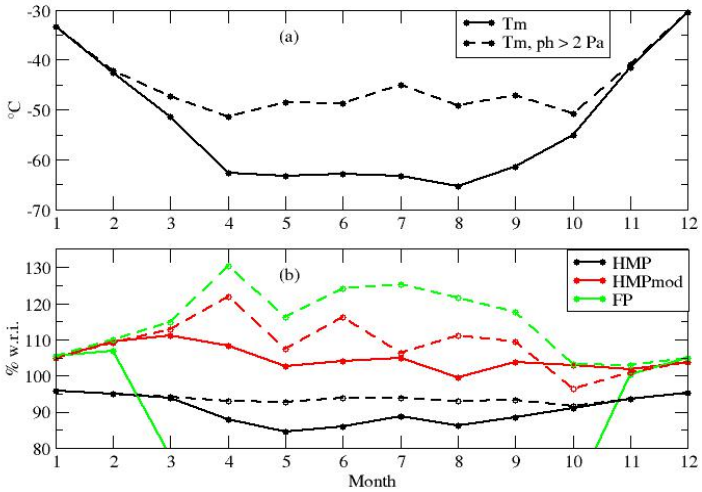

Figure 9: Seasonal variability of monthly-mean temperature (a) and RHi (b) for all reports (solid lines) and reports with moisture partial pressure above 2 Pa only (dashed lines). With all reports, the curve for FP reaches below 30%, well beyond the plot scale (green solid line).

Atmos. Chem. Phys. Discuss., doi:10.5194/acp-2016-670, 2016
Manuscript under review for journal Atmos. Chem. Phys.
Published: 18 August 2016

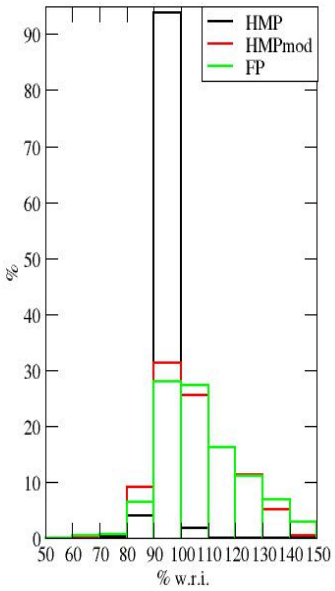

Figure 10, same as Figure 7a but for moisture partial pressure above 2 Pa only.

450

3.3 Impact on surface sublimation calculations

There are very few direct estimations of surface evaporation on the antarctic plateau. This is firstly because eddy correlation techniques use delicate high frequency sampling instruments such as sonic
455 anemometers which are hard to operate and maintain at the required level of performance in the extreme environment of the antarctic plateau. Moreover, due to the very low temperature, the water vapor content is very small and moisture sensors are not both fast and sensitive enough for such measurements in such conditions. For instance, Van As et al. [2005] report that eddy correlation measurements of latent heat flux were unsuccessful even in the summer at Kohnen station in
460 Antarctica ~3000 m above sea level. The authors thus resigned themselves to use bulk methods, a most widely employed approach in Antarctica [Stearns and Weidner, 1993]. However, bulk methods

Atmos. Chem. Phys. Discuss., doi:10.5194/acp-2016-670, 2016
Manuscript under review for journal Atmos. Chem. Phys.
Published: 18 August 2016

are equally affected by measurement biases such as underestimation of water vapor content due to failure to measure supersaturation. The magnitude of the error can be estimated at Dome C by comparing bulk calculations using HMP and HMPmod water vapor reports.

The water vapor flux E from the snow surface (subscript 's ') to the atmosphere is calculated using bulk-transfer formulae :

$$E=\rho C_Q U(z)[q_s - q(z)]$$

where ρ is the air density, $U(z)$ and $q(z)$ the wind speed and the specific humidity at the height z in the atmospheric surface layer and q_s the specific humidity at the surface, assuming saturation with respect to ice at the snow surface temperature. Here the wind speed and specific humidity are measured a z=~3m above th surface, and the snow surface temperature is obtained from measurement of the upwelling infrared radiation [Vignon et al., 2016] considering a snow emissivity of 0.99 [Brun et al., 2011]. C_Q is a bulk transfer coefficient which writes :

$$C_Q=\kappa^2 [ln(z/z_0)-\psi_m(z/L)]^{-1} [ln(z/z_{0q})-\psi_q(z/L)]^{-1}$$

where κ is the Von Kármán's constant, z_0 et z_{0q} the roughness lengths for momentum and water vapor respectively and ψ_m and ψ_q are the corresponding surface-layer similarity stability functions. Stability functions depend solely on the dimensionless height z/L, where L is the Monin-Obukhov length. The same 4 function schemes taken for stable conditions in Vignon et al. [2016] are tested here, and the functions from Hogström [1996] are selected for unstable conditions because they provide reasonable results for momentum and heat fluxes at Dome C [Vignon et al, 2016] . L and thus C_Q are calculated with an iterative resolution of the Monin-Obukhov equations system. The

Atmos. Chem. Phys. Discuss., doi:10.5194/acp-2016-670, 2016
Manuscript under review for journal Atmos. Chem. Phys.
Published: 18 August 2016

value of z_0 is the mean value reported by Vignon et al [2016] for Dome C (0.56 mm). The value of z_{0q} is difficult to estimate at Dome C because the very low vapor content of the atmosphere induces high uncertainties and because the scarcity of near-neutral conditions prevents an independent selection of a scheme for the stability functions. Two different approaches are used. In the first one, $z_{0q}=z_0$ as in King et al [2001], whereas in the second one, z_{0q} is calculated with Andreas [1987] theoretical formula which, at Dome C, yields z_{0q} values lower than z_0 by approximately one order of magnitude. Uncertainties on flux calculations are estimated from the variance of results obtained with the different choices of stability functions and roughness length.

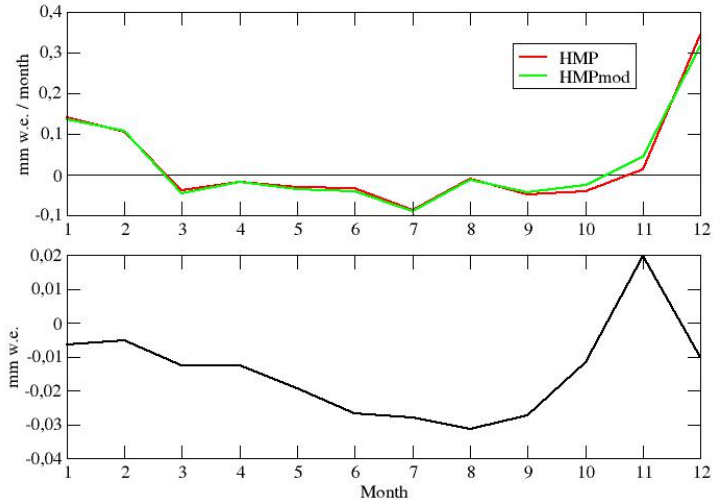

Figure 11. Annual march of the monthly vapor vapor flux at the surface according to HMP (red) and HMPmod(green), the black line showing 0, and cumulated difference (HMPmod – HMP, lower plot).

Figure 11 shows the monthly seasonal and cumulated water flux calculated by the bulk method for

Atmos. Chem. Phys. Discuss., doi:10.5194/acp-2016-670, 2016
Manuscript under review for journal Atmos. Chem. Phys.
Published: 18 August 2016

2015 using either HMP data or HMPmod reports. The flux is positive during the summer months indicating sublimation of snow while during winter months, the flux is negative indicating condensation to the surface. Such seasonality is in agreement with that reported by King et al [2001] at Halley station, coastal Antarctica but at a latitude similar to that of Dome C. The positive summer values reflect the predominance of snow sublimation during the summer diurnal cycle [Genthon et al., 2013] because, in summer, the surface-atmosphere exchanges are larger during convective activity in the afternoon than in the night hours when the boundary layer becomes stable (King et al. [2006], Vignon et al. [2016]). Integrated over the full year 2015, the net water vapor flux is 0.2763 cm w.e using HMPmod data and 0.2863 cm w.e using HMP data. These numbers can vary by as much as ±100% with the different choices of stability functions and roughness length values. They are very small anyway compared to the total surface water budget, given that the mean annual accumulation is about 2.5 cm water equivalent [Genthon et al., 2015]. However, a mean positive evaporation agrees with Stearns and Weidner [1993] who, for other regions of Antarctica, conclude that the annual-mean net sublimation exceeds the annual-mean net deposition. In fact, Figure 11 shows very little difference between calculations made with HMP and HMPmod data: the impact of supersaturation on the water heat flux is thus very small. This is because supersaturations predominantly occur when the wind speed and thus turbulence is weak (not shown) and under cold temperatures associated to low values of specific humidity (Figure 12). A possible contribution of blowing or drifting snow sublimation (King et al [2001], Frezzotti et al. [2004], Barral et al. [2014]) is not taken into account here.

Atmos. Chem. Phys. Discuss., doi:10.5194/acp-2016-670, 2016
Manuscript under review for journal Atmos. Chem. Phys.
Published: 18 August 2016

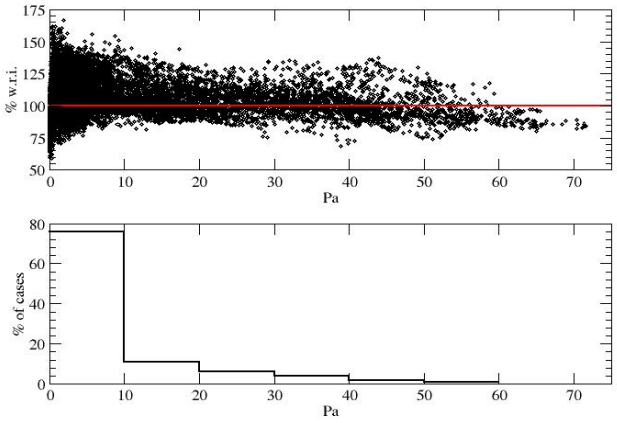

525 *Figure 12 : According to HMPmod, relative humidity vs water vapor partial pressure, saturation shown by the red line (upper plot), and probability distribution function of RHi above 105% with respect to water vapor partial pressure (lower plot).*

530

4. Discussion and conclusions

Major ice supersaturations are observed in the surface atmosphere of Dome C on the antarctic plateau in atmospheric temperature and moisture conditions close to those of the upper troposphere.

535 Fog formation can be observed in the field at temperatures for which heterogeneous freezing of the supercooled droplets would occur if ice nuclei were present. This suggests that the atmosphere is devoid of ice nuclei and that ice crystals, when present, are mostly formed by homogeneous freezing of supercooled droplets. This needs to be confirmed by detecting fog formation and analysing its properties. Meanwhile, to our knowledge it is the first time such strong

540 supersaturations (up to 200%) are observed in the natural surface atmosphere of the Earth.

Atmos. Chem. Phys. Discuss., doi:10.5194/acp-2016-670, 2016
Manuscript under review for journal Atmos. Chem. Phys.
Published: 18 August 2016

Atmospheric supersaturations are frequent in the high troposphere where cirrus clouds form [Spichtinger et al., 2003]. On the other hand, atmospheric supersaturation is a very infrequent situation in the surface atmosphere because of the high concentration of aerosols and relatively mild temperatures which are both favorable to liquid and solid cloud formation. In this respect, the surface atmosphere of the high antarctic plateau is an exception. Because of the high albedo of snow and high elevation, the temperature is close to that of the high troposphere elsewhere even in summer. Long distance transport to such remote area is insufficient to import significant amounts of cloud and ice condensation nuclei even from the closest sources at the oceans, thus the possibility of strong and frequent supersaturation.

Because they are compact, light-weight and comparatively low cost , both to buy and to operate, solid state hygrometers (thin film capacitive sensors such as Vaisala's Humicap) are widely used to report atmospheric moisture from radiosondes or automatic weather stations. However, these sensors are subject to icing in supersaturated environment [Rädel and Shine, 2010] and require correction and/or adaptation. There are not many measurements of atmospheric moisture in Antarctica, and most including by the radiosondes are made using unadapted solid state sensors. The atmospheric humidity of the antarctic atmosphere where supersaturation is frequent is likely often underestimated from observations. Thus, the evaluation of meteorological an climate models from these data may be biased. Observations at Dome C using modified sensors to ensure that supersaturations can be sampled show that models that implement parameterizations of cold cloud microphysics intended to simulate cirrus clouds at high altitude qualitatively reproduce frequent supersaturations but fail with respect to the the statistics of supersaturation events. Moreover, they fail differently, both models producing too much supersaturation but one model simulating much more frequent occurrences of supersaturations that the other.

Atmos. Chem. Phys. Discuss., doi:10.5194/acp-2016-670, 2016
Manuscript under review for journal Atmos. Chem. Phys.
Published: 18 August 2016

Estimations of the moisture budget of the antarctic atmosphere may be erroneous. Because it is comparatively undersampled by observation, studies of the antarctic atmosphere rely more than elsewhere on models and meteorological analyses. However, only models which microphysics parameterization account for supersaturation may, but not necessarily do, correctly reproduce antarctic atmospheric moisture. One consequence of underestimating surface moisture, whether in observations or models not accounting for supersaturations, is likely that the surface turbulent moisture exchange (evaporation or sublimation) is wrong. Although the ground is made of thousands of meters of snow and ice slowly accumulated through millions of years, the antarctic plateau is one of the driest places on Earth. At Dome C, only about ~3 kg m^{-2} of water accumulates each year [Genthon et al. 2015]. Out of this, the relative contribution of precipitation and evaporation is an open question. The direct measurement of both quantities is an unsolved challenge. For the turbulent fluxes, bulk and profile method parameterizations have their intrinsic limits because Monin-Obukov similarity theory requires empirical corrections functions which are not necessarily well established in very stable conditions [Vignon et al. 2016]. However, even the best theory and best parameterization deployed based on this theory will poorly apply if the observations are wrong. The consequences are limited on the antarctic plateau though, because supersaturations are stronger and more frequent as temperature is lower, and moisture content and thus turbulent moisture flux smaller.

Finally, supersaturation has an important impact on the isotopic fractionation occurring during the formation of snow [Dansgaard 1964]. Indeed, supersaturation can only occur in condition with a small number of condensation nuclei during which the growth of the snowflakes is limited by the diffusion of water molecules. The difference in diffusivity of the different isotopes of water will therefore lead to kinetic fractionation. Jouzel and Merlivat [1984] have experimentally established the impact of supersaturation on isotopic composition by a kinetic fractionation factor

Atmos. Chem. Phys. Discuss., doi:10.5194/acp-2016-670, 2016
Manuscript under review for journal Atmos. Chem. Phys.
Published: 18 August 2016

Atmospheric Chemistry and Physics Discussions

$\alpha_{kin} = \frac{S_i}{\alpha_{eq} D/D' (S_i - 1) + 1}$. Here, Si is the supersaturation, a_{eq} is the equilibrium fractionation, D/D' is the diffusivity ratio between light and heavy isotope. This formulation is still used nowadays in most atmospheric models that include water isotopes (e.g. Risi et al. [2010]). In order to provide quantitative interpretation of ice core signal, it is important to include the impact of kinetic fractionation which is significantly affecting the isotopic composition during the formation of the precipitation in the clouds, but also of the snow after the deposition. However, recent studies highlight important limitations of the Jouzel and Merlivat [1984] approach [Casado et al., 2016]. More importantly, all climatic models that include isotopic composition variables only estimate supersaturation from a parametrization from temperature and important discrepancies remain in this parametrization. Although snow forms higher above the surface, our observations provide new constraints on ice supersaturation and will help improve these parameterizations.

Measurement of ice supersaturation as high as 200% in this very dry atmosphere is a game changer for understanding physical processes of the water cycle in Antarctica. The deployment of more hygrometers that can measure supersaturation on the ~45-m meteorological mast is underway and will give more insights into water vapor fluxes. Comparisons to surface observations will also improve our understanding of dry deposition and formation of frost hoar, and possibly of diamond dust. These results open new possibilities of using stations in remote polar regions to study and understand phenomena normally occurring in clouds at several km of altitude.

Acknowledgements:

Support for field measurements was provided by the French polar institute IPEV through program CALVA (1013). Concordia station is jointly operated by the IPEV and PNRA. INSU provided support through programs LEFE CLAPA and DEPHY2. Support by OSUG through observatory

program GLACIOCLIM is also acknowledged. The BSRN upwelling infrared radiation data which served to calculate the snow surface temperature were kindly provided by Christian Lanconelli, CNR ISAC. The research leading to these results has received funding from the European Research Council under the European Union's Seventh Framework Programme (FP7/2007-2013) / ERC grant agreement n° [306045].

References:

Anderson, 1994. Mechanism for the behaviour of hydroactive materials in humidity sensors, J. Atm Oc. Tech, 12, 662-667.

Andreas, E. L., 1987. A theory for scalar roughness and the scalar transfer coefficients over snow and sea ice. Boundary-Lay. Meteorol., 38, 159-184.

Andreas, E. L., 2002. Parametrizing scalar transfer over snow and ice : A review. J. Hydrometeorol., 3, 417-432.

Arthern, R. J., D. P. Winebrenner, D. G. Vaughan, 2006. Antarctic snow accumulation mapped using polarization of 4.3-cm wavelength microwave emission. J. Geophys. Res. 111, D06107, DOI:10.1029/2004JD005667.

Barral, H., Genthon C., Trouvilliez A., Brun C., and Amory C., 2014. Blowing snow in coastal Adélie Land, Antarctica : three atmospheric moisture issues, The Cryosphere, 8, 1905–1919, doi:10.5194/tc-8-1905-2014.

Brun, E., D. six, G. Picard, V. Vionnet, L. Arnaud, E. Bazile, A. Boone, O. Bouchard, C. Genthon, V. Guidard, P. Le Moigne, F. Rabier, and Y. Seity, 2011. Snow-atmosphere coupled simulation at Dome C, Antarctica, J. Glaciol. **57**,721-736

Casado, M., Cauquoin, A., Landais, A., Israel, D., Orsi, A., Pangui, E., Landsberg, J., Kerstel, E., Prie, F. and Doussin, J.-F., 2016. Experimental determination and theoretical framework of kinetic fractionation at the water vapour–ice interface at low temperature. Geochimica et Cosmochimica Acta 174, 54-69.

Dansgaard, W., 1964. Stable isotopes in precipitation. Tellus 16, 436-468.

Frezzotti, M., Pourchet, M., Flora O., Gandolfi, S., Gay, M., Urbini, S., Vincent, C., Becagli, S., Gragnani, R., Proposito, M., Severei, M., Traversi, R., Udisti, R. and Fily, M., 2004, New estimation of precipitation and surface sublimation in East Antarctica from snow accumulation measurements. Clim. Dyn., 23, 803-813.

Gallée, H. and Gorodetskaya, I. V. (2010). Validation of a limited area model over Dome C, Antarctic Plateau, during winter. Climate Dynamics, 34:61–72.

Genthon, C., M. S. Town, D. Six, V. Favier, S. Argentini, and A. Pellegrini, 2010. Meteorological atmospheric boundary layer measurements and ECMWF analyses during summer at Dome C, Antarctica, J. Geophys. Res. **115**, D05104, doi:10.1029/2009JD012741.

Genthon, C., D. Six, V. Favier, M. Lazzara, L. Keller, 2011. Atmospheric temperature measurement biases on the Antarctic plateau, J. Atm. Oceanic Technol., DOI 10.1175/JTECH-D-11-00095.1 **28**, No. 12, 1598-1605.

Genthon C., Six D., Gallée H., Grigioni P., and Pellegrini A., 2013. Two years of atmospheric boundary layer observations on a 45-m tower at Dome C on the Antarctic plateau, J. Geophys. Res. Atmos., 118, 3218–3232, doi:10.1002/jgrd.50128.

Genthon, C., D. Six, C. Scarchilli, V. Giardini, M. Frezzotti, 2015. Meteorological and snow accumulation gradients across dome C, east Antarctic plateau, Int. J. Clim.,36, 455-466, DOI: 10.1002/joc.4362

Goff J. A., and S. Gratch,1945. Thermodynamics properties of moist air, Tans. Amer. Soc. Heat. Vent. Eng., 51, 125-157.

Jouzel J., Lorius C., Petit J. R., Genthon C., Barkov N. I., Korotkevitch Y. S., and Kotlyakov V. M., 1987. Vostok ice core: A continuous isotope temperature record over the last climatic cycle (160000 years), *Nature* **329**, 403-408.

Jouzel, J. and Merlivat, L., 1984. Deuterium and oxygen 18 in precipitation: Modeling of the isotopic effects during snow formation. J. Geophys. Res. 89, 11749-11757.

Kämpfer N (ed), 2013. Monitoring Atmospheric Water Vapor. Ground-based Remote Sensing and In-situ Methods, ISSI Scientific Report Series, 10, Springer, New York.

King, J. C. and Anderson, P.S., 1999, A humidity climatology for Halley, Antarctica, based on frost-point hygrometer measurements. Antarctic Science, 11, 100-104

King, J.C., Anderson, P.S. and Mann, G.W., 2001. The seasonal cycle of sublimation at Halley, Antarctica. J. Glaciology, 47, 56

King, J.C., Argentini, S. A. and Anderson, P. S., 2006. Contrast between the summertime surface energy balance and boundary layer structure at Dome C and Halley stations, Antarctica. J. Geophys. Res., 111, D02105

Meyer, M. P., P. J. Demott, and W. R. Cotton, 1992. New primary ice nucleation parameterizations in an explicit cloud model, J. Appl. Meteorol., 31, 708–721.

Rädel, G., and K. P. Shine, 2010. Validating ECMWF forecasts for occurrences of ice supersaturation using visual observations of persistent contrails and radiosonde measurements over England, Q. J. R. Meteorol. Soc., 136, 1723-1732.

Risi, C., Bony, S., Vimeux, F. and Jouzel, J. (2010) Water-stable isotopes in the LMDZ4 general circulation model: Model evaluation for present-day and past climates and applications to climatic interpretations of tropical isotopic records. J. Geophys. Res. 115, D12118.

Schwerdtfeger, W., 1970. The climate of the Antarctic, Vol. 14, S. Orvig Ed., World survey of climatology, H. E. Landsberg Ed. Elsevier, 253-355.

Spichtinger, P., Gierens, K., Read, W.: The global distribution of ice-supersaturated regions as seen by the microwave limb sounder. Q. J. R. Meteorol. Soc. 129, 3391–3410 (2003). doi: 10.1256/qj.02.141

Atmos. Chem. Phys. Discuss., doi:10.5194/acp-2016-670, 2016
Manuscript under review for journal Atmos. Chem. Phys.
Published: 18 August 2016

Atmospheric Chemistry and Physics Discussions

Spichtinger, P., K. Gierens1 , H. G. J. Smit2 , J. Ovarlez3 , and J.-F. Gayet4, 2004. On the distribution of relative humidity in cirrus clouds, Atmos. Chem. Phys., 4, 639–647.

720 Stearns, C. R. and Weidner, G. A., 1993, Sensible and Latent heat flux estimates in Antarctica. Antarctic research series, 61, 109-138.

Tompkins, A. M., Gierens, K. and Rädel, G., 2007. Ice supersaturation in the ECMWF integrated forecast system. Q. J. R. Meteorol. Soc., 133, 53–63.

725

Van As, D., van den Broeke, M., Reijmer, C., and van de Wal,, M., 2005. The summer surface energy balance of the high antarctic plateau, Boundary-Layer Metorol. 115, 289-317.

Vignon, E., Genthon C., Barral, H., Amory, C., Picard, G., Gallée, H., Casasanta, G. and Argentini,
730 S., 2016. Momentum and heat flux parametrization at Dome C, Antarctica : a sensitivity study, Boundary-Lay. Meteorol., in press.

List of Figures

List of Tables

Bibliography

Aemisegger, F., Spiegel, J. K., Pfahl, S., Sodemann, H., Eugster, W., and Wernli, H. (2015). Isotope meteorology of cold front passages: A case study combining observations and modeling. *Geophysical Research Letters*, 42(13):5652–5660.

Alley, R. B. (1980). Densification and recrystallization of firn at Dome C, East Antarctica.

Alnis, J., Matveev, A., Kolachevsky, N., Udem, T., and Hänsch, T. W. (2008). Subhertz linewidth diode lasers by stabilization to vibrationally and thermally compensated ultralow-expansion glass Fabry-Perot cavities. *Physical Review A*, 77(5):53809.

Altnau, S., Schlosser, E., Isaksson, E., and Divine, D. (2015). Climatic signals from 76 shallow firn cores in Dronning Maud Land, East Antarctica. *The Cryosphere*, 9(3):925–944.

Angert, A., Lee, J.-E., and Yakir, D. (2008). Seasonal variations in the isotopic composition of near-surface water vapour in the eastern Mediterranean. *Tellus B*, 60(4):674–684.

Baertschi, P. (1976). Absolute18O content of standard mean ocean water. *Earth and Planetary Science Letters*, 31(3):341–344.

Bao, H., Cao, X., and Hayles, J. A. (2016). Triple Oxygen Isotopes: Fundamental Relationships and Applications. *Annual Review of Earth and Planetary Sciences*, 44(1).

Barkan, E. and Luz, B. (2005). High precision measurements of 17O/16O and 18O/16O ratios in H2O. *Rapid Communications in Mass Spectrometry*, 19(24):3737–3742.

Barkan, E. and Luz, B. (2007). Diffusivity fractionations of H216O/H 217O and H 216O/H 218O in air and their implications for isotope hydrology. *Rapid Communications in Mass Spectrometry*, 21(18):2999–3005.

Baroni, M., Bard, E., Petit, J. R., Magand, O., and Bourlès, D. (2011). Volcanic and solar activity, and atmospheric circulation influences on cosmogenic 10Be fallout at Vostok

and Concordia (Antarctica) over the last 60years. *Geochimica et Cosmochimica Acta*, 75(22):7132–7145.

Bergeron, T. (1935). On the Physics of clouds and precipitation. *Proc. 5th Assemb. UGGI Lisbon*, 2:156.

Berkelhammer, M., Noone, D. C., Steen-Larsen, H. C., Bailey, A., Cox, C. J., O'Neill, M. S., Schneider, D., Steffen, K., and White, J. W. C. (2016). Surface-atmosphere decoupling limits accumulation at Summit, Greenland. *Science Advances*, 2(4).

Bernhardt, B., Ozawa, A., Jacquet, P., Jacquey, M., Kobayashi, Y., Udem, T., Holzwarth, R., Guelachvili, G., Hansch, T. W., and Picque, N. (2010). Cavity-enhanced dual-comb spectroscopy. *Nat Photon*, 4(1):55–57.

Bigeleisen, J. and Mayer, M. G. (1947). Calculation of Equilibrium Constants for Isotopic Exchange Reactions. *The Journal of Chemical Physics*, 15(5).

Boato, G., Scoles, G., and Vallauri, M. E. (1962). Vapour pressure of isotopic solids by a steady flow method: Argon between 72° K and triple point. *Il Nuovo Cimento (1955-1965)*, 23(6):1041–1053.

Bond, G., Broecker, W., Johnsen, S., McManus, J., Labeyrie, L., Jouzel, J., and Bonani, G. (1993). Correlations between climate records from North Atlantic sediments and Greenland ice. *Nature*, 365(6442):143–147.

Bonne, J. L., Masson-Delmotte, V., Cattani, O., Delmotte, M., Risi, C., Sodemann, H., and Steen-Larsen, H. C. (2014). The isotopic composition of water vapour and precipitation in Ivittuut, southern Greenland. *Atmos. Chem. Phys.*, 14(9):4419–4439.

Bonne, J.-L., Steen-Larsen, H. C., Risi, C., Werner, M., Sodemann, H., Lacour, J.-L., Fettweis, X., Cesana, G., Delmotte, M., Cattani, O., Vallelonga, P., Kjær, H. A., Clerbaux, C., Sveinbjörnsdóttirffilmark, Á. E., and Masson-Delmotte, V. (2015). The summer 2012 Greenland heat wave: in situ and remote sensing observations of water vapour isotopic composition during an atmospheric river event. *Journal of Geophysical Research: Atmospheres*, page 2014JD022602.

Boyle, E. A. (1997). Cool tropical temperatures shift the global δ18O-T relationship: An explanation for the ice core δ18O - borehole thermometry conflict? *Geophysical Research Letters*, 24(3):273–276.

Brun, E., Six, D., Picard, G., Vionnet, V., Arnaud, L., Bazile, E., Boone, A., Bouchard, A., Genthon, C., Guidard, V., Le Moigne, P., Rabier, F., and Seity, Y. (2011).

Snow/atmosphere coupled simulation at Dome C, Antarctica. *Journal of Glaciology*, 57(204):721–736.

Brutsaert, W. (1975). A theory for local evaporation (or heat transfer) from rough and smooth surfaces at ground level. *Water Resources Research*, 11(4):543–550.

Burkart, J. (2015). *Optical feedback frequency-stabilized cavity ring-down spectroscopy - Highly coherent near-infrared laser sources and metrological applications in molecular absorption spectroscopy*. PhD thesis, University Grenoble Alpes.

Burkart, J. and Kassi, S. (2015). Absorption line metrology by optical feedback frequency-stabilized cavity ring-down spectroscopy. *Applied Physics B*, 119(1):97–109.

Burkart, J., Romanini, D., and Kassi, S. (2013). Optical feedback stabilized laser tuned by single-sideband modulation. *Optics letters*, 38(12):2062–2064.

Burkart, J., Romanini, D., and Kassi, S. (2014). Optical feedback frequency stabilized cavity ring-down spectroscopy. *Optics Letters*, 39(16):4695–4698.

Burkart, J., Sala, T., Romanini, D., Marangoni, M., Campargue, A., and Kassi, S. (2015). Communication: Saturated CO2 absorption near 1.6 μm for kilohertz-accuracy transition frequencies. *The Journal of chemical physics*, 142(19):191103.

Cappa, C. D., Hendricks, M. B., DePaolo, D. J., and Cohen, R. C. (2003). Isotopic fractionation of water during evaporation. *Journal of Geophysical Research-Atmospheres*, 108(D16):10.

Casado, M., Cauquoin, A., Landais, A., Israel, D., Orsi, A., Pangui, E., Landsberg, J., Kerstel, E., Prie, F., and Doussin, J.-F. (2016a). Experimental determination and theoretical framework of kinetic fractionation at the water vapour-ice interface at low temperature. *Geochimica et Cosmochimica Acta*, 174:54–69.

Casado, M., Landais, A., Masson-Delmotte, V., Genthon, C., Kerstel, E., Kassi, S., Arnaud, L., Picard, G., Prie, F., Cattani, O., Steen-Larsen, H. C., Vignon, E., and Cermak, P. (2016b). Continuous measurements of isotopic composition of water vapour on the East Antarctic Plateau. *Atmospheric Chemistry and Physics*, 16(13):8521–8538.

Casey, K. A., Fudge, T. J., Neumann, T. A., Steig, E. J., Cavitte, M. G. P., and Blankenship, D. D. (2014). The 1500 m South Pole ice core: recovering a 40 ka environmental record. *Annals of Glaciology*, 55(68):137–146.

Charles, C. D., Rind, D., Jouzel, J., Koster, R. D., and Fairbanks, R. G. (1994). Glacial-Interglacial Changes in Moisture Sources for Greenland: Influences on the Ice Core Record of Climate. *Science*, 263(5146):508–511.

Ciais, P. and Jouzel, J. (1994). Deuterium and oxygen 18 in precipitation: Isotopic model, including mixed cloud processes. *Journal of Geophysical Research: Atmospheres*, 99(D8):16793–16803.

Ciurylo, R. (1998). Shapes of pressure- and Doppler-broadened spectral lines in the core and near wings. *Physical Review A*, 58(2):1029–1039.

Craig, H. (1957). Isotopic standards for carbon and oxygen and correction factors for mass spectrometric analysis of carbon dioxide. *Geochimica et Cosmochimica Acta*, 12(1-2):133–149.

Craig, H. (1961). ISOTOPIC VARIATIONS IN METEORIC WATERS. *Science*, 133(346):1702–&.

Craig, H., Boato, G., and White, D. E. (1955). ISOTOPIC GEOCHEMISTRY OF THERMAL WATERS. *American Mineralogist*, 40(3-4):313.

Craig, H. and Gordon, A. (1965). Deuterium and oxygen 18 variations in the ocean and the marine atmosphere. *Stable Isotopes in Oceanic Studies and Paleotemperatures*, 1(9):130.

Craig, H., Gordon, L. I., and Horibe, Y. (1963). ISOTOPIC EXCHANGE EFFECTS IN EVAPORATION OF WATER .1. LOW-TEMPERATURE EXPERIMENTAL RESULTS. *Journal of Geophysical Research*, 68(17):5079–&.

Criss, R. E. (1999). *Principles of stable isotope distribution*, volume 254. Oxford University Press New York.

Crosson, E. R. (2008). A cavity ring-down analyzer for measuring atmospheric levels of methane, carbon dioxide, and water vapor. *Applied Physics B*, 92(3):403–408.

Cuffey, K. M. and Clow, G. D. (1997). Temperature, accumulation, and ice sheet elevation in central Greenland through the last deglacial transition. *Journal of Geophysical Research: Oceans*, 102(C12):26383–26396.

Dansgaard, W. (1954). The O18-abundance in fresh water. *Geochimica et Cosmochimica Acta*, 6(5):241–260.

Dansgaard, W. (1964). Stable isotopes in precipitation. *Tellus*, 16(4):436–468.

Dansgaard, W., Johnsen, S. J., Clausen, H. B., Dahl-Jensen, D., Gundestrup, N., Hammer, C. U., and Oeschger, H. (1984). North Atlantic climatic oscillations revealed by deep Greenland ice cores. *Climate processes and climate sensitivity*, pages 288–298.

de Wit, J. C., van der Straaten, C. M., and Mook, W. G. (1980). Determination of the Absolute Hydrogen Isotopic Ratio of V-SMOW and SLAP. *Geostandards Newsletter*, 4(1):33–36.

DeConto, R. M. and Pollard, D. (2016). Contribution of Antarctica to past and future sea-level rise. *Nature*, 531(7596):591–597.

Delaygue, G., Jouzel, J., Masson, V., Koster, R. D., and Bard, E. (2000). Validity of the isotopic thermometer in central Antarctica: limited impact of glacial precipitation seasonality and moisture origin. *Geophysical Research Letters*, 27(17):2677–2680.

Di Domenico, G., Schilt, S., and Thomann, P. (2010). Simple approach to the relation between laser frequency noise and laser line shape. *Applied Optics*, 49(25):4801–4807.

Diddams, S. A., Jones, D. J., Ye, J., Cundiff, S. T., Hall, J. L., Ranka, J. K., Windeler, R. S., Holzwarth, R., Udem, T., and Hänsch, T. W. (2000). Direct link between microwave and optical frequencies with a 300 THz femtosecond laser comb. *Physical Review Letters*, 84(22):5102.

Dole, M. (1935). THE RELATIVE ATOMIC WEIGHT OF OXYGEN IN WATER AND IN AIR. *Journal of the American Chemical Society*, 57(12):2731.

Donnelly, T., Waldron, S., Tait, A., Dougans, J., and Bearhop, S. (2001). Hydrogen isotope analysis of natural abundance and deuterium-enriched waters by reduction over chromium on-line to a dynamic dual inlet isotope-ratio mass spectrometer. *Rapid Communications in Mass Spectrometry*, 15(15):1297–1303.

Dutton, A., Carlson, A. E., Long, A. J., Milne, G. A., Clark, P. U., DeConto, R., Horton, B. P., Rahmstorf, S., and Raymo, M. E. (2015). Sea-level rise due to polar ice-sheet mass loss during past warm periods. *Science*, 349(6244).

Ekaykin, A. (2003). *Meteorological regime of central Antarctica and its role in the formation of isotope composition of snow thickness*. PhD thesis, Geography Faculty of Saint Petersbourg.

Ekaykin, A. A., Kozachek, A. V., Lipenkov, V. Y., and Shibaev, Y. A. (2014). Multiple climate shifts in the Southern Hemisphere over the past three centuries based on central Antarctic snow pits and core studies. *Annals of Glaciology*, 55(66):259–266.

Ekaykin, A. A. and Lipenkov, V. Y. (2009). Formation of the ice core isotopic composition. *Physics of ice core records, Low Temperature Science*, 68(Supplement):299–314.

Ekaykin, A. A., Lipenkov, V. Y., Barkov, N. I., Petit, J. R., and Masson-Delmotte, V. (2002). Spatial and temporal variability in isotope composition of recent snow in the vicinity of Vostok station, Antarctica: implications for ice-core record interpretation. *Annals of Glaciology*, 35(1):181–186.

Ekaykin, A. A., Lipenkov, V. Y., Kuzmina, I. N., Petit, J. R., Masson-Delmotte, V., and Johnsen, S. J. (2004). The changes in isotope composition and accumulation of snow at Vostok station, East Antarctica, over the past 200 years. *Annals of Glaciology*, 39(1):569–575.

Ellehøj, M. D., Steen-Larsen, H. C., Johnsen, S. J., and Madsen, M. B. (2013). Ice-vapor equilibrium fractionation factor of hydrogen and oxygen isotopes: Experimental investigations and implications for stable water isotope studies. *Rapid Communications in Mass Spectrometry*, 27(19):2149–2158.

EPICA (2004). Eight glacial cycles from an Antarctic ice core. *Nature*, 429(6992):623–628.

EPICA (2006). One-to-one coupling of glacial climate variability in Greenland and Antarctica. *Nature*, 444(7116):195–198.

Epstein, S. and Mayeda, T. (1953). VARIATION OF O-18 CONTENT OF WATERS FROM NATURAL SOURCES. *Geochimica et Cosmochimica Acta*, 4(5):213–224.

Fawcett, P. J., Ágústsdóttir, A. M., Alley, R. B., and Shuman, C. A. (1997). The Younger Dryas Termination and North Atlantic Deep Water Formation: Insights from climate model simulations and Greenland Ice Cores. *Paleoceanography*, 12(1):23–38.

Fischer, H., Severinghaus, J., Brook, E., Wolff, E., Albert, M., Alemany, O., Arthern, R., Bentley, C., Blankenship, D., and Chappellaz, J. (2013). Where to find 1.5 million year old ice for the IPICS "Oldest Ice" ice core. *Climate of the Past*, 9:2489–2505.

Fisher, D. A., Reeh, N., and Clausen, H. B. (1985). Stratigraphic noise in time series derived from ice cores. *Ann. Glaciol*, 7:76–83.

Frezzotti, M., Gandolfi, S., La Marca, F., and Urbini, S. (2002). Snow dunes and glazed surfaces in Antarctica: new field and remote-sensing data. *Annals of Glaciology*, 34(1):81–88.

Frezzotti, M., Urbini, S., Proposito, M., Scarchilli, C., and Gandolfi, S. (2007). Spatial and temporal variability of surface mass balance near Talos Dome, East Antarctica. *Journal of Geophysical Research: Earth Surface*, 112(F2).

Fujita, K. and Abe, O. (2006). Stable isotopes in daily precipitation at Dome Fuji, East Antarctica. *Geophysical Research Letters*, 33(18).

Gallée, H. and Gorodetskaya, I. V. (2010). Validation of a limited area model over Dome C, Antarctic Plateau, during winter. *Climate dynamics*, 34(1):61–72.

Gat, J. R. (1996). OXYGEN AND HYDROGEN ISOTOPES IN THE HYDROLOGIC CYCLE. *Annual Review of Earth and Planetary Sciences*, 24(1):225–262.

Genthon, C., Piard, L., Vignon, E., Madeleine, J.-B., Casado, M., and Gallée, H. (2016). Atmospheric moisture supersaturation in the near-surface atmosphere at Dome C, antarctic plateau. *Atmos. Chem. Phys. Discuss.*, 2016:1–37.

Genthon, C., Six, D., Favier, V., Lazzara, M., and Keller, L. (2011). Atmospheric Temperature Measurement Biases on the Antarctic Plateau. *Journal of Atmospheric and Oceanic Technology*, 28(12):1598–1605.

Genthon, C., Six, D., Gallée, H., Grigioni, P., and Pellegrini, A. (2013). Two years of atmospheric boundary layer observations on a 45-m tower at Dome C on the Antarctic plateau. *Journal of Geophysical Research: Atmospheres*, 118(8):3218–3232.

Genthon, C., Six, D., Scarchilli, C., Ciardini, V., and Frezzotti, M. (2015). Meteorological and snow accumulation gradients across Dome C, East Antarctic plateau. *International Journal of Climatology*, pages n/a–n/a.

Gkinis, V., Popp, T. J., Blunier, T., Bigler, M., Schüpbach, S., Kettner, E., and Johnsen, S. J. (2011). Water isotopic ratios from a continuously melted ice core sample. *Atmos. Meas. Tech.*, 4(11):2531–2542.

Gkinis, V., Simonsen, S. B., Buchardt, S. L., White, J. W. C., and Vinther, B. M. (2014). Water isotope diffusion rates from the NorthGRIP ice core for the last 16,000 years–Glaciological and paleoclimatic implications. *Earth and Planetary Science Letters*, 405:132–141.

Goff, J. A. and Gratch, S. (1945). Thermodynamic properties of moist air. *ASHVE Trans*, 51:125–158.

Grilli, R., Marrocco, N., Desbois, T., Guillerm, C., Triest, J., Kerstel, E., and Romanini, D. (2014). Invited Article: SUBGLACIOR: An optical analyzer embedded in an Antarctic ice probe for exploring the past climate. *Review of Scientific Instruments*, 85(11):111301.

Groot Zwaaftink, C. D., Cagnati, A., Crepaz, A., Fierz, C., Macelloni, G., Valt, M., and Lehning, M. (2013). Event-driven deposition of snow on the Antarctic Plateau: analyzing field measurements with SNOWPACK. *The Cryosphere*, 7(1):333–347.

Guillevic, M., Bazin, L., Landais, A., Kindler, P., Orsi, A., Masson-Delmotte, V., Blunier, T., Buchardt, S. L., Capron, E., and Leuenberger, M. (2013). Spatial gradients of temperature, accumulation and δ 18 O-ice in Greenland over a series of Dansgaard–Oeschger events. *Climate of the Past*, 9(3):1029–1051.

Hall, J. L. (2006). Nobel Lecture: Defining and measuring optical frequencies. *Reviews of Modern Physics*, 78(4):1279–1295.

Hänsch, T. W. (2006). Nobel Lecture: Passion for precision. *Reviews of Modern Physics*, 78(4):1297–1309.

Helliker, B. R., Roden, J. S., Cook, C., and Ehleringer, J. R. (2002). A rapid and precise method for sampling and determining the oxygen isotope ratio of atmospheric water vapor. *Rapid Communications in Mass Spectrometry*, 16(10):929–932.

Hellmann, R., Bich, E., Vogel, E., and Vesovic, V. (2014). Intermolecular potential energy surface and thermophysical properties of the CH4–N2 system. *The Journal of Chemical Physics*, 141(22).

Hoffmann, G., Werner, M., and Heimann, M. (1998). Water isotope module of the ECHAM atmospheric general circulation model: A study on timescales from days to several years. *Journal of Geophysical Research: Atmospheres*, 103(D14):16871–16896.

Imbrie, J. and Imbrie, J. Z. (1980). Modeling the climatic response to orbital variations. *Science*, 207(4434):943–953.

Johnsen, S. J. (1977). Stable isotope homogenization of polar firn and ice. *Isotopes and impurities in snow and ice*, 1.

Johnsen, S. J., Clausen, H. B., Cuffey, K. M., Hoffmann, G., and Creyts, T. T. (2000). Diffusion of stable isotopes in polar firn and ice: the isotope effect in firn diffusion. *Physics of ice core records*, pages 121–140.

Jones, D. J., Diddams, S. A., Ranka, J. K., Stentz, A., Windeler, R. S., Hall, J. L., and Cundiff, S. T. (2000). Carrier-envelope phase control of femtosecond mode-locked lasers and direct optical frequency synthesis. *Science*, 288(5466):635–639.

Jouzel, J., Alley, R. B., Cuffey, K. M., Dansgaard, W., Grootes, P., Hoffmann, G., Johnsen, S. J., Koster, R. D., Peel, D., Shuman, C. A., Stievenard, M., Stuiver, M., and White, J. (1997). Validity of the temperature reconstruction from water isotopes in ice cores. *Journal of Geophysical Research: Oceans*, 102(C12):26471–26487.

Jouzel, J., Delaygue, G., Landais, A., Masson-Delmotte, V., Risi, C., and Vimeux, F. (2013). Water isotopes as tools to document oceanic sources of precipitation. *Water Resources Research*, 49(11):7469–7486.

Jouzel, J. and Masson-Delmotte, V. (2010). Paleoclimates: what do we learn from deep ice cores? *Wiley Interdisciplinary Reviews: Climate Change*, 1(5):654–669.

Jouzel, J. and Merlivat, L. (1984). Deuterium and oxygen 18 in precipitation: Modeling of the isotopic effects during snow formation. *Journal of Geophysical Research: Atmospheres*, 89(D7):11749–11757.

Jouzel, J., Merlivat, L., Petit, J. R., and Lorius, C. (1983). Climatic information over the last century deduced from a detailed isotopic record in the south pole snow. *Journal of Geophysical Research: Oceans*, 88(C4):2693–2703.

Jouzel, J., Russell, G. L., Suozzo, R. J., Koster, R. D., White, J. W. C., and Broecker, W. S. (1987). Simulations of the HDO and H218O atmospheric cycles using the NASA GISS general circulation model: The seasonal cycle for present-day conditions. *Journal of Geophysical Research: Atmospheres*, 92(D12):14739–14760.

Jouzel, J., Stievenard, M., Johnsen, S. J., Landais, A., Masson-Delmotte, V., Sveinbjornsdottir, A., Vimeux, F., von Grafenstein, U., and White, J. W. C. (2007). The GRIP deuterium-excess record. *Quaternary Science Reviews*, 26(1-2):1–17.

Kassi, S. and Campargue, A. (2012). Cavity ring down spectroscopy with 5 x 10-13 cm-1 sensitivity. *The Journal of Chemical Physics*, 137(23).

Kastler, A. (1962). Atomes à I'intérieur d'un interféromètre Perot-Fabry. *Applied Optics*, 1(101):67–74.

Kavanaugh, J. L. and Cuffey, K. M. (2003). Space and time variation of δ18O and δD in Antarctic precipitation revisited. *Global Biogeochemical Cycles*, 17(1):n/a–n/a.

Kawanishi, T., Sakamoto, T., Miyazaki, T., Izutsu, M., Fujita, T., Mori, S., Higuma, K., and Ichikawa, J. (2006). High-speed optical DQPSK and FSK modulation using integrated Mach-Zehnder interferometers. *Optics Express*, 14(10):4469–4478.

Kerstel, E. R. T., Iannone, R. Q., Chenevier, M., Kassi, S., Jost, H.-J., and Romanini, D. (2006). A water isotope (2H, 17O, and 18O) spectrometer based on optical feedback cavity-enhanced absorption for in situ airborne applications. *Applied Physics B*, 85(2-3):397–406.

Kiehl, J. T. and Trenberth, K. E. (1997). Earth's annual global mean energy budget. *Bulletin of the American Meteorological Society*, 78(2):197–208.

Koster, R. D., Jouzel, J., Suozzo, R. J., and Russell, G. L. (1992). Origin of July Antarctic precipitation and its influence on deuterium content: a GCM analysis. *Climate Dynamics*, 7(4):195–203.

Krinner, G., Genthon, C., and Jouzel, J. (1997). GCM analysis of local influences on ice core delta signals. *Geophysical Research Letters*, 24(22):2825–2828.

Küttel, M., Steig, E. J., Ding, Q., Monaghan, A. J., and Battisti, D. S. (2012). Seasonal climate information preserved in West Antarctic ice core water isotopes: relationships to temperature, large-scale circulation, and sea ice. *Climate Dynamics*, 39(7):1841–1857.

Laepple, T., Hörhold, M., Münch, T., Freitag, J., Wegner, A., and Kipfstuhl, S. (2016). Layering of surface snow and firn at Kohnen Station, Antarctica: Noise or seasonal signal? *Journal of Geophysical Research: Earth Surface*.

Laepple, T., Werner, M., and Lohmann, G. (2011). Synchronicity of Antarctic temperatures and local solar insolation on orbital timescales. *Nature*, 471(7336):91–94.

Landais, A., Barkan, E., and Luz, B. (2008). Record of δ18O and 17O-excess in ice from Vostok Antarctica during the last 150,000 years. *Geophysical Research Letters*, 35(2):L02709.

Landais, A., Barkan, E., Yakir, D., and Luz, B. (2006). The triple isotopic composition of oxygen in leaf water. *Geochimica et Cosmochimica Acta*, 70(16):4105–4115.

Landais, A., Caillon, N., Goujon, C., Grachev, A. M., Barnola, J. M., Chappellaz, J., Jouzel, J., Masson-Delmotte, V., and Leuenberger, M. (2004). Quantification of rapid temperature change during DO event 12 and phasing with methane inferred from air isotopic measurements. *Earth and Planetary Science Letters*, 225(1–2):221–232.

Landais, A., Ekaykin, A., Barkan, E., Winkler, R., and Luz, B. (2012a). Seasonal variations of 17O-excess and d-excess in snow precipitation at Vostok station, East Antarctica. *Journal of Glaciology*, 58(210):725–733.

Landais, A., Steen-Larsen, H. C., Guillevic, M., Masson-Delmotte, V., Vinther, B., and Winkler, R. (2012b). Triple isotopic composition of oxygen in surface snow and water vapor at NEEM (Greenland). *Geochimica et Cosmochimica Acta*, 77:304–316.

Landais, A., Winkler, R., and Prié, F. (2014). Triple Isotopic Composition of Oxygen in Water from Ice Cores. Technical report, LSCE.

Landau, L. D. and Lifshitz, E. M. (1958). *Statistical physics*. Pergamon Press ; Addison-Wesley Pub. Co., London; Reading, Mass.

Landsberg, J. (2014). *Development of an OF-CEAS laser spectrometer for water vapor isotope measurements at low water concentrations*. PhD thesis, University of Groningen.

Landsberg, J., Romanini, D., and Kerstel, E. (2014). Very high finesse optical-feedback cavity-enhanced absorption spectrometer for low concentration water vapor isotope analyses. *Optics Letters*, 39(7):1795–1798.

Langway, C. C. (1970). *Stratigraphic analysis of a deep ice core from Greenland*, volume 125. Geological Society of America.

Laurent, P., Clairon, A., and Breant, C. (1989). Frequency noise analysis of optically self-locked diode lasers. *Quantum Electronics, IEEE Journal of*, 25(6):1131–1142.

Lazzara, M. A., Keller, L. M., Markle, T., and Gallagher, J. (2012). Fifty-year Amundsen–Scott South Pole station surface climatology. *Atmospheric Research*, 118:240–259.

Libois, Q., Picard, G., Arnaud, L., Dumont, M., Lafaysse, M., Morin, S., and Lefebvre, E. (2015). Summertime evolution of snow specific surface area close to the surface on the Antarctic Plateau. *The Cryosphere*, 9(6):2383–2398.

Libois, Q., Picard, G., Arnaud, L., Morin, S., and Brun, E. (2014). Modeling the impact of snow drift on the decameter-scale variability of snow properties on the Antarctic Plateau. *Journal of Geophysical Research: Atmospheres*, 119(20):11,611–662,681.

Lide, D. R. (2004). *CRC handbook of chemistry and physics*. CRC press.

Lisak, D., Havey, D. K., and Hodges, J. T. (2009). Spectroscopic line parameters of water vapor for rotation-vibration transitions near 7180 cm-1. *Physical Review A*, 79(5):52507.

Liu, C. and Barnes, E. A. (2015). Extreme moisture transport into the Arctic linked to Rossby wave breaking. *Journal of Geophysical Research: Atmospheres*, 120(9):3774–3788.

Loewe, F. (1936). The greenland Ice Cap as seen by A Meteorologist. *Quarterly Journal of the Royal Meteorological Society*, 62(266):359–378.

Lorius, C., Merlivat, L., and Hagemann, R. (1969). Variation in the mean deuterium content of precipitations in Antarctica. *Journal of Geophysical Research*, 74(28):7027–7031.

Loudon, R. (2000). *The quantum theory of light*. OUP Oxford.

Lu, G. and DePaolo, D. J. (2016). Lattice Boltzmann simulation of water isotope fractionation during ice crystal growth in clouds. *Geochimica et Cosmochimica Acta*, 180:271–283.

Ludlow, A. D., Huang, X., Notcutt, M., Zanon-Willette, T., Foreman, S. M., Boyd, M. M., Blatt, S., and Ye, J. (2007). Compact, thermal-noise-limited optical cavity for diode laser stabilization at 1.10-15. *Optics Letters*, 32(6):641–643.

Luz, B. and Barkan, E. (2010). Variations of 17O/16O and 18O/16O in meteoric waters. *Geochimica et Cosmochimica Acta*, 74(22):6276–6286.

Luz, B., Barkan, E., Yam, R., and Shemesh, A. (2009). Fractionation of oxygen and hydrogen isotopes in evaporating water. *Geochimica et Cosmochimica Acta*, 73(22):6697–6703.

Majoube, M. (1971a). FRACTIONATION IN O-18 BETWEEN ICE AND WATER VAPOR. *Journal De Chimie Physique Et De Physico-Chimie Biologique*, 68(4):625–&.

Majoube, M. (1971b). OXYGEN-18 AND DEUTERIUM FRACTIONATION BETWEEN WATER AND STEAM. *Journal De Chimie Physique Et De Physico-Chimie Biologique*, 68(10):1423–&.

Martin, P. and Gröning, M. (2009). Reference Sheet for International Measurement Standards VSMOW2 and SLAP2. *International Atomic Energy Agency, Vienna*.

Masson-Delmotte, V., Delmotte, M., Morgan, V., Etheridge, D., Van Ommen, T., Tartarin, S., and Hoffmann, G. (2003). Recent southern Indian Ocean climate variability inferred from a Law Dome ice core: New insights for the interpretation of coastal Antarctic isotopic records. *Climate Dynamics*, 21(2):153–166.

Meijer, H. A. J. and Li, W. J. (1998). The use of electrolysis for accurate delta O-17 and delta O-18 isotope measurements in water. *Isotopes in Environmental and Health Studies*, 34(4):349–369.

Merlivat, L. (1978a). MOLECULAR DIFFUSIVITIES OF (H2O)-O-1 6 HD16O, AND (H2O)-O-18 IN GASES. *Journal of Chemical Physics*, 69(6):2864–2871.

Merlivat, L. (1978b). The dependence of bulk evaporation coefficients on air-water interfacial conditions as determined by the isotopic method. *Journal of Geophysical Research: Oceans*, 83(C6):2977–2980.

Merlivat, L. and Jouzel, J. (1979). Global climatic interpretation of the deuterium-oxygen 18 relationship for precipitation. *Journal of Geophysical Research: Oceans*, 84(C8):5029–5033.

Merlivat, L. and Nief, G. (1967). Fractionnement isotopique lors des changements d'état solide-vapeur et liquide-vapeur de l'eau à des températures inférieures à 0°C. *Tellus*, 19(1):122–127.

Milankovitch, M. (1941). *Kanon der Erdebestrahlung und seine Anwendung auf das Eiszeitenproblem*. Königlich Serbische Akademie.

Millot, G., Pitois, S., Yan, M., Hovhannisyan, T., Bendahmane, A., Hänsch, T. W., and Picqué, N. (2015). Frequency-agile dual-comb spectroscopy. *Nature Photonics*.

Mook, W. G. and Grootes, P. M. (1973). The measuring procedure and corrections for the high-precision mass-spectrometric analysis of isotopic abundance ratios, especially referring to carbon, oxygen and nitrogen. *International Journal of Mass Spectrometry and Ion Physics*, 12(3):273–298.

Morgan, V. I. (1985). An oxygen isotope—climate record from the Law Dome, Antarctica. *Climatic Change*, 7(4):415–426.

Morville, J., Kassi, S., Chenevier, M., and Romanini, D. (2005). Fast, low-noise, mode-by-mode, cavity-enhanced absorption spectroscopy by diode-laser self-locking. *Applied Physics B*, 80(8):1027–1038.

Moyer, E., Sarkozy, L., Lamb, K., Clouser, B., Stutz, E., Kuhnreich, B., Landsberg, J., Habig, J., Hiranuma, N., Wagner, S., Ebert, V., Kerstel, E., Moehler, O., and Saathoff, H. (2013). Applications of Absorption Spectroscopy for Water Isotopic Measurements in Cold Clouds.

Münch, T., Kipfstuhl, S., Freitag, J., Meyer, H., and Laepple, T. (2016). Regional climate signal vs. local noise: a two-dimensional view of water isotopes in Antarctic firn at Kohnen Station, Dronning Maud Land. *Climate of the Past*, 12(7):1565–1581.

NEEM community members, N. (2013). Eemian interglacial reconstructed from a Greenland folded ice core. *Nature*, 493(7433):489–494.

Nicolas, J. P. and Bromwich, D. H. (2014). New Reconstruction of Antarctic Near-Surface Temperatures: Multidecadal Trends and Reliability of Global Reanalyses. *Journal of Climate*, 27(21):8070–8093.

Nief, G. and Botter, R. (1958). Analyse de composés hydrogénés simples au spectromètre de masse. *Advances in Mass Spectrometry, Pergamon Press, London*, page 515.

North Greenland Ice Core Project members (2004). High-resolution record of Northern Hemisphere climate extending into the last interglacial period. *Nature*, 431(7005):147–151.

Nyquist, H. (1924). Certain Factors Affecting Telegraph Speed1. *Bell System technical journal*, 3(2):324–346.

Oerter, H., Wilhelms, F., Jung-Rothenhäusler, F., Göktas, F., Miller, H., Graf, W., and Sommer, S. (2000). Accumulation rates in Dronning Maud Land, Antarctica, as revealed by dielectric-profiling measurements of shallow firn cores. *Annals of Glaciology*, 30(1):27–34.

Orsi, A. J., Cornuelle, B. D., and Severinghaus, J. P. (2014). Magnitude and temporal evolution of Dansgaard–Oeschger event 8 abrupt temperature change inferred from nitrogen and argon isotopes in GISP2 ice using a new least-squares inversion. *Earth and Planetary Science Letters*, 395:81–90.

Paillard, D. (1998). The timing of Pleistocene glaciations from a simple multiple-state climate model. *Nature*, 391(6665):378–381.

Paldus, B. A. and Zare, R. N. (1999). Absorption Spectroscopies: From Early Beginnings to Cavity-Ringdown Spectroscopy. In *Cavity-Ringdown Spectroscopy*, volume 720 of *ACS Symposium Series*, pages 5–49. American Chemical Society.

Petit, J. R., Jouzel, J., Pourchet, M., and Merlivat, L. (1982). A detailed study of snow accumulation and stable isotope content in Dome C (Antarctica). *Journal of Geophysical Research: Oceans*, 87(C6):4301–4308.

Petit, R. J., Raynaud, D., Basile, I., Chappellaz, J., Ritz, C., Delmotte, M., Legrand, M., Lorius, C., and Pe, L. (1999a). Climate and atmospheric history of the past 420,000 years from the Vostok ice core, Antarctica. *Nature*, 399:429–413.

Petit, R. J., Raynaud, D., Basile, I., Chappellaz, J., Ritz, C., Delmotte, M., Legrand, M., Lorius, C., Pe, L., Petit, J. R., Jouzel, J., Raynaud, D., Barkov, N. I., Barnola, J. M., Basile, I., Bender, M., Chappellaz, J., Davis, M., Delaygue, G., Delmotte, M., Kotlyakov, V. M., Legrand, M., Lipenkov, V. Y., Lorius, C., Pepin, L., Ritz, C., Saltzman, E., and Stievenard, M. (1999b). Climate and atmospheric history of the past 420,000 years from the Vostok ice core, Antarctica. *Nature*, 399(6735):429–436.

Picard, G., Arnaud, L., Panel, J.-M., and Morin, S. (2016a). Design of a scanning laser meter for monitoring the spatio-temporal evolution of snow depth and its application in the Alps and in Antarctica. *The Cryosphere*, 10(4):1495–1511.

Picard, G., Domine, F., Krinner, G., Arnaud, L., and Lefebvre, E. (2012). Inhibition of the positive snow-albedo feedback by precipitation in interior Antarctica. *Nature Climate Change*, 2(11):795–798.

Picard, G., Libois, Q., Arnaud, L., Verin, G., and Dumont, M. (2016b). Development and calibration of an automatic spectral albedometer to estimate near-surface snow SSA time series. *The Cryosphere*, 10(3):1297–1316.

Pinilla, C., Blanchard, M., Balan, E., Ferlat, G., Vuilleumier, R., and Mauri, F. (2014). Equilibrium fractionation of H and O isotopes in water from path integral molecular dynamics. *Geochimica et Cosmochimica Acta*, 135:203–216.

Pol, K., Masson-Delmotte, V., Cattani, O., Debret, M., Falourd, S., Jouzel, J., Landais, A., Minster, B., Mudelsee, M., Schulz, M., and Stenni, B. (2014). Climate variability features of the last interglacial in the East Antarctic EPICA Dome C ice core. *Geophysical Research Letters*, 41(11):4004–4012.

Rayleigh, L. (1902). LIX. On the distillation of binary mixtures. *Philosophical Magazine Series 6*, 4(23):521–537.

Raynaud, D., Jouzel, J., Barnola, J. M., Chappellaz, J., Delmas, R. J., and Lorius, C. (1993). The Ice Record of Greenhouse Gases. *Science*, 259(5097):926–934.

Ricaud, P., Carminati, F., Courcoux, Y., Pellegrini, A., Attié, J.-L., El Amraoui, L., Abida, R., Genthon, C., August, T., and Warner, J. (2014). Statistical analyses and correlation between tropospheric temperature and humidity at Dome C, Antarctica. *Antarctic Science*, 26(03):290–308.

Ricaud, P., Genthon, C., Durand, P., Attié, J. L., Carminati, F., Canut, G., Vanacker, J. F., Moggio, L., Courcoux, Y., Pellegrini, A., and Rose, T. (2012). Summer to Winter Diurnal Variabilities of Temperature and Water Vapour in the Lowermost Troposphere as Observed by HAMSTRAD over Dome C, Antarctica. *Boundary-Layer Meteorology*, 143(1):227–259.

Rieker, G. B., Giorgetta, F. R., Swann, W. C., Kofler, J., Zolot, A. M., Sinclair, L. C., Baumann, E., Cromer, C., Petron, G., and Sweeney, C. (2014). Frequency-comb-based remote sensing of greenhouse gases over kilometer air paths. *Optica*, 1(5):290–298.

Risi, C., Bony, S., and Vimeux, F. (2008). Influence of convective processes on the isotopic composition (δ18O and δD) of precipitation and water vapor in the tropics: 2. Physical interpretation of the amount effect. *Journal of Geophysical Research: Atmospheres*, 113(D19):D19306.

Risi, C., Bony, S., Vimeux, F., and Jouzel, J. (2010). Water-stable isotopes in the LMDZ4 general circulation model: Model evaluation for present-day and past climates and applications to climatic interpretations of tropical isotopic records. *Journal of Geophysical Research: Atmospheres*, 115(D12):D12118.

Ritter, F., Steen-Larsen, H. C., Werner, M., Masson-Delmotte, V., Orsi, A., Behrens, M., Birnbaum, G., Freitag, J., Risi, C., and Kipfstuhl, S. (2016). Isotopic exchange on the diurnal scale between near-surface snow and lower atmospheric water vapor at Kohnen station, East Antarctica. *The Cryosphere Discuss.*, 2016:1–35.

Romanini, D., Kachanov, A. A., Sadeghi, N., and Stoeckel, F. (1997). CW cavity ring down spectroscopy. *Chemical Physics Letters*, 264(3-4):316–322.

Romanini, D., Ventrillard, I., Méjean, G., Morville, J., and Kerstel, E. (2014). Introduction to Cavity Enhanced Absorption Spectroscopy. In Gagliardi, G. and Loock, H.-P., editors, *Cavity-Enhanced Spectroscopy and Sensing*, volume 179, chapter 1, pages 1–60. Springer Berlin Heidelberg.

Rosenboum, E. J. (1941). The Mathematical Theory of Non-Uniform Gases (Chapman, S.; Cowling, T. G.). *Journal of Chemical Education*, 18(1):48.

Röthlisberger, R., Hutterli, M. A., Sommer, S., Wolff, E. W., and Mulvaney, R. (2000). Factors controlling nitrate in ice cores: Evidence from the Dome C deep ice core. *Journal of Geophysical Research: Atmospheres*, 105(D16):20565–20572.

Rothman, L. S., Gordon, I. E., Babikov, Y., Barbe, A., Benner, D. C., Bernath, P. F., Birk, M., Bizzocchi, L., Boudon, V., and Brown, L. R. (2013). The HITRAN2012 molecular

spectroscopic database. *Journal of Quantitative Spectroscopy and Radiative Transfer*, 130:4–50.

Schlosser, E., Reijmer, C., Oerter, H., and Graf, W. (2004). The influence of precipitation origin on the d18O-T relationship at Neumayer station, Ekströmisen, Antarctica. *Annals of Glaciology*, 39(1):41–48.

Schmidt, G. A., Hoffmann, G., Shindell, D. T., and Hu, Y. (2005). Modeling atmospheric stable water isotopes and the potential for constraining cloud processes and stratosphere-troposphere water exchange. *Journal of Geophysical Research: Atmospheres*, 110(D21):D21314.

Schmidt, G. A., LeGrande, A. N., and Hoffmann, G. (2007). Water isotope expressions of intrinsic and forced variability in a coupled ocean/atmosphere model. *Journal of Geophysical Research: Atmospheres*, 112(D10).

Schneebeli, M. and Sokratov, S. A. (2004). Tomography of temperature gradient metamorphism of snow and associated changes in heat conductivity. *Hydrological Processes*, 18(18):3655–3665.

Schoenemann, S. W., Schauer, A. J., and Steig, E. J. (2013). Measurement of SLAP2 and GISP δ17O and proposed VSMOW-SLAP normalization for δ17O and 17Oexcess. *Rapid Communications in Mass Spectrometry*, 27(5):582–590.

Schoenemann, S. W., Steig, E. J., Ding, Q., Markle, B. R., and Schauer, A. J. (2014). Triple water-isotopologue record from WAIS Divide, Antarctica: Controls on glacial-interglacial changes in 17Oexcess of precipitation. *Journal of Geophysical Research: Atmospheres*, 119(14):8741–8763.

Schotterer, U., Oldfield, F., and Fröhlich, K. (1996). GNIP. Global Network for Isotopes in Precipitation. *INIS*, 30(12).

Severinghaus, J. P., Sowers, T., Brook, E. J., Alley, R. B., and Bender, M. L. (1998). Timing of abrupt climate change at the end of the Younger Dryas interval from thermally fractionated gases in polar ice. *Nature*, 391(6663):141–146.

Shannon, C. E. (1949). Communication in the presence of noise. *Proceedings of the IRE*, 37(1):10–21.

Sime, L. C., Risi, C., Tindall, J. C., Sjolte, J., Wolff, E. W., Masson-Delmotte, V., and Capron, E. (2013). Warm climate isotopic simulations: what do we learn about interglacial signals in Greenland ice cores? *Quaternary Science Reviews*, 67:59–80.

Sime, L. C., Wolff, E. W., Oliver, K. I. C., and Tindall, J. C. (2009). Evidence for warmer interglacials in East Antarctic ice cores. *Nature*, 462(7271):342–345.

Sodemann, H. and Stohl, A. (2009). Asymmetries in the moisture origin of Antarctic precipitation. *Geophysical research letters*, 36(22).

Sokratov, S. A. and Golubev, V. N. (2009). Snow isotopic content change by sublimation. *Journal of Glaciology*, 55(193):823–828.

Steen-Larsen, H. C., Johnsen, S. J., Masson-Delmotte, V., Stenni, B., Risi, C., Sodemann, H., Balslev-Clausen, D., Blunier, T., Dahl-Jensen, D., Ellehøj, M. D., Falourd, S., Grindsted, A., Gkinis, V., Jouzel, J., Popp, T., Sheldon, S., Simonsen, S. B., Sjolte, J., Steffensen, J. P., Sperlich, P., Sveinbjörnsdóttir, A. E., Vinther, B. M., and White, J. W. C. (2013). Continuous monitoring of summer surface water vapor isotopic composition above the Greenland Ice Sheet. *Atmos. Chem. Phys.*, 13(9):4815–4828.

Steen-Larsen, H. C., Masson-Delmotte, V., Hirabayashi, M., Winkler, R., Satow, K., Prié, F., Bayou, N., Brun, E., Cuffey, K. M., and Dahl-Jensen, D. (2014a). What controls the isotopic composition of Greenland surface snow? *Climate of the Past*, 10(1):377–392.

Steen-Larsen, H. C., Sveinbjörnsdottir, A. E., Peters, A. J., Masson-Delmotte, V., Guishard, M. P., Hsiao, G., Jouzel, J., Noone, D., Warren, J. K., and White, J. W. C. (2014b). Climatic controls on water vapor deuterium excess in the marine boundary layer of the North Atlantic based on 500 days of in situ, continuous measurements. *Atmos. Chem. Phys.*, 14(15):7741–7756.

Steig, E. J., Gkinis, V., Schauer, A. J., Schoenemann, S. W., Samek, K., Hoffnagle, J., Dennis, K. J., and Tan, S. M. (2014). Calibrated high-precision 17O-excess measurements using cavity ring-down spectroscopy with laser-current-tuned cavity resonance. *Atmos. Meas. Tech.*, 7(8):2421–2435.

Stenni, B., Scarchilli, C., Masson-Delmotte, V., Schlosser, E., Ciardini, V., Dreossi, G., Grigioni, P., Bonazza, M., Cagnati, A., Frosini, D., Karlicek, D., Risi, C., Udisti, R., and Valt, M. (2016). Three-year monitoring of stable isotopes of precipitation at Concordia Station, East Antarctica. *The Cryosphere*, 2016(special issue IPICS 2016):1–30.

Tennyson, J., Bernath, P. F., Campargue, A., Császár, A. G., Daumont, L., Gamache, R. R., Hodges, J. T., Lisak, D., Naumenko, O. V., Rothman, L. S., Tran, H., Zobov, N. F., Buldyreva, J., Boone, C. D., De Vizia, M. D., Gianfrani, L., Hartmann, J.-M., McPheat, R., Weidmann, D., Murray, J., Ngo, N. H., and Polyansky, O. L. (2014). Recommended isolated-line profile for representing high-resolution spectroscopic transitions (IUPAC Technical Report). *Pure and Applied Chemistry*, 86(12):1931–1943.

Touzeau, A., Landais, A., Stenni, B., Uemura, R., Fukui, K., Fujita, S., Guilbaud, S., Ekaykin, A., Casado, M., Barkan, E., Luz, B., Magand, O., Teste, G., Le Meur, E., Baroni, M., Savarino, J., Bourgeois, I., and Risi, C. (2016). Acquisition of isotopic composition for surface snow in East Antarctica and the links to climatic parameters. *The Cryosphere*, 10(2):837–852.

Town, M. S., Warren, S. G., Walden, V. P., and Waddington, E. D. (2008). Effect of atmospheric water vapor on modification of stable isotopes in near-surface snow on ice sheets. *Journal of Geophysical Research: Atmospheres*, 113(D24).

Tran, H., Ngo, N. H., and Hartmann, J.-M. (2013). Efficient computation of some speed-dependent isolated line profiles. *Journal of Quantitative Spectroscopy and Radiative Transfer*, 129:199–203.

Tremoy, G., Vimeux, F., Cattani, O., Mayaki, S., Souley, I., and Favreau, G. (2011). Measurements of water vapor isotope ratios with wavelength-scanned cavity ring-down spectroscopy technology: new insights and important caveats for deuterium excess measurements in tropical areas in comparison with isotope-ratio mass spectrometry. *Rapid Communications in Mass Spectrometry*, 25(23):3469–3480.

Tulegenov, A. S., Wheatley, R. J., Hodges, M. P., and Harvey, A. H. (2007). Intermolecular potential and second virial coefficient of the water-nitrogen complex. *The Journal of Chemical Physics*, 126(9).

Udem, T., Holzwarth, R., and Hansch, T. W. (2002). Optical frequency metrology. *Nature*, 416(6877):233–237.

Uemura, R., Abe, O., and Motoyama, H. (2010a). Determining the 17 O/16 O ratio of water using a water–CO 2 equilibration method: Application to glacial–interglacial changes in 17 O-excess from the Dome Fuji ice core, Antarctica. *Geochimica et Cosmochimica Acta*, 74(17):4919–4936.

Uemura, R., Barkan, E., Abe, O., and Luz, B. (2010b). Triple isotope composition of oxygen in atmospheric water vapor. *Geophysical Research Letters*, 37(4):L04402.

Uemura, R., Matsui, Y., Yoshimura, K., Motoyama, H., and Yoshida, N. (2008). Evidence of deuterium excess in water vapor as an indicator of ocean surface conditions. *Journal of Geophysical Research: Atmospheres*, 113(D19).

Urey, H. C. (1947). The thermodynamic properties of isotopic substances. *Journal of the Chemical Society (Resumed)*, 0(0):562–581.

van As, D., van den Broeke, M. R., and Helsen, M. M. (2007). Strong-wind events and their impact on the near-surface climate at Kohnen Station on the Antarctic Plateau. *Antarctic Science*, 19(4):507–519.

Van Den Broeke, M. R. (1998). The semi-annual oscillation and Antarctic climate. Part 1: Influence on near surface temperatures (1957–79). *Antarctic Science*, 10(02):175–183.

Van Hook, W. A. (1968). Vapor pressures of the isotopic waters and ices. *The Journal of Physical Chemistry*, 72(4):1234–1244.

Vimeux, F., Masson, V., Jouzel, J., Stievenard, M., and Petit, J. R. (1999). Glacial-interglacial changes in ocean surface conditions in the Southern Hemisphere. *Nature*, 398(6726):410–413.

Vinther, B. M., Jones, P. D., Briffa, K. R., Clausen, H. B., Andersen, K. K., Dahl-Jensen, D., and Johnsen, S. J. (2010). Climatic signals in multiple highly resolved stable isotope records from Greenland. *Quaternary Science Reviews*, 29(3–4):522–538.

Voigt, W. (1912). *Das Gesetz der Intensitätsverteilung innerhalb der Linien eines Gasspektrums*. Verlagd. KB Akad. d. Wiss.

Waddington, E. D., Steig, E. J., and Neumann, T. A. (2002). Using characteristic times to assess whether stable isotopes in polar snow can be reversibly deposited. *Annals of Glaciology*, 35(1):118–124.

WAIS Divide Project members, W. (2013). Onset of deglacial warming in West Antarctica driven by local orbital forcing. *Nature*, 500(7463):440–444.

Weissbluth, M. (2012). *Atoms and molecules*. Elsevier.

Wendler, G. and Kodama, Y. (1984). On the climate of Dome C, Antarctica, in relation to its geographical setting. *J. Climatol*, 4:495–508.

Werner, M., Langebroek, P. M., Carlsen, T., Herold, M., and Lohmann, G. (2011). Stable water isotopes in the ECHAM5 general circulation model: Toward high-resolution isotope modeling on a global scale. *Journal of Geophysical Research: Atmospheres*, 116(D15):D15109.

Whillans, I. M. and Grootes, P. M. (1985). Isotopic diffusion in cold snow and firn. *Journal of Geophysical Research: Atmospheres*, 90(D2):3910–3918.

Whitlow, S., Mayewski, P. A., and Dibb, J. E. (1992). A comparison of major chemical species seasonal concentration and accumulation at the South Pole and Summit, Greenland. *Atmospheric Environment. Part A. General Topics*, 26(11):2045–2054.

Winkler, R. (2012). Triple-oxygen isotopic composition of meteoric waters: 17 O-excess a new tracer of the hydrological cycle.

Winkler, R., Landais, A., Sodemann, H., Dümbgen, L., Prié, F., Masson-Delmotte, V., Stenni, B., and Jouzel, J. (2012). Deglaciation records of 17O-excess in East Antarctica: reliable reconstruction of oceanic normalized relative humidity from coastal sites. *Clim. Past*, 8(1):1–16.

Wong, W. W. and Klein, P. D. (1986). A review of techniques for the preparation of biological samples for mass-spectrometric measurements of hydrogen-2/hydrogen-1 and oxygen-18/oxygen-16 isotope ratios. *Mass Spectrometry Reviews*, 5(3):313–342.

Zilitinkevich, S. S., Elperin, T., Kleeorin, N., Rogachevskii, I., Esau, I., Mauritsen, T., and Miles, M. W. (2008). Turbulence energetics in stably stratified geophysical flows: Strong and weak mixing regimes. *Quarterly Journal of the Royal Meteorological Society*, 134(633):793–799.